

Endwall Profiling for the Reduction of Secondary Flow in Turbines

Grant Laidlaw Ingram

A Thesis presented for the degree of
Doctor of Philosophy



School of Engineering
University of Durham
England
July 2003

Dedicated to
Claire Bloom

Endwall Profiling for the Reduction of Secondary Flow in Turbines

Grant Laidlaw Ingram

Submitted for the degree of Doctor of Philosophy
July 2003

Abstract

This thesis describes investigations into the use of a technique for improving the efficiency of axial flow turbines. The flow in the turbine component of axial flow machines is complex, with a number of three-dimensional features. In order to extract power from a stream of high pressure and high temperature flow this flow must be turned through a large angle, this high turning introduces a phenomenon known as "secondary flow". This secondary flow introduces additional loss, unsteadiness and regions of high heat transfer into the machine - all of which are undesirable features.

Endwall profiling aims to reduce these undesirable features by shaping the endwall between the turbine blades. The shaping either accelerates the flow which reduces the local static pressure or retards the flow which increases the static pressure. These effects are confined to a region near the endwall so the overall performance of the blade row is not affected. However due to the complexity of the flow it is easy to make things worse rather than better! - careful design is needed. This thesis aims to understand how and why the reductions may be achieved so that they can be better exploited as well as providing information of the performance of a major engine manufacturers design system.

The thesis describes pressure probe measurements inside and outside of the blade passage of a low speed linear cascade with a number of profiled endwall geometries. The aerofoils used in the cascade are already relatively efficient and the overall loss changes are small, accurate measurement is therefore very difficult. The current best profiled endwall reduces secondary loss by $30\% \pm 5\%$ compared to the planar case.

Hot film measurements have been conducted on the endwalls and suction surface of the blade to determine if these benefits are substantially due to changing the boundary layer state. The results from this thesis indicate that this is not the case.

This thesis describes measurements on three generations of profiled endwalls, two of which successfully reduce loss, one does not. The success of the first two endwalls indicates the power of current CFD based design practices, the failure of the third design to reduce loss illustrates some of the shortcomings of current CFD based design practices.

The information from this thesis is being used in the design of the next generation of aircraft engines to which non-axisymmetric profiled endwalls are being fitted.

Declaration

The work in this thesis is based on research carried out in the School of Engineering at the University of Durham. No part of this thesis has been submitted elsewhere for any other degree or qualification and it is all my own work unless referenced to the contrary in the text.

Copyright © 2003 by Grant Ingram.

“The copyright of this thesis rests with the author. No quotations from it should be published without the author’s prior written consent and information derived from it should be acknowledged”.

Acknowledgements

No project is carried out in isolation and this section allows the author to say thank you to the many people that have helped him in the production of this thesis.

Many thanks are due to David Gregory-Smith for his enthusiasm throughout the entire project and for finding the money to do the project in the first place! David Sims-Williams has always been unfailing cheerful and keen to discuss any fluid dynamics problem, I am particularly grateful for his help in calculating tool offsets. Rob Dominy was also extremely helpful especially in setting up and running the hot film experiments as well as loaning us some valuable equipment.

Thanks are also due to Ray Mand and Gary Parker from the thermo lab for their technical support in the lab and lots of useful practical advice. I am grateful to Alan Swan for his excellent work in conducting the CNC machining. Stuart Watson did a fine job of manufacturing the pressure probes. The Electrical and Electronic workshop were also of great help Ian Hutchinson, Colin Wintrip and Ian Garret deserve special mention.

Duncan Simpson was not only great fun to share an office with but worked with an enterprising spirit that is far from common. I'd also like to thank Paul Gordon for his many helpful discussions. I'm very grateful to Sue Crossland for her help in producing the photographs of the probes found in the Appendix.

This project has been a collaboration with Rolls-Royce and I'd like to thank Neil Harvey, Martin Rose, Graham Brennan and Mark Taylor for their interest and help throughout the project and for their input during our progress meetings.

Very few acknowledgement sections mention the essential contribution made by the Engineering coffee bar to the production of world class research work, the author would like to redress this by saying thank to Andrea and Margaret for making over a thousand cups of tea for the author over the three and a half years of research without which I'm sure this thesis would be much the poorer.

Finally I'd like to thank the Durham University KDS Club, they didn't do a thing to help but the practice was fun.

Contents

Abstract	iii
Declaration	iv
Acknowledgements	v
Nomenclature	xxiii
1 Introduction	1
2 Literature Review	4
2.1 Axial Turbines and the Benefits of Improved Efficiency.	4
2.2 Gas Turbines.	5
2.3 Cascade Secondary Flow.	6
2.3.1 Classical Secondary Flow Theory	8
2.3.2 The Passage Vortex	10
2.3.3 The Horseshoe Vortex	10
2.3.4 The Corner Vortex	11
2.3.5 Secondary Flow Models.	11
2.3.6 Boundary Layers.	13
2.3.7 Blade Exit	14
2.4 Real Turbine Flow Fields.	14
2.5 Loss Production	16
2.5.1 Definitions of Loss.	16
2.5.2 Loss Production and Secondary Flow	18
2.6 Methods of Loss Reduction.	20
2.7 Previous Research in the Durham Facility.	23
2.8 3D Endwall Profiling.	25
2.9 Overview	27
3 Experimental Technique	29
3.1 The Durham Cascade	29
3.1.1 Profiled End Walls	31
3.2 Flow Visualisation Technique	32
3.2.1 Smoke Visualisation.	32
3.2.2 Oil/Dye Visualisations.	32
3.2.3 Experimental Method.	33

3.3	Pressure Probe Measurements	34
3.3.1	Probe Calibration	36
3.3.2	Cascade Traverses	38
3.3.3	Measurement Grids.	41
3.4	Data Processing	41
3.4.1	Recovery of Flow Variables.	42
3.4.2	Corrections.	43
3.4.3	Derived Quantities.	45
3.4.4	Pitch Averaging.	47
3.5	Area Averaging.	50
3.5.1	Mixed out loss.	50
3.5.2	Contour and Vector Plots.	53
3.6	Validation	53
3.6.1	Pre and Post Reading System Tests.	53
3.6.2	Software Validation.	54
3.6.3	Hardware Improvements.	54
3.7	Overview	55
4	Flow Visualisation Results	56
4.1	Description	57
4.1.1	Endwall Flows	58
4.1.2	Blade Surface Flows	60
4.1.3	Perspective Views	60
4.2	Overview	61
4.3	Flow Visualisation Photographs	61
5	Pressure Probe Results	76
5.1	Validation	77
5.2	Inlet Boundary Layer	78
5.3	Slot 1 (-9% C_{ax})	79
5.3.1	Five Hole Readings at Slot 1 (-9% C_{ax})	79
5.3.2	Three Hole Readings at Slot 1 (-9% C_{ax})	80
5.4	Slot 2 (6% C_{ax})	81
5.4.1	Five Hole Readings at Slot 2 (6% C_{ax})	81
5.4.2	Three Hole Readings at Slot 2 (6% C_{ax})	82
5.5	Slot 3 (22% C_{ax})	83
5.6	Slot 4 (38% C_{ax})	83
5.7	Slot 5 (55% C_{ax})	84
5.8	Slot 6 (71% C_{ax})	85
5.9	Slot 8 (97% C_{ax})	85
5.10	Slot 10 (128% C_{ax})	86
5.10.1	Five Hole Probe Results for Slot 10 (128% C_{ax})	87
5.10.2	Three Hole Probe Results for Slot 10 (128% C_{ax})	89
5.11	Axial Variation of Area Averaged Values	89
5.11.1	Repeatability: Five Hole Probe Results	91
5.11.2	Repeatability: Three Hole Probe Results	92
5.11.3	Synthesised Data Set.	93

5.11.4	Mixed Out Loss	94
5.12	Vortex Core Movement	95
5.13	Overview	96
5.14	Figures for Pressure Probe Results	97
6	Hot Film Readings	136
6.1	Hot Film Measurement System	136
6.2	Hot Film Results	140
6.2.1	Suction Surface Measurements	141
6.2.2	Endwall Measurements	142
6.2.3	Repeatability and Angle Variation	144
6.3	Overview	144
6.4	Figures for Hot Film Results	145
7	Comparison with CFD Data	165
7.1	Methodology	165
7.2	Solution Details	166
7.3	Comparison at Different Axial Locations	167
7.3.1	Slot 1 (-9% C_{ax})	167
7.3.2	Slot 2 (6% C_{ax})	168
7.3.3	Slot 3 (22% C_{ax})	168
7.3.4	Slot 4 (38% C_{ax})	169
7.3.5	Slot 5 (55% C_{ax})	170
7.3.6	Slot 6 (71% C_{ax})	170
7.3.7	Slot 8 (97% C_{ax})	171
7.3.8	Slot 10 (128% C_{ax})	171
7.4	Comparison of Pitch and Area Averaged Quantities at Slot 10	172
7.5	Three Dimensional CFD Visualisation	175
7.6	Overview	177
7.7	Computational Fluid Dynamics Results	178
8	Third Generation Endwall	209
8.1	Pressure Probe Measurement	209
8.1.1	Validation	210
8.1.2	Slot 6 (71% C_{ax})	211
8.1.3	Slot 8 (97% C_{ax})	212
8.1.4	Five Hole Probe Readings at Slot 10 (128% C_{ax})	213
8.1.5	Three Hole Probe Readings at Slot 4 (38% C_{ax})	213
8.1.6	Three Hole Probe Readings at Slot 10 (128% C_{ax})	214
8.1.7	Pitch Averaged Results	214
8.1.8	Area Averaged Results	217
8.2	Flow Visualisation Results	219
8.3	Measurement Overview	220
8.4	Comparison with CFD Results	220
8.4.1	CFD results for Slot 6 (71% C_{ax})	221
8.4.2	CFD for Slot 8 (97% C_{ax})	221
8.4.3	CFD at Slot 10 (128% C_{ax})	222

8.4.4	Pitch Average CFD Results	222
8.4.5	Area Averaged Results	225
8.4.6	Comparison of the Two Planar CFD Solutions	225
8.5	Computation Fluid Dynamics for P3 Overview	227
8.6	P3 Overview	227
8.7	Third Generation Endwall Graphs.	228
9	Overall Discussion	259
9.1	Publication of Experimental Technique	259
9.2	Flow Visualisation	260
9.3	Transitional Flow in the Durham Cascade	260
9.4	Comparison with previous work in the Durham Cascade	261
9.5	Pitch Averaged Yaw Angle Calculation	262
9.6	Absolute Yaw Angle Measurement.	263
9.7	Experimental Loss Evaluation	264
9.8	Classical Secondary Flow Theory	265
9.9	CFD predictions of endwall profiling	266
9.10	Third generation endwall	266
9.11	C_{ske} as a design parameter	267
9.12	Application to Real Machines	268
9.13	Key Results	268
9.14	Secondary flows and endwall profiling	269
10	Conclusions and Recommendations	273
10.1	Conclusions	273
10.2	Recommendations	274
	Appendix	284
A	Profiled Endwall Geometries	284
B	Cascade Coordinates	288
C	Supplemental Information on Experiment Labels and Technique	290
C.1	Labels for Pressure Probe Traverses	290
C.2	Labels for Hot Film Readings	291
C.3	Different ways of calculating Table 7.1	291
C.4	Pressure Probe Data Processing Programs	292
C.5	Repeatability Results	292
D	Estimating the effects of Profiled Endwalls on Stage Efficiency	295
E	Photographs of Pressure Probes.	297

List of Figures

2.1	Operation of the Gas Turbine	5
2.2	Relationship between Linear Cascades and Real Machines	6
2.3	Simple Definition of Secondary Flow	7
2.4	Vorticity Vector at Inlet and Exit of a Cascade	9
2.5	Formation of the Passage Vortex	10
2.6	Model of Secondary Flow from Sieverding and Bosche (1983)	12
2.7	h-s diagram.	17
2.8	Schematic of <i>Russian Kink</i>	22
2.9	Streamline Curvature:- basic idea.	26
3.1	The Durham Cascade	31
3.2	Profiled and Planar Endwall Fitting	32
3.3	Schematic of Measuring System	35
3.4	Operation of Multi-tube probe.	35
3.5	Five Hole Probe	37
3.6	Cranked Three Hole Probe	37
3.7	Example of a Contoured Measurement Grid	42
3.8	Sample Three Hole Probe Calibration Map	43
3.9	Five Hole Probe Calibration Map (Probe 5HA)	44
3.10	C_{total} Map for Probe 5HA	44
3.11	Magnitude of Midspan Loss Coefficient Adjustment	45
3.12	Definition of Secondary Flow Vectors.	46
3.13	Calculation of Δr for Pitch Averaging.	48
3.14	Control Volume for the Mixed Out Loss Calculation	51
4.1	Gravity Force Direction.	57
4.2	Annotated View of P0.	62
4.3	Annotated View of P1.	63
4.4	Annotated View of P2.	64
4.5	Flow Visualisation P0 Inlet View.	65
4.6	Flow Visualisation P1 Inlet View.	65
4.7	Flow Visualisation P2 Inlet View.	65
4.8	Flow Visualisation P0 Blade Row View.	66
4.9	Flow Visualisation P1 Blade Row View.	66
4.10	Flow Visualisation P2 Blade Row View.	66
4.11	Flow Visualisation P0 Exit View.	67
4.12	Flow Visualisation P1 Exit View.	67
4.13	Flow Visualisation P2 Exit View.	67

4.14 Suction Surface P0	68
4.15 Suction Surface P1	68
4.16 Suction Surface P2	68
4.17 Pressure Surface P0	69
4.18 Pressure Surface P1	69
4.19 Pressure Surface P2	69
4.20 Leading Edge P0.	70
4.21 Leading Edge P1.	70
4.22 Leading Edge P2.	70
4.23 Blade and Endwall Showing Suction Surface P0.	71
4.24 Blade and Endwall Showing Suction Surface P1.	71
4.25 Blade and Endwall Showing Suction Surface P2.	71
4.26 Blade and Endwall Showing Pressure Surface P0.	72
4.27 Blade and Endwall Showing Pressure Surface P1.	72
4.28 Blade and Endwall Showing Pressure Surface P2.	72
4.29 Blade and Endwall Showing Leading Edge P0.	73
4.30 Blade and Endwall Showing Leading Edge P1.	73
4.31 Blade and Endwall Showing Leading Edge P2	73
4.32 P1 Stagnant Region - Fan Running	74
4.33 Suction Surface Flow Features.	75
5.1 Data Processing Chain for Repeated Data	87
5.2 Nomenclature for Vortex Labels	89
5.3 Five Hole Probe Measurement Locations.	98
5.4 Three Hole Probe Measurement Locations.	98
5.5 Typical pre readings C_{P0} Error - five hole.	98
5.6 Typical pre readings Yaw Error - five hole.	98
5.7 Typical pre readings Pitch Error - five hole.	99
5.8 Typical post readings C_{P0} Error - five hole.	99
5.9 Typical post readings Yaw Error - five hole.	99
5.10 Typical post readings Pitch Error - five hole.	99
5.11 Typical C_{P0} Error - three hole probe.	100
5.12 Typical Yaw Error - three hole probe.	100
5.13 Inlet Boundary Layer: Raw Data	100
5.14 Inlet Boundary Layer: Final Profile	100
5.15 Slot 1 P0 Loss	101
5.16 Slot 1 P1 Loss	101
5.17 Slot 1 P2 Loss	101
5.18 Slot 1 Pitch Averaged Loss	101
5.19 Slot 1 P0 Secondary Vectors	102
5.20 Slot 1 P1 Secondary Vectors	102
5.21 Slot 1 P2 Secondary Vectors	102
5.22 Slot 1 Pitch Averaged Yaw Angle	102
5.23 Close Wall Loss at Slot 1 P0	103
5.24 Close Wall Loss at Slot 1 P1	103
5.25 Close Wall Loss at Slot 1 P2	103
5.26 3H and 5H Pitch Averaged Loss at Slot 1	103

5.27 Secondary Vectors at Slot 1 P0	104
5.28 Secondary Vectors at Slot 1 P1	104
5.29 Secondary Vectors at Slot 1 P2	104
5.30 3H and 5H Pitch Averaged Yaw Angle at Slot 1	104
5.31 Slot 2 P0 Loss	105
5.32 Slot 2 P1 Loss	105
5.33 Slot 2 P2 Loss	105
5.34 Slot 2 Pitch Averaged Loss	105
5.35 Slot 2 P0 Secondary Vectors	106
5.36 Slot 2 P1 Secondary Vectors	106
5.37 Slot 2 P2 Secondary Vectors	106
5.38 Slot 2 Pitch Averaged Yaw Angle	106
5.39 Close Wall Loss at Slot 2 P0	107
5.40 Close Wall Loss at Slot 2 P1	107
5.41 Close Wall Loss at Slot 2 P2	107
5.42 3H and 5H Pitch Averaged Loss at Slot 2	107
5.43 Secondary Vectors at Slot 2 P0	108
5.44 Secondary Vectors at Slot 2 P1	108
5.45 Secondary Vectors at Slot 2 P2	108
5.46 3H and 5H Pitch Averaged Yaw Angle at Slot 2	108
5.47 Slot 3 P0 Loss	109
5.48 Slot 3 P1 Loss	109
5.49 Slot 3 P2 Loss	109
5.50 Slot 3 Pitch Averaged Loss	109
5.51 Slot 3 P0 Secondary Vectors	110
5.52 Slot 3 P1 Secondary Vectors	110
5.53 Slot 3 P2 Secondary Vectors	110
5.54 Slot 3 Pitch Averaged Yaw Angle	110
5.55 Slot 4 P0 Loss	111
5.56 Slot 4 P1 Loss	111
5.57 Slot 4 P2 Loss	111
5.58 Slot 4 Pitch Averaged Loss	111
5.59 Slot 4 P0 Secondary Vectors	112
5.60 Slot 4 P1 Secondary Vectors	112
5.61 Slot 4 P2 Secondary Vectors	112
5.62 Slot 4 Pitch Averaged Yaw Angle	112
5.63 Slot 5 P0 Loss	113
5.64 Slot 5 P1 Loss	113
5.65 Slot 5 P2 Loss	113
5.66 Slot 5 Pitch Averaged Loss	113
5.67 Slot 5 P0 Secondary Vectors	114
5.68 Slot 5 P1 Secondary Vectors	114
5.69 Slot 5 P2 Secondary Vectors	114
5.70 Slot 5 Pitch Averaged Yaw Angle	114
5.71 Slot 6 P0 Loss	115
5.72 Slot 6 P1 Loss	115

5.73 Slot 6 P2 Loss	115
5.74 Slot 6 Pitch Averaged Loss	115
5.75 Slot 6 P0 Secondary Vectors	116
5.76 Slot 6 P1 Secondary Vectors	116
5.77 Slot 6 P2 Secondary Vectors	116
5.78 Slot 6 Pitch Averaged Yaw Angle	116
5.79 Slot 6 P0 C_{ske}	117
5.80 Slot 6 P1 C_{ske}	117
5.81 Slot 6 P2 C_{ske}	117
5.82 Slot 6 Pitch Averaged C_{ske}	117
5.83 Slot 6 P0 Streamwise Vorticity Coefficient	118
5.84 Slot 6 P1 Streamwise Vorticity Coefficient	118
5.85 Slot 6 P2 Streamwise Vorticity Coefficient	118
5.86 Slot 6 Pitch Averaged Vorticity	118
5.87 Slot 8 P0 Loss	119
5.88 Slot 8 P1 Loss	119
5.89 Slot 8 P2 Loss	119
5.90 Slot 8 Pitch Averaged Loss	119
5.91 Slot 8 P0 Secondary Vectors	120
5.92 Slot 8 P1 Secondary Vectors	120
5.93 Slot 8 P2 Secondary Vectors	120
5.94 Slot 8 Pitch Averaged Yaw Angle	120
5.95 Slot 8 P0 C_{ske}	121
5.96 Slot 8 P1 C_{ske}	121
5.97 Slot 8 P2 C_{ske}	121
5.98 Slot 8 Pitch Averaged C_{ske}	121
5.99 Slot 8 P0 Streamwise Vorticity Coefficient	122
5.100 Slot 8 P1 Streamwise Vorticity Coefficient	122
5.101 Slot 8 P2 Streamwise Vorticity Coefficient	122
5.102 Slot 8 Pitch Averaged Vorticity	122
5.103 Slot 10 P0 Loss	123
5.104 Slot 10 P1 Loss	123
5.105 Slot 10 P2 Loss	123
5.106 Slot 10 Pitch Averaged Loss	123
5.107 Slot 10 P0 Secondary Vectors	124
5.108 Slot 10 P1 Secondary Vectors	124
5.109 Slot 10 P2 Secondary Vectors	124
5.110 Slot 10 Pitch Averaged Yaw Angle	124
5.111 Slot 10 P0 C_{ske}	125
5.112 Slot 10 P1 C_{ske}	125
5.113 Slot 10 P2 C_{ske}	125
5.114 Slot 10 Pitch Averaged C_{ske}	125
5.115 Slot 10 P0 Streamwise Vorticity Coefficient	126
5.116 Slot 10 P1 Streamwise Vorticity Coefficient	126
5.117 Slot 10 P2 Streamwise Vorticity Coefficient	126
5.118 Slot 10 Pitch Averaged Vorticity	126

5.119	Close Wall Loss at Slot 10 P0	127
5.120	Close Wall Loss at Slot 10 P1	127
5.121	Close Wall Loss at Slot 10 P2	127
5.122	3H and 5H Pitch Averaged Loss at Slot 10	127
5.123	Secondary Vectors at Slot 10 P0	128
5.124	Secondary Vectors at Slot 10 P1	128
5.125	Secondary Vectors at Slot 10 P2	128
5.126	3H and 5H Pitch Averaged Yaw Angle at Slot 10	128
5.127	Area Averaged Mass Flow for Slots 1 to 10.	129
5.128	Area Averaged Yaw Angle for Slots 1 to 10.	129
5.129	Area Averaged C_{ske}	129
5.130	Area Averaged Loss Coeficient.	129
5.131	Area Averaged Secondary Loss Coeficient.	130
5.132	Repeated Traverses at Slot 10 - Loss.	130
5.133	Repeated Traverses at Slot 10 - Yaw.	130
5.134	Maximum Variation between repeated Traverses - Loss.	130
5.135	Maximum Variation between repeated Traverses - Yaw.	131
5.136	Area Averaged Total Loss.	131
5.137	Area Averaged Secondary Loss.	131
5.138	Secondary and Total Loss.	131
5.139	Mean Loss \pm two standard deviations.	132
5.140	Yaw Angle Variations at Slot 10.	132
5.141	Repeated Traverses Three Hole Probe Loss.	132
5.142	Repeated Traverses Three Hole Probe Yaw.	132
5.143	Area Averaged Total Loss - 3H Probe.	133
5.144	Pitch Averaged Loss 3H and 5H Data set.	133
5.145	Pitch Averaged Yaw 3H and 5H Data set.	133
5.146	Pitch Averaged Axial Velocity 3H and 5H Data Set.	133
5.147	Combined Data Set (three and five hole) Loss.	134
5.148	Change in Secondary Loss caused by adding close wall results.	134
5.149	Area Averaged Mixed Out Secondary Loss for a Five Hole Probe.	134
5.150	Area Averaged Mixed Out Secondary Loss for the Synthesised Data Set.	134
5.151	Vortex Centre Movement.	135
5.152	Vortex Centre Movement Measured from the Suction Surface/Blade Wake Centreline.	135
5.153	Why Loss Measurement is Difficult.	135
5.154	Summary Figure of P0, P1 and P2 Area Averaged C_{P0}	135
6.1	Hot Film Layout	137
6.2	Film Attachment	138
6.3	$V_{zeroflow}$ Variation with time.	140
6.4	Gauge Locations for Suction Surface.	146
6.5	Slot 2,6% C_{ax} : Suction Surface $(Q - Q_0)/Q_0$	147
6.6	Slot 3, 22% C_{ax} : Suction Surface $(Q - Q_0)/Q_0$	148
6.7	Slot 5, 55% C_{ax} : Suction Surface $(Q - Q_0)/Q_0$	149
6.8	Slot 6, 71% C_{ax} : Suction Surface $(Q - Q_0)/Q_0$	150

6.9	Slot 7, 87% C_{ax} : Suction Surface $(Q - Q_0)/Q_0$	151
6.10	$P0 V^2 - V_0^2$ traces on endwall.	152
6.11	$P1 V^2 - V_0^2$ traces on endwall.	153
6.12	$P2 V^2 - V_0^2$ traces on endwall.	154
6.13	$P0 V^2 - V_0^2$ showing absolute level.	155
6.14	$P1 V^2 - V_0^2$ showing absolute level.	156
6.15	$P2 V^2 - V_0^2$ showing absolute level.	157
6.16	Contours of $V^2 - V_0^2$ for $P0$	158
6.17	Contours of $V^2 - V_0^2$ for $P1$	159
6.18	Contours of $V^2 - V_0^2$ for $P2$	160
6.19	Repeatability Test: Upstream I	161
6.20	Repeatability Test: Upstream II	161
6.21	Repeatability Test: Inside Blade Row I	162
6.22	Repeatability Test: Inside Blade Row II	162
6.23	Angle Variation: Gauge Lined up with Flow.	163
6.24	Angle Variation: Twenty Degrees Anti-clockwise.	163
6.25	Angle Variation: Twenty Degrees Clockwise.	164
7.1	Experimental and CFD Secondary Loss	174
7.2	Slot 1 $P0$ Loss CFD Prediction.	179
7.3	Slot 1 $P1$ Loss CFD Prediction.	179
7.4	Slot 1 $P2$ Loss CFD Prediction.	179
7.5	Slot 1 Pitch Averaged Loss CFD Prediction.	179
7.6	Slot 1 $P0$ Secondary Vectors CFD Prediction.	180
7.7	Slot 1 $P1$ Secondary Vectors CFD Prediction.	180
7.8	Slot 1 $P2$ Secondary Vectors CFD Prediction.	180
7.9	Slot 1 Pitch Averaged Yaw Angle CFD Prediction.	180
7.10	Slot 2 $P0$ Loss CFD Prediction.	181
7.11	Slot 2 $P1$ Loss CFD Prediction.	181
7.12	Slot 2 $P2$ Loss CFD Prediction.	181
7.13	Slot 2 Pitch Averaged Loss CFD Prediction.	181
7.14	Slot 2 $P0$ Secondary Vectors CFD Prediction.	182
7.15	Slot 2 $P1$ Secondary Vectors CFD Prediction.	182
7.16	Slot 2 $P2$ Secondary Vectors CFD Prediction.	182
7.17	Slot 2 Pitch Averaged Yaw Angle CFD Prediction.	182
7.18	Slot 3 $P0$ Loss CFD Prediction.	183
7.19	Slot 3 $P1$ Loss CFD Prediction.	183
7.20	Slot 3 $P2$ Loss CFD Prediction.	183
7.21	Slot 3 Pitch Averaged Loss CFD Prediction.	183
7.22	Slot 3 $P0$ Secondary Vectors CFD Prediction.	184
7.23	Slot 3 $P1$ Secondary Vectors CFD Prediction.	184
7.24	Slot 3 $P2$ Secondary Vectors CFD Prediction.	184
7.25	Slot 3 Pitch Averaged Yaw Angle CFD Prediction.	184
7.26	Slot 4 $P0$ Loss CFD Prediction.	185
7.27	Slot 4 $P1$ Loss CFD Prediction.	185
7.28	Slot 4 $P2$ Loss CFD Prediction.	185
7.29	Slot 4 Pitch Averaged Loss CFD Prediction.	185

7.30 Slot 4 P0 Secondary Vectors CFD Prediction.	186
7.31 Slot 4 P1 Secondary Vectors CFD Prediction.	186
7.32 Slot 4 P2 Secondary Vectors CFD Prediction.	186
7.33 Slot 4 Pitch Averaged Yaw Angle CFD Prediction.	186
7.34 Slot 5 P0 Loss CFD Prediction.	187
7.35 Slot 5 P1 Loss CFD Prediction.	187
7.36 Slot 5 P2 Loss CFD Prediction.	187
7.37 Slot 5 Pitch Averaged Loss CFD Prediction.	187
7.38 Slot 5 P0 Secondary Vectors CFD Prediction.	188
7.39 Slot 5 P1 Secondary Vectors CFD Prediction.	188
7.40 Slot 5 P2 Secondary Vectors CFD Prediction.	188
7.41 Slot 5 Pitch Averaged Yaw Angle CFD Prediction.	188
7.42 Slot 6 P0 Loss CFD Prediction.	189
7.43 Slot 6 P1 Loss CFD Prediction.	189
7.44 Slot 6 P2 Loss CFD Prediction.	189
7.45 Slot 6 Pitch Averaged Loss CFD Prediction.	189
7.46 Slot 6 P0 Secondary Vectors CFD Prediction.	190
7.47 Slot 6 P1 Secondary Vectors CFD Prediction.	190
7.48 Slot 6 P2 Secondary Vectors CFD Prediction.	190
7.49 Slot 6 Pitch Averaged Yaw Angle CFD Prediction.	190
7.50 Slot 6 P0 C_{ske} CFD Prediction	191
7.51 Slot 6 P1 C_{ske} CFD Prediction	191
7.52 Slot 6 P2 C_{ske} CFD Prediction	191
7.53 Slot 6 Pitch Averaged C_{ske} CFD Prediction	191
7.54 Slot 6 P0 Streamwise Vorticity Coefficient CFD Prediction	192
7.55 Slot 6 P1 Streamwise Vorticity Coefficient CFD Prediction	192
7.56 Slot 6 P2 Streamwise Vorticity Coefficient CFD Prediction	192
7.57 Slot 6 Pitch Averaged Vorticity Flow CFD Prediction	192
7.58 Slot 8 P0 Loss CFD Prediction.	193
7.59 Slot 8 P1 Loss CFD Prediction.	193
7.60 Slot 8 P2 Loss CFD Prediction.	193
7.61 Slot 8 Pitch Averaged Loss CFD Prediction.	193
7.62 Slot 8 P0 Secondary Vectors CFD Prediction.	194
7.63 Slot 8 P1 Secondary Vectors CFD Prediction.	194
7.64 Slot 8 P2 Secondary Vectors CFD Prediction.	194
7.65 Slot 8 Pitch Averaged Yaw Angle CFD Prediction.	194
7.66 Slot 8 P0 C_{ske} CFD Prediction	195
7.67 Slot 8 P1 C_{ske} CFD Prediction	195
7.68 Slot 8 P2 C_{ske} CFD Prediction	195
7.69 Slot 8 Pitch Averaged C_{ske} CFD Prediction	195
7.70 Slot 8 P0 Streamwise Vorticity Coefficient CFD Prediction	196
7.71 Slot 8 P1 Streamwise Vorticity Coefficient CFD Prediction	196
7.72 Slot 8 P2 Streamwise Vorticity Coefficient CFD Prediction	196
7.73 Slot 8 Pitch Averaged Vorticity Flow CFD Prediction	196
7.74 Slot 10 P0 Loss CFD Prediction.	197
7.75 Slot 10 P1 Loss CFD Prediction.	197

7.76 Slot 10 P2 Loss CFD Prediction.	197
7.77 Slot 10 Pitch Averaged Loss CFD Prediction.	197
7.78 Slot 10 P0 Secondary Vectors CFD Prediction.	198
7.79 Slot 10 P1 Secondary Vectors CFD Prediction.	198
7.80 Slot 10 P2 Secondary Vectors CFD Prediction.	198
7.81 Slot 10 Pitch Averaged Yaw Angle CFD Prediction.	198
7.82 Slot 10 P0 C_{ske} CFD Prediction	199
7.83 Slot 10 P1 C_{ske} CFD Prediction	199
7.84 Slot 10 P2 C_{ske} CFD Prediction	199
7.85 Slot 10 Pitch Averaged C_{ske} CFD Prediction	199
7.86 Slot 10 P0 Streamwise Vorticity Coefficient CFD Prediction	200
7.87 Slot 10 P1 Streamwise Vorticity Coefficient CFD Prediction	200
7.88 Slot 10 P2 Streamwise Vorticity Coefficient CFD Prediction	200
7.89 Slot 10 Pitch Averaged Vorticity Flow CFD Prediction	200
7.90 Experimental and CFD Pitch Averaged Loss at Slot 10.	201
7.91 Experimental and CFD Secondary Loss.	201
7.92 Experimental and CFD Pitch Averaged C_{ske} at Slot 10.	201
7.93 Experimental and CFD Pitch Averaged Yaw at Slot 10	201
7.94 CFD and Experimental Pitch Averaged Loss at Slot 10 - comparison by profile.	202
7.95 CFD and Experimental Pitch Averaged C_{ske} at Slot 10 - comparison by profile.	203
7.96 CFD and Experimental Pitch Averaged Yaw Angle at Slot 10 - comparison by profile.	204
7.97 CFD Endwall Flow Suction Surface P0.	205
7.98 CFD Endwall Flow Suction Surface P1.	205
7.99 CFD Endwall Flow Suction Surface P2.	205
7.100 CFD Endwall Flow Pressure Surface P0.	206
7.101 CFD Endwall Flow Pressure Surface P1.	206
7.102 CFD Endwall Flow Pressure Surface P2.	206
7.103 CFD Saddle Point P0.	207
7.104 CFD Saddle Point P1.	207
7.105 CFD Saddle Point P2.	207
7.106 CFD Streamlines associated with loss cores P0.	208
7.107 CFD Streamlines associated with loss cores P1.	208
7.108 CFD Streamlines associated with loss cores P2	208
 8.1 Experimental and CFD Secondary Loss	224
8.2 Effect of mixing length on C_{P0}	227
8.3 Pre-readings Loss Error	229
8.4 Pre-readings Yaw Error	229
8.5 Pre-readings Pitch Error	229
8.6 Post-readings Loss Error	229
8.7 Post-readings Yaw Error	230
8.8 Post-readings Pitch Error	230
8.9 Repeatability of Planar Loss Readings (P0).	230
8.10 Repeatability of Yaw Readings (P0).	230

8.11 Planar Area Loss at Slot 6.	231
8.12 P3 Area Loss at Slot 6.	231
8.13 Planar Secondary Vectors at Slot 6.	231
8.14 P3 Secondary Vectors at Slot 6.	231
8.15 Planar C_{ske} at Slot 6.	232
8.16 P3 C_{ske} at Slot 6.	232
8.17 Streamwise Vorticity Coefficient at Slot 6 P0.	232
8.18 Streamwise Vorticity Coefficient at Slot 6 P3.	232
8.19 Planar Area Loss at Slot 8.	233
8.20 P3 Area Loss at Slot 8.	233
8.21 Planar Secondary Vectors at Slot 8.	233
8.22 P3 Secondary Vectors at Slot 8.	233
8.23 Planar C_{ske} at Slot 8.	234
8.24 P3 C_{ske} at Slot 8.	234
8.25 Streamwise Vorticity Coefficient at Slot 8 P0.	234
8.26 Streamwise Vorticity Coefficient at Slot 8 P3.	234
8.27 Planar Area Loss at Slot 10.	235
8.28 P3 Area Loss at Slot 10.	235
8.29 Planar Secondary Vectors at Slot 10.	235
8.30 P3 Secondary Vectors at Slot 10.	235
8.31 Planar C_{ske} at Slot 10.	236
8.32 P3 C_{ske} at Slot 10.	236
8.33 Streamwise Vorticity Coefficient at Slot 10 P0.	236
8.34 Streamwise Vorticity Coefficient at Slot 10 P3.	236
8.35 Close Wall Loss Readings at Slot 4 P0.	237
8.36 Close Wall Loss Readings at Slot 4 P3.	237
8.37 Close Wall Secondary Flow at Slot 4 P0.	237
8.38 Close Wall Secondary Flow at Slot 4 P3.	237
8.39 Close Wall Loss Readings at Slot 10 P0.	238
8.40 Close Wall Loss Readings at Slot 10 P3.	238
8.41 Close Wall Secondary Flow at Slot 10 P0.	238
8.42 Close Wall Secondary Flow at Slot 10 P3.	238
8.43 Pitch Averaged Loss at Slot 6.	239
8.44 Pitch Averaged Yaw at Slot 6.	239
8.45 Pitch Averaged C_{ske} at Slot 6.	239
8.46 Pitch Averaged Streamwise Vorticity Coefficient at Slot 6.	239
8.47 Pitch Averaged Loss at Slot 8.	240
8.48 Pitch Averaged Yaw at Slot 8.	240
8.49 Pitch Averaged C_{ske} at Slot 8.	240
8.50 Pitch Averaged Streamwise Vorticity Coefficient at Slot 8.	240
8.51 Pitch Averaged Loss at Slot 10.	241
8.52 Pitch Averaged Yaw at Slot 10.	241
8.53 Pitch Averaged C_{ske} at Slot 10.	241
8.54 Pitch Averaged Streamwise Vorticity Coefficient at Slot 10.	241
8.55 Pitch Averaged Loss at Slot 4 - Close Wall Results.	242
8.56 Pitch Averaged Yaw at Slot 4 - Close Wall Results.	242

8.57	Pitch Averaged Loss at Slot 10 - Close Wall Results.	242
8.58	Pitch Averaged Yaw at Slot 10 - Close Wall Results.	242
8.59	$\overline{\overline{C}_{P0}}$ growth through the cascade for P0 and P3.	243
8.60	Secondary loss growth through the cascade for P0 and P3.	243
8.61	\overline{C}_{ske} growth through the cascade for P0 and P3.	243
8.62	Pitch averaged loss, combined data set P0 and P3.	243
8.63	Pitch averaged yaw Angle, combined data set P0 and P3.	244
8.64	Area Averaged Loss Coefficient - effect of including three hole data.	244
8.65	Area Averaged Loss Coefficient - effect of mixing out loss.	244
8.66	Summary Figure of P0 and P3 Area Averaged C_{P0} .	244
8.67	P0 Endwall Flow Visualisation.	245
8.68	P3 Endwall Flow Visualisation.	245
8.69	P0 Leading Edge Flow Visualisation.	245
8.70	P3 Leading Edge Flow Visualisation.	245
8.71	P0 Suction Surface Flow Visualisation.	246
8.72	P3 Suction Surface Flow Visualisation.	246
8.73	P0 Perspective View of Blade and Endwall.	246
8.74	P3 Perspective View of Blade and Endwall	246
8.75	Annotated View of P0.	247
8.76	Annotated View of P3.	248
8.77	Planar Area Loss at Slot 6 - CFD.	249
8.78	P3 Area Loss at Slot 6 - CFD.	249
8.79	Planar Secondary Vectors at Slot 6 - CFD.	249
8.80	P3 Secondary Vectors at Slot 6 - CFD.	249
8.81	Planar C_{ske} at Slot 6 - CFD.	250
8.82	P3 C_{ske} at Slot 6 - CFD.	250
8.83	Streamwise Vorticity Coefficient at Slot 6 P0 - CFD.	250
8.84	Streamwise Vorticity Coefficient at Slot 6 P3 - CFD.	250
8.85	Planar Area Loss at Slot 8 - CFD.	251
8.86	P3 Area Loss at Slot 8 - CFD.	251
8.87	Planar Secondary Vectors at Slot 8 - CFD.	251
8.88	P3 Secondary Vectors at Slot 8 - CFD.	251
8.89	Planar C_{ske} at Slot 8 - CFD.	252
8.90	P3 C_{ske} at Slot 8 - CFD.	252
8.91	Streamwise Vorticity Coefficient at Slot 8 P0 - CFD.	252
8.92	Streamwise Vorticity Coefficient at Slot 8 P3 - CFD.	252
8.93	Planar Area Loss at Slot 10 - CFD.	253
8.94	P3 Area Loss at Slot 10 - CFD.	253
8.95	Planar Secondary Vectors at Slot 10 - CFD.	253
8.96	P3 Secondary Vectors at Slot 10 - CFD.	253
8.97	Planar C_{ske} at Slot 10 - CFD.	254
8.98	P3 C_{ske} at Slot 10 - CFD.	254
8.99	Streamwise Vorticity Coefficient at Slot 10 P0 - CFD.	254
8.100	Streamwise Vorticity Coefficient at Slot 10 P3 - CFD.	254
8.101	Pitch Averaged Loss at Slot 6 - CFD.	255
8.102	Pitch Averaged Yaw at Slot 6 - CFD.	255

8.103	Pitch Averaged C_{ske} at Slot 6 - CFD.	255
8.104	Pitch Averaged Streamwise Vorticity Coefficient at Slot 6 - CFD.	255
8.105	Pitch Averaged Loss at Slot 8 - CFD.	256
8.106	Pitch Averaged Yaw at Slot 8 - CFD.	256
8.107	Pitch Averaged C_{ske} at Slot 8 - CFD.	256
8.108	Pitch Averaged Streamwise Vorticity Coefficient at Slot 8 - CFD.	256
8.109	Pitch Averaged Loss at Slot 10 - CFD.	257
8.110	Pitch Averaged Yaw at Slot 10 - CFD.	257
8.111	Pitch Averaged C_{ske} at Slot 10 - CFD.	257
8.112	Pitch Averaged Streamwise Vorticity Coefficient at Slot 10 - CFD.	257
8.113	Loss predictions from the Two Planar CFD Solutions.	258
8.114	Yaw angle predictions from the Two Planar CFD Solutions.	258
8.115	C_{ske} predictions from the Two Planar CFD Solutions	258
8.116	Comparison of Grids for the Two Planar CFD Solutions	258
9.1	Pitch Averaged C_{P0} for a number of experimenters.	262
9.2	Pitch Averaged yaw angle for a number of experimenters.	263
9.3	Effect of endwall Profiling on Streamwise Vorticity	265
9.4	Bar Chart of Key Results from this Thesis.	270
9.5	Effect of endwall profiling on the horseshoe vortex	271
A.1	P1 Geometry.	285
A.2	P2 Geometry.	286
A.3	P3 Geometry.	287
B.1	Cascade Coordinates including sign of pitch and yaw angles.	289
C.1	Data Processing Programs written by the author.	293
D.1	Labelling for Simple Efficiency Estimate	296
E.1	Photograph of probe 5HB.	298
E.2	Photograph of probe 3HE.	299

List of Tables

1	Symbols used in this thesis.	xxvi
3.1	Design Data for the Durham Cascade	30
3.2	The Standard Day	30
3.3	Inlet Boundary Layer	30
3.4	Slot Locations	39
3.5	The effect of removing the Δr weighting	49
5.1	Measurement Planes for P0,P1 and P2.	77
5.2	Typical maximum and minimum angles relative to the probe at Slot 10.	78
5.3	Yaw Angle Corrections Slot 1 to Slot 8.	79
5.4	Yaw Angle Corrections Slot 10.	87
5.5	Slot 10 Repeated Traverses	91
5.6	Mean Loss and Error Estimate for Five Hole Probe Readings.	92
5.7	Slot 10 Repeated Traverses: three hole probe.	93
5.8	Mean Loss and Error Estimate for Three Hole Probe Readings. (0-7.5% Span)	93
5.9	Combined Three and Five Hole Probe Readings.	94
5.10	Mixed out loss for five hole probe readings.	95
5.11	Mixed out loss for synthesised data set.	95
6.1	Suction Surface Measurement Locations	141
7.1	CFD Loss Predictions Compared to Experimental Values	173
7.2	CFD C_{ske} Predictions compared to Experimental Values	174
7.3	C_{ske} and C_{P0} Reductions Compared. (% of planar values)	175
8.1	Axial Measurement Planes for the Third Generation Endwall	210
8.2	P0 Repeatability Secondary Loss Coefficient	211
8.3	Area Averaged Massflow	211
8.4	Peak Turning (estimate from Figure 5.110).	216
8.5	$\overline{\overline{C_{P0}}}$ for Five Hole Probe Readings P3 endwall.	217
8.6	$\overline{\overline{C_{P0}}}$ for Three Hole Probe Readings (0-7.5% Span) P3 endwall.	217
8.7	Combined Three and Five Hole Probe Readings for P3.	218
8.8	Mixed out loss for synthesised data set - P3.	218
8.9	CFD Loss Predictions Compared to Experimental Values - P3	225
8.10	CFD C_{ske} Predictions compared to Experimental Values -P3	225

8.11	C_{P0} at Midspan compared to freestream turbulence length scale.	226
9.1	$\overline{\overline{C_{P0}}}$ error estimates from literature.	264
9.2	Estimated Efficiencies with Profiled Endwalls	268
9.3	Key Loss Results from this Thesis.	269
C.1	Five Hole Traverse Labels and corresponding calibration.	290
C.2	Three Hole Traverse Labels and corresponding calibration.	291
C.3	P3 Measurement Traverse Labels	291
C.4	Area Averaged Loss Results at Slot 10.	294
D.1	Calculation of efficiency estimate.	296

Nomenclature and Symbols

A Area

A Calibration constant for hot films

B Calibration constant for hot films

CFD Computation fluid dynamics

C_{ax} Axial chord

C_{P0} Total pressure loss coefficient

C_{Pitch} Calibration pitch coefficient

$C_{Pstatic}$ Calibration static pressure coefficient

C_{Ptotal} Calibration total pressure coefficient

C_{Pyaw} Calibration yaw coefficient

C_{ske} Secondary kinetic energy coefficient

C_Ω Streamwise vorticity coefficient

h Radial height for integration or enthalpy

i Hot film gauge current

OHR Over heat ratio for hot film gauges

P Pressure

\bar{P} $(P_{left} + P_{right} + P_{bottom} + P_{top})/4$ for five hole probes.

\bar{P} $(P_{left} + P_{right})/2$ for three hole probes

P_{atm} Atmospheric pressure

P_{bottom} Pressure from “lower” hole on three or five hole probe

P_{centre} Pressure from “centre” hole on three or five hole probe

P_{left} Pressure from “left” hole on three or five hole probe

P_{right} Pressure from “right” hole on three or five hole probe

P_{static} Static pressure

P_{top} Pressure from “top” hole on three or five hole probe

P_{total} Total pressure

P0 Planar endwall

P1 First generation endwall

P2 Second generation endwall

P3 Third generation endwall

Q Gross heat transfer rate

Q_0 Zero flow heat transfer rate

r Radial coordinate

R Tool radius or hot film gauge resistance or gas constant

Δr Radial distance covered by a particular measurement point

s Pitch or entropy

t Tangential coordinate

T_{atm} Atmospheric temperature

V Velocity

V Hot film voltage

V_0 Zero flow hot film voltage

V_{plot} Velocity component used for plotting

V_r Radial component of velocity

V_{sec} Secondary flow velocity

V_t Tangential component of velocity

V_{ups} Upstream free stream velocity

V_x Axial component of velocity

$V_{zeroflow}$ The hot film voltage with no flow over it

x Axial coordinate

Y Pressure Loss Coefficient

α	Yaw angle
α_{mid}	Midspan yaw angle
α_p	Primary flow angle
β	Pitch angle
ρ	Density
Ω	Vorticity
Ω	Electrical resistance
Ω_r	Radial component of vorticity
Ω_s	Streamwise component of vorticity
Ω_t	Tangential component of vorticity
Ω_x	Axial component of vorticity
η	Energy or enthalpy loss coefficient
τ_w	Wall shear stress
ΔT_0	Temperature difference between wall and free stream

Pitch averages are designated by a single bar $\bar{\alpha}$ and area averages are designated by a double bar $\overline{\overline{\alpha}}$. The subscript ∞ as in $C_{P0\infty}$ refers to a mixed out quantity at an infinite distance downstream of the cascade. The subscript *ups* as in V_{ups} refers to the upstream reference position. The subscript 0 generally indicates stagnation conditions and the subscript *s* denotes isentropic conditions.

Symbol	Case
—●—	P0 experimental results
—○—	P0 CFD
—■—	P1 experimental results
—□—	P1 CFD
—▲—	P2 experimental results
—△—	P2 CFD
—▼—	P3 experimental results
—▽—	P3 CFD
—▲—	P3 experimental results (alternate symbol)
—△—	P3 CFD (alternate symbol)

Table 1: Symbols used in this thesis.

Chapter 1

Introduction

SECONDARY FLOWS can account for around half the total loss in a highly loaded low aspect ratio turbine blade (Gregory-Smith et al., 2001). The aim of non-axisymmetric endwall profiling is to reduce these losses and improve the flow inside the blade passage. Although component efficiencies are very high in modern components the high massflows and power outputs of modern machines means that even small gains are worth pursuing. This thesis is the result of a three and a half year programme of research at Durham University in collaboration with Rolls-Royce. The genesis of the current work comes from a paper by Rose (1994) who proposed that flat endwalls were no longer a necessary design constraint and benefits could arise from profiling the endwalls. This approach has proved successful and profiled endwalls have been successfully tested in machine representative rigs Harvey et al. (2002), Brennan et al. (2001) and Rose et al. (2001) and the technology is now appearing on the next generation of engine designs.

This work programme with Rolls-Royce had several aims:-

1. To understand the effects of three dimensional endwall profiling on loss reduction.
2. To exploit this increased understanding with the design, manufacture and testing of a third generation profiled endwall.
3. To provide information to Rolls Royce about the performance of their design system by testing it against an experiment.

This thesis attempts to contribute to all of those aims, though much of the design work has been carried out by Rolls-Royce. At the start of the project two different endwall geometries had been manufactured and tested in the Durham Cascade. Harvey et al. (1999) and Hartland et al. (1999b) describe the testing of a first generation profiled endwall which was extremely successful. Jayaraman (2000) carried out tests on a second profile which performed worse than the first, contrary to design predictions and one of the first tasks was to examine the reasons behind this differing performance. The following principal activities have been carried out:-

- A review and refurbishment of the test rig and instrumentation.
- Oil/Dye surface flow visualisation.

- Extensive pressure probe traverses within the blade passage and at the exit plane for three geometries, the planar reference case and two generations of profiled endwalls.
- Close wall pressure traverses using a flattened three hole probe.
- Surface hot film measurements to determine the state of the endwall boundary layer on the endwalls and on the blade suction surface.
- The design, manufacture and testing of a third generation endwall.

In order to facilitate a comparison between profiled endwalls a new planar endwall was manufactured. Contour plots of endwall height may be found in Figures A.1-A.3 on pages 285-287. This thesis therefore has results from four endwalls:-

P0 planar endwall.

P1 first generation profiled endwall, with profiling extending over the whole of the computation domain.

P2 second generation of profiled endwall, with profiling restricted to inside the blade passage.

P3 third generation endwall, designed, manufactured and tested during the project. This profile has the highest “hump” and the lowest “dip” of profiles available for the Durham Cascade.

The author has endeavoured to go into some detail about the experimental techniques used to obtain the results described herein, the aim being that equipped with this thesis one would be able to repeat the experiments with the minimum of effort.

Another key element of this thesis is that it attempts to provide a realistic estimate of the accuracy and repeatability of results. In many cases repetitions of the experiments have been carried out as part of the thesis. The performance differences between different endwalls are small and accurate and repeatable measurements are difficult to obtain. To attempt to gloss over the problem does the reader a great disservice.

This thesis contains the following chapters:-

1. Introduction - this section.
2. Literature Review - this puts the work into a wider context and discusses other work on three dimensional turbine flows.
3. Experimental Technique - this explains the layout and structure of the experimental equipment and the techniques used for flow visualisation and pressure probe measurements. The data processing for the pressure probe data is also described in some detail. Hot film experiments and data processing is left until Chapter 6.
4. Flow Visualisation Results - results for the P0,P1 and P2 flow visualisation studies. P3 results are left until a later chapter.

5. Experimental Pressure Probe Results for P0,P1 and P2 - this includes both three and five hole probe readings. As well as repeated traverses to estimate the error associated with loss measurements.
6. Hot Film Results - how endwall profiling changes the boundary layer state on both the endwall and the blade suction surface for P0,P1 and P2.
7. Comparison with CFD Data for P0,P1 and P2. Data is extracted from the CFD solution and treated as experimental data to enable a direct comparison to be made. Additional information about the CFD solution is extracted using post processing software.
8. Third Generation Endwall (P3) - the design, manufacture and test of the third generation endwall. The design aim behind this profile was to find the greatest secondary loss reduction that could be obtained in the Durham Cascade.
9. Overall Discussion. The flow changes occurring inside profiled passages are described. The reasons for the differing results in this thesis and those of earlier researchers are discussed in some detail.
10. Conclusions and Recommendations.
11. Appendices. Supplementary information such as contour plots of the geometry of each endwall is included here.

There is a great deal of experimental data presented in this thesis, in order to make the data more manageable all the pitch averaged plots follow the conventions shown in Table 1 on page xxvi with closed symbols being used for experimental data and open symbols used for CFD data as illustrated.

A number of data processing programs were written by the author during the production of this thesis, a diagram of how the various data processing programs fit together is provided in Figure C.1 on page 293. A list of all computer programs used or written for this thesis is also included in section C.4 on page 292

The design of P3 and all of the CFD studies reported in this thesis were carried out at Rolls-Royce. The analysis described here is the work and sole responsibility of the author.

Chapter 2

Literature Review

LITERATURE relevant to this thesis is reviewed in this chapter. It explains why axial flow turbines are important. It describes how the work described in this thesis fits into the wider picture of turbomachinery and real world turbine designs. It illustrates why the work described in this thesis is important and relevant to the world at large.

2.1 Axial Turbines and the Benefits of Improved Efficiency.

Since Charles Parsons demonstrated the power of the axial flow turbine at Spithead in June 1897 it has become the machine of choice for large scale, high temperature applications. The axial flow turbine is used in steam turbines varying in size from a few hundred kilowatts to over one thousand megawatts in size and axial flow turbines are an essential part of the modern gas turbine which powers the vast majority of airborne transport.

The steam turbine has declined in importance somewhat over recent years being replaced in many applications, such as ship propulsion by diesel engines or gas turbines and in the field of electrical generation by the increasing importance of gas turbine based plant. However smaller applications of steam turbines in combined heat and power plants are increasing and it plays a crucial role in the high efficiency of the combined cycle generating plant. The steam turbine will typically operate at a maximum temperature of around 540°C. Materials suitable for operating above that temperature are currently prohibitively expensive and there are no easy mechanisms for cooling steam turbine blades. This can be compared to gas turbines where a turbine inlet temperature of 1300°C is not untypical.

Since Parsons invented the axial flow turbine numerous performance improvements and enhancements have been made to the machine and component efficiencies of over 90% are reported (Haller and Anderton, 2002). Despite the high efficiency of modern turbines, the large number of them sold every year (Rolls-Royce estimate that 55,000 of their engines are still in service) and the large size of modern gas or steam turbines (330 MW for Gas Turbines (GE 9H) and 660 MW typical United Kingdom generating set size for Steam Turbines) mean that even small gains in efficiency are well worth obtaining. Rose (1994) reported that an 0.1% improvement

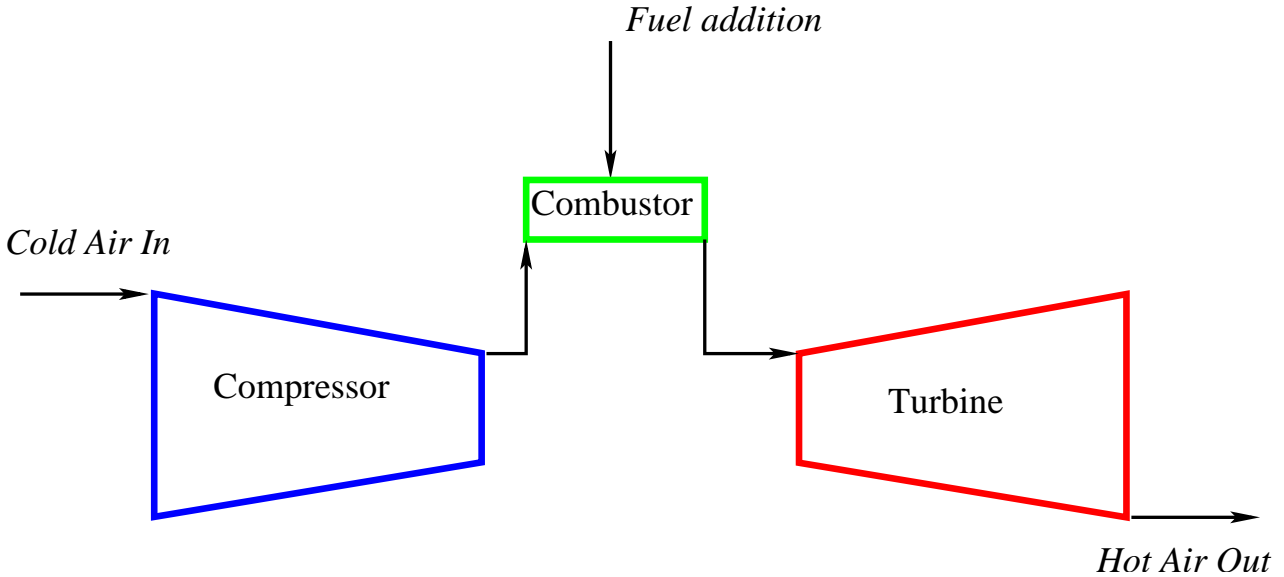


Figure 2.1: Operation of the Gas Turbine

in specific fuel consumption was worth around \$22,000 a year on a Boeing 747 aeroplane. There are over one thousand 747s in operation around the world. A simple calculation based on a 265 MW Siemen's V94.3a electrical generating unit indicates that for UK operation a 0.1% increase in efficiency would be worth over £100,000 per year in increased electrical output.

This explains the motivation behind the current study which is to understand the performance of axial turbine stages when three dimensional contouring of the stage endwalls is applied. This will enable engine designers to reduce the loss in the component and increase the overall efficiency of the machine. Previous studies at Durham (Hartland et al. (1999a) and Jayaraman (2000)) and in machine representative rigs (Harvey et al. (2002), Brennan et al. (2001) and Rose et al. (2001)) have shown an overall reduction of loss across the blade row when using this technique as well as an improvement in the uniformity of the flow pattern exiting the blade row.

2.2 Gas Turbines.

The gas turbine is in theory an extremely simple machine. In its most basic form it requires only three components: compressor, combustion chamber and turbine.

The basic principle of the gas turbine is very well known (See Figure 2.1). Air is compressed, fuel is added and the resultant hot gases are passed through a turbine to generate enough power to drive the compressor and either provide propulsive power by producing a jet of air or turn a shaft and produce a torque. A well known introduction to the gas turbine is found in Cohen et al. (1996).

However the modern machine has evolved to an extremely complex machine, for example:

1. modern aeroengines can have up to three shafts concentric with each other to match the required speeds of the fan, compressor and turbines

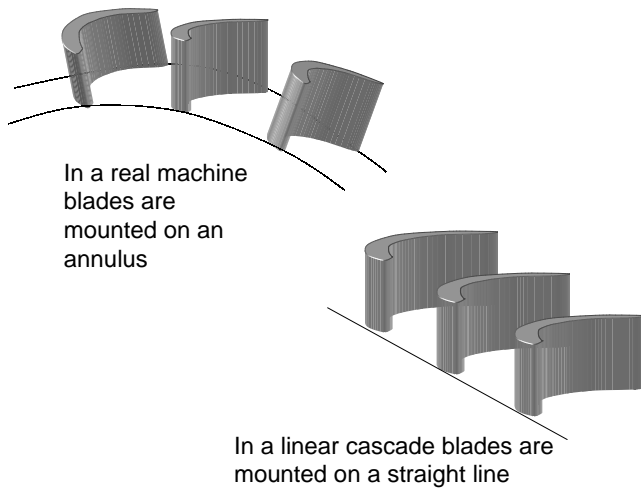


Figure 2.2: Relationship between Linear Cascades and Real Machines

2. combustion chambers have to comply with emissions requirements necessitating two or even three stages of combustion
3. blades and combustion chambers have a complex pattern of film cooling, to avoid the mainstream hot fluid melting the blade/combustion chamber surface
4. in order to achieve high component efficiencies, blades for turbines and compressors take on complex three dimensional shapes
5. in order to achieve a long life at elevated temperature blades now have to made out of exotic materials
6. to reduce tip leakage over the ends of the blades, complex sealing systems may be deployed around the tip of the blades

Hence the successful design of high performance machines is very difficult and requires considerable research and development effort to achieve even relatively small gains.

2.3 Cascade Secondary Flow.

In order to understand the extremely complex flows in turbomachinery itself, the simplified cascade flow model has been developed which in its basic form (and the form used in the research described here) removes the annular features of the geometry and the moving parts. This is shown in Figure 2.2. Even with this considerable simplification of the actual case the flow remains highly complex and many of the flow features found in simple cascades can also be seen in real machines. For example see Haller (1997), Eymann et al. (2002) who show measurements of real machines with flow features that are found in cascade flow.

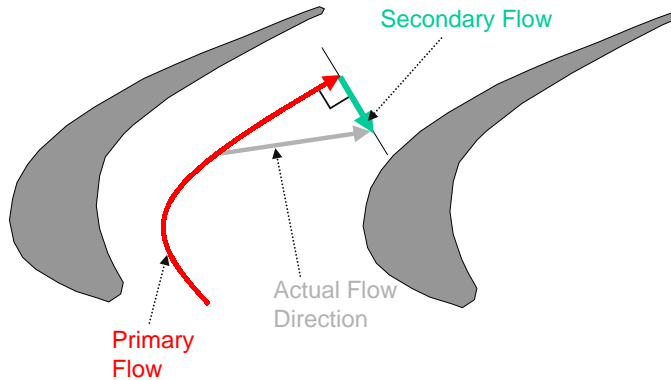


Figure 2.3: Simple Definition of Secondary Flow

There are a number of ways of classifying secondary flows. Secondary flows can be looked at as a small disturbance on a primary flow where the primary flow is the main two dimensional flow e.g. midspan flow through a blade row. Although considered as a small perturbation superimposed on a larger flow, the secondary flow can be of the same order of magnitude as the primary flow. (See Figure 2.3). More rigorous definitions of secondary flow are available, for example Gregory-Smith (1997) quoted Marsh who described secondary flows as

The difference between the flow in a cascade of finite blade spacing and that in the corresponding many bladed cascade giving the same primary flow

This takes into account secondary flows produced by the vorticity shed from the trailing edges of the blades.

Many modern turbomachinery components contain three dimensional geometries and it is not obvious what the primary flow direction should be defined as. One way of defining the primary flow direction is to use an inviscid calculation with no inlet boundary layer to give a three dimensional flow field and secondary flow is defined as deviations from this flow. For this thesis the primary flow direction is very clear so such complexity is not required, Figure 3.12 on page 46 shows the secondary flow definition used in this thesis.

It is equally possible to come up with a more prosaic definition of secondary flows (Moore and Adhye, 1985):

unplanned three-dimensional flow effects in a turbine which lead to unexplained (secondary) losses

The review paper of Sieverding (1985) summarised much of the progress in understanding the effects of secondary flow in turbine blades. When a flow is turned in a cascade of blades there are a number of prominent features namely:

1. the passage vortex
2. the pressure side leg of the horseshoe vortex
3. the suction side leg of the horseshoe vortex
4. the corner vortex

Secondary flows have a number of undesirable effects as described by Gregory-Smith (1997):

1. the work output from a turbine stage depends on the turning of the flow. Secondary flow alters the flow angle in the tangential direction which changes the work output
2. extra loss is produced
3. a non uniform flow is provided at exit of the blade row reducing the efficiency of the blade row downstream
4. secondary flows can introduce unsteadiness into the flow which can cause mechanical problems
5. the secondary flow provides non uniform heat transfer across the blade and endwall surface, for example Goldstein and Spores (1988), Roy et al. (2000) and Burd and Simon (2002) all describe the problem.

The uniformity of exit flow is very important though actually calculating benefits is extremely difficult. For example one study on the effects of leaned blades Harrison (1990) showed that there was no loss reduction in a linear cascade but the exit flow was considerably more uniform - this appears to have been sufficient motivation for blade lean to become commonly used.

2.3.1 Classical Secondary Flow Theory

Classical Secondary Flow Theory considers vorticity dynamics, which examines the changes produced in the vorticity vector by turning the flow. Simplistically the vorticity vector represents the amount of rotating fluid in a flow.

Gregory-Smith (1997) reviewed classical secondary flow theory as part of a series of lectures. He commented that classical secondary flow theory has a role to play in understanding the reasons behind secondary flow and also in providing very fast estimates of secondary flow effects compared to a full three dimensional CFD solution. Using the rule of thumb that computer power double approximately every eighteen months it will only be a matter of time before a fully three dimensional CFD solution can be completed in a matter of seconds.

The production of secondary flow can be viewed as being down to the turning of the vorticity vector Ω . For a uniform flow with inlet boundary layer there is no variation in any velocity except in axial velocity and this only varies in the

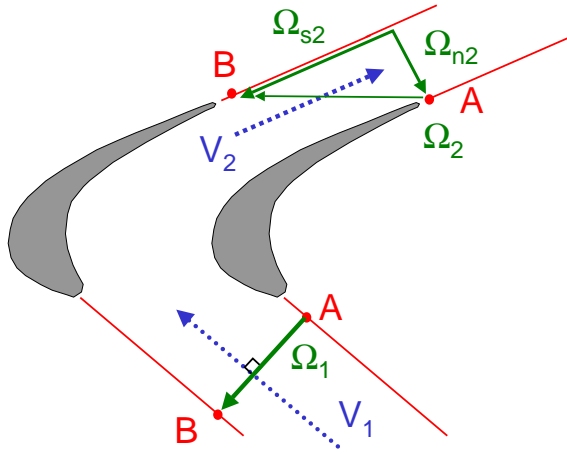


Figure 2.4: Vorticity Vector at Inlet and Exit of a Cascade

radial direction. Therefore the inlet vorticity is normal to the streamwise direction and:

$$\Omega_n = \frac{\partial V_x}{\partial r} \quad (2.1)$$

Figure 2.4 shows the turning of the vorticity vector (Ω). As the flow passes through the blade row, the suction surface flow moves faster than that on the pressure surface and the vorticity vector is turned so that it has a streamwise component.

The simplest equation for the streamwise component of vorticity was derived by Squire and Winter (1951). The Squire and Winter formula states that the distributed vorticity is twice the inlet normal vorticity times the turning angle of the flow, i.e.

$$\Omega_s = -2\Omega_n(\alpha_2 - \alpha_1) \quad (2.2)$$

where Ω_s is the streamwise vorticity, Ω_n is the inlet normal vorticity and α_1 and α_2 are the inlet and exit yaw angles respectively.

The Squire & Winter formula can now explain fairly simply some of the observed features of secondary flow. Firstly the magnitude of the streamwise vorticity is proportional to the turning angle which explains the observations that the magnitude of secondary flows depends on the turning angle. Secondly, with a turbulent inlet boundary layer the vorticity is concentrated nearer the wall. This means the resulting secondary flow is also concentrated near the end wall. For laminar flow the streamwise vorticity will extend further up the blade span but will be less intense. This explains why laminar secondary flow studies tend to produce more elaborate and extensive flow structures than turbulent ones.

A recent application of secondary flow theory is found in Prasad and Hendricks (2000) who used secondary flow theory to understand the migration of hot streaks introduced by the turbine's combustion system.

The passage vortex is caused by a sheared flow being turned:

- A. Inlet boundary layer is a sheared flow
- B. Lower Energy Fluid turns on a tighter radius
- C. To preserve continuity a vortical flow is formed

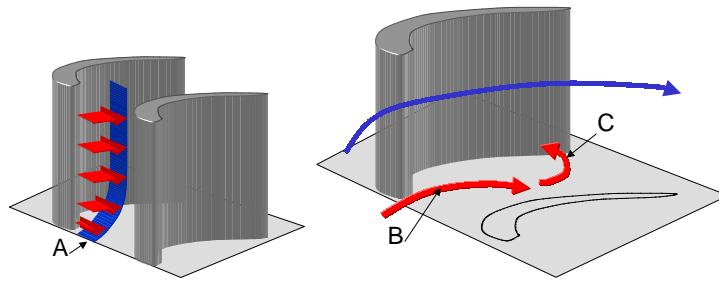


Figure 2.5: Formation of the Passage Vortex

2.3.2 The Passage Vortex

This is the dominant flow feature of secondary flow and numerous researchers have seen evidence of it, such as Harrison (1990), Hodson and Dominy (1987), Moore and Adhye (1985), Moustapha et al. (1985), Marchal and Sieverding (1977) and Gregory-Smith and Graves (1983) to name but a few. Gregory-Smith (1997) describes the basic physics behind the generation of the passage vortex. When a sheared flow e.g. a boundary layer is turned, the slower moving fluid follows a tighter radius of curvature leading to a tangential flow across the passage. Then in order to preserve continuity a vortical flow is formed (See Figure 2.5). The above description only applies to the formation of the passage vortex which is the most noticeable flow feature in real machines and the largest secondary flow feature.

2.3.3 The Horseshoe Vortex

This less obvious feature of the flow is not always seen in reports of experimental work as quite often the resolution of the experiments is not great enough to show its formation. Evidence for the horseshoe vortex is found in Marchal and Sieverding (1977) and Gregory-Smith and Graves (1983) but not in Moore and Adhye (1985).

The horseshoe vortex is formed when a boundary layer flow meets a blunt object. The process is described in some detail in Eckerle and Langston (1987) who describe their experiments with a large cylinder in a low speed wind tunnel. The process of the horseshoe vortex formation is quite complex, but it essentially arises from the mainstream flow outside the boundary layer having a higher stagnation pressure than the flow nearer the wall. This results in a downward flow at the cylinder leading edge and the formation of the vortex structures. Eckerle & Langston report that the vortex does however not form directly ahead of the cylinder but some 15 degrees from the axial direction. Initially the returning flow from the cylinder is deflected and does not form a vortex structure. Eckerle & Langston report a displacement to

momentum thickness ratio of 1.35 which indicates a turbulent boundary, although their turbulence intensity was low at less than 1%.

In a cascade flow the two sides of the horseshoe vortex are labelled the pressure side and suction side according to which part of the blade they are nearest to and they interact with the passage vortex. The exact form of that interaction or its importance is not clear from the literature. A number of different pictures are presented in the literature, for example Sharma and Butler (1987) show a model in which the suction side of the horseshoe vortex rotates around the passage vortex whereas Sieverding and Bosche (1983) show the suction side of the passage vortex rotate with the passage vortex through a much smaller angle. Goldstein and Spores (1988) present a model with seven separate vortices in it, their model is expanded upon in Wang et al. (1997) where the laser light sheet technique is used to make a series of detailed visualisations. The “Wang” model contains another two vortices taking the total up to nine separate structures. Takeshi et al. (1989) present yet another model of secondary flow through a turbine blade.

For the moment it is sufficient to say that the pressure side leg of the horseshoe vortex crosses the blade passage and interacts with the passage vortex in a significant manner. The suction side leg of the horseshoe vortex interacts with the passage vortex. The sense of rotation of the passage vortex and the pressure side leg of the horseshoe vortex is the same, so the two structures can combine. The suction side of the horseshoe vortex rotates in the opposite sense to the passage vortex.

2.3.4 The Corner Vortex

The corner vortex is a flow feature formed by the strong cross flows on the endwall meeting the blade suction surface. The exact physics would appear to be similar to the formation of the horseshoe vortex (see Sieverding (1985)) but there appear to be no detailed studies of the evolution of this vortex. This feature is relatively small and is only seen in experiments with high turning. Its existence is rarely seen in velocity vector plots of the cascade flow as the three or five hole probes used to measure it do not give sufficient resolution near the wall. This fluid structure can be seen in flow visualisations (e.g. Sieverding (1985) or in the reduction of overturning at the wall Gregory-Smith et al. (1987)).

An interesting example of the corner vortex is seen in Yamamoto (1987) who presented results from two cascades one representing a stator with a turning angle of around 68° the other a rotor cascade with a turning angle of around 100° , the effect of the corner vortex is clearly seen in the reduction in overturning in the rotor case at exit which is not seen in the stator case.

A novel use of the corner vortex was described in Harvey et al. (1999) where the corner vortex was enhanced by the use of non-axisymmetric end wall profiling to reduce exit angle deviations at the exit from the flow.

2.3.5 Secondary Flow Models.

As discussed briefly above there are a number of diagrams of what secondary flow looks like in the literature, many of them contradictory and often quite vague in their description of the flow. Of the models described earlier, the model of Sieverding

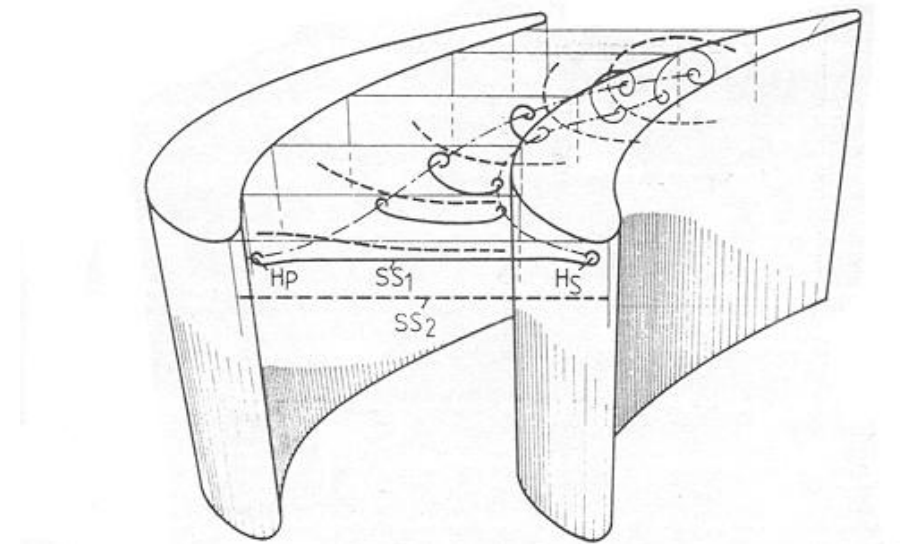


Figure 2.6: Model of Secondary Flow from Sieverding and Bosche (1983)

and Bosche (1983) seems the best description of the interlinked development of the horseshoe vortex and the passage vortex. (The model is included as Figure 2.6.) It matches up best with the detailed visualisations reported in Marchal and Sieverding (1977) and Sieverding and Bosche (1983) as well as the flow visualisations reported in this report. Most secondary flow diagrams in the literature also present a highly stylised representation of vortex structures which imply a much higher number of rotations of the vortex structure than is actually shown in Sieverding & Van Den Bosche's smoke visualisations.

The model of Sharma and Butler (1987) cannot be supported by the flow visualisations referred to above or indeed in the detailed five and three hole traverse seen in Gregory-Smith and Graves (1983) or Yamamoto (1987). Goldstein and Spores (1988) show more vortices than are generally shown elsewhere but there is evidence for the detailed structure they describe in Marchal and Sieverding (1977) and Eckelerle and Langston (1987), Wang et al. (1997) show a smoke visualisation showing many of the extra details that they put into their secondary flow model. However their model was produced under laminar flow conditions where for the same inlet boundary layer thickness the secondary flows are greater. This is because although the integrated vorticity must be the same, the distribution of vorticity is further from the endwall in a laminar boundary layer. Thus the vortex structures tend to be more stable as the action of turbulence is not present to destroy the detailed structure.

There are a number of reasons behind the apparently contradictory flow models presented:

1. Firstly, secondary flow is highly dependent on the turning angle, nozzle guide vanes turning thorough typically 60 degrees exhibit considerably less secondary flow effects than rotor blades turning through typically 110 degrees.
2. Secondly, various studies use instruments and techniques of quite different resolutions.

3. Thirdly, heat transfer studies which find high heat transfer rates near the corners of the blade and endwall tend to ascribe these high rates to the existence of a vortex structure e.g. Goldstein and Spores (1988) and Roy et al. (2000). This is not to say that the structures they describe do not exist, merely that they are not shown up in conventional flow field measurements.

In the author's view detailed models of secondary flow such as Wang et al. (1997) are unlikely to yield much information about the flow in real turbomachinery, which is after all the aim of the engineer. Real turbines tend to operate with turbulent inlet flow and high pressure stages also have appreciable fillet radii; they are inherently unsteady and can contain large temperature gradients. The detailed and small flow structures that Wang et al describe are likely to be swamped by other effects and the generality of such a detailed flow model can be called into question.

Langston (2001) reviewed progress in secondary flow research since Sieverding (1985) and came to the following conclusions:-

- new details of the secondary flow structure have emerged but detailed measurements are needed to determine their significance.
- the horseshoe vortex and the inlet boundary layer separation are important and not fully understood. The recent success of Sauer et al. (2000) shows the need for understanding of basic endwall flows
- the underlying mechanisms causing secondary flow losses are not understood and there is still a need for basic experiments

Langston's review indicates that despite the progress made in recent years there is still much work to be done.

2.3.6 Boundary Layers.

One of the concerns of investigators some years ago was the effect that varying the inlet boundary layer thickness would have on the secondary flow. Sharma and Butler (1987) present a review of three particularly detailed experiments Langston et al. (1977), Marchal and Sieverding (1977) and Gregory-Smith and Graves (1983) in which they conclude that the inlet boundary layer loss convect through the passage without causing additional loss and can be distinguished from the passage loss.

A new boundary layer is formed on the endwall after the passage vortex system has swept up the fluid from the endwall towards midspan. This is highly skewed relative to the midspan flow and the experiments of Moore and Gregory-Smith (1996) and Harrison (1989) have shown that large parts of the new boundary layer are laminar or transitional in nature. Moore and Gregory-Smith (1996) showed that when the intermittency for a mixing layer model of turbulence was specified from the measurement excellent loss predictions resulted in a 3D viscous CFD solution. This indicates that the transitional nature of the flow is important in the production of losses.

2.3.7 Blade Exit

Once the flow exits the blade, interactions with the wake of the blades and mixing losses as the vortices dissipate increase the losses attributable to the cascade. Once the flow exits the blade row the mixing losses are fully determined, a control volume analysis (See Chapter 3) shows that this does not depend on the detail of the mixing process.

Moore and Adhye (1985) describe the losses downstream of a turbine cascade. These experimenters measured the losses and secondary kinetic energy at a number of planes from 96% of axial chord to 140% of axial chord. They found that the increase in total pressure loss could be explained almost entirely by the decrease in secondary kinetic energy. They also found that one third of their losses occurred downstream of the trailing edge. Gregory-Smith (1997) reports on the vortices downstream of the blades and comments that the streamwise vorticity shed from the trailing edges rolls up rapidly into one or two distinct vortices which further complicate the flow field.

2.4 Real Turbine Flow Fields.

The flow through a real turbine is considerably more complicated than that through a low speed stationary cascade namely:

1. the flow is inherently unsteady as blades wakes from preceding blade rows interact with subsequent blade rows
2. the presence of the downstream blade row alters the flow patterns around the preceding blade row even when steady flow is examined (often called the “potential effect”)
3. some modern turbines operate in the transonic region, this means that compressible flow effects are very important
4. real turbines have an annular not a linear geometry which leads to radial pressure gradients
5. the inlet boundary layer of real machines is often skewed due the change of frame of reference caused by the change from a stationary nozzle to a rotating blade row. (See Walsh (1987)).
6. cooling flows are present in high pressure turbines
7. tip leakage flows may be significant
8. “hot streaks” are quite often present from the combustor section, indeed the flow pattern from the combustion may not only have temperature variations but be non-uniform in velocity as well
9. real machines may operate at “off design” conditions for much of their service life

Unsteady Flow Effects

Unsteady effects are the subject of much interest. Perhaps the biggest difference between the flow in a simple linear cascade and that in a real turbine is due to the rotation of the blade rows. Miller et al. (2001), describe the effect of an upstream and downstream vane on the time resolved surface pressures around a high pressure blade. At the leading of the blade the unsteady interactions cause a variation of nearly 10% of in the inlet total pressure. Anderson and Pendery (2001) describe unsteady measurements on a transonic industrial HP turbine stage, the measurements in the paper show clearly the effects of the rotor passing in the wake of the turbine. Breisig et al. (2001) show measurements on a one and a half stage axial turbine with two identical stators. The flow in the second stator which experiences unsteady flow from the rotor is very different from the first. Of particular interest is the use of unsteady transition spots to increase the blade loading in low pressure turbines, see for example Howell et al. (2000).

Compressible Flow

Perdichizzi (1990) examined the effect of Mach number variations on secondary flow development. The location of the passage vortex migrated towards the endwall and secondary flow effects were confined closer to the endwall at higher Mach numbers. At higher Mach numbers the importance of the shed vortices from the blades and the corner vortex is much higher than the main passage vortex. At higher Mach numbers the exit angle deviations are less than at lower Mach numbers. Secondary losses are dependent on Mach number, rising to a local maximum in the just subsonic region then falling in the supersonic region before rising as the flow reaches $M = 1.5$. These changes were attributed to the complex compressible flow.

In real turbines compressibility effects could lead to shock waves and their associated losses will affect the performance of the turbine stage. Denton (1993) describes some of the undesirable effects of shock waves at the trailing edge of transonic turbines.

The Annular Cascade

The annular geometry of real machines introduces a pressure gradient causing low energy fluid to migrate from the blade tip to hub in stationary blades and hub to tip in rotating blades. Moustapha et al. (1985) illustrate the effects of flow in both an annular and a flat cascade. The level of loss observed in the annular cascade is much higher although it is much more concentrated. The exit angle deviations are also much greater though again they are more concentrated over a shorter span.

The Effect of Inlet Skew

Walsh (1987) extensively investigated the effects of inlet skew he concluded that inlet skew as found in turbines makes the situation regarding loss much worse than the case found in compressor which reduces the secondary flow.

Cooling Flows

The effect of cooling flows in the turbine passage have become the subject of recent research; for example Smith et al. (2000) describe the effects on heat transfer coefficients of a film cooling technique representative of those used in real engines. The effects on the aerodynamic performance was not quantified. Day et al. (1999) and Day et al. (2000) carried out studies of the effects of film cooling under engine representative conditions and concluded that the aerodynamic loss could be increased by up to 15% by the introduction of film cooling flows. Another study which includes the effect of coolant injection on the aerodynamics of the blade row is Friedrichs et al. (1996), this study is also notable for the quality of the flow visualisation produced. Friedrichs et al. (1996) conclude that coolant ejection under the lift off lines of the various vortices is inefficient because the coolant is rapidly carried away from the blade surface. Conversely coolant ejection near the blade pressure surface is efficient as the coolant is distributed more effectively.

Tip Leakage Flows

Tip leakage flows introduce additional complexity and losses into the turbine flow field, this process is described in Wallis et al. (2000) and Harvey and Ramsden (2000) along with strategies for reducing the losses introduced by the tip leakage flows.

Combustor Non-uniformities

Some recent attempts to model the transport of “hot streaks” from the combustion section of the engine around nozzle blades are described in Dorney and Gundy-Burlet (2002). The interaction of the hot streak from the combustion chamber and the blade can lead to local overheating of the blade and premature failure. Dorney and Gundy-Burlet describe a strategy for minimising damage to the engine by optimising the “clocking” of the hot streak with the first stage nozzle guide vane. Prasad and Hendricks (2000) describe computational studies of the varying blade twist to ameliorate the effects of hot streaks.

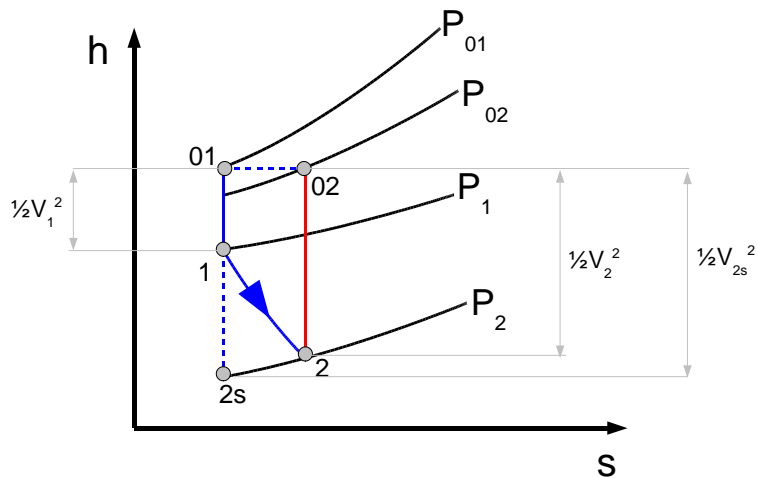
Off Design Performance

The off and on design performance of a low pressure turbine blades was investigated by Hodson and Dominy (1987). The loss was increased with increasing Reynolds number and increasing incidence, however the effects were not straightforward with variations induced by suction surface separation and endwall flow interaction for example.

2.5 Loss Production

2.5.1 Definitions of Loss.

Denton (1993) commented that:-



Enthalpy-Entropy Diagram for a Turbine.

Figure 2.7: h-s diagram.

In general any flow feature that reduces the efficiency of a turbomachine will be called loss but this does not include factors that affect the cycle efficiency as opposed to the turbine or compressor efficiency.

Denton also concluded that the only rational measurement of loss in an adiabatic machine was entropy production. In this section these concepts are related to the measurements taken later on in this thesis. Figure 2.7 shows an enthalpy-entropy diagram for a stationary blade row. There are several common definitions of loss coefficient and blade efficiency in use, two of them are used in this section.

A commonly found definition of loss coefficient is that of pressure loss coefficient:-

$$Y = \frac{P_{01} - P_{02}}{P_{01} - P_{2s}} = \frac{\Delta P_0}{\frac{1}{2}\rho V_{2s}^2} \quad (2.3)$$

This is simply the change in stagnation pressure normalised by the ideal or isentropic downstream dynamic head. An inspection of the h-s diagram reveals the connection with entropy changes immediately for no change in entropy points 01 and 02 will be in the same place and Y will be zero.

Another commonly found definition of loss production is an isentropic efficiency which is more useful for design purposes:-

$$\eta = \frac{h_{01} - h_2}{h_{01} - h_{2s}} \quad (2.4)$$

This is simply the enthalpy change that we obtain divided by the enthalpy change that occurs in a reversible (isentropic) expansion. For a stator blade or for a cascade arrangement, no work is done therefore $h_{01} = h_{02}$, and it is more logical to think of η as the ratio of actual kinetic energy leaving the cascade to the kinetic energy leaving the cascade in an isentropic case.

There is a simple relationship between Y and η for the cascade case:-

$$\eta = \frac{h_{01} - h_2}{h_{01} - h_{2s}} = 1 - \frac{h_2 - h_{2s}}{h_{01} - h_{2s}} = 1 - \frac{h_2 - h_{2s}}{\frac{1}{2}V_{2s}^2} \quad (2.5)$$

where V_{2s} is the isentropic exit velocity. Recalling from basic thermodynamics that:-

$$Tds = dh - \frac{1}{\rho}dP \quad (2.6)$$

So for 2→2s, $P = \text{constant}$ and assuming incompressible flow $T \simeq \text{constant}$, therefore:-

$$s_2 - s_{2s} = \frac{h_2 - h_{2s}}{T} \quad (2.7)$$

Once again recalling from basic thermodynamics that:-

$$T_0 ds = dh_0 - \frac{1}{\rho_0} dP_0 \quad (2.8)$$

For 01→02, $h = \text{constant}$ and for incompressible flow $\rho = \rho_0 = \text{constant}$ and $T \simeq T_0$ therefore:-

$$s_{02} - s_{01} = \frac{\Delta P_0}{T\rho} \quad (2.9)$$

but (see Figure 2.7)

$$s_{2s} - s_2 = s_{02} - s_{01} \quad (2.10)$$

$$\Rightarrow h_2 - h_{2s} = \frac{\Delta P_0}{\rho} \quad (2.11)$$

$$\Rightarrow \eta = 1 - \frac{\Delta P_0}{\frac{1}{2}\rho V_{2s}^2} \quad (2.12)$$

$$\Rightarrow \eta = 1 - Y \quad (2.13)$$

In this thesis the *upstream* dynamic head is used to normalise the change in stagnation pressure, this in contrast to Y where the *downstream* dynamic head is used to normalise. The upstream dynamic head is much more easily measured for the Durham cascade than the downstream dynamic head which explains its use. Walsh (1987), Cleak (1989), Biesinger (1993), Moore (1995) and Hartland (2001) all worked on the Durham Cascade and used the same pressure loss coefficient. If the two dynamic heads are known converting between each one is trivial and this is done in Appendix D as part of a calculation to relate loss coefficient changes to real machine efficiencies.

2.5.2 Loss Production and Secondary Flow

Although the production of loss and secondary flow are linked the two are not synonymous. In particular when a sheared flow is turned secondary flows are in theory be produced without the action of viscosity and therefore without any production of loss. In the numerous secondary flow studies that have been carried out the loss peaks and vortex centres do not necessarily coincide. Fundamentally loss occurs when velocity gradients between adjacent elements of fluids are high, bringing viscous dissipation of energy into play. In the early years of gas turbine development several correlations of experimental data were produced to attempt to predict loss. A particularly well known example is the prediction method of Ainley and Mathieson (1951). Provided that the prediction is applied to blade designs that closely

resemble the ones used to produce the correlation then the method will produce results within $\pm 2\%$ for efficiency. However this sort of method provides little insight into the physical processes that cause the loss, nor can they evaluate any novel method of reducing the loss.

Some attempts have been made to put more of the increased physical understanding of secondary flow into practical use. Gregory-Smith (1983) produced a method that predicted loss, three components modelling the physical nature of the flow; a triangular loss core made up from the inlet boundary layer, a new boundary layer loss calculated from a two dimensional calculation and the assumption that the third loss component was proportional to the secondary kinetic energy predicted by secondary flow theory. The procedure appears to agree well with some nozzle guide vanes data, however the applicability to high turning rotor blade flows is probably limited by the assumptions that the secondary flow theory rests upon.

Sharma and Butler (1987) present another method that attempts to use the “penetration height” of the secondary flow region to predict the losses, though this of necessity makes simplifying assumptions about the secondary flow. The authors quote an accuracy of $\pm 10\%$ for this method.

The current “state of the art” methods for predicting loss without empirical data are CFD calculations. Denton (1993) suggested that even for a two dimensional cascade the best available methods would be within $\pm 20\%$ of the actual loss which explains why empirical data is used even today.

Denton (1993) and Denton and Cumpsty (1987) describe the process of loss production in turbomachines. They make the valid point that most descriptions of loss in the literature are rather vague and that a more rigorous description would be to use increase in entropy rather than increase in loss. Denton and Cumpsty list the generic forms of loss found in turbomachines:

1. profile loss
2. tip leakage loss
3. trailing edge loss, due to finite thickness of trailing edge blades
4. annulus loss due to skin friction outside the blade rows
5. secondary loss
6. leaving loss due to wasted kinetic energy leaving the machine
7. shock loss due to shock waves at the trailing edge of the blades
8. windage loss

Denton’s 1993 paper expands on theme of entropy being the only sensible way of regarding loss generation in real turbomachines.¹ He also included an in depth discussion of the generation of “secondary loss” although he called it endwall loss.

¹This thesis uses total pressure but for steady, incompressible flow the entropy and total pressure are proportional to each other

This concerned the losses produced by the secondary flow patterns described above and the growth of the boundary layer at exit from the blade or nozzle row. Denton commented that:

In all the situation [loss production] is too complex and too dependent on details of the flow and the geometry for simple quantitative predictions to be made.

He regarded the best hope for accurate loss prediction as being the development of three dimensional Naiver Stokes solvers.

However some ten years after Denton's paper CFD predictions of loss remain somewhat poor. Examples of this can be seen (although somewhat out of date) in Gregory-Smith (1995), who showed the results of some twenty or so computations of the Durham Cascade that illustrate wide variations in the loss prediction. Further examples of the CFD predictions of the Durham Cascade may be found in Chapters 7 and 8. For the purpose of design, capturing the trend in loss with geometry changes may be useful even if the absolute values are in error. However it is not the case that the CFD solution is guaranteed to obtain the correct trend.

2.6 Methods of Loss Reduction.

Not surprisingly methods of loss reduction have been the subject of much discussion in the literature. There have been a great many attempts at geometry changes to improve blade performance, namely:

1. Profile Aerodynamics - Aft Loading.
2. Radial variations in blade shape. Such as lean or sweep.
3. Improved Film Cooling Schemes.
4. Utilising Unsteady Flow Interactions.
5. Leading Edge Modifications.
6. Axisymmetric end wall profiling.
7. 3D Non-Axisymmetric End Wall Profiling.

Haller (1997) presents a review of the work conducted at the then GEC-ALSTHOM (now ALSTOM) to improve the efficiency of steam turbines. Haller attests to the importance of having good two dimensional profile designs before three dimensional effects are considered. "Aft loaded" profiles where the cross passage pressure gradient is greatest across the blade at the rear of the blade passage is considered to reduce the secondary flows by reducing the cross passage pressure gradient where the secondary flows are formed at the start of the passage. Haller described GEC-ALSTHOM's development of what were termed "controlled flow" blades which reduced the throat openings at hub and tip thereby reducing the mass flow and therefore secondary loss at the hub and the tip.

Harrison (1989) describes a comprehensive investigation into the performance of leaned blades. He reported that simple lean reduces velocities at one endwall and increases them at the opposite wall. Compound lean reduces endwall losses but at the expense of increased midspan losses. This meant that compound lean in particular had no effect on overall loss coefficient but did substantially reduce the exit angle deviations as well as producing more uniform loss at the exit. This is likely to accrue benefits further downstream in real machines.

Improved film cooling schemes and loss reduction from them has received considerable attention but with mixed results. A recent work of note is Sargison et al. (2002a) who described the testing of a novel design of cooling hole geometry that produced an effectiveness equivalent to that of a slot. Sargison et al. (2002b) describe the testing of this design in engine representative conditions and they conclude that their design produced cooling effectiveness comparable to conventional cooling methods but with a greatly reduced aerodynamic penalty. The work of Biesinger (1993) is discussed below, Biesinger worked on air injection into the Durham cascade to reduce the overall loss and his work is discussed in the section referring to previous work on the Durham Cascade.

A novel scheme developed for low pressure turbines is to use the transitional nature of turbomachinery flows to increase blade loading and reduce the blade numbers for a given power output. Howell et al. (2000) describes this work which is applicable mainly to low pressure blades. In high pressure turbines the secondary flow dominates the flow structure through the blade and this would reduce the scope for such a technique to be applied. Due to the high aspect ratio blades (tall and thin) used in low pressure turbines the two-dimensional profile loss is extremely important and this is what the work of Howell et al. (2000) aims to reduce. However this is more of a profile loss control method rather than a secondary loss reduction method.

A recent paper Sauer et al. (2000) describes loss reduction by leading edge modifications at the endwall. This paper is of note since unlike many loss reduction techniques, Biesinger (1993), Aunapu et al. (2000) and Burd and Simon (2002) for example, it actually reduces losses. Sauer et al manufactured a bulb for the leading edge of the turbine blade at the endwall, this bulb reduced in size so that at 5% of blade span the blade profile was normal. The rationale behind this loss reduction methodology was to increase the strength of the suction side of the horseshoe vortex so that it would prevent the impingement of the passage vortex on the suction surface of the blade. The authors report a phenomenal 47% reduction in secondary loss, although they present no results for overall loss and no measurements within the blade passage. A similar method was used by Zess and Thole (2002) who describe the design, manufacture and test of a leading edge fillet which eliminated the horseshoe vortex and produced large reductions in turbulent kinetic and streamwise vorticity - the study used laser doppler velocimetry so no loss results are available.

A form of loss reduction which was reportedly being put into production steam turbines some time ago is axisymmetric end wall profiling (Warner and Tran, 1987). The work on these axisymmetric end wall profiles was first suggested by Russian engineers, hence they are sometimes called a *Russian Kink*. See for example Deich et al. (1965) and Figure 2.8 for a schematic diagram. Warner & Tran describe the use

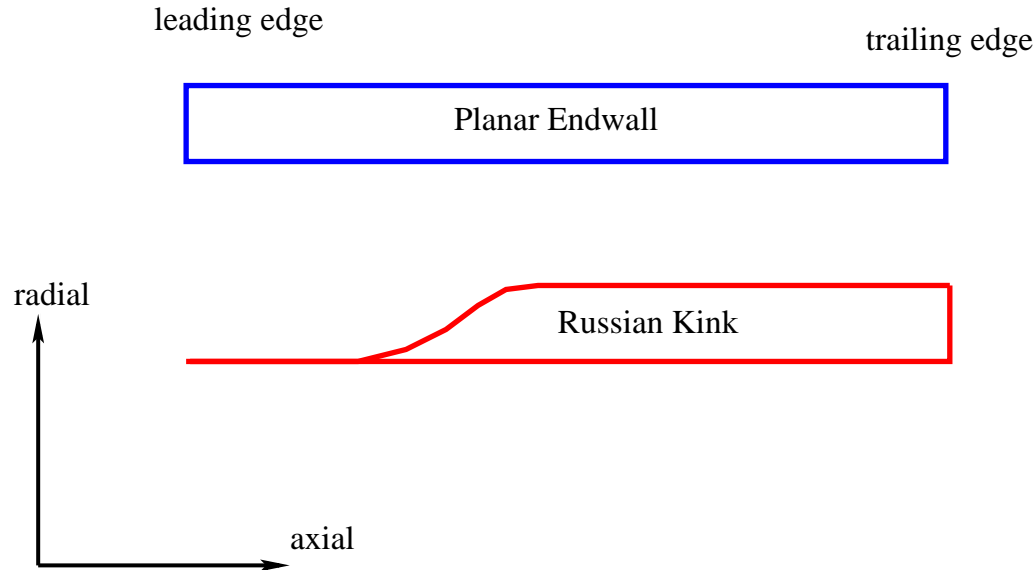


Figure 2.8: Schematic of *Russian Kink*

of a *Russian Kink* and the explanation for its success is based on acceleration of the boundary layer along the contour leading to a thinner boundary layer. The second reason is the “turn then accelerate” philosophy imposed on the flow rather than the “turn and accelerate” one taken in the then Westinghouse Electric’s machines. As there is a higher aspect ratio at the region of highest turning the fluid turns at minimum velocity which aims to reduce the secondary flows.

Recent research on axisymmetric endwalls includes Duden et al. (1999) who redesigned a low pressure turbine profile along with axisymmetric endwall profiling to reduce loss. Overall loss reduced by 5% with secondary loss reducing by 29%. Their rationale for the reduced losses was that they had reduced the radial pressure gradient and obstructed the radial movement of the secondary flow. They also commented on the benefits of aft loading the blade profiles.

Dossena et al. (1999) reported on an axisymmetric end wall design for a first stage nozzle guide vane. The authors reported a reduction of 35% overall loss and a 54% reduction for secondary loss. This is remarkably successful but it is suspected that they have reduced the blade loading in their cascade which would reduce loss and secondary flow without being beneficial as a greater number of blades would be required to do the same amount of work.

Burd and Simon (2002) examined end wall profiling. They used a two passage cascade and installed a contoured endwall on only one of the blade passages, making their results somewhat suspect.

With the ready availability of three dimensional viscous CFD solutions a number of automated design systems are being produced which optimise the geometry of the blade and endwall automatically, see for example Shahpar (2000). The basic problem with these systems lies in the unreliability of certain aspects of the CFD prediction. Harvey and Ramsden (2000) list in decreasing order of accuracy the results from CFD predictions:

1. static pressure

2. mass flow and exit flow angle distributions
3. secondary flows
4. overall entropy rise
5. shocks and separations
6. local skin friction / heat transfer rates

Despite the limited quality of flow predictions from current CFD codes, these techniques have been shown to be extremely useful design tools. Substantial reductions in loss have been obtained using CFD based design systems, for example Harvey et al. (1999), Duden et al. (1999), Brennan et al. (2001) and Harvey et al. (2002) all used CFD to optimise shapes before any testing was carried out.

Denton and Xu (1999) provide a useful summary of the “thought models” behind recent three dimensional blade and passage design. Denton and Xu remark that are actually at least three theories for the reasons behind the success of blade lean in reducing endwall losses.

- the increase in load at mid-span means that most work is done at the most efficient location
- low-energy fluid near the endwall is redistributed by the spanwise pressure gradients and this prevents separation and loss accumulation near the endwalls
- the entropy creation (loss generation) per unit surface area is proportional to the local velocity to the power two or three. For compound lean the area exposed to an increase in velocity is much less than that exposed to a decrease in velocity.

The third theory is regarded as the most credible by Denton and Xu. The authors remark that although the effects of three dimensional flow and design features on inviscid flow can be clearly understood and exploited to improve efficiency, the viscous part of the flow is much more difficult to understand and predict qualitatively. The authors further remark that although three dimensional features have been introduced into real machines and provided tangible benefits there is a limited understanding of how these features actually work. This is of course relatively common in engineering, where the motivation is to produce a solution to a problem and leave the detailed understanding of how the device works until a later date.

2.7 Previous Research in the Durham Facility.

Endwall profiling research on the Durham facility is described in the next section, however previous to this work there have been a large number of papers and PhD theses on secondary flow using the same facility. Graves (1985) described the building of the original cascade which provided detailed information on secondary flows in turbine blades. Walsh (1987) studied the effects of inlet skew of the boundary layer on secondary flow in the cascade. This was achieved by placing a moving belt

upstream of the cascade and rotating the belt to provide skew on the boundary layer. Skew is experienced in real machines as a result of the changing frame of reference when the flow passes from the stationary hub to a rotating blade row. The incoming boundary layer is “skewed” to point in a different direction from the mainstream flow by the action of the casing surface.

Walsh found that skew profoundly affected the secondary flow in the cascade. The effect of inlet skew is to increase the overall loss by 56% of the base case value, when the skew was reversed substantial reductions in loss occurred. The test rig that Walsh used however only represented the case where the boundary layer is skewed. It does not represent the action of an upstream blade row.

Cleak (1989) presented a detailed investigation of the capability of three-dimensional Navier-Stokes solvers to predict losses and flow features in the Durham Cascade. He found in common with other researchers that accurate predictions of pressure fields were possible but that loss prediction and prediction of the Reynolds stress in the cascade were poor. Although Cleak’s conclusions must now be viewed with caution as CFD technology has advanced at a very fast rate, the general conclusion seems to hold.

Biesinger (1993) investigated the possibility of reducing losses by injection of air through an upstream slot in the Durham Cascade, the air was injected tangentially so as to oppose the production of secondary flows. Although a reduction in loss was observed, when the additional kinetic energy added by the tangential injection is taken into account, no net reduction in loss was calculated. However when the mixed out losses were considered some blowing configurations did produce some overall benefit, and the detailed operation of each blowing system was crucial to the results obtained. Many other investigations on end wall blowing have been conducted such as Burd and Simon (2002) which have shown mixed results. As Biesinger (1993) pointed out many investigations tended to ignore the energy input to the injected air.

The attraction of using air injection is that air is injected to the blades and stators in gas turbines for cooling purposes in any case, so that if successful this loss reduction method would be easily applicable. Two comments are worthwhile here, the first is that since Biesinger has shown small variations in injection flow have significant results on the loss and flow structures, some sort of systematic design of the injection system should be used. The second is that since cooling flows are already injected into engines the criteria for success for such a loss reduction scheme should be if it reduces losses without increasing the amount of energy required for blowing as well as satisfying the cooling duties. There is no doubt that the design of such a system would be difficult but as Rose (1994) pointed out current injection methods are judged to disturb the flow rather than aid it.

The key to a successful cooling/loss reduction scheme would be CFD predictions of the injection process, that would capture the effects of the small variations described in Biesinger’s Thesis. Biesinger (1993) showed that the CFD codes available at the time did not accurately capture the flow features associated with injection.

Moore (1995) investigated the Durham cascade using hot wires to provide data for the validation of turbulence and transition models. Moore found that significant areas of the blade and endwall surfaces were in fact under laminar or transitional flow

conditions, rather than being fully turbulent. Moore and Gregory-Smith (1996) also found that much better results were obtained from CFD predictions for loss when the correct laminar/turbulent boundary layer distribution was imposed onto the CFD solution. However predicting transition in complex three dimensional flow is difficult.

2.8 3D Endwall Profiling.

Only a few researchers have attempted to use non-axisymmetric profiles in cascades or machines. Morris and Hoare (1975) and Atkins (1984) are two early examples.

Atkins carried out a systematic design of endwall profiling by trying out a large number of profiles designed using an inviscid CFD flow solver. He criticised the ad hoc way in which profiles were designed in the past and indeed designed axisymmetric profiles that successfully reduced loss.

Atkins put down the success of the *Russian Kink* profile down to a reduced cross passage pressure gradient at the endwall. In profiles where the exit area is reduced compared to the entry of the cascade the acceleration of the flow was reported to aid in the reduction of loss.

However Atkin's three dimensional profiles were not as successful, both worked on the principle of reducing the cross passage pressure gradient. Each profile attempted to modify the pressure distribution on one side of the blade passage and then reduced linearly to zero height at the other side of the passage. Atkins showed at best an overall loss reduction of 9.2% and the increase in loss for the two three dimensional end wall profiles. Atkins also completed experiments which related the total loss to the change in aspect ratio and found an inverse relationship. Atkins also reported that the passage vortex appears even in the absence of inlet vorticity as the new boundary layer generated on the endwall within the blade passage is overturned.

The current work at Durham University was started by the work of Rose (1994). Rose describes a CFD study into the use of non-axisymmetric profiling to reduce static pressure variations in the flow field downstream of a nozzle. The idea was that if the static pressure variation is reduced then the coolant pressure can be set at the lowest possible value meaning that only just enough coolant goes into the rotor, improving machine efficiency. Rose concluded that:

the use of axisymmetric endwalls can be viewed as an arbitrary and unnecessary design constraint

Rose produced a design of endwall that CFD predicted would reduce the static pressure variations.

Rose's idea was used by Hartland et al. (1998) and implemented in the Durham Cascade. A new endwall was designed which reduced the static pressure variations at exit from the blade row. The secondary loss however increased by around 21%, with the overall loss increasing by 11%. However the research did prove the soundness of the basic idea.

Rose's profile used the principle of streamline curvature, where a concave curvature was used to increase the local static pressure by reducing the local velocity

high speed – low pressure

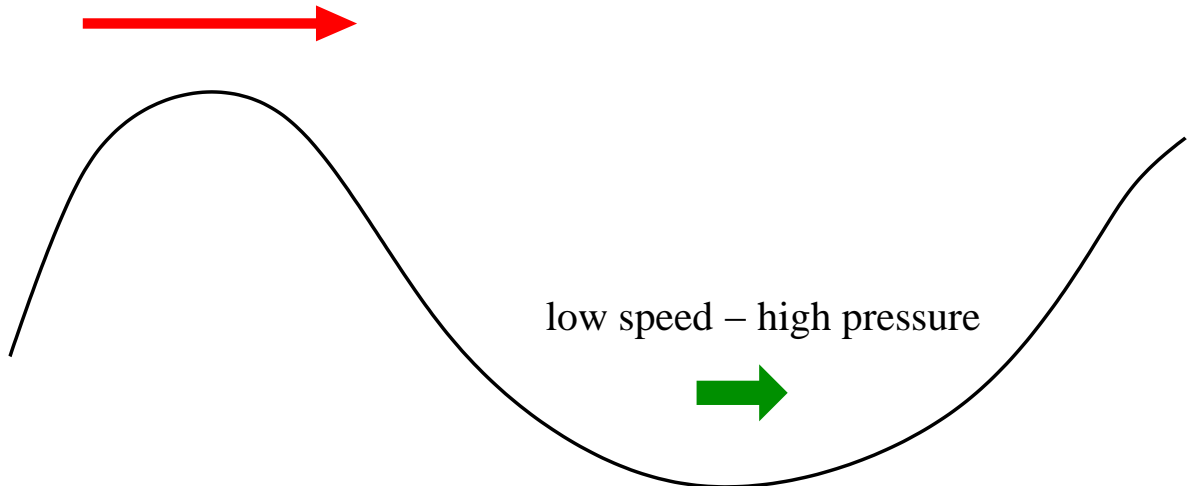


Figure 2.9: Streamline Curvature:- basic idea.

and a convex curvature used to increase local velocity and decrease the static pressures, see Figure 2.9. The streamline curvature approach was then used to try to reduce the cross passage gradient in the blade passage and reduce the secondary flows caused by it.

Yan (1999) described work on non-axisymmetric endwall profiling applied to a model of a steam turbine nozzle. Yan designed his profile without the aid of any automated design systems and designed with the maximum profiling in the latter half of the blade passage. He reported a total loss reduction of just over 4%. Although less than the loss reduction obtained by Hartland et al (1999) it is perhaps understandable as the nozzle will have less secondary flow and less potential for loss reduction than a rotor blade. Yan's cascade turned the flow through 77° where as the "Durham Cascade" which Hartland used has a turning angle of 111° .

Harvey et al. (1999) describes the design of a non-axisymmetric endwall profile for the Durham Cascade. Previous profiles were designed using a largely trial and error approach with considerable skill required on the part of the designer. Harvey et al describe a novel design method that introduces a systematic approach. This approach is as follows:

1. generate a systematic set of perturbations for the endwall
2. complete a 3D viscous calculation for each perturbation
3. construct a linear sensitivity matrix
4. use linear superposition to construct new flow fields and geometries
5. from these new flow fields generate the endwall profile

The method was then applied to the Durham Cascade. The aim of the design study was to reduce the exit angle deviations from the blade row as exit angles are predicted well by CFD, but other quantities such as loss are predicted unreliably.

The final design incorporated a novel feature near the trailing edge of the blade, a bump which enhanced the corner vortex in order to reduce the overturning near the endwall.

Hartland et al. (1999a) describes the testing of the profile designed by Harvey et al in the Durham Cascade. Hartland's tests show a reduction in secondary loss of 29% with an overall loss reduction of 20%. However this was not the design intent which was to reduce the exit angle deviations at the cascade exit. Hartland showed a reduction in exit angle deviation of around two degrees. This profile is used in the current work and is generally referred to as P1. The profile used for Hartland's work was designed with perturbations well upstream and downstream of the blade passage. Clearly this is unrealistic for a real turbine and a second profile was designed with the profiling restricted to the blade passage. This profile designed by Rolls-Royce was built and tested in the Durham Cascade by Jayaraman (2000). This second profile is used in the current research and is generally referred to as P2. This profile demonstrated a reduction in secondary loss and a reduction in exit angle deviation of around three degrees. The level of reduction of secondary loss is less than for Hartland's profile at 8% reduction on secondary loss and 5% overall.

At the start of this programme of work the reasons for the widely differing performance between Profile P1 and P2 were not apparent and one of the main reasons for conducting this research was to understand the differing performance of the profiles.

Following the successful work in Durham, Rolls-Royce have conducted several machine representative tests on endwall profiles, operating in 3/4 scale rotating rigs. Brennan et al. (2001) describes the design process for a redesign of the Trent 500 HP stage to take advantage of profiled end walls. The testing of this design is described in Rose et al. (2001) who found a 0.59% increase in stage efficiency (with an accuracy of $\pm 0.25\%$) which exceeded the design intent. Though this is a relatively small change in efficiency the remarks made above indicate that it is well worth having. Furthermore the Trent 500 HP blade represented "state of the art" aerodynamics in the first place and had weak secondary flows, so the case chosen was not perhaps the best approach to demonstrate the benefits of endwall profiling. Harvey et al. (2002) presented results from tests in a multi-row test environment and showed that endwall profiling still provided benefits. Endwall profiling is now being deployed onto real turbomachinery.

2.9 Overview

Despite the high level of efficiency of modern components, due to the large size and large number of modern machines even small gains in efficiency are well worth while. This chapter has described secondary flow in linear cascades. The flow is complex and the major flow structures; passage vortex, horseshoe vortex and corner vortex are well known, although the production of loss from these features is not currently well understood.

Real turbine flow fields are much more complicated than the flow in linear cascades incorporating unsteadiness, heat transfer, shock waves, tip clearance to name a few of the effects. Despite this the secondary flow features seen in cascade studies

seem to carry over into real turbine measurements, see for example Haller (1997).

A number of methods of loss reduction using the enhanced knowledge of the flow field have been proposed. Actually achieving reliable methods of loss reduction is quite difficult as a large proportion of authors show a lack of success in reducing the loss. Three dimensional non-axisymmetric end wall profiling has been shown to be an effective method of loss reduction both in University test rigs and in real machine representative test rigs.

Chapter 3

Experimental Technique

EXPERIMENT METHODS used in the so-called Durham Cascade are the subject of this chapter. The techniques used to obtain the flow visualisation and pressure probe results in this thesis are described here. There is also an extensive section on the data processing used for the cascade. The descriptions contained here are detailed; readers who do not want to read about the experimental technique can skip directly to chapters with the results in them. Details of the hot film work can be found in the chapter with the experimental work. The results from the hot film work cannot be understood without careful reference to the hot film methods whereas pressure probe and flow visualisation techniques are very similar from one experimenter to the next.

3.1 The Durham Cascade

The Durham Cascade is a low speed, large scale linear cascade of six rotor blades taken from a high pressure rotor design. The blades are designed to have aerodynamic similarity with the real machine rather than geometric similarity as the real blades operate in the transonic region. The cascade has been a popular computational test case and has been in use since 1983 and the subject for six PhD studies and numerous publications.

Air is supplied to the cascade by means of a variable speed centrifugal fan. The fan is completely enclosed and the incoming air is filtered by means of a number of Vokes filters. The air then passes through a number of screens and settling chambers before emerging through a honeycomb into the working section. In the working section a grid of bars is mounted 1.4 m in front of the leading edge of the blades in order to give a turbulence intensity of around 5% at inlet. A boundary layer bleed is provided 150mm downstream of the turbulence grid before the cascade is reached. The flow is turned through 111° and discharges upwards. The design data for the cascade is given in Table 3.1. The boundary layer bleed is only present on one side of the cascade so the inlet flow is slightly asymmetric. The inlet boundary layer is characterised in Table 3.3 and as is immediately apparent it is large relative to the instrumentation size and is turbulent. Table 3.3 is derived from the inlet boundary measurements described in Chapter 5. Moore (1995) describes the construction of the cascade in more detail.

Inlet Flow Angle	42.75°
Blade Exit Angle	-68.7°
Blade Chord	224 mm
Blade Axial Chord	181 mm
Blade Pitch	191 mm
Blade Half-Span	200 mm
Reynolds Number (Axial Chord and Exit Velocity)	4.0×10^5

Table 3.1: Design Data for the Durham Cascade

Dynamic Head	215 Pa
Free stream Velocity	19.1 ms^{-1}
Density of Air	1.179 kgm^{-3}
Dynamic Viscosity	$1.814 \times 10^{-5} \text{ Nsm}^{-2}$

Table 3.2: The Standard Day

The rig is set to operate as close as possible to the correct Reynolds number, making some attempt to vary the speed of the airflow through the tunnel to compensate for the variations in atmospheric conditions. Once this is set all the pressure probe readings are compensated to standard day conditions, so that readings from different days can be compared to one another. Table 3.2 lists the the standard day conditions to which all pressure readings are corrected.

The cascade blades have a span of 400mm and a chord of 224mm. This gives an aspect ratio of 1.78 which means there is a large region of undisturbed midspan flow. The blades are cantilevered from one endwall, into which a total of twelve slots are cut to provide access for measurement probes. Only one passage is instrumented. The other endwall consists of a series of panels which cover a blade passage. These panels which can be either profiled or flat are locked in place when running by a large hardboard sheet (see Figure 3.2). This means that for profiled endwalls only one side of the passage is profiled. Measurements are however only taken in half the blade passage (i.e. up to 200mm from the endwall), later chapters will show that the midspan flow is identical for the planar and profiled geometries so this slight asymmetry has not affected the flow.

Static pressure measurement tapings are provided on the endwall for the instrumented passage and along the surface of one of the blades. Figure 3.1 shows the general layout of the cascade. Figure B.1 in Appendix B shows the direction of the ordinates relative to the blade shapes as well as defining yaw and pitch angles.

99% Thickness	30 mm
Displacement Thickness	2.13 mm
Momentum Thickness	1.76 mm
Shape Factor	1.21

Table 3.3: Inlet Boundary Layer

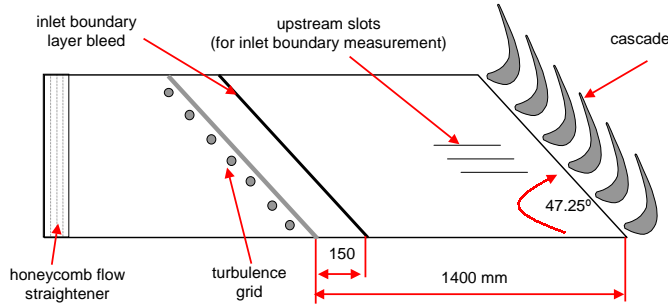


Figure 3.1: The Durham Cascade

3.1.1 Profiled End Walls

Four different endwall geometries were used during the course of this thesis, P1 and P2 were originally manufactured and tested by Hartland (2001) and Jayaraman (2000) respectively. The third was designed by Rolls-Royce during this project and was manufactured and tested by the author. The results for the P3 profile are discussed separately from the P0, P1 and P2 results.

Profile P1 was designed using an early version of Rolls-Royce's design system (FAITH)¹ and the profiling extends over the entire computational domain. The computational domain is actually larger than the cascade so the P1 results do not include all the profiling that Rolls-Royce designed but this is felt to be a minor effect. A contour plot of endwall heights is shown in Figure A.1 on page 285.

Profile P2 was designed with a later version of the FAITH code and has the profiling restricted to the blade passage. This means that there is a region of extremely sharp curvature around the leading edge pressure surface. This can be seen in Figure A.2 on page 286.

The design of P3 is discussed in the relevant chapter, but the aim was to achieve the maximum possible loss reduction so it has the most extreme curvature of all three profiles. P3 is also the only profiled endwall that has the same maximum reduction in height as increase in height. P1 and P2 both have higher peaks than troughs. Height contours for P3 can be found in Figure A.3 on page 287.

¹FAITH stands for Forward And Inverse THree dimensional linear design system.

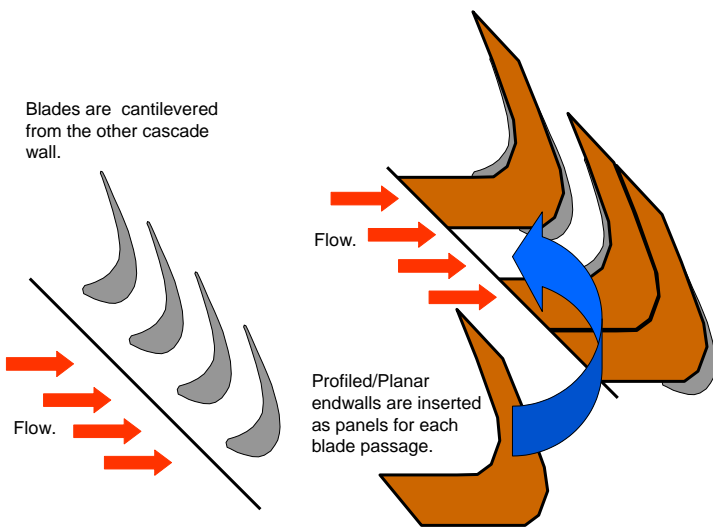


Figure 3.2: Profiled and Planar Endwall Fitting

3.2 Flow Visualisation Technique

3.2.1 Smoke Visualisation.

Smoke Visualisation was attempted in the cascade but did not produce worthwhile results. The smoke produced no discernible pattern by eye and the experiments were not carried further. Cleak (1989) reported a turbulence intensity of 5%. These high levels of turbulence in the Durham cascade appeared to be the main factor against achieving good results. This turbulence intensity is in place to represent real turbine conditions and is achieved by a grid of bars 1.4m upstream of the cascade. Marchal and Sieverding (1977) report excellent smoke flow visualisation results but their turbulence intensities were of the order of 0.5%, although they experimented with similar speeds to obtain their results.

3.2.2 Oil/Dye Visualisations.

The principle of oil/dye surface flow visualisations is that a mixture of an oil (diesel or paraffin) and some dye is applied to the surface of the model of interest. This model is then placed in the wind tunnel, where the flow is applied at the speed of interest. The oil/dye mixture then follows the path of the flow on the model surface, with regions of low velocity showing up as the oil/dye stays largely in place. Separation bubbles are easily identified as a “slug” of fluid builds up in the region of recirculation. Finally regions of high shear stress near the wall are identified as the oil/dye mixture is removed from the model surface altogether. The technique is described extensively in Barlow et al. (1999), Merzkirch (1974) and Maltby (1962) which contains the best information on the technique.

It is important in oil/dye work to ensure that a sufficiently high velocity is obtained in the wind tunnel, otherwise gravity will cause the pattern on the blades and endwall to be meaningless. In regions of low velocity the oil/dye can also re-

main in place leading to a pattern from the paintbrush used to apply the mixture and nothing else. The velocities in the Durham cascade are just high enough to start getting acceptable flow visualisation results. For example on the suction side of the blade and in the blade passage good flow visualisation was obtained without too much difficulty. The pressure side and upstream of the blade leading edge on the endwall however presented more problems as the velocity in these regions was relatively low. The effect of velocity increase on flow visualisation results is illustrated with great clarity in Marchal and Sieverding (1977) where oil visualisations are illustrated showing exit velocities from 20 m/s to 160 m/s, although it should be noted that oil of differing viscosity was used in the tests.

3.2.3 Experimental Method.

The following general procedure was used when performing the tests:

- Oil/dye was mixed together in ratios of 4:1 (diesel: dye by volume) to 2:1. The diesel was standard road going diesel and the dye was a mixture of Fiesta daylight colours and an inert bulking agent. The dye had the useful property of fluorescing under ultraviolet (UV) light meaning the pattern can be observed much more clearly by the naked eye under UV light.
- The oil/dye was applied to the endwall or blade in a uniform manner as possible using a paintbrush. As far as possible the brush strokes were kept perpendicular to the expected direction of flow so that any brush marks would be distinguishable from flow streaks.
- The model was placed into the wind tunnel, secured and then the wind tunnel was brought up to speed as rapidly as possible to avoid the dye 'running' while the tunnel was stationary.
- The tunnel was run at full speed for between six and thirty minutes, although the main pattern appeared to have formed within the first five minutes. The longer runs gave the pattern time to dry out.
- Once the pattern had established itself on the blades the tunnel was stopped and the panel/blades removed for photography.
- Each flow visualisation run was given a unique number to identify it.

As well as coating the entire surface of the endwall or blade with oil/dye a number of variations on the technique were attempted. Areas which had not moved under action of the original flow were sprayed with oil in an attempt to get them moving. However only limited success was observed. The flow patterns that appeared on the blade when only the endwall was painted were also recorded showing the migration of fluid from the endwall to the blade. The blades were also coated in a sticky backed plastic film, which allowed the pressure and suction surfaces of the blades to be investigated by forming a pattern and then removing the plastic film. This enables the suction and pressure surfaces to be viewed 'folded out' but it was felt that this did not produce better results than simple suction surface flow visualisation.

Parts of the panels were painted with dye with other sections left blank but this was of limited value. Some useful information can be obtained by painting the blade surface a different colour to the endwall which shows some of the migration of fluid from the endwall up the blade surface.

Photographing the flow visualisation image requires almost as much effort as obtaining the image in the first place. Considerably better results were found when the endwalls were painted white and cleaned thoroughly before flow visualisation commenced, which provided better contrast with the red dye. Details of the photography are very camera specific so are not included here.

3.3 Pressure Probe Measurements

The method used for pressure probe measurements in this thesis is that of Treaster and Yocom (1979) who describe the use of five hole probes and pressure coefficients. Other researchers have examined the performance of pressure probe measurement systems Dominy and Hodson (1992) describe the effect of Reynolds number variations on the performance of five hole probes, they found that although in many cases the effect could be very small, the measurement of dynamic pressure with a five hole probe could have had an error of more than 3% due to Reynolds number effects. Main et al. (1996) describe a four hole probe that obtains all the flow variables a five hole probe does, the particular advantage over a five hole being that for high speed flow probe size is much more important. Christiansen and Bradshaw (1981) describe the effect of turbulence on pressure probes and conclude that in turbulent flows yaw angles should be obtained using the nulling technique. Alternatively though not suggested in their paper, it may be more desirable to calibrate the probe in a turbulent flow.

The rest of this section describes the automated data acquisition system used for pressure probe measurements in this thesis. A 486 PC provided control to the stepper motors which moved the traverse gear. The rig PC also read the signals from the pressure transducers or hot wire probes through an A/D converter card. All differential pressure measurements are taken relative to the upstream total pressure. (See Figure 3.3 for a schematic)

The probes used in the Durham Cascade were conventional three and five hole pressure probes. The principle of multi-hole pressure probes is straightforward, in general holes aligned with the flow will read a higher pressure than those that are not. (See Figure 3.4) With a five holed probe the top and bottom holes will give an indication of pitch angle and the left and right holes an indication of yaw. The exact difference in pressure between two holes depends very much on the individual probe geometry and in general there is no analytical solution to obtain this pressure difference. Therefore in practice the differences have to be measured before the probe is used in tests and the information stored in what is normally called a “calibration map”. As well as obtaining yaw and pitch angles a five hole probe can also measure static and total pressure leading to a very complete description of the flow field. The three hole probes used for this thesis could only obtain yaw angles, total pressure and static pressure. If there are large pitch angles present in the flow the probe may not produce accurate readings.

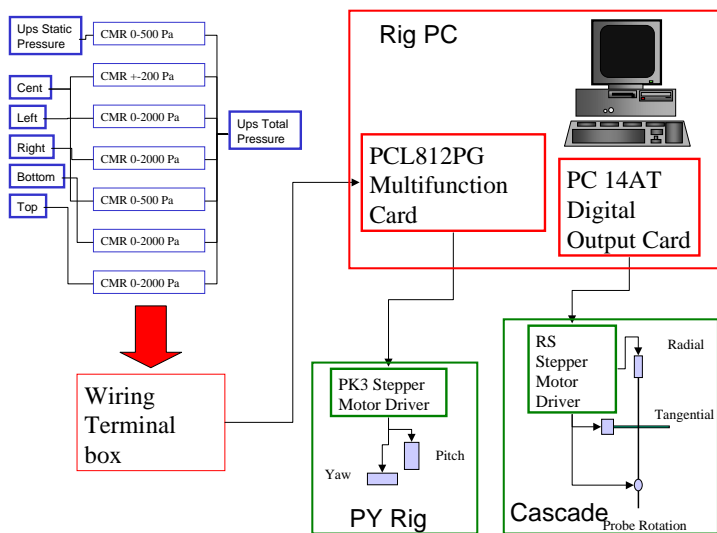


Figure 3.3: Schematic of Measuring System

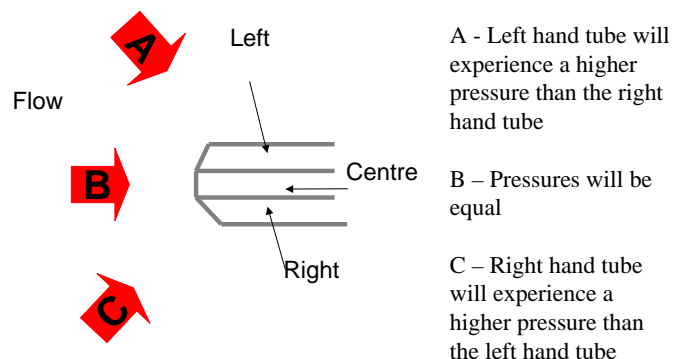


Figure 3.4: Operation of Multi-tube probe.

3.3.1 Probe Calibration

In order to produce a calibration map the probe has to be rotated in pitch and yaw through all the expected flow angles to be encountered in the traverse. The response of the probe is measured, recorded and used later to recover the flow variables from the cascade tests.

The Calibration Rig or Pitch-Yaw Rig has two stepper motors which can alter the pitch and yaw of the probe. The rig also has an air jet of variable speed supplied by a centrifugal fan and passing through a large diameter flexible hose to the test point. Just before the test point a smooth contraction is provided which helps to ensure that the flow quality is reasonably good. The probe is placed in this rig and rotated around in yaw and pitch. For three hole probes $\pm 42^\circ$ in yaw was used with increments of two degrees. For five hole probes $\pm 36^\circ$ in yaw and pitch with increments of two degrees were typically used. Thus for a three hole probe a calibration consisted of forty three points but for a five hole probe a calibration consisted of 1369 points. Measurements of the pressure are taken with the data acquisition system and a specially written computer program *logpy*.²

The three hole probe and five hole probes used consist of a number of small tubes bound together into a “cobra” type arrangement. The manufacturing drawings are shown in Figure 3.5 and 3.6 (The figures are not to scale) and photographs of the probes are included in Figures E.1 and E.2 in Appendix E. The “cobra” arrangement ensures that when the probe is rotated about its axis the probe tip stays in the same place. In practice deflections from wind loading and self weight mean that this is not quite true. Each tube of the probe is piped away via small bore metal tubing and then plastic tubing to differential pressure transducers. The three hole probe design is a result of experience with conventional three hole probe “cobra” head design and features a cranked head to avoid contacting the curved endwall when taking measurements up the wall. The five hole probe is essentially a copy of an existing probe used by Hartland (2001) with a much smaller stem - the aim being to be able to traverse closer to the blade surfaces than Hartland did, the design is otherwise conventional and was chosen as it had been successful in the past.

The chosen reference for the differential pressure transducers is upstream total pressure. This reference is measured from a pitot static probe inserted upstream of the cascade or just upstream of the measuring point in the Calibration Rig (See Figure 3.3 for the connections).

In order to improve the accuracy of the measuring system the calibration is conducted using the same equipment as used for the cascade tests. The Rig PC with transducers is mounted on a trolley and transported from the cascade to the calibration jet as required. The actual measurement of pressures is again conventional. Pressures measured from the various probes in the cascade are piped up to a series of sensitive transducers which convert the pressure signals to voltages. These voltages are converted into digital information by the analogue to digital converter whereupon they are converted back into pressures by the logging software. Probe

²This program along with all the other programs for data processing were entirely written by the author during the project. A list of the programs used can be found in section C.4 on page 292 and a diagram is found in Figure C.1 on page 293

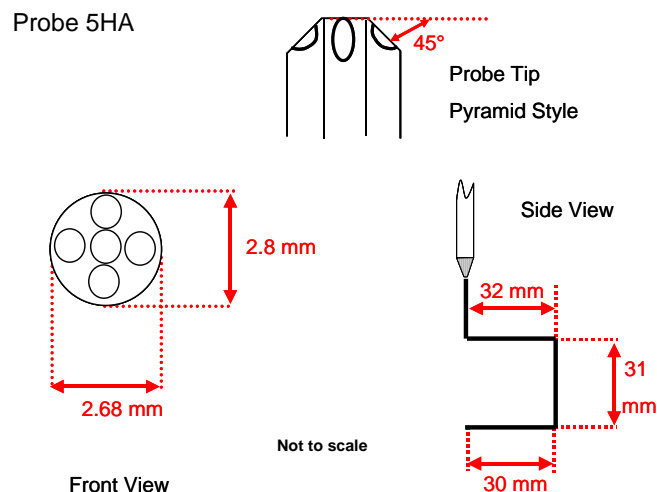


Figure 3.5: Five Hole Probe

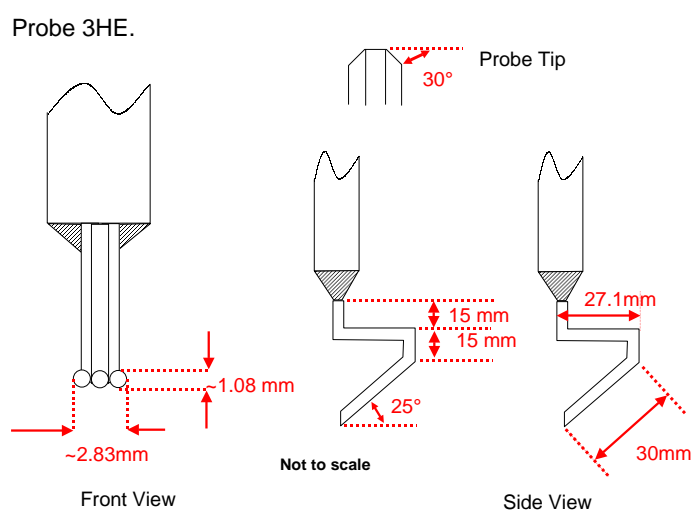


Figure 3.6: Cranked Three Hole Probe

positioning is achieved by means of stepper motor and slides driven from the Rig PC. The stepper motor system is an “open loop” control system. (See Figure 3.3 for a schematic)

The transducers used have a range of ± 200 Pa for the centre hole and 0-2000 Pa for each of the outer holes. A 0-500 Pa transducer is used to measure the upstream dynamic pressure. Two additional transducers of 0-500 Pa and 0-2000 Pa are used as extra measurements on the centre hole as when the boundary layer is measured the ± 200 Pa transducer has insufficient range. The best ranged transducer is selected during processing in the *calib* program.

The initial probe position in the calibration jet was set by eye with visual aids. Probe yaw was set using a large set square to align the probe tip to the jet. Probe pitch was zeroed using a plumb line and measuring by eye. Care was taken to ensure that the probe tip lies on the axis of rotation of both pitch and yaw.

The calibration data is made non-dimensional by using the following variables:

$$C_{P_{yaw}} = \frac{P_{left} - P_{right}}{P_{centre} - \bar{P}} \quad (3.1)$$

$$C_{P_{pitch}} = \frac{P_{bottom} - P_{top}}{P_{centre} - \bar{P}} \quad (3.2)$$

$$C_{P_{total}} = \frac{P_{centre} - P_{total}}{P_{centre} - \bar{P}} \quad (3.3)$$

$$C_{P_{static}} = \frac{\bar{P} - P_{static}}{P_{centre} - \bar{P}} \quad (3.4)$$

where

$$\bar{P} = (P_{left} + P_{right} + P_{bottom} + P_{top})/4 \quad (3.5)$$

for five hole probes. For three hole probes $C_{P_{pitch}}$ does not exist and

$$\bar{P} = (P_{left} + P_{right})/2 \quad (3.6)$$

Once a complete probe calibration has been obtained a test in the cascade may be conducted. Note that Hartland (2001) used the true dynamic head to normalise the pressure coefficients. This has the advantage that it produces smoother calibration maps at the edges of the map and the disadvantage that an iteration is required to recover flow variables.

3.3.2 Cascade Traverses

The Durham Cascade is a conventional linear low speed cascade with six blades based on the geometry of an HP rotor blade. It has full span of 400mm and a blade pitch of 191mm, this relatively large scale allows instrumentation to be used that is much larger (and cheaper) than would be acceptable for a smaller cascade. A number of tangential traverse planes are provided in the cascade known as “Slots” into which the three or five hole probes can be inserted. The measurement slots are located in the axial locations listed in Table 3.4.

Cascade Traverse are carried out using the program *log3h* for three hole probes and *log5h* for five hole probes. The operation of each program is identical:

Slot No.	$\% C_{ax}$	x/mm
1	-9%	-197
2	6%	-170
3	22%	-141
4	38%	-112
5	55%	-81
6	71%	-52
7	87%	-24
8	97%	-5
9	116%	29
10	128%	51

Table 3.4: Slot Locations

1. The zero offset from the transducer is measured.
2. Atmospheric pressure and temperature are entered
3. The current co-ordinates of the probe are entered
4. The rig is run up to speed, in order to provide Reynolds number similarity the speed is altered depending on atmospheric conditions.
5. The probe is moved to each point on the measurement grid in turn and the pressure sampled.
6. The rig waits until the probe reading has settled before taking a reading. Each transducer was sampled at a frequency of 286 Hz for around 4.37 s which meant that 1250 samples were taken. This is a relatively low frequency to sample at but the transducers used in this thesis already contain some damping so sampling at a higher frequency results in no additional information.
7. A test is carried out on the data to determine whether there is too much scatter in the data. If the scatter is too great the data is re-sampled until acceptable results are obtained.
8. Once all measurement points in the grid file have been sampled the traverse is finished.

The rig is set to operate as close as possible to the correct Reynolds number, making some attempt to vary the speed of the tunnel to compensate for the variations in atmospheric conditions. Generally good agreement between the demanded upstream dynamic head and the achieved dynamic head is found. With patience an error of 1% can be achieved. This error in Reynolds number is unlikely to affect the flow.

All the pressure probe readings are compensated to standard day conditions, so that readings from different days can be compared to one another. This is done by multiplying by the ratio of the actual upstream dynamic head to the upstream dynamic head on the standard day.

The logging software contain subroutines which test whether or not the readings have settled before allowing the program to commence logging. The change in voltage is measured over approximately one second and if the change is less than 0.01 V or twenty seconds have elapsed the program is allowed to commence logging. The aim is to ensure maximum accuracy in the minimum traverse time. The data from each measurement point undergoes a statistical test to eliminate measurements with too much scatter in the data. If the data from a particular sample fails the test the measurement point is repeated until the data is acceptable. In practice failure of the test is extremely rare 1 in 1000 points typically and sampling again seems to produce acceptable data. Some of the pressure probe results were taken without these tests applied, but all of the readings used for numerical results have been repeated where necessary with the latest version of the measuring system.

Probe positioning in the cascade was achieved by a number of different methods:

1. The angle of the probe was set using a plumb line. Tests conducted with a three hole probe indicate that this can line up the probe with a repeatability of slightly more than one degree if care is taken.
2. For downstream slots the tangential position is measured using a pair of digital callipers and the reference mark on the cascade. The probe stem is used to measure the probe position, so it is important that the probe is straight.
3. For upstream slots the tangential positioning is set by lining up the probe stem to the reference marks on outside of the cascade using a large set square as a visual aid, as access to the upstream slots in the cascade is extremely limited.
4. The radial positioning is achieved by moving the probe in small increments until a piece of paper inserted between the probe tip and the endwall no longer moves freely. For curved endwalls the tangential position must be known as well and then the height of the endwall found at that position. The position of the probe was then considered to be half the probe diameter away from the endwall.
5. For three hole probes the endwall was located using a pressure measurement technique. Firstly the probe was driven manually until it touched the endwall, then a traverse run carried out. The traverse consisted of a series of steps of 0.1mm away from the assumed zero position. A graph of P_{centre} vs. radial coordinate then showed where the true wall position occurred.
6. The above method of radial positioning is only practicable when the endwall is accessible. For slots with inaccessible endwalls the following method was first adopted:
 - The probe was set to a known radial position in a slot with an accessible endwall.
 - The traverse gear was then moved to the required slot without rotating the radial stepper motor. The traverse gear detaches from the cascade as one unit.

- Once the probe had been reinserted into the cascade the radial position was then assumed to be the same as that set on the accessible endwall.
7. For the second half of the project, axial positioning was set by means of metal inserts into the traverse gear, this ensures that the axial location is identical when the traverse gear is repositioned, previously there was some variation between runs as the gear was set by “eye”.

The method of point 6 about is however rather unsatisfactory and for most of the traverses in this thesis it was not used. The technique was only used for traverses within the blade row for the P0,P1 and P2 endwalls and not at all for the P3 work.

3.3.3 Measurement Grids.

The measurement grids in this thesis differ from those used by previous workers. There is generally a uniform tangential spacing of 7mm rather than a varying tangential spacing. The radial steps of 5mm close to the wall and 10mm above $r=100\text{mm}$ have been retained.

The contoured grids are generated so that the perturbations from the endwall reduce towards midspan. This is accomplished as follows:

- The radial distance between the endwall and midspan is calculated at a given tangential position.
- The ratio of this and the planar distance between the endwall and midspan is calculated.
- The radial step size for that tangential location (5mm or 10mm for the planar five hole probe readings) is adjusted by the above ratio.

By way of example consider a tangential location on a contoured grid with the endwall at $r=4.7\text{mm}$. The midspan to endwall distance would be 195.3mm meaning that ratio required is $195.3/200 = 0.9765$. For this tangential location instead of 5mm steps 4.88mm steps would be taken close to the endwall and 9.77mm steps would be taken further away from the endwall.

Therefore for contoured grids the radial step size varies in the tangential direction. A contoured grid is illustrated in Figure 3.7.

3.4 Data Processing

There are a number of programs used to process the data. Most of which are written in the “C” programming language. Plotting is conducted using the proprietary GSHARP program. Previous experimenters (Hartland, 2001) had used spreadsheets to do the pitch and area averaging. It was felt that whilst a program is more difficult to write than a spreadsheet solution it has several advantages. The analysis can be done much more rapidly and one is absolutely certain that the data from different profiles have been operated on in an identical manner.

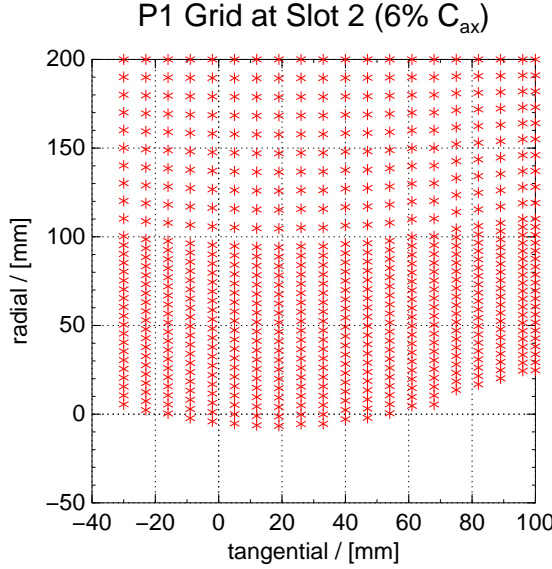


Figure 3.7: Example of a Contoured Measurement Grid

3.4.1 Recovery of Flow Variables.

Flow variables are extracted from the pressure data and the calibration map using the program *calib*.

The process for extracting flow variables from the measurements is explained with reference to a three hole probe. A three hole probe calibration map is illustrated in Figure 3.8, the process of extracting flow variables from pressure measurements is explained with reference to this map. When measurements are taken in the cascade three pressure measurements are available, P_{centre} , P_{left} and P_{right} . This information allows C_{Pyaw} to be calculated directly. The yaw angle is then obtained by “looking up” the appropriate angle from the graph of C_{Pyaw} . This yaw angle is then used to look up the values of C_{Ptotal} and $C_{Pstatic}$. The coefficients then yield the total and static pressure as follows:

$$\bar{P} = (P_{left} + P_{right})/2 \quad (3.7)$$

$$P_{total} = P_{centre} - C_{Ptotal}(P_{centre} - \bar{P}) \quad (3.8)$$

$$P_{static} = \bar{P} - C_{Pstatic}(P_{centre} - \bar{P}) \quad (3.9)$$

The difference between total and static pressure gives the dynamic head, from which the velocity can be determined. Various parameters such as loss coefficient (C_{P0}) can then be obtained. How each coefficient or parameter is determined is described in a later section.

The process for a five hole probe is identical although the implementation is much more complicated because as well as the Yaw coefficient a Pitch Coefficient has to be accounted for. A Five hole Calibration Map is illustrated in Figures 3.9 to 3.10. The “vertical” lines in Figure 3.9 are lines of constant pitch angle and the “horizontal” lines are for constant yaw. Data can be extracted as follows: C_{Pyaw} and C_{Ppitch} can be calculated from the pressure data directly. The point will lie in a “box” formed by the lines of constant yaw and pitch angle on the calibration map. This box is found by the program and the value of yaw and pitch angle estimated

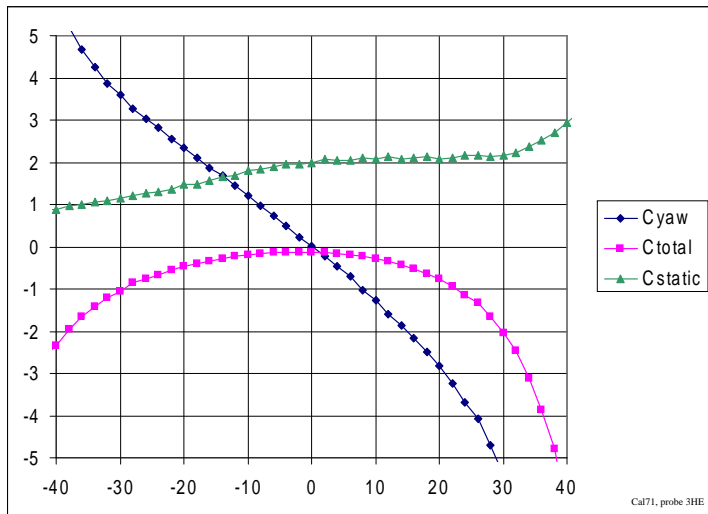


Figure 3.8: Sample Three Hole Probe Calibration Map

by linear interpolation. Using the values of yaw and pitch the values of total and static coefficient are then found. Linear interpolation was used to estimate the exact values. Then from the total and static coefficients the total and static pressure can be calculated in a very similar manner to a three hole probe.

3.4.2 Corrections.

The *field* program produces files containing all the information necessary for an area plot. In this program total and static coefficients are calculated as well as the velocity component, the secondary velocity component used for the vector plots, C_{ske} and vorticity. Three corrections are applied to the data.

The corrections are either obtained automatically by the *field* program and a supplemental input file or they can be entered manually. In either case they are obtained by taking the output from *calib* and examining the midspan ($r=200\text{mm}$) data. All corrections are applied to every data point in the traverse. The three corrections are as follows:

- Pitch Angle correction. This angle is added to all pitch angles in the traverse and is the angle required to ensure that the average pitch angle at midspan over one pitch is zero. This is designed to compensate for any misalignment of the probe.
- Yaw Angle correction. This is the angle required to adjust the average midspan yaw angle to be the same as a specified value. This is to correct for probe misalignment between traverses of the same slot taken at different times.
- Loss Coefficient correction. This is the loss coefficient required to adjust the midspan and midpitch value of loss coefficient to zero. The rationale behind this correction is that it compensates for misalignment of the upstream reference probe and possible errors in the calibration of the probe. For slots inside

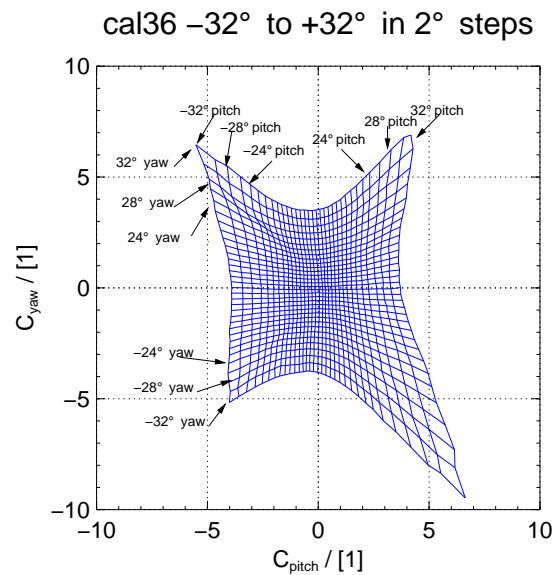


Figure 3.9: Five Hole Probe Calibration Map (Probe 5HA)

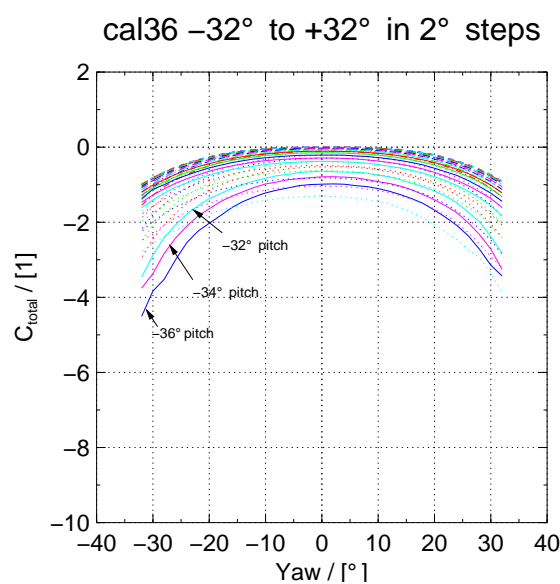


Figure 3.10: C_{total} Map for Probe 5HA

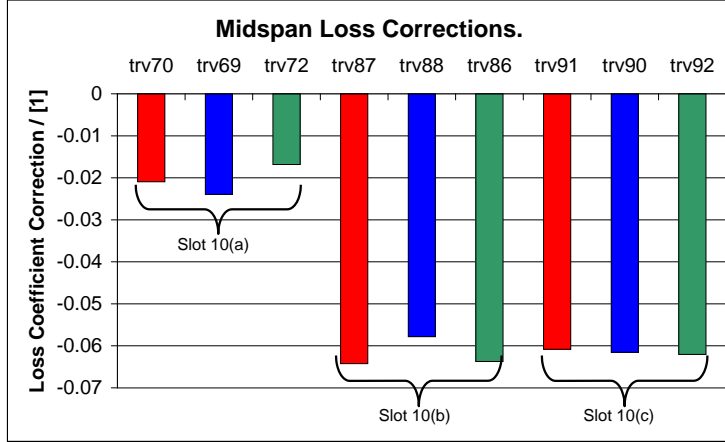


Figure 3.11: Magnitude of Midspan Loss Coefficient Adjustment

the blade passage this correction is the loss coefficient required to adjust the average midspan loss to zero.

The value of the corrections depends how well the probe is set up, with care typical corrections are around two degrees for pitch and less than one degree for yaw. The yaw corrections may be much higher in cases where the probe is not easily aligned, such as inside the blade row. Loss coefficient corrections at the reference plane are typically of the order of -0.02 up to a maximum of -0.06. These corrections appear large relative to the secondary loss but very little variation occurs during a series of “back to back” readings, supporting the assertion that these corrections compensate for misalignment of the upstream reference probe. The magnitude of these corrections is shown in Figure 3.11.

3.4.3 Derived Quantities.

The three components of velocity are calculated thus:

$$V = \sqrt{\left(\frac{2(P_{total} - P_{static})}{\rho} \right)} \quad (3.10)$$

$$V_x = V \cos \alpha \cos \beta \quad (3.11)$$

$$V_t = V \sin \alpha \cos \beta \quad (3.12)$$

$$V_r = V \sin \beta \quad (3.13)$$

Secondary Velocity vectors are calculated on the basis of a midspan yaw angle α_{mid} . α_{mid} is calculated for each tangential position in the traverse, so the midspan angle varies across the pitch of the cascade. In the calculations the midspan angle is taken to be the angle at half span ($r=200\text{mm}$). Figure 3.12 provides a diagram which explains the origin of the formulas. Figure B.1 in Appendix B shows the

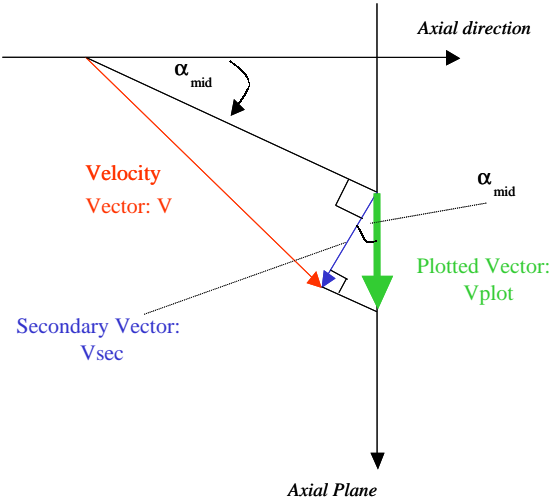


Figure 3.12: Definition of Secondary Flow Vectors.

direction of the ordinates relative to the blade shapes as well as defining yaw and pitch angles.

V_{plot} is the variable that is output, the velocity vector plots show V_{plot} as the tangential component and V_r as the radial component of velocity.

C_{P0} is defined relative to the upstream total pressure.

$$C_{P0} = \frac{P_{total_{ups}} - P_{total}}{\frac{1}{2}\rho V_{ups}^2} \quad (3.14)$$

C_P is defined in a similar manner.

$$C_P = \frac{P_{static_{ups}} - P_{static}}{\frac{1}{2}\rho V_{ups}^2} \quad (3.15)$$

C_{ske} is calculated in a very straightforward manner.

$$C_{ske} = \frac{V_{sec}^2 + V_r^2}{V_{ups}^2} \quad (3.16)$$

where

$$V_{sec} = V \sin(\alpha - \alpha_{mid}) \quad (3.17)$$

This is entirely consistent with the method described in Moore (1995) or Hartland (2001). This is the “classic” definition of secondary kinetic energy and does not take account of the inviscid effects of endwall profiling. All the coefficients used in this thesis are normalised using the *inlet* flow conditions as the inlet conditions are well defined. It is more common to use the exit flow conditions and this should be kept in mind when comparing the results of different experimenters.

Streamwise vorticity is a more complicated parameter to extract from the data. It is carried out using the method of Gregory-Smith et al. (1987). Vorticity is defined

as the curl of the velocity vector and the components are defined to be Ω_x , Ω_r and Ω_t in the axial, radial and tangential directions respectively. There are given by:-

$$\Omega_x = \frac{\partial V_r}{\partial t} - \frac{\partial V_t}{\partial r} \quad (3.18)$$

$$\Omega_t = \frac{\partial V_x}{\partial r} - \frac{\partial V_r}{\partial x} \quad (3.19)$$

$$\Omega_r = \frac{\partial V_t}{\partial x} - \frac{\partial V_x}{\partial t} \quad (3.20)$$

Streamwise vorticity is taken as the component of vorticity in the primary flow direction which is given by

$$\Omega_s = \Omega_x \cos \alpha_p + \Omega_t \sin \alpha_p \quad (3.21)$$

where α_p is the primary flow angle, in this case this is equal to the yaw angle at midspan. The axial measurement planes are too far apart to allow an accurate measurement of $\partial/\partial x$ to be made so an alternative method is required.

This method is to use the incompressible Helmholtz equation and take the radial component to obtain Ω_t thus:-

$$\Omega_t = \frac{1}{V_x} \left(\frac{1}{\rho} \frac{\partial P_{total}}{\partial r} - V_t \Omega_x \right) \quad (3.22)$$

Differentiating experimental data is difficult as spurious values are introduced by experimental scatter. To get around this problem a spline is fitted to the data points and the gradient calculated from that. This is done with a freely available numerical library routine Galassi et al. (2001) and the resulting values of vorticity are normalised using the axial blade chord and the upstream velocity. The vorticity readings plotted in this thesis are therefore a vorticity coefficient:-

$$C_\Omega = \frac{\Omega_x C_{ax}}{V_{ups}} \quad (3.23)$$

3.4.4 Pitch Averaging.

The program *pitch* carries out the pitch and area averaging. Yaw angle, Loss, mass flow, C_{ske} and vorticity are pitch and area averaged.

The program operates as follows:

- The number of points that cover 191mm (one blade pitch) is calculated, this is to deal with slots after the blade trailing edge to ensure that pitch averaging only takes place over one blade pitch. Pitch averaging takes place from the smallest tangential value upwards. This gives better results by ensuring that the pitch averaging boundaries are not inside the blade wakes.
- The parameters (yaw, loss, massflow, C_{ske} and Vorticity) are pitch averaged and the results written to the output file.
- The parameters are averaged over the measurement area.

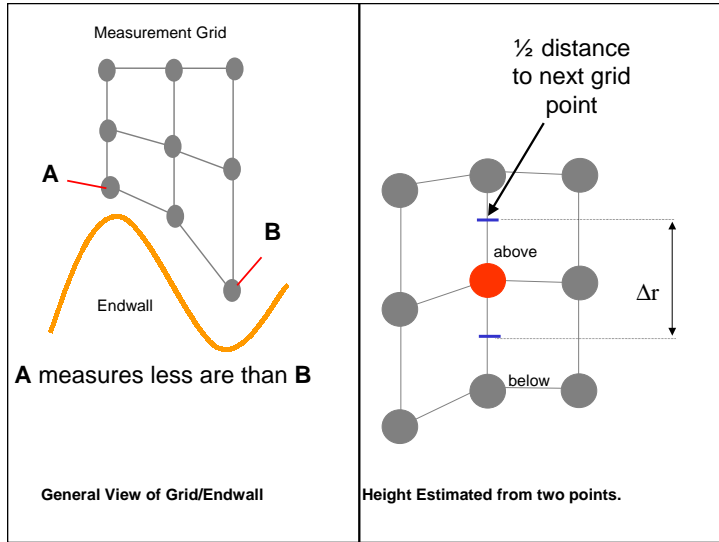


Figure 3.13: Calculation of Δr for Pitch Averaging.

For pitch averaged plotting each endwall was given a symbol and a colour to allow results to be understood “at a glance”. The symbol used is listed in the legend on each plot and also in Table 1 on page xxvi. Experimental results use filled in symbols and CFD results use open symbols.

The pitch averaging process attempts to take into account the varying area introduced by the contoured grids that are used on profiled endwalls. Previous work such as that of Moore (1995) pitch averaged quantities, such as loss, weighted with the axial velocity, V_x . In the current work measurement grids are curved and the radial spacing varies in the tangential direction (see Figure 3.7). Thus for a given tangential line each point represents a slightly different area. In order to take account of this the current work uses $\Delta r V_x$ as the weighting function, where Δr represents the radial height which the measurement point represents. Figure 3.13 illustrates this.

The pitch averaged loss coefficient is therefore:

$$\overline{C_{P0}} = \frac{\int_0^s C_{P0} \Delta r V_x dt}{\int_0^s \Delta r V_x dt} \quad (3.24)$$

With a contoured endwall, Δr will vary with tangential position. In practice the integration is done numerically using the trapezium rule as follows:

$$\begin{aligned} \overline{C_{P0}} = & \left[\left(\frac{t_2 - t_1}{2} \right) (C_{P0_2} \Delta r_2 V_{x_2} + C_{P0_1} \Delta r_1 V_{x_1}) + \dots + \right. \\ & \left. \left(\frac{t_n - t_{n-1}}{2} \right) (C_{P0_n} \Delta r_n V_{x_n} + C_{P0_{n-1}} \Delta r_{n-1} V_{x_{n-1}}) \right] \times \\ & \left[\left(\frac{t_2 - t_1}{2} \right) (\Delta r_2 V_{x_2} + \Delta r_1 V_{x_1}) + \dots + \right. \\ & \left. \left(\frac{t_n - t_{n-1}}{2} \right) (\Delta r_n V_{x_n} + \Delta r_{n-1} V_{x_{n-1}}) \right]^{-1} \end{aligned} \quad (3.25)$$

<i>trv69</i>	With Δr weighting	Uniform Spacing
Total C_{P0}	0.1186	0.1204
Secondary C_{P0}	0.0781	0.0790

Table 3.5: The effect of removing the Δr weighting

This equation is included to highlight the fact that although more sophisticated methods of integration (e.g. Simpsons' rule) are available they generally require regularly spaced points, which the measurement grids used in this thesis do not provide.

Essentially the pitch averaging process takes place on lines of constant proportion to midspan rather than constant radial distance. That is it takes place along the measurement grid. The $\Delta r V_x$ weighting is an attempt to take that into account. Pitch averaged plots do not have r in mm as the abscissa but % to midspan to reflect this fact.

Using the Δr method to account for profiled endwalls is an approximation, however at Slot 10 (128% C_{ax}) the profiling is either zero (P0, P2) or very small (P1, P3) so in actual fact the difference that this weighting makes is very small. Table 3.5 shows the difference between area averaged values of P1 traverse calculated using the Δr method and area averaged values calculated as if there was no radial variation. As can be seen the difference in results is small and certainly does not effect the conclusions found in later chapters.

The pitch averaged quantities are listed with their formula below. Pitch averaged axial velocity:

$$\overline{V_x} = \frac{\int_0^s V_x \Delta r dt}{\int_0^s \Delta r dt} \quad (3.26)$$

Pitch averaged tangential velocity:

$$\overline{V_t} = \frac{\int_0^s V_t V_x \Delta r dt}{\int_0^s V_x \Delta r dt} \quad (3.27)$$

For yaw angle:

$$\overline{\alpha} = \tan^{-1} \frac{\overline{V_t}}{\overline{V_x}} \quad (3.28)$$

Using this method rather than averaging the local values of yaw angle means that the pitch averaged yaw angle corresponds to the correct tangential momentum and mass flow. Pitch averaged streamwise vorticity coefficient:

$$\overline{C_\Omega} = \frac{\int_0^s C_\Omega V_x \Delta r dt}{\int_0^s V_x \Delta r dt} \quad (3.29)$$

Pitch averaged C_{ske} :

$$\overline{C_{ske}} = \frac{\int_0^s C_{ske} V_x \Delta r dt}{\int_0^s V_x \Delta r dt} \quad (3.30)$$

3.5 Area Averaging.

The area averaging is straightforward. The algorithm uses the pitch averaged values as calculated above and performs a simple trapezium rule calculation weighted by the pitch averaged axial velocity, \bar{V}_x . For contoured endwalls the pitch averaged values are assumed to lie on the same radial locations as the planar endwall. For Loss:

$$\overline{\overline{C}}_{P0} = \frac{\int_0^h \overline{C}_{P0} \bar{V}_x dr}{\int_0^h \bar{V}_x dr} \quad (3.31)$$

where h is the radial extent of the traverse. Again this is implemented numerically using the trapezium rule.

The other area averaged quantities calculated are $\overline{\overline{C}}_{ske}$, $\overline{\overline{V}}_x$ and $\overline{\overline{V}}_t$ which are defined below.

$$\overline{\overline{C}}_{ske} = \frac{\int_0^h \overline{C}_{ske} \bar{V}_x dr}{\int_0^h \bar{V}_x dr} \quad (3.32)$$

It is possible to calculate a value for $\overline{\overline{C}}_\Omega$ and this is in fact implemented in the data processing programs but is not included in the thesis due to limitations of space.

Area averaged velocities are calculated as follows:

$$\overline{\overline{V}}_x = \frac{1}{h} \int_0^h \bar{V}_x dr \quad (3.33)$$

$$\overline{\overline{V}}_t = \frac{\int_0^h \bar{V}_t \bar{V}_x dr}{\int_0^h \bar{V}_x dr} \quad (3.34)$$

For Yaw Angle again this is calculated from the area averaged velocities rather than averaging the pitch averaged yaw angle.

$$\overline{\overline{\alpha}} = \tan^{-1} \frac{\overline{\overline{V}}_t}{\overline{\overline{V}}_x} \quad (3.35)$$

Massflow can be obtained from the area averaged axial velocity as follows:-

$$\dot{m} = \rho s h \overline{\overline{V}}_x \quad (3.36)$$

3.5.1 Mixed out loss.

Mixed out loss is implemented according to the method of Moore (1995). Using the continuity and momentum equations, a derivation may be made to obtain values at a plane an infinite distance downstream of the cascade. At this plane the flow will be mixed out to obtain uniform values of C_{P0} etc.

This derivation applies only to linear, incompressible cascades with no cooling flows or heat transfer effects. More complicated methods to deal with annular, compressible and cooled mixing processes are available such as Main et al. (1997) however the general solution to Main et al. (1997) requires a numerical solution so

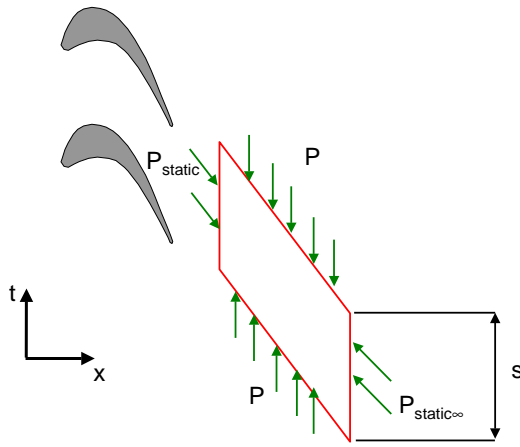


Figure 3.14: Control Volume for the Mixed Out Loss Calculation

it is not easily compared to the one in this chapter. It is however trivial to reduce the conservation equations (mass, momentum etc) from the compressible annular cascade to their linear, incompressible case.

The derivation is slightly simplified from the one outlined in Moore (1995). The control volume is illustrated in Figure 3.14. Assume that $V_{r\infty} = 0$.

Continuity requires that:

$$\rho \bar{V}_x sh = \rho V_{x\infty} sh \quad (3.37)$$

$$\Rightarrow V_{x\infty} = \bar{V}_x \quad (3.38)$$

Strictly this only applies to profiles with no perturbations at the plane of interest, so that the profiled area is equal to $s \times h$, however for the profiles used in this thesis the difference should be small.

Equating tangential momentum (assuming no wall friction):

$$\rho \bar{V}_x \bar{V}_t sh = \rho V_{x\infty} V_{t\infty} sh \Rightarrow V_{t\infty} = \bar{V}_t \quad (3.39)$$

Strictly speaking this only applies to profiles with no perturbations at the plane of interest as it is assumed that the static pressure on the top and bottom of the control volume cancel out. With profiling this assumption is no longer true, however this is ignored as there is no obvious way of dealing with this variation and the effect is not expected to be large.

Thus the mixed out yaw angle is the same as the area averaged yaw angle.

Axial momentum equation

$$\int_0^h \int_0^s P_{static} dt dr - P_{static\infty} sh = \rho V_{x\infty}^2 sh - \rho \int_0^h \int_0^s V_x^2 dt dr \quad (3.40)$$

$$\Rightarrow \int_0^h \int_0^s P_{static} dt dr = P_{static\infty} sh + \rho V_{x\infty}^2 sh - \int_0^h \int_0^s V_x^2 dt dr \quad (3.41)$$

Consider the static pressure coefficient C_P .

$$\int_0^h \int_0^s C_P dx dr = \frac{1}{\frac{1}{2} \rho V_{ups}^2} \int_0^h \int_0^s (P_{static_{ups}} - P_{static}) dt dr \quad (3.42)$$

Since $P_{static_{ups}}$ is a constant

$$\frac{1}{2} \rho V_{ups}^2 \int_0^h \int_0^s C_P dt dr = P_{static_{ups}} sh - \int_0^h \int_0^s P_{static} dt dr \quad (3.43)$$

Combining 3.41 and 3.43 gives

$$\frac{1}{2} \rho V_{ups}^2 \int_0^h \int_0^s C_P dt dt = P_{static_{ups}} sh - P_{static_\infty} sh - \rho V_{x\infty}^2 sh + \rho \int_0^h \int_0^s V_x^2 dt dr \quad (3.44)$$

$$[P_{static_{ups}} - P_{static_\infty}] sh = \rho V_{x\infty}^2 sh - \rho \int_0^h \int_0^s V_x^2 dt dr - \frac{1}{2} \rho V_{ups}^2 \int_0^h \int_0^s C_P dt dt \quad (3.45)$$

Defining a mixed-out total pressure coefficient $C_{P0\infty}$ as

$$C_{P0\infty} = \frac{P_{total_{ups}} - P_{total_\infty}}{\frac{1}{2} \rho V_{ups}^2} \quad (3.46)$$

Applying Bernoulli gives

$$P_{static_{ups}} = P_{total_{ups}} - \frac{1}{2} \rho V_{ups}^2 \quad (3.47)$$

$$P_{static_\infty} = P_{total_\infty} - \frac{1}{2} \rho V_\infty^2 \quad (3.48)$$

$$\Rightarrow P_{static_{ups}} - P_{static_\infty} = P_{total_{ups}} - P_{total_\infty} + \frac{1}{2} \rho (V_\infty^2 - V_{ups}^2) \quad (3.49)$$

Substituting 3.49 into 3.45.

$$\begin{aligned} & \left[P_{total_{ups}} - P_{total_\infty} + \frac{1}{2} \rho (V_\infty^2 - V_{ups}^2) \right] sh = \\ & \rho V_{x\infty}^2 sh - \rho \int_0^h \int_0^s V_x^2 dt dr - \frac{1}{2} \rho V_{ups}^2 \int_0^h \int_0^s C_P dt dt \end{aligned} \quad (3.50)$$

Rearranging.

$$\begin{aligned} & P_{total_{ups}} - P_{total_\infty} \\ &= \rho V_{x\infty}^2 - \frac{\rho}{sh} \int_0^h \int_0^s V_x^2 dt dr - \frac{1}{2sh} \rho V_{ups}^2 \int_0^h \int_0^s C_P dt dt \end{aligned} \quad (3.51)$$

Divide by the upstream dynamic head ($1/2\rho V_{ups}^2$) to get mixed out loss coefficient $C_{P0\infty}$. The upstream dynamic head is used as it is a well defined quantity for the Durham Cascade has been used extensively by previous experimenters on the

Durham Cascade such as Walsh (1987), Cleak (1989), Biesinger (1993), Moore (1995) and Hartland (2001).

$$C_{P0\infty} = 1 + \frac{1}{V_{ups}^2} \left[-V_\infty^2 + 2V_{x\infty}^2 - \frac{2}{sh} \int_0^h V_x^2 dt dr + \frac{V_{ups}^2}{sh} \int_0^h \int_0^s C_P dt dr \right] \quad (3.52)$$

Recall that $V_{r\infty} = 0$ therefore $V_\infty^2 = V_x^2 + V_t^2$ so

$$C_{P0\infty} = 1 + \frac{1}{V_{ups}^2} \left[V_{x\infty}^2 - V_{t\infty}^2 - \frac{2}{sh} \int_0^h V_x^2 dt dr + \frac{V_{ups}^2}{sh} \int_0^h \int_0^s C_P dt dr \right] \quad (3.53)$$

The trapezium rule is used for numerical integration as before. A midspan mixed out loss is defined as well, this is calculated by applying the above calculation on the four radial measurement points near midspan, i.e. for the planar case this uses $r=170, 180, 190$ and 200 mm. Since $V_{x\infty} = \bar{V}_x$ and $V_{t\infty} = \bar{V}_t$ the mixed out yaw angle is the same as the area averaged yaw angle.

3.5.2 Contour and Vector Plots.

Contour and Vector Plots are produced using the “GSHARP” plotting software which runs on the University UNIX system. This program essentially is a user interface for a series of graphics functions. It is operated by writing a program in the “GSHARP scripting language” and a large number of these scripts have been generated and saved for different sorts of plots. This has meant that the plots can be reproduced relatively rapidly and with the minimum of effort should different data processing methods be applied to the data, provided of course that one has access to the GSHARP program.

3.6 Validation

Given that some of the results in this thesis disagree with those presented by other workers working in the same cascade, some discussion of the validity of the results presented in herein is essential. Considerable care has been taken in producing the current results in ensuring firstly that they were as accurate as is reasonably possible and secondly that the quantitative results were completed back to back, with the same process used to take each reading. This section describes the efforts made to ensure that the results are accurate and that they remained so during the tests.

3.6.1 Pre and Post Reading System Tests.

Before and after the five hole logging the operation of all the logging programs and the most significant data processing programs were tested. The probe was calibrated as normal then this “System” or “Hand” test was conducted. The hand test took the following form.

- The probe was lined up in the calibration rig and two protractors with pointers were added to the calibration rig to indicate the position of the probe.

- The logging program *log5h* was then run on a fictitious grid of some fifty points. The probe was manually traversed using the protractors as a guide through $\pm 30^\circ$ in yaw and pitch in ten degree steps.
- The output from this run was then processed through the *calib* program along with the calibration map. The yaw and pitch angles returned by this run were then directly compared to the desired yaw and pitch angles that had been rotated manually.

These “hand tests” also give some indication of the error in the loss measurement as the loss returned at all angles should be zero. For a three hole probe no pitch variation was conducted and the probe was rotated though $\pm 40^\circ$ with a five degree step. For both three and five hole probes the zero pitch and zero yaw point is taken twice. Results from the “hand tests” can be found in the Chapter 5 for the P0,P1 and P2 measurements and Chapter 8 for the third generation endwall.

3.6.2 Software Validation.

The programs *logpy*, *coeff*, *log3h* and *log5h* and *calib* have all been shown to be functioning by the testing described above. The pitch program which produces the pitch and area averaged results has been tested by generating a fictitious loss surface in the shape of a triangle and checking to see that it produces the correct pitch and area averaged values, which can be worked out theoretically. This triangular loss shape has been tried with variation in the radial direction only and with variation in the tangential direction only. It has also been carried out with different grid spacing in the radial and tangential direction. For all the above cases the program returned the correct area and pitch averaged values. Finally a variation in the axial velocity produced the expected trends in the calculation of pitch and area averaged loss.

This is a simplistic test but does give some confidence that there is nothing grossly wrong with the algorithm for pitch and area averaging. A desirable further step might be to use a more complicated test shape. Further confidence in the system is given by the close agreement which can be found between the circumferentially averaged experimental data and the computational fluid dynamics data produced by Rolls-Royce, if there were major errors in the algorithms used in the author’s programs the agreement would not be so good.

3.6.3 Hardware Improvements.

The actual physical structure of the cascade is now some fourteen years old and has seen numerous modifications. In particular the blades are showing signs of age with several running repairs being conducted, the leading edge of one of the blades used for the instrumented passage has a distinct bulbous shape at the endwall leading edge due to the various repairs carried out. Several small pieces of work have been carried out under the current project to try and improve the geometry of the cascade.

- a new backing sheet was made for the cascade to ensure that the endwall panels were locked firmly in place

- in order to fit profiled endwalls onto the original cascade endwall extensions had been added to the blades, these extended the blades so that the “dips” in the endwall could be accommodated. However these extensions were of poor geometric quality and were replaced by extensions that are mounted at the cantilevered end of the cascade so that the geometry around the blade/endwall interface is much improved.
- the axial position of the traverse gear has been improved by adding slides of fixed length to position the traverse gear. Previously the traverse gear was fixed by eye.

The cascade is a large scale low speed cascade so small changes to the geometry are not critical and measurements are made back to back so the imperfections remain the same for different geometries. This means that the effect on the results should be limited.

3.7 Overview

This chapter has provided detailed descriptions of the cascade hardware (the so called Durham Cascade). The experimental techniques for flow visualisation results and the pressure probe traversing have also been elucidated in some detail. Finally the detailed data processing algorithms have been explained and discussed. The motivation behind the detailed explanations is that the loss changes described in the later chapters are relatively small and if small changes are made to the way data is processed then the results will not be directly comparable.

Chapter 4

Flow Visualisation Results

LOW VISUALISATION using the oil/dye on surface technique are described in this chapter for the P0, P1 and P2 profiles. The P3 visualisations are left until Chapter 8.

The oil/dye surface flow visualisations were photographed onto conventional film, printed and then scanned in for incorporation into the final text. Digital photography was not available at a low enough quality-cost tradeoff at the time of the experiments to justify using it. The scanned images are grouped by image type to allow comparison between endwalls, i.e. a general view of P0, P1 and P2 is followed by a close up of the inlet for P0, P1 and P2. The photographs are organised as follows:-

- General views of the endwall with blades removed showing the overall flow pattern.
- Close up of the endwall inlet.
- Close up of the blade passage portion of the endwall.
- Close up of the exit portion of the endwall.
- Blade suction surface.
- Blade pressure surface.
- Blade leading edge.
- Perspective view showing the suction surface and the endwall.
- Perspective view showing the pressure surface and the endwall.
- Perspective view showing the leading edge of the blade and the endwall.

Care must be taken when interpreting the photographs because the effect of gravity on the oil/dye mixture in regions of low flow velocity is quite high, meaning that useful information is not obtained from some areas of the visualisation. The direction of the gravity force on a panel is shown in Figure 4.1. Particularly near the inlet and on the pressure side of the blade/endwall, the flow velocities are too

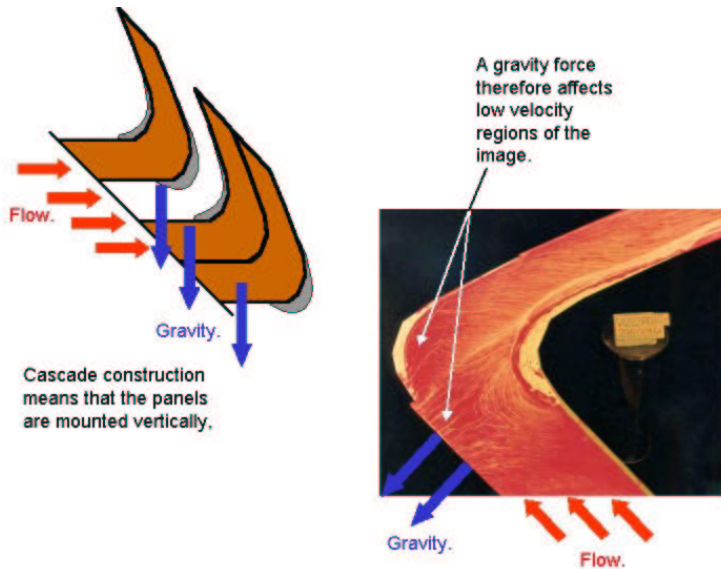


Figure 4.1: Gravity Force Direction.

low to produce useful results, however the flow may move under the action of gravity creating a flow pattern that is open to misinterpretation.

Photographs annotated to show the flow features discussed are included as Figure 4.2 on page 62 for P0, Figure 4.3 on page 63 for P1 and Figure 4.4 on page 64 for the second generation endwall.

4.1 Description

In general the flow visualisation results show significant differences between the profiled endwalls and the planar geometry. However flow features that appear relatively dramatic in surface flow visualisation may not penetrate very far into the mainstream flow and may be therefore relatively unimportant. The general flow features of each profiled geometry are discussed before describing the salient features of each photograph in detail.

The pictures are interpreted on the following basis:

- streamlines of the surface flow will be parallel to the lines shown in the oil/dye mixture
- regions of low shear stress at the wall will show an accumulation of oil/dye
- regions of high shear stress will show an absence of dye
- the blades were painted black and a lighter coloured dye (typically red) was used on the blade surfaces - absence of dye is therefore a dark line on the photographs
- the endwalls were painted white and again red dye was used on - absence of dye is therefore a pale line or region on the photographs

4.1.1 Endwall Flows

Planar Case

The planar endwall shows features that have been seen by Cleak (1989) in the Durham Cascade and in other flow visualisation studies Marchal and Sieverding (1977) for example. Specifically there are strong traces of the passage vortex, the corner vortex and both legs of the horseshoe vortex. The saddle point associated with the horseshoe vortex is not discernible though this is put down to the relatively low flow velocities at inlet to the cascade. The new boundary layer formed after the passage vortex also shows a large amount of overturning. These features are labelled and enlarged in Figure 4.2 on page 62.

Figure 4.5 shows the inlet flow, this clearly shows the regions where the oil/dye mixture has not moved under action of the flow but shows details of both the suction and pressure sides of the horseshoe vortex. Figure 4.8 illustrates the blade passage where the passage vortex trace is the dominant feature. The detailed interactions of the horseshoe vortex with the passage vortex are not clear from a simple surface flow visualisation but it appears that there is some significant interaction between the two. The formation of the corner vortex in the top right of the picture is also apparent. Figure 4.11 shows the exit flow - the development of the corner vortex is apparent as is the highly skewed nature of the exit flow. It is apparent that the oil/dye lines which are parallel to the streamlines do not follow the exit angle of the blades.

First Generation Endwall

The P1 endwall (Figure 4.3 on page 63 shows an annotated view) illustrates dramatically different flow features. The pressure side of horseshoe vortex trace is difficult to determine and really cannot be made out at all. The corner vortex appears to have a similar size and intensity as the planar case as shown by the flow visualisation, though this does not necessarily mean that the feature is identical as the corner vortex might have lifted off the endwall. The suction side of the horseshoe vortex remains clearly visible, however, it looks in fact slightly larger than the planar case however the quality of the flow visualisation (mainly the oil-dye ratio) is better for P1 and P2 than for P0. The most striking feature that can be seen is a large area of stagnant flow along the upstream ridge.

As noted earlier the profiling for P1 extends far upstream and downstream of the blade passage. Upstream of the blade row there is a large ridge which runs parallel to the mainstream flow in the upstream direction about 100mm (55% C_{ax}). (See Figure A.1 on page 285). It is at the peak of this ridge that this large region of stagnant flow appears. In Figures 4.6 and 4.3 etc it appears as a region of high shear stress (no dye left in place) however this is due to the effect of gravity when the tunnel is turned off, fluid that has accumulated in this region of low shear stress then dribbles away. This process was observed several times during the production of this thesis by the author. Figure 4.32 shows a view taken of the endwall in the cascade and the fan running - a region of pooled oil/dye mixture can clearly be seen.

The new highly-skewed boundary layer for P1 can also be clearly seen, by inspection it can be seen that it is more aligned with the midspan flow direction than the

boundary layer found in the planar case within the blade passage, after the blade exit the situation is less clear with the planar endwall and the P1 profile exhibiting similar oil/dye traces.

Figure 4.6 shows the inlet flow. The large stagnant region discussed earlier is immediately apparent. The suction side of the horseshoe vortex whilst slightly larger than for the planar case appears to be less strong - that is the oil/dye traces are more evenly spaced. Figure 4.9 shows the endwall inside the blade passage. The lack of pressure side horseshoe vortex trace is immediately apparent and the corner vortex can clearly be seen. Also of note is the direction of the streamlines on the endwall, for the planar case the streamline direction was further overturned than for the P1 case. Figure 4.12 shows the exit flow for the profiled geometry. Profiling for the first generation endwall extends further downstream than the trailing edge, though this is not apparent from plan view photographs. A feature of P1 is that there is a ridge which is designed to enhance the corner vortex and reduce the overturning at the endwall. This increased corner vortex which can clearly be seen in secondary vector plots in later chapters, is not noticeably larger than the planar case in this photograph.

Second Generation Endwall.

The P2 endwall (Figure 4.4 on 64 shows an annotated view) has more similarities with the planar flow visualisation than the first generation endwall but again there are significant differences. The pressure side horseshoe vortex migration is not visible - this is quite significant as it is normally a dominant feature of secondary flows surface visualisation. However for P2 both the suction and pressure side legs of the horseshoe vortex are present. The pressure side trace is however very weak. The new skewed boundary layer appears to have an overturning that is greater than for P1 and about the same as for P0 at exit from the blade row. Inside the blade passage passage the turning appears less than for the planar case.

Figure 4.7 exhibits the horseshoe vortex flows as described earlier, both the suction surface and the pressure surface trace are visible. The pressure surface trace is much weaker than the planar case but stronger than the P1 trace. The suction surface trace looks stronger than even the planar case, though that is in part due to the increased quality of the flow visualisation for P2. Figure 4.10 shows the endwall flow inside the blade passage. The lack of pressure side horseshoe vortex trace is particularly notable as well as the direction of streamlines in the upper half of the photograph. The streamline directions are again less overturned than for the planar case. Figure 4.13 illustrates the exit flow for P2. The corner vortex appears similar to the planar case but of more interest is the exit angle of the endwall flow. Although within the blade passage the overturning is not as great for P2 as it is for the planar case, by the time the P2 flow reaches the blade exit the overturning has returned to the same sort of level as the planar case. A quantitative judgement is hard to make but it would appear that the flow visualisation shows a greater overturning at blade exit for P2 than for the planar case.

4.1.2 Blade Surface Flows

Blade surface flow visualisations are included in Figures 4.14-4.22.

The suction surface photographs show that the suction surface flow is in general similar for the three geometries. Figure 4.14 shows the planar case, the passage vortex is shown very clearly. On the right of the photograph the suction side of the horseshoe vortex leaves a distinct trace on the blade surface which remains distinct from the passage vortex until the trailing edge. Figure 4.15 shows the P1 case with the passage vortex trace still being clearly shown but the intensity and height at exit from the blade are reduced in magnitude. The angle of the oil/dye traces from the horizontal is also reduced for the P1 case. Figure 4.16 show the P2 case, again the passage vortex trace is the dominant feature but with reduced intensity and angle from the horizontal compared to the planar case.

The suction side of the horseshoe vortex appears to remain distinct a considerable way along the blade surface and sits considerably above the passage vortex trace for all endwalls. The precise form of the interaction between the suction side of the horseshoe vortex and the passage vortex is not clear, though it appears very similar for different endwalls. Figure 4.33 shows the flow features of P0 with annotations.

The pressure side of the blade yields no useful information as the flow velocity is generally too low and the flow patterns in the regions of interest are virtually identical between endwalls. The pressure surface figures are included for completeness rather for new insights that they provide into the flow. Pressure side flow visualisations are found in Figure 4.17, 4.18 and 4.19. The pressure side photographs do reveal two things, the velocity near the trailing edge increases so that the flow visualisation starts to work at that point and that the flow has low radial components at any point shown by the oil/dye traces.

Leading edge views of the endwall are shown in Figures 4.20, 4.21 and 4.22 for P0, P1 and P2 respectively. The flows are very similar. For P2 the radial movement of the suction side of the horseshoe vortex appears to have been delayed slightly resulting in a “kinked” shape to the trace. For both P1 and P2 the suction side of the horseshoe vortex leaves a signature that is dark line (absence of dye) next to a bright line (presence of dye). The effect is most pronounced on P2, this may be due to changes in the strength of the horseshoe vortex brought about by endwall profiling.

4.1.3 Perspective Views

Perspective views provide a useful way of locating flow features on geometric features. In this chapter three views are included for each endwall. Figures 4.23, 4.24 and 4.25 show the suction surface and the endwall together. This allows the interaction between the suction surface trace and the endwall flow to be seen more clearly. In particular the P1 picture highlights the ridge that enhances the corner vortex flow.

The pressure surface and endwall are shown in Figure 4.26, 4.27 and 4.28 for P0, P1 and P2 respectively. The P0 photograph shows the horseshoe vortices particularly well, something that is not so clear when only one endwall panel is used. The P1 photograph shows how the large stagnant region sits on top of the upstream

ridge.

The leading edge and endwall are shown in Figure 4.29, 4.30 and 4.31 for P0, P1 and P2 respectively. The perspective view again shows the position of the stagnant region relative to the P1 geometry. This perspective view also shows the interaction of the horseshoe vortex and the suction surface for all geometries.

4.2 Overview

A comprehensive collection of photographs of oil/dye flow visualisations have been presented in this chapter. These photographs show a reduced pressure side of the horseshoe vortex migration in both profiled cases with no discernible trace seen at all on the endwall. Significant changes are observed regarding the horseshoe vortex for both profiled cases with a large stagnant area being observed for the P1 geometry. Blade surface visualisations confirm the reduced strength of the passage vortex but indicate that the fundamental flow dynamics are the same.

4.3 Flow Visualisation Photographs

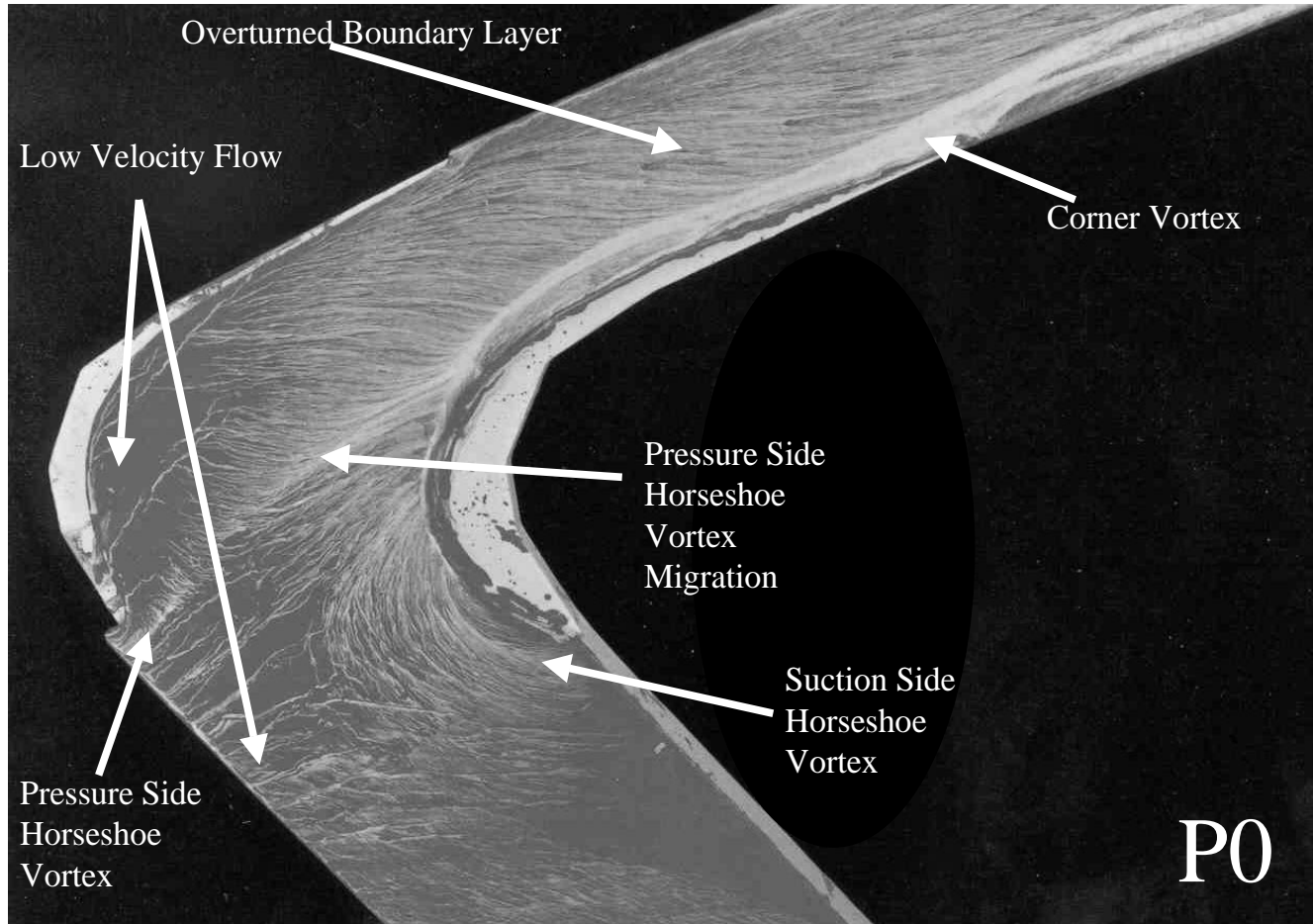


Figure 4.2: Annotated View of P0.

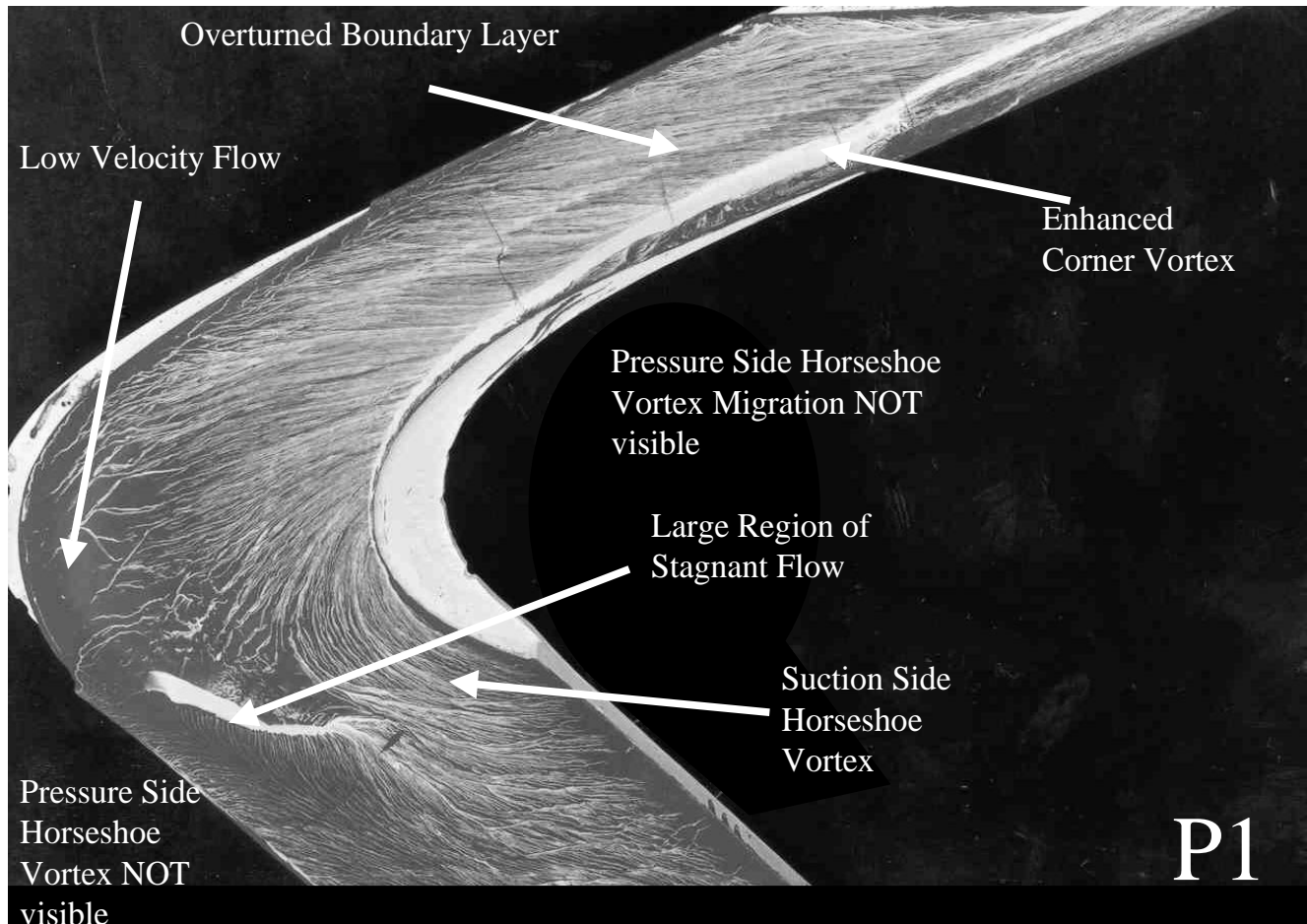


Figure 4.3: Annotated View of P1.

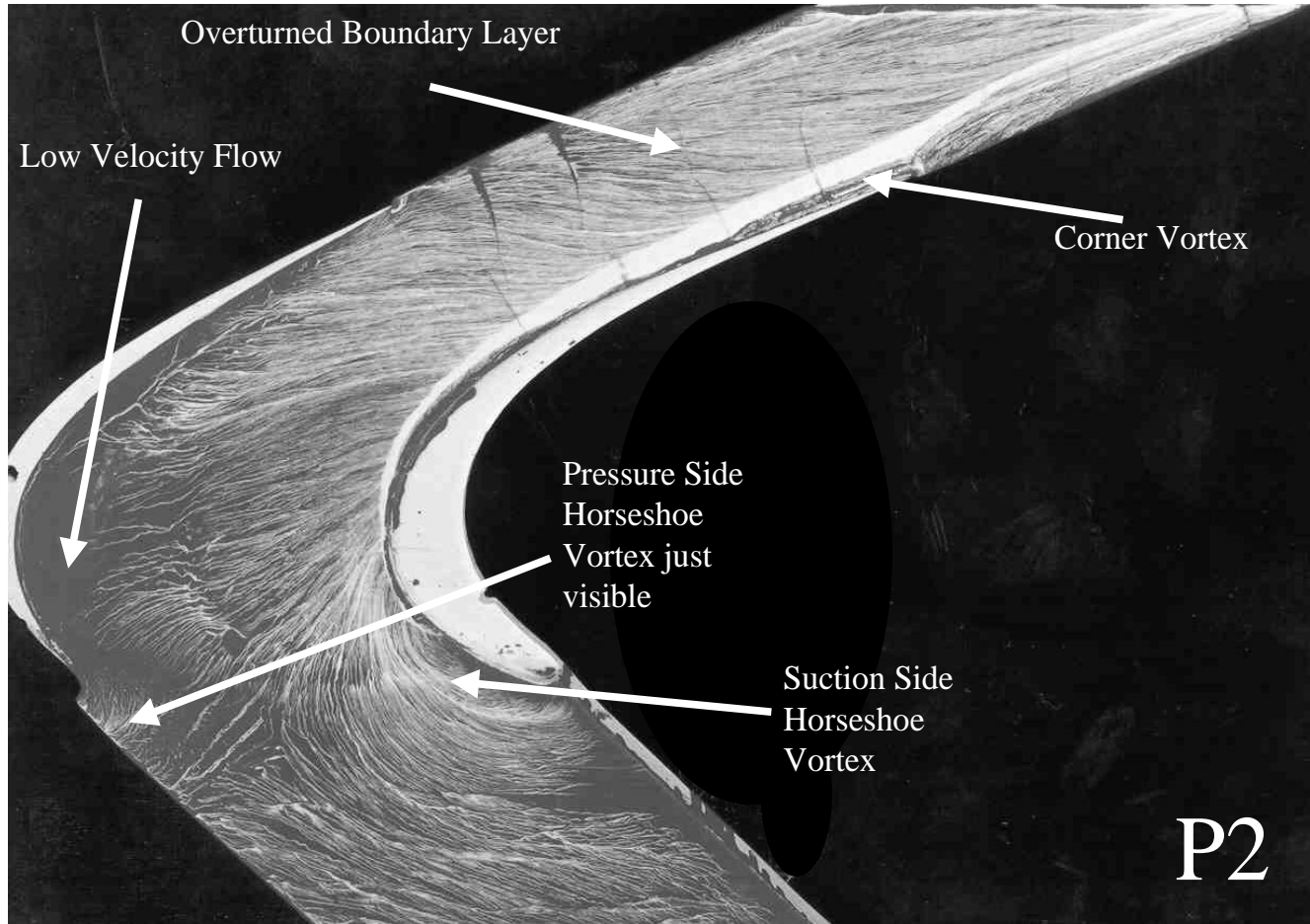


Figure 4.4: Annotated View of P2.

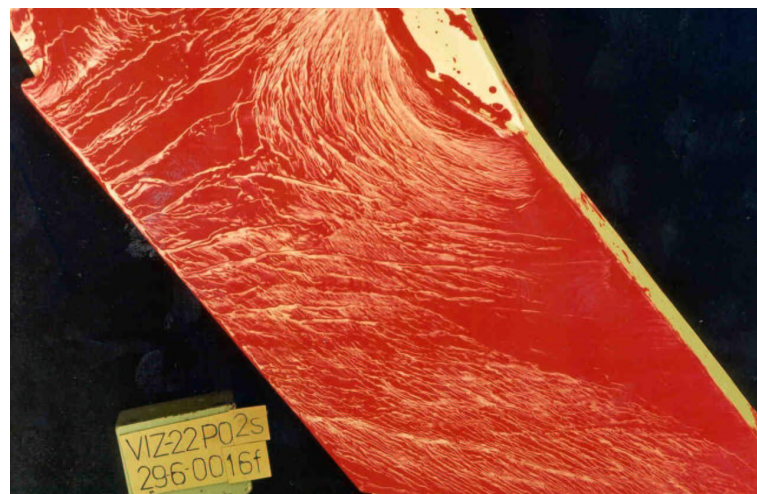


Figure 4.5: Flow Visualisation P0 Inlet View.

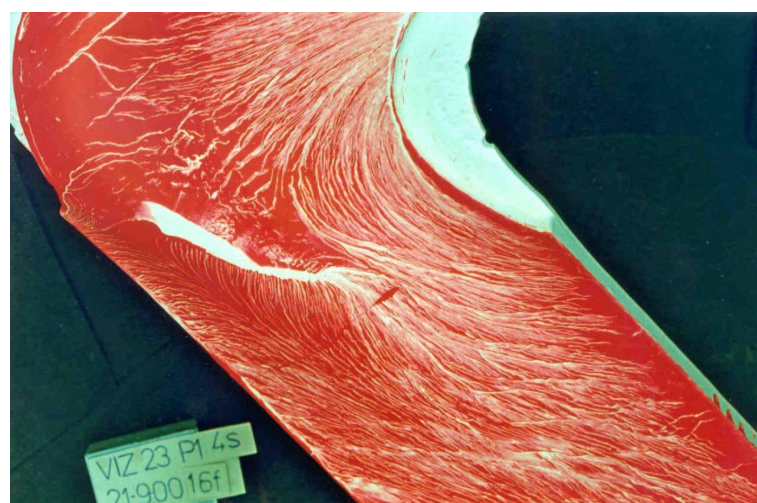


Figure 4.6: Flow Visualisation P1 Inlet View.

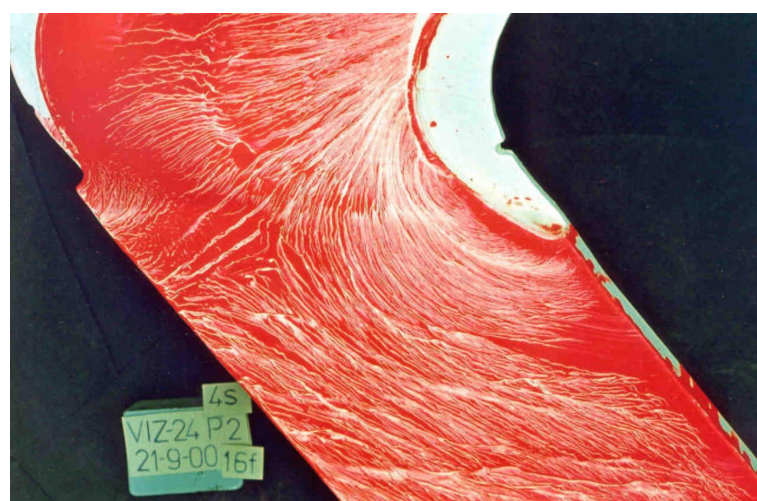


Figure 4.7: Flow Visualisation P2 Inlet View.



Figure 4.8: Flow Visualisation P0 Blade Row View.

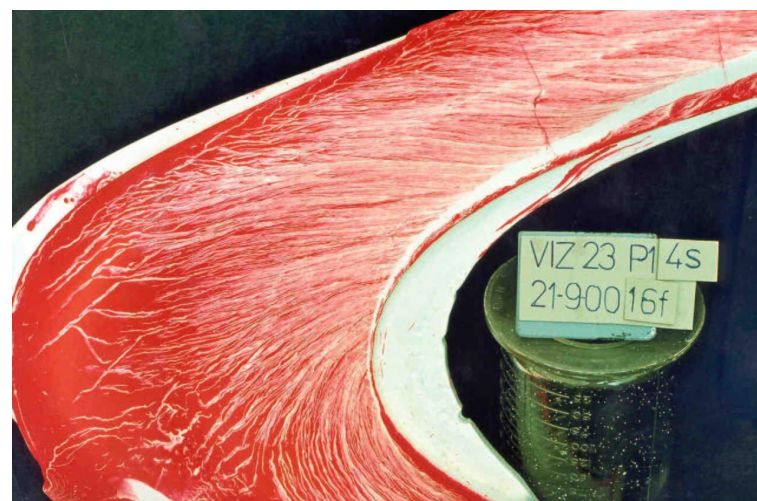


Figure 4.9: Flow Visualisation P1 Blade Row View.



Figure 4.10: Flow Visualisation P2 Blade Row View.



Figure 4.11: Flow Visualisation P0 Exit View.

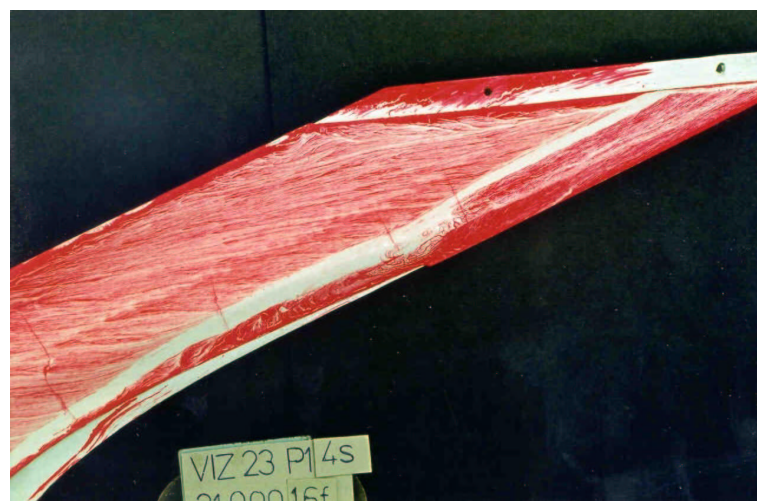


Figure 4.12: Flow Visualisation P1 Exit View.



Figure 4.13: Flow Visualisation P2 Exit View.

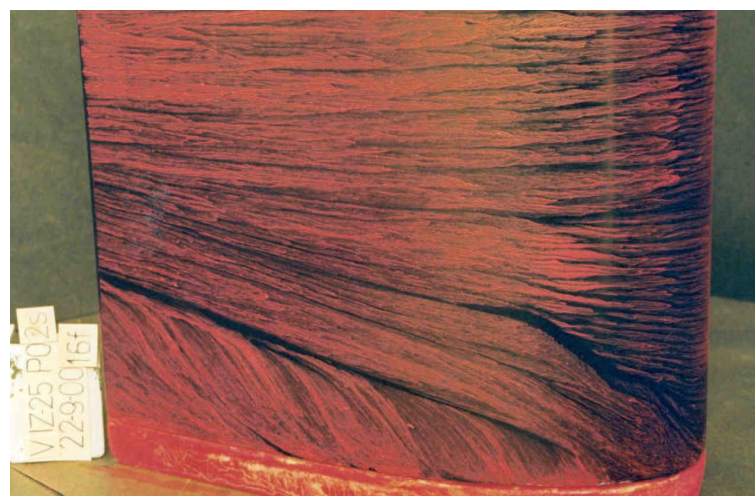


Figure 4.14: Suction Surface P0.

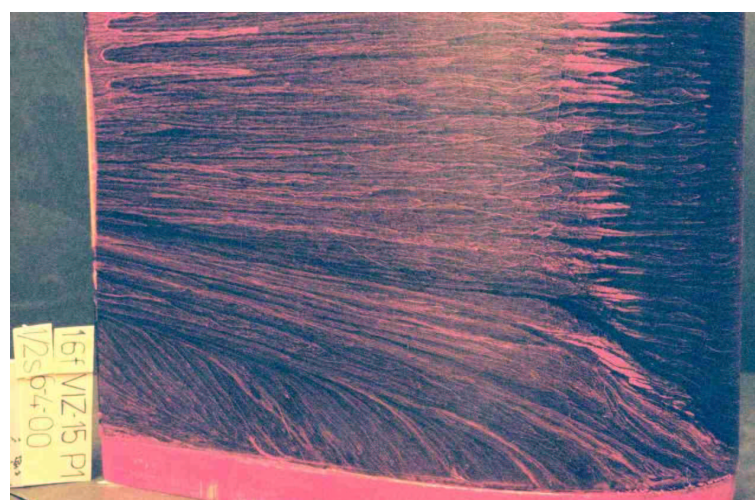


Figure 4.15: Suction Surface P1.



Figure 4.16: Suction Surface P2.



Figure 4.17: Pressure Surface P0.



Figure 4.18: Pressure Surface P1.

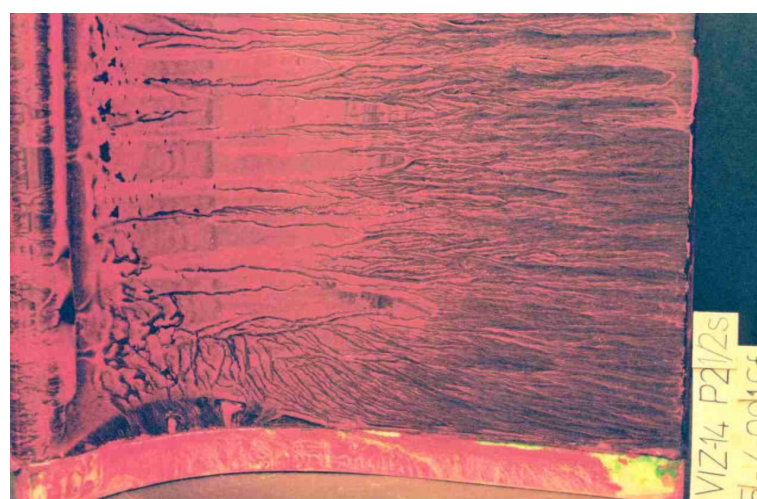


Figure 4.19: Pressure Surface P2.



Figure 4.20: Leading Edge P0.

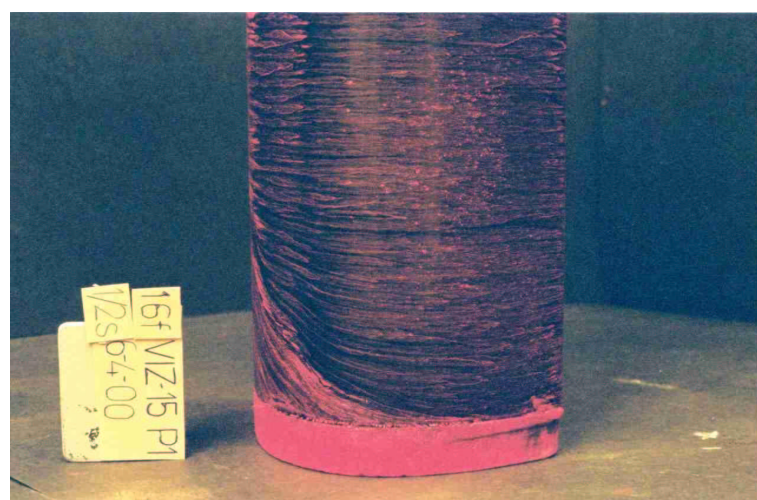


Figure 4.21: Leading Edge P1.

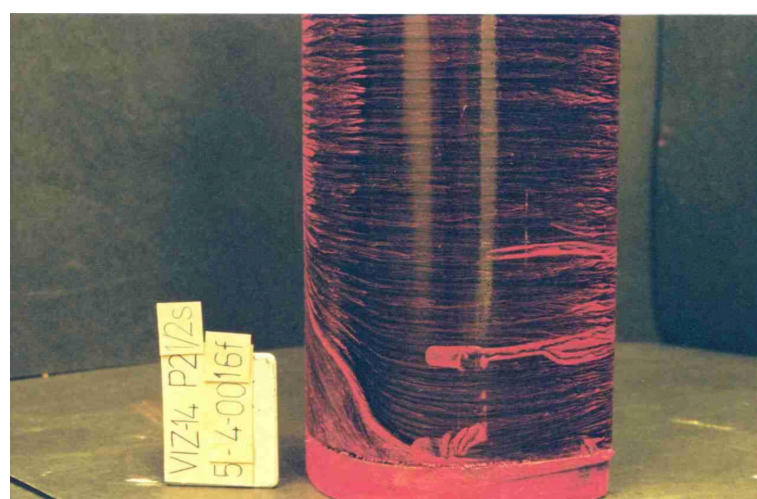


Figure 4.22: Leading Edge P2.

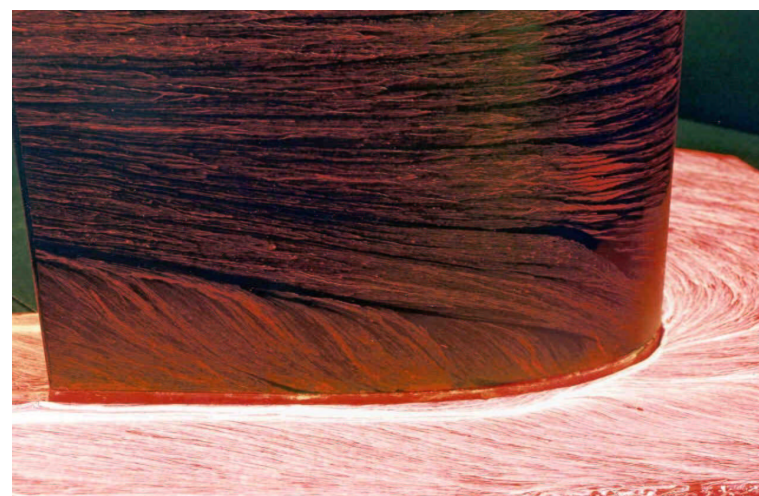


Figure 4.23: Blade and Endwall Showing Suction Surface P0.

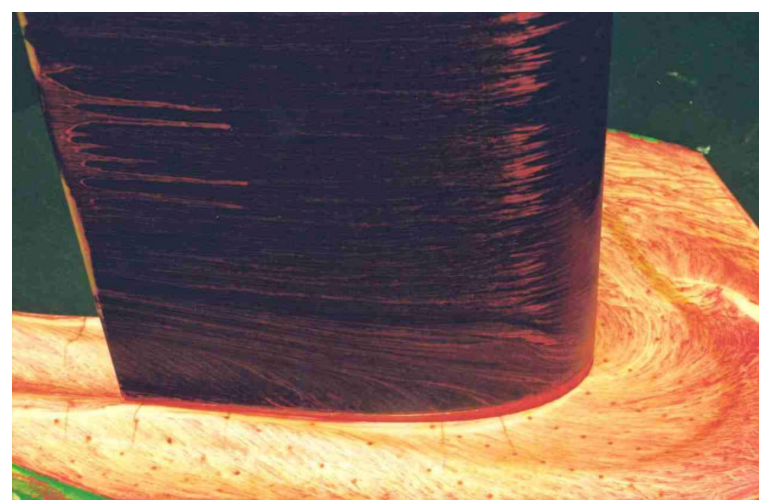


Figure 4.24: Blade and Endwall Showing Suction Surface P1.

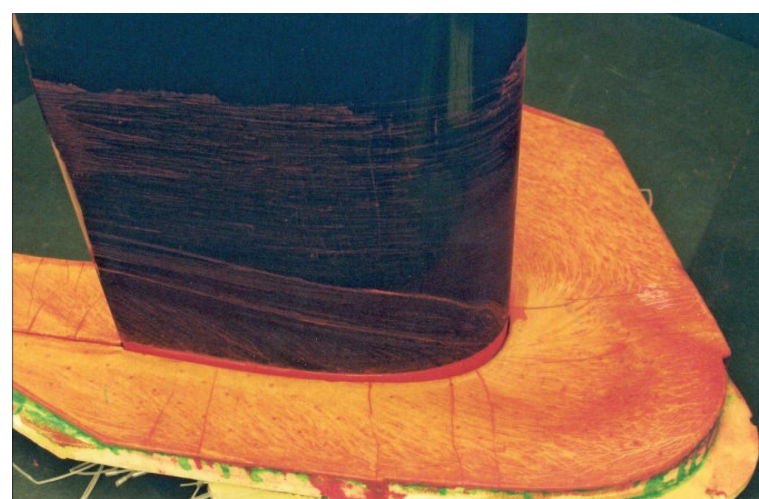


Figure 4.25: Blade and Endwall Showing Suction Surface P2.



Figure 4.26: Blade and Endwall Showing Pressure Surface P0.

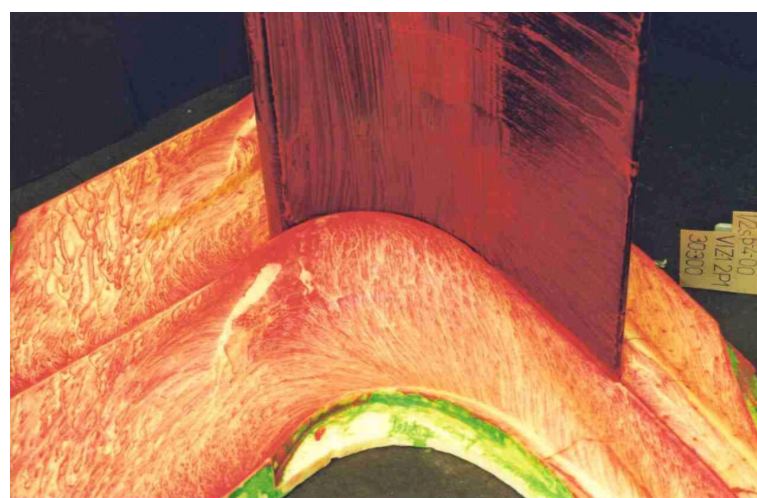


Figure 4.27: Blade and Endwall Showing Pressure Surface P1.

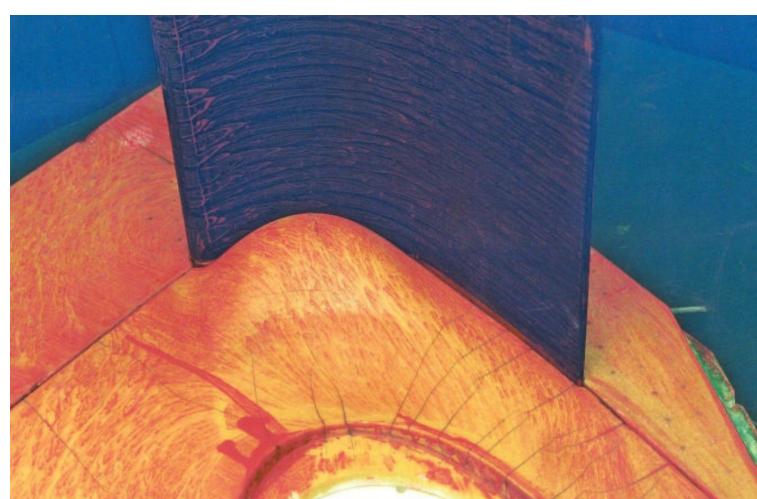


Figure 4.28: Blade and Endwall Showing Pressure Surface P2.

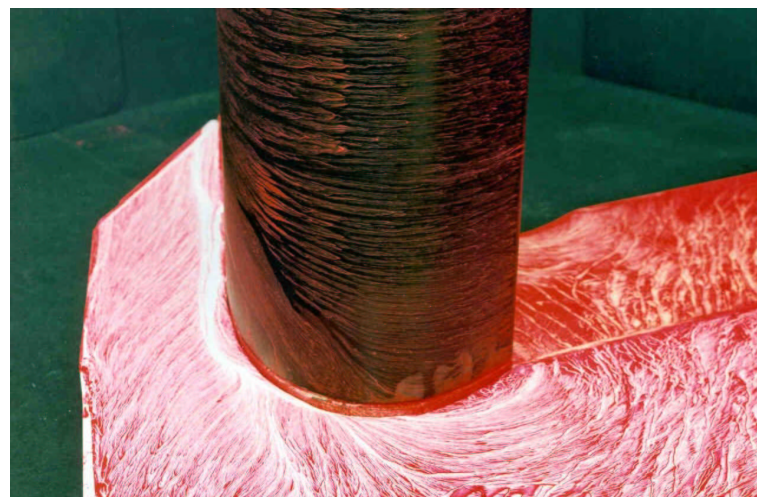


Figure 4.29: Blade and Endwall Showing Leading Edge P0.

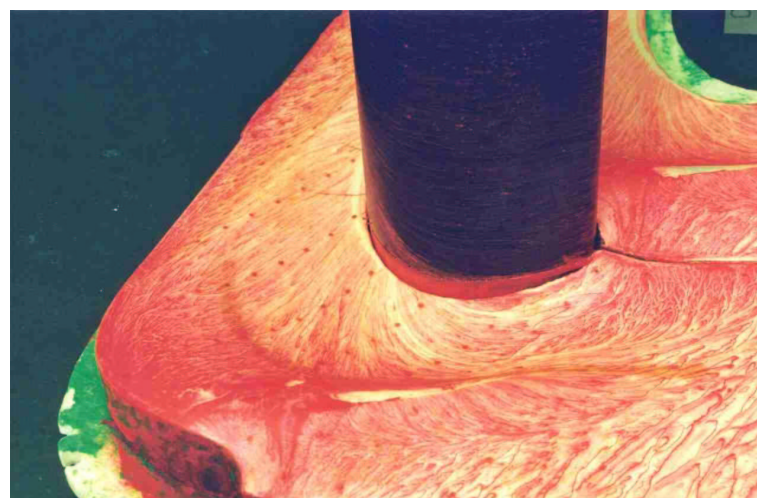


Figure 4.30: Blade and Endwall Showing Leading Edge P1.

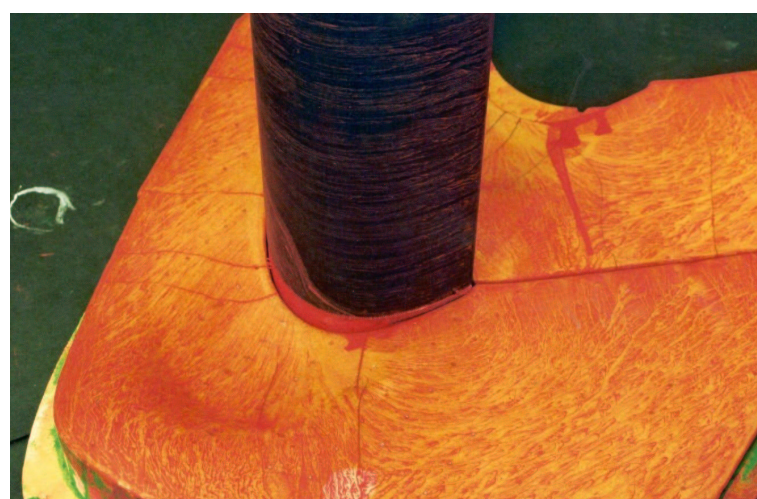


Figure 4.31: Blade and Endwall Showing Leading Edge P2

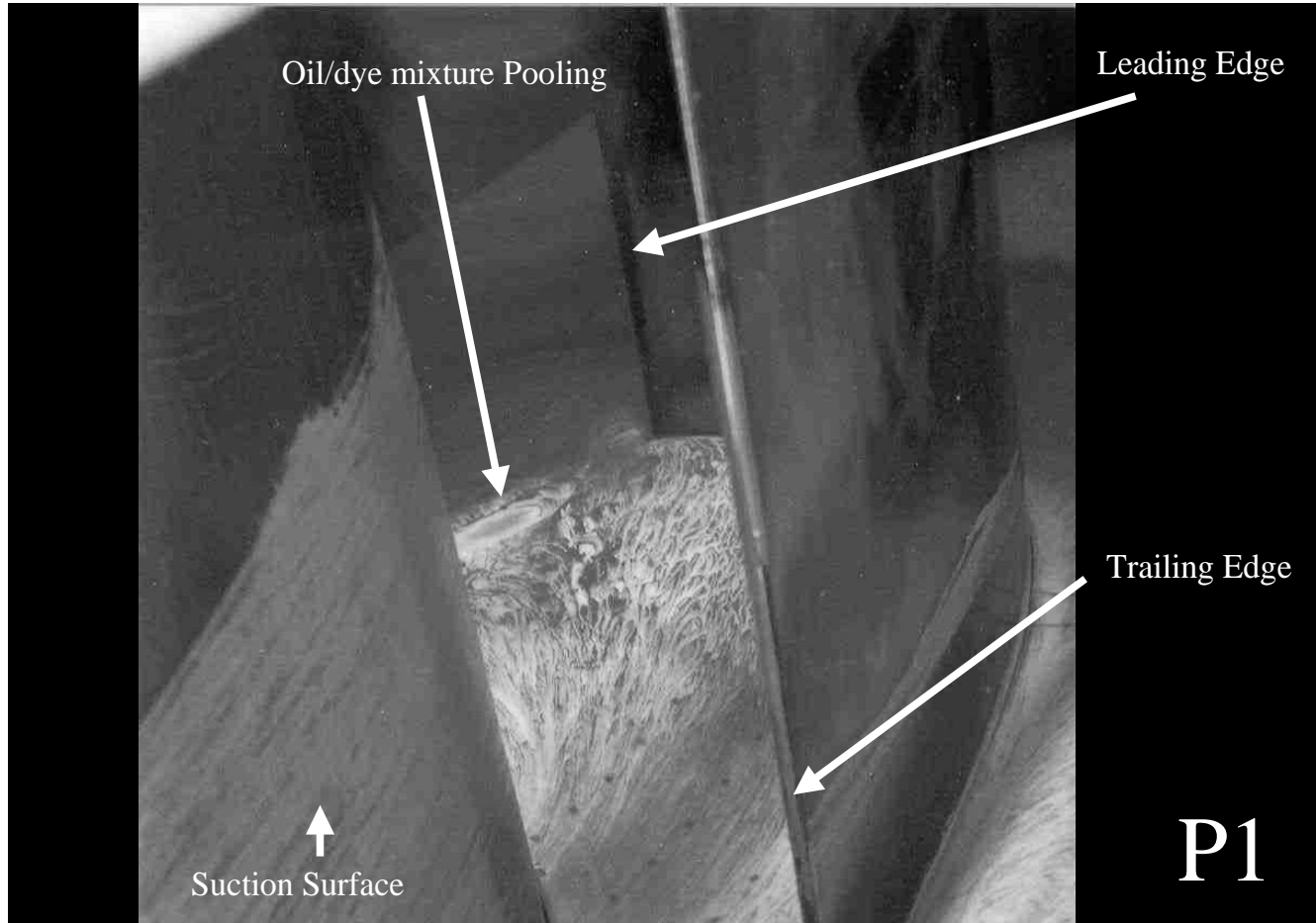


Figure 4.32: P1 Stagnant Region - Fan Running.

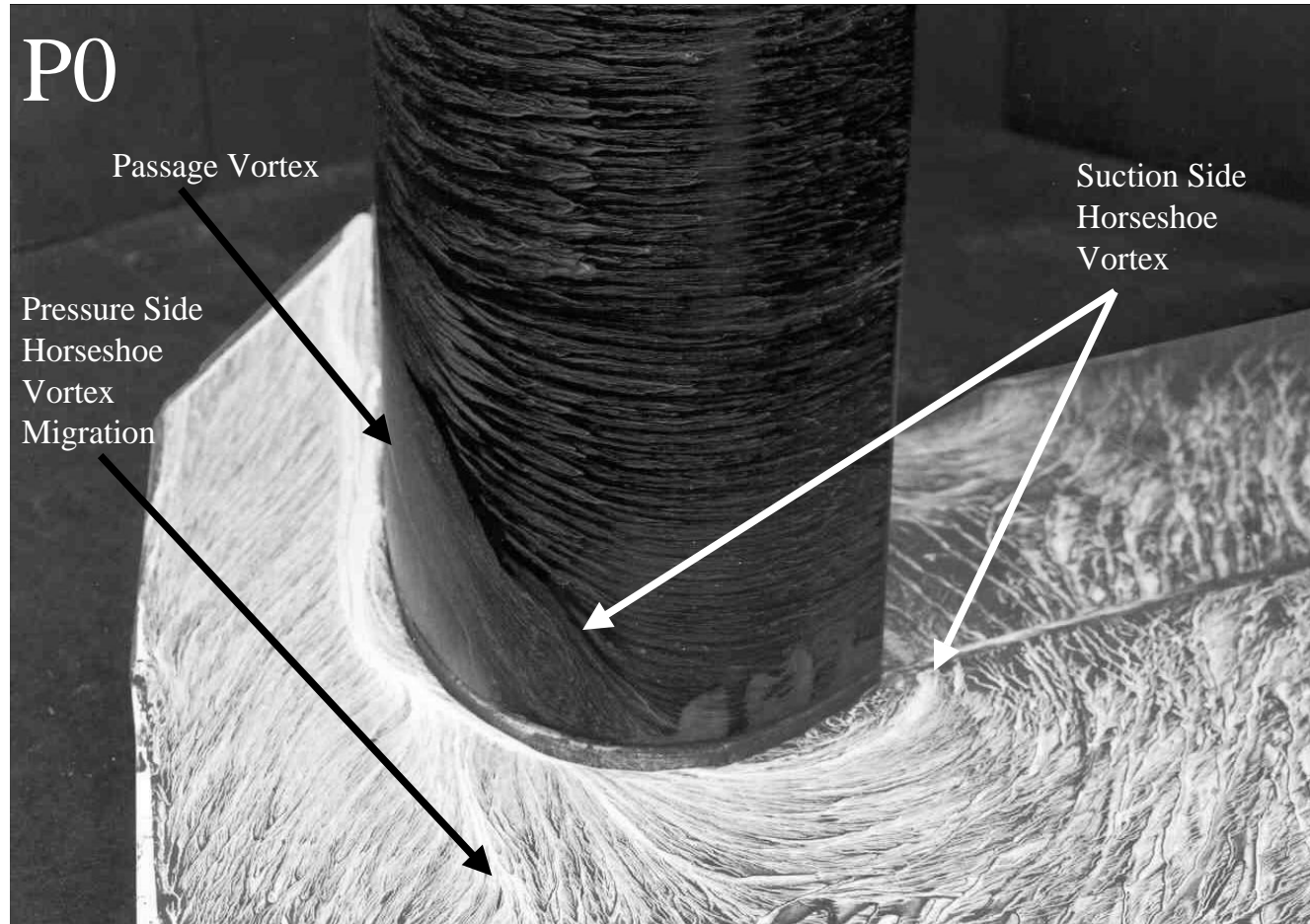


Figure 4.33: Suction Surface Flow Features.

Chapter 5

Pressure Probe Results

THIS LARGE chapter details the pressure probe results for the planar and the first two profiled endwalls. Comparison with the CFD results is left until a separate chapter. This chapter contains four different presentations of results:-

- contour plots and line graphs of the results of instrument checks before and after measurements
- contour plots of loss coefficient, secondary vectors, C_{ske} and vorticity coefficient. Plots of yaw angle contours, pitch angle contours, and static pressure coefficient were made but do not yield enough new information to justify their inclusion.
- graphs of pitch averaged loss coefficient, yaw angle, C_{ske} and vorticity coefficient.
- area averaged values for various traverses and combination of traverses

Contour plots and pitch averaged results are presented in order of increasing axial chord, so the inlet boundary layer studies come first followed by Slot 1 (-9% C_{ax}) through to Slot 10 (128% C_{ax}) results. Following this area averaged results are presented, these values include “net loss” which aims to determine the loss generated inside the cascade by subtracting the inlet boundary loss from the number in question. All area plots and pitch averaged plots are “gross loss” which does not subtract the inlet boundary layer loss.

Contour plots of C_{ske} and streamwise vorticity coefficient are not included for Slots 1 (-9% C_{ac}) to Slot 5 (55% C_{ax}) inclusive as they do not provide enough information to justify their inclusion.

Table 5.1 shows the measurements conducted. Three types of readings are shown in the table the first “5H Readings” refers to five hole probe readings which start 5mm from the endwall, “3H Readings” refers to three hole probe readings which start nominally on the wall ($r=0\text{mm}$) and extend up to 15mm from the endwall and finally “Multiple Readings” refers to whether or not three traverses were conducted at the same plane to give an idea of the repeatability of the measurements. Figure 5.3 shows the locations of the traverse planes for five hole probe readings and Figure 5.4 shows the measurement locations for three hole probe readings. Measurements

Slot No.	% C_{ax}	x/mm	5H Readings	3H Readings	Multiple Readings
1	-9%	-197	Yes	Yes	-
2	6%	-170	Yes	Yes	-
3	22%	-141	Yes	-	-
4	38%	-112	Yes	-	-
5	55%	-81	Yes	-	-
6	71%	-52	Yes	-	-
8	97%	-5	Yes	-	-
10	128%	51	Yes	Yes	Yes

Table 5.1: Measurement Planes for P0,P1 and P2.

of the inlet boundary layer have also been carried out with a three hole probe. The results of the tests of the measuring system are included where appropriate.

All measurements in this section were conducted by the author for the current thesis. Some of them replicate previous measurements taken by Hartland (2001) or Jayaraman (2000) and a comparison of the new results with older published data is included in a later section.

The measurements presented in this chapter were taken over a relatively long period of time and with slightly different versions of the measuring system described in a previous chapter. In particular several of the five hole probe readings inside the blade passage were not conducted with a “back to back” methodology and quite large midspan yaw angle corrections are required to give the same midspan flow values. This was the genesis for the “back to back” methodology. Since flow information inside the blade passage does not extend to the blade pressure and suction surface boundary layers the data yields only qualitative information so the measurements were not repeated with the updated measurement system. The blade positions are plotted on all the plots within the blade passage so that the data is seen in context. For traverses inside the blade passage at different axial locations a different area is measured so mass flow conservation is not expected at each internal slot.

5.1 Validation

For each set of readings the performance of the measurement system was checked by performing a “hand test” as described in Chapter 3. In summary this involves recording readings with the probe through a number of known angles at zero loss and then plotting the error between the known angles and loss value and the ones returned by the instrumentation system. Included in this chapter are only typical results for “before and after” tests - some thirty different “hand tests” were conducted for this thesis and to include them all would have taken an inordinate amount of space.

Figure 5.5 shows contours of error in C_{P0} for the test conducted before measurements for Slot 10(b) and Slot10(c). Figure 5.6 and Figure 5.7 show contours of yaw and pitch error respectively. All the figures show acceptable levels of error, the peaks in the corners of the contour plot are where the calibration map is stretched and although the errors in the corners are too high for accurate readings in practice

<i>trv70</i>	Yaw/[°]	Pitch/[°]
max	11.4	12.7
min	-13.3	-6.9

Table 5.2: Typical maximum and minimum angles relative to the probe at Slot 10.

the edges of the calibration map are not reached very often. At the only plane where the quantitative measurements are used the maximum ranges of yaw and pitch angle relative to the probe are typically $\pm 14^\circ$, Table 5.2 shows typical values of maximum and minimum angle relative to the probe from a P0 Slot 10 traverse.

Figure 5.8 shows contours of C_{P0} error after the tests conducted for Slot 10(b) and Slot 10(c). Figure 5.9 and Figure 5.10 show contours of pitch and yaw error for the post-readings tests. The results are acceptable which shows that there was no deterioration of the measurement system during the test. There appears to be a systematic error of some two degrees in pitch but this is put down to a misalignment when setting up the probe in the calibration jet for the post readings test. These results are representative of the pre and post readings test carried out for five hole probes throughout the thesis.

For three hole probe readings a similar process was carried out, Figure 5.11 shows C_{P0} errors before and after readings were carried out with a three hole probe. Figure 5.12 shows the corresponding yaw angle error plot. These results are representative of those conducted throughout the thesis and indicate an acceptable level of error.

The point of carrying out the “hand test” is to identify major and minor problems with the instrumentation system. In particular if a major leak had developed during traversing it might affect the results considerably without the experimenter being aware of it. The hand test ensures that such errors can be located and dealt with in a timely manner.

5.2 Inlet Boundary Layer

Inlet boundary layer measurements are taken one axial chord upstream of the blade leading edge and three tangential locations are available to take measurements. Figure 5.13¹ shows all the results and Figure 5.14 shows the final inlet boundary layer.

It is immediately apparent that measurement differences due to changes in tangential position are greater than measurement differences due to changing endwalls. The profiling for P1 extends far upstream of the leading edge and concerns had been raised about the effect on the inlet conditions but these fears are shown to be unfounded. The area of “negative loss” shown in Figure 5.14 is a well known feature of the Durham Cascade and is due to the non-uniform spacing of the turbulence grid upstream of the cascade. For further details see Cleak (1989) or Moore (1995).

The inlet boundary layer was first averaged and then corrected to give zero loss at midspan, in the same way that other traverses were. This data is then averaged

¹A list of symbols used for pitch averaged graphs may be found on page xxvi

Case	Slot 1	Slot 2	Slot 3	Slot 4	Slot 5	Slot 6	Slot 8
P0	-3.0	-4.3	5.1	0.1	-0.0	-2.1	-2.3
P1	-2.4	-4.2	-2.9	-1.4	0.9	-0.5	-0.0
P2	-3.1	-4.2	-2.2	-0.1	0.0	2.6	-0.0

Table 5.3: Yaw Angle Corrections Slot 1 to Slot 8.

using the standard mass weighting technique to give a final inlet boundary layer loss coefficient. This is calculated to be: -0.01513. This value is used to calculate the net loss for the combined data sets. Due to the large area of “negative loss” in the boundary layer the area averaged value is negative, i.e. it represents an energy gain relative to the probe reference position.

The values in Table 3.3 on page 30 are taken from the measurements described in this section.

5.3 Slot 1 (-9% C_{ax})

Three and five hole probe readings were conducted for Slot 1. In order to negotiate the leading edge of the blades very high angles of incidence of flow on to the probe head are required.

5.3.1 Five Hole Readings at Slot 1 (-9% C_{ax})

A special calibration had to be conducted for the five hole readings at Slot 1 to ensure that only a very small number of points were out of range. This involved rotating the probe by 24° in the calibration rig before a calibration was conducted. (The special calibration covered +12° in Yaw to -60° in Yaw) This produced reasonable results but a large number of the points in the Slot 1 traverse had an incidence to the probe of 60° or so. With these measures four points remained out of range for P2 and three for P1. They were estimated by linear extrapolation (using a spreadsheet) in the radial direction only. The traverse consisted of around one thousand points so the effect of the estimated points should not be too great.

The P1 traverse for Slot 1 also missed the last radial line closest to the endwall to avoid probe/endwall interference. (Profile P1 is contoured at this measurement plane, the other geometries are not). This can clearly be seen on the contour plots. In order to make the results comparable the area averaging for Slot 1 is carried on P0 and P2 for an equivalent number of points.

A correction was applied to the midspan yaw angle to match them up to a 42.5° inlet angle. Previous studies have suggested that the actual inlet to the cascade is 43.5° as there is a deflection caused by the upstream turbulence grid. The main point of the present work is to compare the results for different endwalls so a correction to the nominal inlet yaw angle was felt to be acceptable. The differences between corrections for each endwall are quite small which provides some justification for examining relative yaw angles rather than absolute ones. Table 5.3 lists the corrections used for Slots 1 to 8.

Figures 5.15 to 5.17 show the loss results and Figures 5.19 to 5.21 show the secondary vectors. Pitch averaged loss is shown in Figure 5.18 and pitch averaged yaw angle in Figure 5.22. The arrangement of figures is such that the area plots and pitch averaged plots for the same quantity appear on the same page for easy comparison, this arrangement is repeated for each slot location.

The following points are immediately apparent from inspection of the figures:-

- The fact that the P1 profiling extends well upstream of the leading edge is immediately apparent.
- The loss profile essentially follows that of the inlet boundary layer, the endwall profiling has no effect at this slot. This is especially clear from the pitch averaged plot of loss in Figure 5.18.
- The midspan yaw angles agree reasonably well to within 0.5° or so. (Figure 5.22). Endwall profiling cause significant changes in the pitch averaged yaw angle up to 30% of midspan height.
- There are significant differences in the secondary vectors for the three endwalls, the leading edge flows of P1 and P2 are much larger than those of P0. Much of this flow might be present within an inviscid flow without an inlet boundary layer, so it is not what is classically considered secondary flow.

5.3.2 Three Hole Readings at Slot 1 (-9% C_{ax})

Three hole probe readings were taken at Slot 1 using a specially made cranked three hole probe (see Figure 3.6 on page 37) which was designed to avoid the cobra head contacting the endwall in regions of high curvature. Testing with more conventional three hole probes indicates that the cranked head and “traditional” probes give very similar results, so the new design does not appear to interfere with the flow.

As with the earlier Slot 1 traverses a special calibration had to be conducted with the probe to get the increased range required for Slot 1, as the blade position means that an extremely high incidence (30°) to the probe head was found even at midspan. The yaw angle range encountered near the endwall was however even greater than the -66° to +18° provided by the special calibration. There were points with yaw angles greater than +18° relative to the probe head. These points are dealt with by using the original ±42° calibration. A combined output file was then created using a spreadsheet, taking the in range points from each calibration.

The three hole probe measurement grid consisted of firstly a midspan traverse at $r=200\text{mm}$ to allow the agreement between three and five hole probe readings to be determined and secondly a series of close wall measurements from $r=0\text{mm}$ (nominal) to $r=15\text{mm}$ or the profiled equivalent. The three hole probe readings were corrected to the same midspan yaw angle (42.5°) and loss (zero) at midspan and midpitch as the five hole probe readings.

The area plots of loss are shown in Figures 5.23 to 5.25 with the pitch averaged values in Figure 5.26. Note that the radial scale on the area plots is different for P1. Plots of secondary velocity vectors are shown in Figures 5.27 to 5.29 with the pitch averaged yaw angles in 5.30. Plotted alongside the three hole probe pitch

averaged points are the five hole probe results to give some idea of the agreement at the endwall. Given that both the three hole and the five hole probes are operating at the absolute limits of their range the agreement is fair.

The secondary velocity vectors do not contain any pitch angle variation as this information is not available with a three hole probe. These plots of “quasi” secondary flow do provide a more useful guide to what is going on in the flow than yaw angle contour plots which are extremely difficult to interpret. Yaw angle plots do not give any indication as to the magnitude of the flow so flows with very low velocities can appear very significant. Although the “quasi” secondary flow vectors are more useful than yaw angle contours care is needed to interpret these plots - especially in areas where there is significant variation in endwall height in the tangential direction.

The data set for three hole probe results is plotted and processed as if it ended at the endwall exactly ($r=0\text{mm}$ for a planar endwall), this is not strictly true as the probe has a finite thickness of approximately 1mm. In reality therefore the actual data set ends at about 0.5mm from the endwall. Assuming that the data set continues to the wall causes problems when trying to compare with CFD data and was only adopted as the most convenient way of plotting the data. Future work should precisely plot the position of the data.

The following points are illustrated by the close wall results:-

- The area loss plots are different for each endwall and the high loss regions are associated with the blade leading edges. (Figures 5.23-5.25)
- The loss cores associated with the blade leading edges are larger for the P1 case (Figure 5.24) than for the other two cases though the overall loss at the endwalls is larger for the other two cases.
- The cross flows seen in Figures 5.28 and 5.29 for profile P1 and P2 are much larger than the planar case (Figure 5.27). Qualitatively the flow appears to be pushed around the leading edge towards the suction side of the blade leading edge.
- The graphs of pitch averaged loss (Figure 5.26) and yaw angle (Figure 5.30) are not at all smooth, this is put down to the high flow angles encountered by the probe and the “out of range” points that are left in the data files.

Presentation and discussion of area averaged results is left until section 5.11 on page 89.

5.4 Slot 2 (6% C_{ax})

5.4.1 Five Hole Readings at Slot 2 (6% C_{ax})

Figures 5.31 to 5.33 show the loss for Slot 2. Figures 5.35 to 5.37 show the secondary flow. Pitch averaged loss is shown in Figure 5.34 and pitch averaged yaw angle in Figure 5.38.

The loss profile still largely reflects the inlet boundary layer. Due to the extremely high curvature just downstream of Slot 2 on profile P2 the last two radial

lines of the traverse were removed. This means that very little flow information of interest is actually obtained.

The traverses are corrected to the same midspan angle to allow easy comparison with the three hole and the five hole results. This angle is simply the average of the midspan ($r=200\text{mm}$) yaw angles that were obtained with a five hole probe (16.6°), the variations between endwall geometries is actually very small. An examination of the results indicates that the secondary flows appear larger for the profiled cases, however this may be simply due to inviscid effects from the large height perturbations that are present on the endwall at this axial location.

The following points can be ascertained:-

- The loss follows closely the pattern of the boundary layer, at least within the measurement plane captured in the traverse (Figure 5.34). The secondary flows seen in Slot 1 have not yet materialised into altered loss patterns.
- Flow patterns are generally similar for the planar and profiled cases. (Figures 5.35-5.37). There is a limited amount of evidence for the existence of the suction side of the horseshoe vortex being seen in P0 and P1 at $t=20\text{mm}$, $r=-5\text{mm}$ and $t=25\text{mm}$, $r=5\text{mm}$. This feature does not appear to be present in P2 where any effect appears dominated by the large crossflow that occurs.
- P2 has the largest crossflow of all endwalls despite the fact that the profiling is of a lower magnitude than for P1. (See Figure 5.38) This is put down to a potential effect of the large curvature on the pressure side of the P2 profiling. The curvature can be seen in the contours of endwall height in Figure A.2 on page 286.

5.4.2 Three Hole Readings at Slot 2 (6% C_{ax})

The area plots of loss are shown in Figures 5.39 to 5.41 with the pitch averaged values in Figure 5.42. Area plots of yaw angle are also included in Figures 5.43-5.45 with the pitch averaged values in 5.46.

The following points can be ascertained:-

- The loss boundary layer is still very large compared to measurement area (Figure 5.42). In fact it is larger than the measurement area, since the 99% thickness of the inlet boundary layer is 30mm this is not surprising.
- The loss distribution at this Slot 6% C_{ax} is now different for each endwall (Figures 5.39-5.41). The P0 loss is relatively evenly distributed along the endwall, the P2 loss is concentrated near the pressure side and the P1 loss is generally smaller than the other two geometries.
- The “quasi” secondary flow plots (Figures 5.43-5.45) indicate that the increased overturning for P2 continues close to the endwall. The lack of pitch information from the three hole probe makes the secondary flows on P1 look smaller than they actually are. For P1 a lot of the flow seen with the five hole probe has quite a large pitch angle directed towards the endwall which is not captured by the three hole probe readings.

- Large parts of the boundary layer are now being overturned, i.e. the secondary flow is from the pressure side to the suction side, whereas as slot 1 it was in the other direction. (Figures 5.43-5.45)

5.5 Slot 3 (22% C_{ax})

The Slot 3 readings were taken with an early version of the measuring system and so are not a “back to back” set, i.e. the probe was moved and the endwall was kept constant during the traverses, this necessitates quite large yaw angle corrections. Additionally the Slot 3 readings do not have the confidence test and the settling time tests applied to them. The yaw angle to which these results are adjusted is selected as 2.48° which is the average of the uncorrected results.

Figures 5.47 to 5.49 show the loss results and Figures 5.51 to 5.53 show the secondary vectors. Pitch averaged figures are included in Figures 5.50 and 5.54 for loss coefficient and yaw angle.

The following key points are made about the plots:-

- The loss is now less evenly distributed with peaks for P0 at $t=100\text{mm}$, P1 $t=50\text{mm}$ and P2 at $t=35\text{mm}$ (Figures 5.47-5.49).
- The profiled endwalls have a very similar or higher loss than the planar case (Figures 5.47-5.49). The loss pattern at this axial location is still dominated by the boundary layer profile.
- There is a clearly defined vortex structure seen in the planar case (Figures 5.51-5.53). This does not occur for P1 or P2 where there is simply a crossflow from pressure surface to suction surface.
- This is reflected in the pitch averaged yaw angle values (Figure 5.54) where there is a clear difference between the bulk flow patterns between P0 and the profiled cases.
- There appears to be a spurious vector on the P2 results (Figure 5.53) at $t=35\text{mm}$, $r=0\text{mm}$. This is most likely due to the confidence tests and settling time not being implemented for this traverse.
- Much of the secondary flow is due to the endwall curvature at this slot - rather than “classical” secondary flow which is due a boundary layer being overturned. (i.e. it would be present in an inviscid flow with no inlet boundary layer)

5.6 Slot 4 (38% C_{ax})

The Slot 4 readings are taken using the “back to back” methodology with the confidence test and settling time functions used. The yaw angle is corrected to the same midspan value (-17.4°) but the magnitude of the corrections is quite small compared to the previous slot. This is shown in Table 5.3 - this shows the benefits of leaving

the traverse gear in place and changing the endwalls. The yaw angle variation between midspan and the endwall is extremely large for these data sets - for the P0 case eleven points all at $r=5\text{mm}$ were out of range and had to be estimated using linear extrapolation using a spreadsheet.

Figures 5.55 to 5.57 show the loss for Slot 4. Figures 5.59 to 5.61 show the secondary flow. Pitch averaged figures are included in Figures 5.58 and 5.62 for loss coefficient and yaw angle.

The following points are noted here:-

- Distinct loss cores are starting to form in each of the geometries (Figures 5.55-5.57).
- Profiled endwalls still have the same or greater loss than the planar case (Figures 5.55-5.57).
- Vortex like structures are now present in the two profiled cases as well as in the planar case. (Figures 5.59-5.61) This is reflected in the pitch averaged yaw angles as well with the midspan flows matching up much better.

5.7 Slot 5 (55% C_{ax})

The Slot 5 readings are taken using the “back to back” methodology with the confidence test and settling time functions used, however the probe had to be recalibrated for the last traverse (the P1 traverse). The yaw angle is corrected to (-38.2°) and again the spread of corrections is quite small. The yaw angle variation between midspan and the endwall is again very high for this slot so six points for the P0 case and two for the P1 case had to be extrapolated to give reasonable data values.

Figures 5.63 to 5.65 show the loss for Slot 5. Figures 5.67 to 5.69 show the secondary flow. Pitch averaged figures are included in Figures 5.66 and 5.70 for loss coefficient and yaw angle.

The following points are noted here:-

- Loss cores are now distinct for each end wall. (Figures 5.63-5.65).
- Profiled endwalls have slightly less loss than the planar one. (Figures 5.63-5.65)
- The passage vortex for the profiled cases is smaller and nearer the endwall than the planar case flow structure (Figures 5.67-5.69). The profiled passage vortices are further away from the suction surface than the planar one. The planar vortex centre is at $t=30\text{mm}$ for P0 and at 45mm and 50mm for P1 and P2 respectively. This links in with the flow visualisation shown in Chapter 4 which shows a reduced crossflow within the blade passage for P1 and P2 (Figures 4.8-4.10 on page 66).
- Thus it would appear that profiled endwalls are delaying the cross passage flow - the pitch averaged yaw angles hide this fact by averaging over a pitch.

5.8 Slot 6 (71% C_{ax})

The Slot 6 readings were taken with an early version of the measuring system and so are not a “back to back” set, i.e. the probe was moved and the endwall was kept constant during the traverses. Additionally the Slot 6 readings do not have the confidence test and the settling time tests applied to them. The yaw angle to which these results are adjusted is selected as -53.7° which is the average of the uncorrected results. The corrections required to achieve this midspan angle are found in Table 5.3. All data points were within the range of the probe so no extrapolation was necessary.

Figures 5.71 to 5.73 show the loss for Slot 6, Figures 5.75 to 5.77 show the secondary flow. From Slot 6 onwards C_{ske} and streamwise vorticity coefficient are plotted, these quantities are shown in Figures 5.79 to 5.81 for C_{ske} and Figures 5.79 to 5.85 for vorticity. Pitch averaged figures are included in Figures 5.74, 5.78, 5.82 and 5.86 for loss coefficient, yaw angle, C_{ske} and vorticity respectively.

The following points are noted here:-

- P0 loss is now much greater than the profiled cases. (Figures 5.71-5.73) This appears to be due to the interaction of the passage vortex with the suction side of the blade. Since the profiled passage vortices are nearer the pressure surface this interaction is delayed and/or reduced.
- The peak loss for all geometries is in nearly the same place (Figures 5.71-5.73).
- The passage vortex for the profiled cases remains smaller and nearer the endwall than the planar case flow structure (Figures 5.75-5.77). This is shown in the pitch averaged yaw angles plot as the P0 case has the greatest under turning and over turning of the three endwalls. The reduced secondary flow activity near the endwall ties in quite well with the flow visualisations reported in Chapter 4, where the endwall oil/dye traces show that P1 and P2 have a smaller amount of overturning than the planar case.
- C_{ske} values for P0 are much larger than those found in P1 and P2 (Figures 5.79-5.81), which reflects the results seen in the secondary vectors plot.
- The increased secondary flows for P0 are also reflected in the streamwise vorticity coefficient plots (Figures 5.83-5.85) which show increased activity for P0 compared to the two profiled cases.

5.9 Slot 8 (97% C_{ax})

The Slot 8 readings were taken with an early version of the measuring system and so are not a “back to back” set, i.e. the probe was moved and the endwall was kept constant during the traverses. Furthermore the Slot 8 readings do not have the confidence test and the settling time tests applied to them. The yaw angle to which these results are adjusted is selected as -69.5° which is the average of the uncorrected results. Table 5.3 lists the actual corrections used. All data points were within the range of the probe so no extrapolation was necessary.

Figures 5.87 to 5.89 show the loss for Slot 8, Figures 5.91 to 5.93 show the secondary flow, C_{ske} and vorticity are shown in Figures 5.95 to 5.101. Pitch averaged figures are included in Figures 5.90, 5.94, 5.98 and 5.102 for loss coefficient, yaw angle, C_{Ske} and vorticity respectively.

The following points are noted here:-

- The planar case exhibits the greatest loss, both in terms of the overall pitch averaged values (Figure 5.90) and the peak value in the contour plots (Figures 5.87-5.89). All of the pitch averaged loss results illustrate a double peak/peak-shoulder pattern of loss.
- The centres of the passage vortex for the planar and profiled cases remain in different positions, with the P0 vortex being much stronger (Figures 5.91-5.93). The P0 profile has the greatest under turning of all three geometries.
- On Figures 5.91-5.93 the position of the suction side of the horseshoe vortex at blade exit determined from flow visualisation studies is plotted. This represents the largest spanwise extent of secondary flow at the blade surface. As can be seen in the figures the secondary vector plots are consistent with the surface flow visualisation with P0 having the greatest extent of secondary flow (See Figures 4.14-4.16 on page 68). Due to the difficulty of estimating axial position from the photographs this is the only slot at which flow visualisation information is included on the area results.
- The P2 profile now has the greatest over turning (though the actual value is close to the planar endwall) the flow at the endwall is also more uniform than for the other geometries. See Figure 5.94.
- The P2 profiling is effectively zero at this point (97% C_{ax}) but the profiling for P1 continues downstream.
- C_{ske} (Figures 5.95-5.97) and Vorticity (Figures 5.99-5.101) plots confirm the remarks above. The C_{ske} plots indicate two areas of secondary flow activity, one associated with the passage vortex loss core and the second on the endwall at midspan.
- The streamwise vorticity plots show positive values above the passage vortex loss core. (Figures 5.99-5.101) This is put down to the presence of the suction side of the horseshoe vortex. In addition the P0 contour plot shows a region of extremely high positive vorticity on the suction side close to the endwall this is evidence of the counter vortex.

5.10 Slot 10 (128% C_{ax})

The Slot 10 readings are taken using the “back to back” methodology with the confidence test and settling time functions used. The yaw angle is corrected to the nominal exit angle of -68.7°. The required correction for each traverse at Slot 10 is shown in Table 5.4. Since Slot 10 is the measuring plane at which profiles are

Case	Slot10a	Slot10b	Slot 10c
P0	3.4	1.0	0.9
P1	3.3	0.9	0.9
P2	3.4	1.0	0.9

Table 5.4: Yaw Angle Corrections Slot 10.

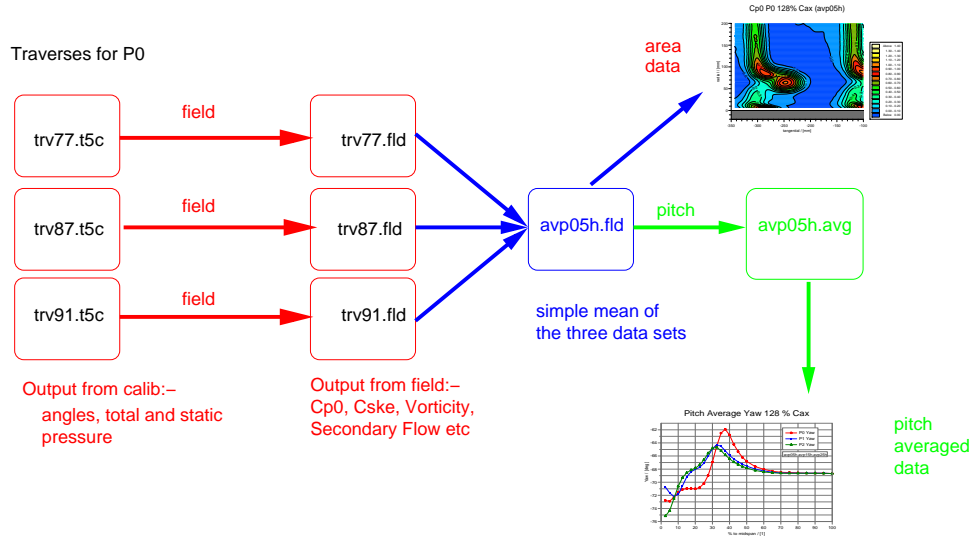


Figure 5.1: Data Processing Chain for Repeated Data

ranked it was the subject of five traverses for each geometry. This thesis presents results for only three of these traverses per endwall as they were completed using the latest version of the measuring system and are the most accurate. The omitted traverses support all the points made in this thesis so no erroneous conclusions are drawn by missing out data that does not “agree”. Having three results for each endwall geometry gives some idea of the repeatability of the experiments and allows a realistic estimate of the error in the measurements to be obtained.

Area averaged traverses are presented for five hole probe and three hole probe readings. These area plots are plots of averages of the three traverses at each point. The data processing “chain” is shown in Figure 5.1. The difference between the averaged area plots and individual area plots is very small and so is not shown. The variation between pitch averaged readings is shown in a later subsection and is worthy of comment.

5.10.1 Five Hole Probe Results for Slot 10 (128% C_{ax})

Figures 5.103 to 5.105 show the loss for Slot 10, Figures 5.107 to 5.109 show the secondary flow, C_{ske} and vorticity coefficient are shown in Figures 5.111 to 5.117. Pitch averaged figures are included in Figures 5.106, 5.110, 5.114 and 5.118 for loss coefficient, yaw angle, C_{ske} and Ω_s respectively. These figures are produced by processing the individual data sets and then averaging the results (see Figure 5.1)-this means that yaw angle corrections etc. can be applied before the averaging takes

place. A few general remarks about the flow at Slot 10 are made:-

- There are three vortical structures in the plots. The first is the passage vortex, the second is the corner vortex and the third is associated with the trailing shed vorticity of the blade/suction side of the horseshoe vortex. These are shown diagrammatically in Figure 5.2.
- Both profiled geometries reduce C_{ske} and Loss (Figure 5.114 for C_{ske} and Figure 5.106 for loss). Both geometries reduce the under turning at 30-40% of mid-height. P2 increases the over turning with respect to the planar case (Figure 5.110).
- The enhanced corner vortex for P1 is clearly seen in the vector plots (Figure 5.108) and alters the pitch averaged yaw angle at the expense of greater loss (Figure 5.106).
- The “kink” on the pitch averaged loss plot for P1 at around 5% of midspan height (Figure 5.106) is due to the increased loss due to the enhanced corner vortex for P1 being offset from the endwall slightly ($t=-280\text{mm}$, $r=10\text{mm}$ see Figure 5.104). More succinctly this “kink” is a real flow feature and not an artifact of the measuring process.
- The altered over turning of P1 is only a *pitch averaged* effect. Across the pitch at $r=5\text{mm}$ the area plots (see Fig 5.108) show there are regions of much increased over turning and regions of suction surface to pressure surface flow.
- The increased over turning on P2 near the endwall is evident in the Secondary Vectors plot (Figure 5.109) as well as the pitch averaged yaw angles graph (Figure 5.110).
- The overturning for both profiled endwalls is consistent with the flow visualisation results which show that *downstream* of the blade passage the overturning for P2 is greater than that for P0 and the overturning for P1 is about the same (See Figures 4.11-4.13 on page 67).
- The C_{ske} (Figures 5.111-5.113) contours show much higher levels of C_{ske} for P0 than P1 or P2. The enhanced corner vortex for P1 also results in increased C_{ske} near the endwall.
- Streamwise vorticity plots show positive and negative vorticity (Figures 5.115-5.117). Positive vorticity represents anti-clockwise flow and negative vorticity represents clockwise flow. The passage vortex (negative vorticity, clockwise rotation) is distinct from the shed vorticity/suction side of horseshoe vortex (positive vorticity, anti-clockwise rotation). Nearer the endwall high values of vorticity result from the existence of the corner vortex. The vorticity coefficient plots show the planar profile with the greatest activity and also highlight the large amount of secondary flow associated with the enhanced counter vortex for P1.
- The flow is reasonably periodic, the traverse covers 127% of a pitch.

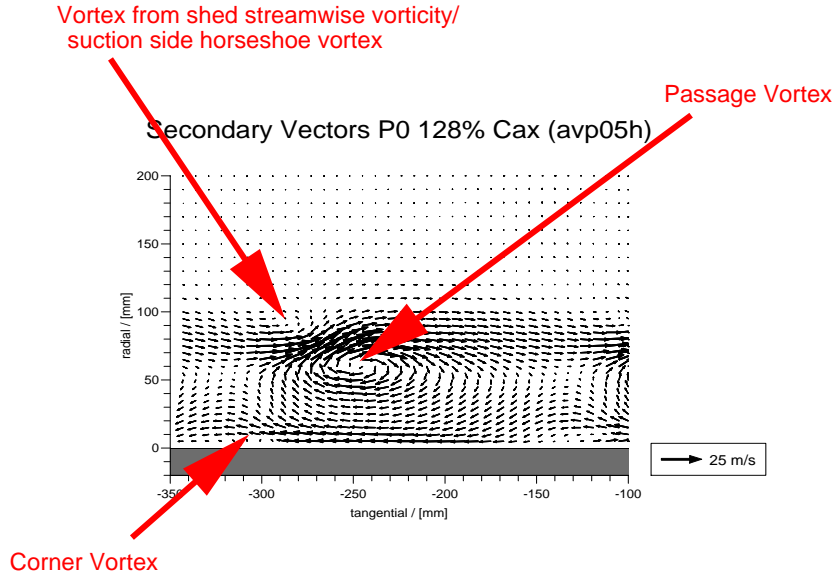


Figure 5.2: Nomenclature for Vortex Labels

5.10.2 Three Hole Probe Results for Slot 10 (128% C_{ax})

The area plots of loss are shown in Figures 5.119 to 5.121 with the pitch averaged values in Figure 5.122. “Quasi” secondary flow is shown in Figures 5.123 to 5.125 with the pitch averaged values in 5.126. Once again the values shown are averaged values of three separate traverses. Plotted alongside the three hole probe results are the corresponding five hole probe results. The agreement at this slot is much better than that in slots 1 or 2 probably because the probe is operating at much less extreme yaw angles. The pitch angles experienced by the probe are also much less at Slot 10 as the profiling is of a much smaller magnitude.

A few general remarks about the flow at Slot 10 are made:-

- The enhanced corner loss means that the P1 case has the greatest loss (Figure 5.120).
- The increased overturning for P2 (Figure 5.125) does not manifest itself as increased loss compared to the planar case (Figure 5.122).
- The agreement with five hole probe readings is excellent for both pitch averaged loss (Figure 5.122) and pitch averaged yaw angle (Figure 5.126).
- Although the enhanced corner vortex appearing on P1 reduces the overturning somewhat the overturning for P1 is still greater than the planar case.

5.11 Axial Variation of Area Averaged Values

In this section the growth in area averaged quantities through the cascade are described, this section uses the results from five hole probe readings only. Care needs to be taken when interpreting the figures in this section as the measurement areas

for blade rows do not include the blade boundary layers and represent slightly different fractions of the total flow depending on the blade/endwall/probe geometry at the slot in question.

Figure 5.127 shows the massflow variation through the cascade. If the measurement volumes were the same at each slot the massflow should be the same. However since the blade boundary layers are missed out of the traverses inside the blade row the massflow is underestimated inside the blade passage. The agreement between different profiles at most slots and the agreement between inlet and exit is however encouraging.

The fact that the massflow in is the same as the massflow out leads to the conclusion that the endwall profiling has not introduced large radial migrations of the flow. The policy of measuring only to half span and only profiling one endwall of the cascade appears to be justified. The fact that the massflows in and out are the same also provides support for the policy of yaw angle corrections since the axial velocity is obtained by $V_x = V \cos \alpha$.

The closeness of the massflow readings at each slot is also encouraging, as this suggests that despite not capturing the whole area of the internal slot the reduced area traverses are giving representative results. That is, endwall profiling has not moved significant amounts of flow into the fraction of the cascade that were not traversed during measurements. Thus comparisons between different endwalls at Slot 5 (55% C_{ax}) for example, are meaningful as the bulk of the flow is captured in all cases.

Figure 5.128 shows the change in yaw angle through the cascade, the yaw angle is corrected at midspan but the level of agreement indicates that endwall profiling is not changing the amount of turning done by the blade row and therefore in a real machine the amount of work done would be the same. The blade exit is at 100% C_{ax} hence there is no change in yaw angle after that point. There is a large difference in the area averaged yaw angle at Slot 3 - the planar case is different from the two profiled cases - this is due to the fact that at Slot 3 there is vertical flow for P0 (Figure 5.51) but not for P1 or P2 (Figures 5.52, 5.53). This results in a large difference in pitch averaged yaw angle between the planar and the profiled cases (Figure 5.54) which leads to a different area averaged yaw angle. The data processing procedure ensures that the *midspan* yaw angles are the same. If as in the case of Slot 3 the yaw angles over the rest of the span are different the $\bar{\alpha}$ value will also be different.

Figure 5.129 shows the growth of secondary kinetic energy through the cascade. Care must be taken when interpreting this figure as the measurement planes inside the blade row (Slots 2 to 8) do not cover the whole blade row. Nevertheless the plot does show dramatic reductions in C_{ske} for both profiled cases relative to the planar case. C_{ske} is based on the square of velocity differences ($C_{ske} = (V_{sec}^2 + V_r^2) / V_{ups}^2$), so small changes in velocity are magnified by C_{ske} . Therefore it is not surprising that there is a dramatic reduction in C_{ske} , but what is surprising is the closeness of C_{ske} values for P1 and P2.

Figure 5.129 also shows the “potential” effect of endwall profiling, much of the C_{ske} in Slots 2,3 and 4 would be present in an inviscid flow through the cascade with no inlet boundary layer. This shows up in the C_{ske} values though is not necessarily

Slot No.	P0	P1	P2
10(a)	trv70	trv69	trv72
10(b)	trv87	trv88	trv86
10(c)	trv91	trv90	trv92

Table 5.5: Slot 10 Repeated Traverses

what one would classify as secondary flow.

Figures 5.130 and 5.131 show the loss growth through the cascade for loss coefficient and secondary loss coefficient respectively. Area averaged loss quantities discussed in this section are gross values - that is the inlet boundary layer loss is not subtracted. The plots confirm the previous remarks about the closeness of loss growth between the planar and the profiled endwalls until Slot 4 (38% C_{ax}) where a difference begins to emerge. The plot of secondary loss, where secondary loss is the total loss minus the midspan loss removes the effects of the blade wakes from the downstream traverses. This means that Figure 5.131 is a better examination of the loss growth through the cascade. The P1 profile performs better than P2 in terms of loss production until after the trailing edge of the blade where the loss associated with the enhanced corner vortex contributes much more to the loss total.

5.11.1 Repeatability: Five Hole Probe Results

As discussed above each profile has three measurements taken at Slot 10. Each of these measurements were conducted from scratch each time, that is they were taken on different days and all the equipment was reset before the next set of repeatability runs was conducted. So for each set of readings Slot 10(a), 10(b) and 10(c) the tangential position and yaw angle of the probe was reset. This allows us to quantify the repeatability of the experiments and estimate the effects of probe setting variation etc. The variation on area plots is very small between traverses and no comparison is therefore made. A small amount of variation can be seen in the pitch averaged plots. In order to aid interpretation of the figures Table 5.5 lists the traverse numbers used for the traverse.

Pitch averaged results for Loss and yaw are show in Figures 5.132 and 5.133. The degree of variation appears to be very small with extremely good qualitative agreement between all the traverses. This is confirmed by Figure 5.134 which shows the maximum difference between pitch averaged loss at each radial position. Figure 5.135 shows an identical plot for yaw angles. These plots show that the maximum loss difference is over 0.1, however this is one point near the endwall on P1 and a much more typical value would be 0.02. Yaw angle agreement is excellent with all angles agreeing within less than half a degree.

Area averaged results are shown in Table C.4 on page 294 as well as in Figures 5.136 and 5.137.

Net loss is obtained by subtracting the inlet boundary loss from the total loss coefficient to give the loss growth in the cascade, the following remarks would apply equally to gross loss however. The level of variation in loss results is quite surprising given the good agreement that is apparently present in the pitch averaged results. For example the planar secondary loss maximum variation between the Slot 10(a)

	P0	P1	P2	Error Estimate
Net total	0.1503	0.1336	0.1289	± 0.005
Net secondary	0.0723	0.0554	0.0517	± 0.004
% Planar Case	100.0	76.5	71.4	± 5.1

Table 5.6: Mean Loss and Error Estimate for Five Hole Probe Readings.

run the Slot 10(c) run is some 3.6% of the mean value which seems quite high when compared to the pitch averaged plots.

The error bars used in Figure 5.136 (total loss) and Figure 5.137 (secondary loss) are 0.005 and 0.004 respectively. For each set of readings for P0,P1 and P2 the mean and standard deviation was taken and twice the largest standard deviation for the total and secondary loss calculation is used for the error bars. Should repeated loss measurements follow a normal distribution this means that the mean value plus or minus two standard deviations should encompass 95.5% of all readings, Kreyszig (1983). Obviously with such a small sample size (three) sophisticated statistical methods are somewhat suspect as a single “rogue” value will have a big effect, but this is at least a rational way of assessing the error associated with endwall measurements that can be logically extended should further experiments be conducted. Figure 5.138 shows the secondary and total loss on the same scale which illustrates that the secondary loss is about half the total loss.

Table 5.6 lists the mean and error margins for loss measurements associated with the three endwalls and the mean net secondary loss with error bars is plotted in Figure 5.139. Significantly it is apparent both profile losses will offer improvements over the planar case, but that the error bars for the P1 and P2 cases overlap. These data represent the best estimate available of loss generation using a five hole probe.

Area averaged yaw angles are shown in Figure 5.140 the variation in yaw angles is much less than for loss. The error bars are again twice the maximum standard deviation for the P0, P1 and P2 data set. The variation is very small, the abscissa on Figure 5.140 is only half a degree. The most notable piece of information that can be extracted from this graph is that the difference in turning between endwalls is very small meaning the overall work output for the blade row is largely unaffected. The maximum change in area averaged yaw angle is between P0 and P2 and amounts to 0.13° or 0.2% of the planar value.

5.11.2 Repeatability: Three Hole Probe Results

A similar exercise in repeating the measurements at Slot 10 was conducted for three hole probe results as for the five hole probe results. Table 5.7 lists the three hole probe traverses that make up each repeatability test. In general similar results were obtained with the pitch averaged values showing good agreement but the area averaged values showing several percentage points of variation between different measurements. Pitch averaged results for loss and yaw are show in Figures 5.141 and 5.142. Again the agreement between different traverses is quite good, for the yaw angles there appears to be some sort of systematic offset for each profile. However the scale is much finer than for the Five Hole results (Figure 5.133) so small differences are much more apparent.

Slot No.	P0	P1	P2
10(a3)	trv77	trv76	trv78
10(b3)	trv94	trv99	trv93
10(c3)	trv97	trv96	trv98

Table 5.7: Slot 10 Repeated Traverses: three hole probe.

	P0	P1	P2	Error Estimate
Gross total C_{P0} 3H	0.3069	0.4149	0.2441	± 0.040
% Planar Case	100.0	135.2	79.5	± 13.0

Table 5.8: Mean Loss and Error Estimate for Three Hole Probe Readings. (0-7.5% Span)

Area averaged values of loss are shown in Figure 5.143, the error bars are once again twice the largest standard deviation. The three hole probe area averaged loss results are the gross figures i.e. without the boundary layer subtracted off them, as subtracting either the whole boundary layer or only the first 15mm from the three hole probe does not have much physical meaning. In the first case one would be comparing a measurement to half span with a measurement to 8% of span and in the second case one would be comparing the inlet boundary layer with a highly skewed new boundary layer.

Figure 5.143 shows that the P1 profile has the largest loss in the close wall region, which is unsurprising given the existence of the enhanced corner vortex. The differences close to the endwall are quite large even as a % of the planar case. One would expect the loss differences to be much larger as near the endwall the boundary layer loss means that the overall loss is much higher. Whereas for the five hole results the average net total loss for P2 was some 14.2% lower than the planar case for the three hole probe results the largest difference is a 35% increase from the planar case to the P1 case. The P2 geometry actually results in a 20% reduction in loss at the endwall. Clearly the enhanced corner vortex is a major loss producing feature, but the enhanced crossflow in P2 does not appear to be contributing to increased loss compared to the planar case. The results are summarised in Table 5.8.

5.11.3 Synthesised Data Set.

In order to obtain the best measurement of loss, the three and five hole probe averaged data sets are combined to produce a synthesised data set. This data set consists of the three hole readings up to and including 5% ($r=10\text{mm}$ for a planar wall) of span, the remainder of the data set is taken up by five hole probe readings. For this combined data set the amount of information available reduces to the lowest common denominator which in this case is C_{P0} , C_P , V_x and V_t . From this one can obtain yaw angle (α) and “quasi” secondary velocity. The point is to look at how the overall loss picture is affected by the addition of the boundary layer loss measurement by our three hole probe. Figures 5.144 and 5.145 show the pitch averaged loss and yaw. The loss shows that although the boundary loss is very high compared to

3H 5H Results	P0	P1	P2	Error Estimate
Net total	0.1574	0.1431	0.1322	± 0.005
Net secondary	0.0807	0.0650	0.0557	± 0.004
% Planar Case	100.0	80.5	69.0	± 5.1
5H Results	P0	P1	P2	Error Estimate
Net total	0.1503	0.1336	0.1289	± 0.005
Net secondary	0.0723	0.0554	0.0517	± 0.004
% Planar Case	100.0	76.5	71.4	± 5.1

Table 5.9: Combined Three and Five Hole Probe Readings.

the passage vortex loss core the % span that it covers is quite small. The yaw plot shows the increase in overturning that occurs with the P2 geometry and the reduction that occurs due to the counter vortex with P1. Although the readings show a very good match up between loss and yaw angle there is a static pressure measurement difference between the three hole probe and the five hole probe at midspan and this is reflected in the axial velocity plot which is shown in Figure 5.146.

The synthesised data set is intended to examine the changes in the area averaged values caused by including the three hole probe measurements as well as provided a definitive measurement of the loss generation from the three endwalls. The P1 data set shows an increase in loss when the three hole measurements are included and the P2 shows a decrease in loss when compared to the planar case. This is shown in Table 5.9 which contains values for the synthesised data set as well as values from Table 5.6 for comparison. Figure 5.147 shows the net secondary loss of the combined data set along with error bars taken from the five hole data set. Figure 5.148 shows the change in secondary loss for each of the geometries when the three hole readings are combined.

The major point from this work is that including the close wall readings captures more of the loss of the P1 enhanced corner vortex and the fact that P2 has a lower close wall loss than the planar case means that the apparent performance of P2 relative to the datum is improved. If the error estimates are kept the same as for the five hole probe the values for P1 and P2 are now outside the expected range of experimental error.

The synthesised data set represents the “state-of-the-art” loss measurement in the Durham Cascade and is the most accurate assessment of the performance of endwall profiling in this thesis.

5.11.4 Mixed Out Loss

A mixed out loss calculation as described in Chapter 3 was carried out on the data at Slot 10. The mixed out loss calculation allows an estimate of the potential for deleterious effects of remaining secondary flow features to be calculated. Whether it should represent the “definitive” loss ranking parameter is open to debate. On the one hand it takes into account loss that has not yet been realised at the measurement plane, on the other hand the subsequent blade rows are not an infinite distance

	128% C_{ax}			Mixed out loss		
	P0	P1	P2	P0	P1	P2
Net total	0.1503	0.1336	0.1289	0.2346	0.1930	0.1828
Net secondary	0.0723	0.0554	0.0517	0.1046	0.0839	0.0694
% Planar Case	100.0	76.5	71.4	100.0	80.2	66.3

Table 5.10: Mixed out loss for five hole probe readings.

	128% C_{ax}			Mixed out loss		
	P0	P1	P2	P0	P1	P2
Net total	0.1574	0.1431	0.1322	0.2086	0.1865	0.1724
Net secondary	0.0807	0.0650	0.0557	0.1082	0.0907	0.0763
% Planar Case	100.0	80.5	69.0	100.0	83.8	70.5

Table 5.11: Mixed out loss for synthesised data set.

downstream and some of the secondary flow which is mixed out may in fact produce useful work.

Five Hole Probe Mixed Out Loss.

Table 5.10 shows the mixed out loss values for P0, P1 and P2. The mixed out calculation does not change the ranking of the profiled endwalls and in fact improves the relative performance of P2 somewhat. This is put down to the higher levels of secondary kinetic energy associated with the enhanced corner vortex of P1. Figure 5.149 shows the changes in secondary loss when the mixed out calculation is applied.

Synthesised Data Set Mixed Out Loss.

Mixed out loss can be calculated from the synthesised data as well. As can be seen from equation 3.53 on page 53, the mixed out loss calculation depends on C_P , V_x , $V_{t\infty}$ and $V_{x\infty}$ all of which can be obtained from a three hole probe. The mixed out loss for the combined data set is show in Table 5.11. When the mixed out loss is included for the synthesised data set, the relative performance of P2 improves relative to P1 as the secondary kinetic energy associated with the enhanced corner vortex is mixed out. Figure 5.150 shows the change in area averaged loss coefficient when the mixed out loss calculation is carried out.

5.12 Vortex Core Movement

The centre of the passage vortex can be identified from the secondary vector plots described earlier and the position plotted as the flow feature moves downstream. As Langston (2001) remarks “vortex” is an inherently fuzzy term and the identification of the vortex centre from the secondary plots is done by eye without a rigorous mathematical basis. More rigorous definitions exist see Langston (2001) for more details but for the purposes of this thesis judging by eye will suffice.

The vortex centres are plotted in Figure 5.151. A noticeable vortex structure exists earlier for the planar case than for the profiled cases. The planar vortex core is also swept more rapidly across the passage than the profiled case, as can be seen at Slots 5 and 6. The planar vortex core also rises faster than the profiled ones ending up at Slot 10 some 10mm higher than the profiled cases.

Figure 5.151 plots the vortex cores with tangential coordinate as the ordinate. Figure 5.152 plots the vortex cores with the ordinate as distance from the suction surface or blade wake centreline. This approach was used by Gregory-Smith and Graves (1983) and reveals the extent changes in passage vortex migration produced by endwall profiling. For the planar case the migration is as measured by Gregory-Smith and Graves (1983) but for the profiled cases the migration is such that the passage vortex centre moves *away* from the suction surface through the blade row. However determining the centre of the vortices is somewhat arbitrary for the profiled cases at Slot 8 (Figures 5.92 and 5.93).

5.13 Overview

This chapter has described the pressure probe results for the first two generations of profiled endwall and compared them to the planar reference case. In contrast to previous work Jayaraman (2000) the P2 profile produces the least loss - this discrepancy will be discussed further in Chapter 9. Results are available at eight different axial planes through the blade row and at three locations close wall measurements are available to supplement the bulk flow measurements made using a five hole probe.

Endwall profiling changes the flow around the leading edge of the blade significantly and delays formation of the passage vortex, which when it is formed migrates more slowly across the blade passage than the planar case. The profiled passage vortices are smaller in size and penetrate a shorter distance up the span than the planar case.

One notable feature of the current work has been to repeat the measurements to examine the accuracy of the overall setup. Yaw angle changes between measurements have been found to be extremely small, however loss changes are significant but smaller than the differences between endwalls. For example an error of $\pm 5\%$ of planar secondary loss is estimated for secondary loss measurement and the difference between P1 and P2 is some 11.5% of planar secondary loss.

This level of errors is quite large, however the blade profile is already relatively efficient and Figure 5.153² shows that ranking the profiles is a difficult exercise as the loss differences are small, for the planar case a loss measurement of 32 Pa is seen and a change of some 4 Pa between the planar case and a profiled case (in this case P0 to P1) is expected, however to compare profiled endwalls is much more difficult with a change of only 1 Pa or so between endwalls.

Figure 5.154 summarises the loss ranking of the three profiles, using the synthesised data set to show a best case reduction in secondary loss of some 31%. Figure 5.154 also shows the mixed out loss values for the synthesised data set.

²The chart shows C_{P0} multiplied by upstream dynamic head to give more manageable numbers.

5.14 Figures for Pressure Probe Results

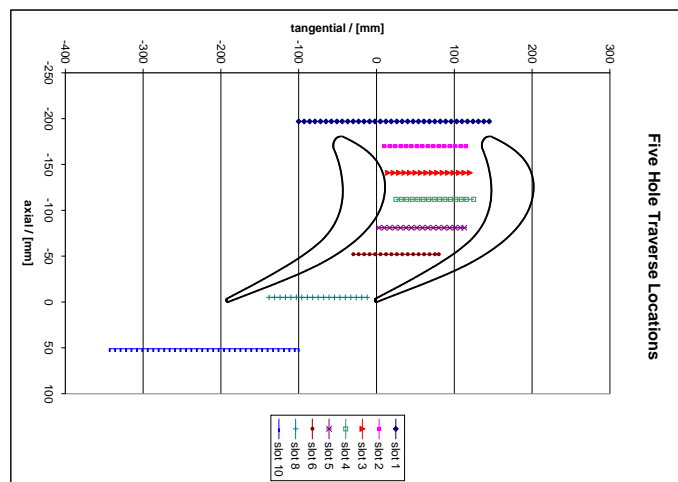


Figure 5.3: Five Hole Probe Measurement Locations.

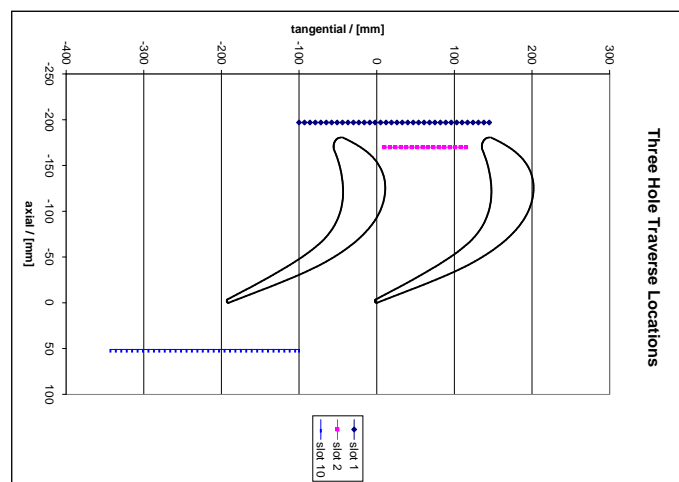


Figure 5.4: Three Hole Probe Measurement Locations.

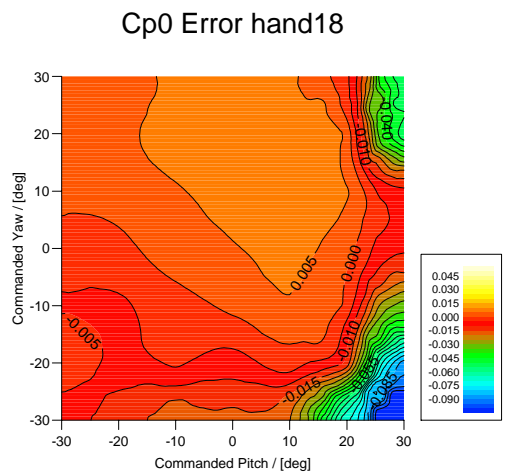


Figure 5.5: Typical pre readings C_{P0} Error - five hole.

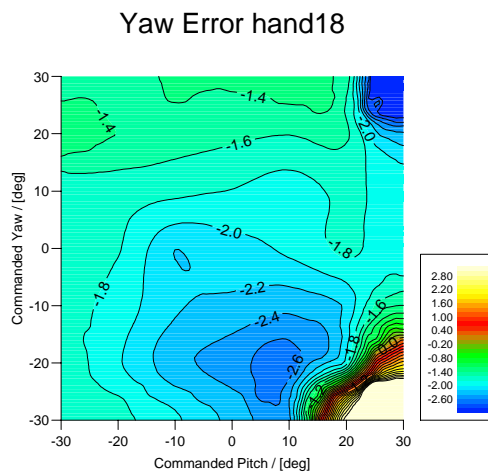


Figure 5.6: Typical pre readings Yaw Error - five hole.

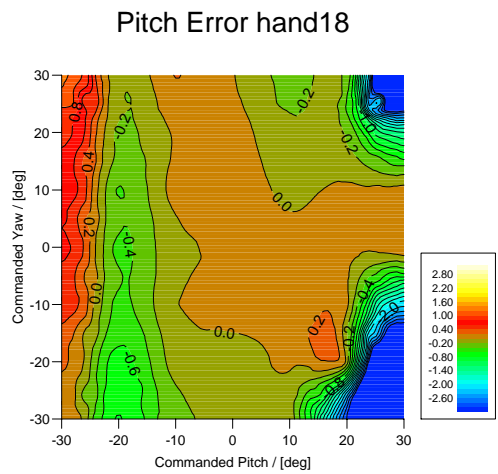


Figure 5.7: Typical pre readings Pitch Error - five hole.

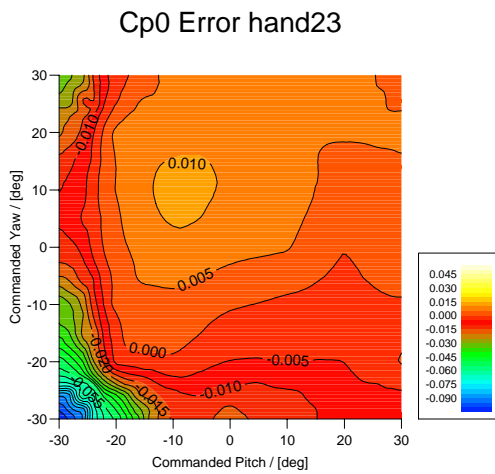


Figure 5.8: Typical post readings C_{P0} Error - five hole.

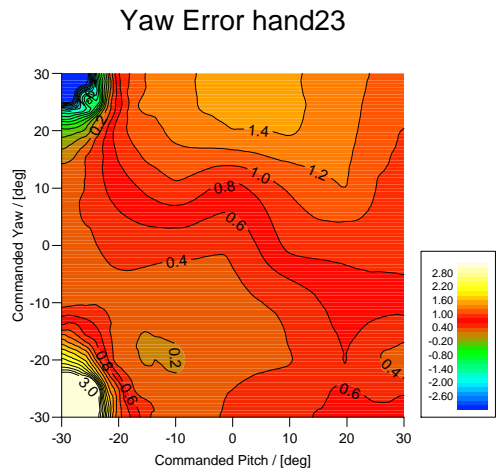


Figure 5.9: Typical post readings Yaw Error - five hole.

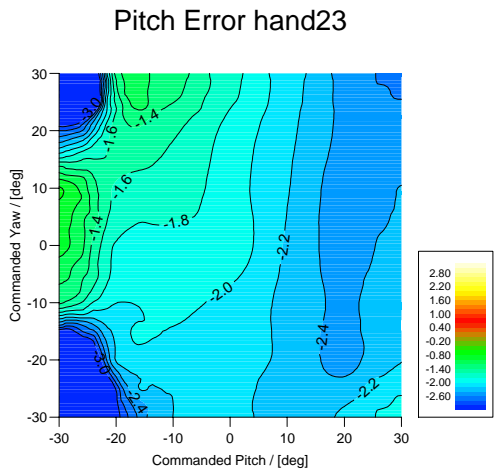


Figure 5.10: Typical post readings Pitch Error - five hole.

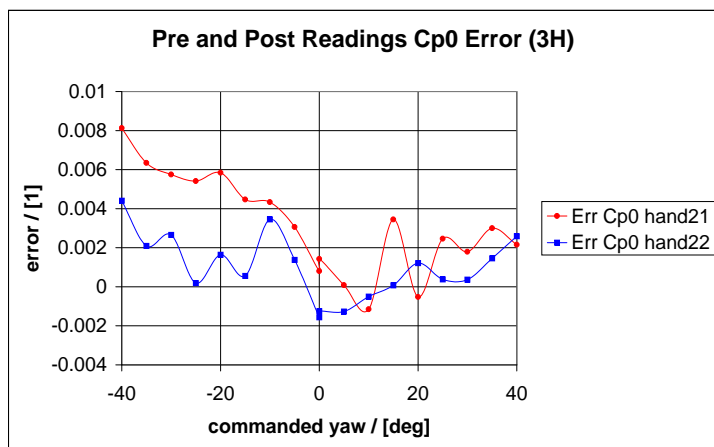


Figure 5.11: Typical C_{P0} Error - three hole probe.

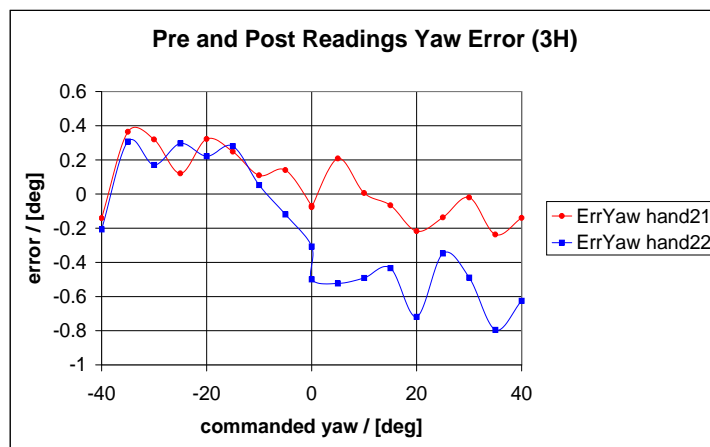


Figure 5.12: Typical Yaw Error - three hole probe.

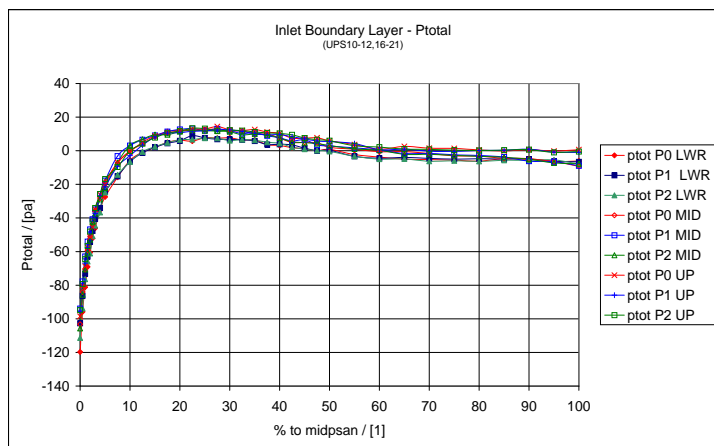


Figure 5.13: Inlet Boundary Layer: Raw Data

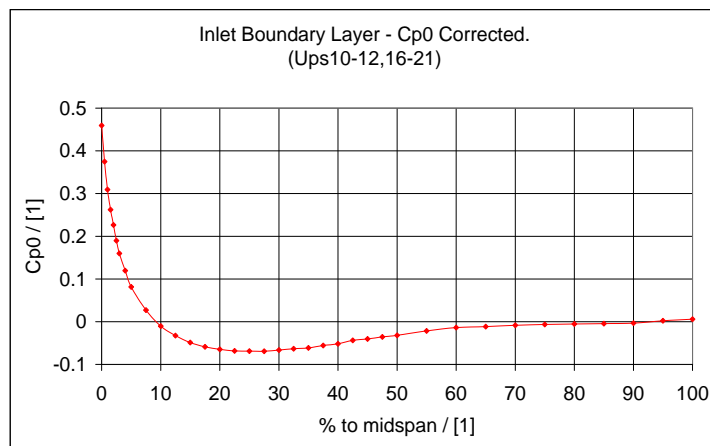


Figure 5.14: Inlet Boundary Layer: Final Profile

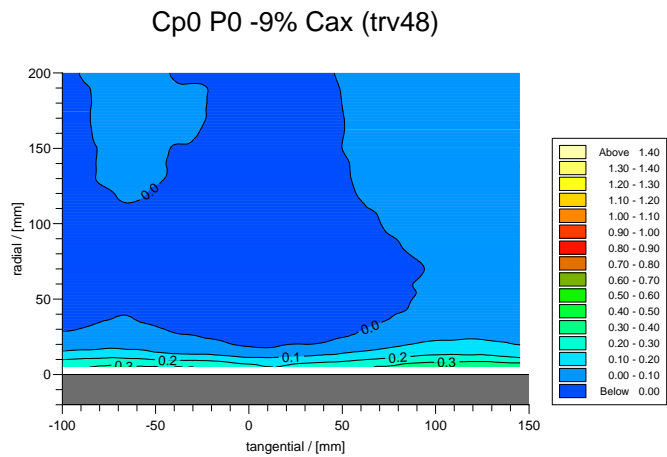


Figure 5.15: Slot 1 P0 Loss

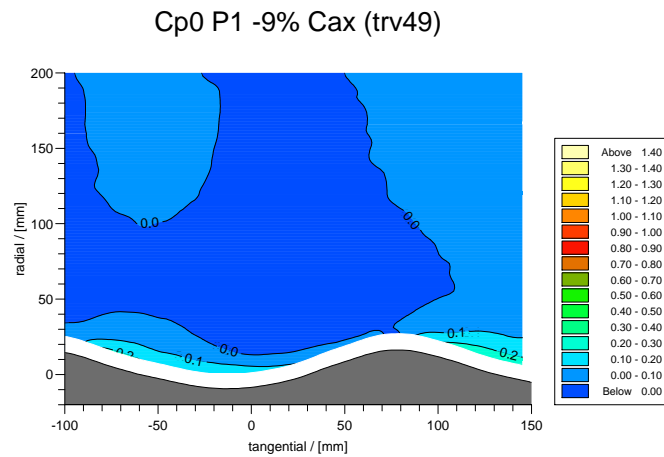


Figure 5.16: Slot 1 P1 Loss

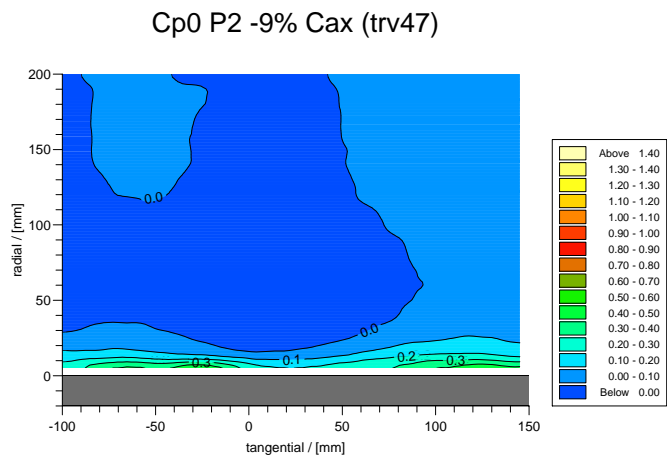


Figure 5.17: Slot 1 P2 Loss

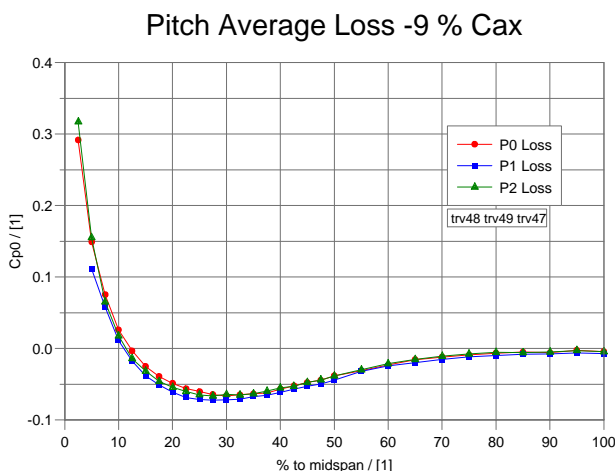


Figure 5.18: Slot 1 Pitch Averaged Loss

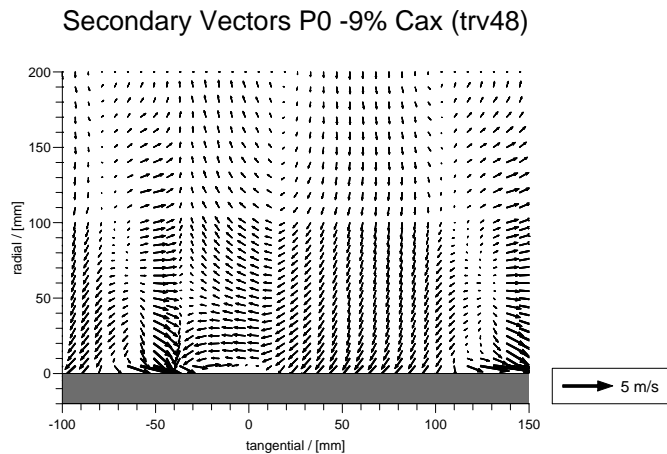


Figure 5.19: Slot 1 P0 Secondary Vectors

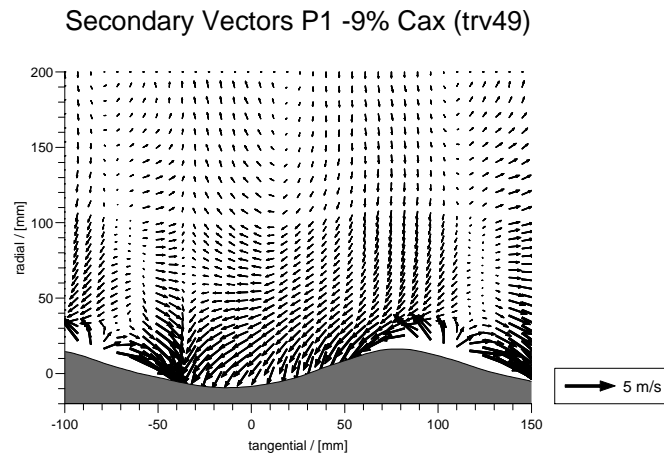


Figure 5.20: Slot 1 P1 Secondary Vectors

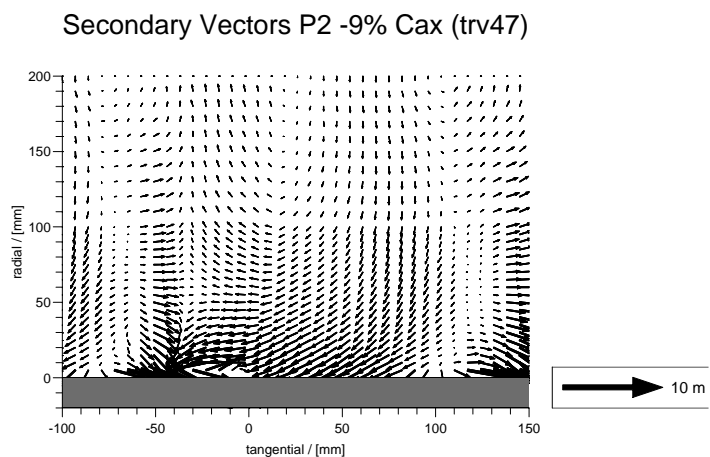


Figure 5.21: Slot 1 P2 Secondary Vectors

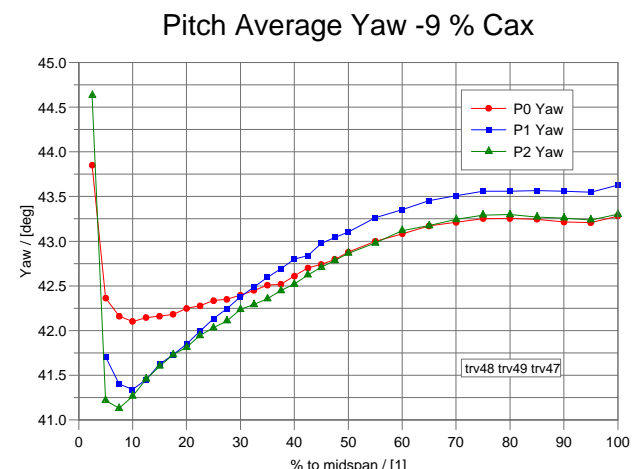


Figure 5.22: Slot 1 Pitch Averaged Yaw Angle

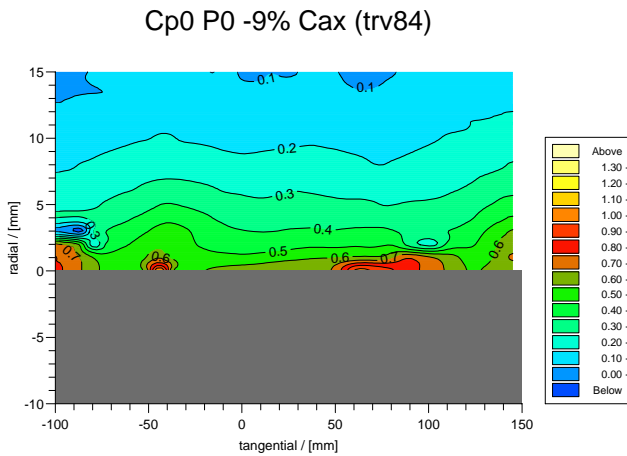


Figure 5.23: Close Wall Loss at Slot 1 P0

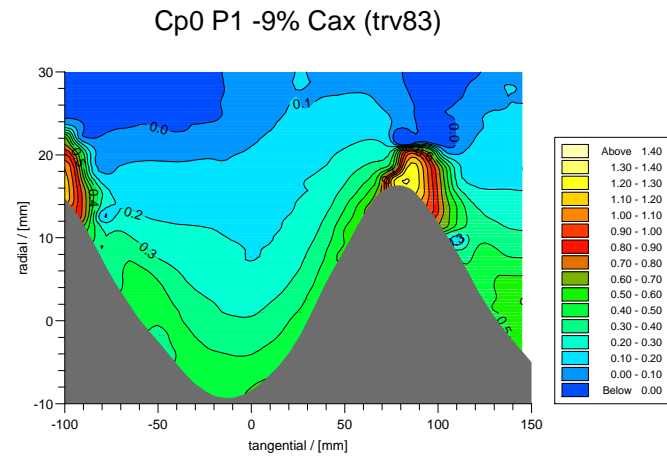


Figure 5.24: Close Wall Loss at Slot 1 P1

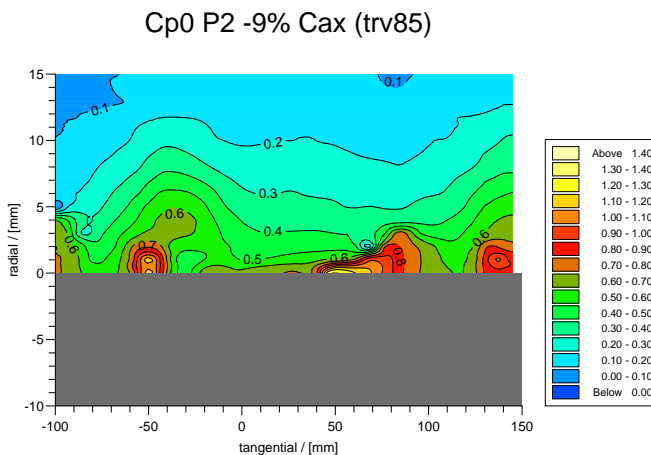


Figure 5.25: Close Wall Loss at Slot 1 P2

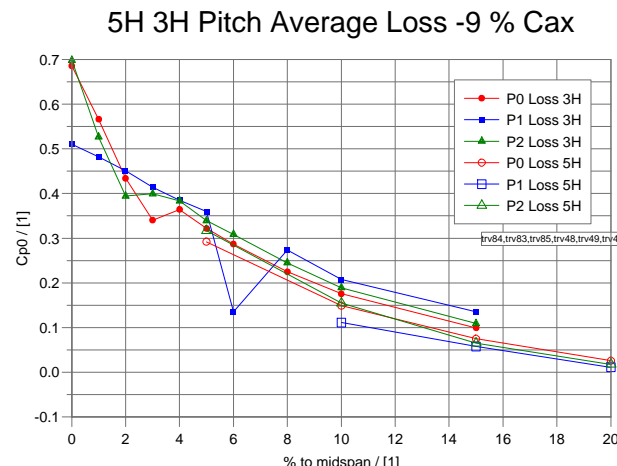


Figure 5.26: 3H and 5H Pitch Averaged Loss at Slot 1

Secondary Vectors P0 -9% Cax (trv84)

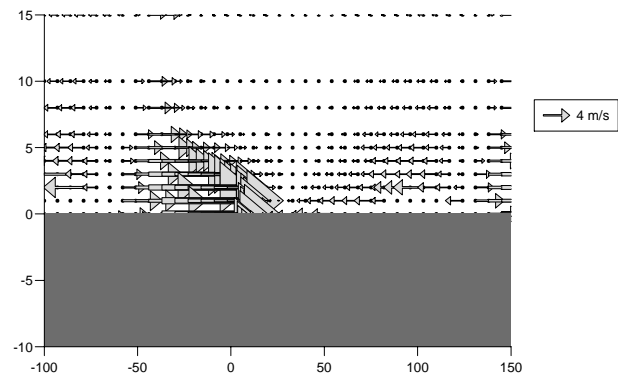


Figure 5.27: Secondary Vectors at Slot 1 P0

Secondary Vectors P1 -9% Cax (trv83)

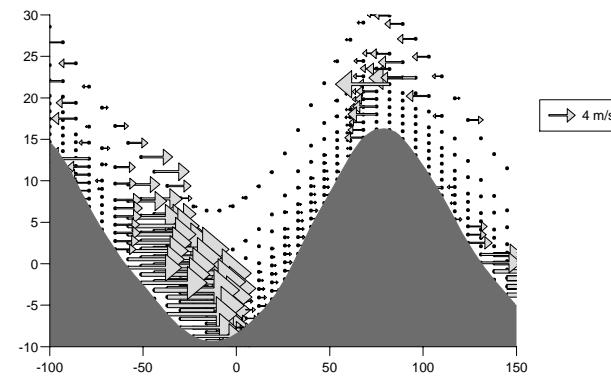


Figure 5.28: Secondary Vectors at Slot 1 P1

Secondary Vectors P2 -9% Cax (trv85)

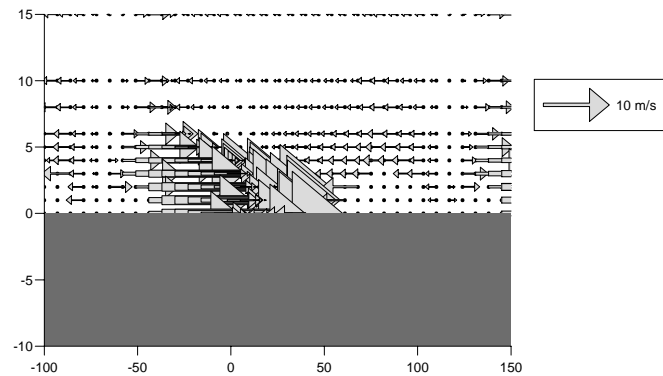


Figure 5.29: Secondary Vectors at Slot 1 P2

5H 3H Pitch Average Yaw -9 % Cax

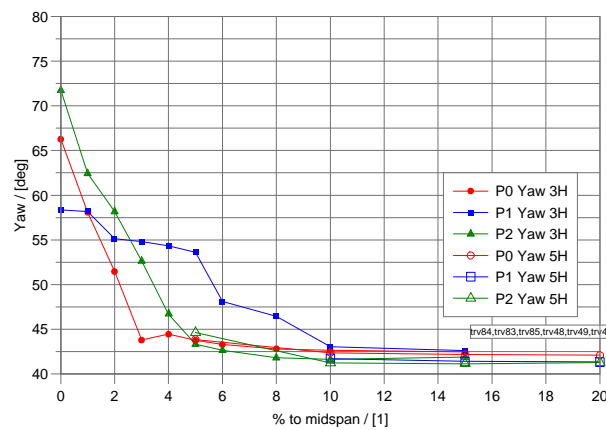


Figure 5.30: 3H and 5H Pitch Averaged Yaw Angle at Slot 1

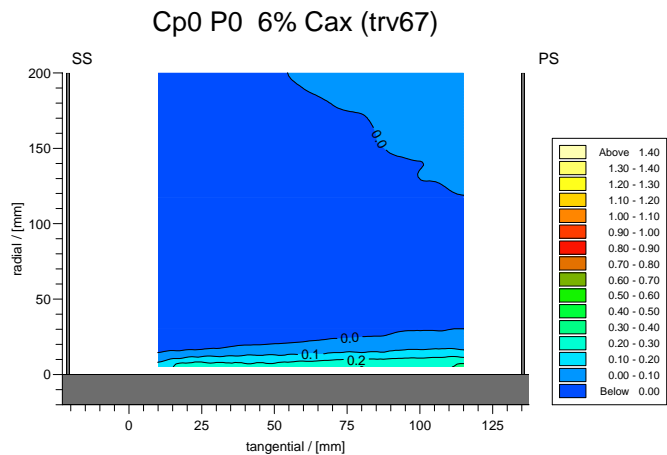


Figure 5.31: Slot 2 P0 Loss

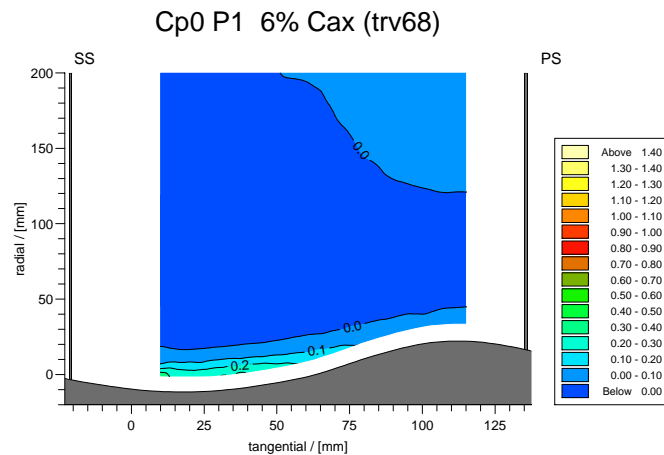


Figure 5.32: Slot 2 P1 Loss

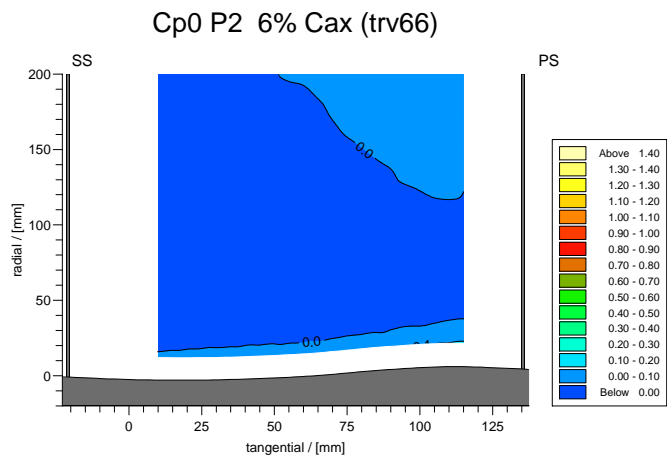


Figure 5.33: Slot 2 P2 Loss

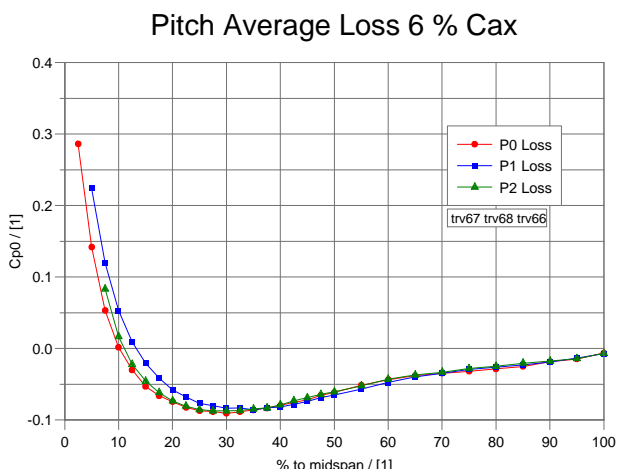


Figure 5.34: Slot 2 Pitch Averaged Loss

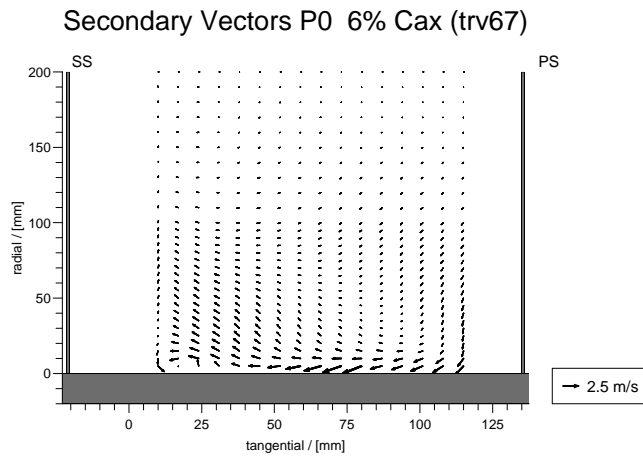


Figure 5.35: Slot 2 P0 Secondary Vectors

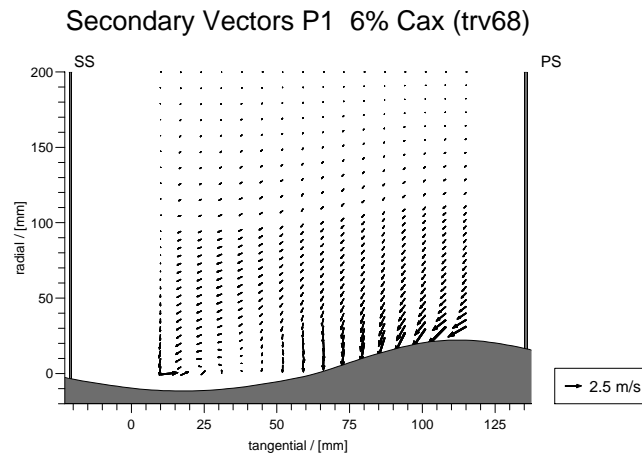


Figure 5.36: Slot 2 P1 Secondary Vectors

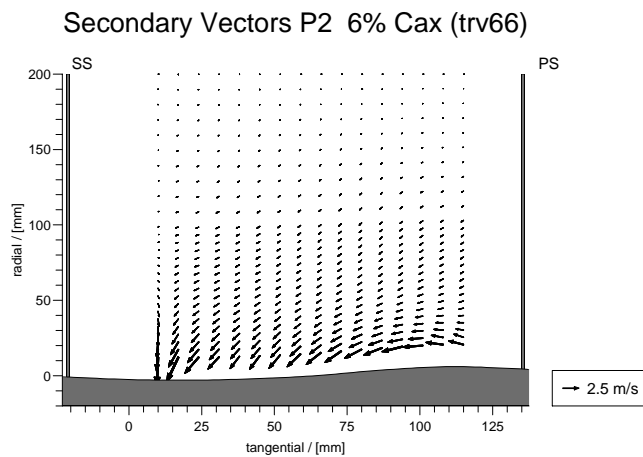


Figure 5.37: Slot 2 P2 Secondary Vectors

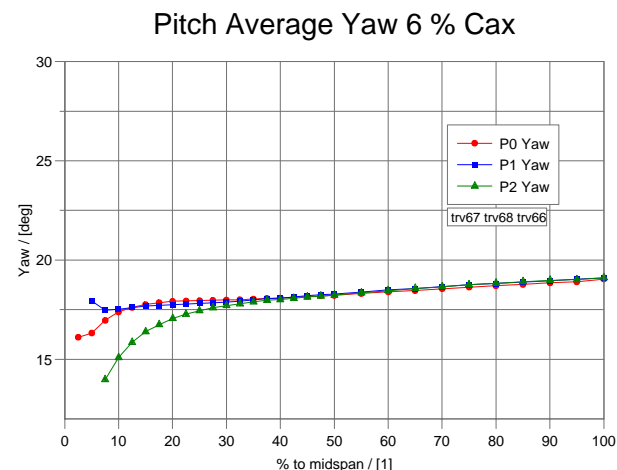


Figure 5.38: Slot 2 Pitch Averaged Yaw Angle

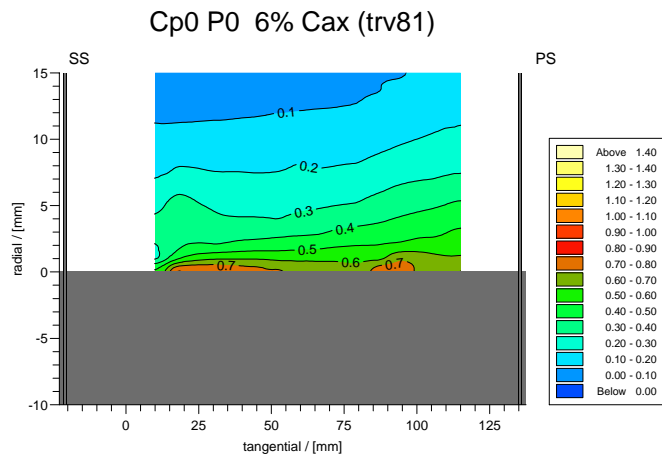


Figure 5.39: Close Wall Loss at Slot 2 P0

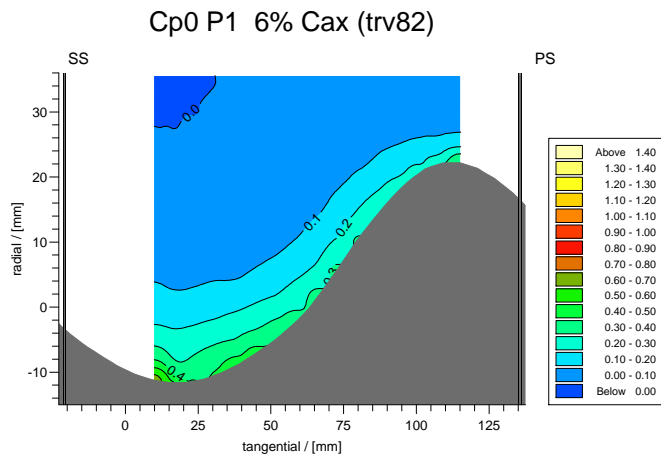


Figure 5.40: Close Wall Loss at Slot 2 P1

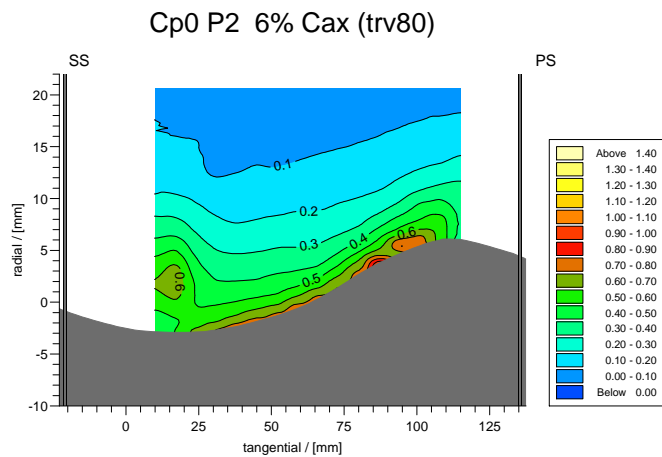


Figure 5.41: Close Wall Loss at Slot 2 P2

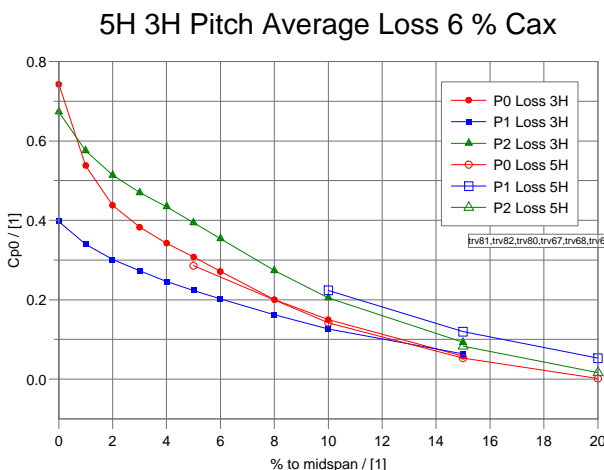


Figure 5.42: 3H and 5H Pitch Averaged Loss at Slot 2

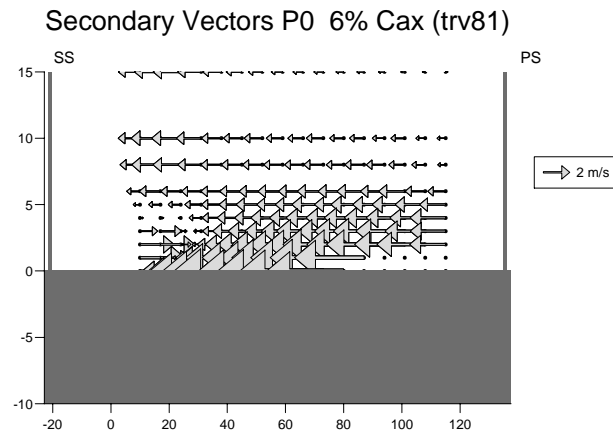


Figure 5.43: Secondary Vectors at Slot 2 P0

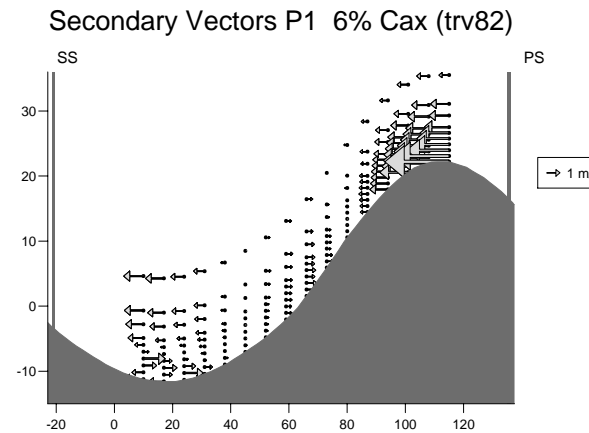


Figure 5.44: Secondary Vectors at Slot 2 P1

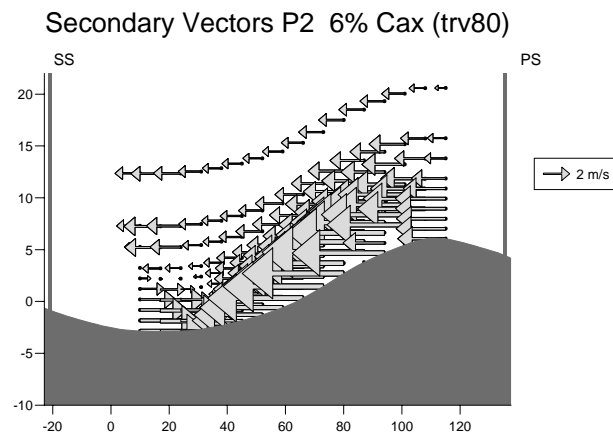


Figure 5.45: Secondary Vectors at Slot 2 P2

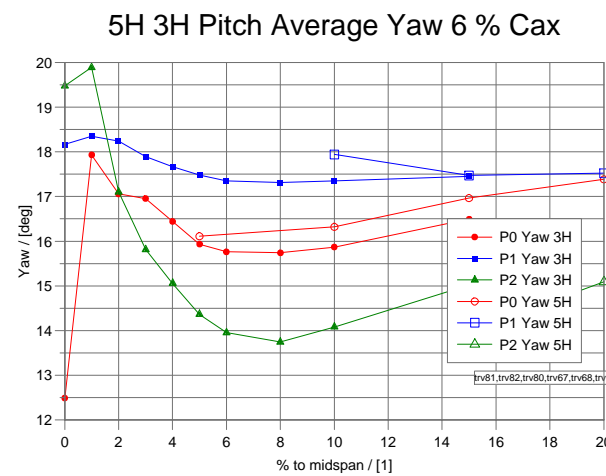


Figure 5.46: 3H and 5H Pitch Averaged Yaw Angle at Slot 2

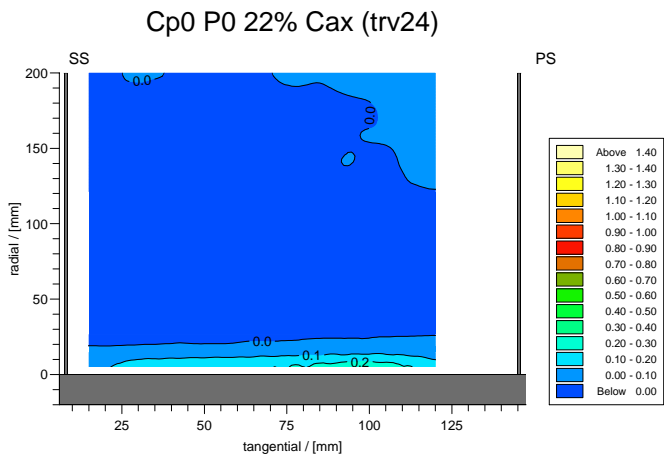


Figure 5.47: Slot 3 P0 Loss

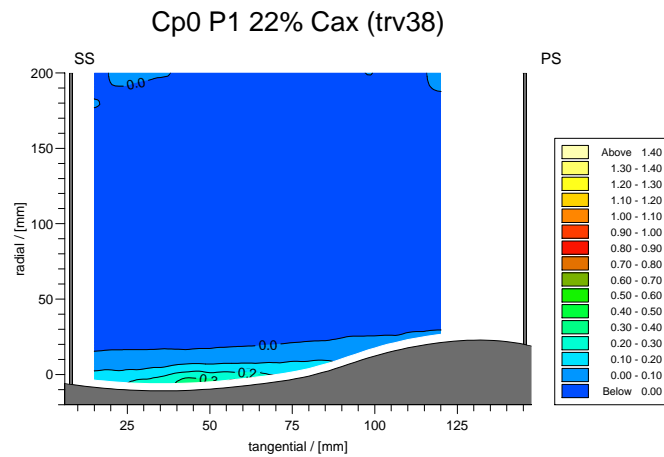


Figure 5.48: Slot 3 P1 Loss

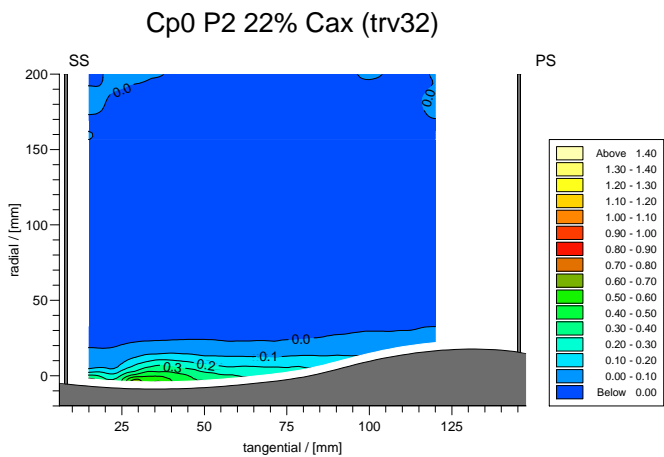


Figure 5.49: Slot 3 P2 Loss

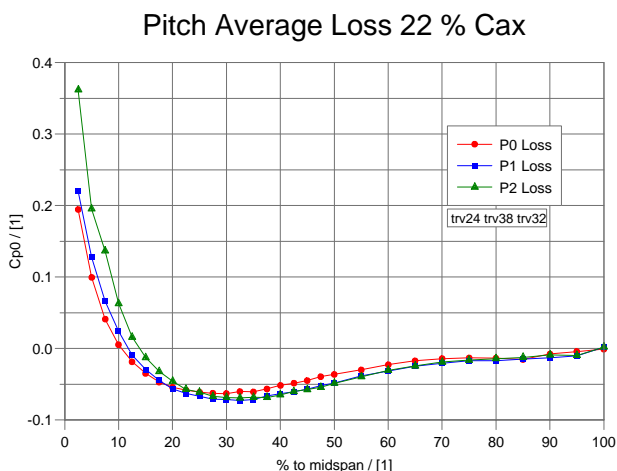


Figure 5.50: Slot 3 Pitch Averaged Loss

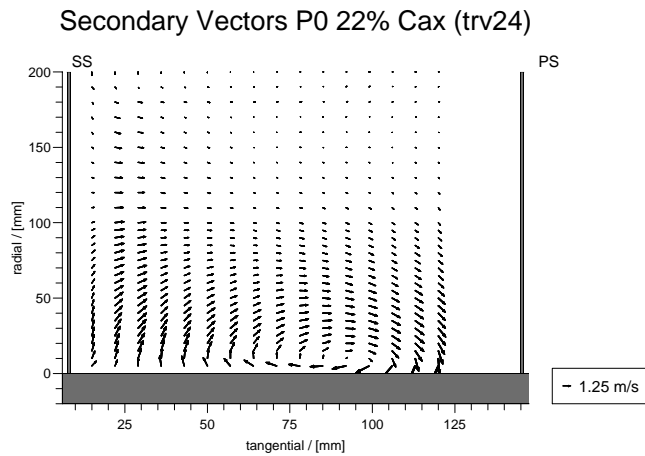


Figure 5.51: Slot 3 P0 Secondary Vectors

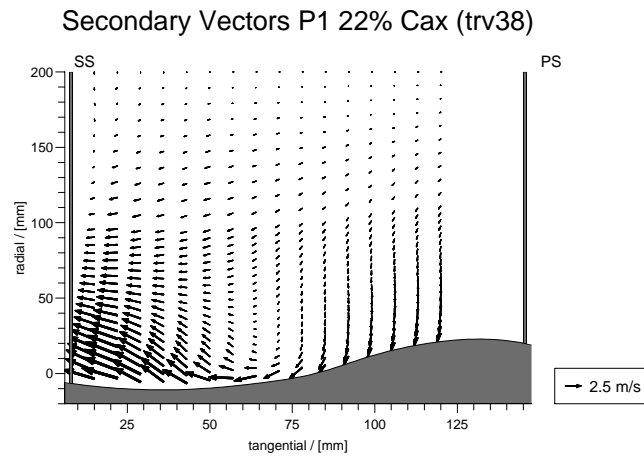


Figure 5.52: Slot 3 P1 Secondary Vectors

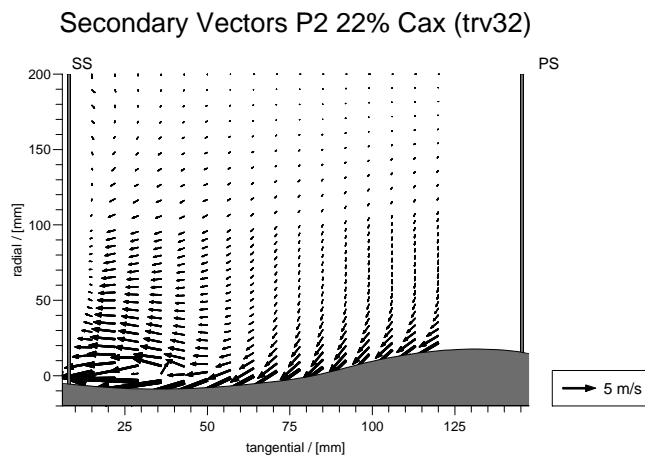


Figure 5.53: Slot 3 P2 Secondary Vectors

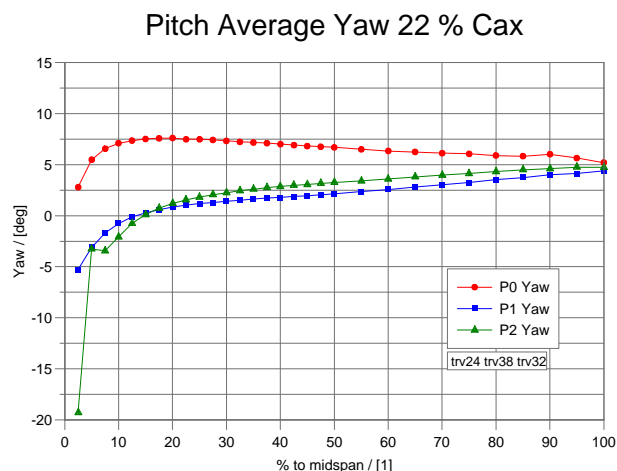


Figure 5.54: Slot 3 Pitch Averaged Yaw Angle

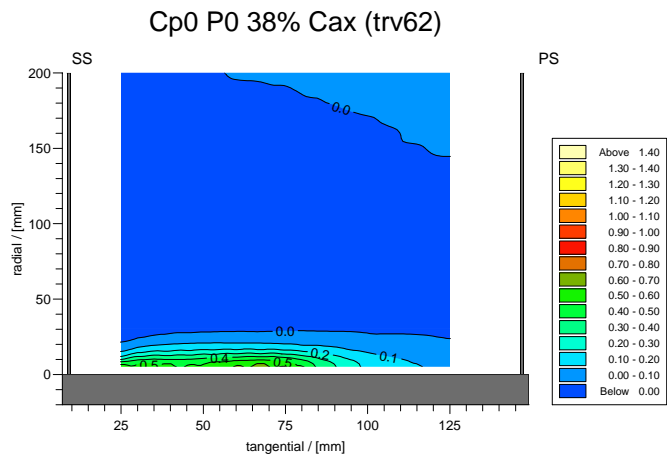


Figure 5.55: Slot 4 P0 Loss

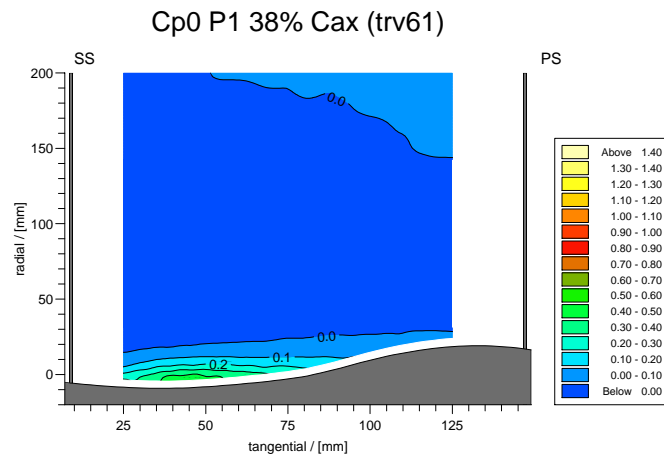


Figure 5.56: Slot 4 P1 Loss

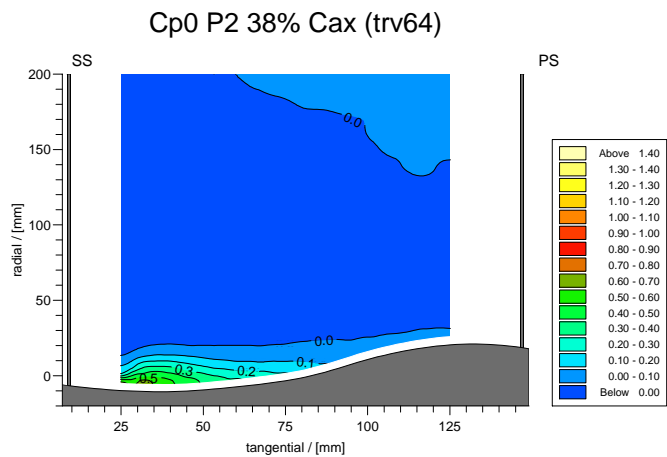


Figure 5.57: Slot 4 P2 Loss

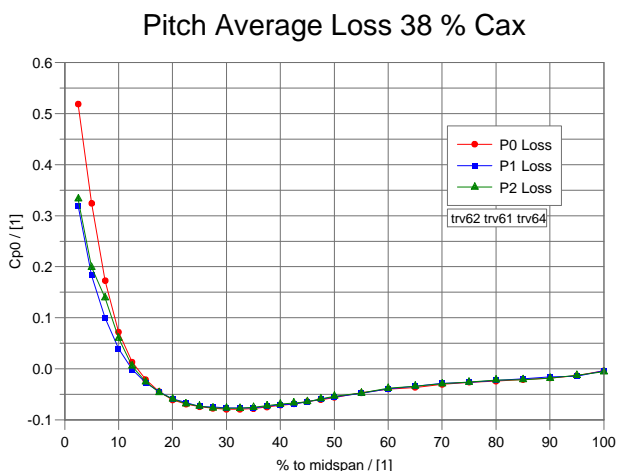


Figure 5.58: Slot 4 Pitch Averaged Loss

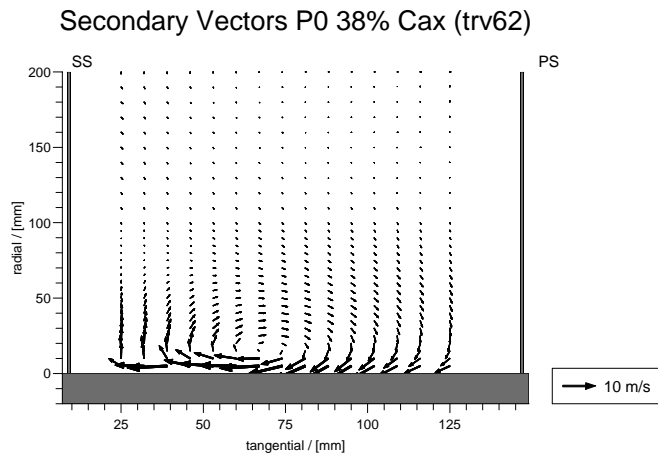


Figure 5.59: Slot 4 P0 Secondary Vectors

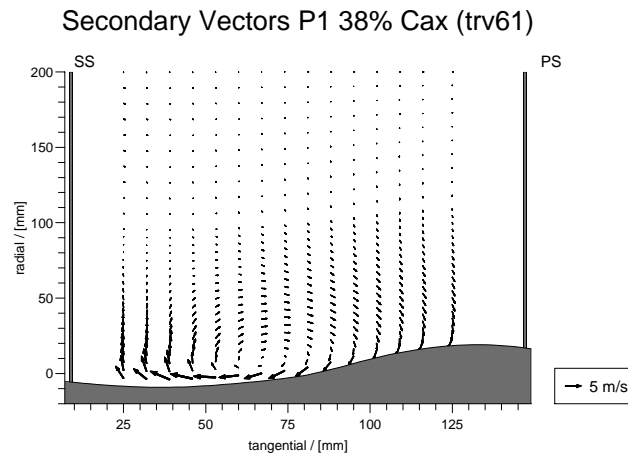


Figure 5.60: Slot 4 P1 Secondary Vectors

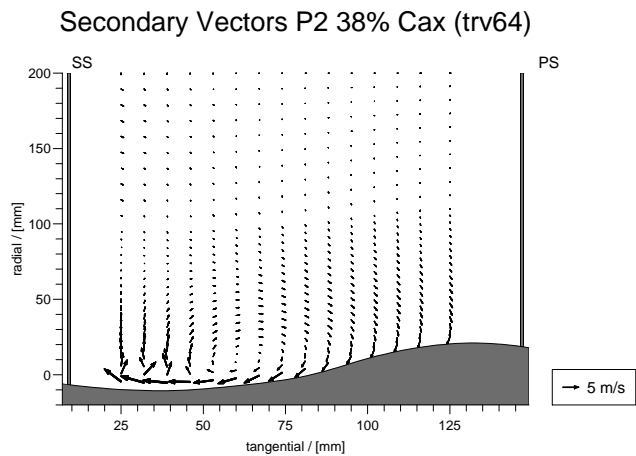


Figure 5.61: Slot 4 P2 Secondary Vectors

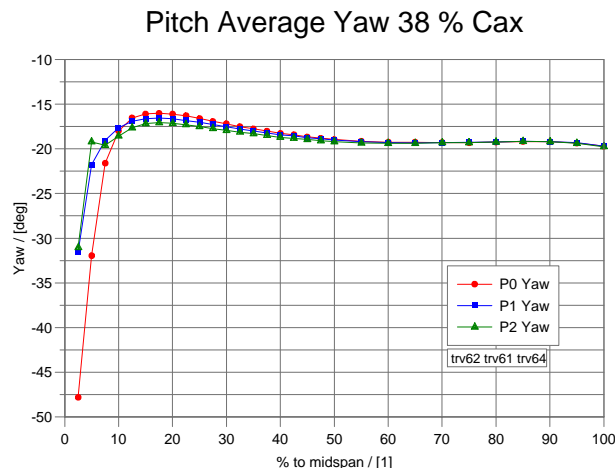


Figure 5.62: Slot 4 Pitch Averaged Yaw Angle

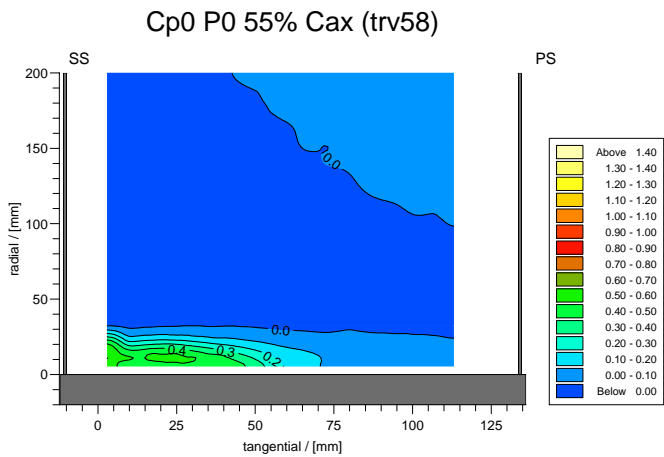


Figure 5.63: Slot 5 P0 Loss

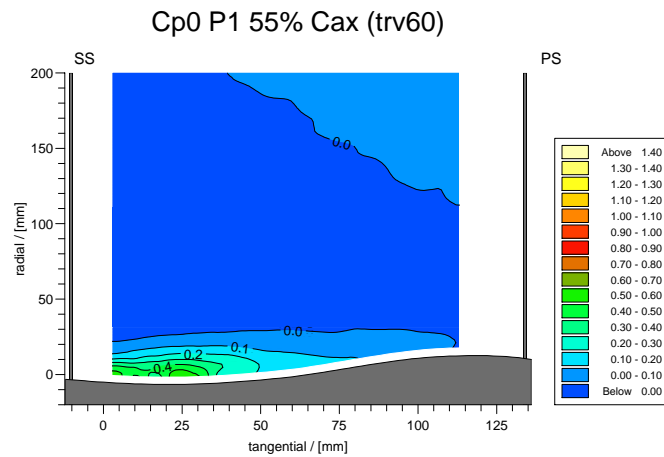


Figure 5.64: Slot 5 P1 Loss

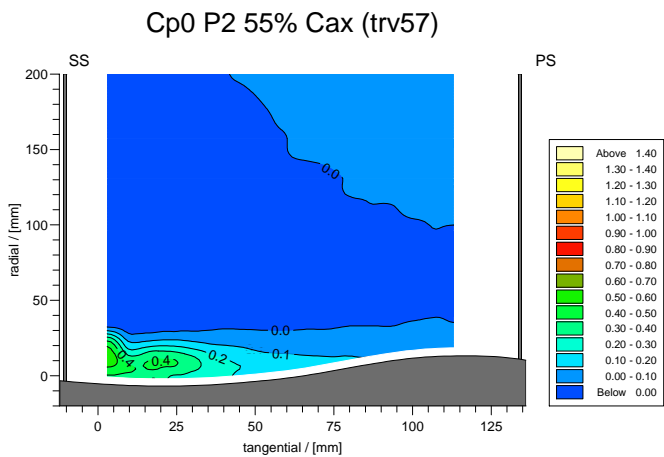


Figure 5.65: Slot 5 P2 Loss

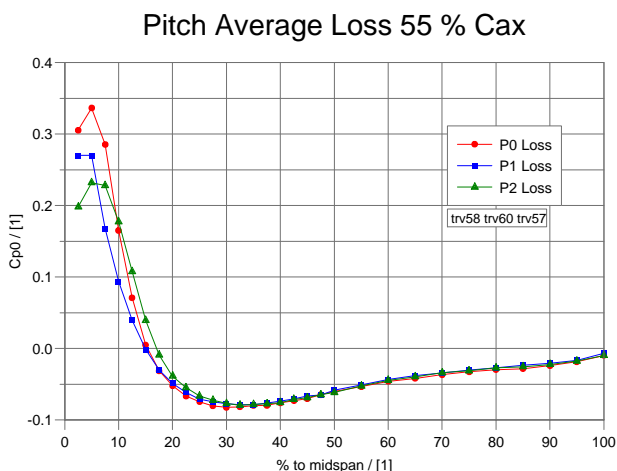


Figure 5.66: Slot 5 Pitch Averaged Loss

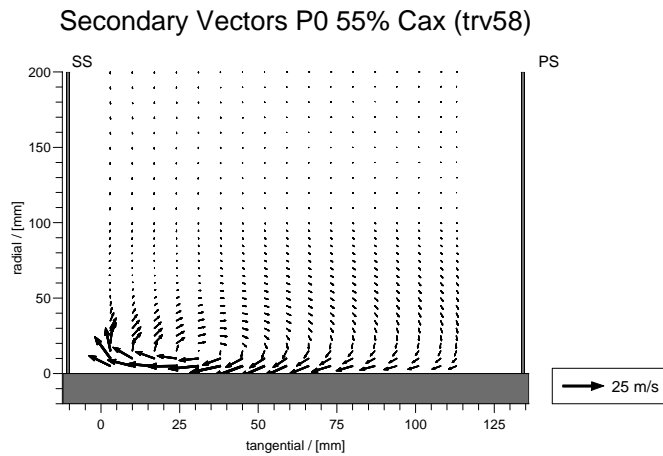


Figure 5.67: Slot 5 P0 Secondary Vectors

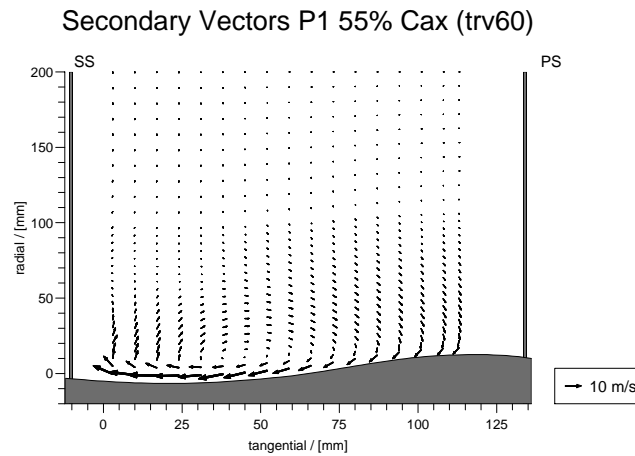


Figure 5.68: Slot 5 P1 Secondary Vectors

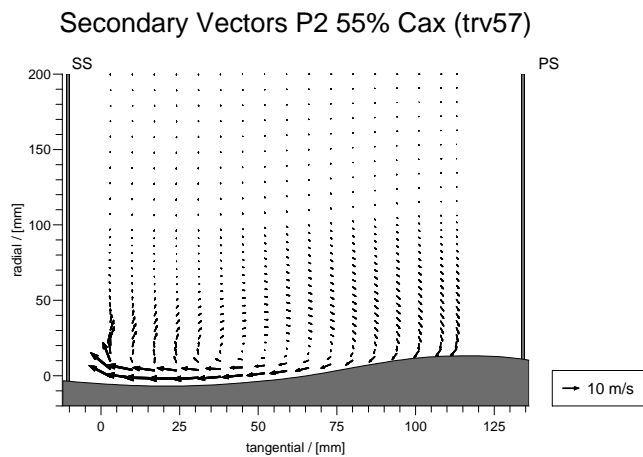


Figure 5.69: Slot 5 P2 Secondary Vectors

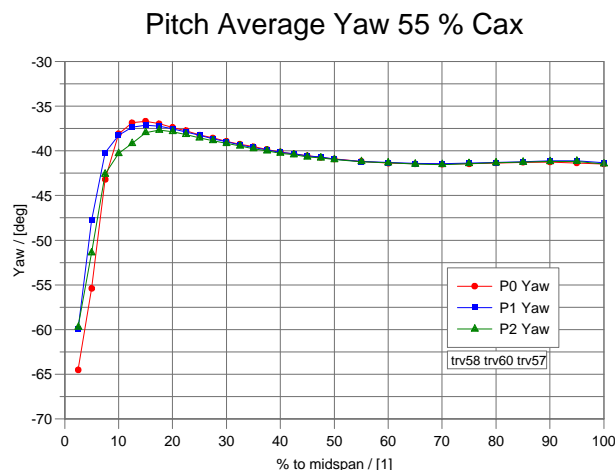


Figure 5.70: Slot 5 Pitch Averaged Yaw Angle

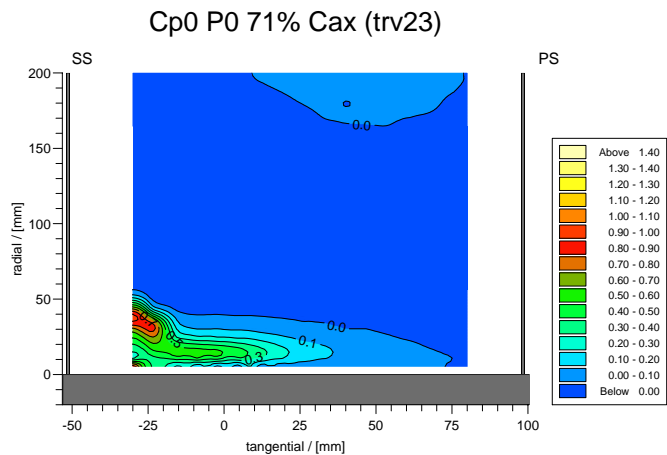


Figure 5.71: Slot 6 P0 Loss

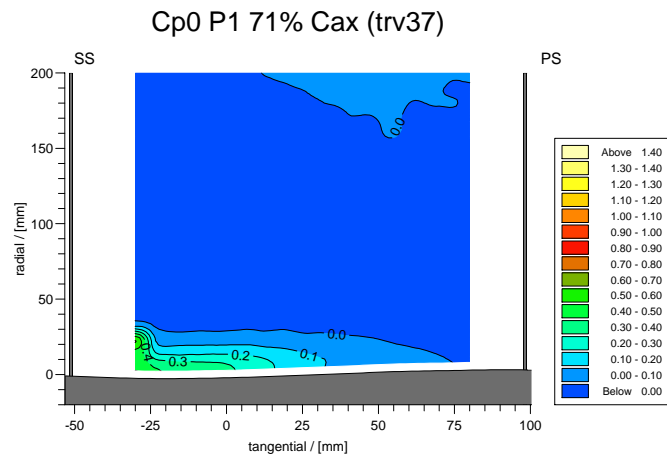


Figure 5.72: Slot 6 P1 Loss

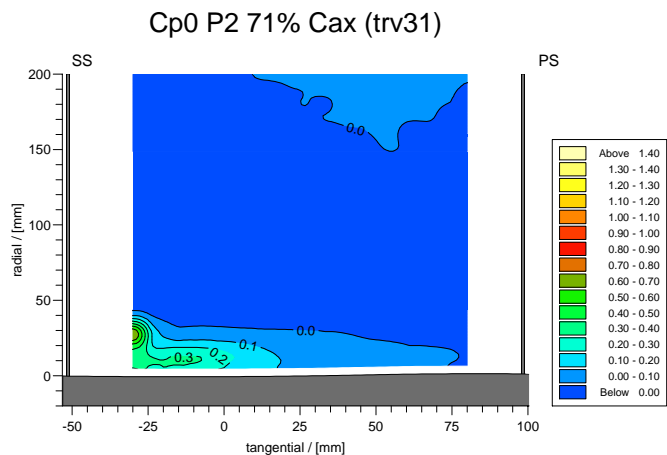


Figure 5.73: Slot 6 P2 Loss

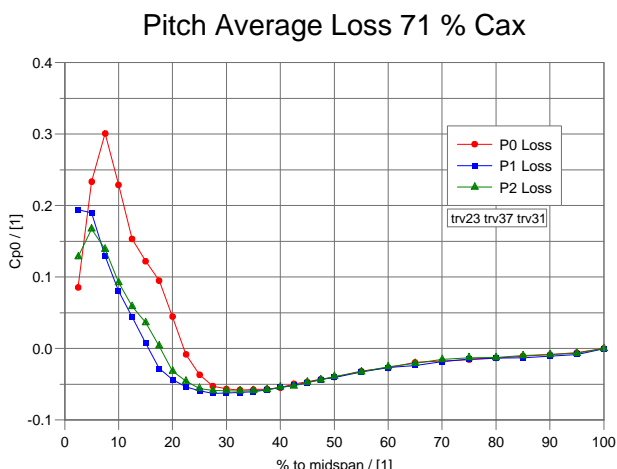


Figure 5.74: Slot 6 Pitch Averaged Loss

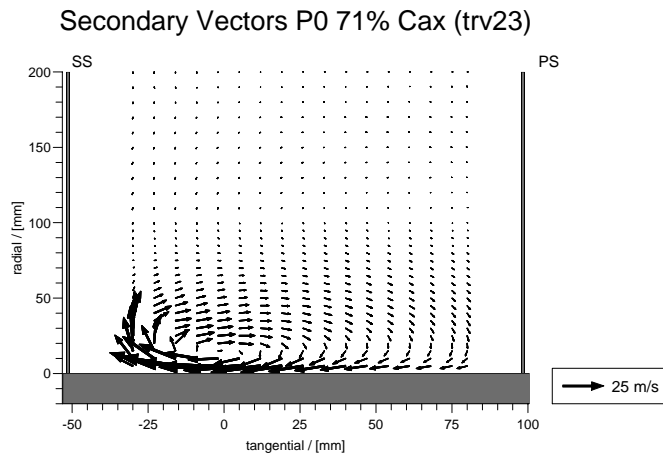


Figure 5.75: Slot 6 P0 Secondary Vectors

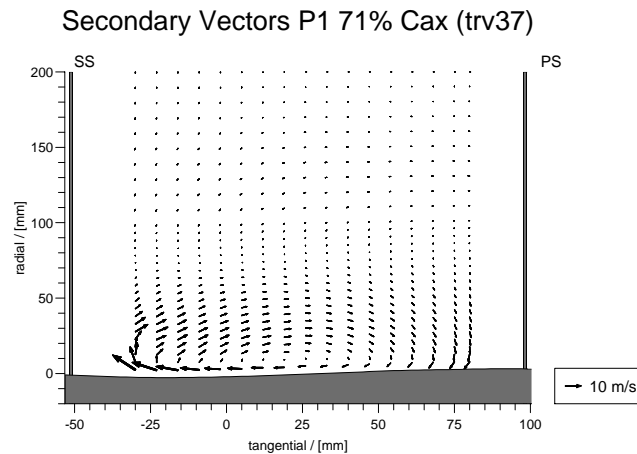


Figure 5.76: Slot 6 P1 Secondary Vectors

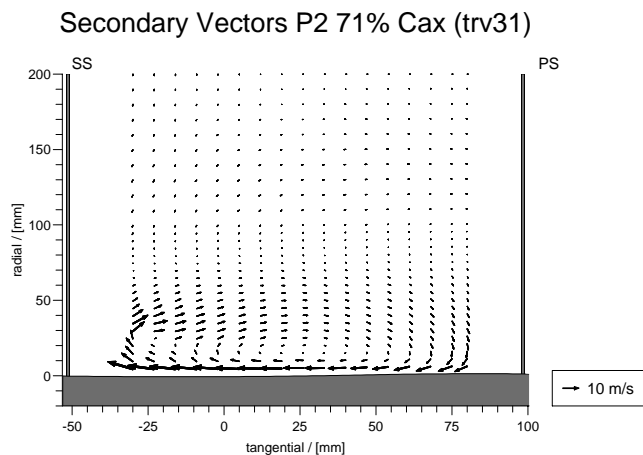


Figure 5.77: Slot 6 P2 Secondary Vectors

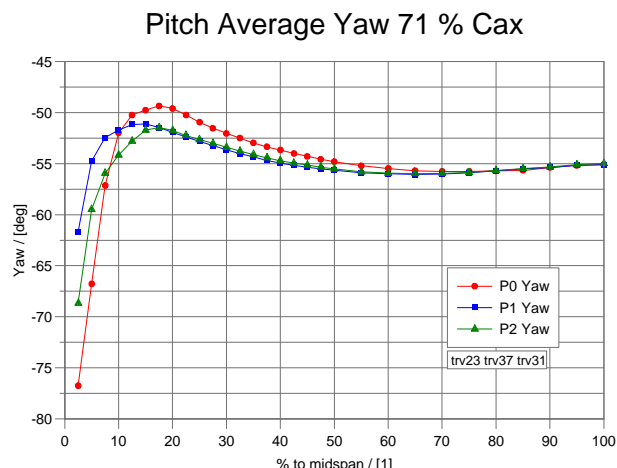


Figure 5.78: Slot 6 Pitch Averaged Yaw Angle

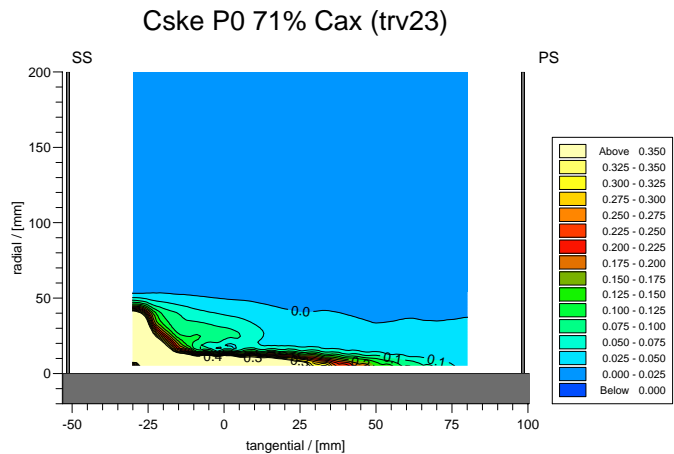


Figure 5.79: Slot 6 P0 C_{ske}

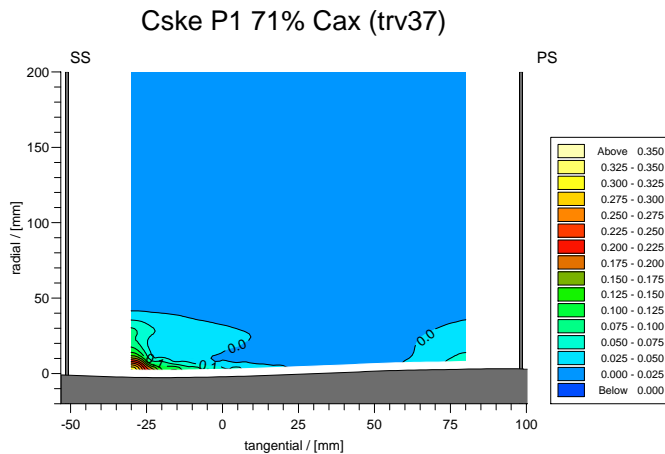


Figure 5.80: Slot 6 P1 C_{ske}

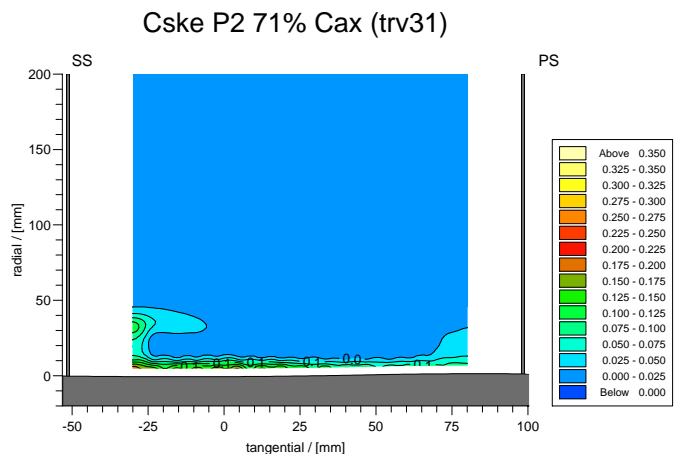


Figure 5.81: Slot 6 P2 C_{ske}

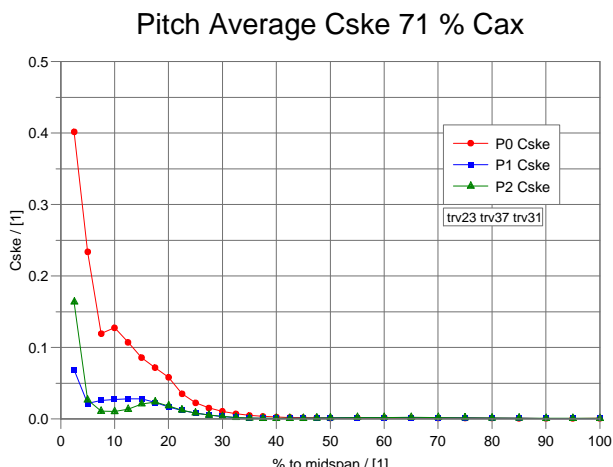


Figure 5.82: Slot 6 Pitch Averaged C_{ske}

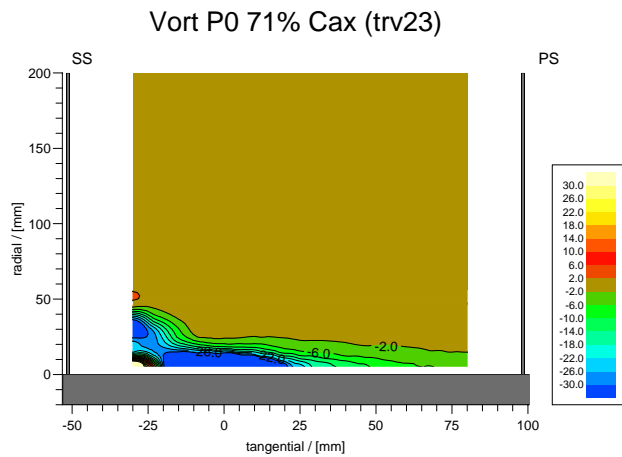


Figure 5.83: Slot 6 P0 Streamwise Vorticity Coefficient

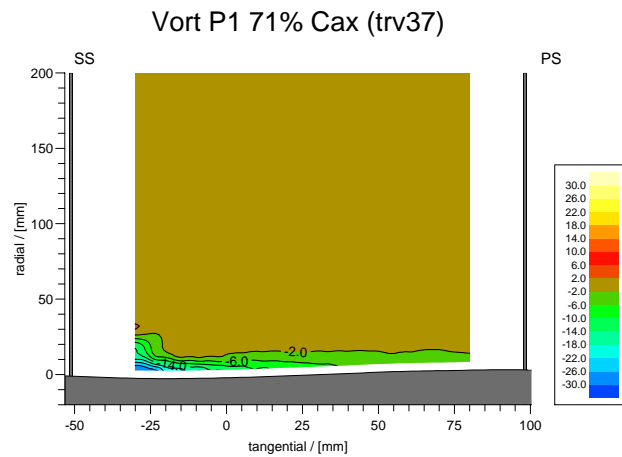


Figure 5.84: Slot 6 P1 Streamwise Vorticity Coefficient

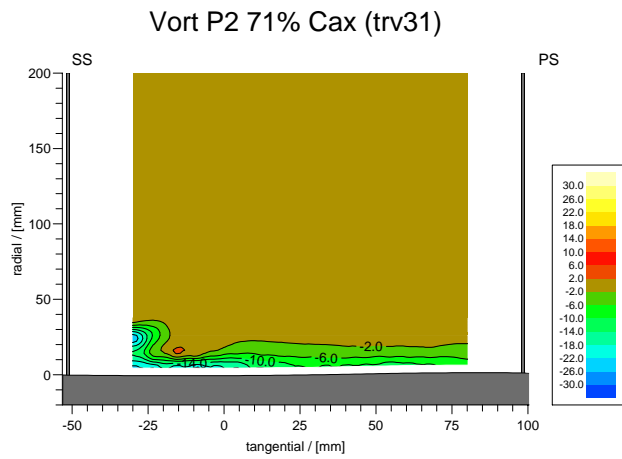


Figure 5.85: Slot 6 P2 Streamwise Vorticity Coefficient

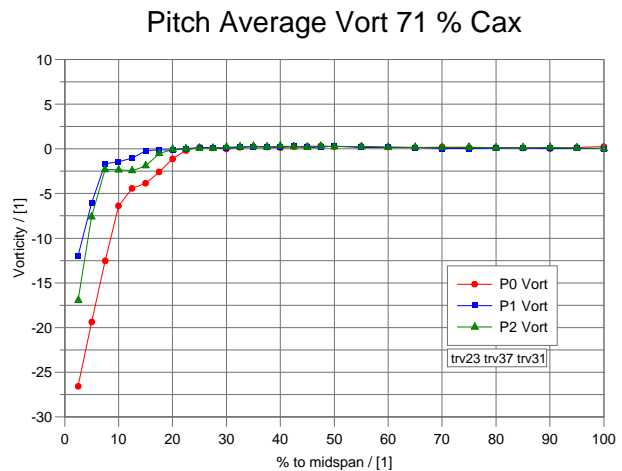


Figure 5.86: Slot 6 Pitch Averaged Vorticity

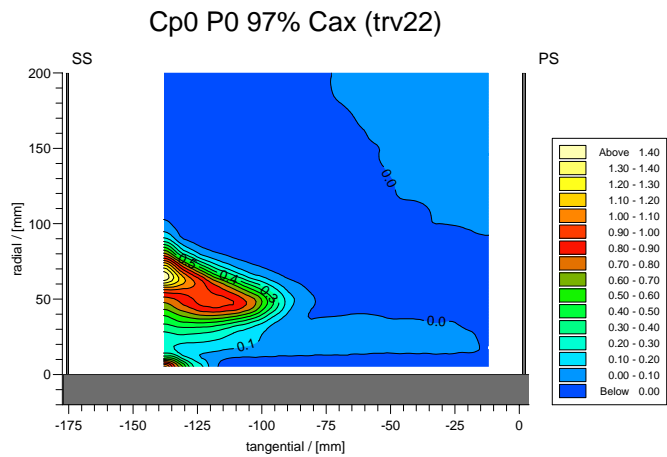


Figure 5.87: Slot 8 P0 Loss

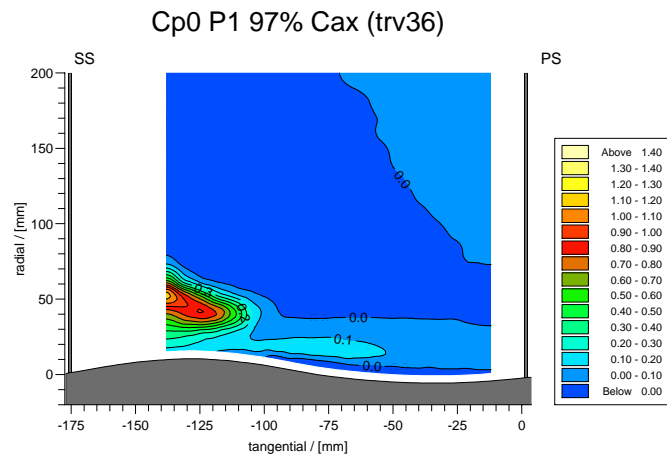


Figure 5.88: Slot 8 P1 Loss

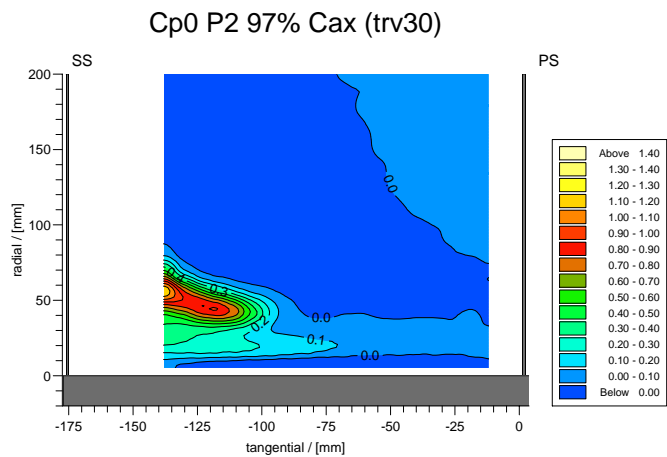


Figure 5.89: Slot 8 P2 Loss

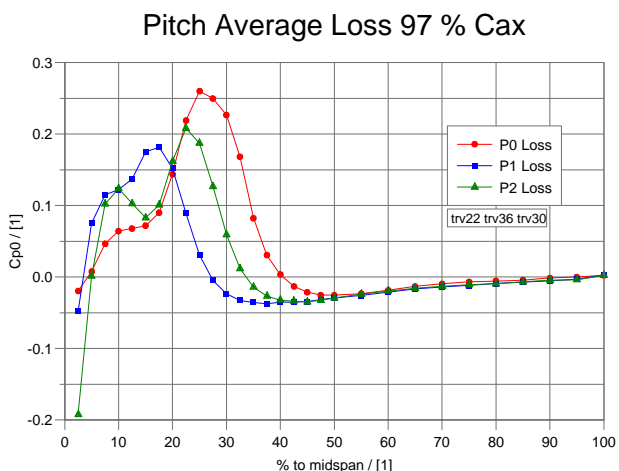


Figure 5.90: Slot 8 Pitch Averaged Loss

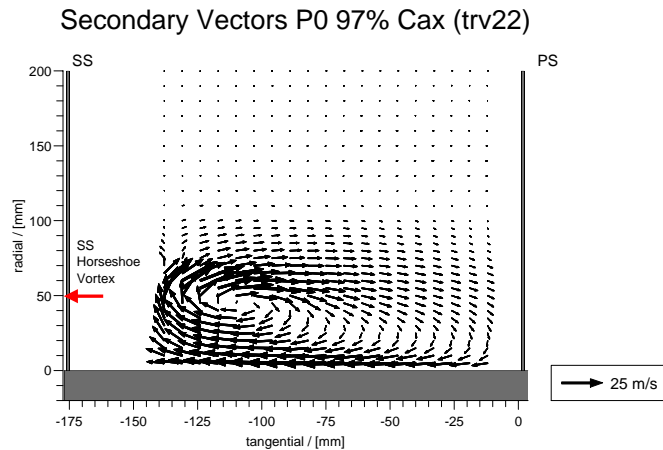


Figure 5.91: Slot 8 P0 Secondary Vectors

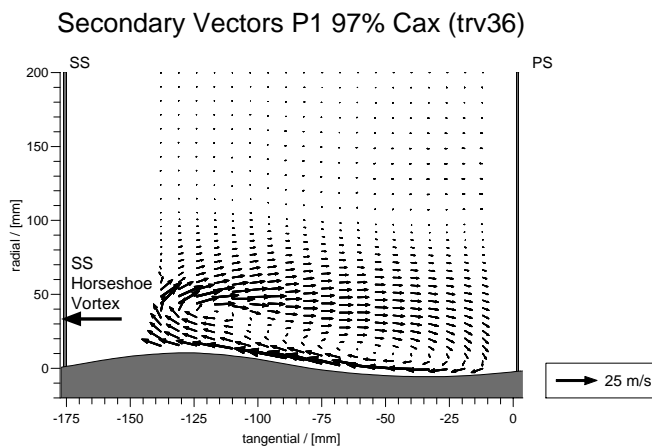


Figure 5.92: Slot 8 P1 Secondary Vectors

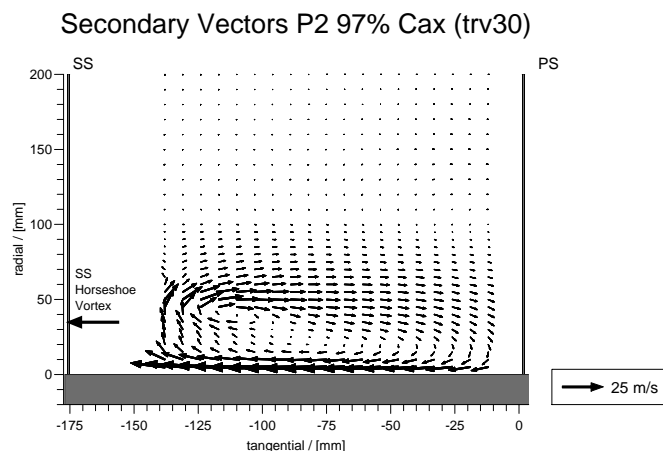


Figure 5.93: Slot 8 P2 Secondary Vectors

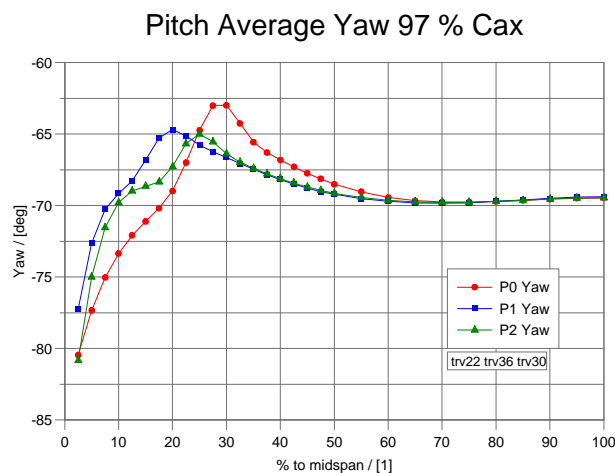


Figure 5.94: Slot 8 Pitch Averaged Yaw Angle

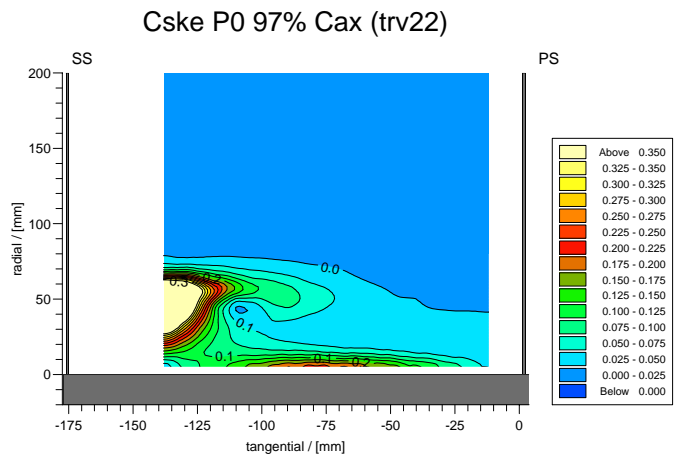


Figure 5.95: Slot 8 P0 C_{ske}

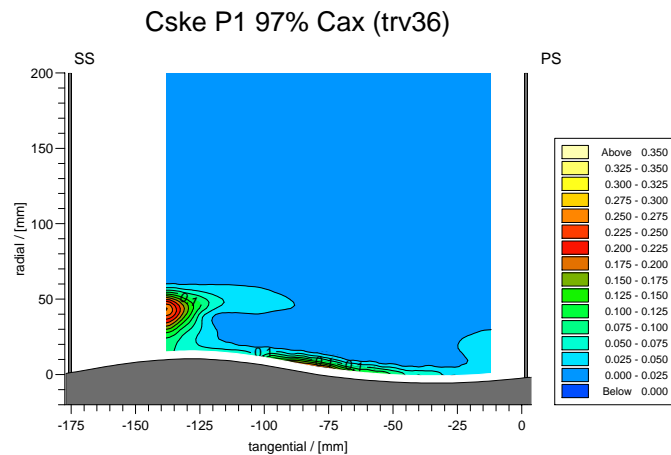


Figure 5.96: Slot 8 P1 C_{ske}

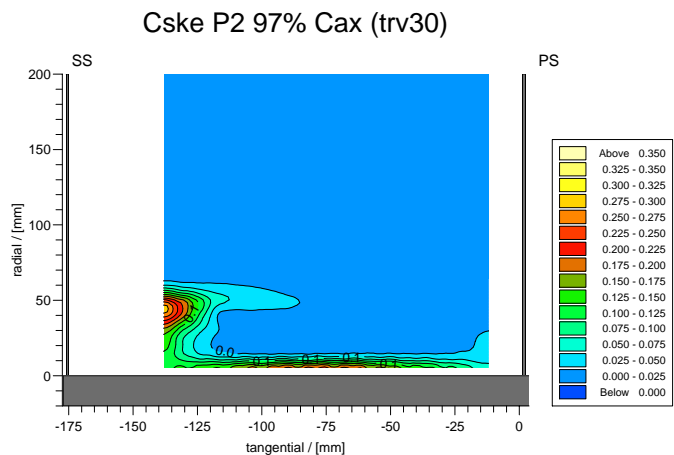


Figure 5.97: Slot 8 P2 C_{ske}

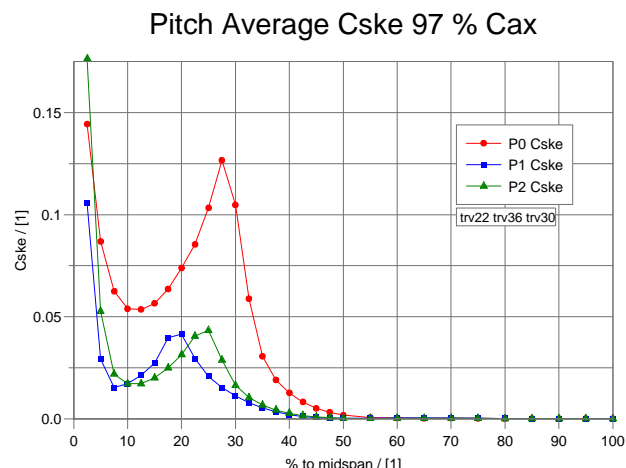


Figure 5.98: Slot 8 Pitch Averaged C_{ske}

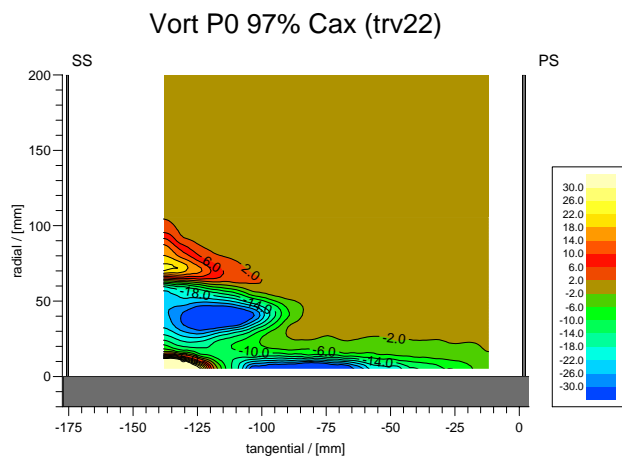


Figure 5.99: Slot 8 P0 Streamwise Vorticity Coefficient

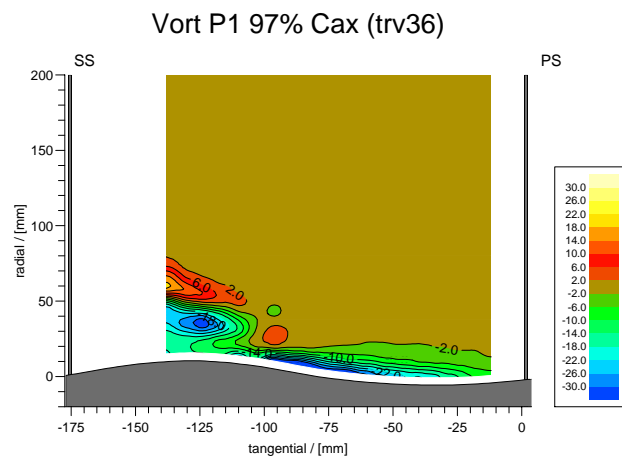


Figure 5.100: Slot 8 P1 Streamwise Vorticity Coefficient

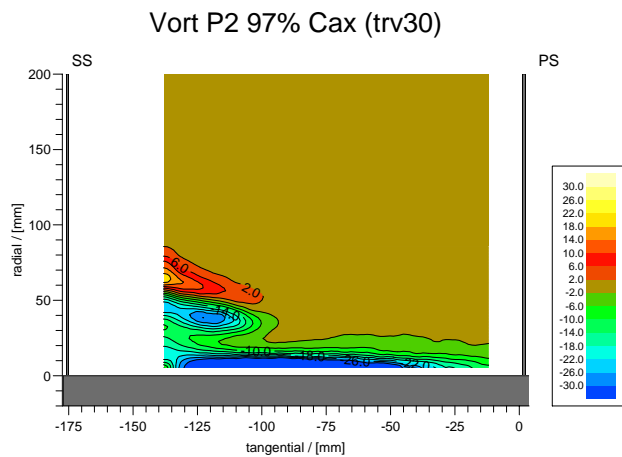


Figure 5.101: Slot 8 P2 Streamwise Vorticity Coefficient

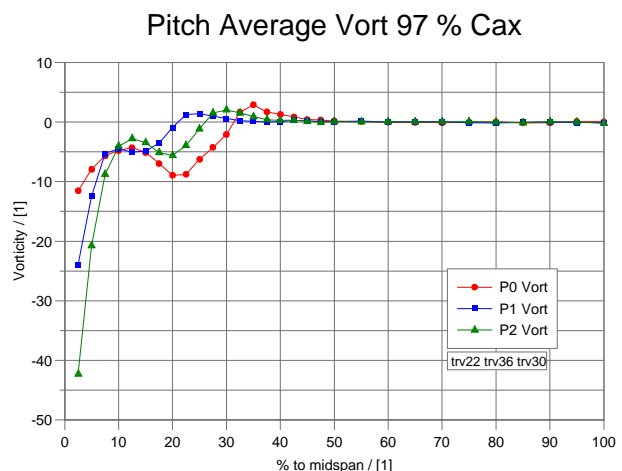


Figure 5.102: Slot 8 Pitch Averaged Vorticity

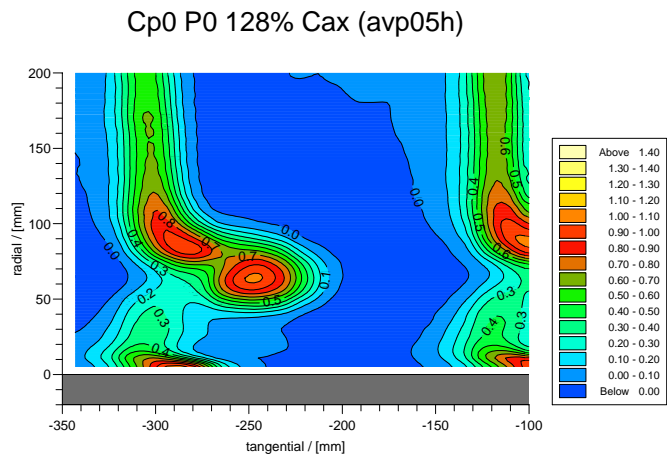


Figure 5.103: Slot 10 P0 Loss

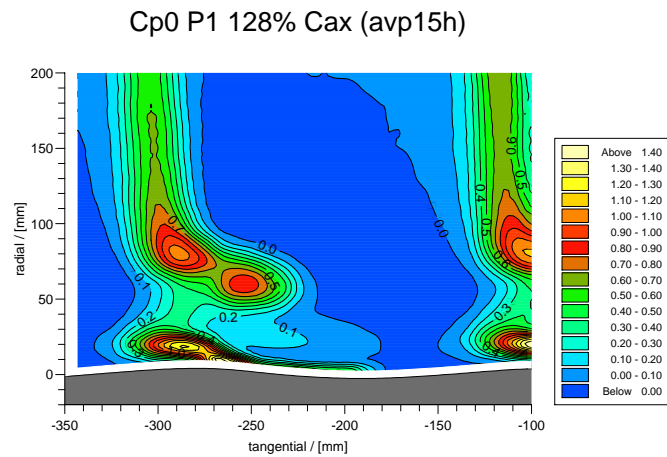


Figure 5.104: Slot 10 P1 Loss

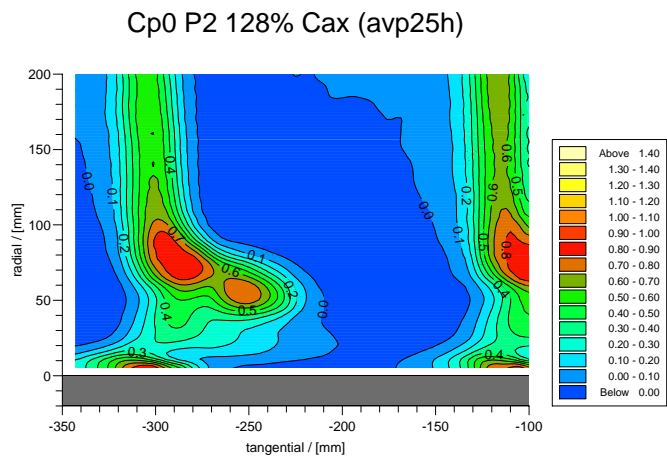


Figure 5.105: Slot 10 P2 Loss

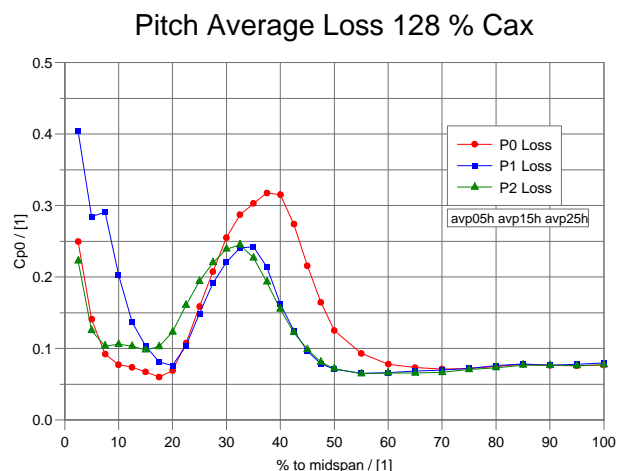


Figure 5.106: Slot 10 Pitch Averaged Loss

Secondary Vectors P0 128% Cax (avp05h)

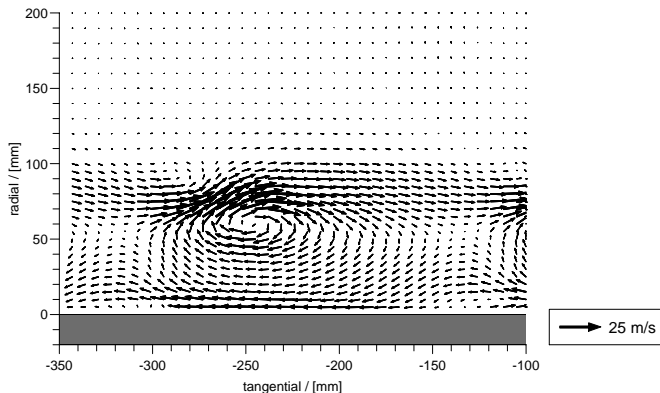


Figure 5.107: Slot 10 P0 Secondary Vectors

Secondary Vectors P1 128% Cax (avp15h)

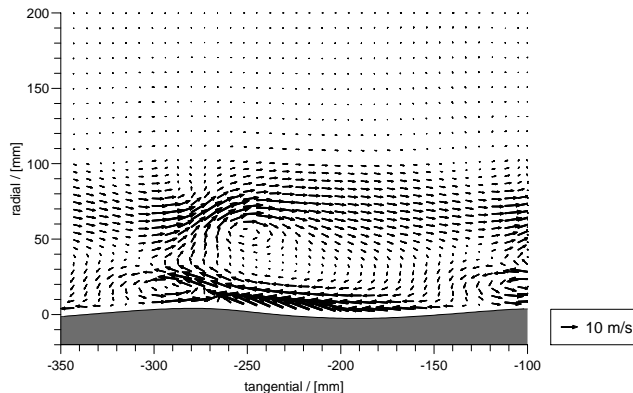


Figure 5.108: Slot 10 P1 Secondary Vectors

Secondary Vectors P2 128% Cax (avp25h)

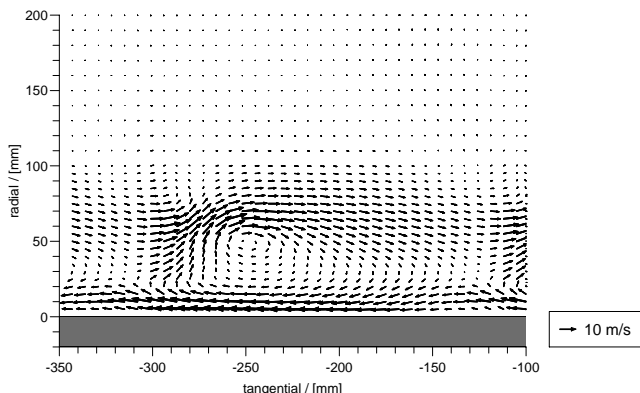


Figure 5.109: Slot 10 P2 Secondary Vectors

Pitch Average Yaw 128 % Cax

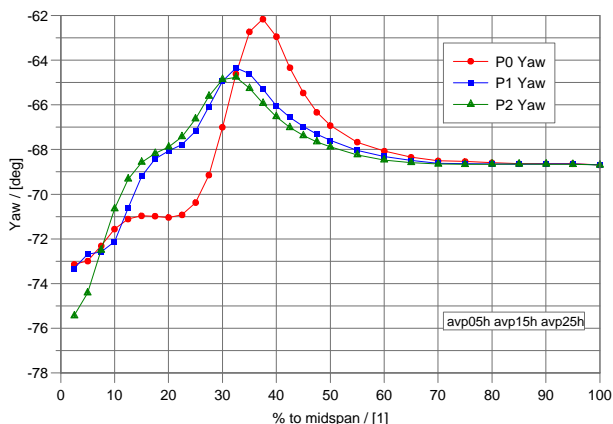


Figure 5.110: Slot 10 Pitch Averaged Yaw Angle

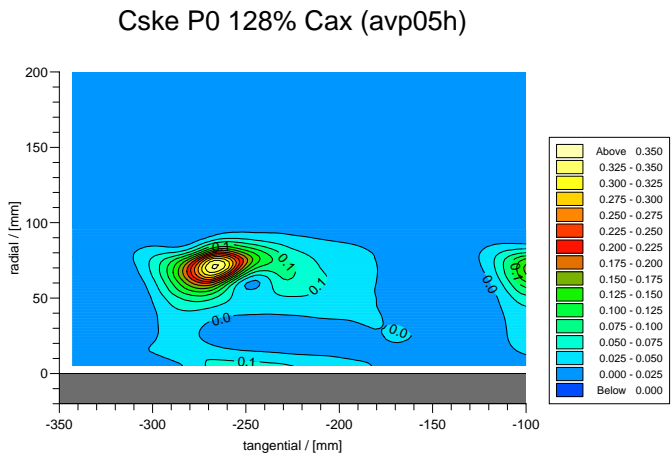


Figure 5.111: Slot 10 P0 C_{ske}

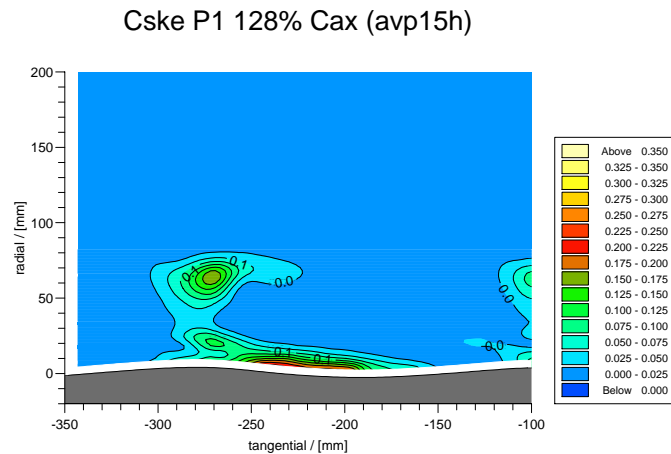


Figure 5.112: Slot 10 P1 C_{ske}

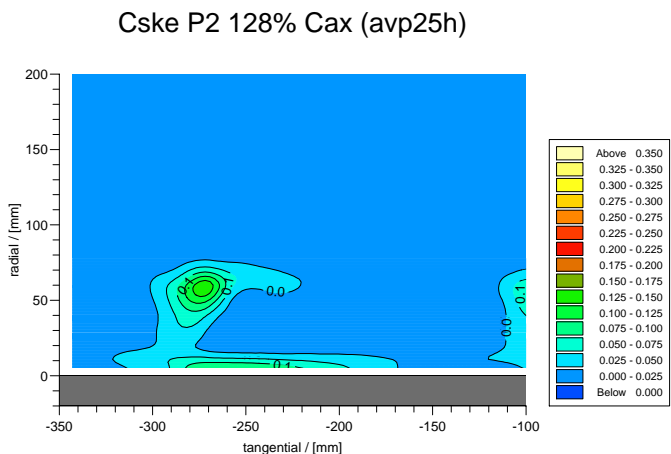


Figure 5.113: Slot 10 P2 C_{ske}

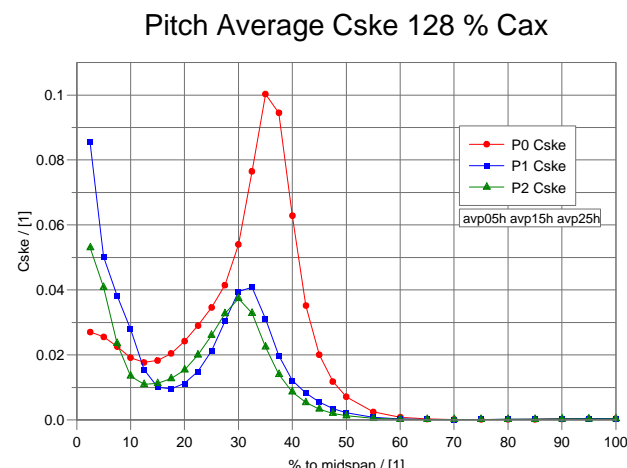


Figure 5.114: Slot 10 Pitch Averaged C_{ske}

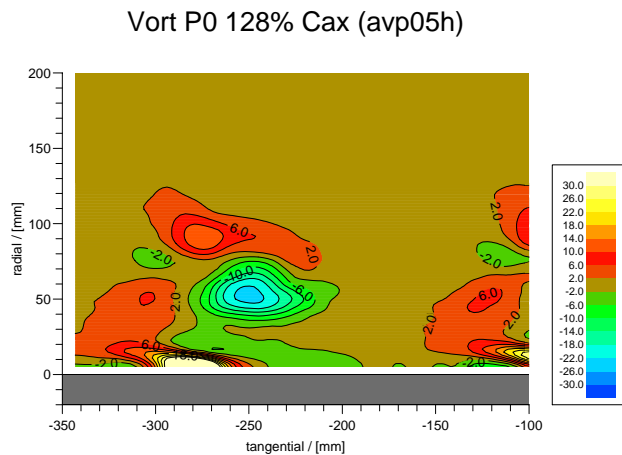


Figure 5.115: Slot 10 P0 Streamwise Vorticity Coefficient

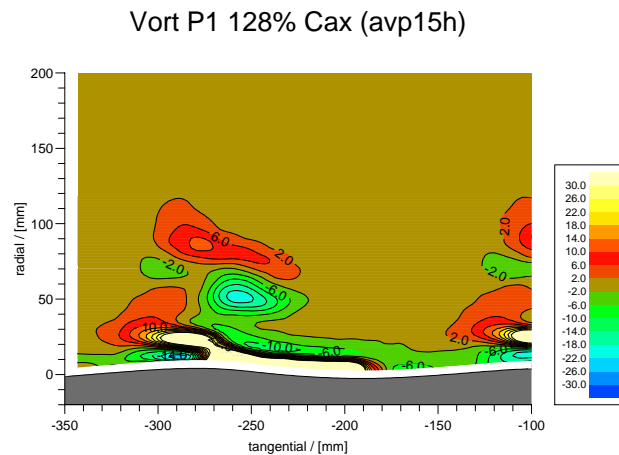


Figure 5.116: Slot 10 P1 Streamwise Vorticity Coefficient

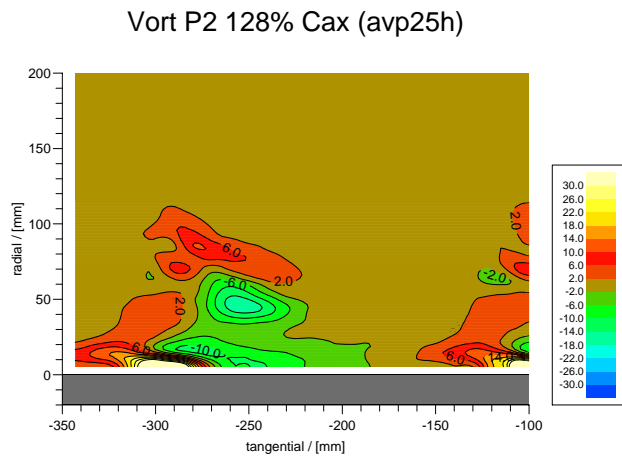


Figure 5.117: Slot 10 P2 Streamwise Vorticity Coefficient

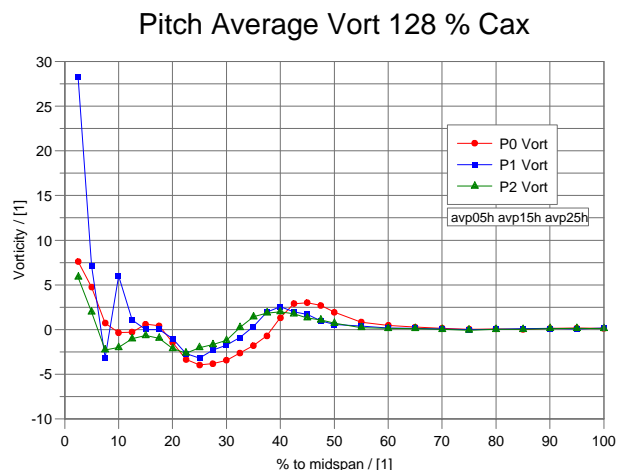


Figure 5.118: Slot 10 Pitch Averaged Vorticity

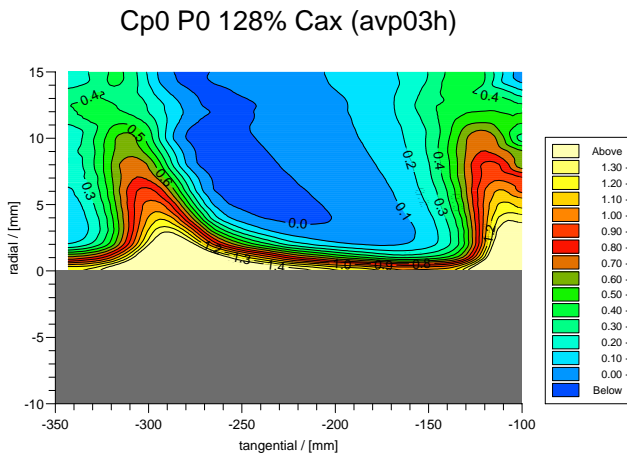


Figure 5.119: Close Wall Loss at Slot 10 P0

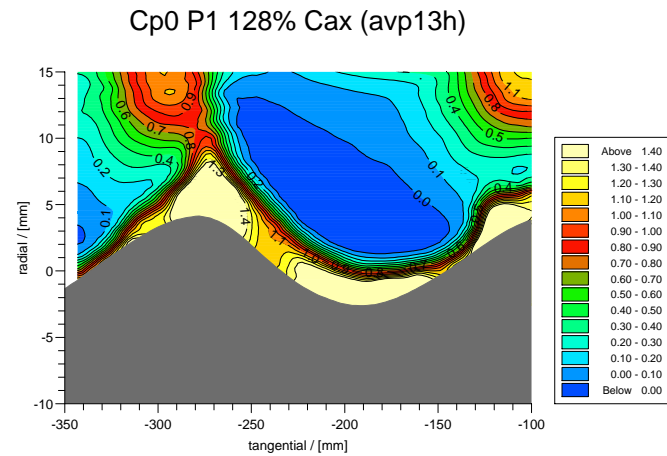


Figure 5.120: Close Wall Loss at Slot 10 P1

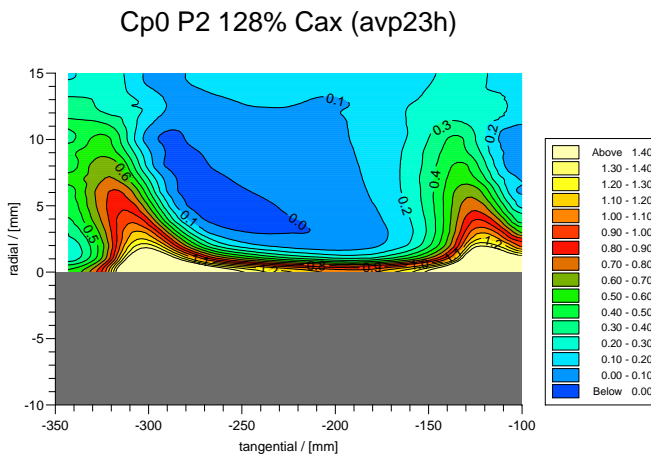


Figure 5.121: Close Wall Loss at Slot 10 P2

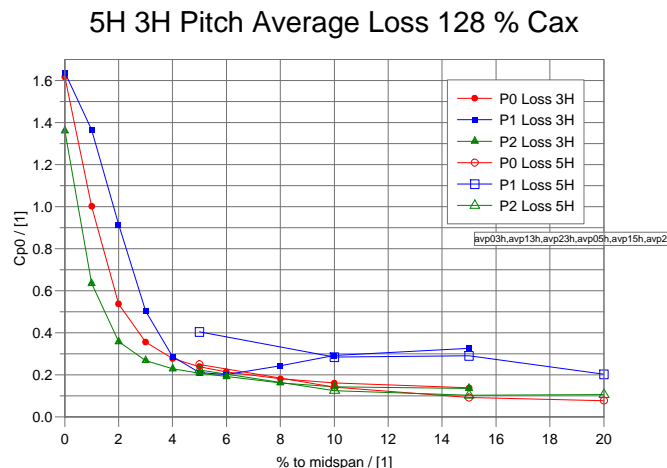


Figure 5.122: 3H and 5H Pitch Averaged Loss at Slot 10

Secondary Vectors P0 128% Cax (avp03h)

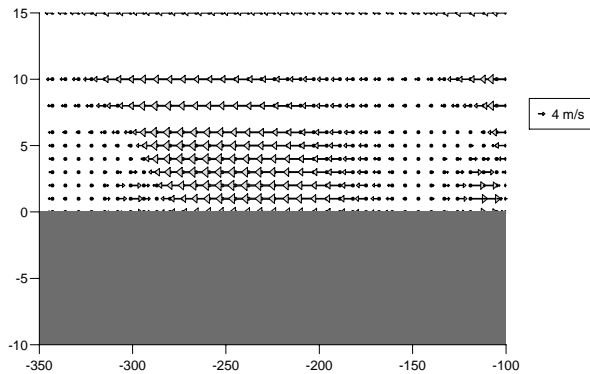


Figure 5.123: Secondary Vectors at Slot 10 P0

Secondary Vectors P1 128% Cax (avp13h)

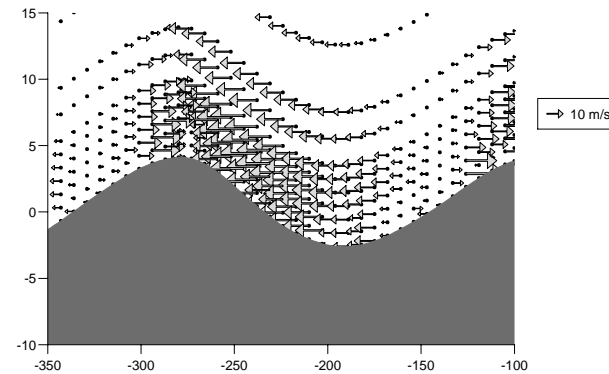


Figure 5.124: Secondary Vectors at Slot 10 P1

Secondary Vectors P2 128% Cax (avp23h)

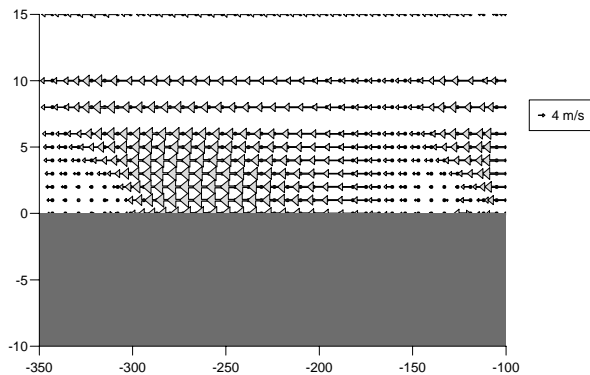


Figure 5.125: Secondary Vectors at Slot 10 P2

5H 3H Pitch Average Yaw 128 % Cax

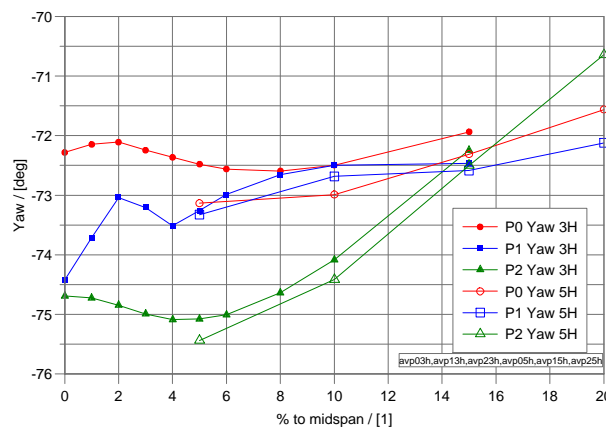


Figure 5.126: 3H and 5H Pitch Averaged Yaw Angle at Slot 10

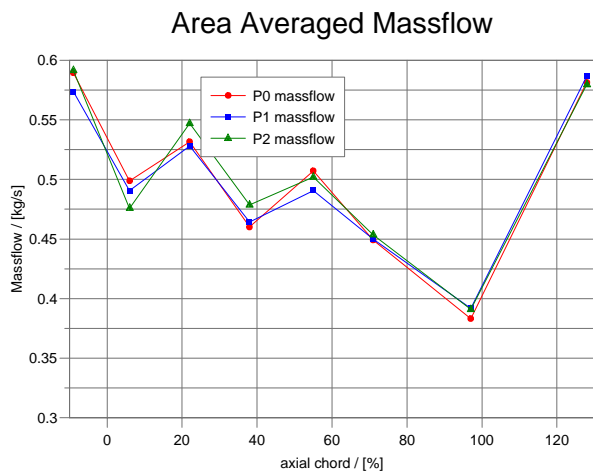


Figure 5.127: Area Averaged Mass Flow for Slots 1 to 10.

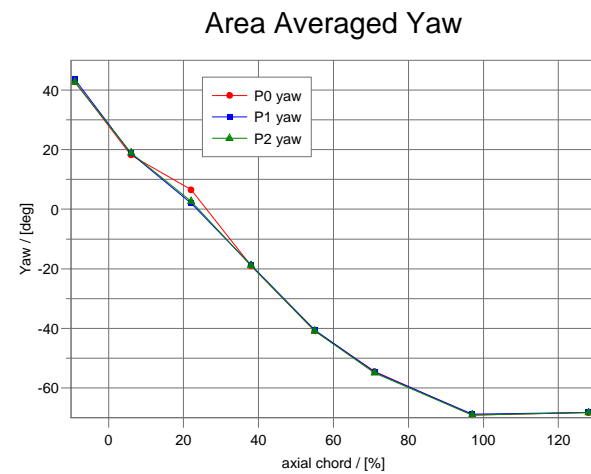


Figure 5.128: Area Averaged Yaw Angle for Slots 1 to 10.

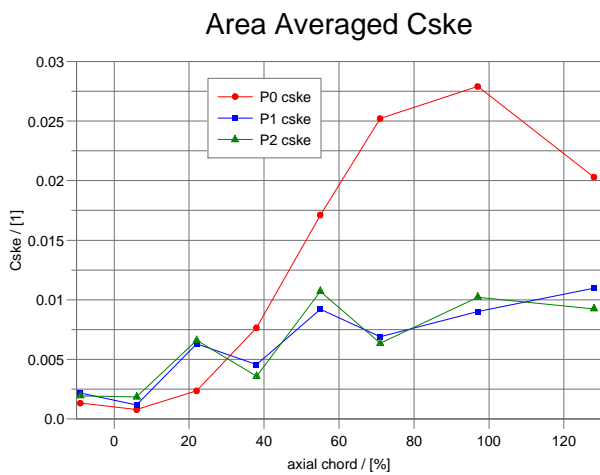


Figure 5.129: Area Averaged C_{ske} .

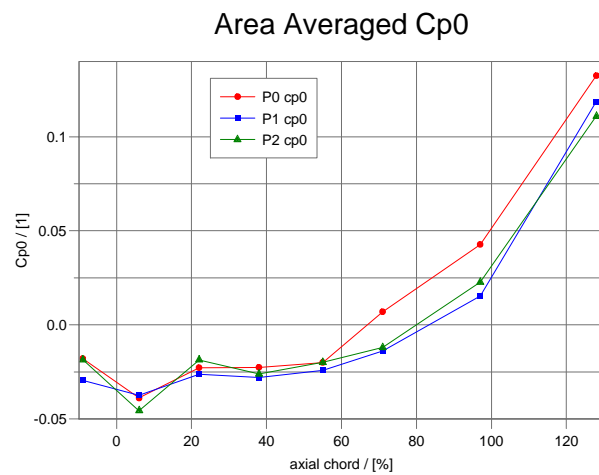


Figure 5.130: Area Averaged Loss Coeficient.

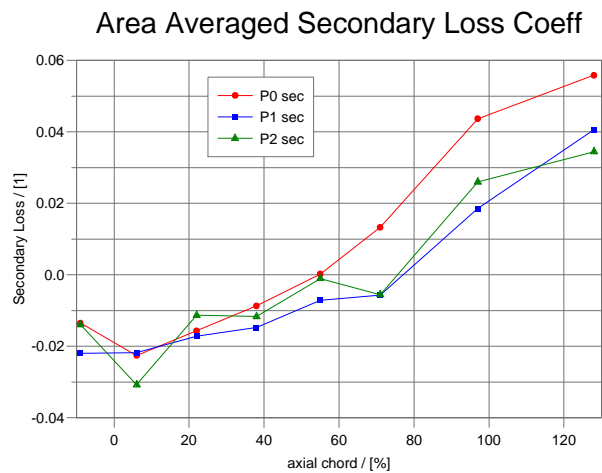


Figure 5.131: Area Averaged Secondary Loss Coeficient.

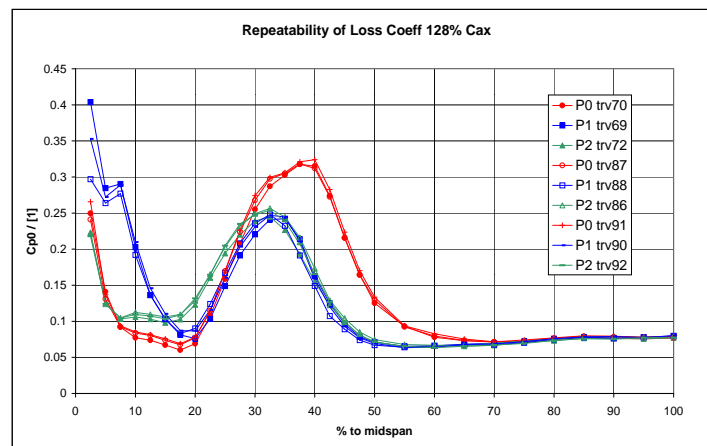


Figure 5.132: Repeated Traverses at Slot 10 - Loss.

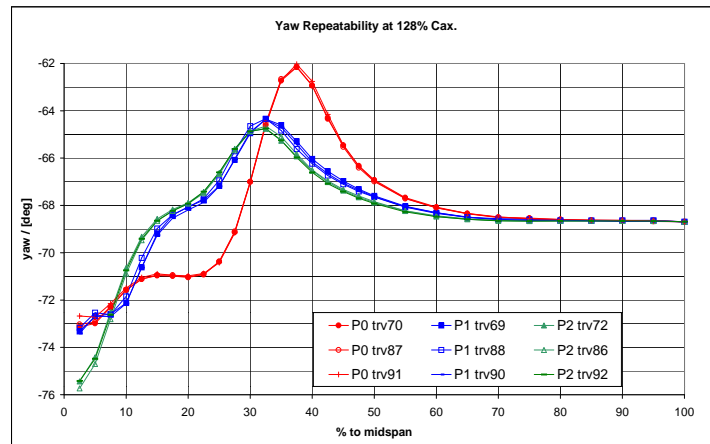


Figure 5.133: Repeated Traverses at Slot 10 - Yaw.

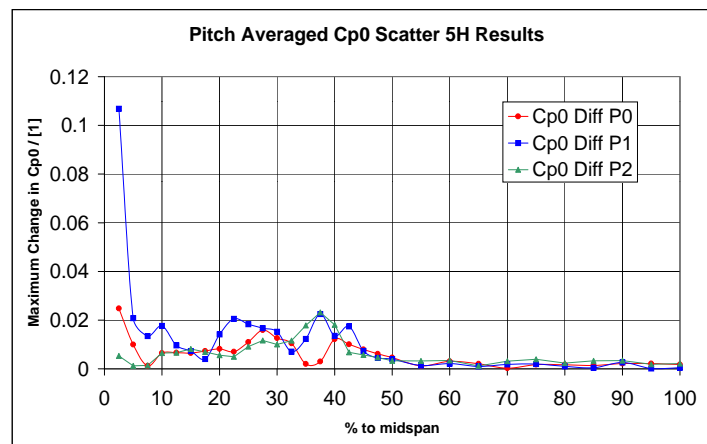


Figure 5.134: Maximum Variation between repeated Traverses - Loss.

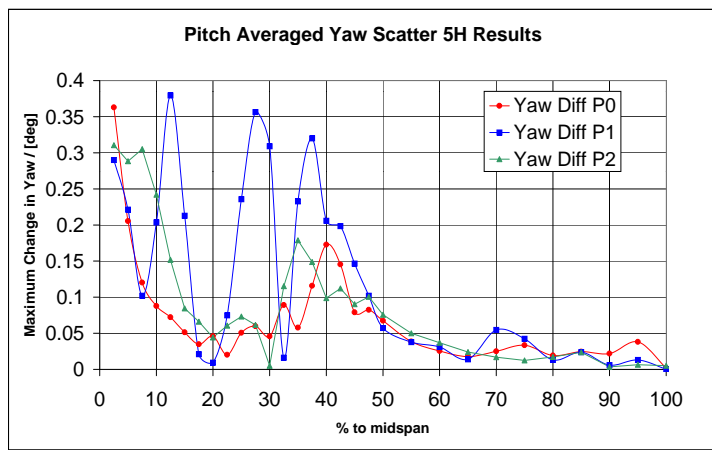


Figure 5.135: Maximum Variation between repeated Traverses - Yaw.

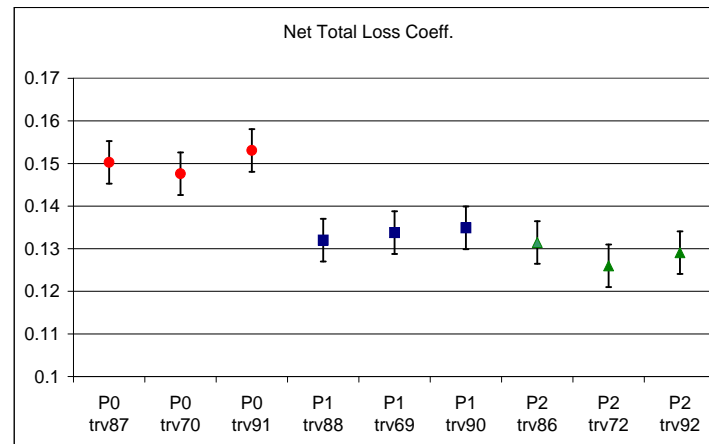


Figure 5.136: Area Averaged Total Loss.

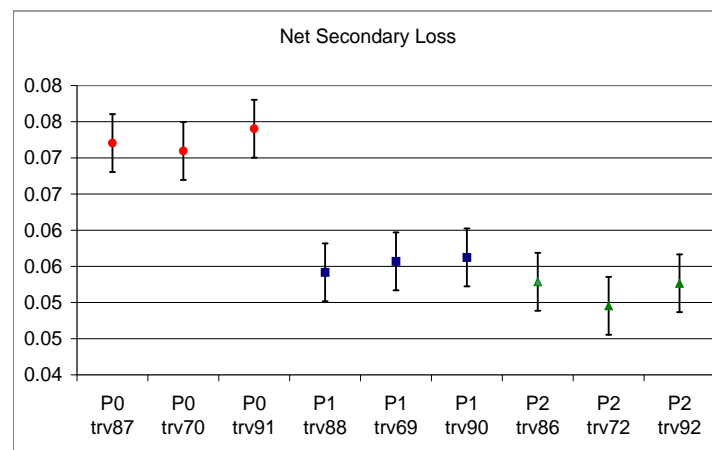


Figure 5.137: Area Averaged Secondary Loss.

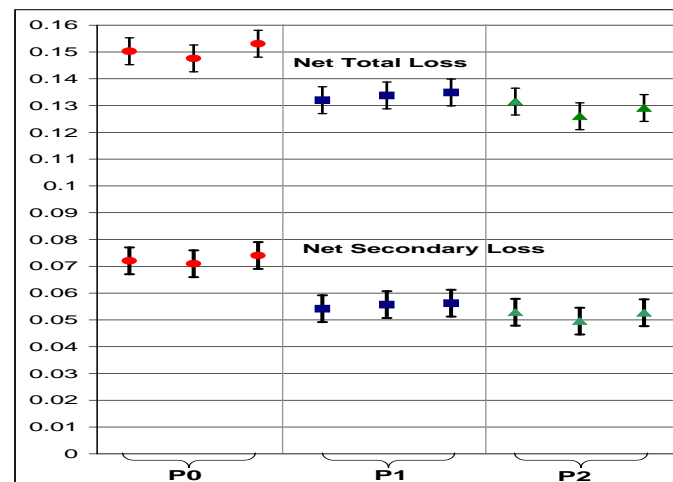


Figure 5.138: Secondary and Total Loss.

5.14. Figures for Pressure Probe Results

132

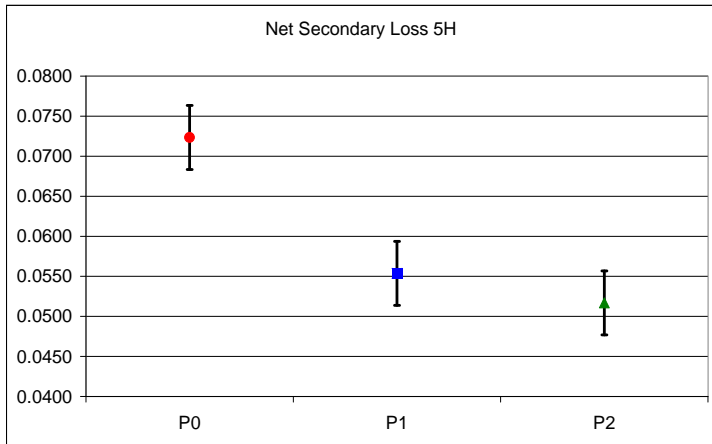


Figure 5.139: Mean Loss \pm two standard deviations.

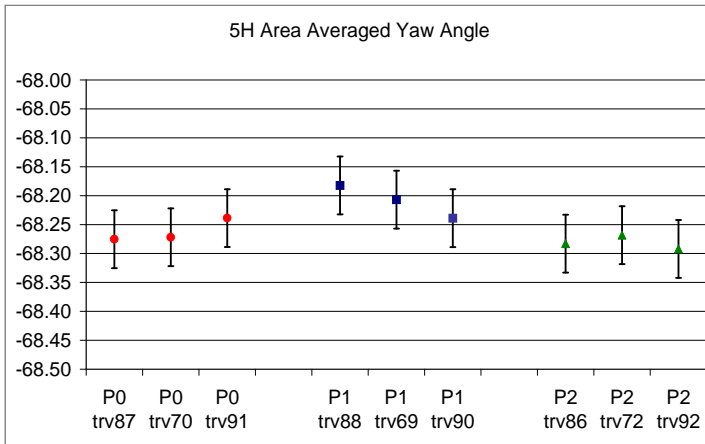


Figure 5.140: Yaw Angle Variations at Slot 10.

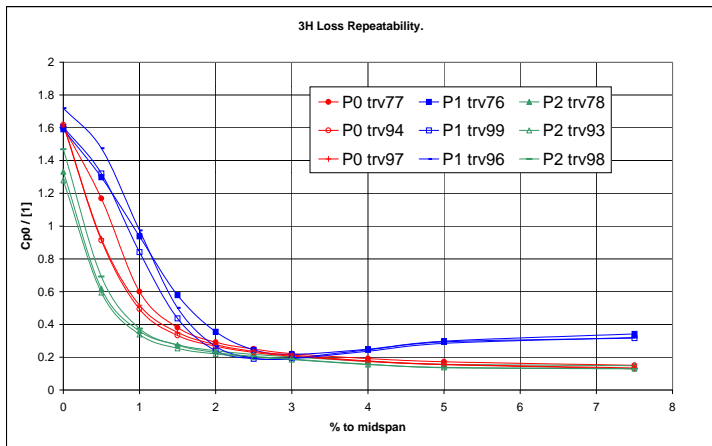


Figure 5.141: Repeated Traverses Three Hole Probe Loss.

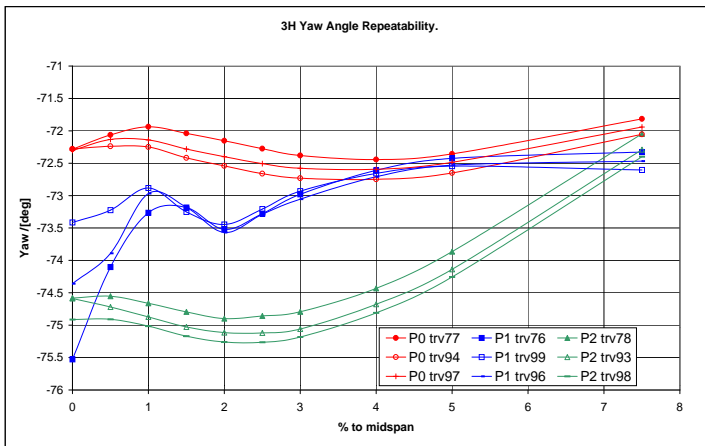


Figure 5.142: Repeated Traverses Three Hole Probe Yaw.

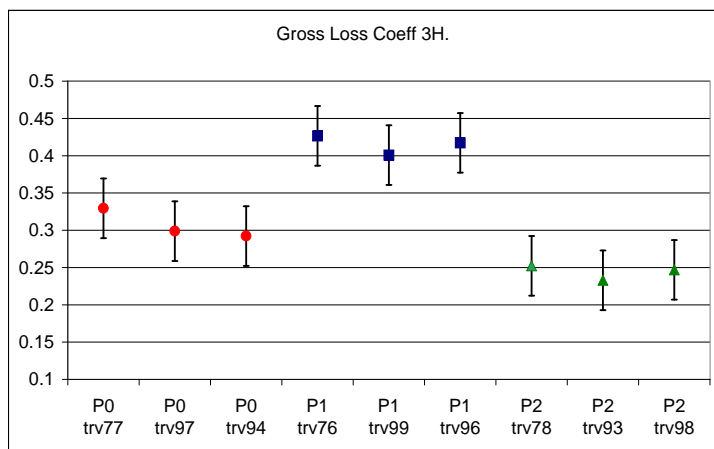


Figure 5.143: Area Averaged Total Loss - 3H Probe.

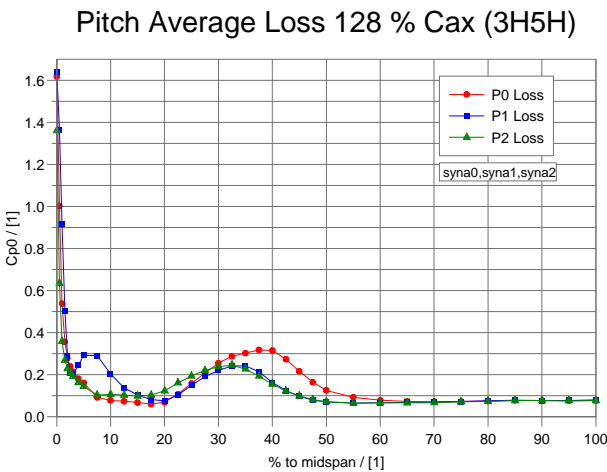


Figure 5.144: Pitch Averaged Loss 3H and 5H Data set.

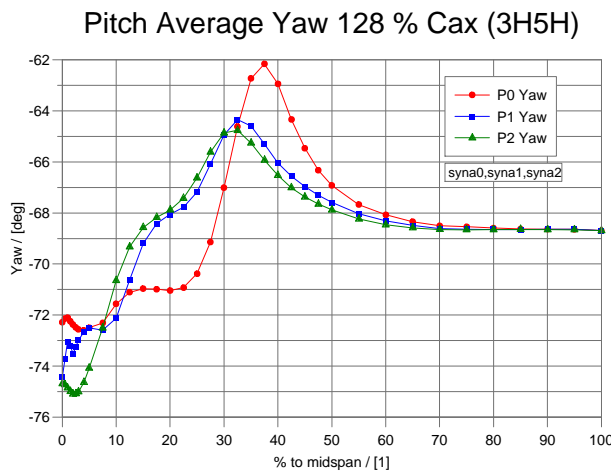


Figure 5.145: Pitch Averaged Yaw 3H and 5H Data set.

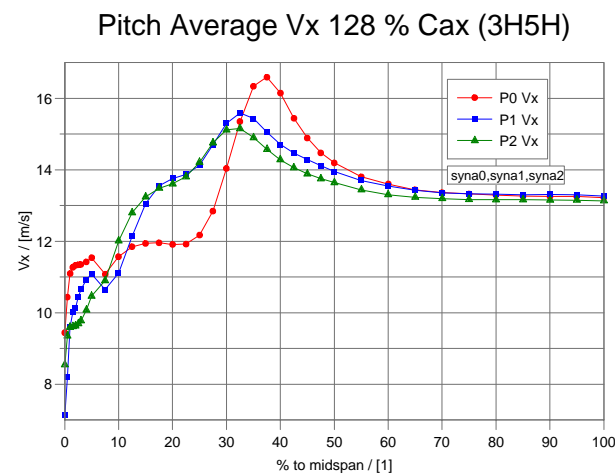


Figure 5.146: Pitch Averaged Axial Velocity 3H and 5H Data Set.

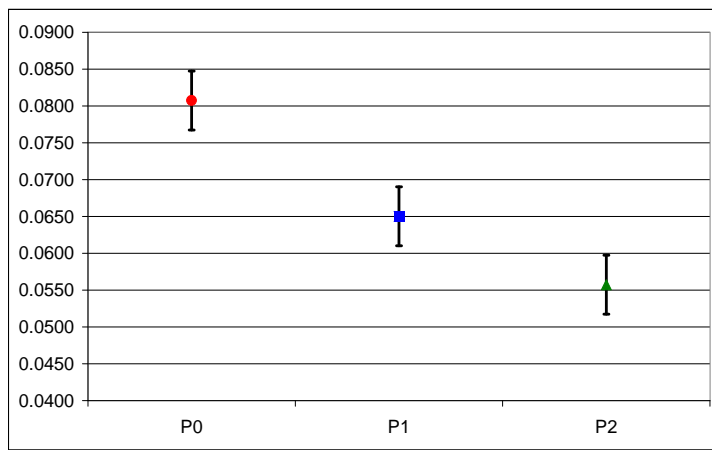


Figure 5.147: Combined Data Set (three and five hole) Loss.

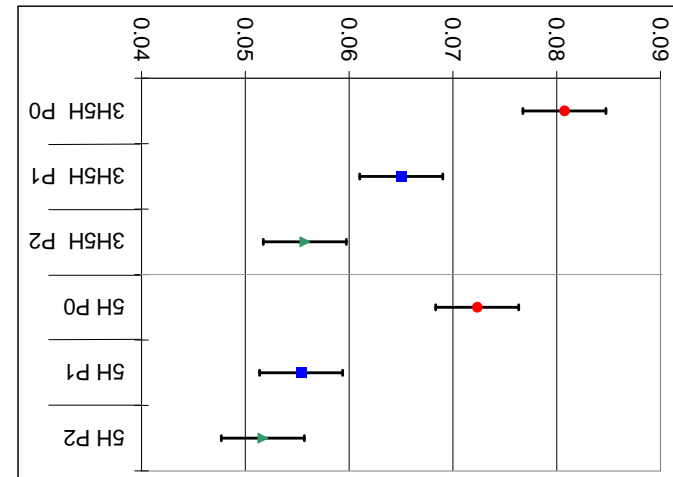


Figure 5.148: Change in Secondary Loss caused by adding close wall results.

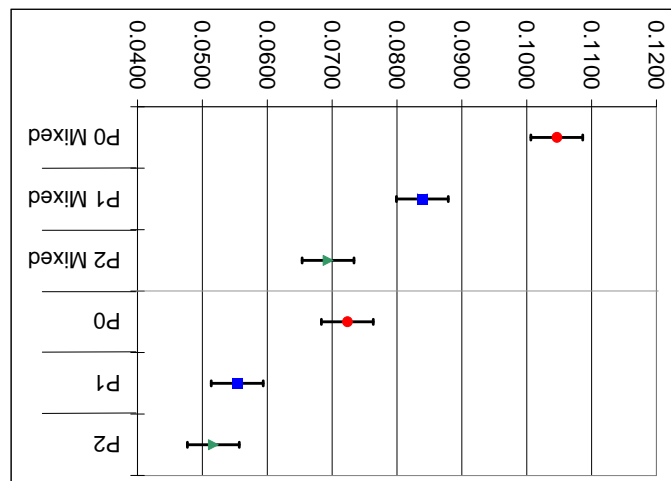


Figure 5.149: Area Averaged Mixed Out Secondary Loss for a Five Hole Probe.

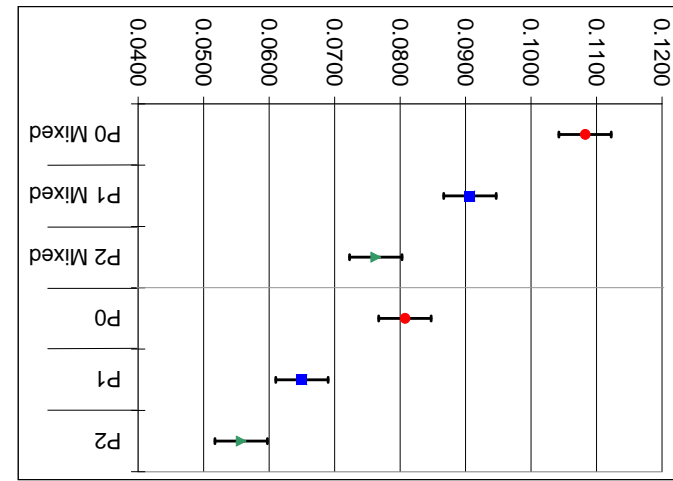


Figure 5.150: Area Averaged Mixed Out Secondary Loss for the Synthesised Data Set.

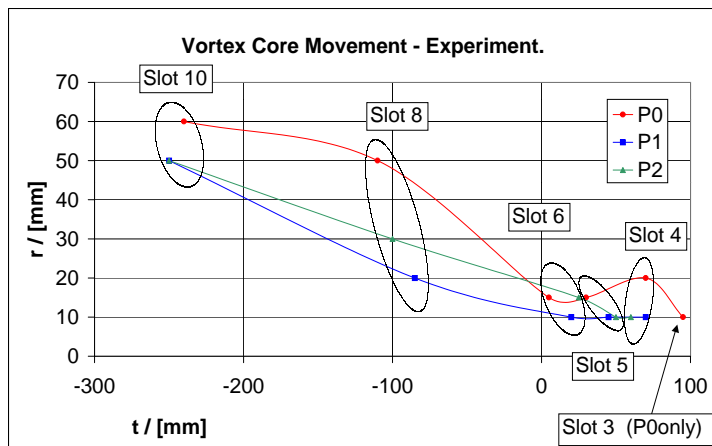


Figure 5.151: Vortex Centre Movement.

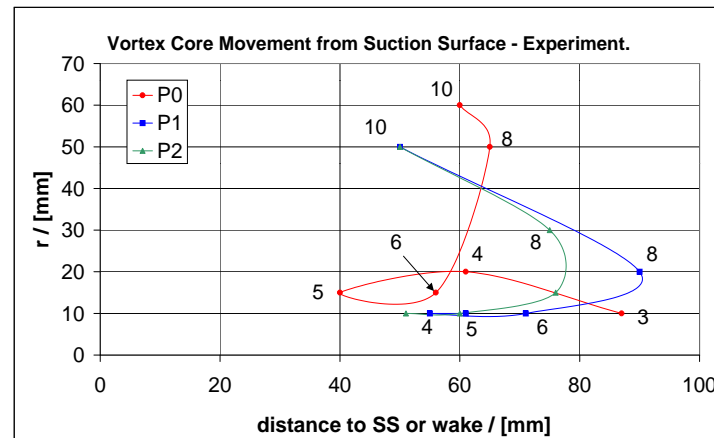


Figure 5.152: Vortex Centre Movement Measured from the Suction Surface/Blade Wake Centreline.

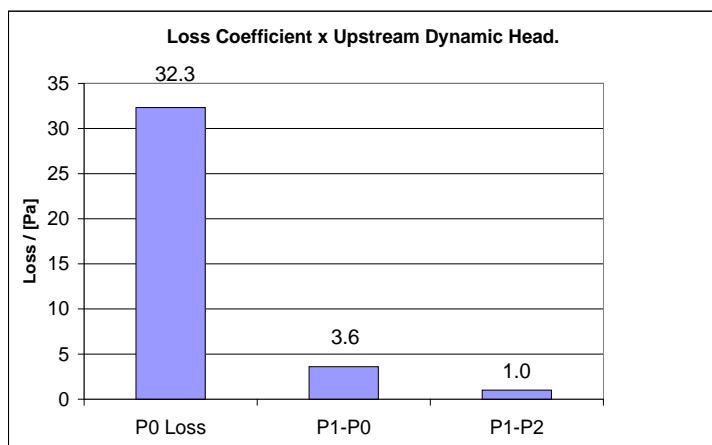


Figure 5.153: Why Loss Measurement is Difficult.

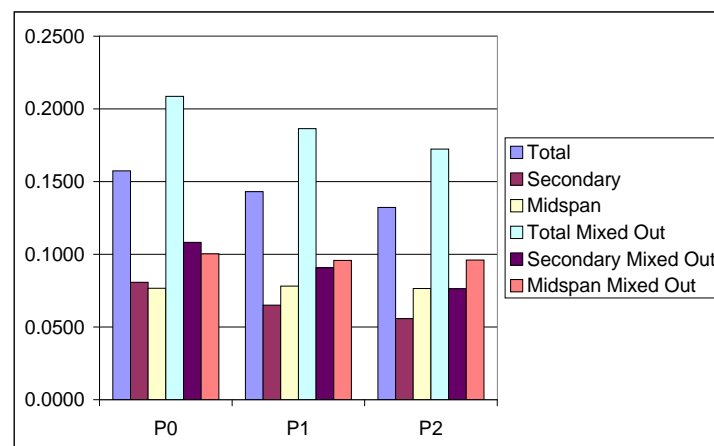


Figure 5.154: Summary Figure of P0, P1 and P2 Area Averaged C_{P0} .

Chapter 6

Hot Film Readings

THIS CHAPTER contains hot film measurements for the planar reference case, P0 and the two older profiled geometries, P1 and P2. Hot film measurements for both the suction surface of the blade and the endwall itself are included. The aim of the measurements was to determine if the benefits of endwall profiling arise from changing the boundary layer state.

The method for measuring intermittency in the cascade using hot films was developed during the course of research. This utilises “off the shelf” hot films and measuring equipment along with a high speed A/D converter and a number of programs written by the author to process the data. The system as deployed does not give quantitative values of intermittency but provides qualitative information by displaying processed hot film traces. Whilst it would have been highly desirable to get quantitative values of intermittency for the endwalls, it is not immediately apparent how the current method could have been extended to accommodate this.

There is a large amount of data presented in this chapter, so each experiment was given a label such as “P0EC7” or “P1S501”. As is evident the labels take the form of Pn il xxx , details of how to decode this label to reference a specific film location are found in the Appendix.

An emphasis is placed on providing a realistic assessment of the accuracy of the results and problems encountered, so that they may be of maximum value.

6.1 Hot Film Measurement System

The basic principles of hot films are well known. The hot film which consists of a very small heated element, Figure 6.1, is one arm of a Wheatstone bridge. The film is placed at the location of interest and if the shear stress increases over the gauge so will the heat transfer and the temperature of the gauge will drop. This reduces gauge resistance and this change is measured and the voltage increased so that the hot film heats up keeping the resistance constant.

It is possible to operate the gauge at constant current rather than at constant temperature, however this necessitates some estimate of the changing performance of the gauge (e.g. re-calibration) with temperature changes which is not required for constant temperature work. Constant temperature work also improves the frequency response of the system which is the main reason for choosing it.

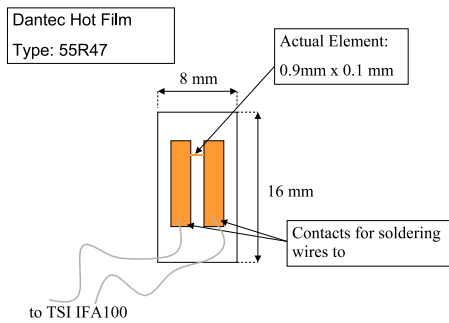


Figure 6.1: Hot Film Layout

In order to obtain accurate values of shear stress from a hot film gauge, two requirements have to be met. Firstly a relationship between the gauge resistance, power dissipated, or some other measured hot film parameter, and the shear stress has to be proposed. Secondly some way of calibrating the gauge to deal with the constants in this relationship needs to be found. Bellhouse and Schultz (1966) described their method of doing both, they proposed a relationship of the form $\tau_w^{1/3} = A(i^2 R / \Delta T_0) + B$ where i and R are the current and resistance of the hot film gauge respectively. This relationship requires that some assumptions are made about the boundary layer flow, principally that the thermal boundary layer is very small compared to the velocity boundary layer and that the pressure gradient is small enough to regard the temperature profile as linear. Additionally in order to obtain values of shear stress, A and B have to be determined by calibration and this requires a known shear stress. Bellhouse and Schultz solved this problem by mounting their gauge on a the flat end of a glass rod which could be moved from location to location, the gauge could then be placed in a location of known shear stress for calibration. This approach is not possible for profiled endwalls due the sharp curvature of the endwall in certain places.

Given the difficulties in obtaining quantitative results from hot film probes the decision was made to obtain qualitative results only.

Hodson (1985) in an investigation of leading edge flow in a high speed linear cascade used the parameter $(Q - Q_0)/Q_0$ to plot hot film traces, Q is the gross heat transfer rate from the hot film and Q_0 is heat transfer at zero flow over the gauge. Q_0 is approximately equal to the heat lost to the substrate which means the parameter $(Q - Q_0)/Q_0$, is a normalised heat transfer rate to the fluid from the gauge. In this chapter the parameter $(Q - Q_0)/Q_0$ is used to plot the hot film suction surface traces and experience has shown that this parameter successfully shows up the transitional flow on the suction surface without difficulty.

For the endwall measurements a different parameter was used. It was found that due to the variation in the zero flow heat transfer rate Q_0 the parameter $(Q - Q_0)/Q_0$ varied too much for nominally similar flows and much better results were obtained by not using the parameter $V^2 - V_0^2$, where V is the voltage applied to the bridge during operation and V_0 is the zero flow voltage.

Given the high cost of the “off the shelf” hot film gauges, a large amount of gauge

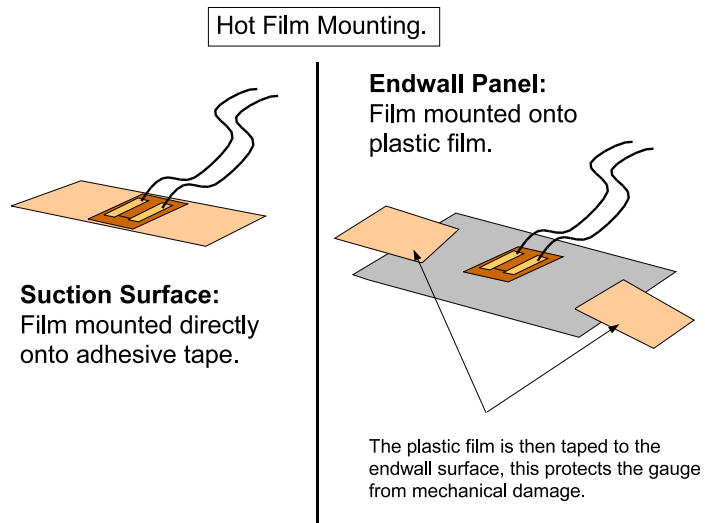


Figure 6.2: Film Attachment

re-use is required to make the process economical. The method of attachment of the gauge to the endwall has an impact both on the measurement and the life of the gauge. For the suction surface work, the gauge was simply stuck down onto adhesive tape which was “sticky” all the way underneath the gauge. However this resulted in a rather short gauge lifetime, as considerable stress is placed on the small gauge when removing it from the suction surface. For the endwall measurements the gauge was stuck down to a small piece (2cm by 2cm) of overhead transparency material and this was then attached firmly to the endwall. See Figure 6.2). The backing material has a thickness of 0.1mm and was not expected to disturb the incoming flow with a boundary layer thickness of around 40mm.

The gauge is connected to a TSI IFA-100, which provides the necessary electronics to heat the hot film and amplify and filter the output. Although it has other possible applications for this thesis the TSI-IFA-100 was used as a constant temperature anemometer control and processing system. For our application the analogue output from the IFA-100 is fed directly into a high speed A/D converter (Strawberry Tree Flash-12) which stores voltage vs. time traces. This data was then processed and plotted. A program written by the author specifically for the project called *film* was used to record the data.

The measurement of the zero flow voltage and therefore Q_0 has to be precise. Figure 6.3 shows the variation in zero flow voltage after switch on for two hot films, one on the endwall and one on the suction surface. In earlier unsuccessful work at Durham, Ingram and Gregory-Smith (2002), no such study was carried out and readings commenced typically after 60 seconds. Figure 6.3 shows that 300 seconds is reasonable time to wait for the gauge to settle. For each reading a careful procedure is followed, namely:-

- Mark position on the endwall.
- Estimate flow direction from flow viz.

- Put probe in place, ensuring good contact with the surface and that it is lined up with the flow direction.
- Stick lead in wires down out of the way.
- Connect to IFA-100
- Ensure that the cascade is properly 'boxed up' with seals applied where necessary.
- Measure the cold resistance.
- Set operating resistance, usually use an overheat ratio (OHR) of 1.5.
- Set probe to run.
- Wait for 300 seconds.
- Read $V_{zero\!flow}$ and record. (This done automatically by the *film* program.)
- Measurement of intermittency.
- Record T_{atm} and P_{atm} if necessary.
- Turn on fan and run cascade up to speed.
- Examine hot film output trace and optimise by adjusting filtering frequency, gain, offset, and bridge compensation.
- Run *film* program to record the hot film traces
- Store the data files.
- Turn the fan off and repeat as necessary.

The processing of results is distinct from the data acquisition. The data acquisition program *film* is written in the “C” programming language as this allows the programmer intimate control of the hardware (see Kernighan and Ritchie (1988)) and runs on the rig PC. The *film* program has the following functions:-

- reads $V_{zero\!flow}$
- allows the operator to run the tunnel to the correct “standard day” conditions
- reads and stores the voltage vs time traces
- allows the user to adjust sampling frequency, no of samples etc.

The data processing programs are relatively simple as they only calculate $(Q - Q_0)/Q_0$ or $V^2 - V_0^2$. Data processing is now done using a high level scripting language called “Python”. Python makes dealing with large amounts of data in many different files much easier than it would be in C as the work of memory management and file input/output details are done by the language not the programmer. (See Beazley (2001) for details.)

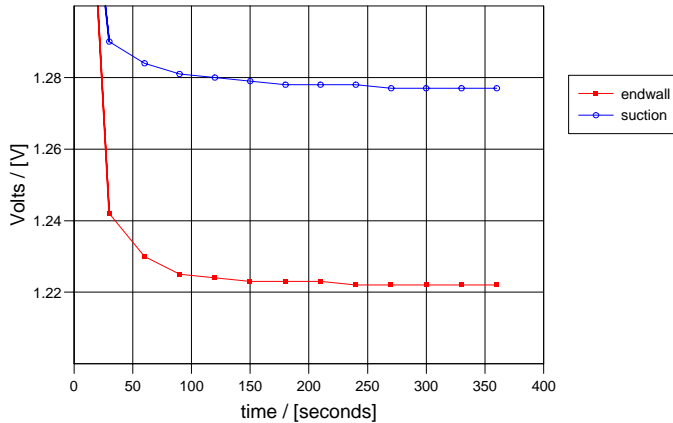


Figure 6.3: $V_{z\text{ero}f\text{low}}$ Variation with time.

The Python script reads in the voltage time trace and calculates $(Q - Q_0)/Q_0$ or $V^2 - V_0^2$ from the information in the file. This is then written out to a separate file which is then plotted using the GSHARP plotting package. For comparison the plots are imported into a drawing program¹ to show the traces side by side in various configurations.

6.2 Hot Film Results

The Hot Film results are split into two sections, the first covers the suction surface measurements the second the endwall traces. Measurements of the pressure surface by Moore (1995) did not reveal any major flow features of interest and it was decided to not repeat these measurements.

It was the original intention to produce intermittency contour plots of the blade and endwall surfaces for all three geometries. The plan in essence was to do what Moore (1995) did for the planar endwall for all three geometries. However this turned out not to be practical and what is presented in this report is a series of hot film measurements at various locations on the endwall that give an indication as to the state of the boundary layer at those locations (laminar, intermittent or turbulent).

The information presented here does however go some way to determining whether or not the benefits of endwall profiling are arrived at by changing the state of the boundary layer, or by some other mechanism such as a smaller passage vortex generating less loss.

Although the sampling frequency and number of samples was variable the results presented here were taken at 20 KHz and 10,000 samples were taken. This means

¹for this chapter OpenOffice.org's Draw program was used but many alternatives exist

Slot No.	% C_{ax}	x/mm
2	6%	-170
3	22%	-141
5	55%	-81
6	71%	-52
7	87%	-24

Table 6.1: Suction Surface Measurement Locations

that the highest possible frequency that could be detected by the system is 10 KHz.

Hodson (1985) quotes a frequency response for surface mounted of hot films of 15-20 KHz. This suggests the limiting factor in the frequency response of the measurements presented in this chapter is the sampling frequency.

The Durham Cascade features an inlet boundary layer thickness of 30 mm (See Table 3.3 on page 30) and if we assume a typical inlet velocity of 20 m/s a very rough estimate of the frequency of events that occur in the boundary layer would be around 6 KHz. With a measuring capability of 10 KHz the system could resolve turbulent events with a length scale of 2 mm assuming that they occurred at the freestream velocity. This very crude estimate suggests that the measurement system can resolve events down to around 6% of inlet boundary layer thickness.

As can be seen in the later sections this resolution is enough to resolve the suction surface boundary layer with some success but the situation on the endwall is not so clear. The fact that the measurement system can show a laminar to turbulent transition gives some confidence that dramatic changes on the endwall would be picked up.

6.2.1 Suction Surface Measurements

Suction surface measurements were conducted in twenty five locations on the suction surface. Five measurements were conducted at five locations, which correspond to Slots 2,3,5,6 and 7 (See Table 6.1 and Figure 6.4 on page 146). Each axial location had hot film traces taken at $r=10,30,50,70$ and 100mm. No attempt is made to take account of endwall curvature and to operate at a constant percentage of midspan as was done for the pressure probe results. A % value to midspan of the planar case is included on the plots however. As mentioned previously the suction surface hot films were attached directly to adhesive film so the area immediately under the gauge is stuck directly to the suction surface. Whilst this provides good contact with the suction surface it proved too expensive in terms of consumption of gauges to measure the endwall surface using the same method. The gauges were attached to the blade and then each endwall (P0, P1 and P2) was tested in turn with the gauges left in place.

The variation in the trace of the hot film is examined. This is obtained by processing the $(Q - Q_0)/Q_0$ traces and plotting the variation around the average value. Figures 6.5 to 6.9 show these plots for Slots 2 to 7 (6% C_{ax} to 87% C_{ax}). The vertical scale is the same (± 1 unit of $(Q - Q_0)/Q_0$) for every plot to allow a comparison between plots to be made.

By inspection of the results it appears that the gauge used for $r=10$ mm (5%

Span for P0) at Slot 2 was not adequately attached to the suction surface, so does not yield useful information.

The boundary layer on the suction surface starts off laminar with more turbulence near the endwall, the turbulent region spreads upwards as the trailing edge is approached. For example Figure 6.6 on page 148 (22% C_{ax}) shows that at 50% of midspan the P0 trace is exhibiting transitional behaviour that is close to laminar flow, there are only a few turbulent peaks and the main flow is relatively calm. Figure 6.7 on page 149 (55% C_{ax}) shows that at 25% of midspan the P0 trace is exhibiting transitional behaviour that is much closer to turbulent flow with a much greater number of peaks in the trace. Finally Figure 6.9 on page 151 (87% C_{ax}) shows that for P0 at 25% of midspan the trace exhibits much more turbulent behaviour with much higher levels of unsteadiness.

In general the boundary layer state is the same as that found in Moore (1995) and it does not change very much depending on the endwall used. There are isolated traces where the hot film trace appears to be different for the profiled endwalls rather than the planar ones (e.g. P0 15% in Figure 6.8 and the P2 50% in Figure 6.6). However these “rogue” traces do not fit with the transition from turbulent to laminar flow with increasing radial height with the same endwall installed so are ignored. Repeating the “rogue” measurements appeared unlikely to deliver any new information as the measurements that were successful showed that the suction surface boundary layer does not change when profiled endwalls are applied.

The fact that the suction surface boundary layer does not change is perhaps unsurprising, the boundary layer state over most of the blade will be dominated by the pressure gradient on the blade surface which as has been shown (Hartland et al., 1999a) does not change much when profiled endwalls are applied. Earlier work in Chapter 4 has shown that there are changes in the extent of secondary flow on the suction surface but that the overall pattern remains largely the same. The suction side of the horseshoe vortex at blade exit is for example at $r=50\text{mm}$ for P0, 42mm for P1 and 43mm for P2 (these heights are estimated from flow visualisation photographs and are marked on Figures 5.91-5.93). It may be that the small changes in flow patterns are reflected in the actual level of intermittency on the suction surface but the twenty five measurement points were not fine enough to pick them up.

By way of comparison Moore (1995) used 112 points to examine the intermittency on the suction surface and 149 for the endwall. Moore (1995) used a hot wire system with automated traversing which was considerably less time consuming than the method used for this thesis. Hot wires were not considered suitable for the endwall as in regions of sharp curvature the wire could not be manoeuvred close enough to the endwall.

6.2.2 Endwall Measurements

Endwall Hot film measurements were conducted in some sixteen locations on each endwall making a total of forty eight endwall measurements for all three panels. More measurements would have been highly desirable but the set obtained gives an indication of whether or not the boundary layer is changed by profiled end walls.

The Hot Film technique was identical to that for the suction surface except that the gauge was attached to a 2cm by 2cm piece of plastic, this gave the gauge some protection and gave it a longer life. For example the suction surface measurements used up five gauges with twenty five separate locations measured (once fixed to the blade the gauge can measure each endwall without being moved). The endwall surface used two gauges and measured forty eight separate locations. Or put another way, using the plastic backing improves gauge life from five separate locations to twenty four separate locations. The results obtained from the endwall appear to show that the plastic backing does not interfere with getting good results.

As discussed earlier the parameter used to look at transition on the endwall is $V^2 - V_0^2$ rather than $(Q - Q_0)/Q_0$, due to variations in Q_0 . $V^2 - V_0^2$ is proportional to the heat transfer into the fluid from the gauge. In order to obtain the actual heat transfer from the gauge one has to multiply by the "hot" resistance i.e. $R(V^2 - V_0^2)$ the resistance of the gauge when operating varied from 17Ω to 19Ω so the effect of neglecting R should be minimal when comparing traces. For the endwall traces both the variation about a mean value is examined as well as the level.

The variation about a mean value is plotted in Figures 6.10 to 6.12 and the level in Figures 6.13 to 6.15. The middle reading at exit for P1 (P1EP4) did not produce useful results and this is due the discontinuity for P1 at exit of the cascade, as the profiling extends further than the cascade. This is normally dealt with by sealant gel during pressure probe measurements but was removed to try and attach the gauge - since the gauge was destroyed during this reading it was decided to leave a gap in the data.

Several additional processing methods such as the Turbulent Energy Recognition Algorithm (TERA) used by Moore (1995) were attempted on the data to try and enhance the features of interest. However these attempts did not yield any more information than can be obtained by examining the trace directly by eye so are not included.

Other investigations such as Harrison (1990) using hot films have yielded greater success on the endwall. However Harrison reported that a movable endwall was available so the gauge had to be attached only once, then the endwall could be moved to the appropriate location. This approach is not possible with the profiled endwalls at Durham.

Moore (1995) also produced much more definitive results for the endwall, though the time dependent traces are not plotted in any detail. Moore used a hot wire which has a much better frequency response than the hot film which may account for the better results.

The following points can be observed about the endwall immediately:-

- In general the endwall results are not as clear as was originally hoped.
- There is agreement for the planar case with previous studies, Harrison (1990) or Moore (1995). A visual inspection of the traces shows a region of what could be classified as transitional flow near the pressure surface.
- There is a general trend in increased level of $V^2 - V_0^2$ through the blade passage in each of the endwalls. This is in according with our understanding of the flow.

- In general the levels and fluctuations of the traces appear to be higher for P0 than P1 or P2, although the change is quite small.
- The state of the boundary layer appears similar for the three endwalls. This suggests that either the benefits of endwall profiling do not come from changing the boundary layer state or our measurement system does not have enough resolution to capture the change. Given that the measurement system picks up the transition on the suction surface without difficulty, it is likely that any dramatic changes would be captured.

The endwall film average levels were calculated and are plotted in Figures 6.16 to 6.18. Given that there are only eighteen data points these contours must be viewed with some care. The actual data points are plotted on the graphs as black squares.

Given the scarcity of data the Figures 6.16 to 6.18 are hard to interpret. However it would appear that the heat transfer levels are similar across the geometries but the level increases more rapidly to the maximum for P0. P1 appears to have the highest value of $V^2 - V_0^2$ which may be associated with the enhanced counter vortex, however the lack of data makes this a somewhat tentative conclusion.

6.2.3 Repeatability and Angle Variation

In order to give some confidence that the results can be repeated. Two gauge locations P0EC3 and P0EI4 were repeated with different gauges on different days. Figure 6.19 and Figure 6.20 show the results for P0EC3 (which is upstream of the blade row) and Figures 6.21 and 6.22 show the results for P0EI4 which is in the middle of the blade row.

The result show a reasonable level of repeatability for what should be the same flow. Note that the plots are of the heat transfer level $V^2 - V_0^2$ as this gives far better repeatability than $(Q - Q_0)/Q_0$. When the hot films readings are taken the flow direction at the endwall was estimated from the flow visualisation results. However this was imprecise so a short study was carried out to assess how the hot film trace changes with angle. A reference position (P0EC7) was taken and the same reading was taken with the gauge rotated twenty degrees clockwise and anti-clockwise. The results in $V^2 - V_0^2$ form as shown in Figure 6.23 to Figure 6.25.

These tests show a reasonable level of repeatability and also strongly suggest that $V^2 - V_0^2$ is a better parameter to examine than $(Q - Q_0)/Q_0$ for the experiments presented here.

6.3 Overview

This chapter has described hot film work to determine the state of the boundary layer on the endwall and suction surface. The hot film work shows little change in the boundary layer state on the aerofoil suction surface when endwall profiling is applied. The measurements presented in this chapter show very clear evidence of transitional flow in all three cases. The endwall boundary layer is much less clear, despite using almost identical instrumentation and techniques to acquire the data.

Again it would appear that endwall profiling does not dramatically change the state of the boundary layer.

6.4 Figures for Hot Film Results

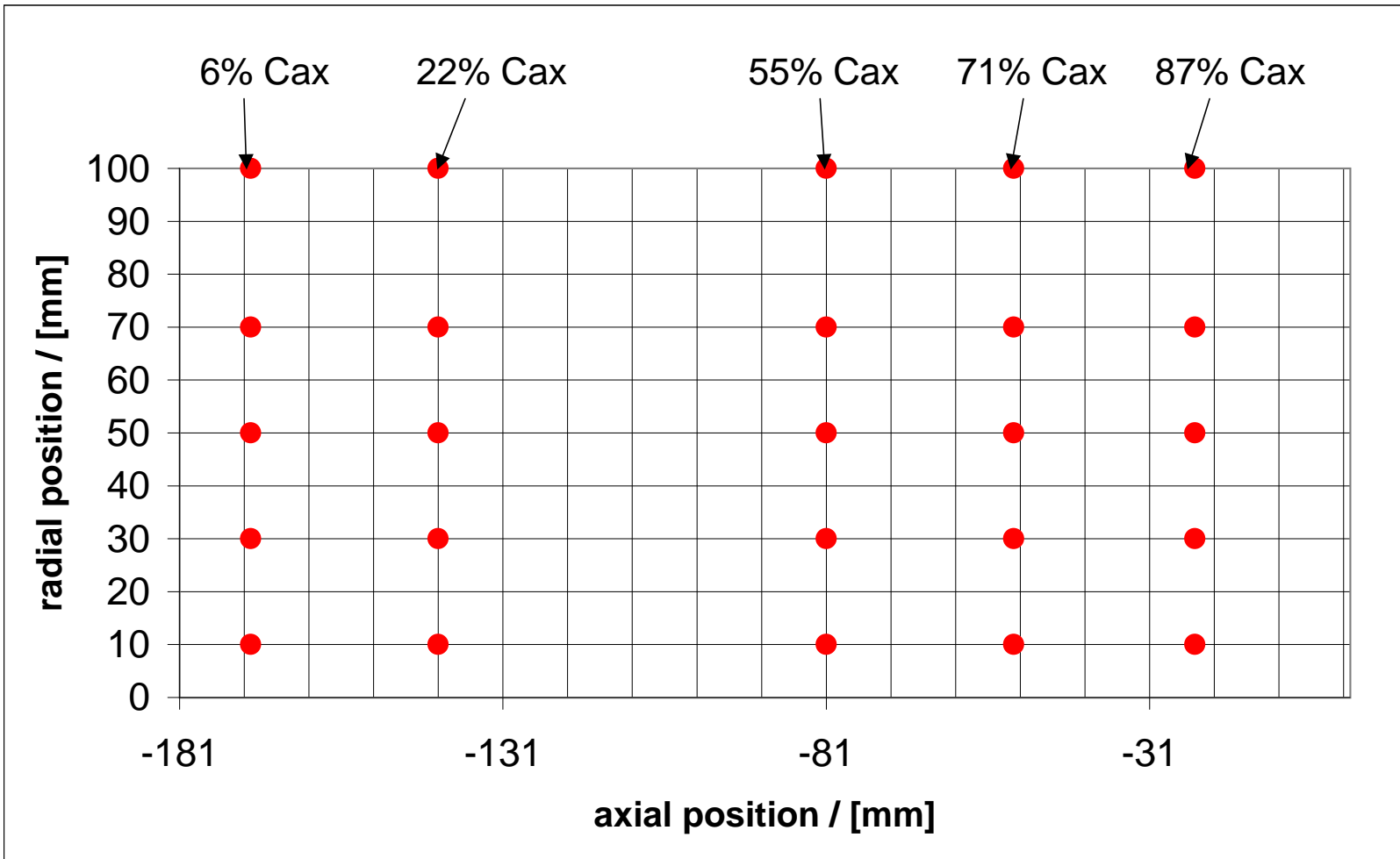
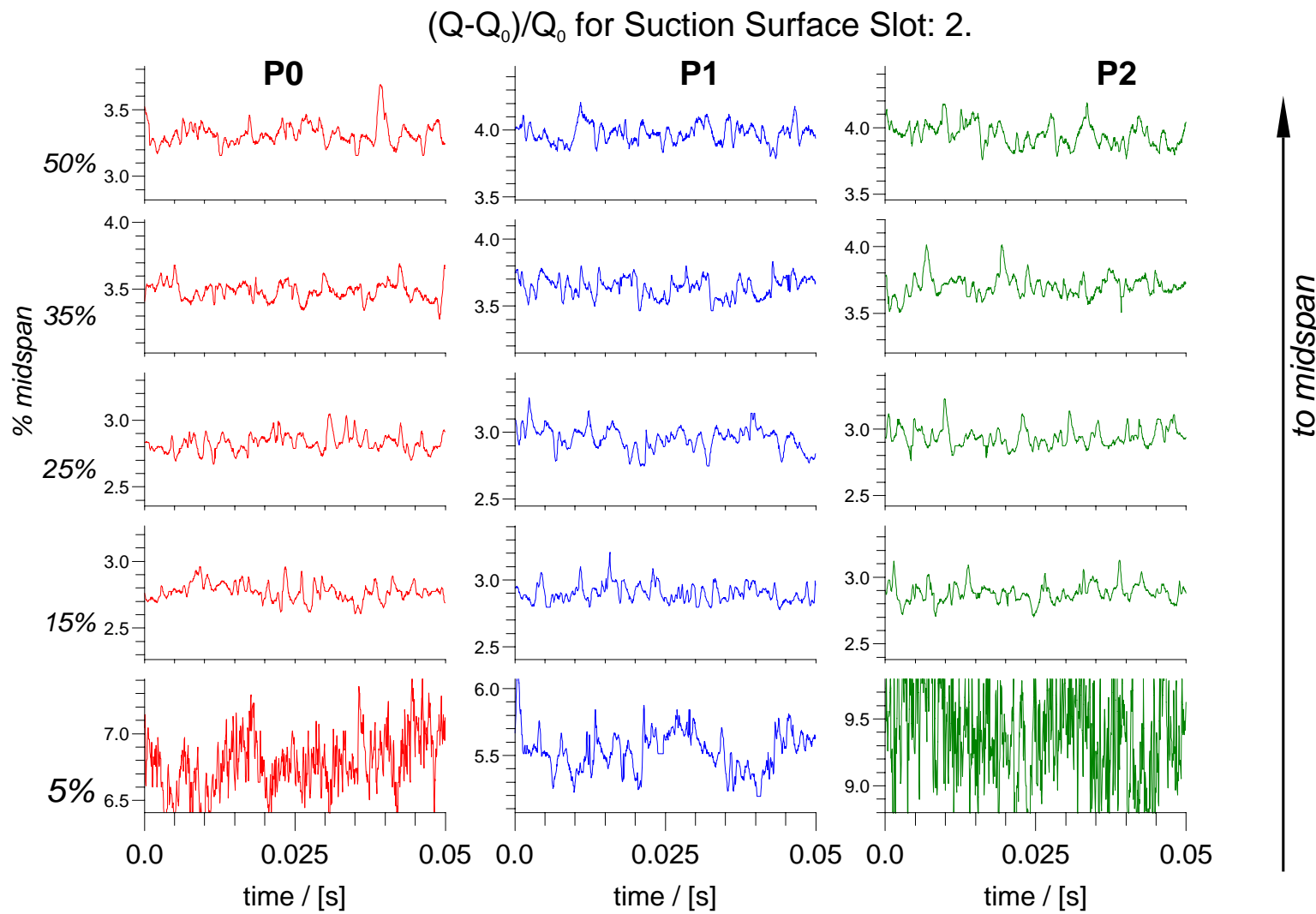
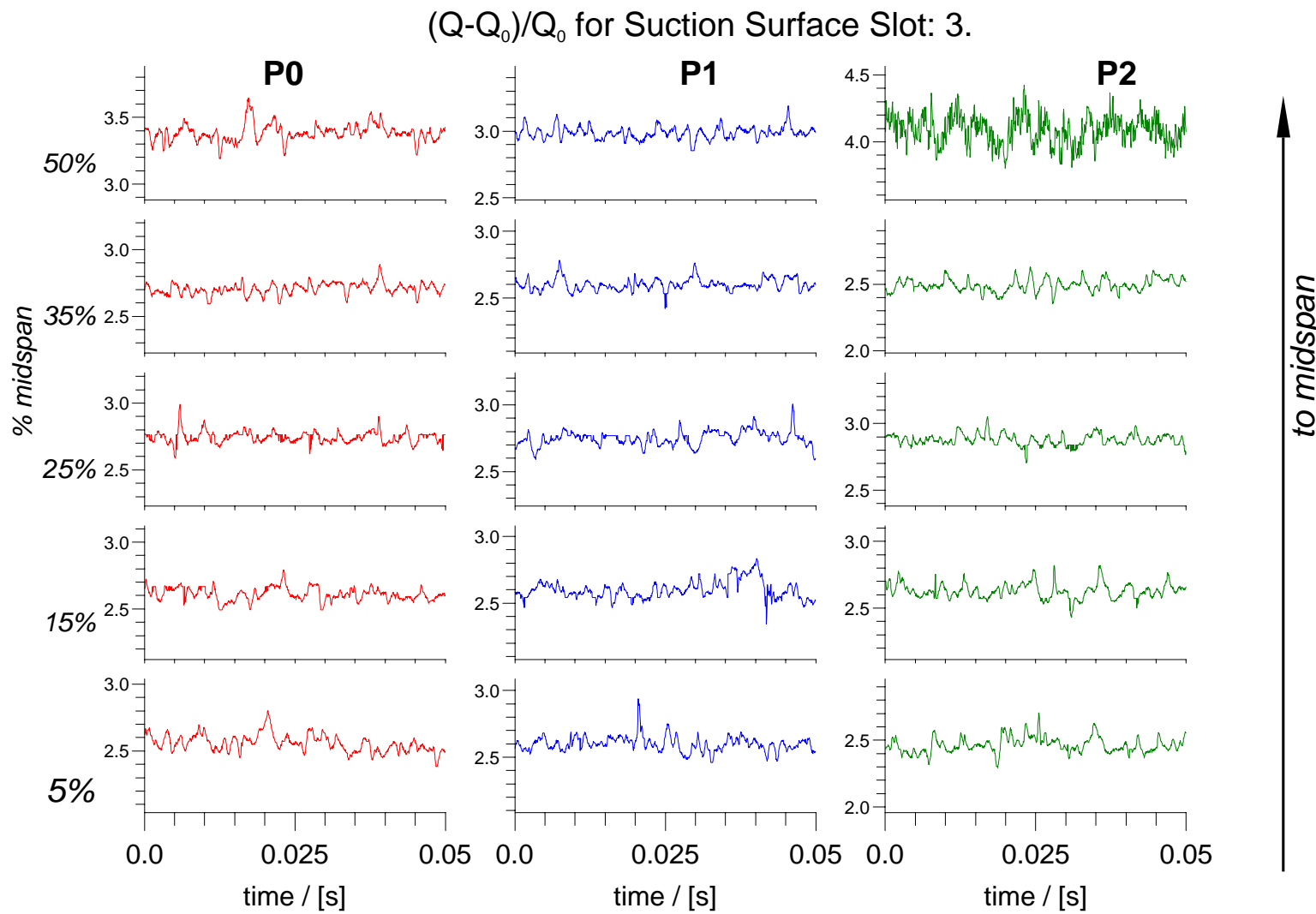
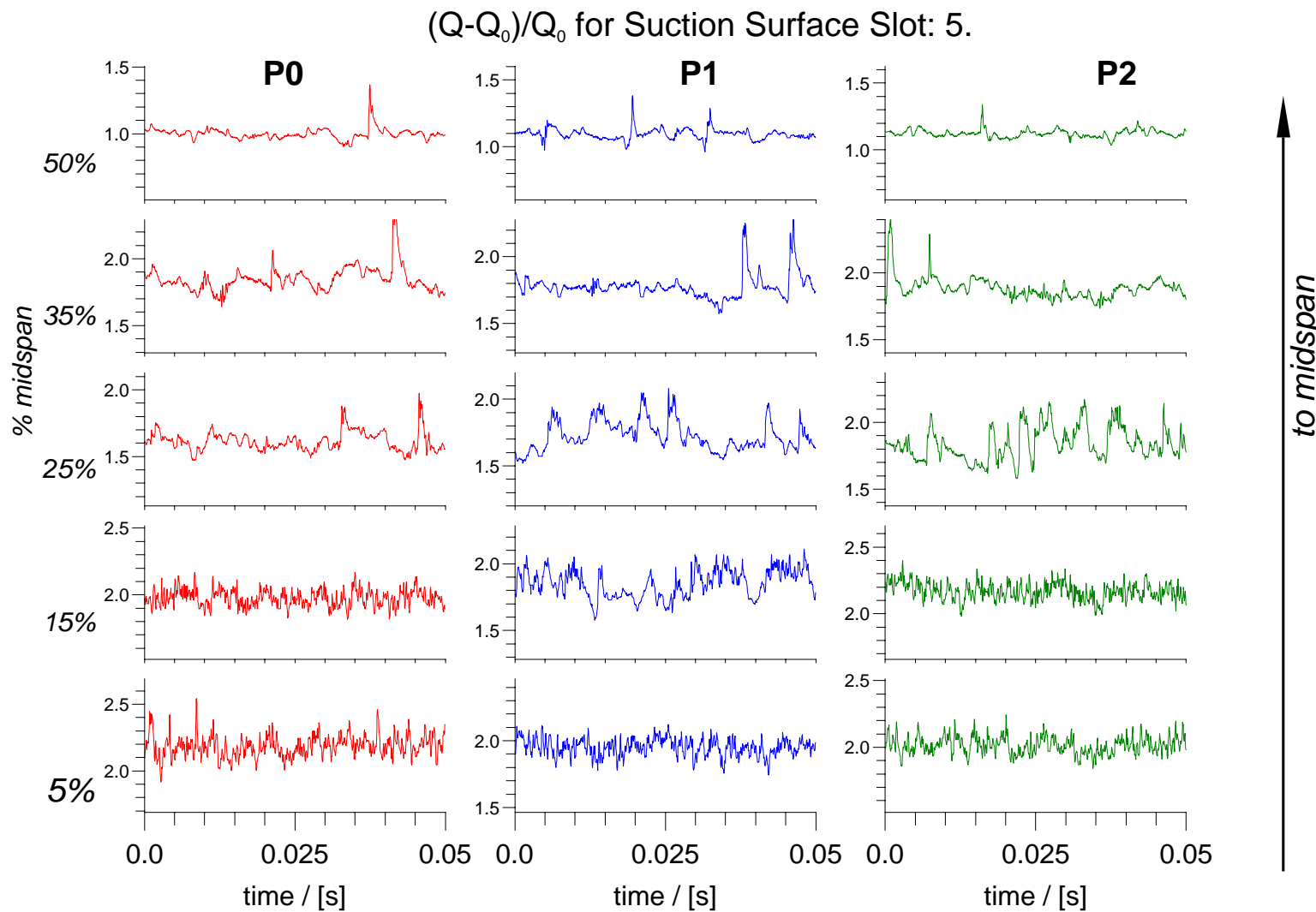
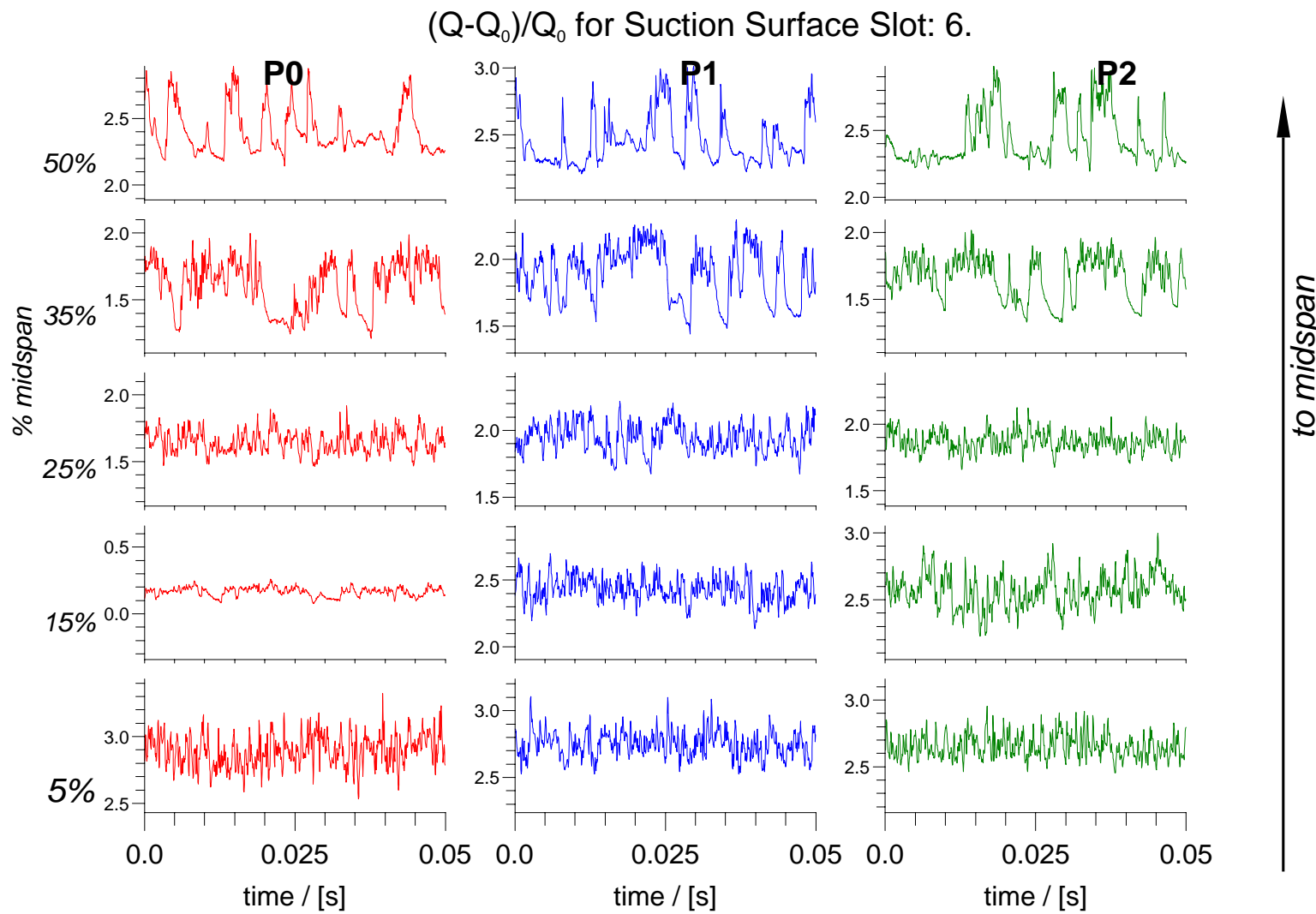


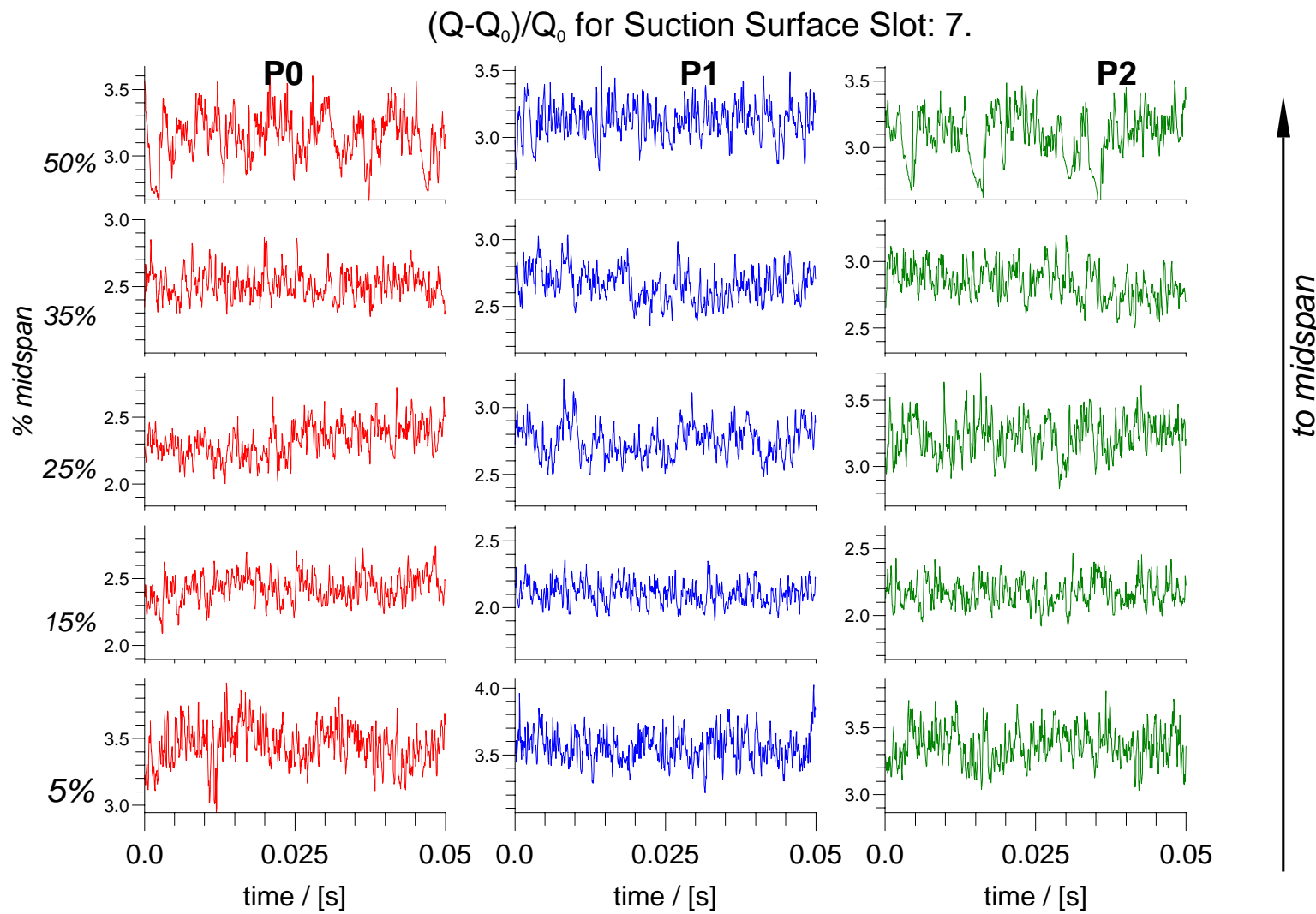
Figure 6.4: Gauge Locations for Suction Surface.

Figure 6.5: Slot 2,6% C_{ax} : Suction Surface $(Q - Q_0)/Q_0$

Figure 6.6: Slot 3, 22% C_{ax} : Suction Surface $(Q - Q_0)/Q_0$

Figure 6.7: Slot 5, 55% C_{ax} : Suction Surface $(Q - Q_0)/Q_0$

Figure 6.8: Slot 6, 71% C_{ax} : Suction Surface $(Q - Q_0)/Q_0$

Figure 6.9: Slot 7, 87% C_{ax} : Suction Surface $(Q - Q_0)/Q_0$

6.4. Figures for Hot Film Results

152

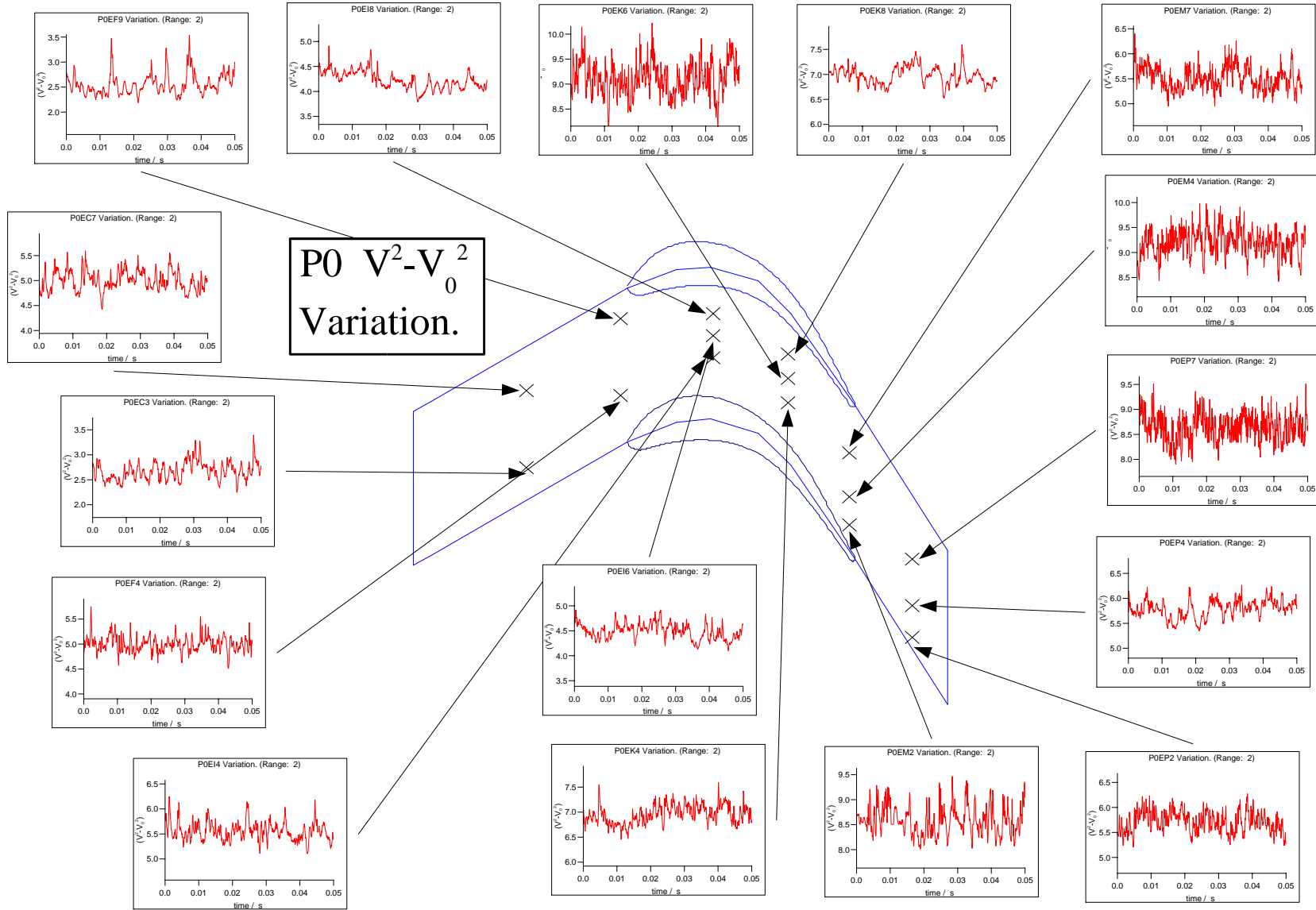


Figure 6.10: $P0 V^2 - V_0^2$ traces on endwall.

6.4. Figures for Hot Film Results

153

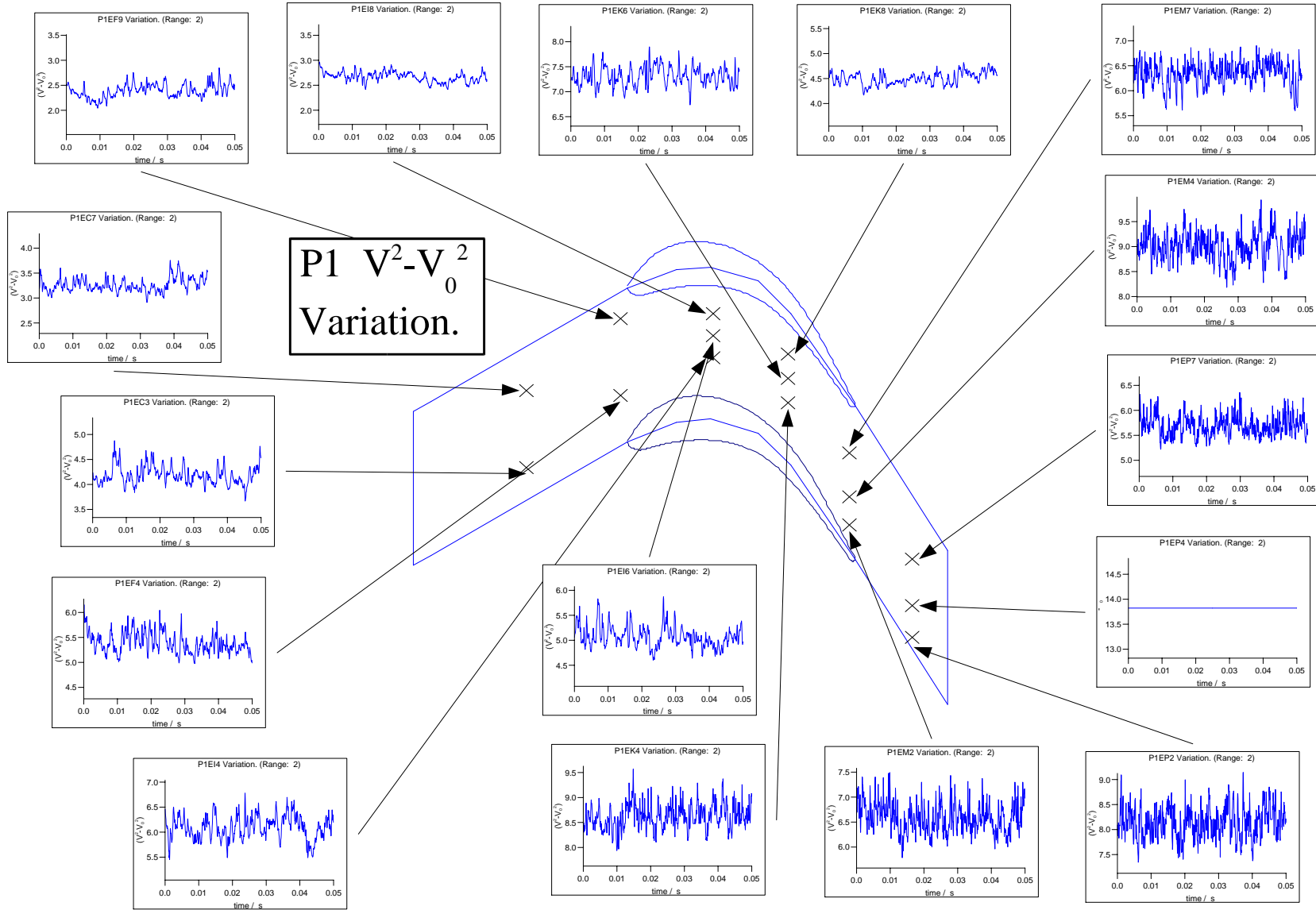


Figure 6.11: P1 $V^2 - V_0^2$ traces on endwall.

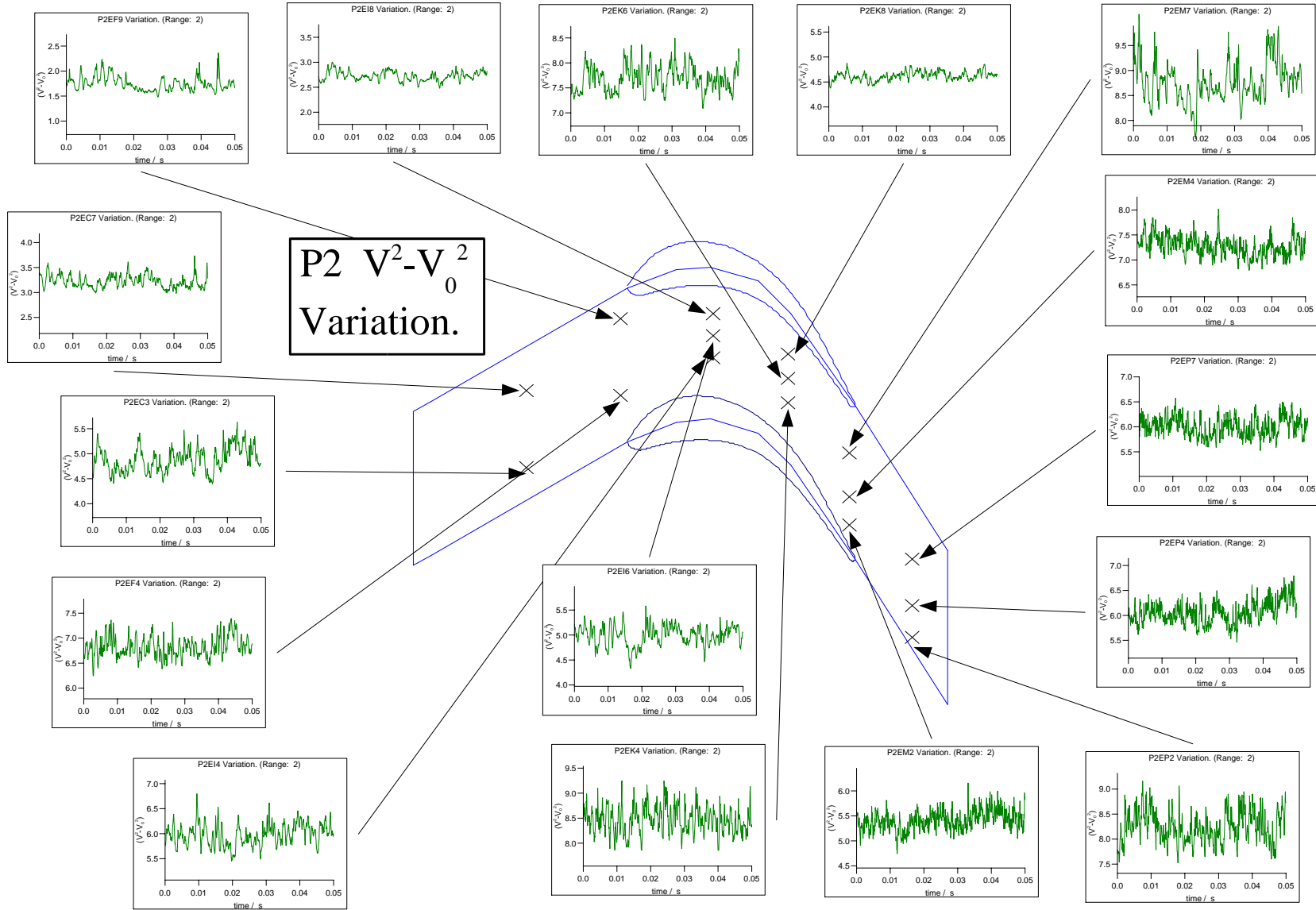


Figure 6.12: P2 $V^2 - V_0^2$ traces on endwall.

6.4. Figures for Hot Film Results

155

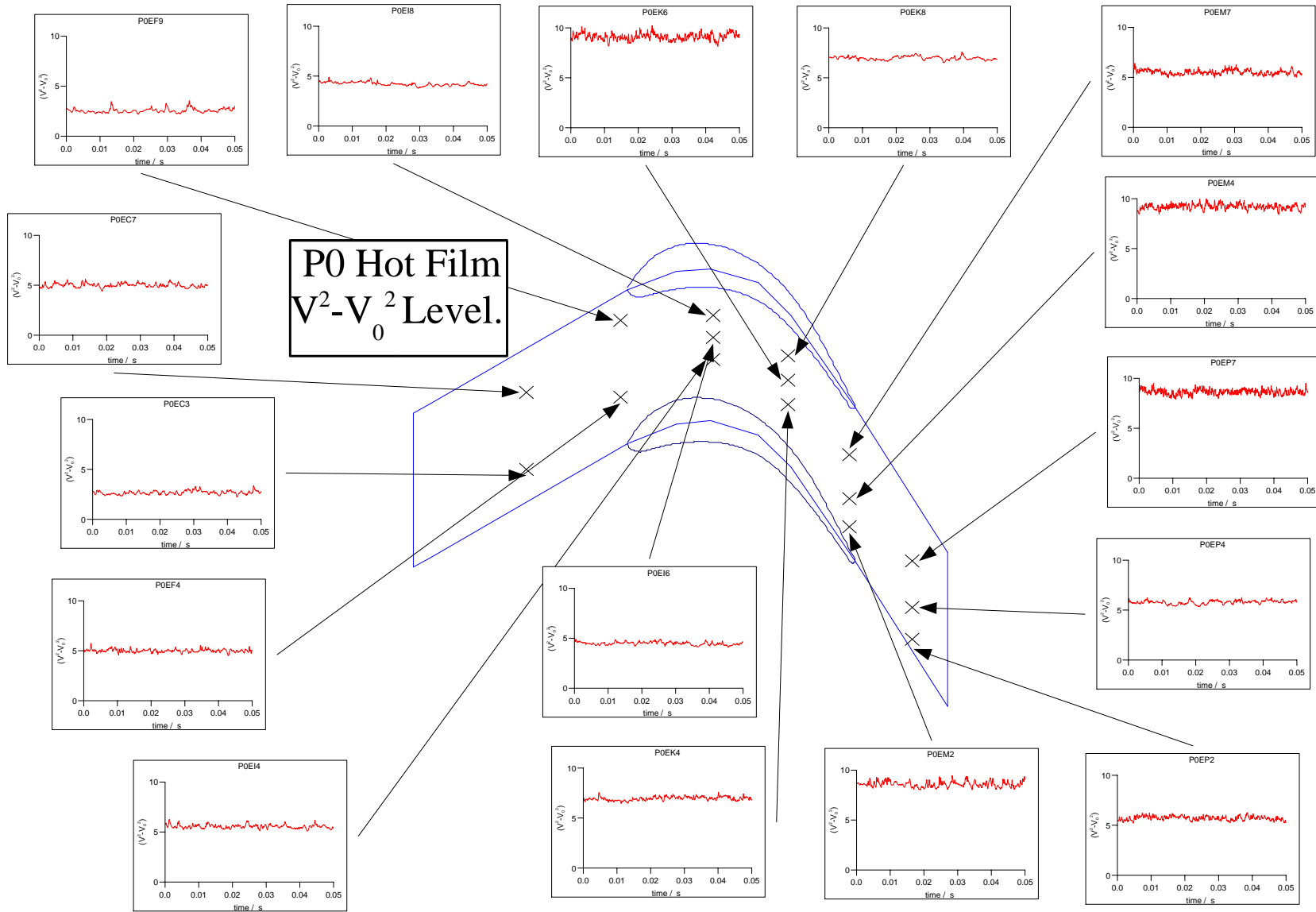


Figure 6.13: $P0 V^2 - V_0^2$ showing absolute level.

6.4. Figures for Hot Film Results

156

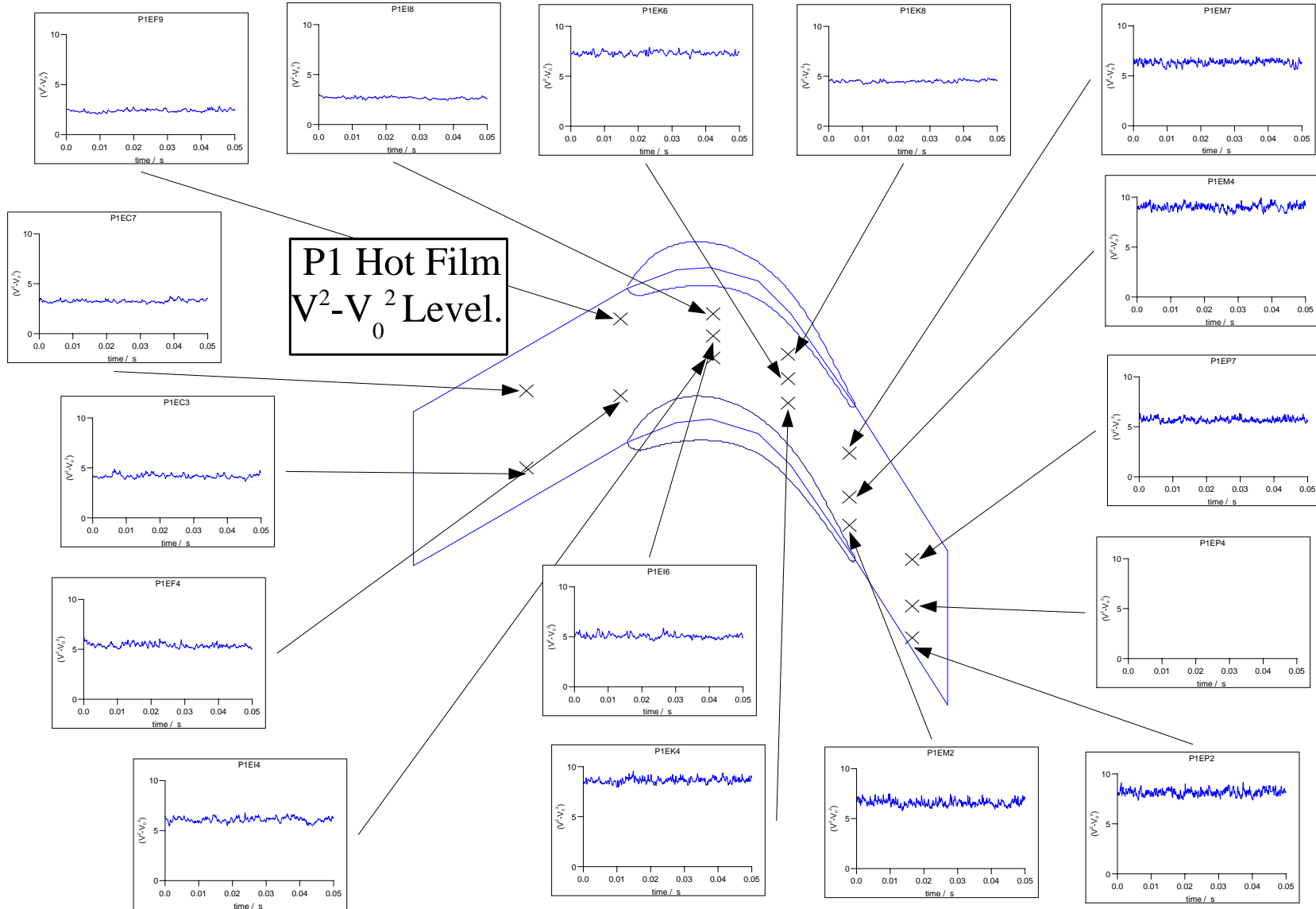


Figure 6.14: P1 $V^2 - V_0^2$ showing absolute level.

6.4. Figures for Hot Film Results

157

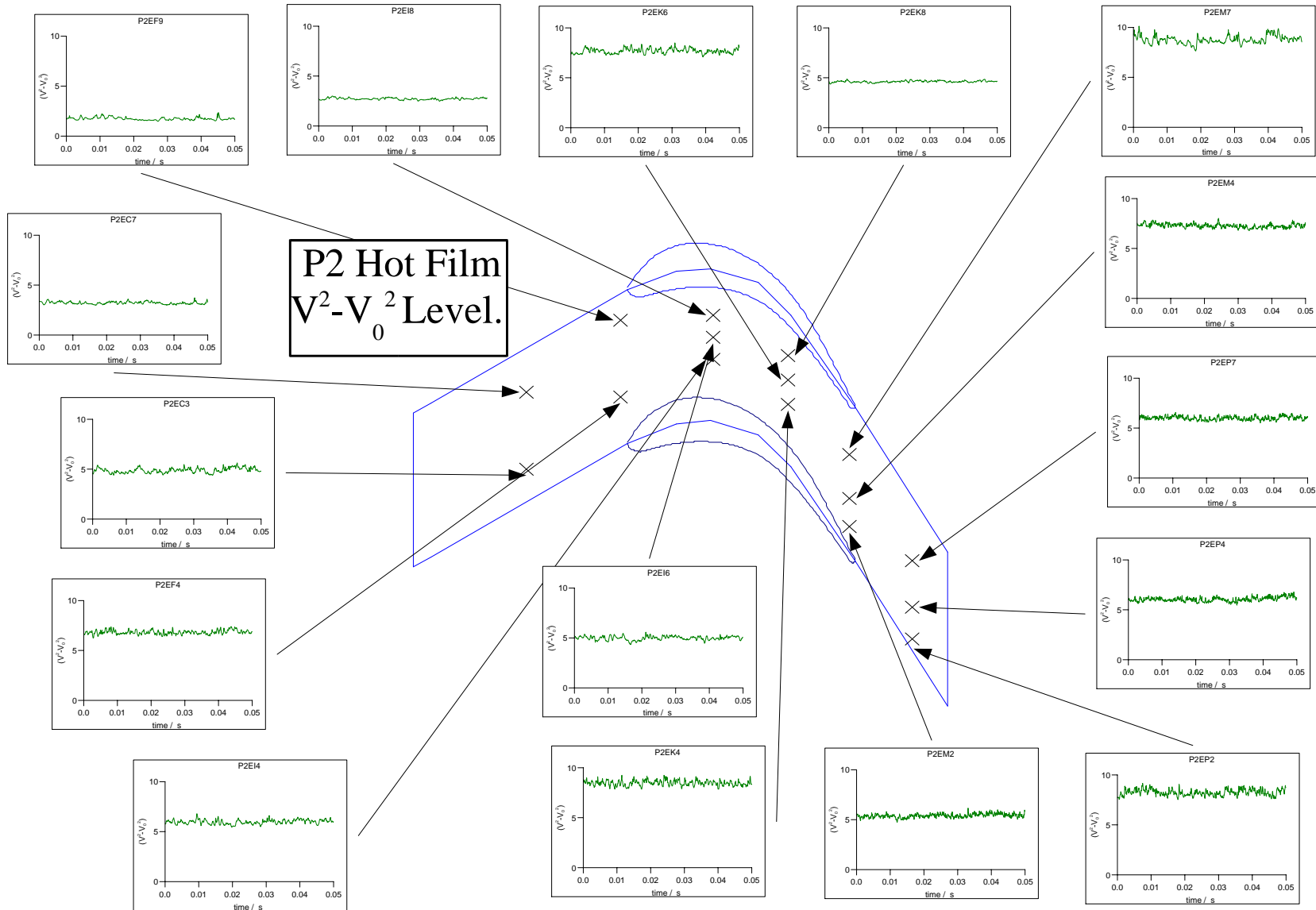


Figure 6.15: P2 $V^2 - V_0^2$ showing absolute level.

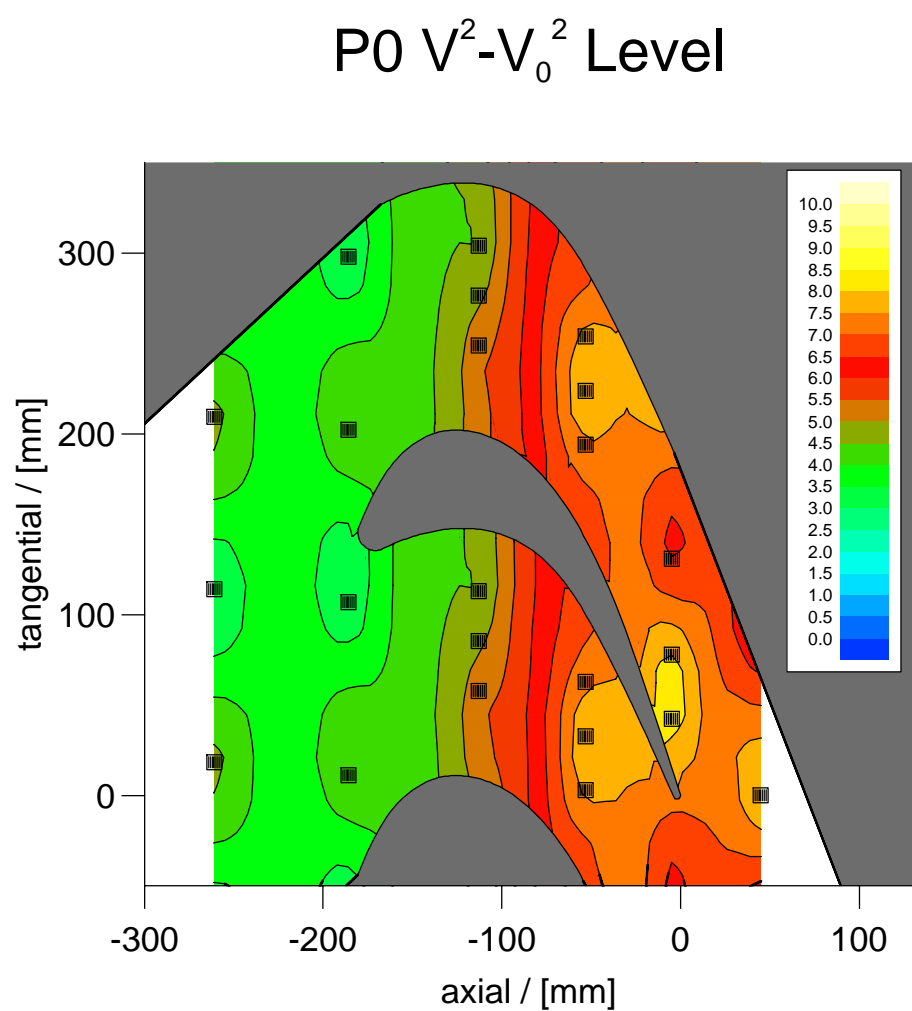


Figure 6.16: Contours of $V^2 - V_0^2$ for P0

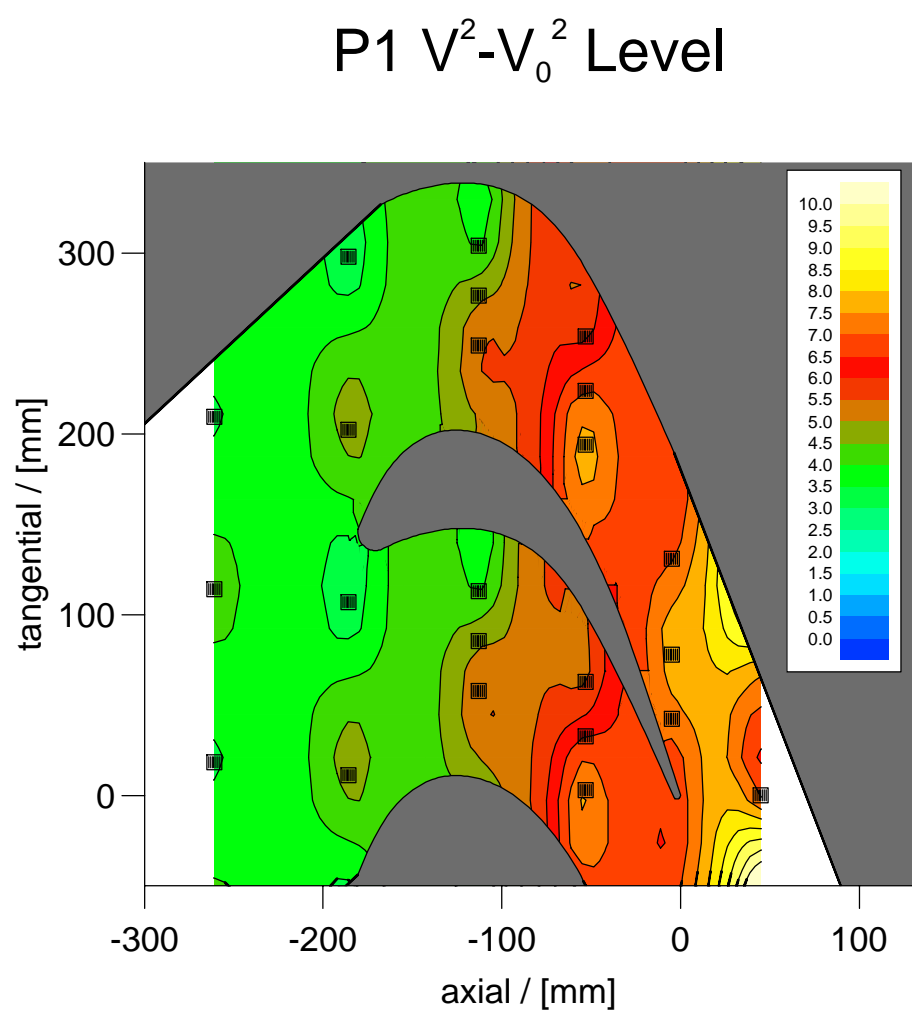


Figure 6.17: Contours of $V^2 - V_0^2$ for P1

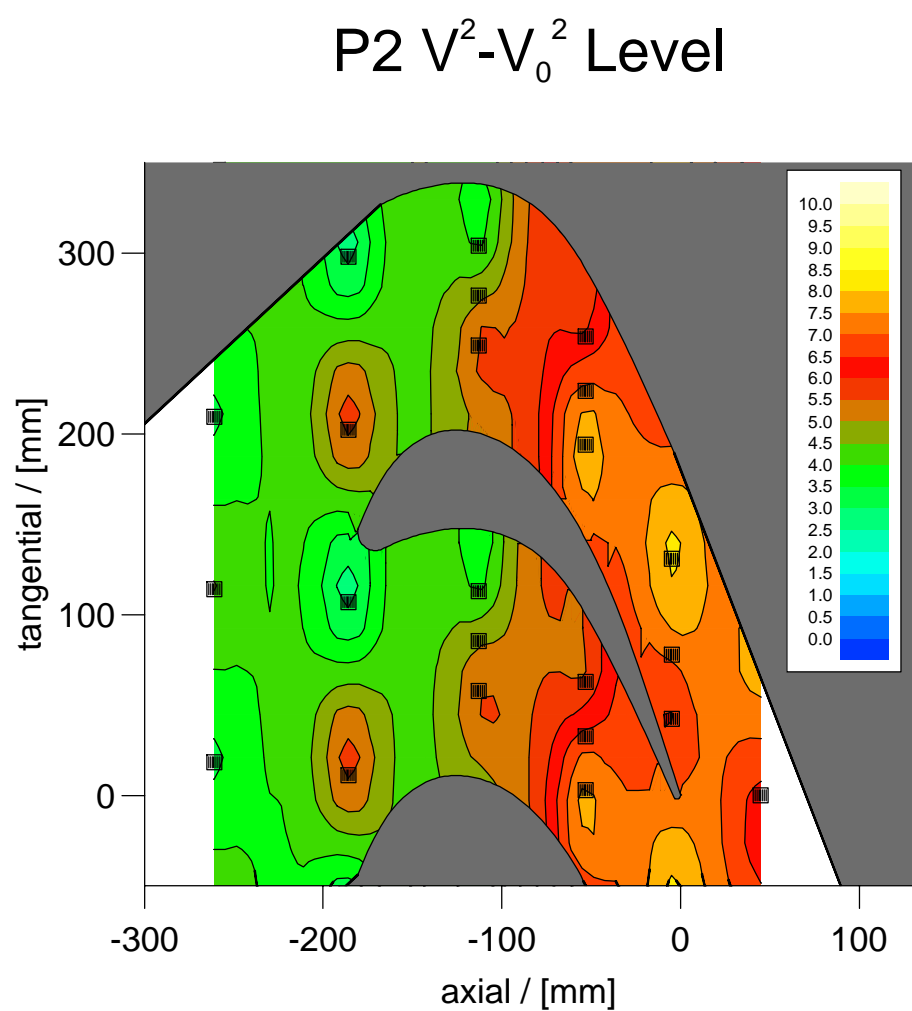


Figure 6.18: Contours of $V^2 - V_0^2$ for P2

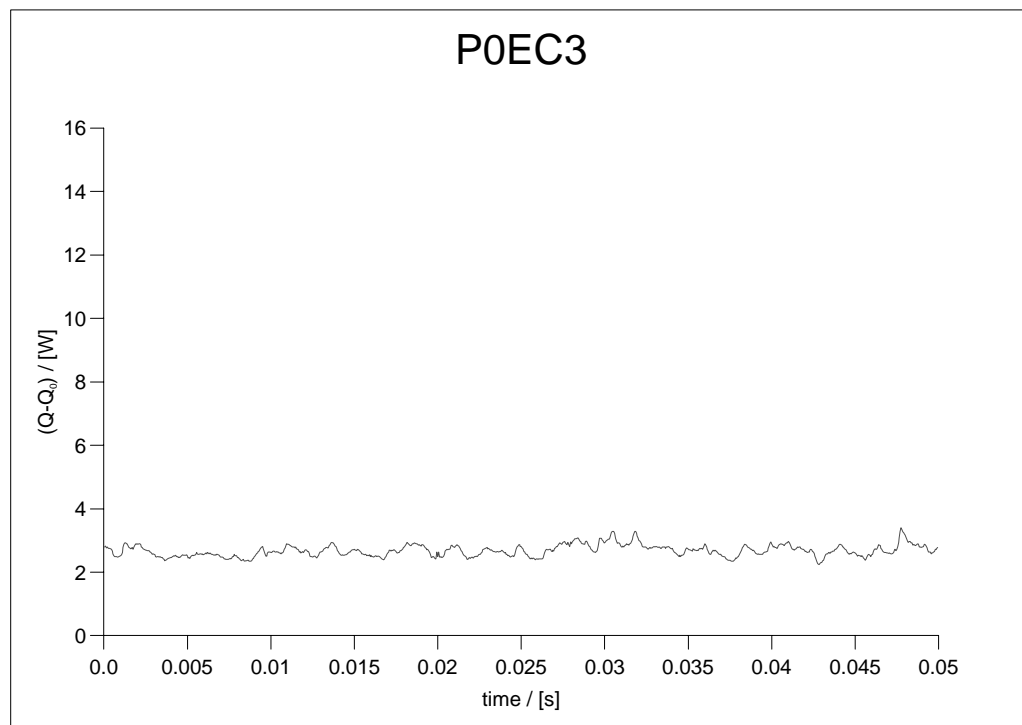


Figure 6.19: Repeatability Test: Upstream I

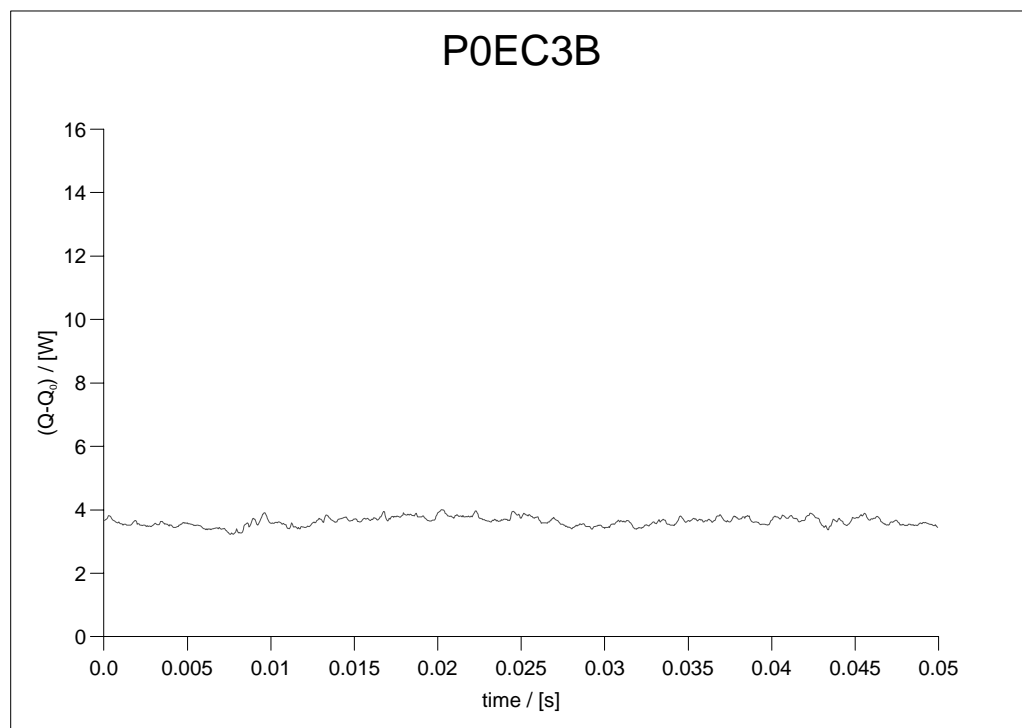


Figure 6.20: Repeatability Test: Upstream II

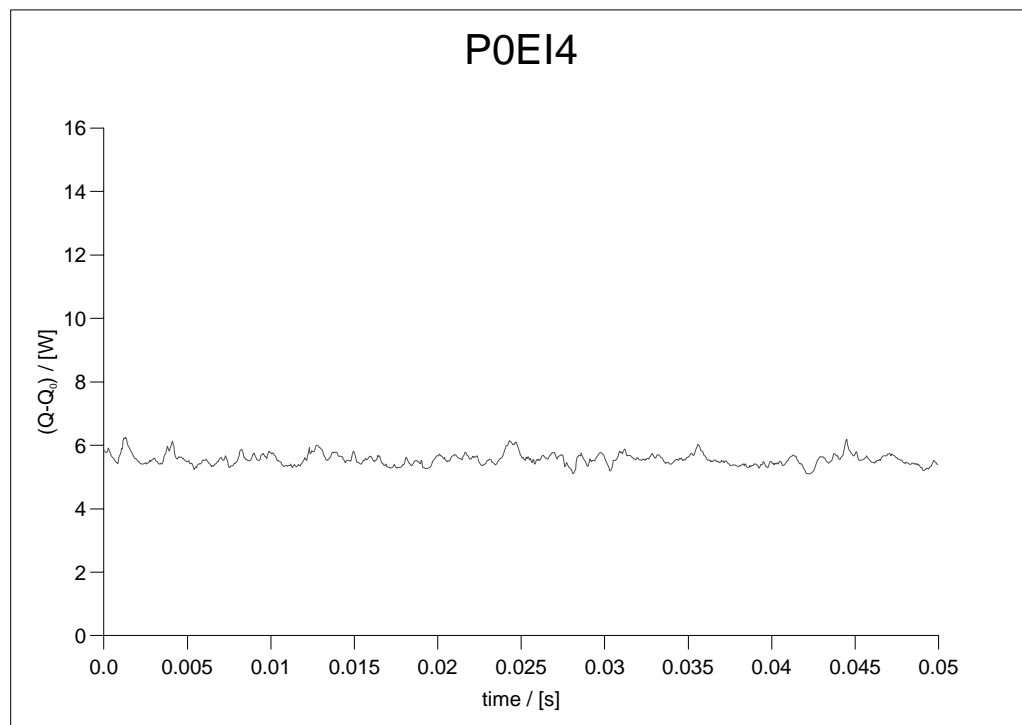


Figure 6.21: Repeatability Test: Inside Blade Row I

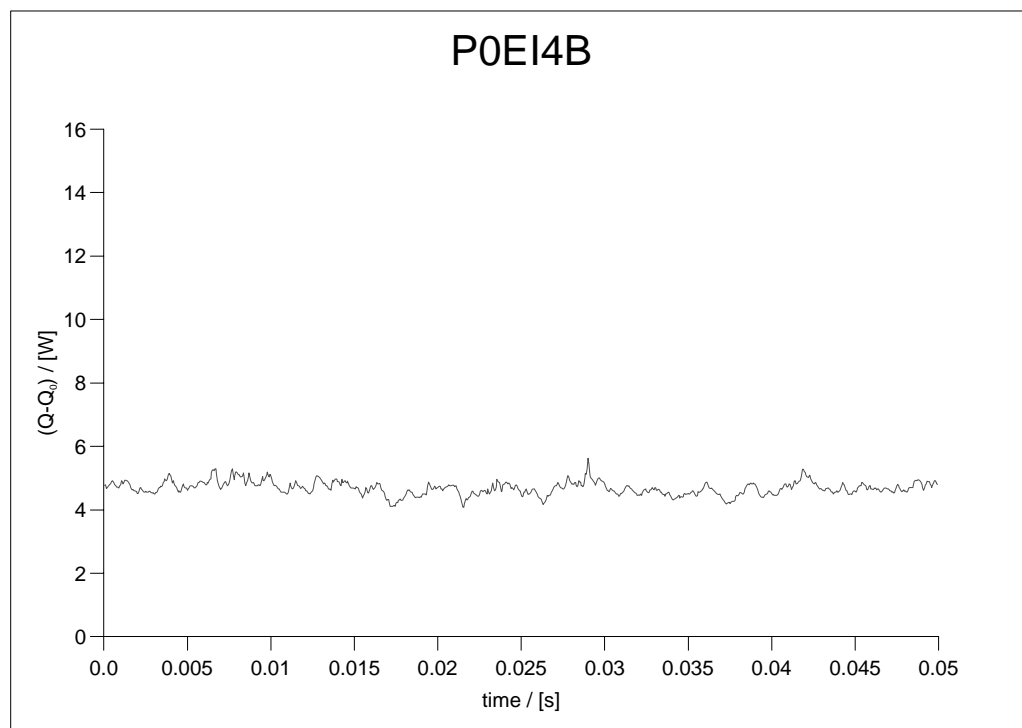


Figure 6.22: Repeatability Test: Inside Blade Row II

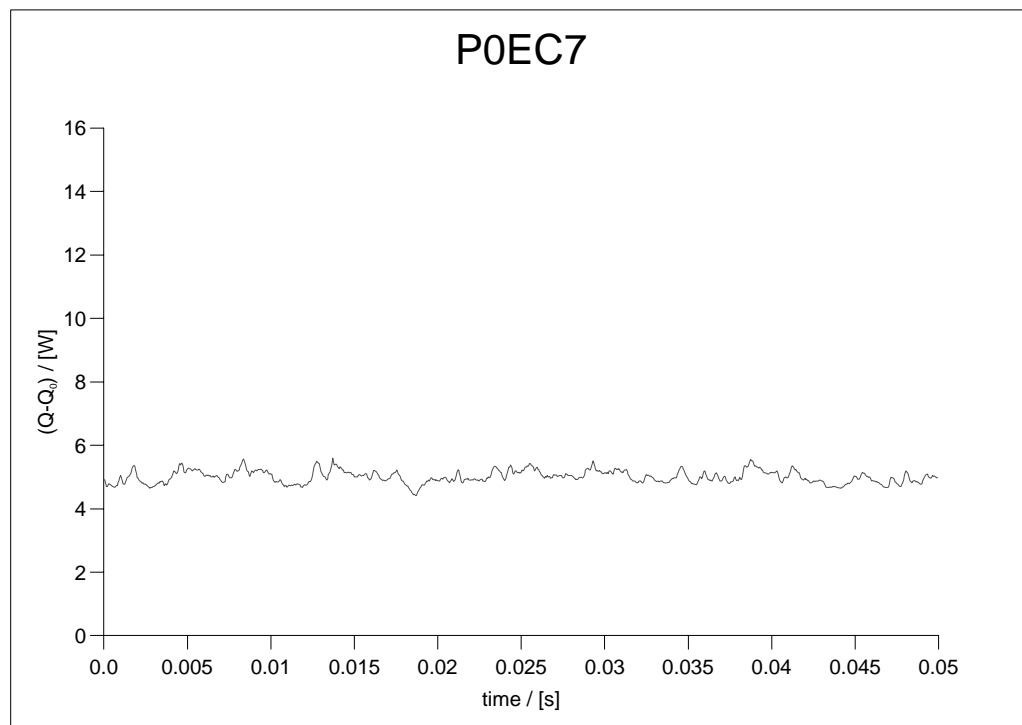


Figure 6.23: Angle Variation: Gauge Lined up with Flow.

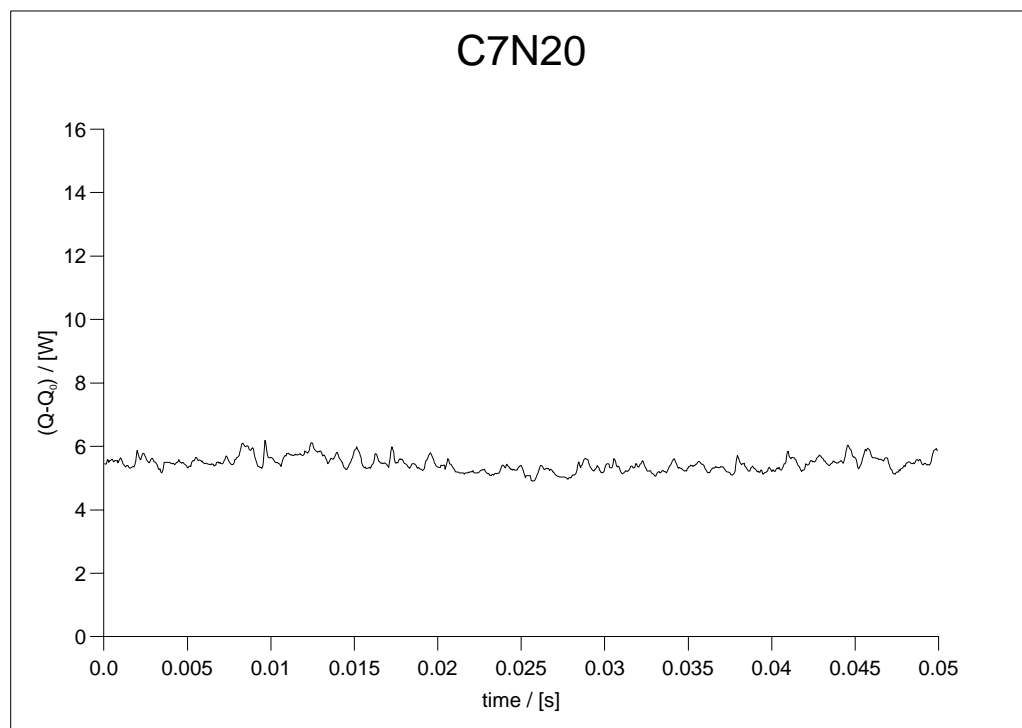


Figure 6.24: Angle Variation: Twenty Degrees Anti-clockwise.

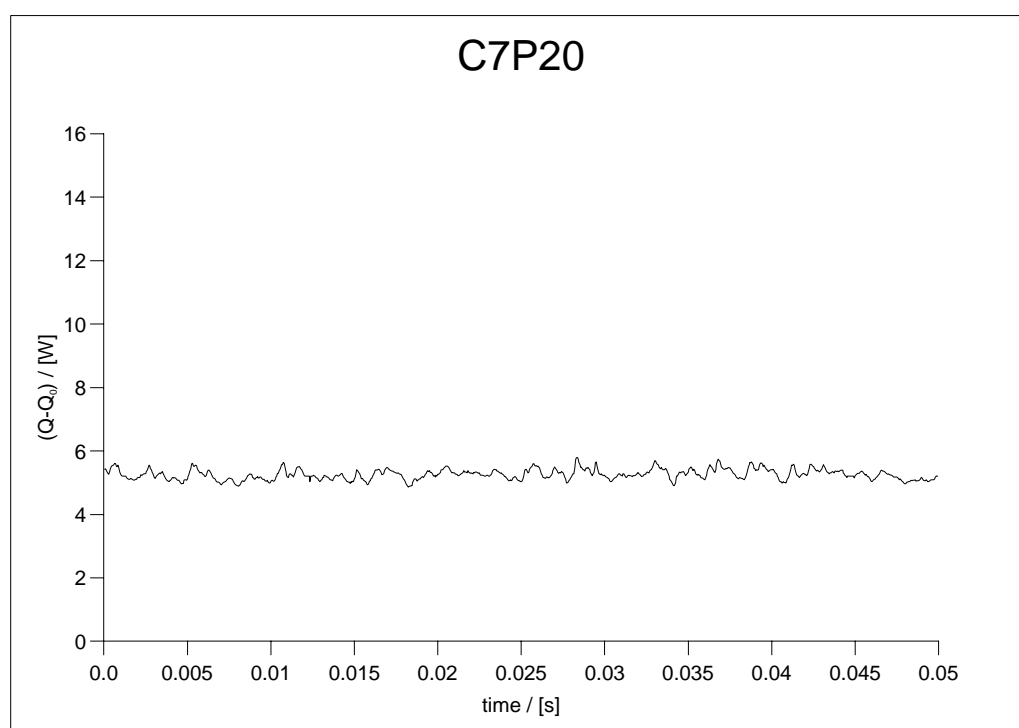


Figure 6.25: Angle Variation: Twenty Degrees Clockwise.

Chapter 7

Comparison with CFD Data

RESULTS FROM computational fluid mechanics calculations are reviewed and compared with measurements of the real flow field in this chapter. The computational fluid dynamics results were obtained by Rolls-Royce during the course of the design, the author was responsible for the data extraction, the plotting and the analysis and conclusions described here. Comparison of experimental and computational data for the third generation endwall (P3) is left until Chapter 8. Comparisons are made firstly at the same axial planes used for the pressure probe measurements, to allow a direct comparison to be made. Secondly useful information about the flow is extracted from the CFD results directly by using the three dimensional visualisation capabilities of modern post processing software.

7.1 Methodology

In order to ensure that the computational fluid dynamics results are comparable to the experimental results the same processing was applied to CFD data as experimental data and the same programs were used to produce the plots for this thesis. The process is as follows:

- Data points are extracted from the CFD solution at the measurement grid locations. This is a non-trivial operation as not only are the CFD results blade centred rather than passage centred as the experimental results are, but the CFD grids are curved in the radial direction.
- These CFD points are placed in a file in experimental format. Again this is a non-trivial operation as the coordinates have to be suitably transformed.
- Each CFD equivalent to an experimental run is given a unique name. For the five hole probe equivalent at slot 1 for the planar case the data is given the label $p0s15h$, for three hole probe results at the same slot $p0s13h$ is used. The label appears on each plot.¹

¹During the design of the third generation endwall Rolls-Royce produced another CFD solution for the planar case. Results from this solution are labelled with a suffix $_b$, results from this solution may be found in Chapter 8.

- This file is processed using *field*² to get area values of loss, C_{ske} , vorticity etc. These outputs are processed in the same way as the experimental data to obtain the figures.
- The output from *field* is processed through *pitch* to produce pitch averaged results.
- The same plotting programs are used to produce the pictures and diagrams found in this chapter as for the experimental chapter. However this is not the case for plots taken directly from the post-processing program.

This process ensures that any approximations introduced by the pitch and area averaging and any effects due to sampling only every 7mm in the tangential direction etc, are the same for the computational data set as for the the experimental data set.

Some information is obtained directly from the CFD solution using the proprietary program FIELDVIEW. This is a post-processing program that was used because Rolls-Royce software could export their CFD solutions into a format that FIELDVIEW could use - all other considerations were secondary. In common with many post processing packages FIELDVIEW can produce many different views of the solution and several of the more meaningful ones were selected for inclusion. The plots taken using FIELDVIEW were not processed using the programs used for the rest of the data as the point of the exercise was to examine the CFD data directly. In order to ensure comparability with other plots the maximum and minimum value and number of levels for the contours were kept the same between two-dimensional plots and the three dimensional plots. Identical definitions of loss coefficient (C_{P0}) etc, were used for the plots.

Computational fluid dynamics results equivalent to the close wall measurements for Slots 1,2 and 10 in Chapter 5 are not included in this chapter. This is for two reasons, one is to keep the thesis down to a manageable length and the second is that there are considerable difficulties in extracting the close wall data from the CFD solution. Extracting close wall data is more difficult than extracting five hole probe data because the close wall data includes points that are nominally on the endwall. Minor differences in interpolation mean that FIELDVIEW will consider many points used in the measurement grid as being outside the computational domain. Moreover CFD data at the endwall has zero velocity which causes the data processing programs *field*, *pitch*, etc to fail. Neither of these difficulties are insurmountable but present a large enough obstacle to prevent inclusion of close wall CFD results.

7.2 Solution Details

The computational fluid dynamics solutions presented here were all conducted at Rolls-Royce and the post-processing described above and analysis was conducted at Durham University. The CFD solution does not represent the “state-of-the-art”

²A list of the programs used can be found in Appendix C.4 and their relationship is shown in Figure C.1 on page 293

in fluid mechanics, rather it represents a typical grid size and configuration usually used in design work. Details of the way the endwalls are designed can be found in Harvey et al. (1999). Essentially a representation of the endwall shape is made using splines passing through a number of control points on the endwall surface. Each control point is perturbed in six ways and computations done on the effect of each perturbation. For the six control points used for P1 and P2 this means that thirty-six fully viscous calculations need to be made to obtain sufficient information to design a profile. An acceptable shape is extracted from each run without further fully viscous calculations, this is done by using linear superposition on the flow fields and the geometries.

The code used was a steady flow solver using the pressure correction algorithm of Moore (1985). The grid consisted of 89 axial, 39 tangential and 29 radial planes giving around 100,000 points. The first generation endwall was originally designed in 1999 but even then the computation did not represent the “state-of-the-art”, this is mainly due to the need to repeat the calculation thirty six times before a geometry can be extracted. The P3 profile designed in 2002 uses considerably more points. The boundary layers are treated as fully turbulent everywhere with an algebraic mixing length model being used to model turbulence in the main flow and wall functions to model the flow for cells adjacent to a the wall.

7.3 Comparison at Different Axial Locations

In this section a comparison is made between different computational results and experimental results at different axial locations. Comparisons are made at all axial locations for which experimental data is available i.e. Slot 1-8 and 10. Table 5.1 on page 77 lists the experimental values that are available. Numerous combinations of results are possible but in this chapter we plot Loss Coefficient, Secondary Vectors, C_{ske} and Vorticity for comparison with the experimental data in the Pressure Probe Results Chapter. The numerical solutions extend fully to the blade and endwall surfaces but for the purposes of comparison only equivalent points are plotted.

7.3.1 Slot 1 (-9% C_{ax})

Figures 7.2 to 7.4 show the loss results, Figures 7.6 to 7.8 show the secondary vectors. Pitch averaged figures are included as Figures 7.5 and 7.9 for loss and yaw angle.³

The following points are made about the Slot 1 results:-

- The Slot 1 CFD results (Figure 7.5) show that the three profiles have very similar loss profiles and this is confirmed by the experimental results (Figure 5.18).
- There is no negative loss associated with the CFD solution as the boundary layer profile that was entered did not model the negative loss found in the real case. The Durham Cascade is a popular computational test case and this is a common method of modelling the boundary layer.

³A list of symbols used for pitch averaged graphs may be found on page xxvi

- Loss peak values are very similar (~ 0.35 for CFD (Figure 7.5), ~ 0.3 for experiments (Figure 5.18)), this is unsurprising as the measured boundary layer is the inlet condition.
- The CFD secondary vectors capture the increased flow around the leading edge of both the P1 and the P2 geometry successfully (Figures 7.6-7.8). The pitch averaged results show a small (half a degree) difference in midspan yaw angle between P1 and the other two geometries (Figure 7.9). This is again reflected in the experimental results (Figure 5.22), although the CFD does not predict the extent of secondary flow activity up the blade span and predicts a lower magnitude of flow than actually occurs.

7.3.2 Slot 2 (6% C_{ax})

Figures 7.10 to 7.12 show the loss results and Figures 7.14 to 7.16 show the secondary vectors. Pitch averaged figures are included as Figures 7.13 and 7.17 for loss and yaw angle.

The following points arise from a comparison of the Slot 2 CFD results and the Slot 2 experimental results:-

- CFD (Figures 7.13) and experimental (Figure 5.34) loss plots both show that the loss is still dominated by the inlet boundary layer. The magnitude of loss is well predicted given that the CFD has no inlet boundary layer “hump”. The CFD loss appears to be identical for each endwall at this axial location.
- The CFD again underestimates the magnitudes of secondary flows produced by endwall profiling (Figures 7.14-7.16). The pattern of pitch averaged yaw angles is also slightly different with the CFD predicting a uniform flow above 35% of span and the experimental results predicting a gradual change all the way until 100% span (Figure 5.38).
- There is a large mismatch between the midspan yaw angle for CFD (Figure 7.17) and experimental data (Figure 5.38). This is put down to a probe misalignment as the experimental data was corrected to the average of the midspan experimental data. Therefore any gross misalignment of the probe will not be corrected by such a method. It would have been much more satisfactory to correct the experimental results to the CFD results for the cases where the experimental yaw angle positioning was poor.
- At first glance at the secondary vector plots (Figures 7.14-7.16) it may appear that the midspan secondary vectors are not zero, however a closer inspection reveals that the midspan points ($r=200\text{mm}$) appear very faintly or not at all at midspan as the vectors at this point are in fact zero. What can be made out is not actually the midspan flow.

7.3.3 Slot 3 (22% C_{ax})

Figures 7.18 to 7.20 show the loss results and Figures 7.22 to 7.24 show the secondary vectors. Pitch averaged figures are included as Figure 7.21 for loss and Figure 7.25

for yaw angle.

The following salient points arise from an examination of the Slot 3 CFD and experimental data.

- The loss profiles (Figure 7.21) remain dominated by the inlet boundary layer and the CFD successfully captures this feature.
- Experimental measurements (Figure 5.50) show an increased loss for P2 relative to the other two profiles, this is not reflected in the CFD.
- CFD predicts quite clear vortex structures for P1 and P2 at this slot (Figures 7.23 and 7.24), which do not occur in the experimental data (Figures 5.52 and 5.53). For the P1 CFD at $t=60\text{mm}, r=0\text{mm}$ a vortex is clear - the experiments on the other hand show a large cross flow with no vortex present. The P2 CFD at $t=40\text{mm}, r=10\text{mm}$ again shows a clear vortex whereas the experiments show a strong crossflow towards the suction surface. For P0 both experiments (Figure 5.51) and CFD (Figure 7.22) predict a vortex like structure at this slot.
- This is reflected in the pitch averaged yaw angle (Figure 7.25), where as noted previously the experimental P0 values (Figure 5.54) differ from the P1 and P2 values up to midspan. For the CFD there is much more uniformity up to midspan. For the experiments only the P0 case exhibits under turning whereas the CFD predicts under turning for both P0 and P1, though the changes are small.
- There is also a two and a half degree difference between the CFD midspan yaw angle (Figure 7.25) and the experimental values (Figure 5.54), this is again put down to probe alignment problems.

7.3.4 Slot 4 (38% C_{ax})

Figures 7.26 to 7.28 show contours of loss coefficient and Figures 7.30 to 7.32 show the secondary vectors. Pitch averaged figures are included as Figures 7.29, 7.33 for loss and yaw angle.

The following key points are noted from an examination of the Slot 4 CFD and experimental results.

- The loss is once again dominated by the inlet boundary layer pattern (Figure 7.29). The magnitude is under predicted by the CFD however with a peak value of 0.4 compared to a peak value of 0.5 for P0 in the experiments. This takes no account of the negative loss in the experimental data, if this negative loss is accounted for the P1 and P2 loss peaks would be lower.
- There is still a large midspan yaw angle discrepancy between the experimental (Figure 5.62) and computation values (Figure 7.33).
- Clearly defined vortex structures are now present in the experimental data (Figures 5.59-5.61) and predicted by the CFD (Figures 7.30-7.32), though the magnitude and position of these vortices is incorrect.

- The maximum under turning predicted by the CFD (Figure 7.33) is similar to that found in the experiments (Figure 5.62).

7.3.5 Slot 5 (55% C_{ax})

Figures 7.34 to 7.36 show the loss results and Figures 7.38 to 7.40 show the secondary vectors. Pitch averaged figures are included as Figures 7.37 and 7.41 for loss and yaw angle respectively.

The following points are noted:-

- At this slot distinct loss cores associated with the passage vortex begin to form (Figures 5.63-5.65). The CFD accurately predicts that this feature occurs (Figures 7.34-7.36).
- There is again a midspan yaw angle discrepancy between the experimental (Figure 5.70) and computation (Figure 7.41) values.
- Although there are minor discrepancies between the positions of the passage vortices, in general the prediction of flow dynamics is good (Figures 5.67-5.69 for experiments and Figures 7.38-7.40 for CFD).

7.3.6 Slot 6 (71% C_{ax})

Figures 7.42 to 7.44 show the loss results, Figures 7.46 to 7.48 show the secondary vectors. C_{ske} and Vorticity pictures are shown in Figures 7.50-7.52 and Figures 7.54-7.56 respectively. Pitch averaged figures are included as Figures 7.45, 7.49, 7.53 and 7.57 for loss, yaw angle, C_{ske} and vorticity coefficient respectively.

The following points are immediately apparent from a comparison of the Slot 6 experimental and computational results:-

- The CFD predicts further loss growth in the passage vortex loss core (Figures 7.42-7.44) but fails to accurately determine its magnitude or determine that P0 should have a significantly higher loss than the other two geometries.
- The CFD (Figures 7.62-7.48) under predicts the magnitude of the secondary flows.
- There is good agreement with the midspan experimental (Figure 5.78) and computational (Figure 7.49) flow angles.
- The pitch averaged loss values for the CFD (Figure 7.45) exhibit a strange dip at 100% of midspan. An inspection of the “raw” CFD results using the FIELDVIEW program indicates that this “dip” in loss is present in the CFD solution. This means that it was not introduced by the data extraction or processing system described earlier. The reason for this “dip” in the CFD is not known it may be due to an imperfection in the boundary conditions at midspan - but that is merely speculation. This feature does not appear to influence the loss results closer to the endwall.

- The CFD C_{ske} results (Figures 7.50-7.52) rank the profiles correctly, however the computations do not predict the extent of the region of increased secondary kinetic energy correctly, i.e. the computations show a much smaller area than is actually present in experiments (Figures 5.79-5.81).
- Vorticity coefficient plots (Figures 7.54-7.56) show that the computational values are predicted at a lower level than occurs in the experiments (Figures 5.83-5.85). This matches up with the lower secondary flow found in the computational prediction.

7.3.7 Slot 8 (97% C_{ax})

Figures 7.58 to 7.60 show the loss results, Figures 7.62 to 7.64 show the secondary vectors. C_{ske} and C_Ω pictures are shown in Figures 7.66-7.68 and Figures 7.70-7.72 respectively. Pitch averaged figures are included as Figures 7.61, 7.65, 7.69 and 7.73 for loss, yaw angle, C_{ske} and vorticity coefficient respectively.

The following observations are made following a comparison of the Slot 8 computational and experimental results:

- The CFD is successful at predicting the trends in loss growth at this axial plane (Figure 7.61). The planar case is clearly seen to have a greater loss core and the trends seen in the pitch averaged experimental results (Figure 5.90) are captured in the CFD as well, though some of the details are not accurate and the magnitude is about half of the experimental value.
- The anomaly in loss results at midspan (Figure 7.61) where a pronounced dip in loss occurs at midspan is present in the Slot 8 data as well as the Slot 6 data. The CFD also gives a slightly negative loss between 40 and 90% of midspan.
- CFD Secondary Velocities once again capture most of the details of the flow (Figure 7.62-7.64). However the magnitude of these changes is under predicted, for example the vortex centres for the CFD results have not migrated as far from the endwall as the experimental vortex centres (Figures 5.91-5.93).
- The CFD C_{ske} results (Figures 7.66-7.68) rank the profiles correctly, however the computations do not predict the extent of the region of increased secondary kinetic energy correctly, i.e. the computations show a much smaller area than is actually present. For example at 25% span the CFD predicts a peak P0 C_{ske} coefficient of 0.03 in the experiments the value is found to be 0.125.
- The vorticity coefficient contours (Figures 7.70-7.72) reflect the reduced secondary flow activity predicted by the CFD.

7.3.8 Slot 10 (128% C_{ax})

Figures 7.74 to 7.76 show the loss results, Figures 7.78 to 7.80 show the secondary vectors and C_{ske} and C_Ω pictures are shown in Figures 7.82-7.84 and Figures 7.86-7.88 respectively. Pitch averaged figures are included as Figures 7.77, 7.81, 7.85 and 7.89 for loss, yaw angle, C_{ske} and C_Ω respectively.

The following observations are made following a comparison of the Slot 10 computational and experimental results:

- As Moore (1995) has shown experimentally, the blade boundary layers are transitional, the CFD models them as fully turbulent and this leads to an over prediction of loss of the blade boundary layers. (Figure 7.77 shows the CFD pitch averaged loss and Figure 5.106 shows the experiment).
- The anomalous midspan loss dip is not present at this axial plane.
- The CFD predicts (Figure 7.74) a much weaker passage vortex loss core for the planar case than occurs in the experiments (Figure 5.103). The CFD does capture the loss in the enhanced loss core but fails to determine the changes in size of the P0, P1 and P2 passage vortex cores at this plane accurately.
- CFD Secondary Velocities (Figures 7.78-7.80) once again capture most of the details of the flow. The magnitude of these changes is quite accurately captured. In particular the agreement between the pitch averaged yaw angle for CFD (Figure 7.81) and experimental (Figure 5.110) cases is very encouraging, although the vortex migration from the endwall is under predicted by the CFD. The CFD also misses the inflection in pitch averaged yaw angle that occurs in the experiment at 15% of midspan in Figure 5.110.
- The CFD C_{ske} results (Figures 7.82-7.84) rank the profiles correctly and manage to capture all the salient flow features.
- The CFD C_Ω contours (Figures 7.86-7.88) show that the CFD predicts stronger vortices for the shed vorticity/suction side of the horseshoe vortex than the experiment - this is in agreement with the secondary vectors.

7.4 Comparison of Pitch and Area Averaged Quantities at Slot 10

In this section the computations are compared to the pitch and area averaged values of loss, yaw angle and secondary kinetic energy. The rationale behind using secondary kinetic energy is that it is a parameter which is related to loss but is better predicted by CFD than loss.

Firstly the pitch averaged parameters are plotted with the CFD and experimental results superimposed. Loss is shown in Figure 7.90 - the effect of the fully turbulent blade boundary layer calculation is immediately apparent with the CFD midspan loss being roughly twice that of the measured values. (0.1496 for the CFD and 0.0771 for the measured case). The effect on secondary loss is much less clear from Figure 7.90 - partly this is a result of having six lines on one graph. In order to assess the effects of secondary loss both the CFD and experimental results are adjusted to give a zero midspan loss value - this means that secondary loss is plotted. This is shown in Figure 7.91. Even when plotting secondary loss, the graph is still difficult to interpret so a graph with each endwall plotted on a separate set of axis is provided in Figure 7.94 on page 202.

5H Results	P0	P1	P2	P0 CFD	P1 CFD	P2 CFD
Net Total	0.1503	0.1336	0.1289	0.2226	0.2212	0.2159
Midspan	0.0780	0.0782	0.0772	0.1509	0.1489	0.1491
Secondary	0.0723	0.0554	0.0517	0.0716	0.0723	0.0668
% Planar Case	100.0	76.5	71.4	100.0	101.0	93.3
5H Mixed Out	P0	P1	P2	P0 CFD	P1 CFD	P2 CFD
Mixed Total	0.2346	0.1930	0.1828	0.2525	0.2435	0.2390
Mixed Midspan	0.1300	0.1091	0.1134	0.1611	0.1495	0.1592
Mixed Secondary	0.1046	0.0839	0.0694	0.0914	0.0940	0.0798
% Planar	100.0	80.2	66.3	100.0	102.8	87.4

Table 7.1: CFD Loss Predictions Compared to Experimental Values

For the P0 case we see that the CFD predicts the passage vortex loss core and the reduction of loss at 10 to 20% of span quite well but gets some details wrong. There is a pronounced hump and dip in the CFD passage vortex loss core which does not occur in the experimental results. This appears to be a consequence of the CFD over predicting boundary layer loss which is then fed into the vortex associated with the trailing edge vorticity/suction side of the horseshoe vortex. The loss core associated with the passage vortex appears to be the lower “hump” at around 25% of span. The point is that the overall good agreement is not the result of an accurate prediction of the loss production by the CFD.

For the P1 case the passage vortex loss core is over predicted in strength but the CFD does capture the increased loss associated with the enhanced corner vortex. The dip in loss between the endwall losses and the passage vortex loss core is under predicted with the CFD predicting more loss than is actually present.

A similar story is seen for P2 with the passage vortex being over predicted and the endwall loss being captured accurately - however the dip in loss between the endwall losses and the passage vortex loss core is greater than occurs in reality.

Table 7.1 shows the CFD and experimental loss, this table also includes the mixed out loss for comparison. This quantifies the remarks made in the previous paragraph. Figure 7.1 shows a bar chart of the secondary loss results (the sixth line of Table 7.1) for reference. Secondary loss is the main parameter under consideration as this largely removes the effect of the blade boundary layer modelling and the turbomachinery designer can examine secondary loss with the prior knowledge that the modelling of the midspan flow is incorrect. However the CFD prediction of loss is incorrect even when examining secondary loss. For P1 a small increase in loss is predicted and for P2 the loss is overestimated considerably. This is not however particularly surprising, loss *measurement* is difficult as the blade rows are already quite efficient and the changes between endwalls are small - the same applies to CFD. Furthermore the endwalls were designed in the expectation that the loss prediction would be poor, and the original profile (P1) was designed on the basis of reducing yaw angle deviations and not on predicted loss reduction.

C_{ske} is used as a substitute for loss as the CFD predicts this somewhat better and it is related to loss. Figure 7.92 shows the CFD predictions superimposed on the experimental values. Once again with six lines on one graph this is hard to

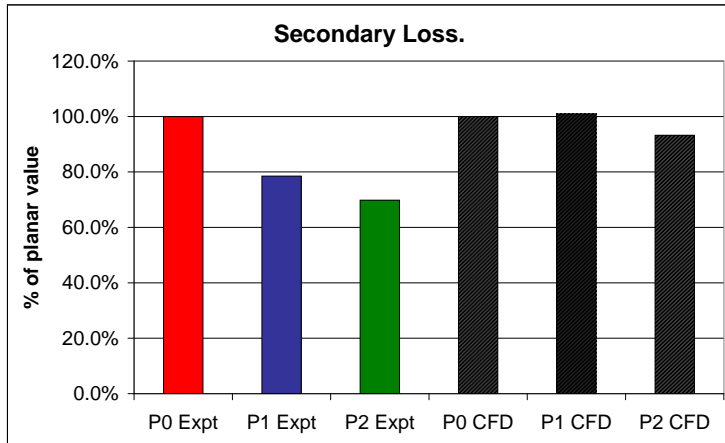


Figure 7.1: Experimental and CFD Secondary Loss

5H Results	P0	P1	P2	P0 CFD	P1 CFD	P2 CFD
C_{ske}	0.0203	0.0110	0.0092	0.0198	0.0101	0.0121
% Planar Case	100.0	54.0	45.5	100.0	51.1	61.4

 Table 7.2: CFD C_{ske} Predictions compared to Experimental Values

decipher so a graph with each profile on a separate set of ordinates is provided in Figure 7.95, this can be found on page 203. C_{ske} prediction is by no means perfect. The planar case in particular is under predicted in the main passage vortex peak at 35% span and over predicted at less than 10% of span. The situation with the profiled geometries is more confused with the CFD under predicting for P1 and over predicting for P2. This is reflected in the area averaged results shown in Table 7.2. As can be seen from the table, the CFD does not rank the profiles in terms of C_{ske} correctly, but the absolute values of computational C_{ske} are much closer than the loss predictions.

With the absence of an accurate loss prediction from the CFD, C_{ske} can be used as a substitute. Table 7.3 details the C_{ske} reductions compared to the loss reductions⁴. As can be seen in the experiments there is a correlation between reduced C_{ske} and reduced loss, however for the CFD such a correlation does not exist. This is to be expected as CFD does not predict loss very well.

A very crude way of estimating the loss reduction from the C_{ske} can be established, the results for P1 and P2 show that the % loss reduction is about half the % C_{ske} reduction. (0.47 for P1 and 0.55 for P2). Using this estimate we could predict the loss from the CFD by dividing the C_{ske} coefficient by two. This would predict the P1 loss reduction as 24% and the P2 loss reduction as 19% - this is still the incorrect ranking but at least it indicates that the loss is going down for both profiles rather than up.

⁴All values are % of planar value.

Expt	P1	P2
C_{ske} reduction	46.0	54.5
C_{P0} reduction	21.5	30.2
CFD	P1	P2
C_{ske} reduction	48.9	38.6
C_{P0} reduction	-1.0	6.7

Table 7.3: C_{ske} and C_{P0} Reductions Compared. (% of planar values)

Yaw angles are shown in Figure 7.93, the CFD data has been adjusted to give the same midspan angle as the experimental data, but the size of this adjustment is very small at less than half a degree. The information is repeated with one set of ordinates for each profile in Figure 7.96 on page 204. In general yaw angle is much better predicted by CFD than the other parameters with the maximum error being 2.5° and typically much less than that.

Again the P0 case actually appears to agree the least well with the experimental data, peak under turning and over turning are predicted in slightly the wrong place and the predicted over turning in the planar case is much greater than that which actually occurs. The under turning and over turning is captured by the CFD although some of the details are wrong.

Predictions for the profiled endwalls appear slightly better with some discrepancies between the position of peak under turning. Near the wall the differences become greater for P2 and there is something of a systematic over prediction of over turning by about 1.5° , this is perhaps due to viscous effects damping out the flow dynamics in a manner which is not captured by CFD. Near the wall for P1 we see that the CFD predicts a reduction in under turning near the wall for P1 which does not occur in practice. A close examination of the secondary vector plots (Figure 7.6 on page 180 for the CFD and 5.108 on page 124 for the experiments) indicates that this is due to the CFD under predicting the crossflow from the new boundary layer that is formed after the passage vortex. This result contradicts some previously published work (Ingram et al., 2002), this is due to a change in the method of pitch averaging and will be discussed in Chapter 9.

7.5 Three Dimensional CFD Visualisation

Modern post-processing software allows many different three dimensional views of the endwall to be produced, a selection of the more informative ones are included in this thesis.

The first set of figures shown illustrates the surface flow on the CFD and these can be compared to the oil/dye visualisation shown in Chapter 4. The method of calculation is described in the manual for the software (IntelligentLight, 2001) and the CFD visualisations are all taken from the same angle. The endwall is coloured grey and the lines represent surface streamlines. The lines are coloured according to FIELDVIEW's calculation of wall shear stress. The authors' purpose in including the wall shear stress colours was to highlight the streamline direction and the geometry of the endwalls and blades, this section does not discuss wall shear

stress or the validity of the calculation.

Figures 7.97-7.99 show the flow on the suction surface on the blade, which show that the CFD is picking up the different heights that the passage vortex reaches at blade exit - this is what Sharma and Butler (1987) called the “penetration height” (The comparable flow visualisation is found in Figures 4.14-4.16 on page 68) The P0 profile is seen to have the greatest “penetration height” of the three profiles as expected. The enhanced corner vortex for P1 is also picked up quite clearly and is not seen in the other two cases. Finally the sharp suction surface dip for P2 is shown up clearly as an area of high shear stress (a red line in the bottom left hand corner of 7.99) since the profiling for P2 was restricted to the blade passage only there is very sharp curvature at this point (see Figure A.2 on page 286) which the CFD highlights. There is also no sign of the additional vortex trace associated with the suction side of the horseshoe vortex that is seen in the flow visualisation (See Figure 4.14 on page 68). The flow visualisation shows an additional vortex trace that starts earlier than the main passage vortex and rapidly migrates up the blade surface. This vortex is associated with the suction side of the horseshoe vortex and is not shown in the CFD.

Pressure surface flow is shown in figures 7.100-7.102. The CFD results show a generally similar pattern on the pressure surface and as is immediately apparent from an inspection of Figures 4.17-4.19 on page 69 there is very little flow visualisation to validate the CFD against. The reduced strength of the passage vortex is not apparent in these figures but can be seen in plots produced by Rolls-Royce for an earlier paper (Ingram et al., 2002).

Details of the horseshoe vortex saddle point are found in Figures 7.103-7.105, comparable flow visualisation figures may be found in Figures 4.29-4.31 on page 73. The geometry of the endwalls is also shown in the plots though it is quite difficult to make out. The CFD does not show quite the same dramatic flow patterns for P1 as the oil/dye experiments do, however the computations do show a differing flow pattern for each endwall. The P0 computation shows the classical horseshoe pattern with a strong passage vortex/pressure side horseshoe vortex migration trace leading off to mid-passage. The P1 picture shows that the saddle point is larger in size, is nearer the pressure side of the blade and is further upstream of the leading edge. The crossflow that forms the passage vortex/pressure side horseshoe vortex migration is still there but is much less concentrated than in the planar case. This perhaps accounts for the lack of a passage vortex/pressure side horseshoe vortex migration trace on the endwall for P1 (see figure 4.9 on page 66). The P2 picture shows further differences: the saddle point is larger than for the planar case, is much more biased towards the pressure side of the blade and is the furthest upstream of the three profiles.

The increased size of the horseshoe vortex can be inferred from the lack of firm traces on the endwall oil/dye traces but the detailed changes that the CFD implies cannot be seen in the oil/dye traces alone.

Finally the origin of the two distinct loss cores in the CFD solution is examined. A number of streamlines which pass through the centres of both loss cores are selected using the post-processing software. The point being to determine the origin of the fluid that ends up in the loss core. The plots are shown in Figures 7.106, 7.107

and 7.108 for profile P0, P1 and P2 respectively. As well as the streamlines also shown is the axial reference plane (Slot 10 128%) with contours of loss coefficient on it. The contour maximum and minimum values are set to be the same in the CFD picture as in the two-dimensional contour plots so that they are comparable. The figures shown that the larger loss core (furthest from the endwall) is associated largely with the blade boundary layer and the smaller loss core derives from the passage vortex. This confirms remarks made earlier, where the CFD over predicts boundary layer loss but under predicts the mixing loss associated with the passage vortex. Therefore the approximate correct size of the loss cores compared to experiment is due to the CFD over predicting boundary layer loss which then migrates to roughly the correct location, whilst the CFD greatly under predicts the actual loss generated by the secondary flow features.

7.6 Overview

The computational fluid dynamics used to design the endwalls did not use an excessive number of points or a particularly sophisticated turbulence model, rather it represents a typical design computation. The sophistication is provided by the thirty-six perturbations that are examined to produce the final endwall design. It is important to bear that in mind when examining the results from the computations.

Due to the use of a turbulent model for the boundary layers the loss on the blade surfaces is over predicted as large areas of this flow are in fact laminar which in general produces less loss than turbulent boundary layers. This means that the blade wakes in the CFD solution (Figures 7.74-7.76) are much larger than in reality and also that the vortex associated with the trailing edge shed vorticity/suction side of the horseshoe vortex appears much larger than in experiments. In fact in the CFD the passage vortex loss core is smaller than that of the shed vorticity/suction side horseshoe vortex whereas in the experiments (Figures 5.103-5.105) the situation is reversed.

It is clear from an examination of the CFD results extracted and put into experimental form that the CFD does not predict the magnitude of the secondary flows inside the blade passage correctly - it underestimates the extent and magnitude of the secondary flow regions. However the trends appear to be captured accurately and after the trailing edge the prediction improves somewhat.

A very crude correlation can be made between reductions in C_{ske} and reductions in secondary loss. Very roughly for a 1% reduction in C_{ske} (as a % of the planar value) a 0.5% reduction in secondary loss may be expected. This is a “rule of thumb” extracted from experimental measurements and may not be widely applicable.

Care needs to be taken when comparing some of the experimental results to the computational results - the large midspan flow angle discrepancies do not necessarily call the computation into doubt - but the other way around. The experiments at Slot 3,6 and 8 (6%, 71% and 97% C_{ax} respectively) were not conducted with the back to back methodology and so some midspan discrepancy is expected here. The experiments have given useful information about the pattern of the flow at that particular location even if they do not capture the numerical values correctly.

The computational fluid dynamics may not be perfect and have significant devi-

ations from reality contained in the results. However it predicts enough flow features with enough accuracy to produce a reasonable design of endwall. Furthermore, CFD can be an extremely useful tool for examination of details of the flow that are not easy to examine using experimental measurements - as has been carried out in this chapter.

7.7 Computational Fluid Dynamics Results

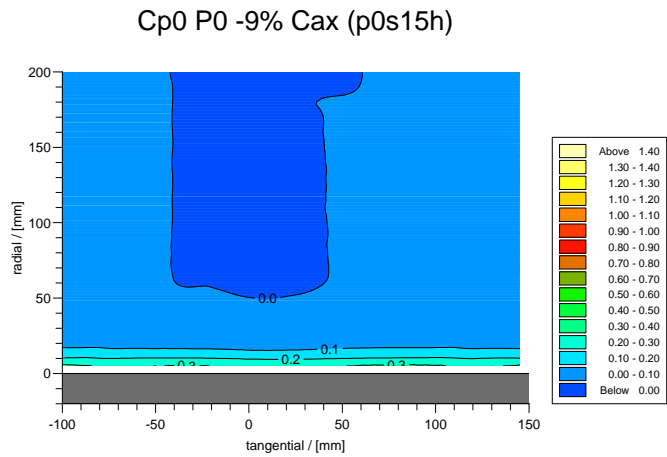


Figure 7.2: Slot 1 P0 Loss CFD Prediction.

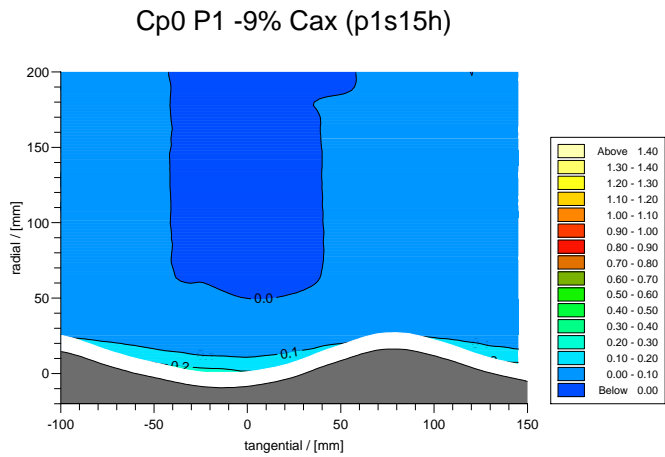


Figure 7.3: Slot 1 P1 Loss CFD Prediction.

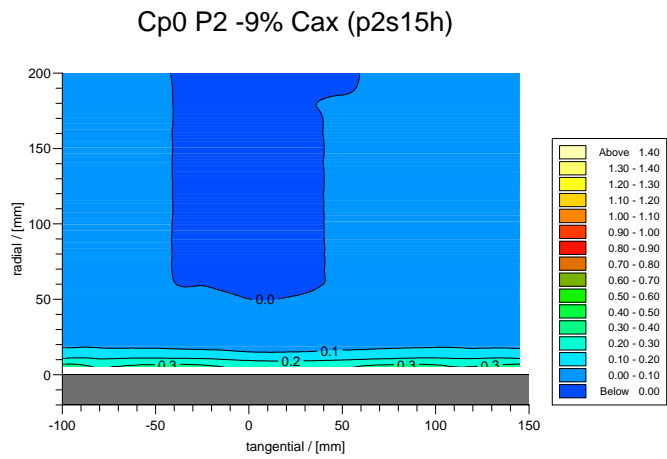


Figure 7.4: Slot 1 P2 Loss CFD Prediction.

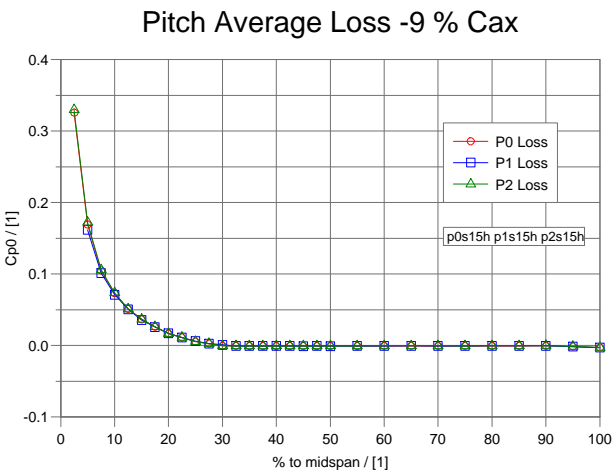


Figure 7.5: Slot 1 Pitch Averaged Loss CFD Prediction.

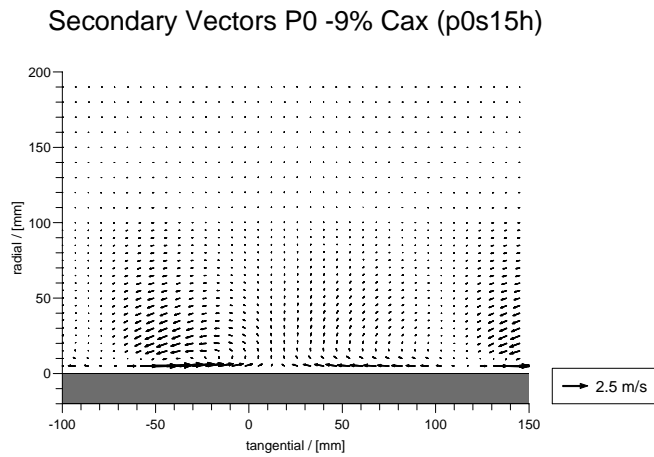


Figure 7.6: Slot 1 P0 Secondary Vectors CFD Prediction.

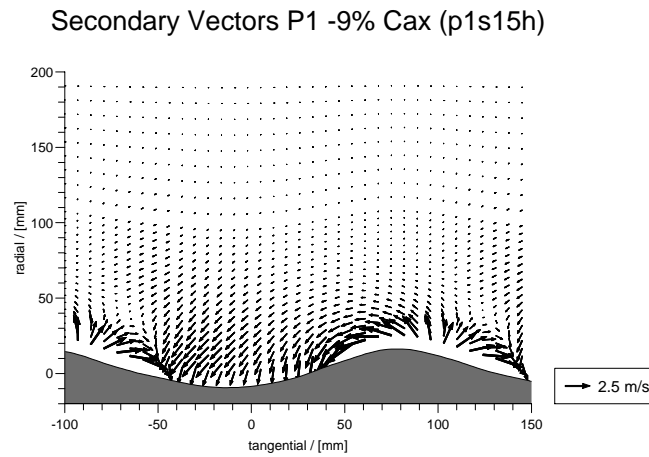


Figure 7.7: Slot 1 P1 Secondary Vectors CFD Prediction.

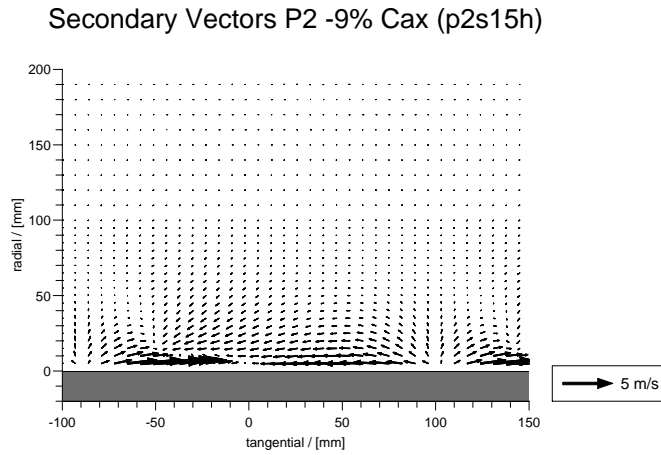


Figure 7.8: Slot 1 P2 Secondary Vectors CFD Prediction.

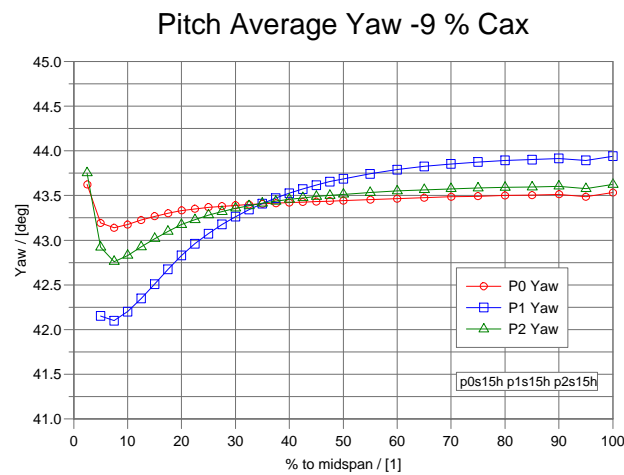


Figure 7.9: Slot 1 Pitch Averaged Yaw Angle CFD Prediction.

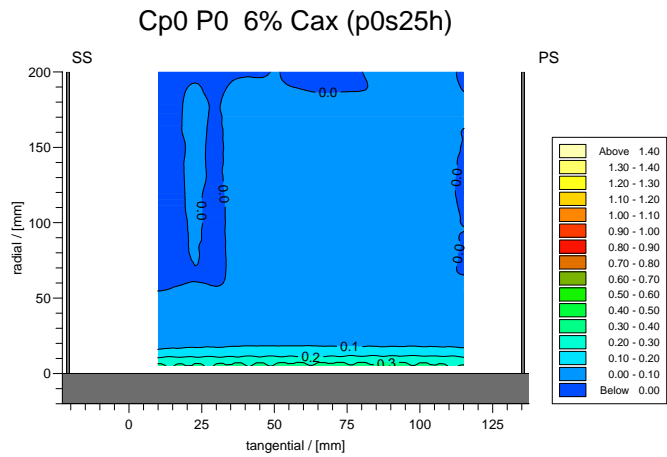


Figure 7.10: Slot 2 P0 Loss CFD Prediction.

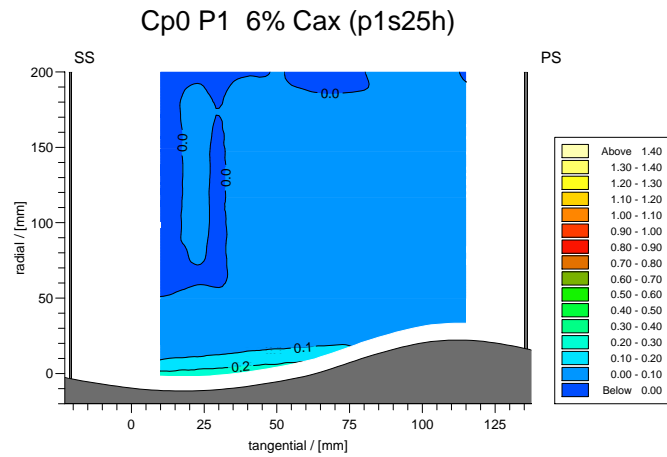


Figure 7.11: Slot 2 P1 Loss CFD Prediction.

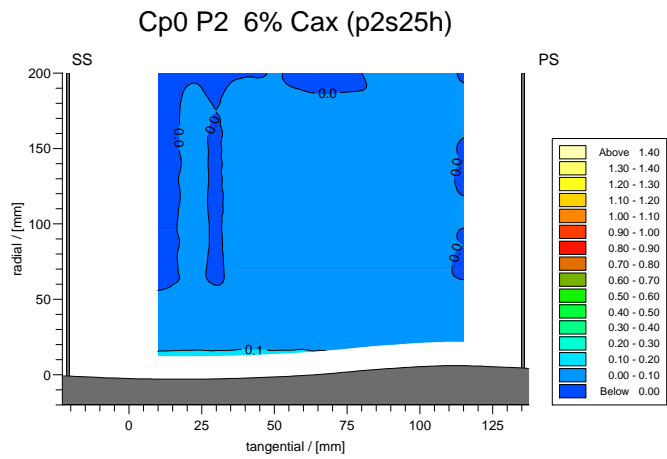


Figure 7.12: Slot 2 P2 Loss CFD Prediction.

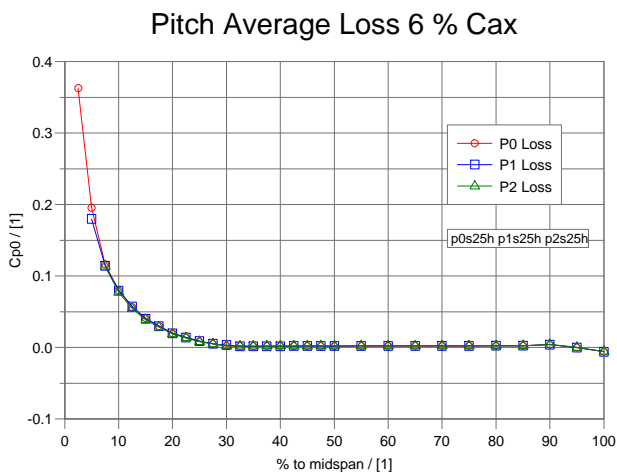


Figure 7.13: Slot 2 Pitch Averaged Loss CFD Prediction.

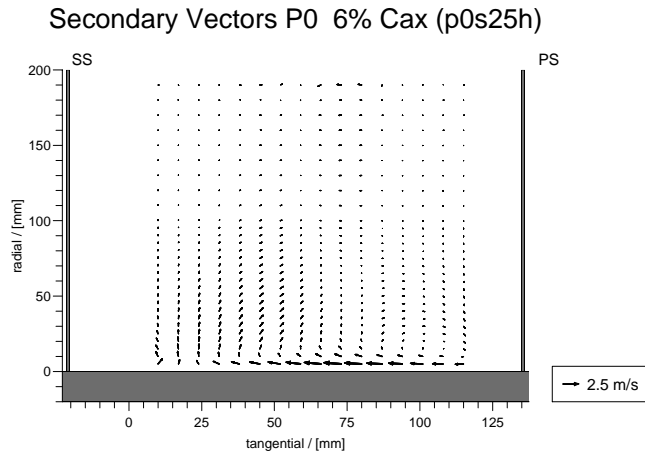


Figure 7.14: Slot 2 P0 Secondary Vectors CFD Prediction.

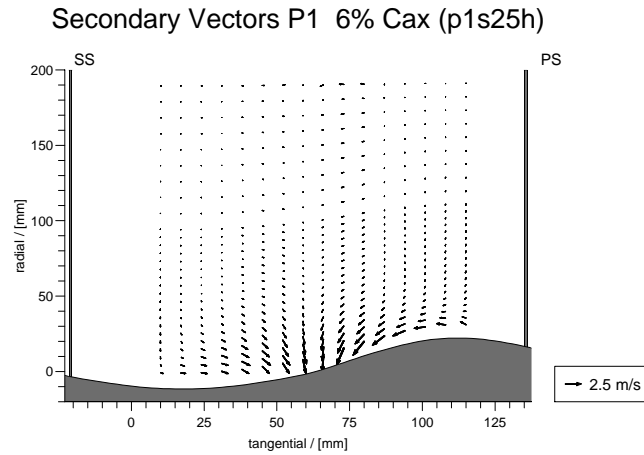


Figure 7.15: Slot 2 P1 Secondary Vectors CFD Prediction.

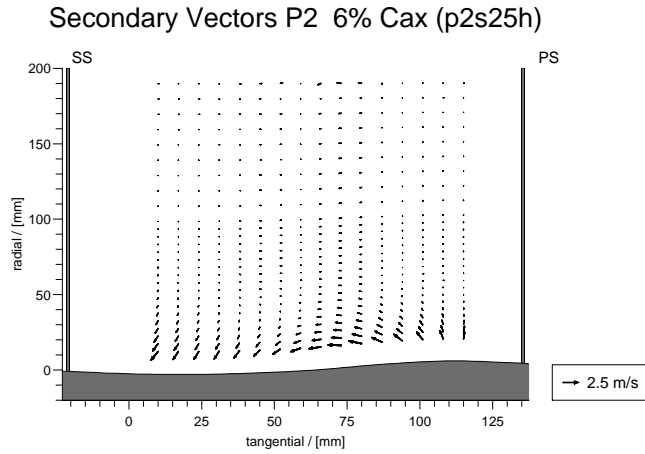


Figure 7.16: Slot 2 P2 Secondary Vectors CFD Prediction.

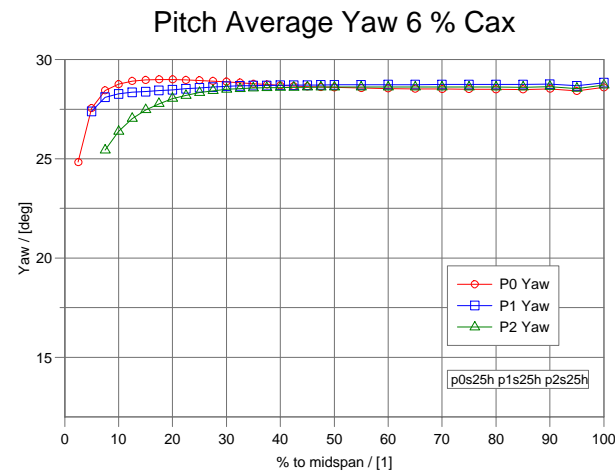


Figure 7.17: Slot 2 Pitch Averaged Yaw Angle CFD Prediction.

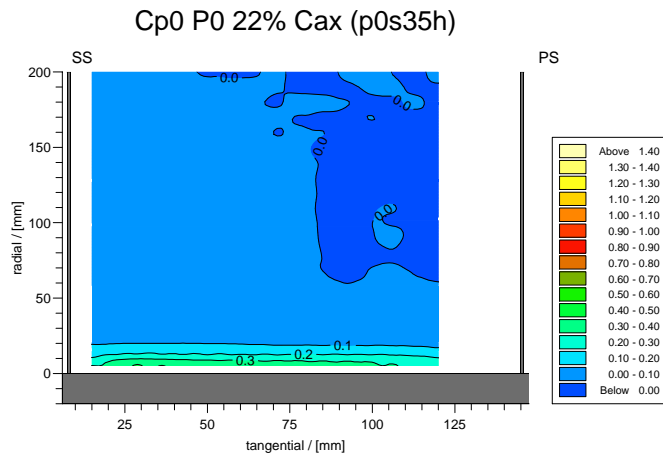


Figure 7.18: Slot 3 P0 Loss CFD Prediction.

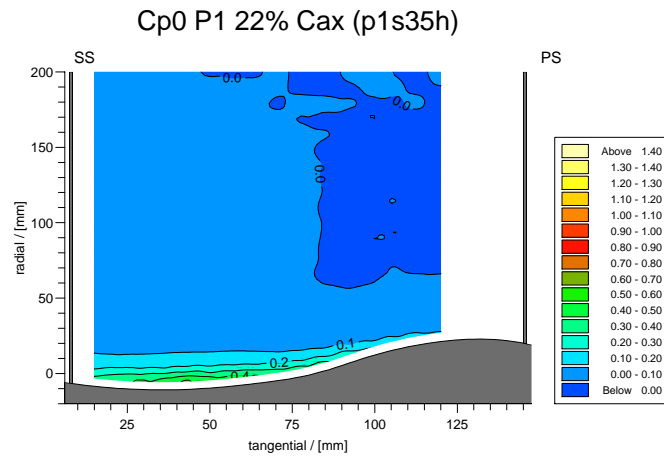


Figure 7.19: Slot 3 P1 Loss CFD Prediction.

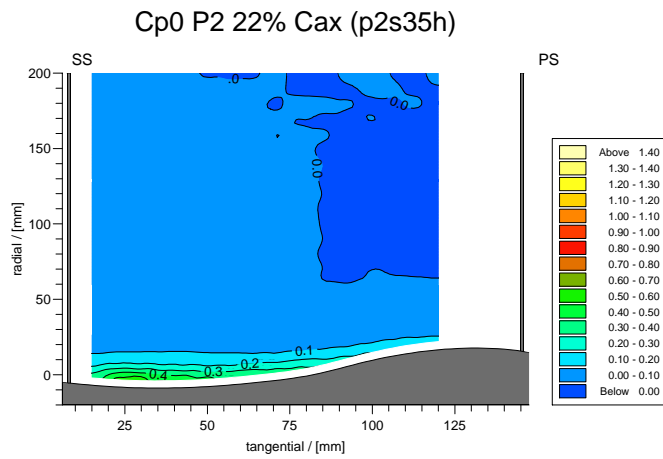


Figure 7.20: Slot 3 P2 Loss CFD Prediction.

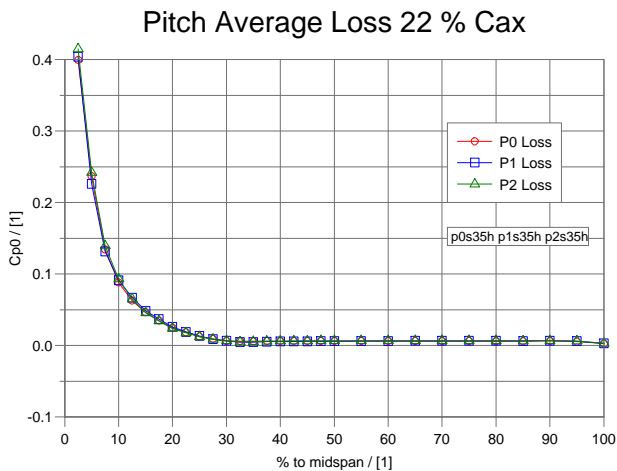


Figure 7.21: Slot 3 Pitch Averaged Loss CFD Prediction.

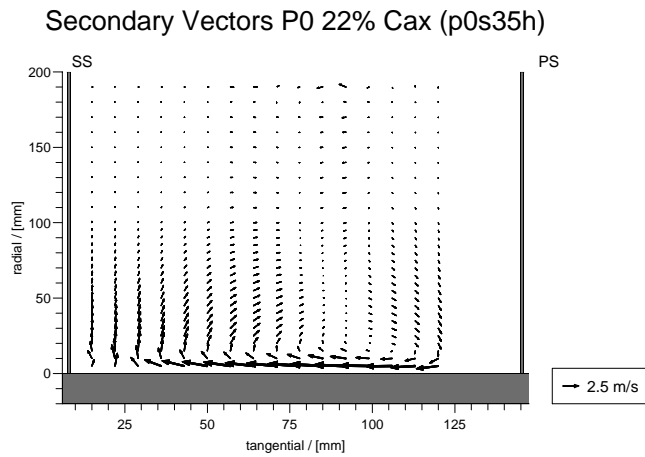


Figure 7.22: Slot 3 P0 Secondary Vectors CFD Prediction.

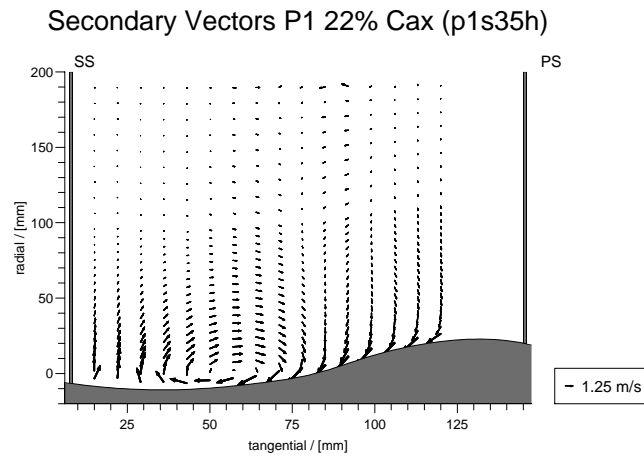


Figure 7.23: Slot 3 P1 Secondary Vectors CFD Prediction.

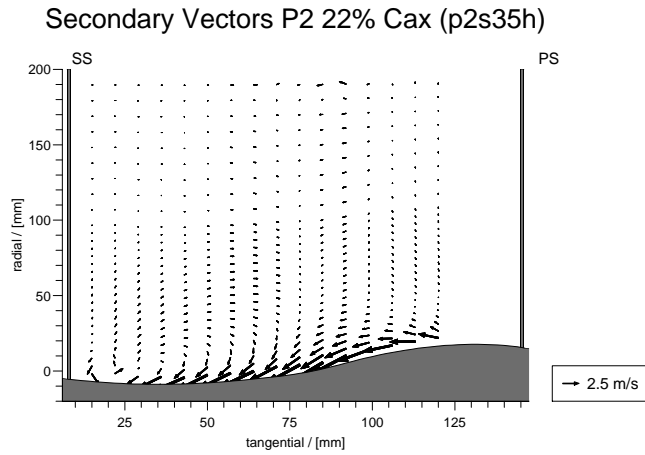


Figure 7.24: Slot 3 P2 Secondary Vectors CFD Prediction.

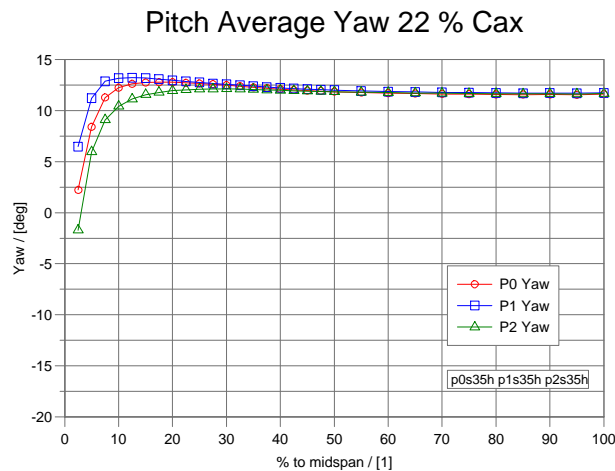


Figure 7.25: Slot 3 Pitch Averaged Yaw Angle CFD Prediction.

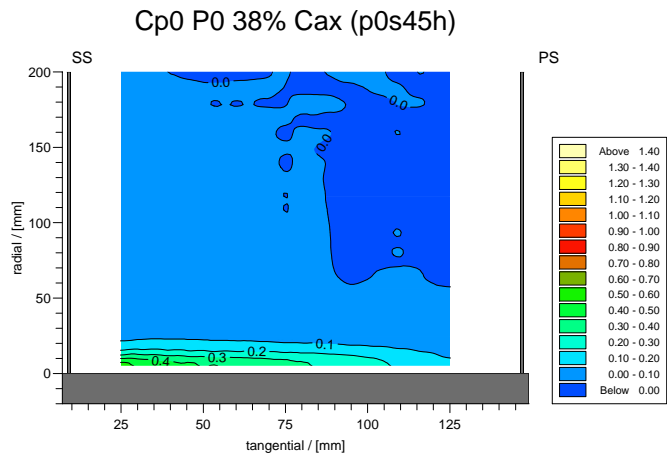


Figure 7.26: Slot 4 P0 Loss CFD Prediction.

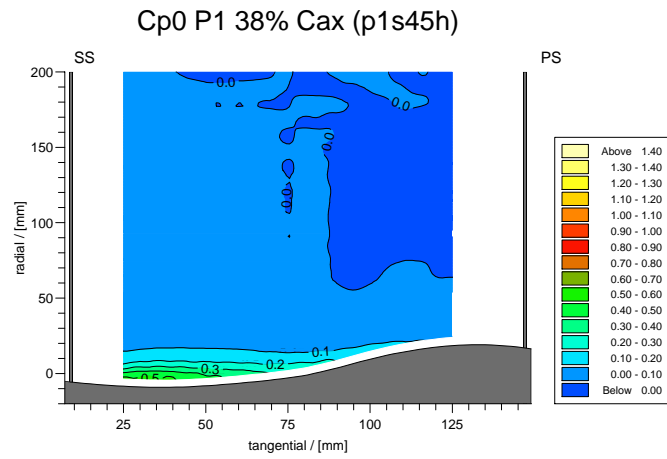


Figure 7.27: Slot 4 P1 Loss CFD Prediction.

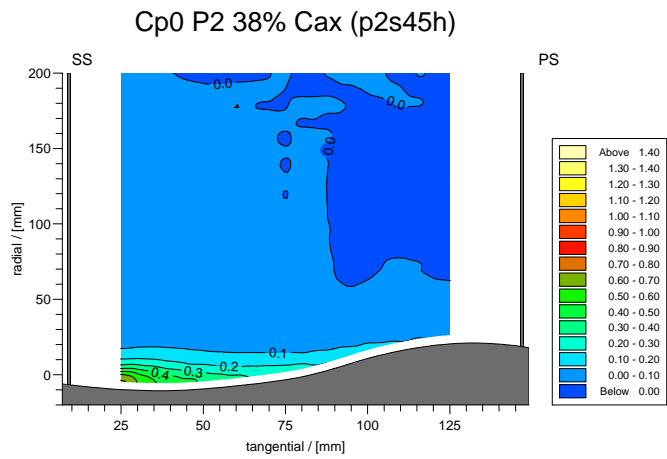


Figure 7.28: Slot 4 P2 Loss CFD Prediction.

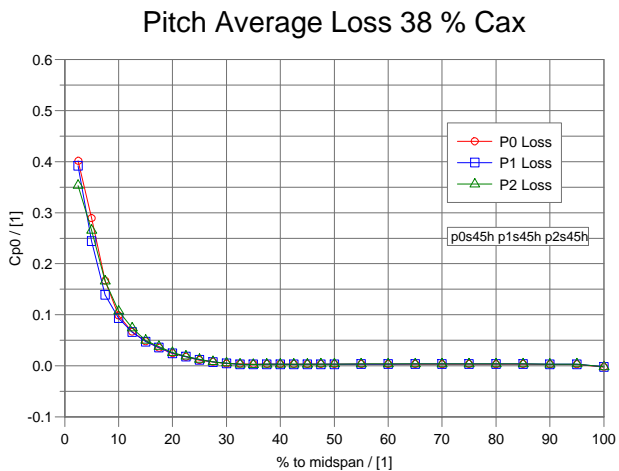


Figure 7.29: Slot 4 Pitch Averaged Loss CFD Prediction.

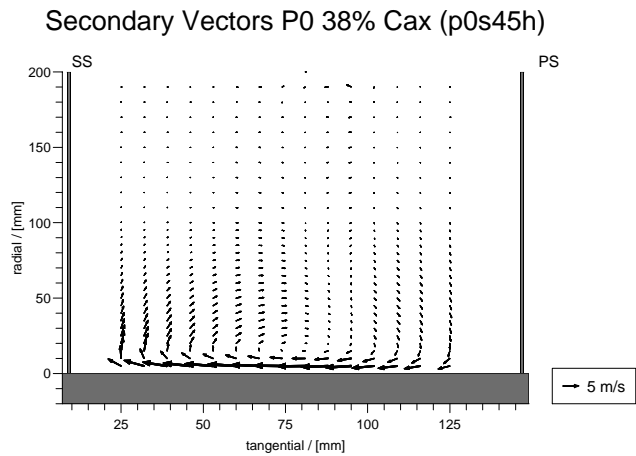


Figure 7.30: Slot 4 P0 Secondary Vectors CFD Prediction.

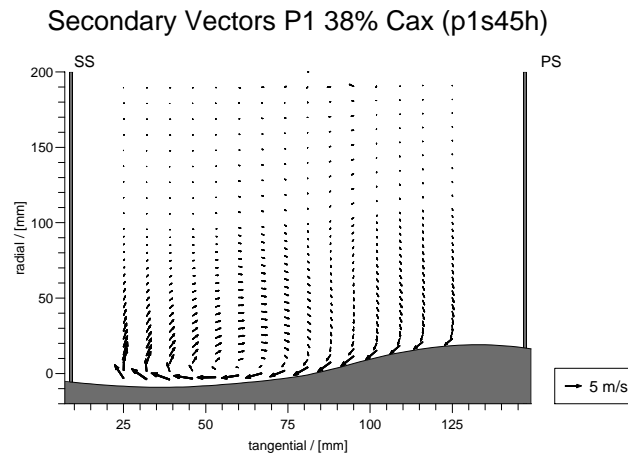


Figure 7.31: Slot 4 P1 Secondary Vectors CFD Prediction.

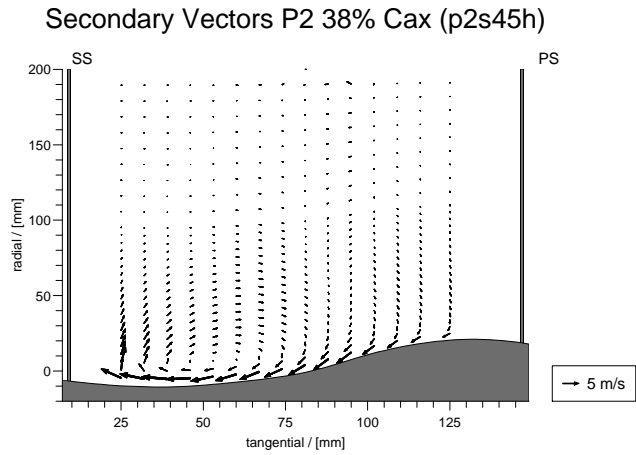


Figure 7.32: Slot 4 P2 Secondary Vectors CFD Prediction.

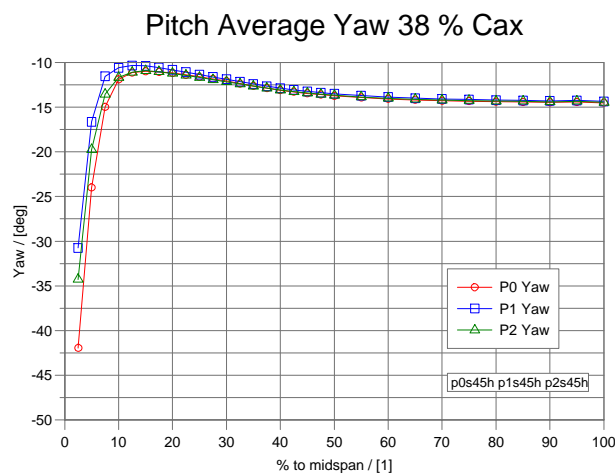


Figure 7.33: Slot 4 Pitch Averaged Yaw Angle CFD Prediction.

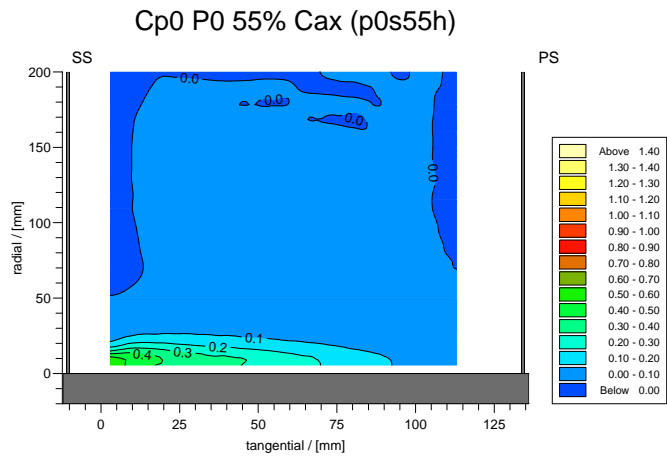


Figure 7.34: Slot 5 P0 Loss CFD Prediction.

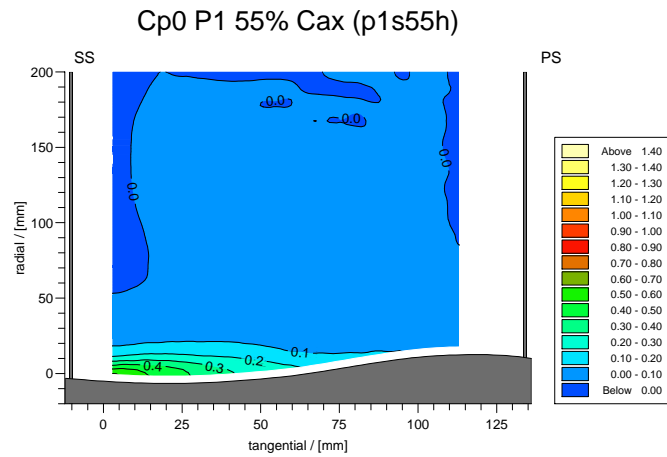


Figure 7.35: Slot 5 P1 Loss CFD Prediction.

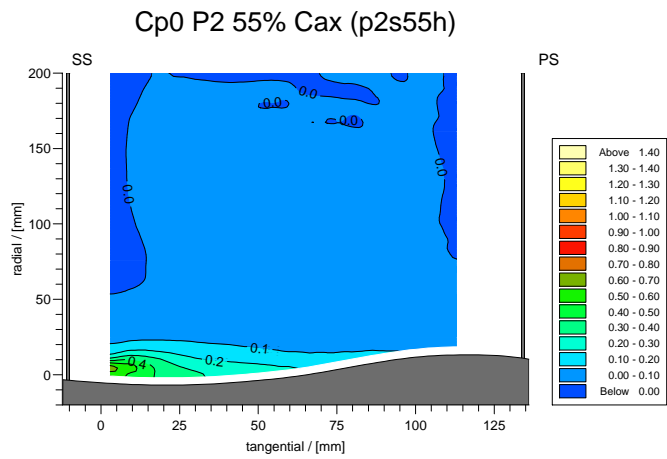


Figure 7.36: Slot 5 P2 Loss CFD Prediction.

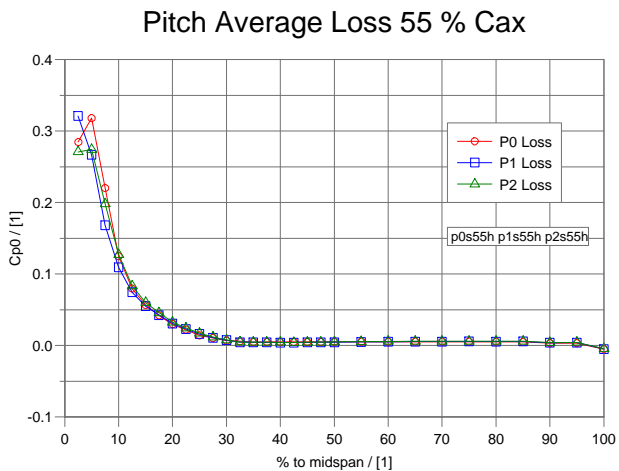


Figure 7.37: Slot 5 Pitch Averaged Loss CFD Prediction.

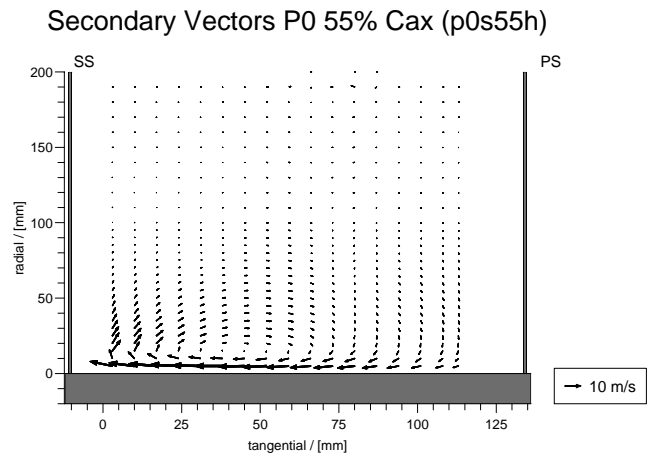


Figure 7.38: Slot 5 P0 Secondary Vectors CFD Prediction.

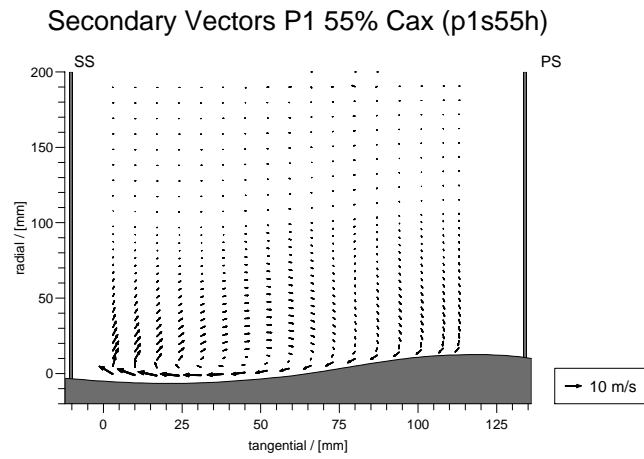


Figure 7.39: Slot 5 P1 Secondary Vectors CFD Prediction.

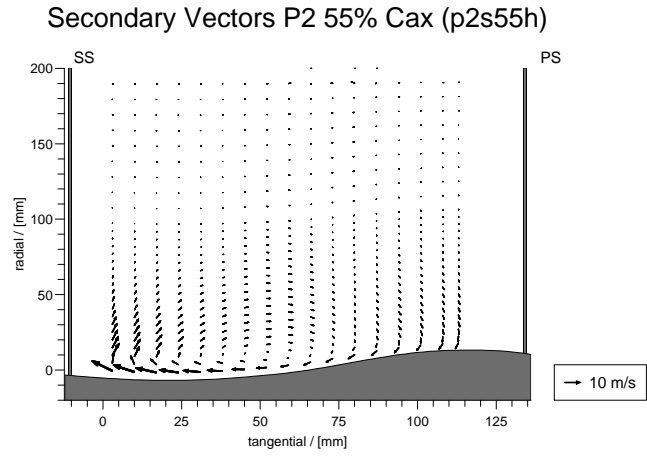


Figure 7.40: Slot 5 P2 Secondary Vectors CFD Prediction.

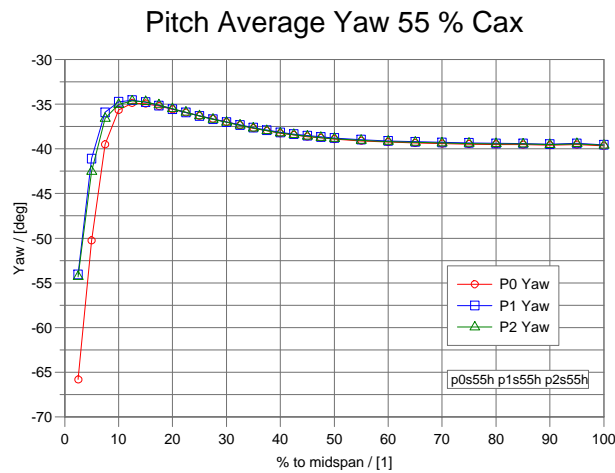


Figure 7.41: Slot 5 Pitch Averaged Yaw Angle CFD Prediction.

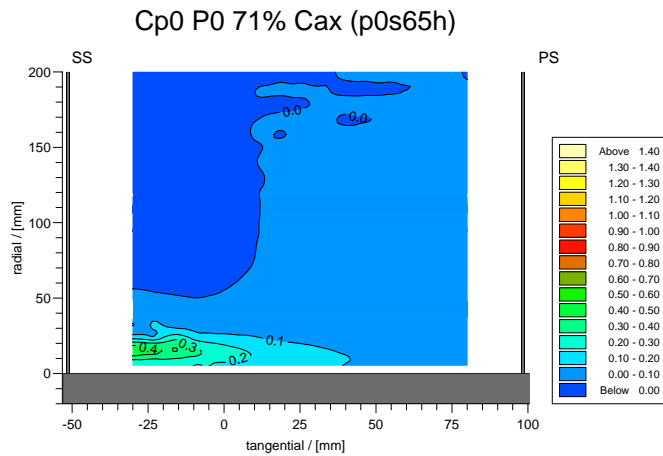


Figure 7.42: Slot 6 P0 Loss CFD Prediction.

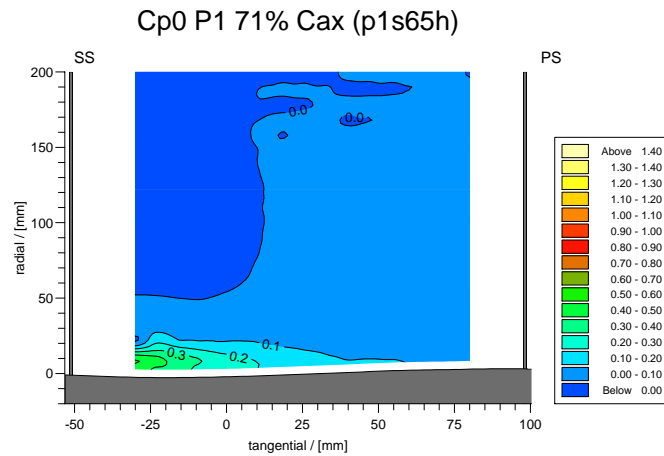


Figure 7.43: Slot 6 P1 Loss CFD Prediction.

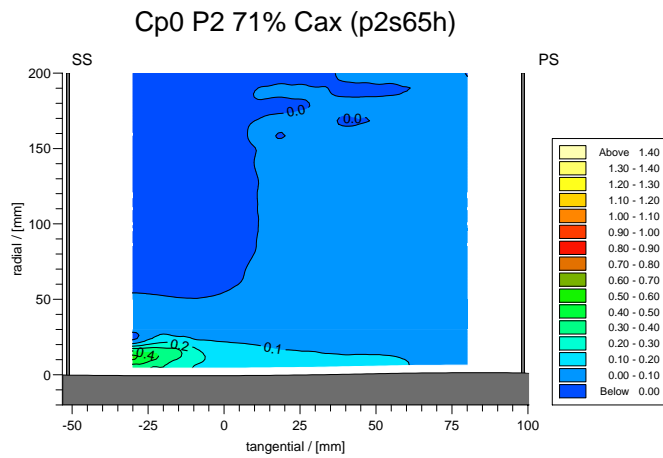


Figure 7.44: Slot 6 P2 Loss CFD Prediction.

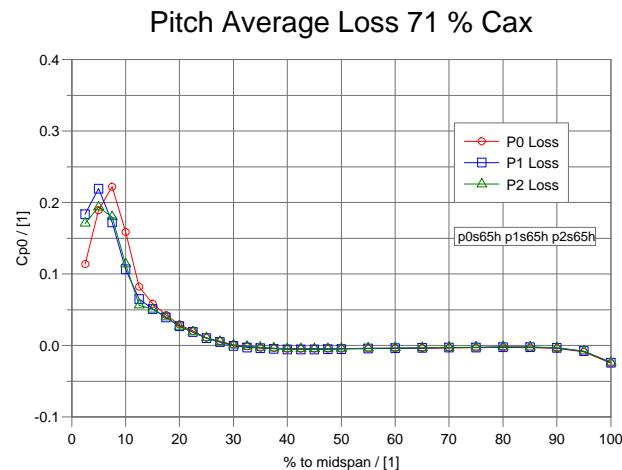


Figure 7.45: Slot 6 Pitch Averaged Loss CFD Prediction.

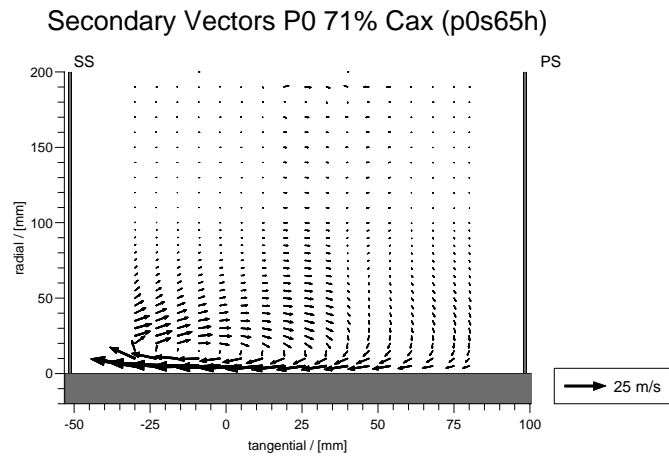


Figure 7.46: Slot 6 P0 Secondary Vectors CFD Prediction.

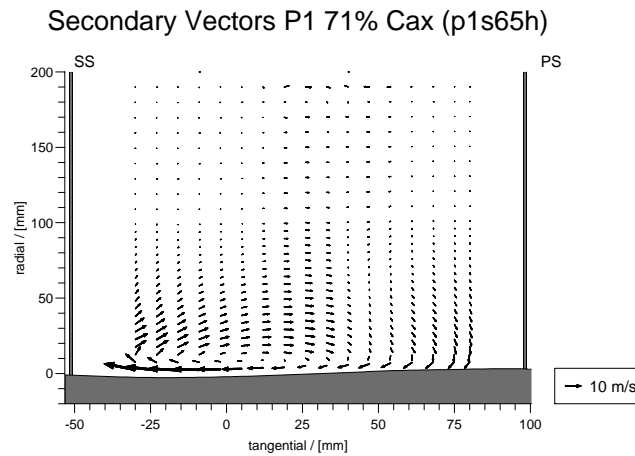


Figure 7.47: Slot 6 P1 Secondary Vectors CFD Prediction.

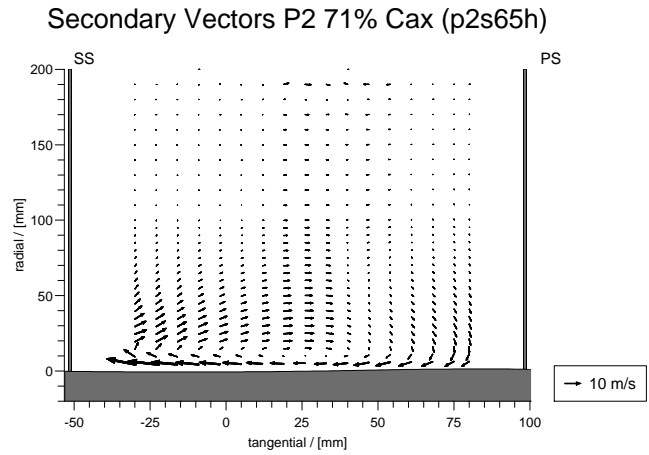


Figure 7.48: Slot 6 P2 Secondary Vectors CFD Prediction.

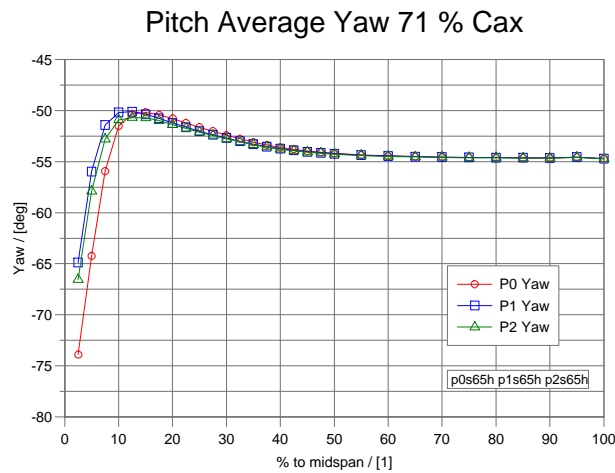


Figure 7.49: Slot 6 Pitch Averaged Yaw Angle CFD Prediction.

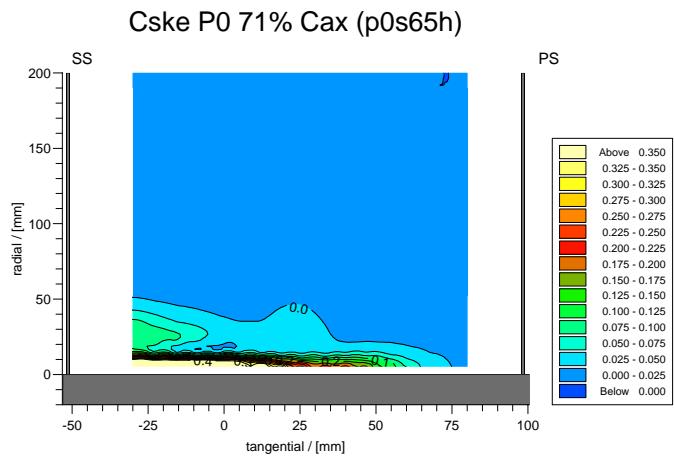


Figure 7.50: Slot 6 P0 C_{ske} CFD Prediction

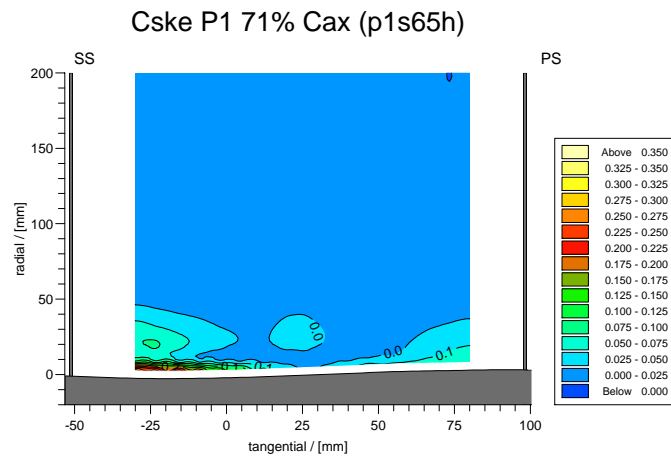


Figure 7.51: Slot 6 P1 C_{ske} CFD Prediction

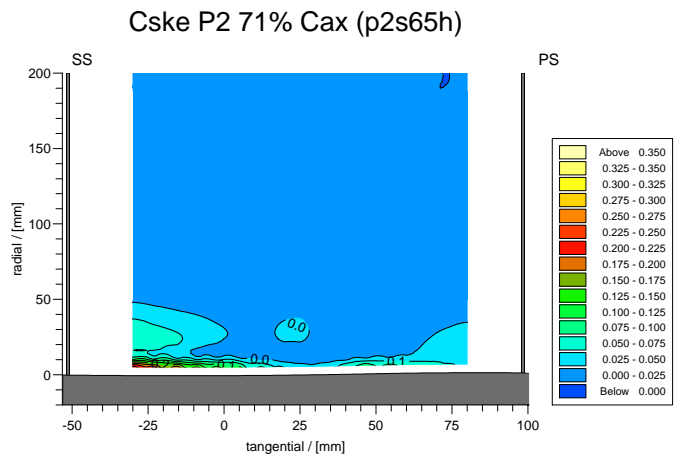


Figure 7.52: Slot 6 P2 C_{ske} CFD Prediction

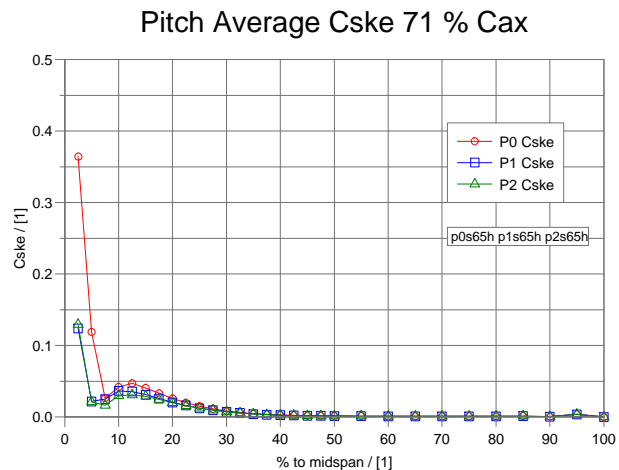


Figure 7.53: Slot 6 Pitch Averaged C_{ske} CFD Prediction

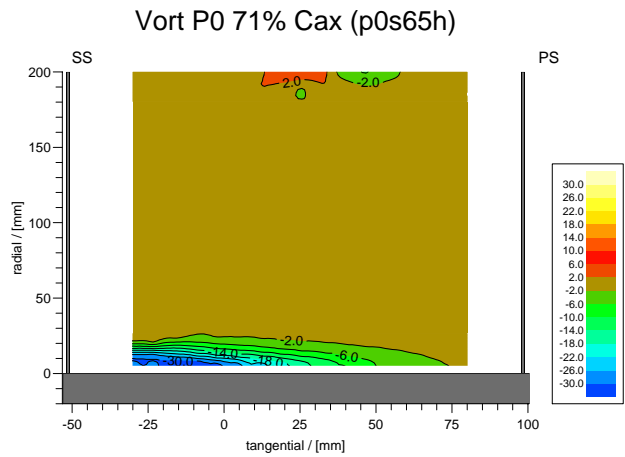


Figure 7.54: Slot 6 P0 Streamwise Vorticity Coefficient CFD Prediction

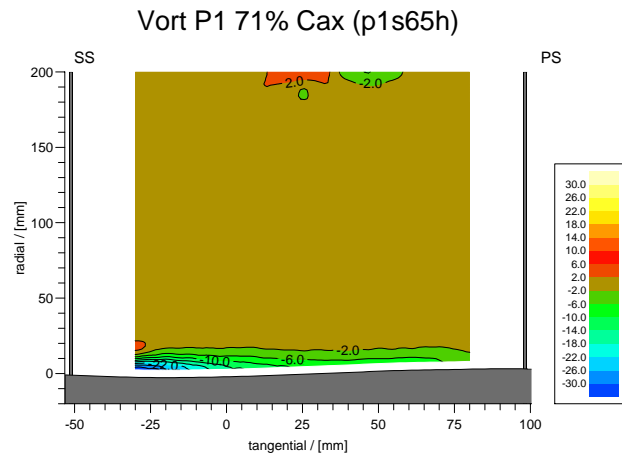


Figure 7.55: Slot 6 P1 Streamwise Vorticity Coefficient CFD Prediction

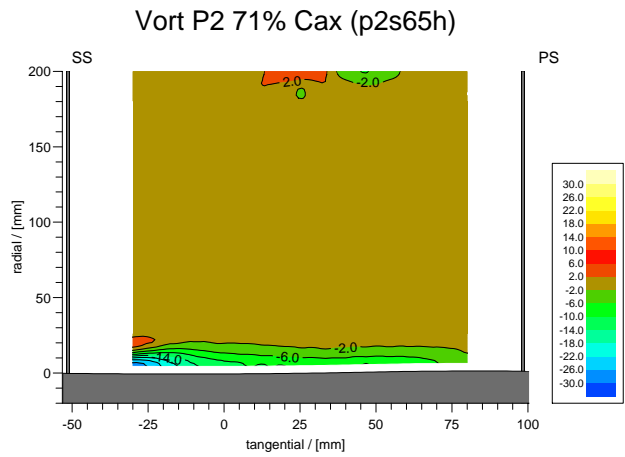


Figure 7.56: Slot 6 P2 Streamwise Vorticity Coefficient CFD Prediction

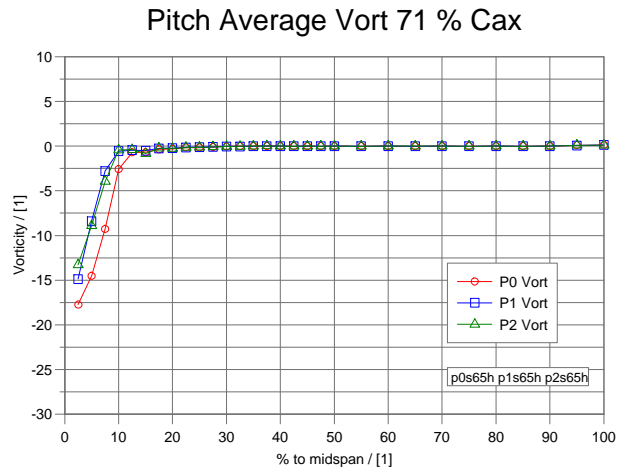


Figure 7.57: Slot 6 Pitch Averaged Vorticity Flow CFD Prediction

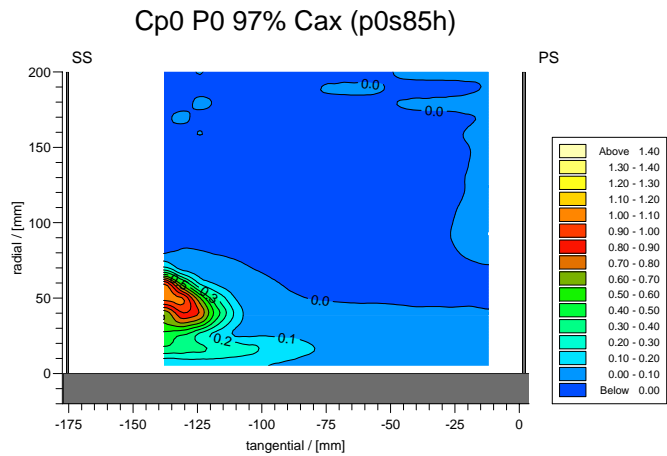


Figure 7.58: Slot 8 P0 Loss CFD Prediction.

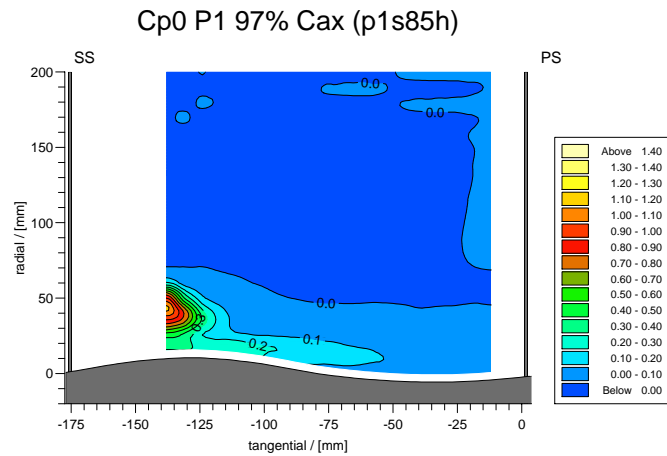


Figure 7.59: Slot 8 P1 Loss CFD Prediction.

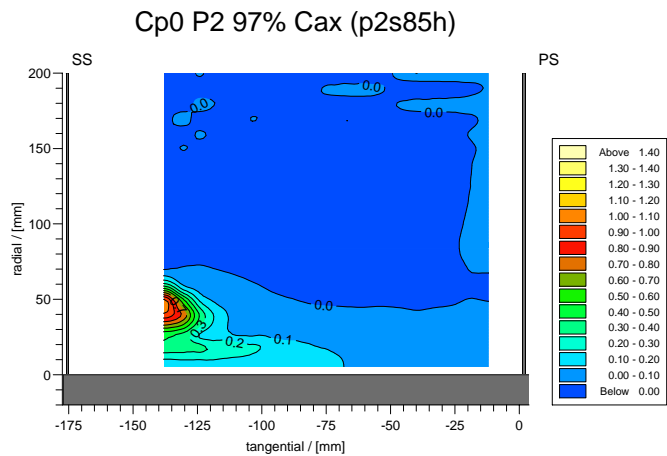


Figure 7.60: Slot 8 P2 Loss CFD Prediction.

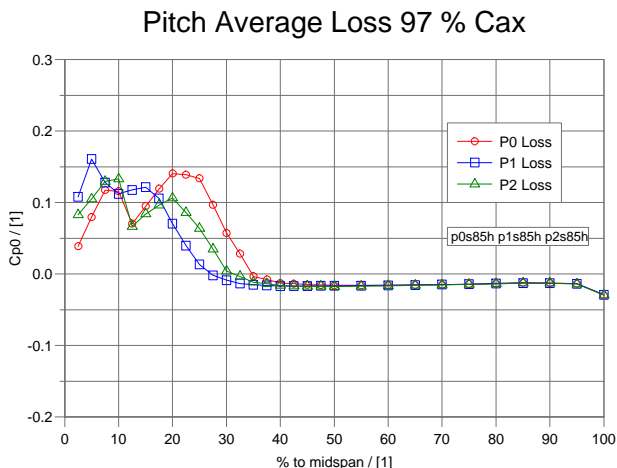


Figure 7.61: Slot 8 Pitch Averaged Loss CFD Prediction.

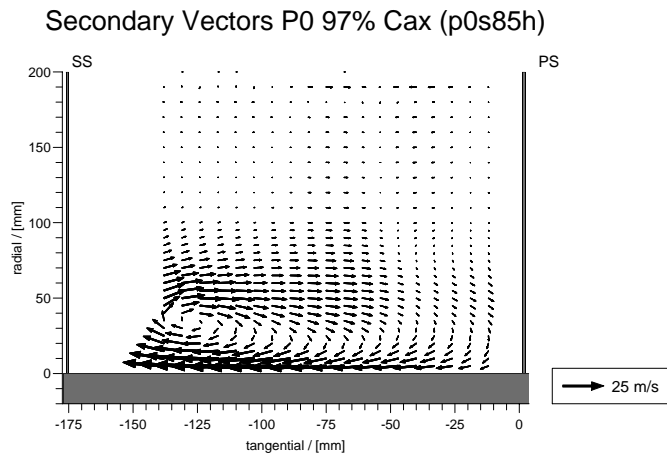


Figure 7.62: Slot 8 P0 Secondary Vectors CFD Prediction.

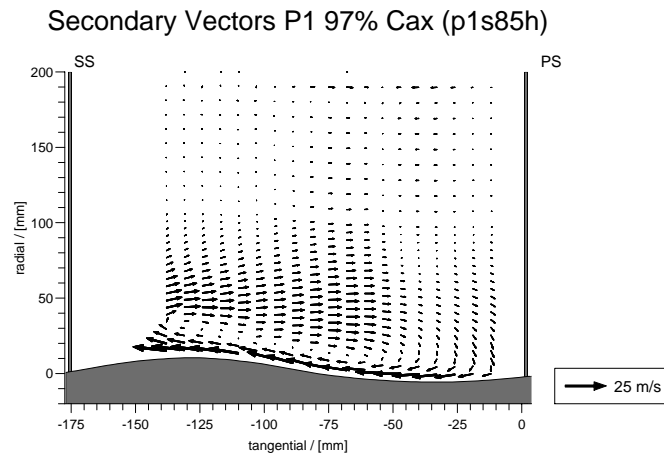


Figure 7.63: Slot 8 P1 Secondary Vectors CFD Prediction.

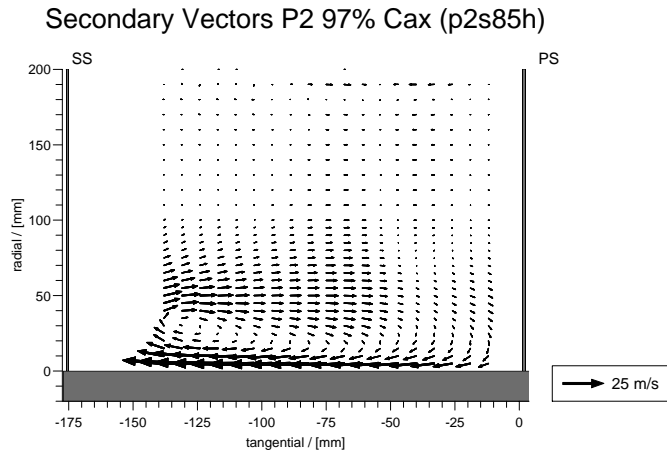


Figure 7.64: Slot 8 P2 Secondary Vectors CFD Prediction.

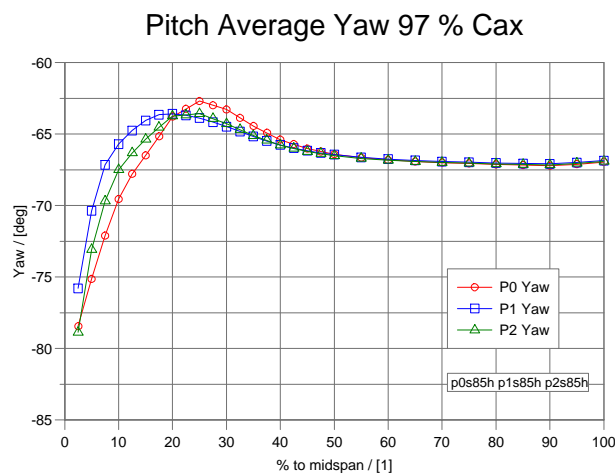


Figure 7.65: Slot 8 Pitch Averaged Yaw Angle CFD Prediction.

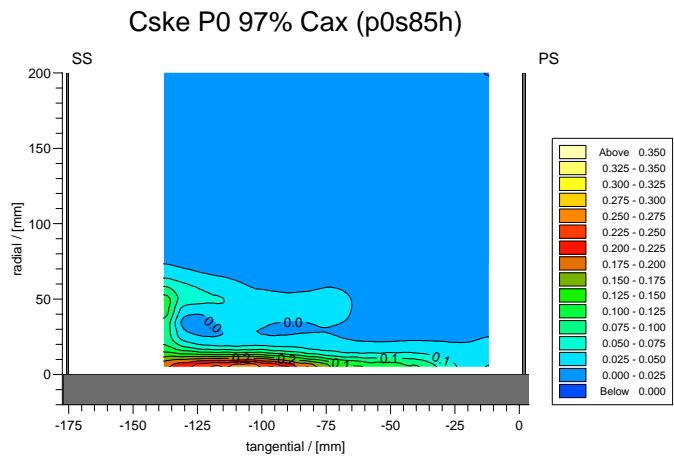


Figure 7.66: Slot 8 P0 C_{ske} CFD Prediction

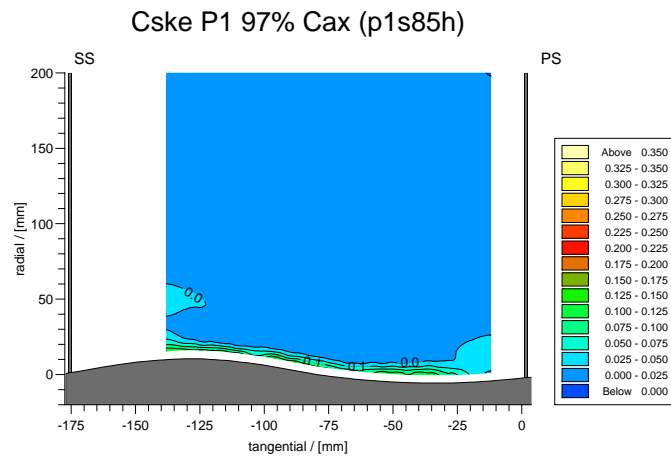


Figure 7.67: Slot 8 P1 C_{ske} CFD Prediction

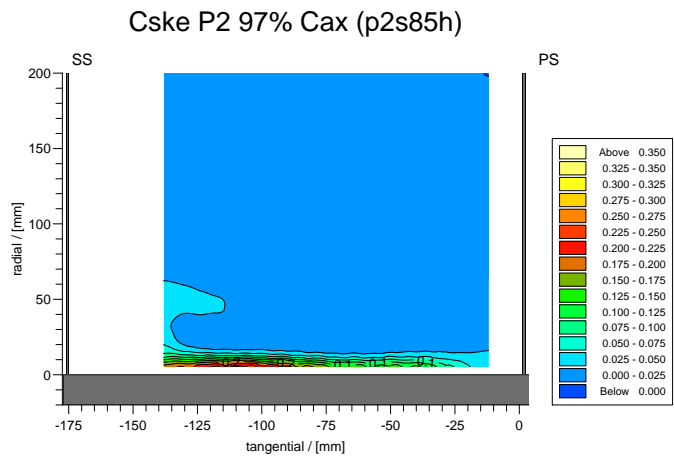


Figure 7.68: Slot 8 P2 C_{ske} CFD Prediction

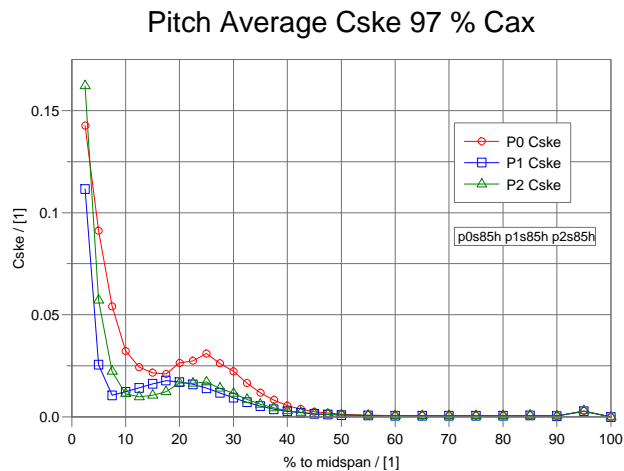


Figure 7.69: Slot 8 Pitch Averaged C_{ske} CFD Prediction

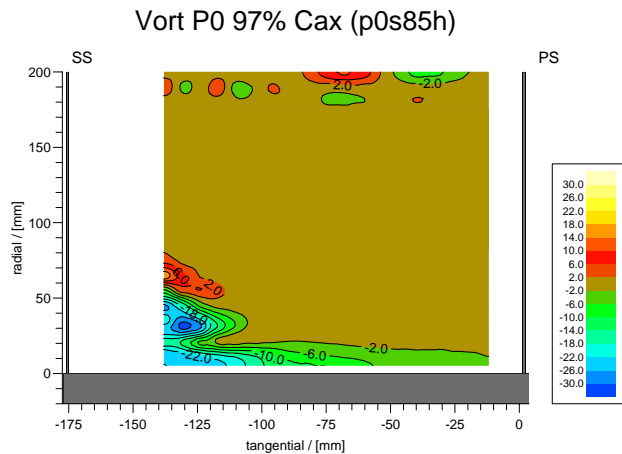


Figure 7.70: Slot 8 P0 Streamwise Vorticity Coefficient CFD Prediction

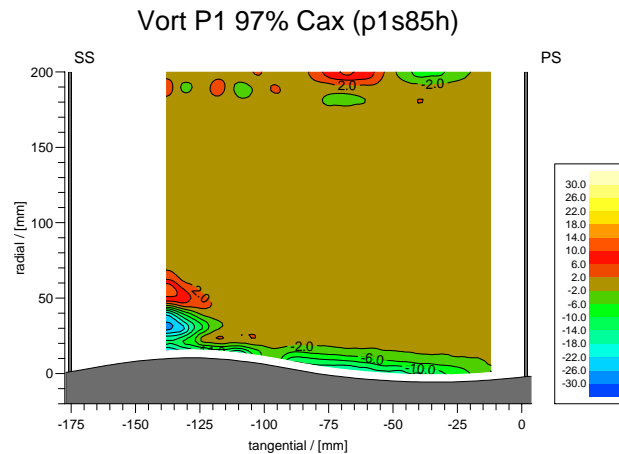


Figure 7.71: Slot 8 P1 Streamwise Vorticity Coefficient CFD Prediction

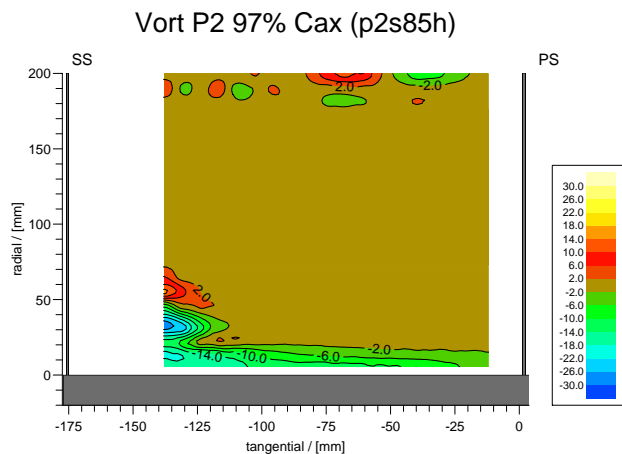


Figure 7.72: Slot 8 P2 Streamwise Vorticity Coefficient CFD Prediction

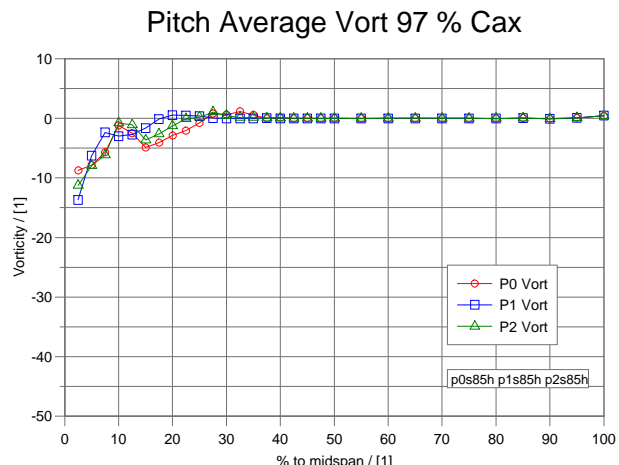


Figure 7.73: Slot 8 Pitch Averaged Vorticity Flow CFD Prediction

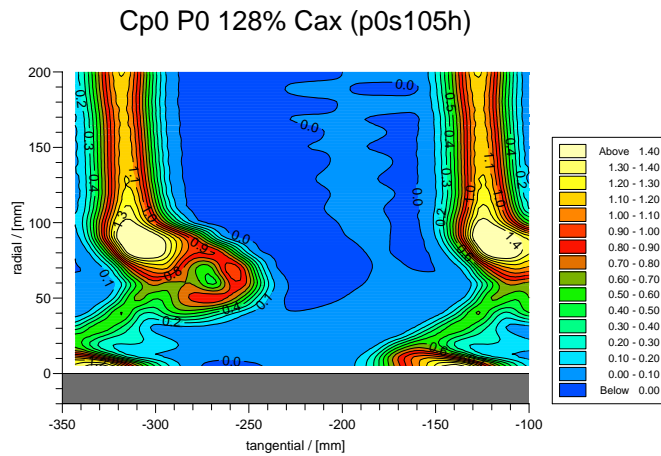


Figure 7.74: Slot 10 P0 Loss CFD Prediction.

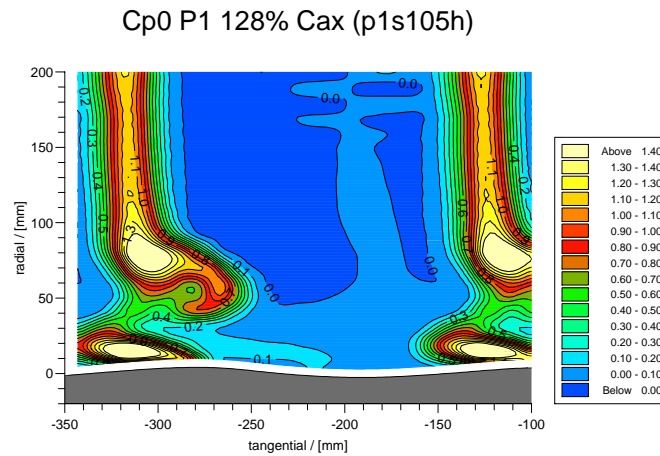


Figure 7.75: Slot 10 P1 Loss CFD Prediction.

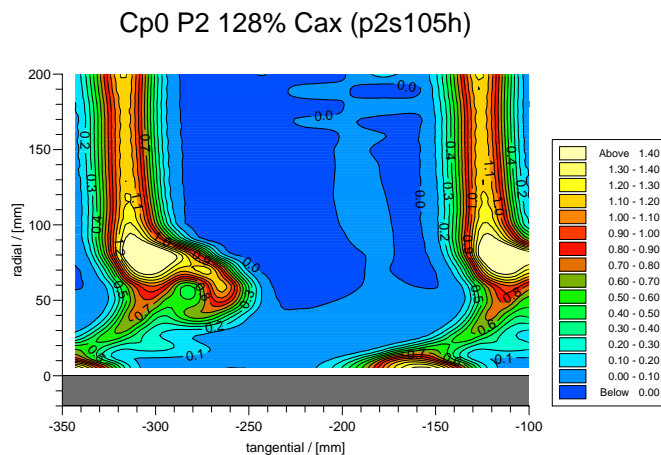


Figure 7.76: Slot 10 P2 Loss CFD Prediction.

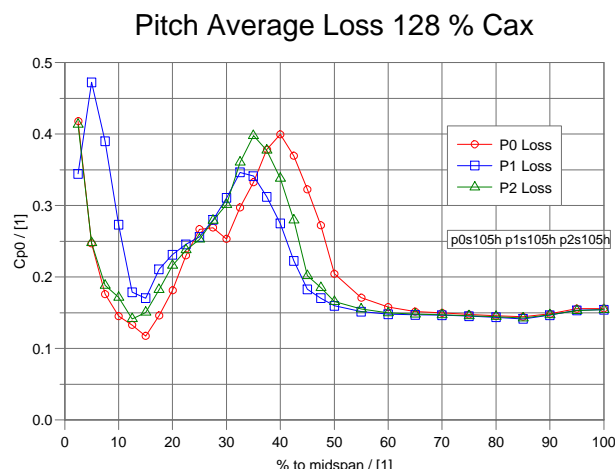


Figure 7.77: Slot 10 Pitch Averaged Loss CFD Prediction.

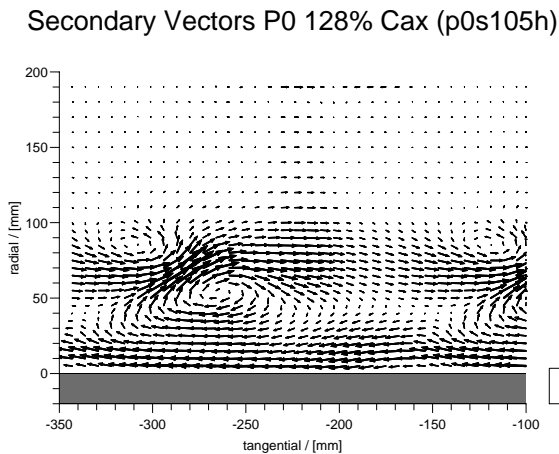


Figure 7.78: Slot 10 P0 Secondary Vectors CFD Prediction.

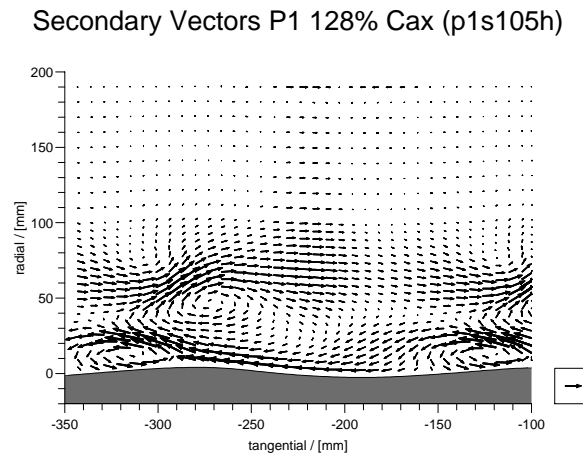


Figure 7.79: Slot 10 P1 Secondary Vectors CFD Prediction.

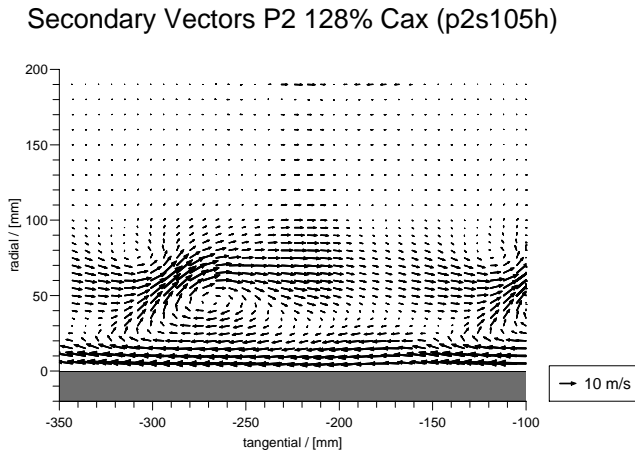


Figure 7.80: Slot 10 P2 Secondary Vectors CFD Prediction.

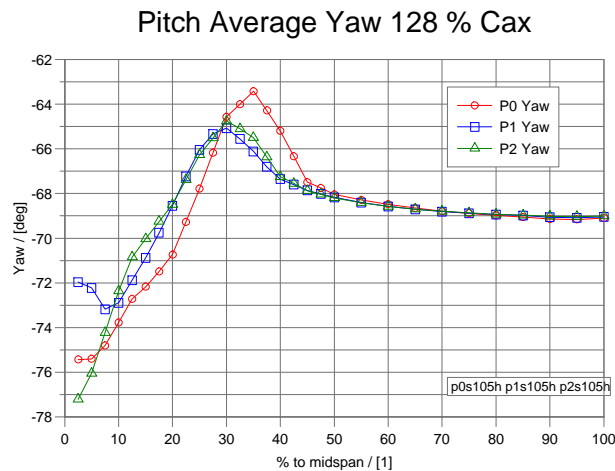


Figure 7.81: Slot 10 Pitch Averaged Yaw Angle CFD Prediction.

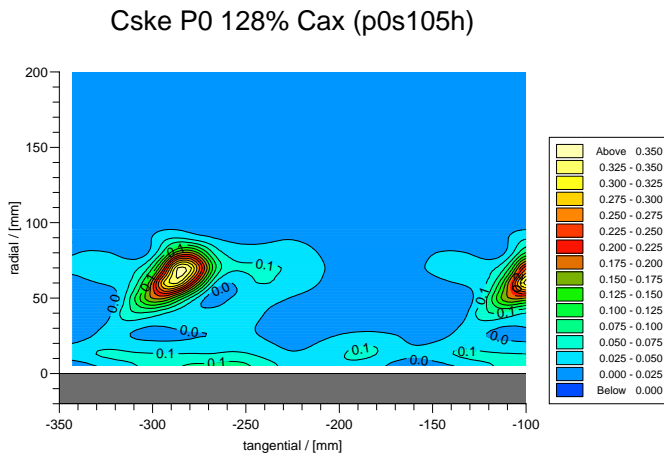


Figure 7.82: Slot 10 P0 C_{skc} CFD Prediction

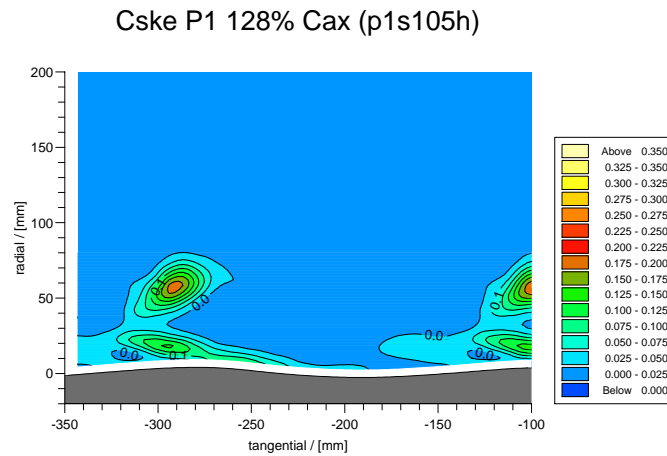


Figure 7.83: Slot 10 P1 C_{skc} CFD Prediction

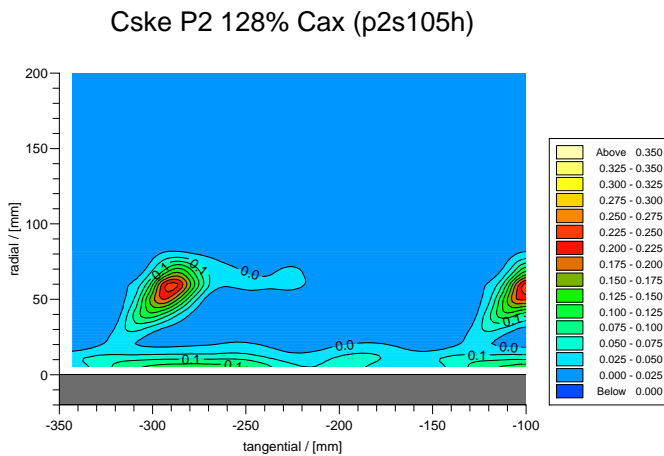


Figure 7.84: Slot 10 P2 C_{skc} CFD Prediction

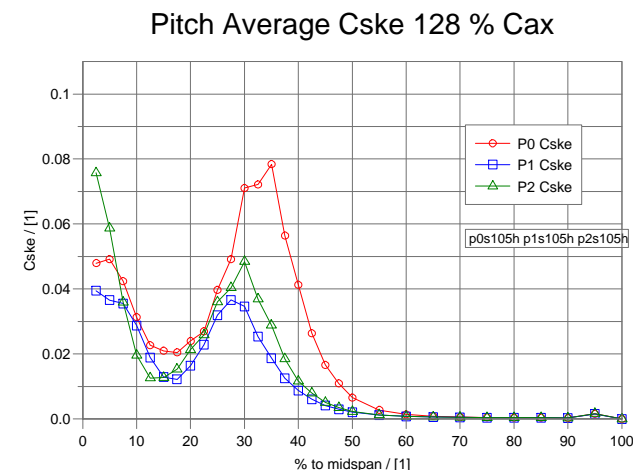


Figure 7.85: Slot 10 Pitch Averaged C_{skc} CFD Prediction

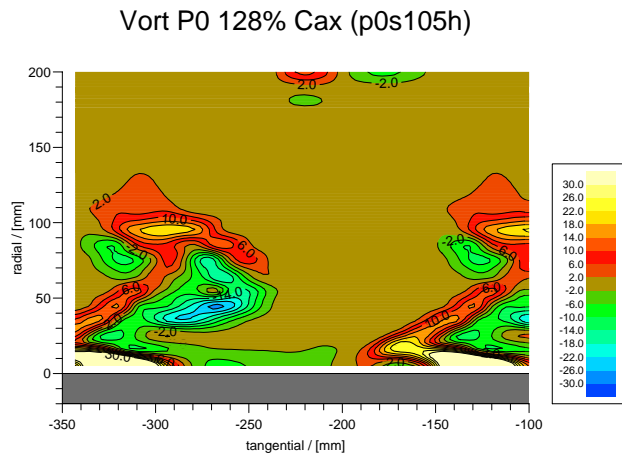


Figure 7.86: Slot 10 P0 Streamwise Vorticity Coefficient CFD Prediction

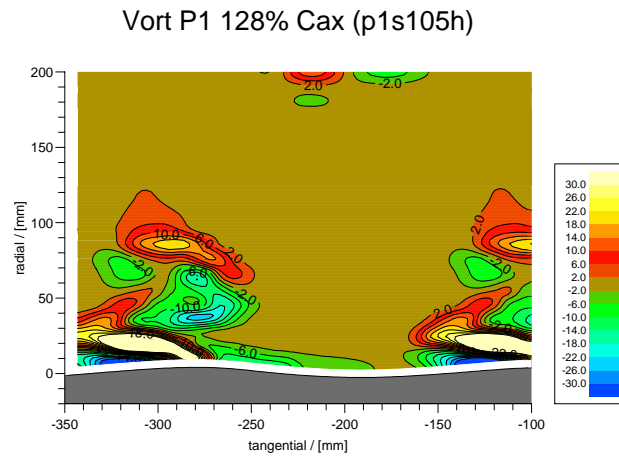


Figure 7.87: Slot 10 P1 Streamwise Vorticity Coefficient CFD Prediction

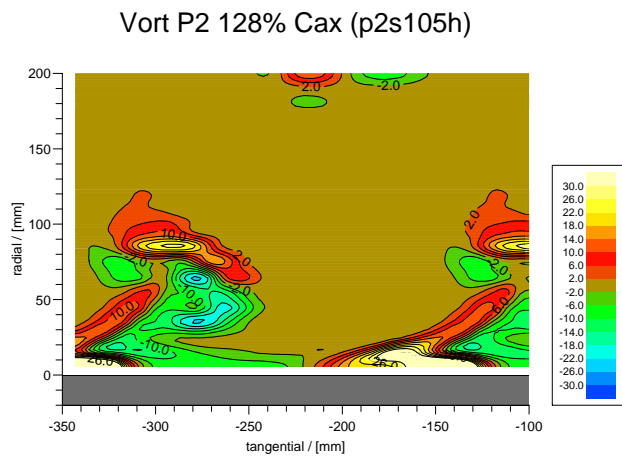


Figure 7.88: Slot 10 P2 Streamwise Vorticity Coefficient CFD Prediction

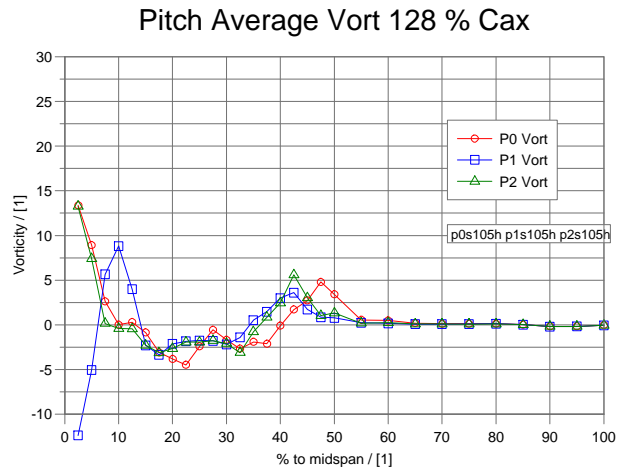


Figure 7.89: Slot 10 Pitch Averaged Vorticity Flow CFD Prediction

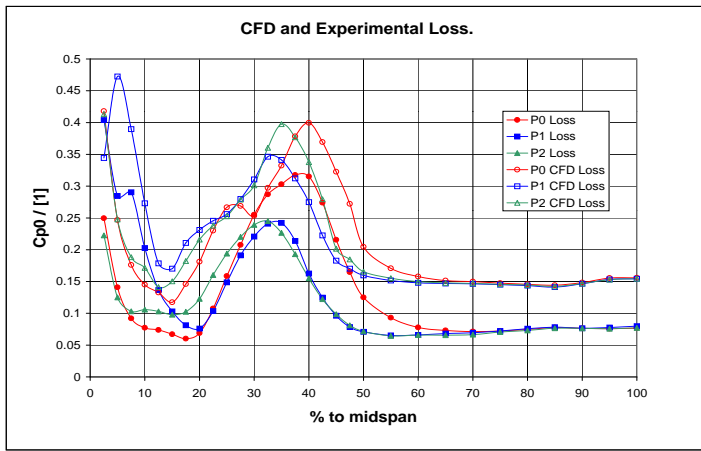


Figure 7.90: Experimental and CFD Pitch Averaged Loss at Slot 10.

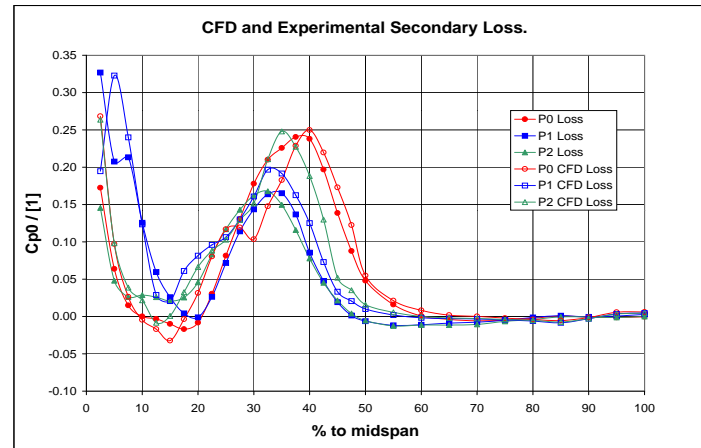


Figure 7.91: Experimental and CFD Secondary Loss.

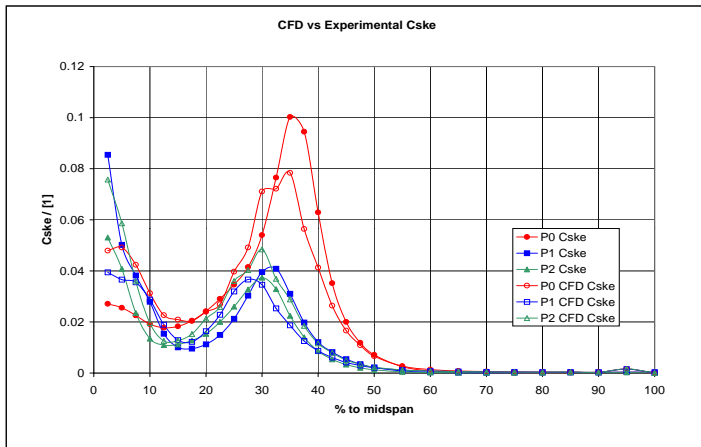


Figure 7.92: Experimental and CFD Pitch Averaged C_{ske} at Slot 10.

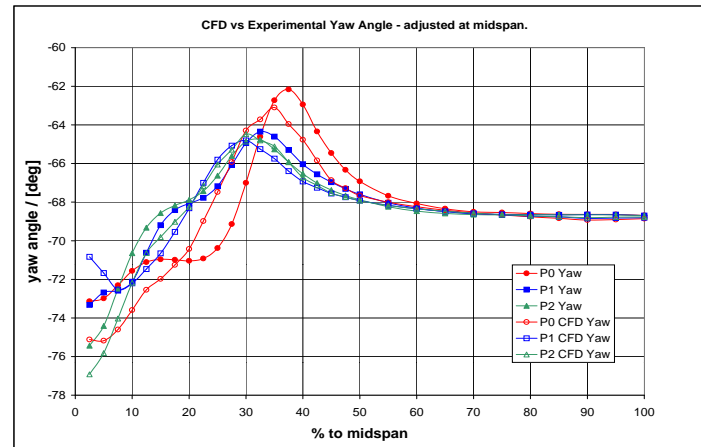


Figure 7.93: Experimental and CFD Pitch Averaged Yaw at Slot 10

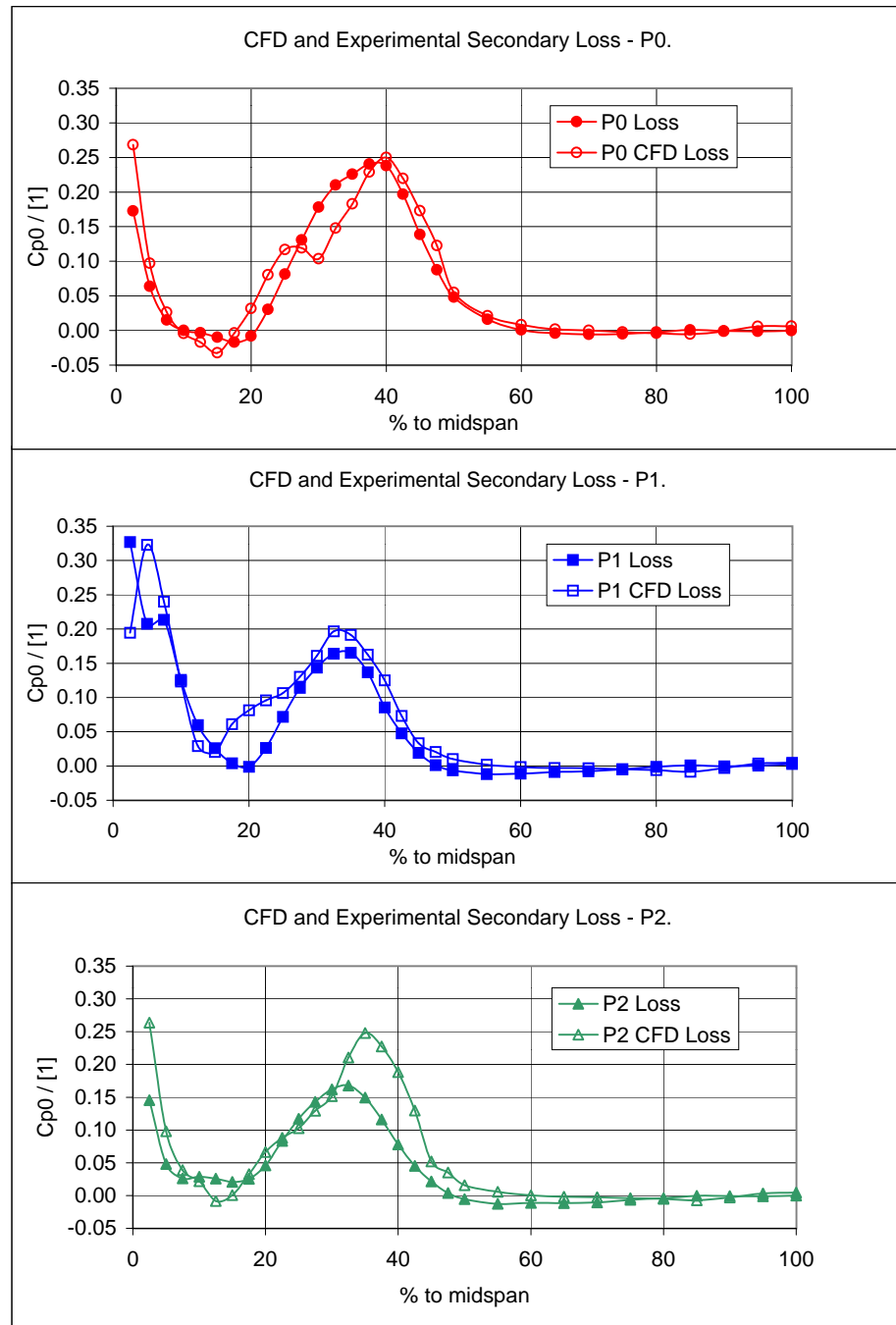


Figure 7.94: CFD and Experimental Pitch Averaged Loss at Slot 10 - comparison by profile.

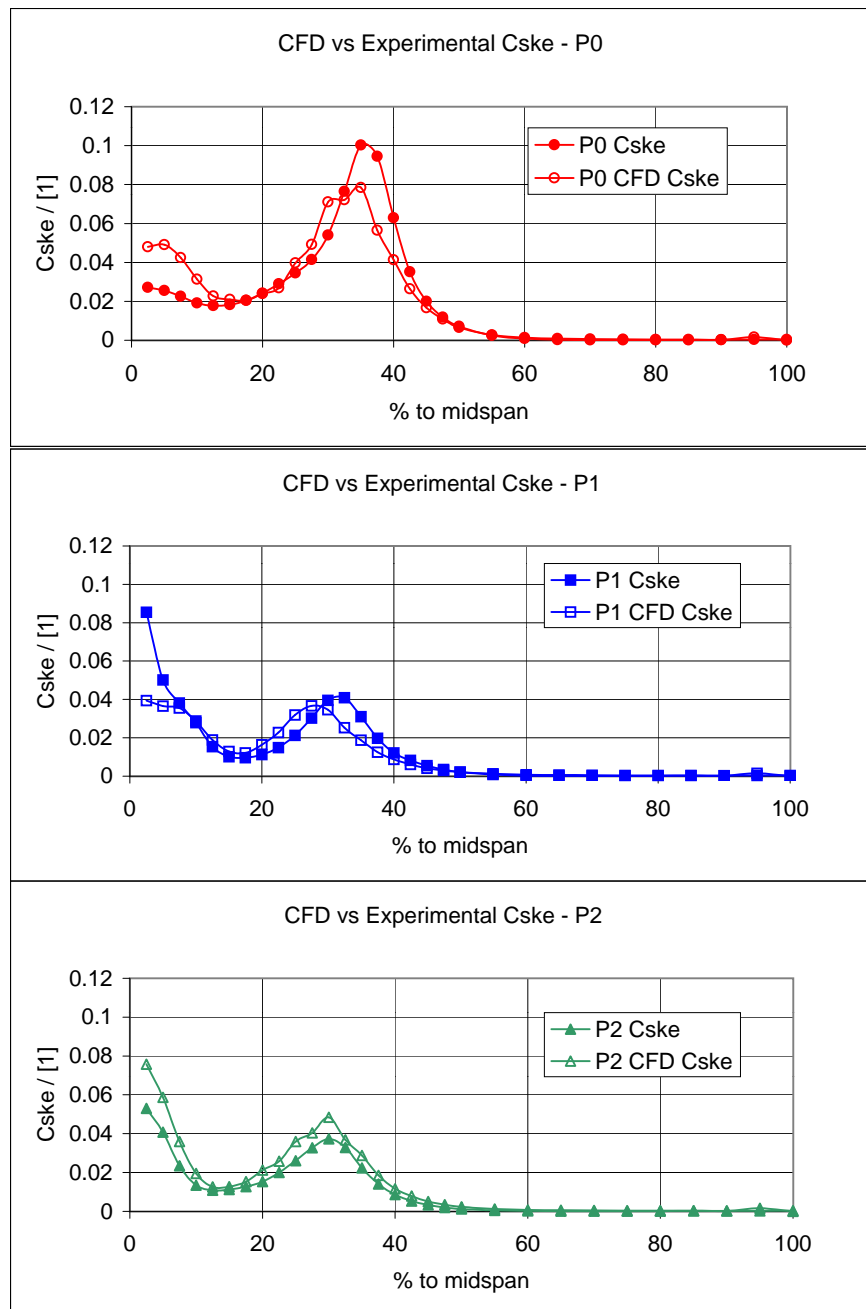


Figure 7.95: CFD and Experimental Pitch Averaged C_{ske} at Slot 10 - comparison by profile.

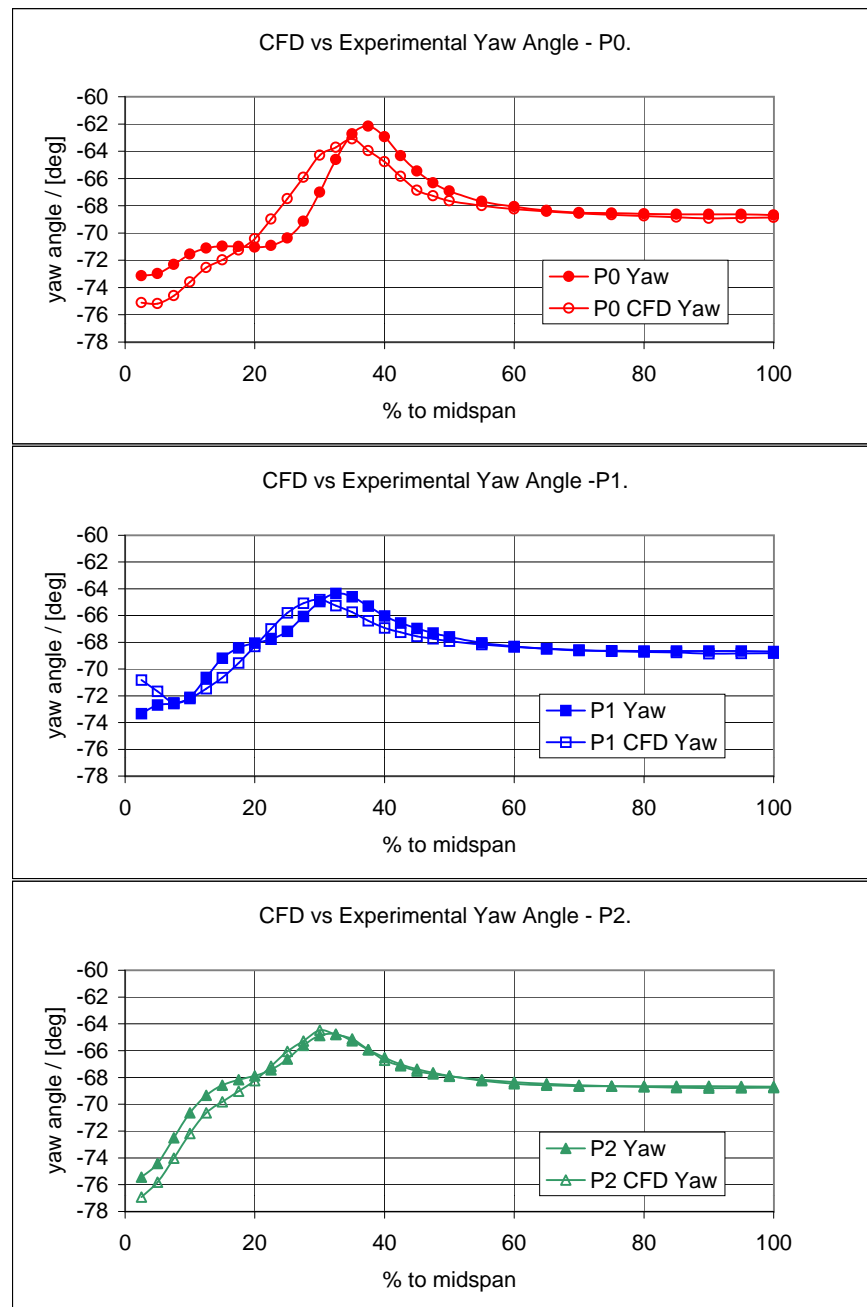


Figure 7.96: CFD and Experimental Pitch Averaged Yaw Angle at Slot 10 - comparison by profile.

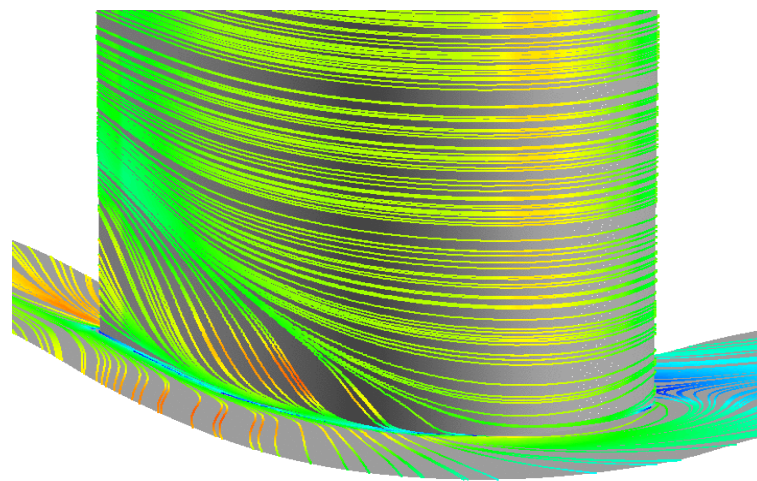


Figure 7.97: CFD Endwall Flow Suction Surface P0.

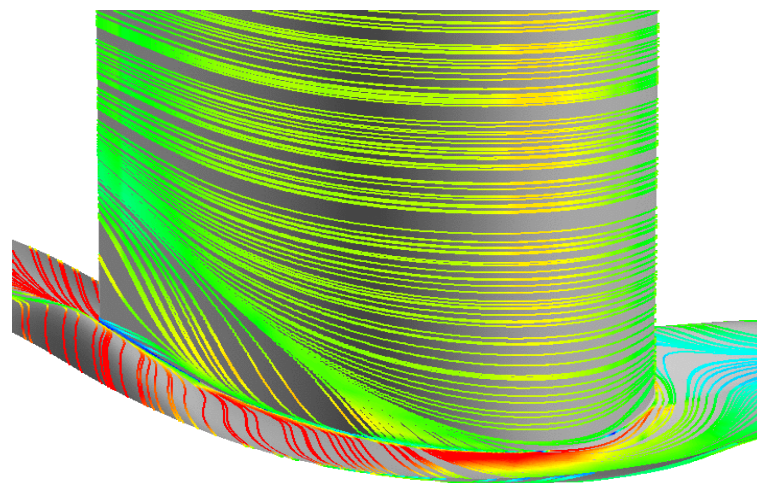


Figure 7.98: CFD Endwall Flow Suction Surface P1.

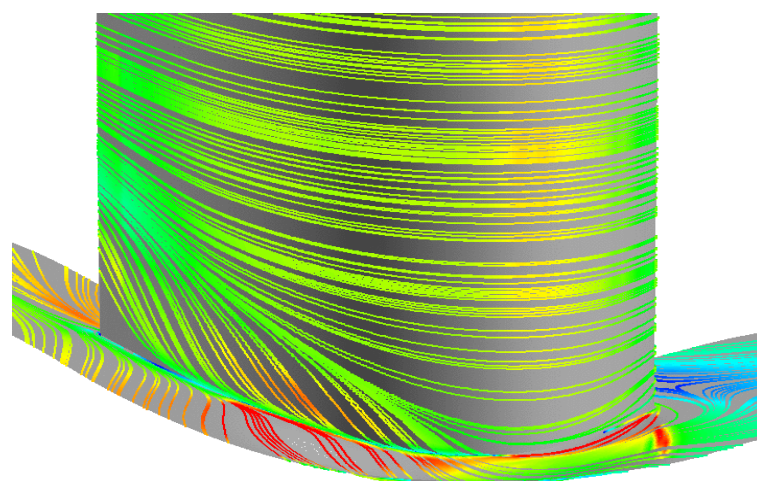


Figure 7.99: CFD Endwall Flow Suction Surface P2.

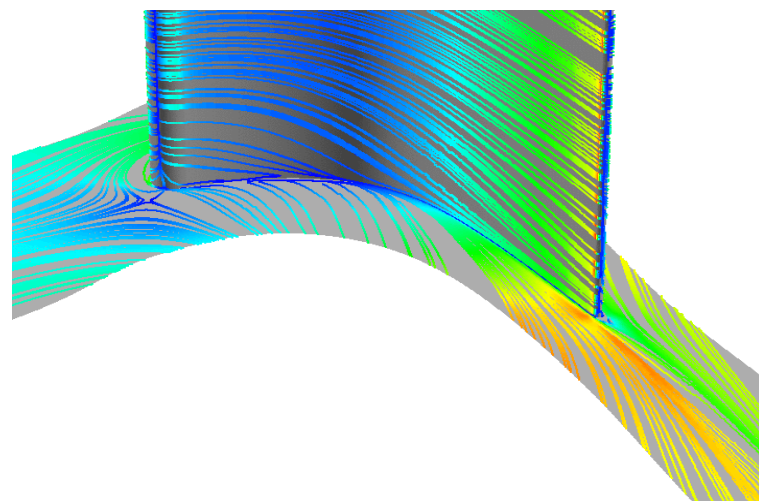


Figure 7.100: CFD Endwall Flow Pressure Surface P0.

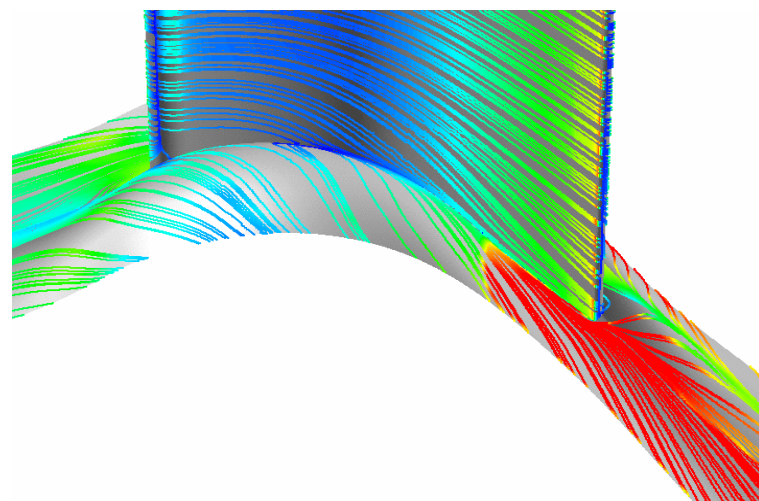


Figure 7.101: CFD Endwall Flow Pressure Surface P1.

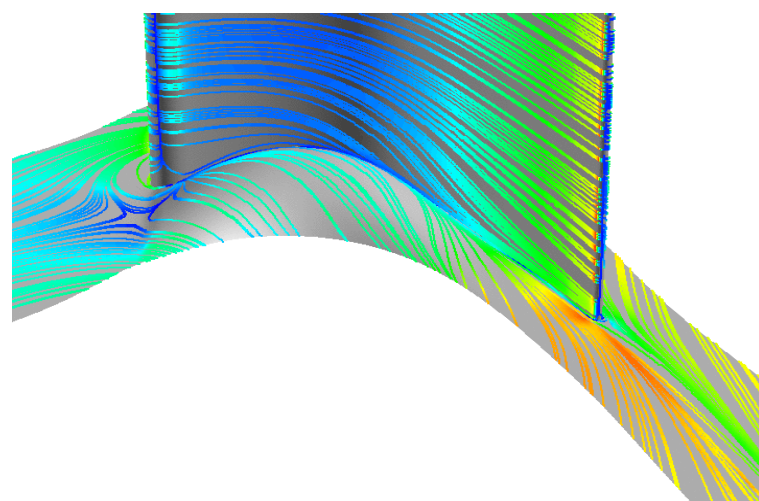


Figure 7.102: CFD Endwall Flow Pressure Surface P2.

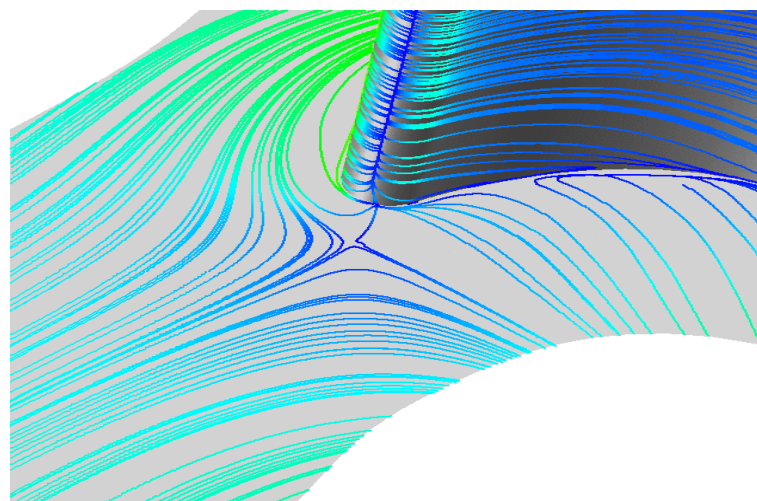


Figure 7.103: CFD Saddle Point P0.

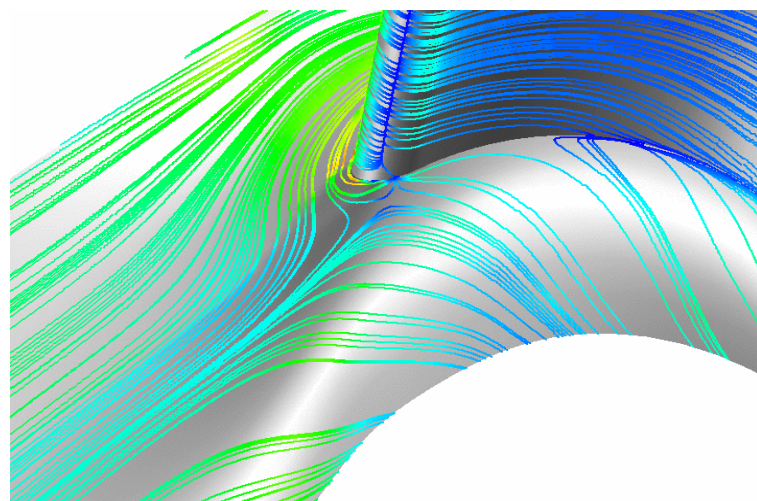


Figure 7.104: CFD Saddle Point P1.

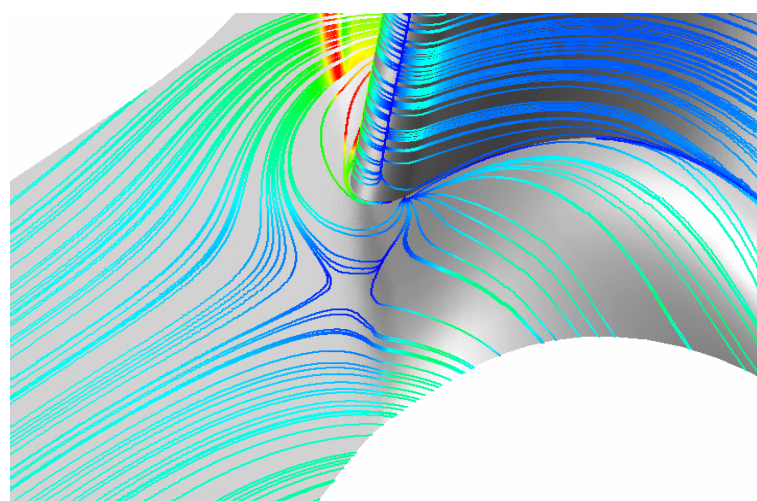


Figure 7.105: CFD Saddle Point P2.

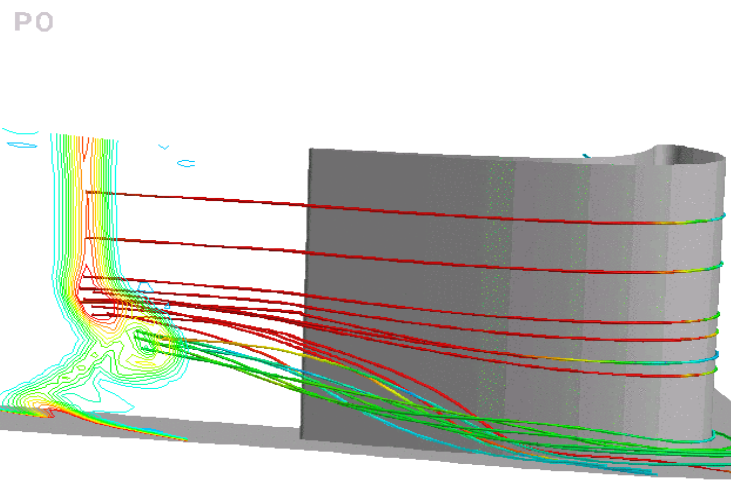


Figure 7.106: CFD Streamlines associated with loss cores P0.

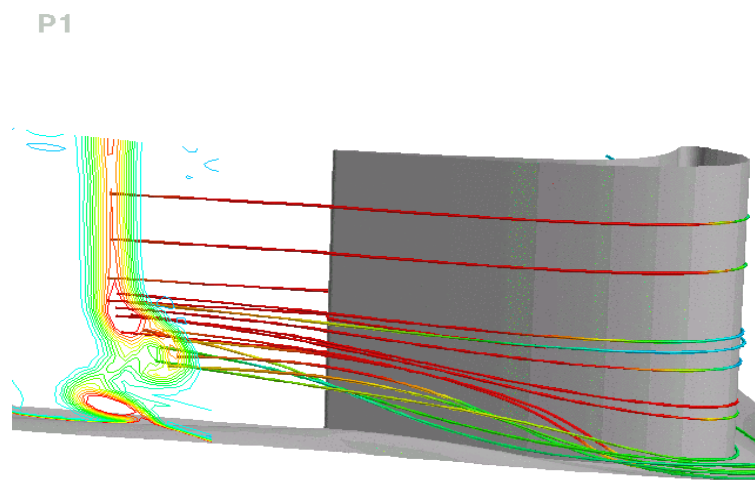


Figure 7.107: CFD Streamlines associated with loss cores P1.

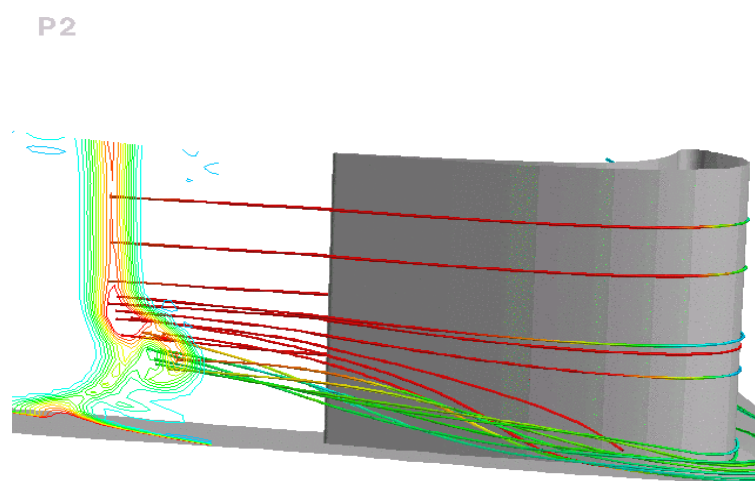


Figure 7.108: CFD Streamlines associated with loss cores P2

Chapter 8

Third Generation Endwall

THIS CHAPTER details the testing of a third generation endwall. This endwall was designed at Rolls-Royce, Derby using a revised version of their design system used to design P1 and P2. The profile was then manufactured and tested at Durham. The profile aimed to get the maximum possible benefit from endwall profiling in terms of loss reduction. Previous profiles were designed on the basis of reducing exit angle deviations with the hope of reducing secondary loss as a result, but P3 was designed from the start with the intention of reducing loss and the exit angles were left to “come out in the wash”. CFD does not predict loss so another parameter based on secondary kinetic energy was used as the design variable, this approach is outlined in Brennan et al. (2001).

The geometry of the endwalls is shown in Figure A.3 on page 287. The manufacture is described in some detail in a separate report (Ingram, 2003). The reader who is attempting to manufacture their own profiled endwalls is encouraged to refer to it. Ingram (2003) contains enough detail to allow the manufacturing process to be repeated with the minimum of effort. Testing follows exactly the methodologies described in the earlier chapters.

In order to meet project requirements for rapid progress a few items were dealt with less attention to detail than desired. The panels were not painted with high contrast paint so the flow visualisation is less effective, the photography for the flow visualisation leaves something to be desired and there was only time to carry out one traverse at each slot. Despite this the author believes that the results contained within this chapter give accurate enough information to judge the performance of the third generation endwall.

8.1 Pressure Probe Measurement

Pressure probe readings with a five hole probe were taken at three slot locations, pressure probe readings with a three hole probe were taken at two locations. Table 8.1 shows the details. The pressure probe readings are conventional pressure probe readings that have been described in Chapter 3. The only point to be made is that although “back to back” tests have been conducted the readings have not been repeated three times and then averaged - only one reading was taken.

The layout of figures in this chapter is slightly different from previous chapters as

Slot No.	% C_{ax}	x/mm (from t.e.)	5H Readings	3H Readings
4	38%	-112	No	Yes
6	71%	-52	Yes	No
8	97%	-5	Yes	No
10	128%	51	Yes	Yes

Table 8.1: Axial Measurement Planes for the Third Generation Endwall

there are only two endwalls to compare (P0 and P3) as opposed to three in previous chapters. Contour plots of loss, C_{ske} , C_Ω and secondary vector plots are included in order of increasing slot number, i.e. from upstream to downstream. Pitch averaged graphs are grouped by axial location and are included after the contour and vector plots.

8.1.1 Validation

Before the readings described here the probe was calibrated and a “hand test” conducted on the system to check for errors. In fact this was done four times as each set of readings was taken. The order was as follows:

1. Five hole probe results were taken at Slots 10, 8 and 6
2. Three hole probe readings were then at Slot 4 to examine the flow near the endwall highlighted by flow visualisation
3. Three hole probe readings were taken at Slot 10
4. Some readings at Slot 10 were repeated with a five hole probe.

The results for the before and after “hand test” for the first set of five hole probe readings are included. In Figures 8.3 to 8.5 the errors before any readings were taken are shown. These results compare well to those from previous chapters and are acceptable. Figures 8.6 to 8.8 show the errors after the first set of five hole probe readings were taken. This allows a check to be made for probe damage, leaks etc that might have been introduced into the system during testing. The results are again acceptable. The large errors found in the corner of the calibration map were discussed in an earlier chapter - in practice the “corners” of the calibration map are never used. This indicates that there was no deterioration in the condition of the measuring system during the tests. Similar results were obtained for the three hole probe and for the other sets of measurements on the third generation endwall, these are not included in the thesis but indicated acceptable accuracy.

For each of the axial measurement planes a planar reference case reading was taken using the “back to back” methodology. This can then be compared to previous planar readings at the same location to give some idea of repeatability and changes between previous data sets. The current set of readings compare well at Slot 10 with previous readings, though not so well for Slot 8 or Slot 6. This is not that surprising as the original planar Slot 8 and Slot 6 readings were taken with a different probe and a much less sophisticated version of the measuring system.

	avp05h	trv100	difference	error
Secondary C_{P0}	0.0558	0.0600	0.0042	± 0.004

Table 8.2: P0 Repeatability Secondary Loss Coefficient

Case	Massflow / [kg/s]	% Difference
Planar	0.5913	-
P3	0.5934	0.4

Table 8.3: Area Averaged Massflow

Figure 8.9 shows the pitch averaged loss for P0 compared to previous five hole readings and Figure 8.10 shows the pitch averaged yaw angle for P0 compared to previous five hole probe readings. The changes in the loss and yaw angle are small and are certainly smaller than those found between the new endwall (P3) and the planar case - giving confidence in the results. The agreement between area averaged values is also encouraging. Table 8.2 shows the secondary loss coefficient for the best five hole probe reading from Chapter 5 and the P0 traverse conducted at the same time as the P3 readings. The error estimate from Chapter 5 of ± 0.004 appears to be a little low since the difference between the best five hole probe loss reading in Chapter 5 and the current loss reading is 0.0042.

One concern was that the new profile with more extreme curvature throughout the passage would be harder to seal with the blade ends etc. and a tip-leakage effect or external leakage effect would result. This can be checked by reference to the flow visualisation which shows no evidence of any leakage effect. Furthermore a comparison of the planar and the P3 massflow shows results within 0.4% of each other (See Table 8.3). This is encouragingly close.

The reader may notice that the location of the five hole probe Slot 10 results do not match up precisely to the endwall curvature (e.g. Figure 8.29). This was due to an error in calculating the grid for the Slot 10 traverse. Given that the curvature of the endwall is very small at that axial plane ($\pm 1.5\text{mm}$) this error was not expected to affect the results significantly. This was confirmed by a later traverse at Slot 10 with a five hole probe and the correct grid which showed virtually identical results.

8.1.2 Slot 6 (71% C_{ax})

Contour plots of loss for P0 and P3 are found in Figures 8.11 and 8.12 respectively. Secondary vectors are shown in Figures 8.13 and 8.14 for P0 and P3. C_{ske} is shown in Figures 8.15 and 8.16. Note that this is the “classic” definition which means that there is no compensation made for the inviscid effects introduced by the endwall profiling. Contours of C_Ω are shown in Figures 8.17 and 8.18 for P0 and P3 respectively.

An examination of the contour and vector plots reveals the following key points:-

- The loss core for P3 (Figure 8.12) is smaller but of much greater intensity than for P0 (Figure 8.11).
- The P3 loss core (Figure 8.12) is further from the endwall than in the planar

case (Figure 8.11).

- The secondary flows are much smaller for P3 than for the planar case, i.e. the secondary vectors (Figure 8.13 for P0 and Figure 8.14 for P3) show a smaller vortex and the C_{ske} plots (Figure 8.15 for P0 and Figure 8.16 for P3) show less secondary kinetic energy. This is in contrast to Slot 8 (downstream) where the passage vortex covers a greater area for P3 than for the planar area.
- The vorticity plots show a region of positive vorticity above the passage vortex on P3 (Figure 8.18). This region is also present in the planar case (Figure 8.17) but is much smaller.

8.1.3 Slot 8 (97% C_{ax})

Contour plots of C_{P0} for P0 and P3 are found in Figures 8.19 and 8.20 respectively. Secondary vectors are shown in Figures 8.21 and 8.22 for P0 and P3. C_{ske} is shown in Figures 8.23 and 8.24 and contours of C_Ω are shown in Figures 8.25 and 8.26 for P0 and P3 respectively.

The following comments are made:-

- The loss core for P3 (Figure 8.20) is smaller in area but much higher in intensity than the planar case (Figure 8.19).
- The traverse does not extend to the blade surfaces so some interesting details are lost. It is not apparent from the plots whether the higher intensity of the P3 loss core (Figure 8.20) extends all the way to the endwall or if there is a reduction in C_{P0} towards the endwall.
- The secondary vectors (Figure 8.21 for P0 and Figure 8.22 for P3) and the C_{ske} plots (Figure 8.23 for P0 and Figure 8.24 for P3) show that the secondary flow “dynamics” for P0 and P3 are much closer to each other at Slot 8 than they are at Slot 10 (downstream).
- The P3 case appears to have less over turning at the endwall than the planar case. This can be seen in the vector plots (Figures 8.21 and 8.22) and in the C_{ske} (Figure 8.23 for P0 and Figure 8.24 for P3) contours.
- The profiled passage vortex (Figure 8.22) appears to be larger but less intense than the planar case (Figure 8.21). The actual vortex centres appear in the same place but the large amplitude of profiling at this axial location for P3 means that the vortex covers a larger area, since the vortex extends to the endwall in both cases.
- The vorticity plots (Figures 8.25 and 8.26) confirm the comments about vortex core strength and C_{ske} distribution.

8.1.4 Five Hole Probe Readings at Slot 10 (128% C_{ax})

Contour plots of C_{p0} are provided in Figure 8.27 and Figure 8.28 for P0 and P3 respectively. Secondary Vectors are found in Figure 8.29 (Planar) and Figure 8.30 (P3). Secondary kinetic energy coefficient is plotted in Figures 8.31 and 8.32 for P0 and P3. Finally streamwise vorticity coefficient is plotted in Figures 8.33 and 8.34.

The following comments are made:-

- The loss core strength associated with the passage vortex at Slot 10 is much larger for the P3 case (Figure 8.28) than the P0 case (Figure 8.27). The loss core associated with the shed vorticity/suction side of the horseshoe vortex is also larger.
- The loss core associated with the corner vortex is in a different place for the planar case (Figure 8.27) and the P3 case (Figure 8.28). For the planar case it is located at $t=-290\text{mm}$ and $r=5\text{mm}$, for P3 it is located at $t=-170$ and $r=5\text{mm}$. The loss core for this vortex has moved across towards the suction surface for at least half a pitch. This loss core is also much more spread out in the tangential plane rather than concentrated as for the planar case.
- The secondary vectors (Figure 8.29 for P0 and Figure 8.30 for P3) and the C_{ske} measurements (Figure 8.31 for P0 and Figure 8.32 for P3) show a reduction in the strength of the secondary flow - but this is not accompanied by a reduction in loss. Close to the endwall the secondary flows are much larger but this was expected from the design.
- The Streamwise Vorticity plots (Figure 8.33 for P0 and Figure 8.34 for P3) confirm the reduction in secondary flow.
- The loss cores (Figures 8.27 and 8.28) and the vortex cores (Figures 8.29 and 8.30) appear to be at the same radial height. This can be compared to the P1/P2 profiles which keep the loss core closer to the endwall than the vortex core.

8.1.5 Three Hole Probe Readings at Slot 4 (38% C_{ax})

Following flow visualisation work, a three hole probe traverse was taken at Slot 4 to examine the flow downstream of a flow feature of interest (See Section 8.2). Area plots of loss are found in Figures 8.35 (P0) and 8.36 (P3). Secondary Vectors are found in Figures 8.37 for P0 and 8.38 for P3. Note that this is “pseudo” secondary flow as it includes no pitch information at all - this is important at this slot as the curvature for P3 is very high in this region. The large turning found at Slot 4 means that some of the data points are out of range of the probe - the data processing simply clips to the maximum value relative to the probe (42°) - so the readings are an under estimate of the secondary flow.

The close wall results at Slot 4 (38% C_{ax}) show a large area of loss concentrated in the bottom left hand corner of the plot (Figure 8.36). This is downstream of a region of quite sharp curvature on the endwall. This is indicative of some sort of loss producing flow feature upstream of this point. The secondary flow plots (Figures 8.37

and 8.38) do not indicate a radical difference in flow between the planar and the P3 case, but there is no pitch information and the curvature of the endwall is very sharp at this axial plane. For the planar case the secondary velocities increase towards the endwall but for the P3 case on the suction side of the traverse the opposite is true, this may be due to the low energy fluid associated with a separation staying close to the endwall. However as can be seen from the flow visualisation (see Section 8.2) the phenomenon upstream of Slot 4 is quite complex and no firm conclusions can be drawn from the “puesdo” secondary flow, though the loss readings provide clear evidence of strong loss production on the endwall upstream of Slot 4.

8.1.6 Three Hole Probe Readings at Slot 10 (128% C_{ax})

Three hole probe readings for Slot 10 were taken to examine the close to the endwall and provide a comprehensive value of the area averaged loss value. Area plots of loss are found in Figures 8.39 for P0 and 8.40 for P3. Secondary Vectors are found in Figures 8.41 for P0 and 8.42 for P3. Once again this “puesdo” secondary flow as it includes no pitch information at all.

The following key points are extracted from the close wall readings at Slot 10:-

- The close wall readings show that the flow near the endwall is significantly different from the planar case, the loss core is much more uniform with only one noticeable peak which is located at mid-pitch rather than associated with a blade wake (Figure 8.39 for P0 and 8.40 for P3) . This supports the findings from the five hole probe traverse.
- It is not obvious from the contour plots of C_{P0} whether the P3 or the planar case has the greatest loss, this can only be determined by reference to the pitch averaged plots.
- The secondary vectors (Figure 8.41 for P0 and 8.42 for P3) show the expected counter vortex for P0, but for P3 the counter vortex structure is evident only in reduced overturning at the endwall and is mid-pitch rather than associated with the suction side blade wake. (P0 corner vortex is at $t=-290\text{mm}$, the P3 corner vortex is at $t=-200\text{mm}$). The single loss peak that is seen in the loss plots appears at $t=-190\text{mm}$.
- The secondary vector plots (Figure 8.41 for P0 and 8.42 for P3) show increased overturning at the endwall for P3 as expected.

8.1.7 Pitch Averaged Results

The pitch averaged results are collated together by slot.¹ Pitch averaged plots of loss coefficient, yaw angle, secondary kinetic energy coefficient and streamwise vorticity are provided.

¹A list of symbols used for pitch averaged graphs may be found on page xxvi

Slot 6 (71% C_{ax})

For Slot 6 (71% C_{ax}) loss is shown in Figure 8.43, yaw angle in Figure 8.44, C_{ske} in Figure 8.45 and C_Ω in Figure 8.46.

For Slot 6 the earlier remarks regards loss core size and position are confirmed (See Figure 8.43). Notably for Slot 6 the overall loss for the P3 endwall is actually greater although the peak intensity of the loss is much less, as it is spread over a greater area - this is not obvious from the pitch averaged graph. The Yaw angle plot (Figure 8.44) shows that the P3 profiling improves the under turning situation slightly although perhaps not as well as previous endwalls. The C_{ske} pitch averaged plot (Figure 8.45) shows a reduced level of C_{ske} for P3. Streamwise vorticity (Figure 8.46) illustrates a change in flow structure between P3 and P0, for P3 there is a double dip in the value as the endwall is approached, for P0 it is a single change. This is because for P0 there is a single continuous area of negative vorticity for P0 (Figure 8.17) whereas for P3 there is a distinct peak (Figure 8.18). Physically this is due to the reduced over turning for P3 at Slot 6 compared to the planar case.

Slot 8 (97% C_{ax})

For Slot 8 (97% C_{ax}) loss is shown in Figure 8.47, yaw angle in Figure 8.48, C_{ske} in Figure 8.49 and C_Ω in Figure 8.50.

The loss core for the P3 case has a greater intensity (at 30% of span) than P0, but is spread over a smaller area (See Figure 8.47). It is not obvious from the plot which case has the larger loss, this has to be determined from area averaged values (See Section 8.1.8). The yaw angle plot (Figure 8.48) shows that at Slot 8 (97% C_{ax}) the under turning is reduced by some 1.8° . The over turning is also significantly reduced by around 4° . The C_{ske} plot (Figure 8.49) shows that the P3 values are well below the planar value. The pattern of the flow is the same for both endwalls with two peaks the outer one at 25-30% span is associated with the passage vortex and the inner one is associated with the over turning at the endwall. The profiling for P3 appears to have reduced the peak associated with the passage vortex less than that associated with the over turning. The vorticity plot (Figure 8.50) shows that the flow patterns are again similar.

Slot 10 (128% C_{ax})

For Slot 10 (128% C_{ax}) loss is shown in Figure 8.51, yaw angle in Figure 8.52, C_{ske} in Figure 8.53 and C_Ω in Figure 8.54. Also shown in the figures are the corresponding values for P1 and P2 to allow an assessment of the differing performance of different endwalls.

Examining the Slot 10 (128% C_{ax}) figures the following comments are made:-

- The pitch averaged loss shows clearly the larger passage vortex for P3 compared to the other profiled cases, though it is not immediately clear the loss core is actually larger than the planar case. The loss close to the endwall (less than 10% span) for the P3 case is comparable to the P1 profile.
- The midspan agreement for loss between different profiles is very good. The data processing applies an offset to the data to try to ensure that it matches

Endwall	Peak under turning	Peak over turning
P0	-62.0°	-71.5°
P1	-64.5°	-72.0°
P2	-64.7°	-75.5°
P3	-64.0°	-76.5°

Table 8.4: Peak Turning (estimate from Figure 5.110).

at midspan. However the minor variations in midspan loss from 80%-100% span are identical between endwalls.

- The reduction in under turning is not as great as the other endwalls but it is very close to P1. See Table 8.4. Over turning is increased relative to the planar case and is comparable to the P2 profile.
- Although there is a C_{ske} reduction it is not as great for P3 as it is for P1 and P2. This is different from the design intent.
- The streamwise vorticity coefficient shows similar flow patterns for all endwalls, with a large peak near the endwall associated with P1 and P3. For the P1 case this is due to the enhanced corner vortex. For P3 case this also appears to be due to the enhanced corner vortex. The close wall plots above (See Figure 8.40) shown the corner vortex in a very different position from that normally found in cascade flows.

Pitch Averaged Three Hole Probe Results

Pitch averaged loss for Slot 4 is illustrated in Figure 8.55, this plot was taken with a three hole probe and extends further than “normal” three hole probe traverses as there is no corresponding five hole probe traverse available for P3 at this slot. The loss plot clearly shows the increased loss for P3 compared to P0. The last point for P3 at a nominal 0% span shows a slightly reduced loss compared to points at 0.5 and 1%, this could be due to the loss feature being convected away from the wall for P3 and being associated with boundary layer loss for P0. Figure 8.56 shows the pitch averaged yaw angle. There is a 50° change in yaw angle from midspan to endwall with the turning for P3 being somewhat less than that for P0.

Pitch averaged C_{P0} for Slot 10 is shown in Figure 8.57. This figure also shows the corresponding five hole probe traverses at Slot 10, and as can be seen the agreement between five hole and three hole probe readings is quite good. The P3 case has a greater loss than the P0 case close to the endwall. Figure 8.58 shows the pitch averaged yaw angle, again the corresponding five hole probe traverse is included on the plot. The agreement between the three and five hole probe readings is good with a small (less than 1°) offset between the two. The close wall readings confirm the four degree increase in over turning caused by the third generation profiled endwall.

	P0	P3	Error Estimate
Net total	0.1531	0.1599	± 0.005
Net secondary	0.0751	0.0821	± 0.004
% Planar Case	100.0	109.2	± 5.1

Table 8.5: $\overline{\overline{C_{P0}}}$ for Five Hole Probe Readings P3 endwall.

	P0	P3	Error Estimate
Gross total	0.3175	0.4384	± 0.040
% Planar Case	100.0	138.1	± 13

Table 8.6: $\overline{\overline{C_{P0}}}$ for Three Hole Probe Readings (0-7.5% Span) P3 endwall.

8.1.8 Area Averaged Results

Figure 8.59 shows the gross loss growth through the cascade for P0 and P3. This is analogous to Figure 5.130 on page 129 except that for P3 only three slot measurement locations are available. Figure 8.60 shows the secondary loss growth through the cascade. Secondary loss removes the blade boundary layers from the downstream results which makes a better comparison to the upstream slots as the blade boundary layers are removed from the upstream slots by virtue of not measuring up to the blade surfaces. As can be see from either figure the loss values for P0 and P3 are very similar at Slot 6 (71% C_{ax}) but show a greater loss for P3 at Slot 8 (97% C_{ax}) and Slot 10 (128% C_{ax}). Figure 8.61 shows the C_{ske} growth through the cascade, P3 exhibits consistently lower area averaged values of C_{ske} than P0. A detailed discussion of C_{ske} values is left until section 8.4 where a comparison with CFD values is made.

Area averaged results are contained in Table 8.5. Table 8.5 is in the same format as Table 5.6 on page 92 to allow a comparison to be made with earlier results. It is immediately apparent that the results show an increase in loss associated with the new endwall. The error in Table 8.5 is taken from Chapter 5 where it was derived from a consideration of a number of tests on the same endwall. The table shows net loss values which have the loss from the inlet boundary layer subtracted from them, the inlet boundary layer loss measurement is taken from Chapter 5.

Table 8.5 shows an increase in loss compared to the planar case, which is expected having examined the contour and pitch averaged plots of loss.

Table 8.6 shows the area averaged loss values for the three hole probe readings alone. As is expected there is a large increase in loss for P3 when compared to the planar reference case. The error margins are again those estimated from Chapter 5.

Three and Five Hole Probe Results

The three hole probe results point to increased loss close to the endwall, so in order to asses the impact of this on the overall loss figure a synthesised data set was produced for P3 in the same manner as in Chapter 5 for P0, P1 and P2. In order to make the results within this chapter consistent a new synthesised data set was produced for P0 which used the back-to-back traverses described in this chapter.

3H 5H Results	P0	P3	Error Estimate
Net total	0.1648	0.1743.	± 0.005
Net secondary	0.0869	0.0964	± 0.004
% Planar Case	100.0	111.0	± 5.1
5H Results	P0	P3	Error Estimate
Net total	0.1531	0.1599	± 0.005
Net secondary	0.0751	0.0821	± 0.004
% Planar Case	100.0	109.2	± 5.1

Table 8.7: Combined Three and Five Hole Probe Readings for P3.

	128% C_{ax}		Mixed out loss	
	P0	P3	P0	P3
Net total	0.1648	0.1743	0.1863	0.2010
Net secondary	0.0869	0.0964	0.1014	0.1101
% Planar Case	100.0	111.0	100.0	108.5

Table 8.8: Mixed out loss for synthesised data set - P3.

Figure 8.62 shows the P0 and P3 synthesised data set when they are pitch averaged. The increased loss at the endwall and the different positions of the passage vortex can be clearly seen. Figure 8.63 shows the pitch averaged yaw angle, the reduced under turning at 30-40% of midspan is shown along with the increased over turning at the endwall.

Table 8.7 shows the area averaged values of loss. Including the three hole probe readings increases the P3 loss generation relative to the planar case. For easy comparison the results from Table 8.5 are included in Table 8.7. The increase in loss from 109% of the planar case to 111% of the planar case is in line with the changes in overall loss value when the close wall results are applied found for P1 and P2 in Chapter 5. Figure 8.64 shows the results in Table 8.7 graphically.

Mixed Out Loss

A mixed out loss calculation as described in Chapter 3 was carried out on the data. The results are shown in Table 8.8, the results are for the combined data set only. The secondary loss is shown graphically in Figure 8.65. The P3 loss as a percentage of the planar value reduces slightly when the mixing calculation is carried out, suggesting that the flow is more developed for the P3 case than for the planar case. The overall loss is of course increasing, the P0 loss increases more than the P3 loss.

The loss results are summarised using Figure 8.66 to illustrate the different components of loss. This figure shows the combined data set not the mixed out loss. The basic point is that the loss for P3 is increasing and not decreasing. It is important to establish the reason for this increase but a detailed quantitative assessment of the loss production as conducted in Chapter 5 for profiles P1 and P2 is not necessary as the ranking of the profile is already clear.

8.2 Flow Visualisation Results

The experimental technique for flow visualisation was the same as that described in Chapter 3. There were only two changes made to the flow visualisation process, firstly there was not sufficient time to repaint the endwalls in brilliant white - so the results are not as clear as those found in Chapter 4. Secondly there was not sufficient time to refine the lighting so some apparent flow features are merely reflections, this is highlighted later in the chapter. Despite these deficiencies the flow visualisation results are good enough to show up significant differences between P3 and previous endwall.

Figures 8.67 and 8.68 show general views of the panel. The P0 photographs are taken from Chapter 4 to provide a direct comparison. Figures 8.69 to 8.72 show the blade surfaces for P0 and P3. Figures 8.73 and 8.74 show a perspective view of the blade and endwall visualisation.

The following features are apparent:-

- The pressure side leg of the horseshoe vortex/passage vortex trace is much stronger initially for P3 than for P0.
- The suction side leg of the horseshoe vortex is much stronger on P3 than on P0.
- The passage vortex traces on the suction surface of the blade exhibit considerable differences between the two endwalls. There are two distinct “lift off lines” on the blade surface for P0. They have two distinct starting points whereas for P3 they both start in the same place.
- The suction surface corner vortex trace is much weaker for P3 than for P0.

Since these features are not immediately apparent from the photographs an additional set of figures: Figure 8.75 and Figure 8.76 are included with the features labelled.

Of most interest is the suction side horseshoe vortex. There is some evidence to suggest a separation of some sort at the start of the profiling where there is a sharp convex curvature. The suction surface flow at this point is almost vertically away from the endwall suggesting low energy fluid being convected up the blade surface (This is not immediately apparent from the photographs presented in this thesis, it is however apparent from an inspection of the actual flow visualisation). This is a physical flow feature we have not seen in previous endwalls. This increased loss early in the passage may then be convected into the loss core, giving the observed high loss downstream. This theory is given support from the results from Slot 4 (38% C_{ax}) which shows large amounts of additional loss downstream from the “separated region”.

One reason for the high loss close to the endwall may be the significant increase in “wetted” area caused by the ridge in the later part of the passage. Also the high crossflow on the wall can be expected to increase the loss there.

8.3 Measurement Overview

Pressure probe measurements have been conducted on the new generation endwall that show despite a reduction in C_{ske} there is in fact a 11% increase in secondary loss. The third generation endwall also provides the smallest reduction in under turning of the profiled endwalls and provides the greatest overturning of any geometry including the planar case.

Flow visualisation studies show an increased strength passage vortex along with an enhanced horseshoe vortex. There is some evidence that the poor performance of P3 may be down to a separated region associated with the initial curvature. This is backed up by a close wall traverse downstream of the suspected separation region which shows a large area of loss.

8.4 Comparison with CFD Results

In a similar manner to the CFD comparison in previous chapters we compare the CFD to experimental results here. The methodology for extracting CFD is the as that described in Chapter 7. The CFD solution is more sophisticated than those used for P1 and P2 however, there are considerably more grid points (280,000 compared to 100,000), the whole cascade is modelled rather than just the half span and the measurements of the inlet boundary layer shown in Chapter 5 are used as boundary conditions for the CFD solution. Detailed changes were also made to the design procedure at Rolls-Royce but it is not appropriate to discuss them in this thesis. The planar reference case was recomputed for the design of the profiled endwalls and it is this solution that is used in this chapter. This allows the author to concentrate on the changes that the CFD predicts rather than the absolute values.

In common with Chapter 7 a meaningful notation was chosen for the CFD results. Each CFD equivalent to an experimental run was given a unique name. For the five hole probe equivalent at slot 1 for the p3 case the data is given the label $p3s15h$. The label appears on each plot.

During the design of the third generation endwall Rolls-Royce produced another CFD solution for the planar case. Results from this solution are labelled with a suffix: “ $_b$ ”. So the label $p0s15h$ refers to the 1999 planar solution (approximately 100,000 points) for slot 1 and $p0s15h_b$ refers to the 2002 planar solution (approximately 280,000 points).

Results from the CFD solutions are presented in the same manner as the experimental results with contour plots of loss coefficient, secondary vectors, C_{ske} and vorticity followed by pitch averaged quantities.

Following the presentation of the P3 CFD results and a comparison with the experimental measurements Section 8.4.6 is included to highlight some of the differences between the second CFD solution (240,000 points) for the planar case and the first (100,000 points).

8.4.1 CFD results for Slot 6 (71% C_{ax})

Contour plots of loss for P0 and P3 are found in Figures 8.77 and 8.78 respectively. Secondary vectors are shown in Figures 8.79 and 8.80 for P0 and P3. C_{ske} is shown in Figures 8.81 and 8.82. Contours of C_Ω are shown in Figures 8.83 and 8.84 for P0 and P3 respectively.

An examination of the contour and vector plots reveals the following key points:-

- The loss core predicted by CFD for P3 (Figure 8.78) is smaller and of similar intensity as for P0 (Figure 8.77).
- The loss core and vortex centre predicted by CFD for P3 (Figure 8.80) is at the same radial position as the planar one (Figure 8.79). This is different from the experimental results which show a different position for the loss cores and vortex centres. (Figure 8.13, 8.14 for the experiments).
- The secondary flows are much more diffuse for P3 than for the planar case, i.e. the secondary vectors show a large vortex and the C_{ske} plots (Figures 8.81, 8.82) show less secondary kinetic energy.
- The region of positive vorticity above the passage vortex on P3 found in the experiments (Figure 8.18) is not seen in the CFD (Figure 8.84).

8.4.2 CFD for Slot 8 (97% C_{ax})

Contour plots of C_{P0} for the P0 and P3 CFD solution are found in Figures 8.85 and 8.86 respectively. Secondary vectors are shown in Figures 8.87 and 8.88 for P0 and P3. C_{ske} is shown in Figures 8.89 and 8.90 and contours of C_Ω are shown in Figures 8.91 and 8.92 for P0 and P3 respectively.

The following comments are made:-

- The CFD predictions of loss show a reduced intensity for P3 (Figure 8.86) compared to P0 (Figure 8.85). This is in contrast to the experiments where an increased loss is found for P3 (Figure 8.20).
- The CFD secondary vectors show that the P3 passage vortex (Figure 8.88) is much less diffuse at Slot 8 than at Slot 6. CFD predicts that the tangential extent of the planar vortex (Figure 8.87) is much larger than the P3 case. In the experiments the vortices are much closer in size. (Figure 8.21 for P0 and Figure 8.22 for P3).
- The CFD C_{ske} values predict that for P3 (Figure 8.90) the secondary kinetic energy coefficient is similar to P0 (Figure 8.89). This is in contrast to the experiments where the two profiles show significant differences.
- The streamwise vorticity values also show a big difference between experiments (Figure 8.25 and 8.26) and CFD (Figure 8.91 and 8.92). The CFD predicts relatively low values of C_Ω the experiments show high values.

8.4.3 CFD at Slot 10 (128% C_{ax})

Contour plots of C_{p0} CFD predictions are provided in Figure 8.93 and Figure 8.94 for P0 and P3 respectively. Predicted secondary Vectors are found in Figure 8.95 (Planar) and Figure 8.96 (P3). Secondary kinetic energy coefficient is plotted in Figures 8.97 and 8.98 for P0 and P3. Finally streamwise vorticity is plotted in Figures 8.99 and 8.100.

The following comments are made:-

- The CFD prediction for the P0 loss core shows only one peak (Figure 8.93) this in contrast to the earlier coarse grid solution (Figure 7.74) which showed two areas of loss. The CFD prediction for P3 also shows one peak (Figure 8.94). Both these predictions contradict the experimental findings which show two loss peaks for both endwalls. (Figure 8.27 and Figure 8.28).
- The CFD loss cores for P0 and P3 are predicted to have roughly the same size. The CFD predicts enhanced loss associated with corner vortex for P3. (Figure 8.94).
- The predictions of secondary vectors (Figure 8.95 and 8.94) show a reduced size and intensity of secondary flow when compared to the experimental results. (Figure 8.29 and 8.28). The cross flows at the endwall predicted by CFD are much higher than occur in the experimental results.
- The C_{ske} contours reflect the low levels of predicted activity for both the P0 and the P3 case (Figure 8.97 for P0 and Figure 8.98 for P3), the C_{ske} values are in general much lower than those found in experiments (Figure 8.31 and 8.32). Significantly the predicted level of C_{ske} for the 2002 planar solution (Figure 8.97) is much lower than that found in the 1999 planar solution (Figure 7.82 on page 199).
- The CFD C_{ske} plot for P3 does predict a high level of C_{ske} associated with the corner counter vortex. (Figure 8.98).
- The CFD plots of streamwise vorticity plots (Figures 8.99 and 8.100) predict a reduction in secondary flow overall but with extremely high values of C_Ω associated with the corner counter vortex.

8.4.4 Pitch Average CFD Results

The pitch averaged results are collated together by slot exactly as for the experimental results. Pitch averaged plots of loss coefficient, yaw angle, secondary kinetic energy coefficient and streamwise vorticity are provided. As only two endwalls are being compared it is reasonable to plot the CFD results on the same ordinates as the experimental results for comparison. CFD results are shown with open symbols and experimental results are shown with filled symbols.

For the pitch averaged plots only the CFD C_{P0} values are adjusted by adding a constant to all pitch averaged values to give the same midspan loss as the experimental case. This allows secondary loss to be visually compared by the reader. For

the area averaged values shown later no such correction is applied - it is used simply to make the plots clearer. A similar process is applied for the yaw angle, though in general the corrections are very small.

Slot 6 (71% C_{ax}) Pitch Averaged CFD

For Slot 6 (71% C_{ax}) loss is shown in Figure 8.101, yaw angle in Figure 8.102, C_{ske} in Figure 8.103 and C_Ω in Figure 8.104.

For Slot 6 the experimental loss core has two peaks which is missed by the CFD. In fact the CFD under predicts the planar loss core as well and predicts that the P3 loss core will be smaller than the planar case. (See Figure 8.101). The trends in the planar loss core are captured adequately though the absolute value is not. The inlet boundary layer “negative” loss has convected to this slot as for the experimental case (Figure 8.43), this is a consequence of supplying accurate inlet boundary layer information into the CFD solution.

The Yaw angle plot (Figure 8.102) shows that although there are some discrepancies in absolute yaw angle the trend is well predicted for the planar case. For the P3 case the CFD fails to predict the reduced overturning between 10-20% of midspan and an error of up to five degrees results. It is notable that the CFD solution predicts slightly different values of midspan yaw angle.

The C_{ske} pitch averaged plot (Figure 8.103) predicts a reduced level of C_{ske} for P3, which does indeed occur. However the CFD misses the local peak in C_{ske} that occurs at 19-25% of midspan. For the planar case the CFD under predicts the value of C_{ske} .

Streamwise vorticity (Figure 8.104) is in general well predicted by the CFD. However there is a region of large changes (10-30% to midspan) in the experimental C_Ω which is not predicted at all by the CFD.

Slot 8 (97% C_{ax}) Pitch Averaged CFD

For Slot 8 (97% C_{ax}) loss is shown in Figure 8.105, yaw angle in Figure 8.106, C_{ske} in Figure 8.107 and C_Ω in Figure 8.108.

The loss core for the P3 case is incorrectly predicted by the CFD (See Figure 8.105). The computations predict a smaller loss core for P3 than the planar case, but in practice the loss core size is very similar.

The yaw angle plot (Figure 8.106) shows that the planar CFD predicts that the passage vortex is closer to the endwall than occurs in practice. The CFD for the P3 case also under predicts the secondary flow activity, for the experimental case there is much more under turning than is predicted by the CFD. For both experimental cases there is a point of inflection in the yaw angle curve (At 18% of midspan for P0 and 21% for P3) which is missed by the CFD.

The C_{ske} plot (Figure 8.107) shows that the CFD predicts the C_{ske} associated with the passage vortex closer to the endwall than occurs in reality. The CFD also underestimates the intensity of the C_{ske} but successfully predicts that the P3 case will have lower values than the planar case.

The vorticity plot (Figure 8.108) shows that the intensity of the secondary flow patterns are again underestimated by CFD.

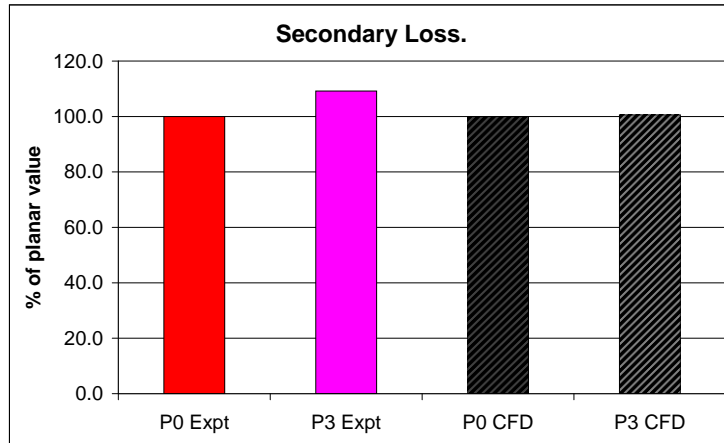


Figure 8.1: Experimental and CFD Secondary Loss

Slot 10 (128% C_{ax}) Pitch Averaged CFD

For Slot 10 (128% C_{ax}) secondary loss is shown in Figure 8.109, using secondary loss rather than loss means that the difference in blade boundary layers can be eliminated to some extent as discussed in Chapter 7. Yaw angle is shown in Figure 8.110, C_{ske} in Figure 8.111 and C_Ω in Figure 8.112.

The following key points are made after examining the figures:-

- The CFD predicts that the loss core for P0 and P3 will be of similar size (Figure 8.109). The size of loss cores in experiments is much larger than predicted by the CFD though they are comparable to each other. The experimental loss cores are also in different positions which is not predicted by CFD.
- The yaw angle CFD for P3 and P0 (Figure 8.110) predicts that the under turning will be almost identical, both in terms of value and position. This does not occur in practice. The CFD yaw angles successfully predict that profile P3 will increase the over turning. The position of the passage vortex is also closer to the endwall in the CFD than it is in the experiments.
- The C_{ske} predictions for P0 and P3 (Figure 8.111) show that the CFD successfully predicts a reduction the main C_{ske} peak away from the endwall when P3 is used. However the absolute value of these peaks are incorrect and the CFD over predicts the level of C_{ske} at the endwall for P3.
- The streamwise vorticity plot (Figure 8.112) confirms the previous remarks. As can be seen the magnitude of the secondary flow activity is generally under predicted and the position is predicted too close to the endwall. Finally the level of C_Ω at the endwall for P3 is over predicted.

5H Results	P0	P3	P0 CFD	P3 CFD
Net Total	0.1531	0.1599	0.2603	0.2574
Midspan	0.0779	0.0779	0.2087	0.2055
Secondary	0.0751	0.0821	0.0516	0.0519
% Planar Case	100.0	109.2	100.0	100.6

Table 8.9: CFD Loss Predictions Compared to Experimental Values - P3

5H Results	P0	P3	P0 CFD	P3 CFD
C_{ske}	0.0205	0.0117	0.0116	0.0099
% Planar Case	100.0	57.1	100.0	84.9

Table 8.10: CFD C_{ske} Predictions compared to Experimental Values -P3

8.4.5 Area Averaged Results

Table 8.9 shows the CFD and experimental loss, and as can be seen from the table the CFD does not predict loss well. The midspan loss prediction from the CFD is higher than that found in Chapter 7, which suggests that there was some difference in the blade boundary calculation or that the solution is somewhat grid dependent. In any case the midspan CFD loss is typically 2.6 times that found in the experiments. Secondary loss is not well predicted either with no change in loss being predicted and the absolute value underestimating the magnitude of the losses. As outlined in Chapter 7 this is expected, it is well known that CFD will not predict loss accurately. Figure 8.1 illustrates this.

Chapter 7 compared the C_{ske} reductions and found a correlation between C_{ske} reductions and loss. As is illustrated in Table 8.10 this correlation does not hold for P3. Although there is a reduction in C_{ske} but there is no corresponding reduction in loss coefficient.

8.4.6 Comparison of the Two Planar CFD Solutions

As has been pointed out in earlier sections there are significant differences between the two solutions for the planar case. Figure 8.113 shows the pitch averaged loss for both solutions compared to an experimental traverse. As can be seen the earlier CFD solution captures the location and magnitude of the loss more accurately than the later solution. Figure 8.114 shows the yaw angle for the two planar CFD solutions and an experimental traverse. The first CFD solution captures the position of the over turning and under turning more accurately than the second. Figure 8.115 shows a similar comparison for C_{ske} - both CFD solutions over predict C_{ske} at the wall and the later CFD solution under predicts the magnitude of the passage vortex C_{ske} peak more than the earlier one.

The origin of the grids for both solutions is different. Although the second solution uses some 280,000 points compared to 100,000 for the first, the second solution includes the unprofiled endwall of the cascade and covers twice the area of the first. Therefore for the region of interest the second solution has 140,000 for the second solution as opposed to 100,000 points for the first solution. The first (1999) grid was copied from one produced by Durham University the second

Length Scale / [mm]	HM Midspan C_{P0}	RR Midspan C_{P0}
9.36	0.494	-
0.936	0.171	-
0.0936	0.104	-
0.936	-	0.151
2.9655	-	0.209

Table 8.11: C_{P0} at Midspan compared to freestream turbulence length scale.

was produced by Rolls-Royce's design system. Despite this the two grids are very similar, the Durham Cascade in planar form is a very simple geometry so that is unsurprising. Figure 8.116 shows the leading and trailing edges of both grids as can be seen the second (2002) solution has more points near the blade surfaces and is generally slightly finer in comparison.

The second significant change in input to the second CFD solution compared to the first is that the second used the measured inlet boundary layer shown in Figure 5.14 on page 100. The measured inlet boundary layer has an area of negative loss caused by a jetting effect from the turbulence grid upstream. The inlet boundary layer to the first (1999) CFD solution did not include this "hump". More accurate modelling of the inlet boundary layer was not expected to change the solution dramatically as the change in inlet conditions is quite small, the difference in inlet vorticity between a boundary layer with a "hump" and a flat one is very small. The way to test this hypothesis would be to conduct two calculations on the planar case with the only difference being the "hump" in the inlet boundary layer.

Finally different values for freestream turbulence length scale were used in the calculations. The first solution (1999) used a freestream turbulence length scale of 0.936mm, the second solution (2002) used a freestream turbulence length scale length of 2.97mm. The first value was obtained from Moore (1995) who carried out calculations with an earlier version of the same code with a variety of length scales. Moore (1995) conducted three calculations with length scales of 9.36mm, 0.936mm and 0.0936mm, interestingly the measured freestream turbulence length scale is 9.36mm so the selection of a 0.936mm is somewhat arbitrary. The second value of 2.97mm is a "default" value in Rolls-Royce's design system, so represents a much more typical result of a design computation. The change in midspan loss between the earlier (1999) and later (2002) planar CFD solutions can be attributed to the change in length scale. Table 8.11 shows the values of midspan loss that Moore (1995) found along with present values compared to mixing length. Figure 8.2 shows the numbers from table 8.11 graphically which shows that the change in midspan loss can be attributed to changes in turbulence model input only.

The difference in midspan loss appears to be entirely attributable to the changed length scale input parameter, the changed inlet boundary layer appears not to be the main cause of the difference between the two planar cases. The first computation (1999) involved taking a grid that was optimised for the Durham Cascade and the second (2002) is more representative of design practice.

Gregory-Smith (1995) compared a number of calculations on the Durham Cascade and the results for the 2002 P0 solution presented in this chapter are typical of

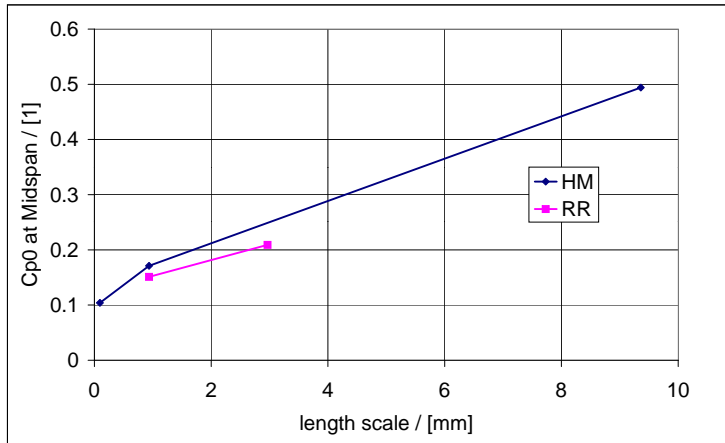


Figure 8.2: Effect of mixing length on C_{P0}

a too active turbulence model where vortex movement is suppressed and too much loss is generated.

A higher freestream turbulence length scale leads to stronger turbulent viscosity which would tend to suppress separation in the predicted flow field. It may be that with a different value for freestream turbulence length scale the separated flow region would have been predicted. Even if this was the case however it is not immediately apparent how a freestream turbulence length scale that produces good results could be obtained without both experimental and computational data being available before the calculation started.

8.5 Computation Fluid Dynamics for P3 Overview

The CFD solution for P3 has been compared to the experimental results. The CFD shows no sign of the separated region that was identified by the experimental results, in fact if it had the design of the profile would certainly have been changed. The fact that this separated region is not picked up by the CFD means that the whole solution for P3 deviates more from the experimental case than the P0 results throughout the comparison made in this chapter.

8.6 P3 Overview

The testing of a third generation endwall has been described in this chapter. This third generation endwall was designed to achieve the best possible loss reduction and used the largest height perturbations that could be manufactured. A detailed description of the manufacturing process is found in Ingram (2003).

The third generation endwall does not however reduce loss, there is in fact a 9 to 11% increase in secondary loss. The increase in loss is put down to the existence

of a complicated flow feature at the start of the “dip” at the profiled endwall. This feature is analogous to a conventional two dimensional separation produces a dramatic rise in loss near the wall as measured by a three hole probe at 38% C_{ax} . The flow feature is associated with a sharp curvature and it may be possible to smooth the geometry and keep the expected benefits for the rest of the design.

The CFD does not predict this separated region and once this has occurred the CFD is missing a very important piece of “information” about the flow field in the blade row and the prediction is generally poorer than those found in Chapter 7 where earlier generations of endwalls are compared to CFD predictions.

The design aim for the P3 endwall was to achieve the best possible loss reduction within the Durham Cascade it would appear that in attempting to achieve the best possible result the suction side dip was made too “dramatic” a feature and the curvature applied on the suction side endwall was too great.

8.7 Third Generation Endwall Graphs.

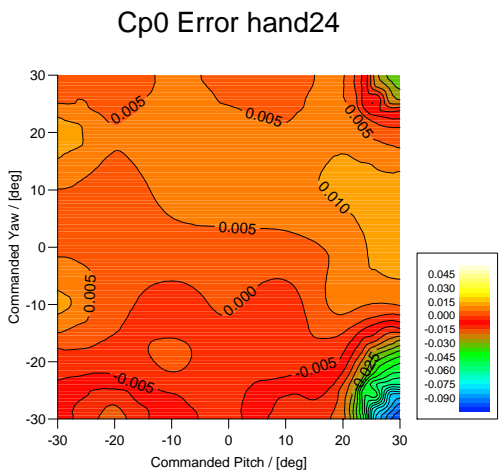


Figure 8.3: Pre-readings Loss Error

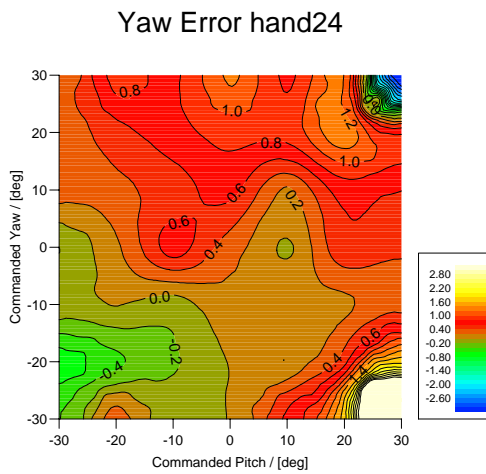


Figure 8.4: Pre-readings Yaw Error

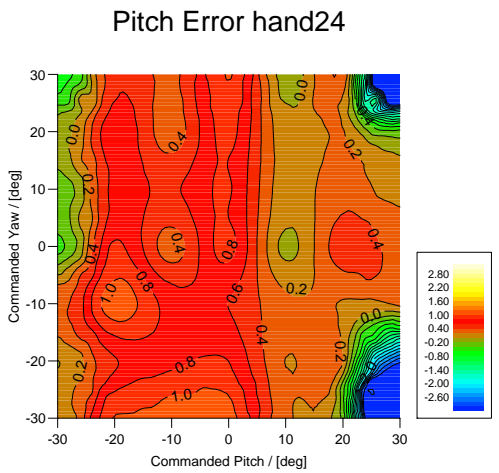


Figure 8.5: Pre-readings Pitch Error

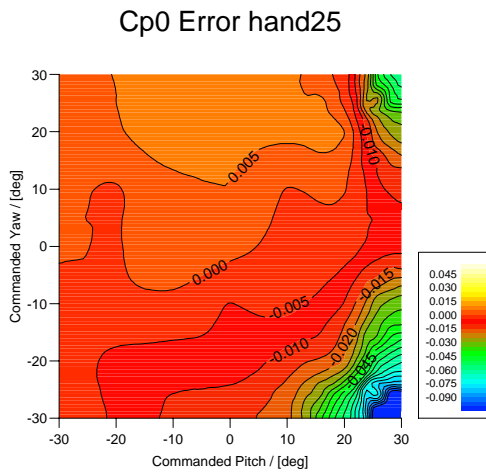


Figure 8.6: Post-readings Loss Error

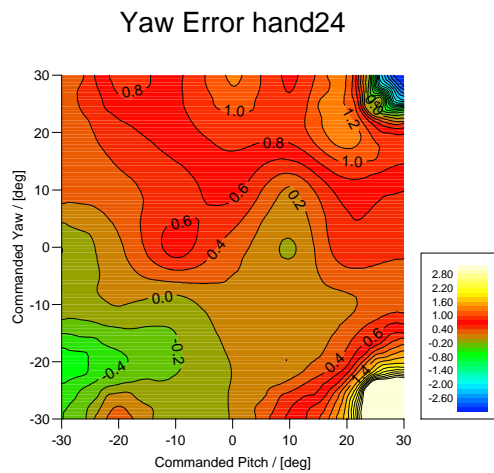


Figure 8.7: Post-readings Yaw Error

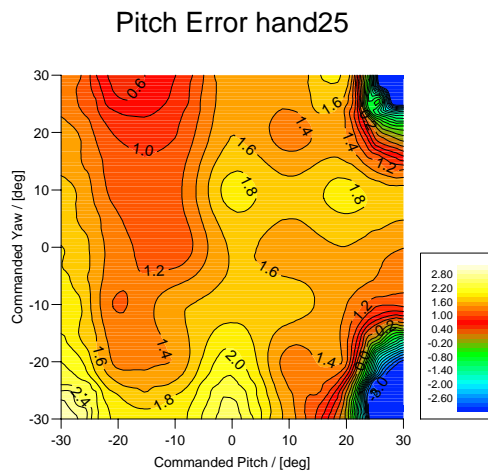


Figure 8.8: Post-readings Pitch Error

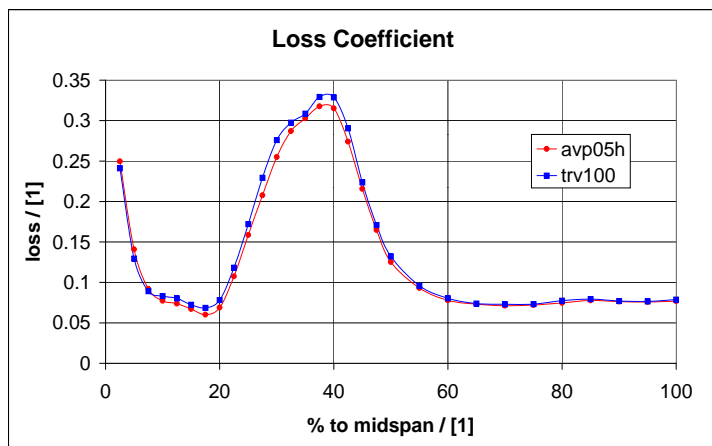


Figure 8.9: Repeatability of Planar Loss Readings (P0).

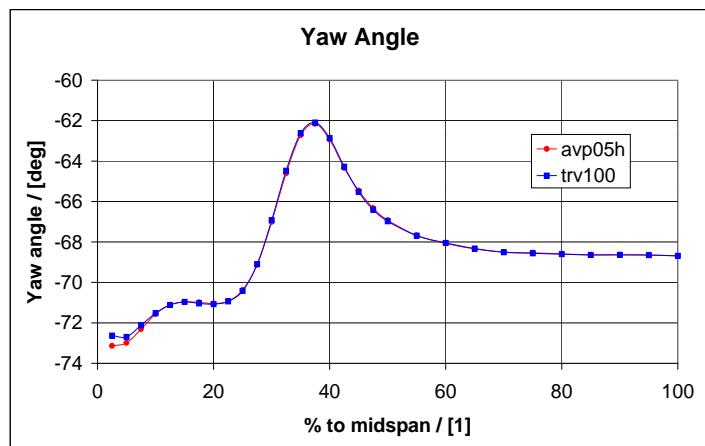


Figure 8.10: Repeatability of Yaw Readings (P0).

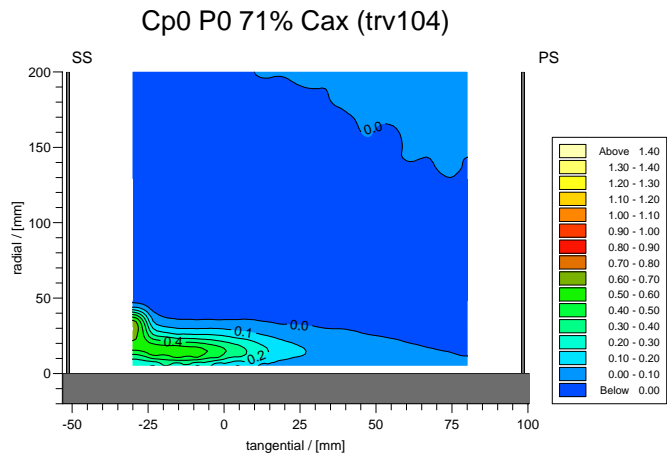


Figure 8.11: Planar Area Loss at Slot 6.

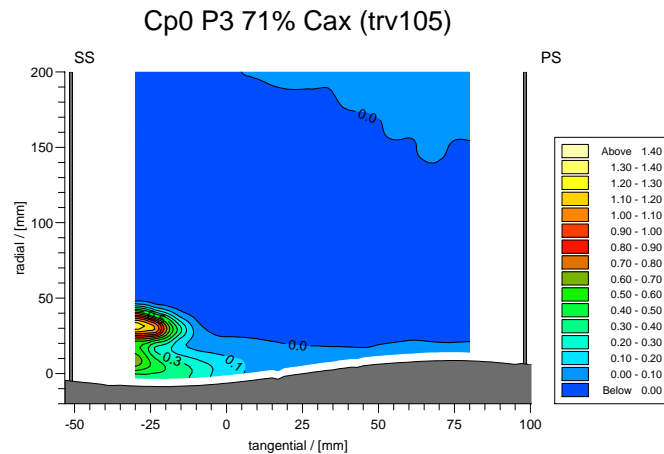


Figure 8.12: P3 Area Loss at Slot 6.

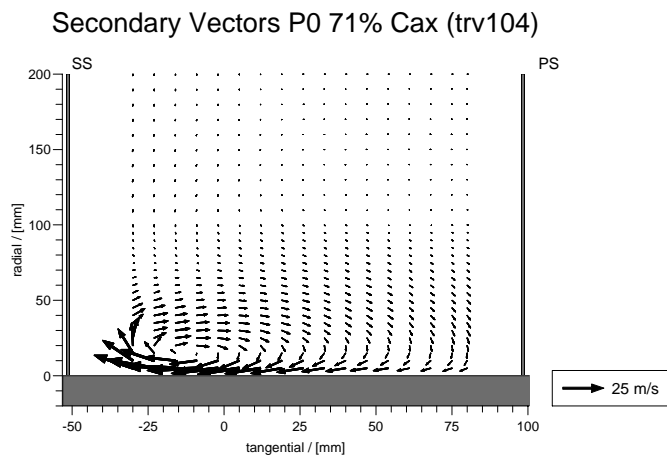


Figure 8.13: Planar Secondary Vectors at Slot 6.

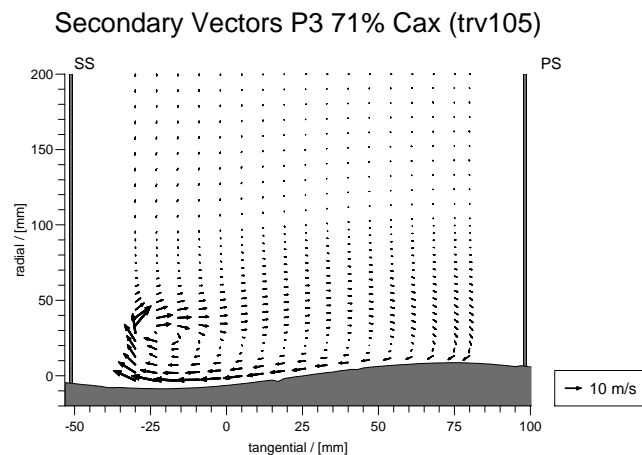


Figure 8.14: P3 Secondary Vectors at Slot 6.

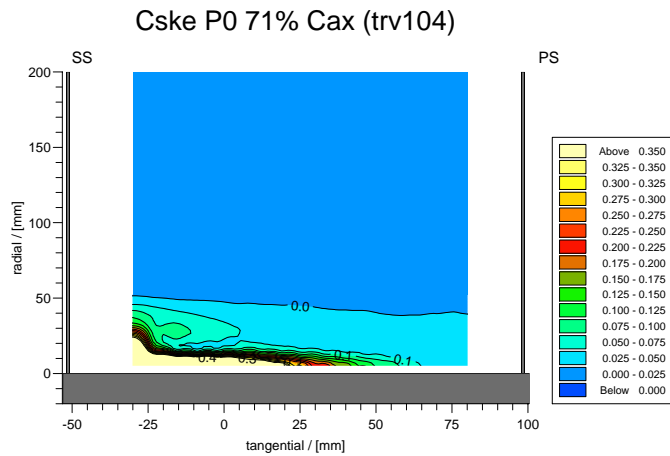


Figure 8.15: Planar C_{ske} at Slot 6.

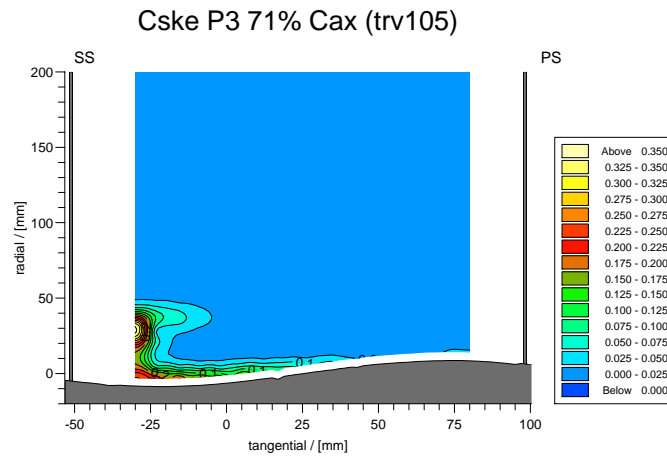


Figure 8.16: P3 C_{ske} at Slot 6.

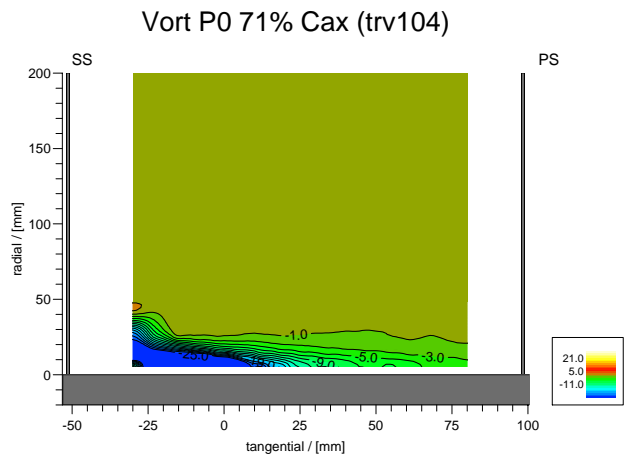


Figure 8.17: Streamwise Vorticity Coefficient at Slot 6 P0.

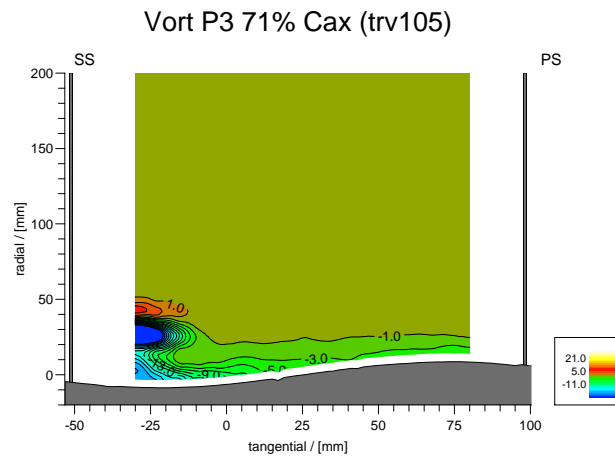


Figure 8.18: Streamwise Vorticity Coefficient at Slot 6 P3.

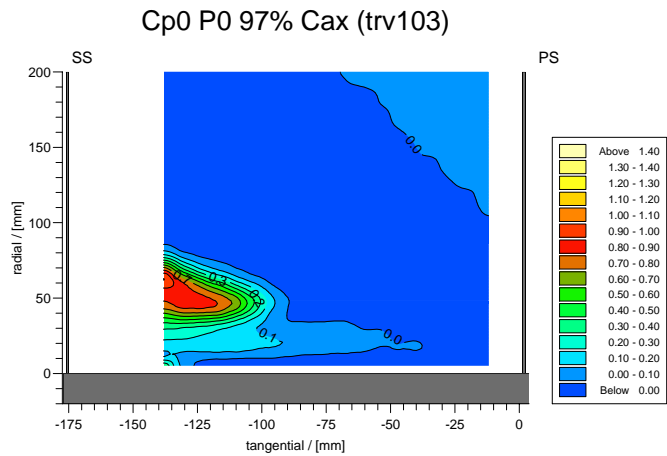


Figure 8.19: Planar Area Loss at Slot 8.

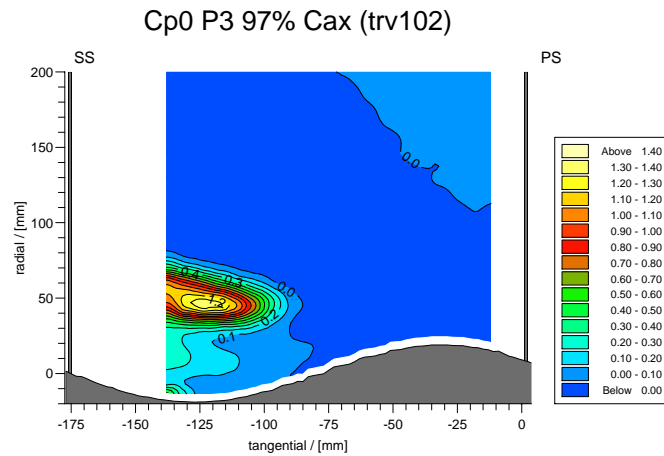


Figure 8.20: P3 Area Loss at Slot 8.

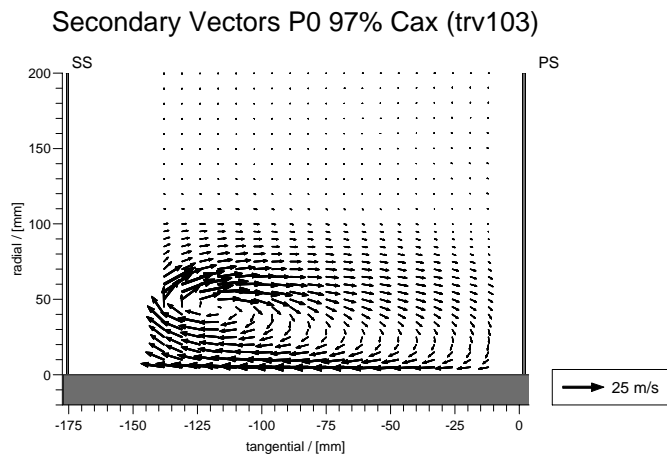


Figure 8.21: Planar Secondary Vectors at Slot 8.

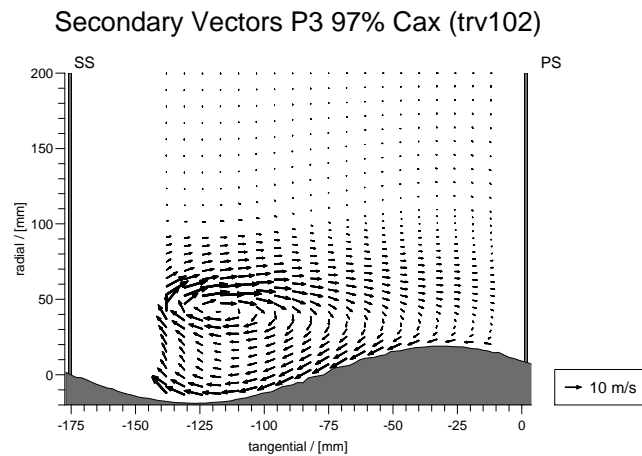


Figure 8.22: P3 Secondary Vectors at Slot 8.

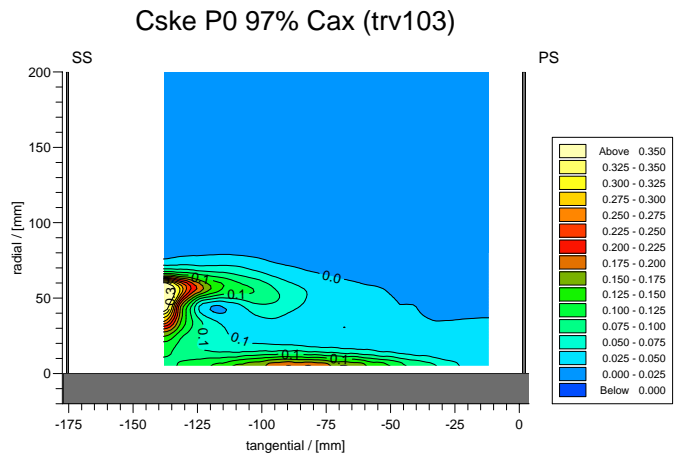


Figure 8.23: Planar C_{ske} at Slot 8.

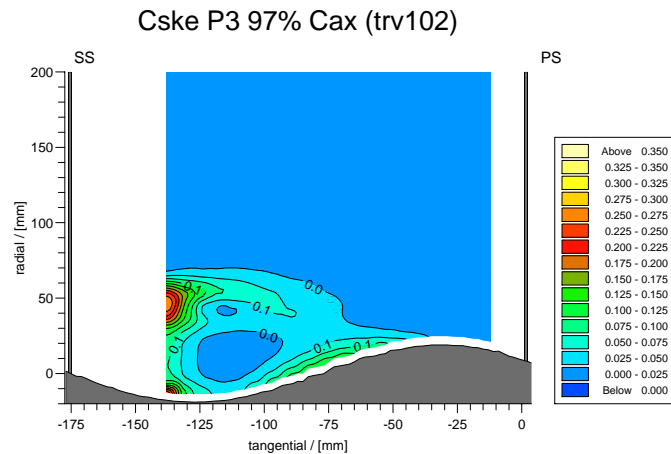


Figure 8.24: P3 C_{ske} at Slot 8.

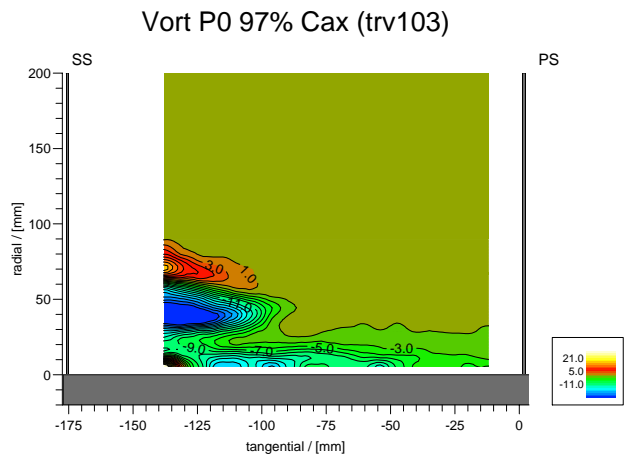


Figure 8.25: Streamwise Vorticity Coefficient at Slot 8 P0.

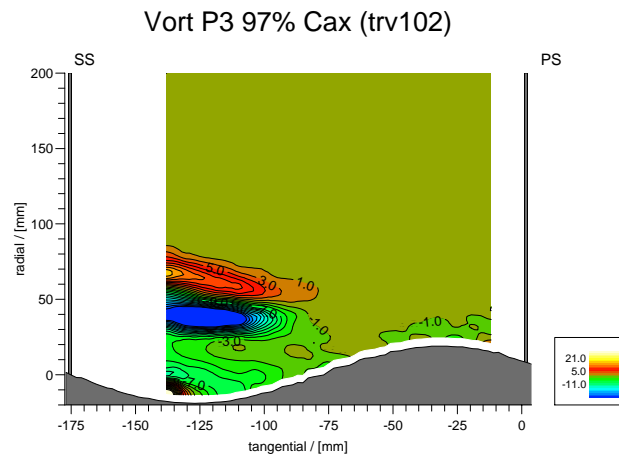


Figure 8.26: Streamwise Vorticity Coefficient at Slot 8 P3.

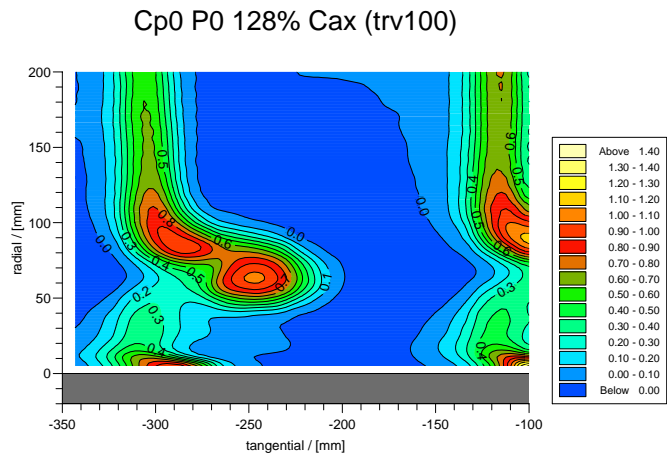


Figure 8.27: Planar Area Loss at Slot 10.

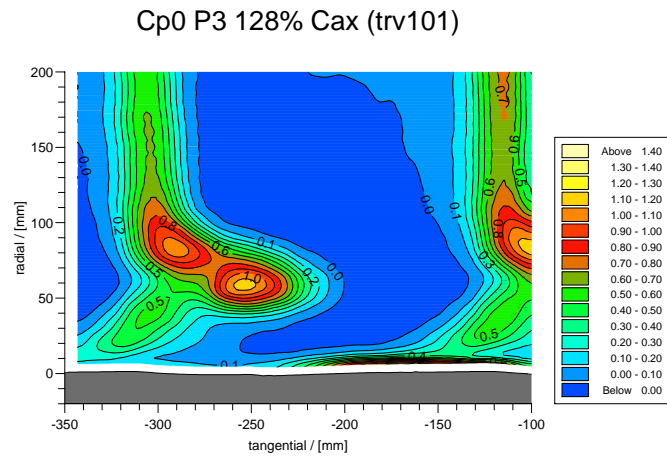


Figure 8.28: P3 Area Loss at Slot 10.

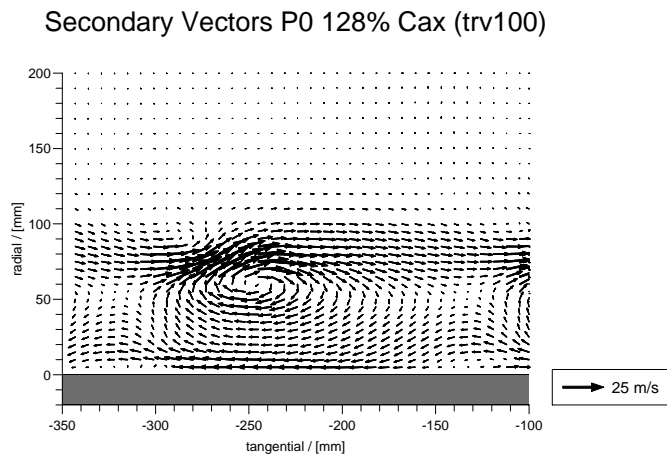


Figure 8.29: Planar Secondary Vectors at Slot 10.

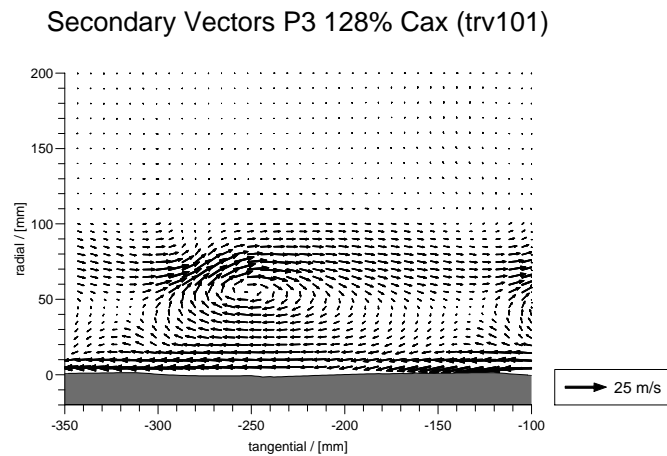


Figure 8.30: P3 Secondary Vectors at Slot 10.

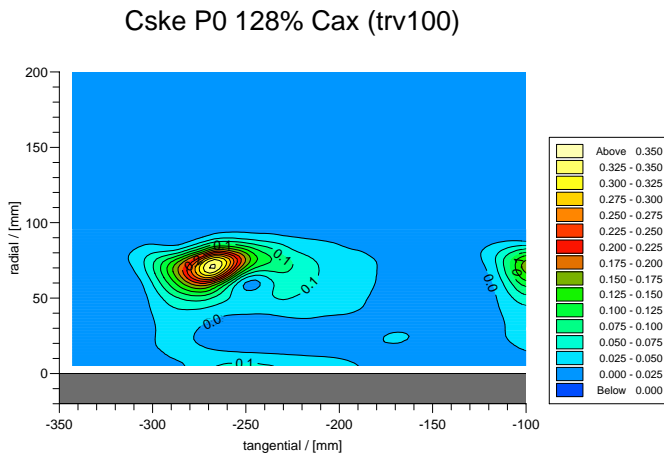


Figure 8.31: Planar C_{ske} at Slot 10.

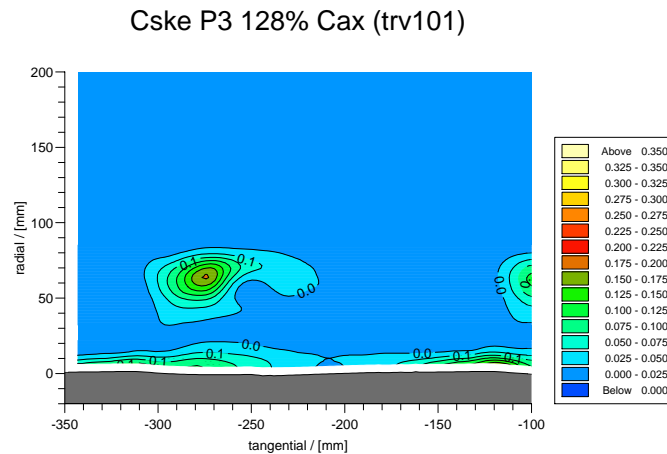


Figure 8.32: P3 C_{ske} at Slot 10.

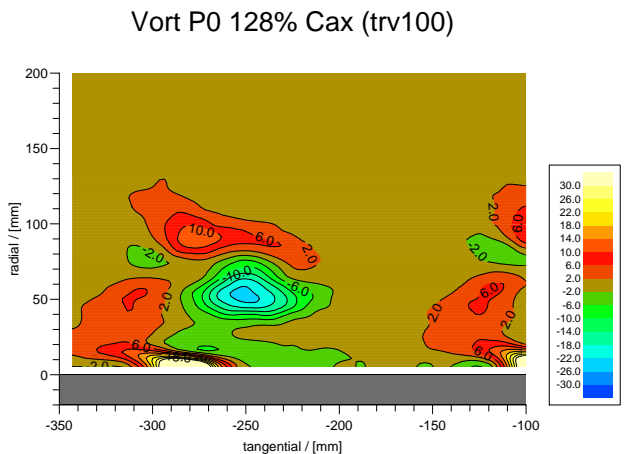


Figure 8.33: Streamwise Vorticity Coefficient at Slot 10 P0.

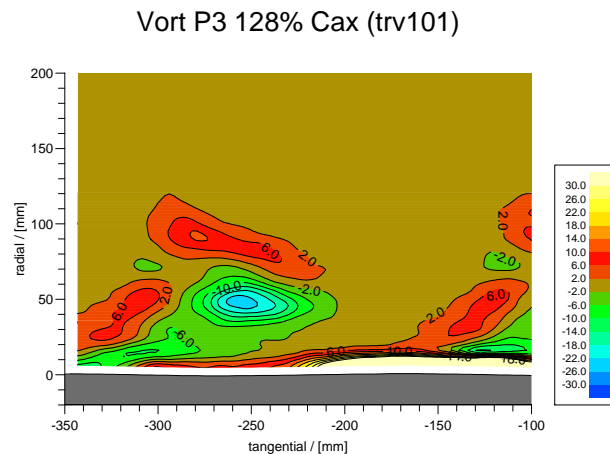


Figure 8.34: Streamwise Vorticity Coefficient at Slot 10 P3.

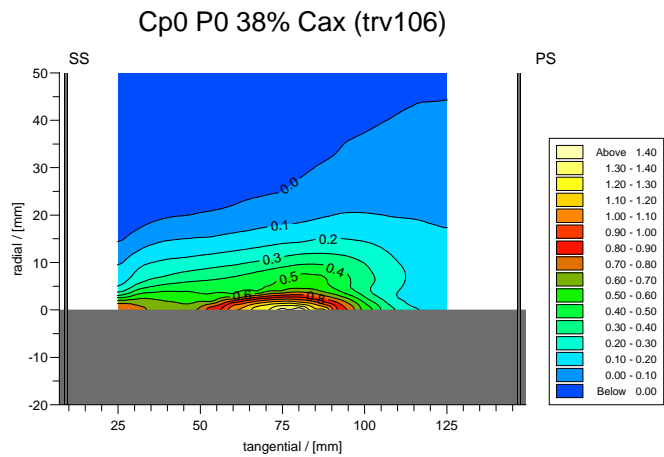


Figure 8.35: Close Wall Loss Readings at Slot 4 P0.

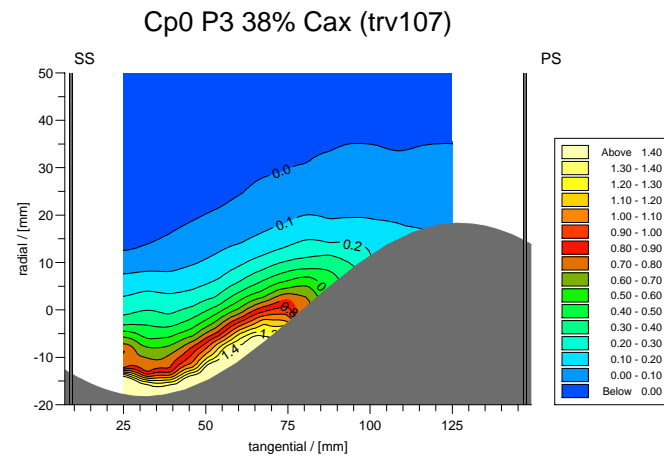


Figure 8.36: Close Wall Loss Readings at Slot 4 P3.

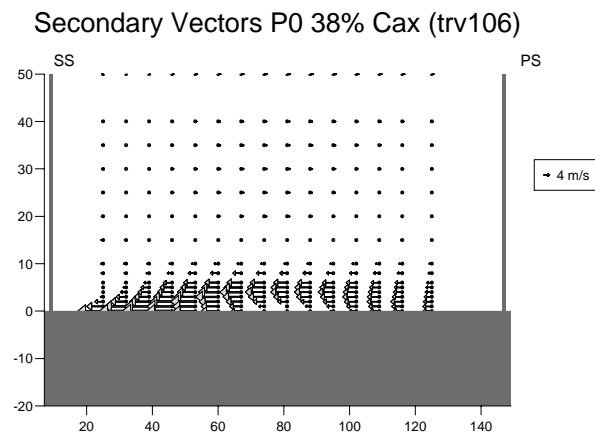


Figure 8.37: Close Wall Secondary Flow at Slot 4 P0.

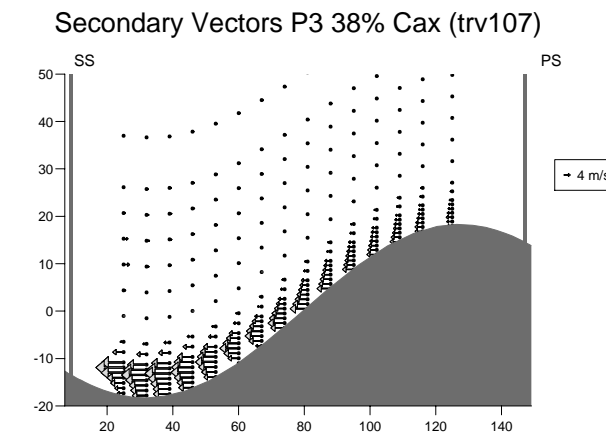


Figure 8.38: Close Wall Secondary Flow at Slot 4 P3.

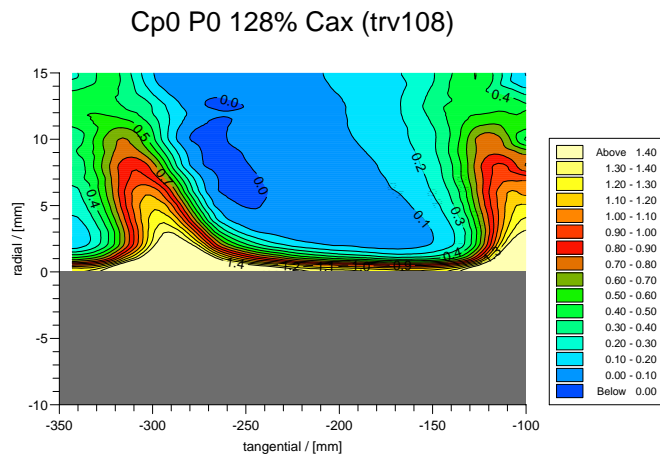


Figure 8.39: Close Wall Loss Readings at Slot 10 P0.

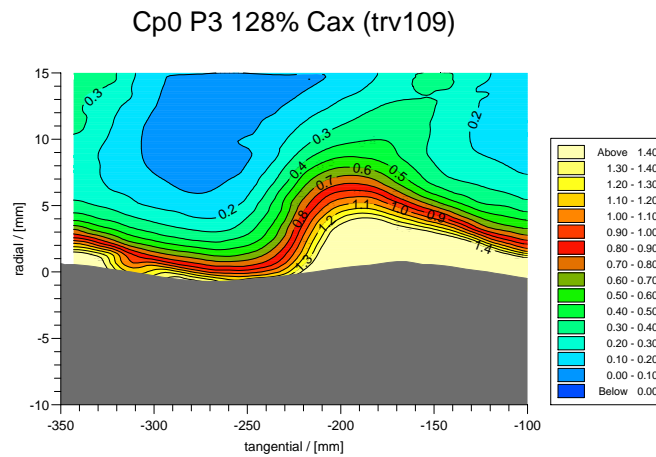


Figure 8.40: Close Wall Loss Readings at Slot 10 P3.

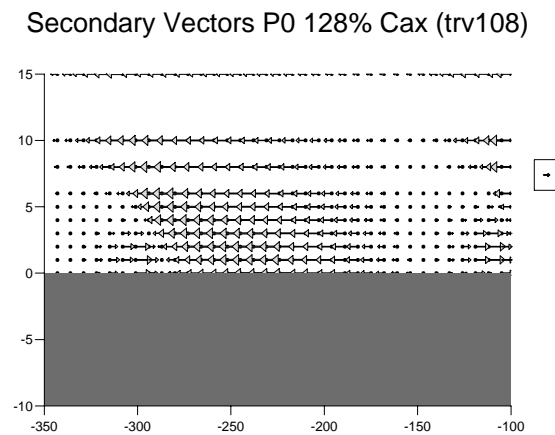


Figure 8.41: Close Wall Secondary Flow at Slot 10 P0.

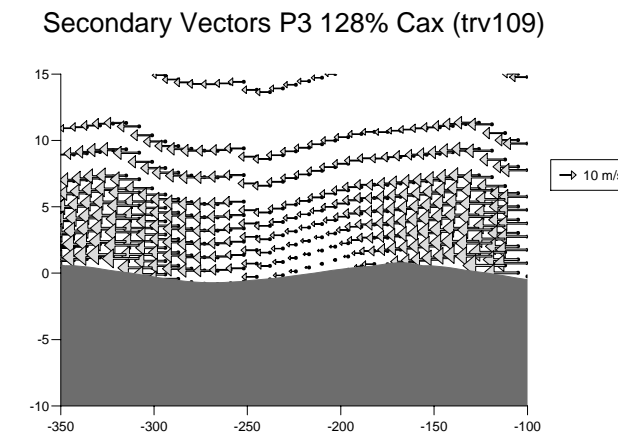


Figure 8.42: Close Wall Secondary Flow at Slot 10 P3.

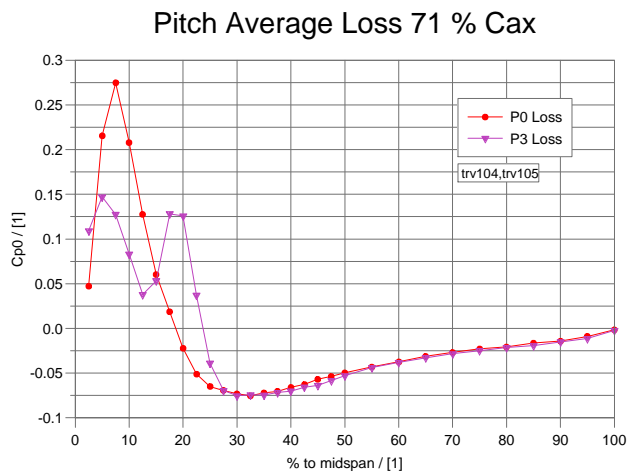


Figure 8.43: Pitch Averaged Loss at Slot 6.

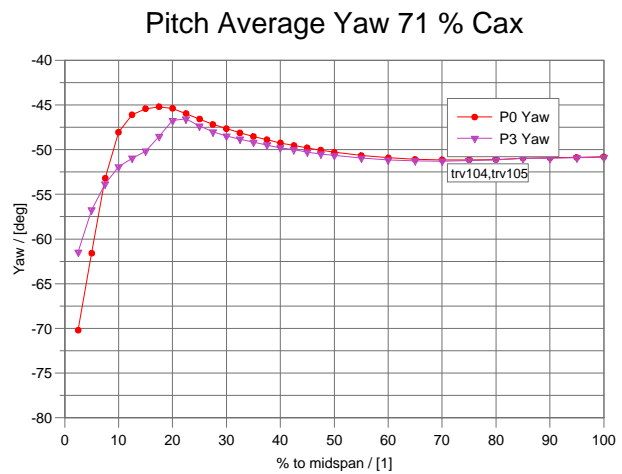


Figure 8.44: Pitch Averaged Yaw at Slot 6.

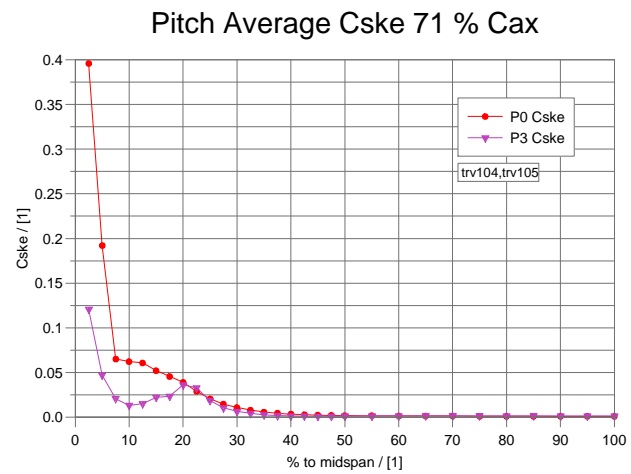


Figure 8.45: Pitch Averaged C_{ske} at Slot 6.

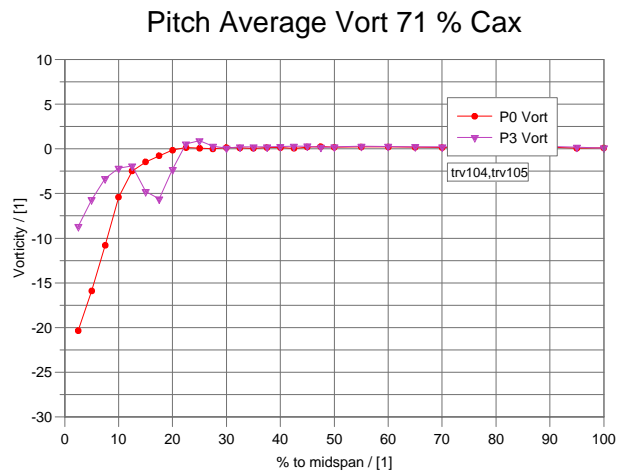


Figure 8.46: Pitch Averaged Streamwise Vorticity Coefficient at Slot 6.

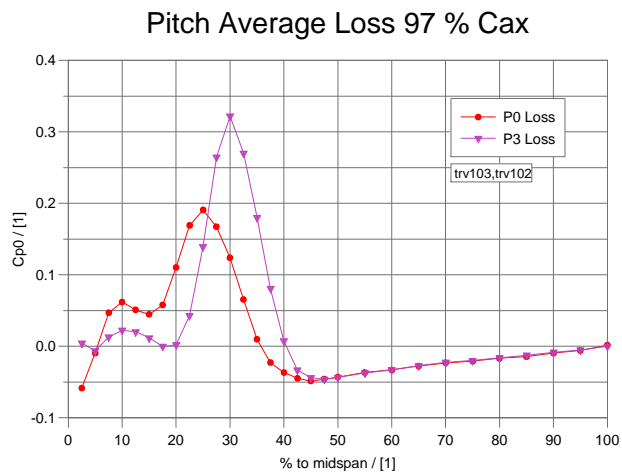


Figure 8.47: Pitch Averaged Loss at Slot 8.

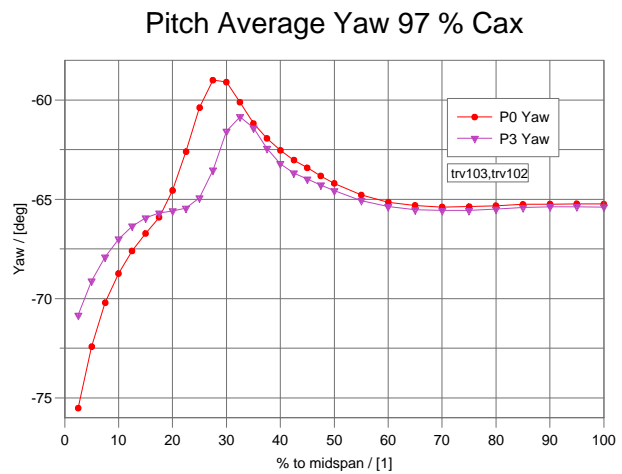


Figure 8.48: Pitch Averaged Yaw at Slot 8.

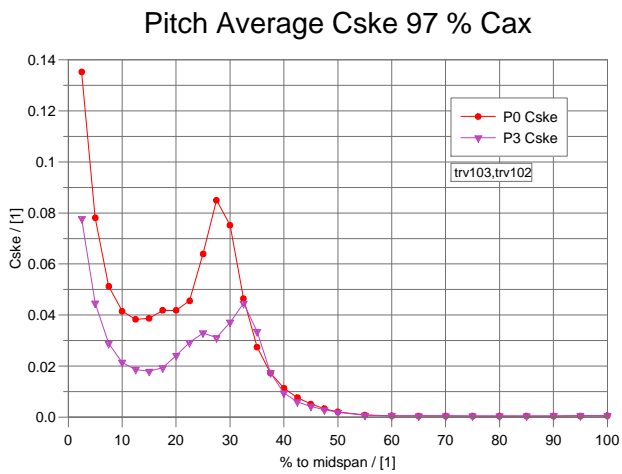


Figure 8.49: Pitch Averaged C_{ske} at Slot 8.

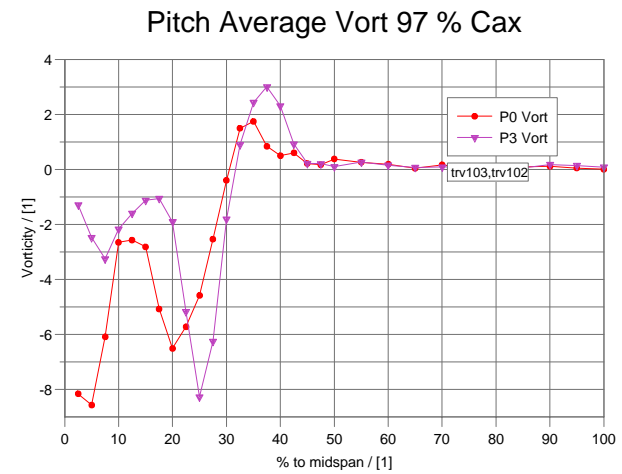


Figure 8.50: Pitch Averaged Streamwise Vorticity Coefficient at Slot 8.

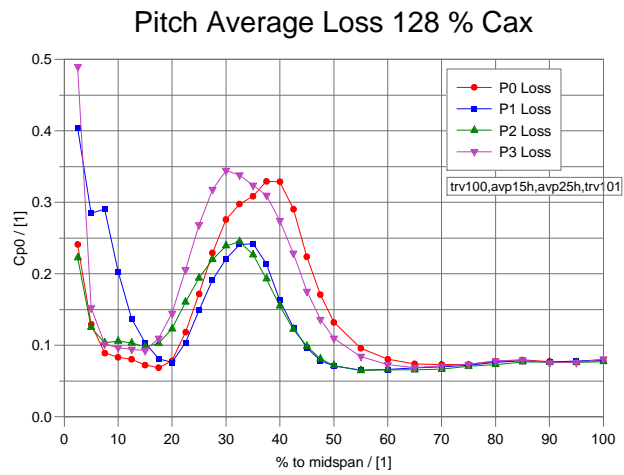


Figure 8.51: Pitch Averaged Loss at Slot 10.

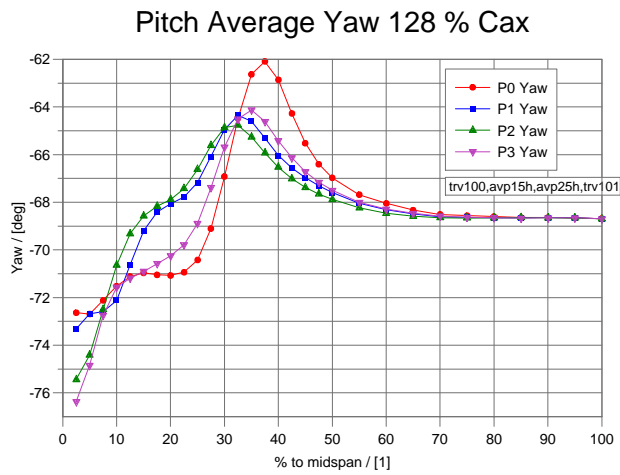


Figure 8.52: Pitch Averaged Yaw at Slot 10.

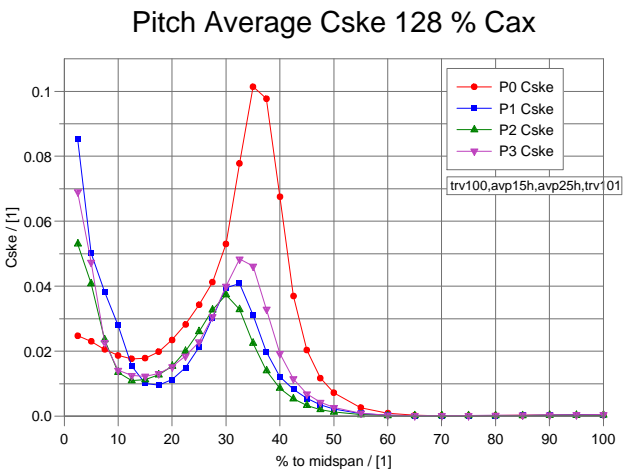


Figure 8.53: Pitch Averaged C_{ske} at Slot 10.

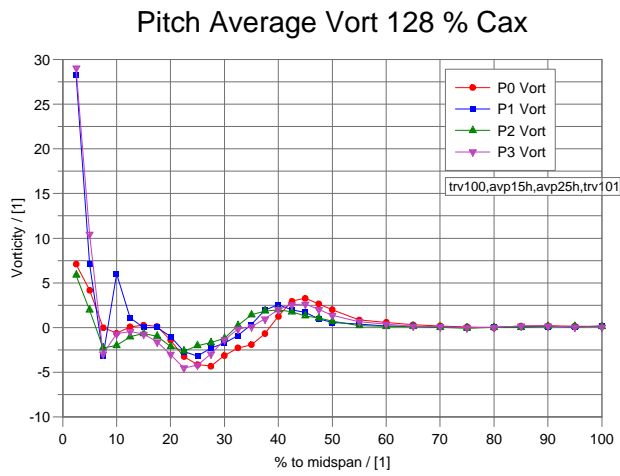


Figure 8.54: Pitch Averaged Streamwise Vorticity Coefficient at Slot 10.

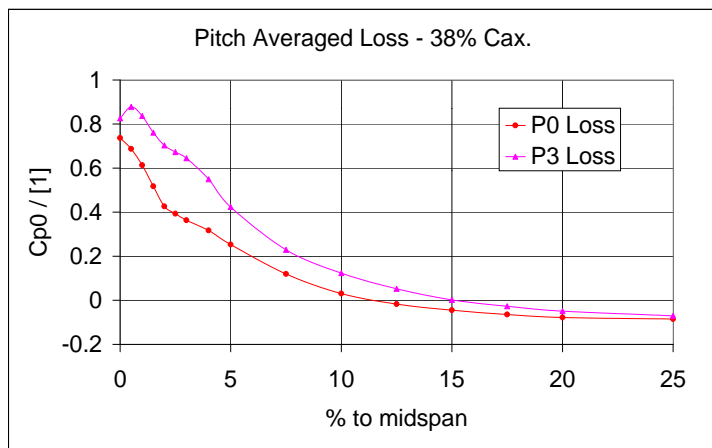


Figure 8.55: Pitch Averaged Loss at Slot 4 - Close Wall Results.

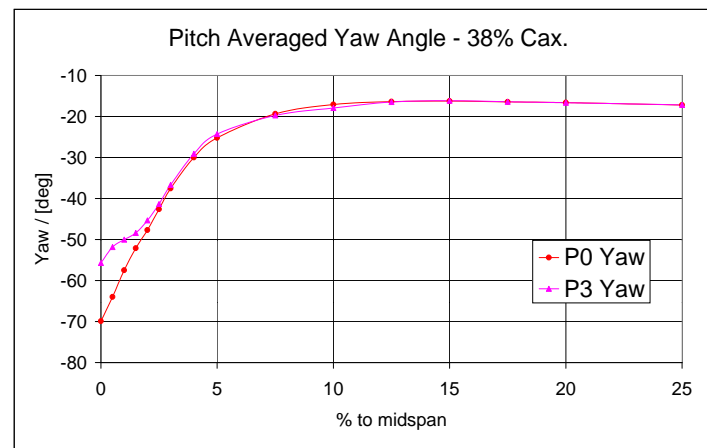


Figure 8.56: Pitch Averaged Yaw at Slot 4 - Close Wall Results.

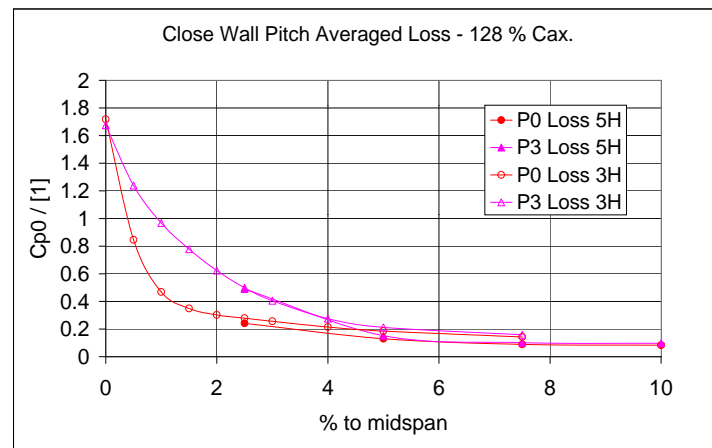


Figure 8.57: Pitch Averaged Loss at Slot 10 - Close Wall Results.

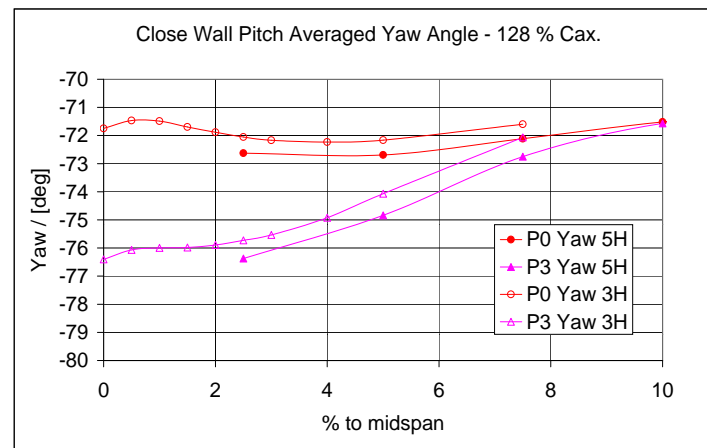


Figure 8.58: Pitch Averaged Yaw at Slot 10 - Close Wall Results.

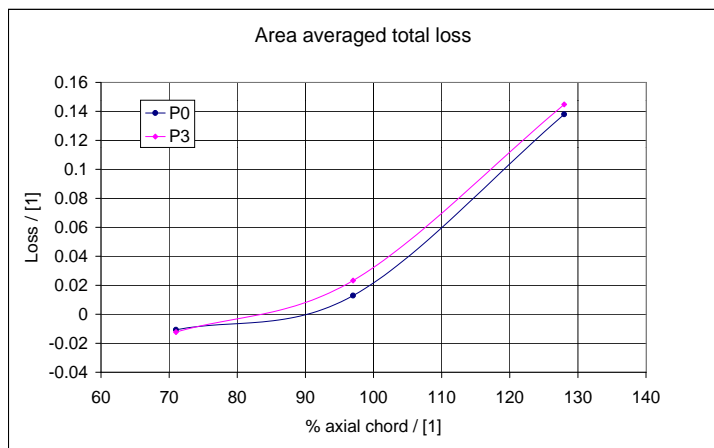


Figure 8.59: $\overline{\overline{C}_{P0}}$ growth through the cascade for P0 and P3.

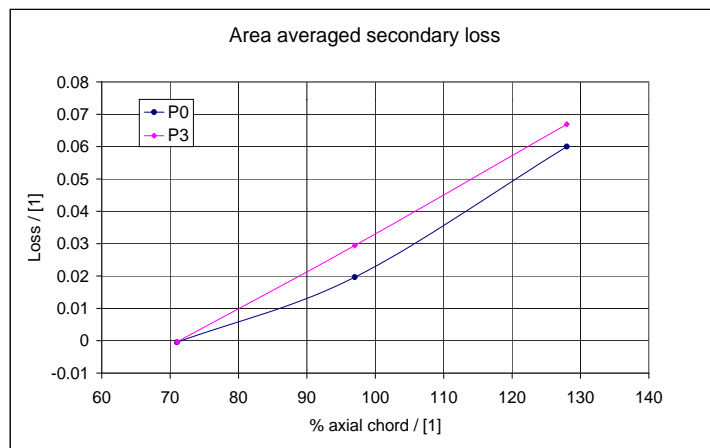


Figure 8.60: Secondary loss growth through the cascade for P0 and P3.

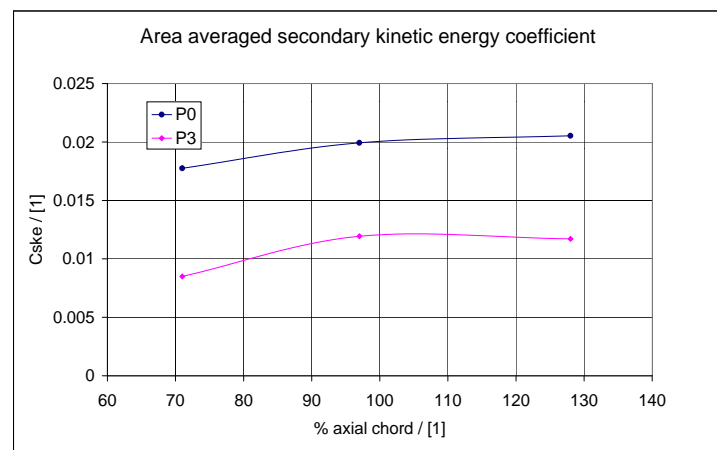


Figure 8.61: $\overline{\overline{C}_{ske}}$ growth through the cascade for P0 and P3.

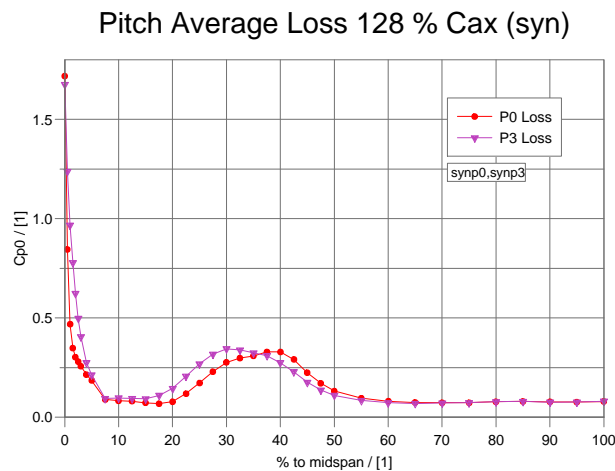


Figure 8.62: Pitch averaged loss, combined data set P0 and P3.

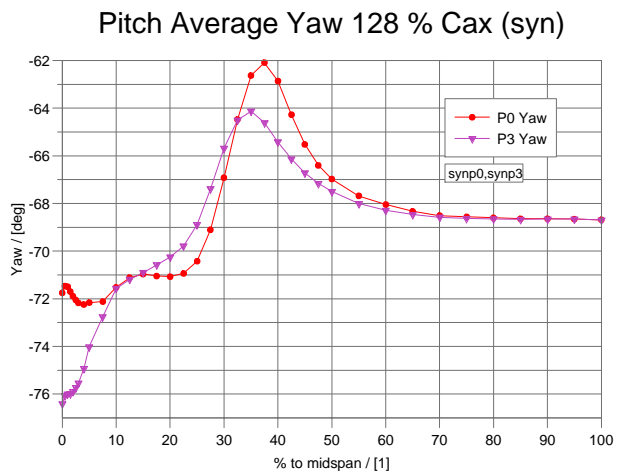


Figure 8.63: Pitch averaged yaw Angle, combined data set P0 and P3.

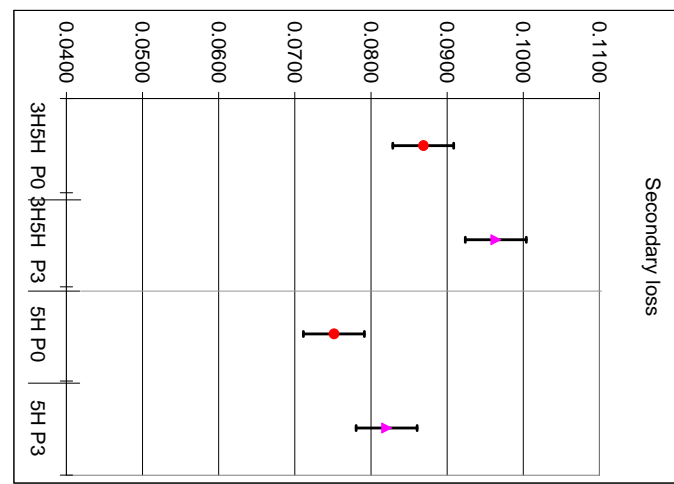


Figure 8.64: Area Averaged Loss Coefficient - effect of including three hole data.

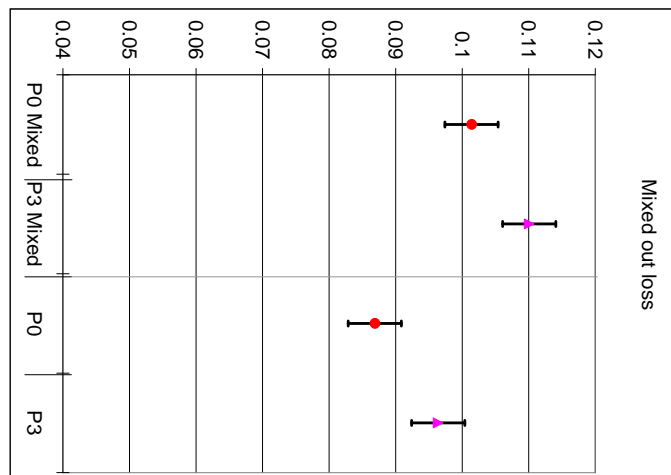


Figure 8.65: Area Averaged Loss Coefficient - effect of mixing out loss.

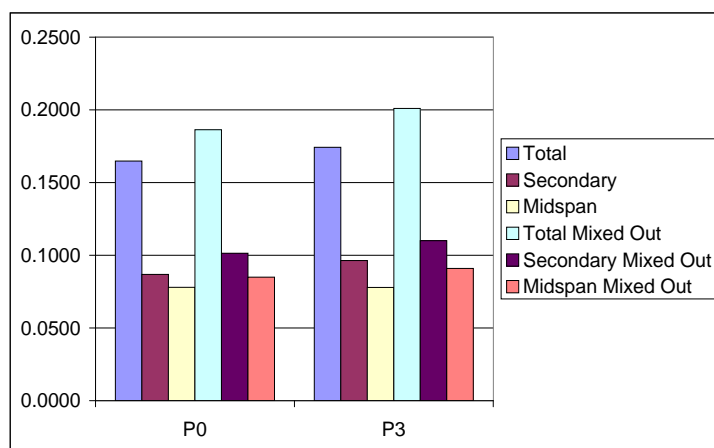


Figure 8.66: Summary Figure of P0 and P3 Area Averaged C_{P0} .



Figure 8.67: P0 Endwall Flow Visualisation.

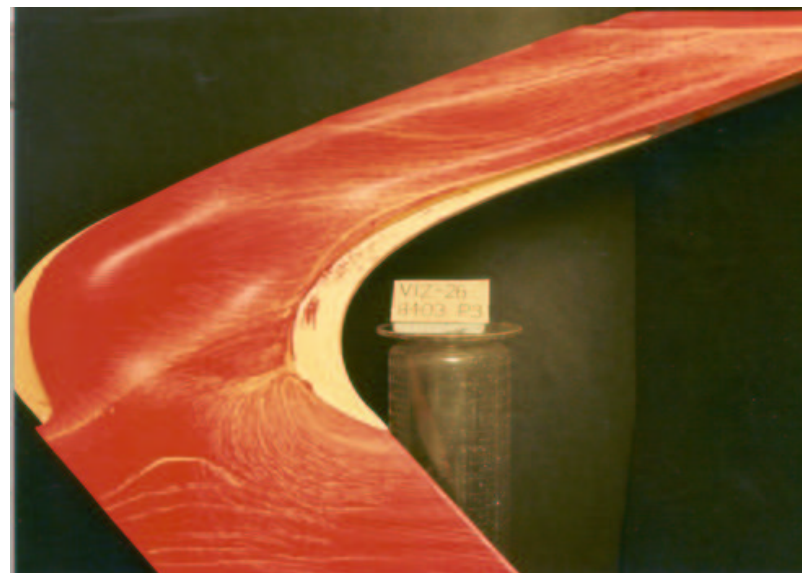


Figure 8.68: P3 Endwall Flow Visualisation.



Figure 8.69: P0 Leading Edge Flow Visualisation.



Figure 8.70: P3 Leading Edge Flow Visualisation.

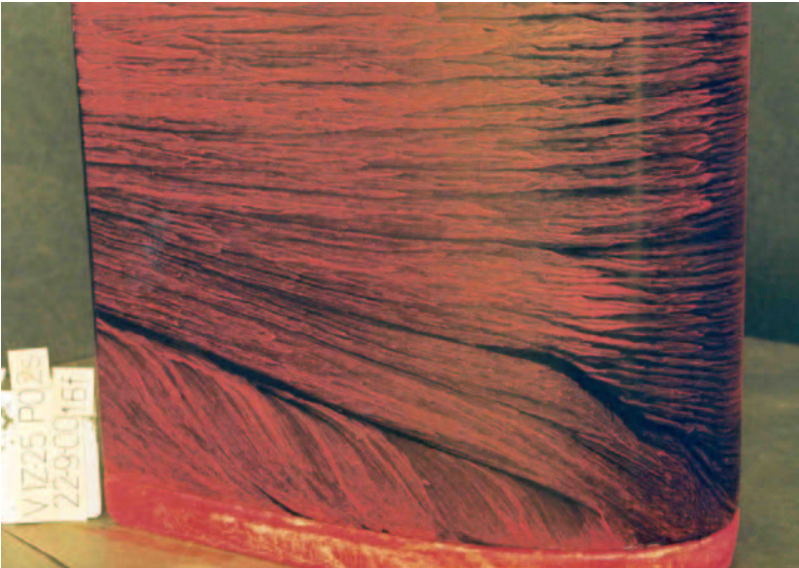


Figure 8.71: P0 Suction Surface Flow Visualisation.

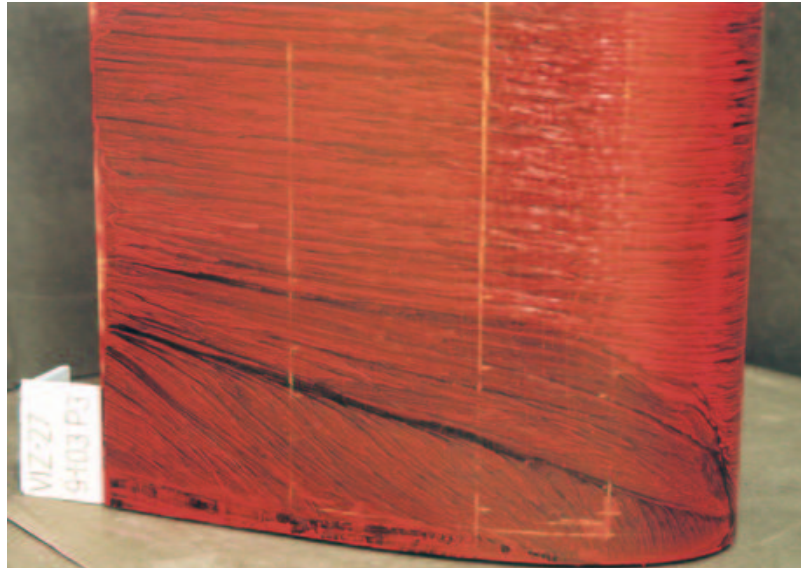


Figure 8.72: P3 Suction Surface Flow Visualisation.

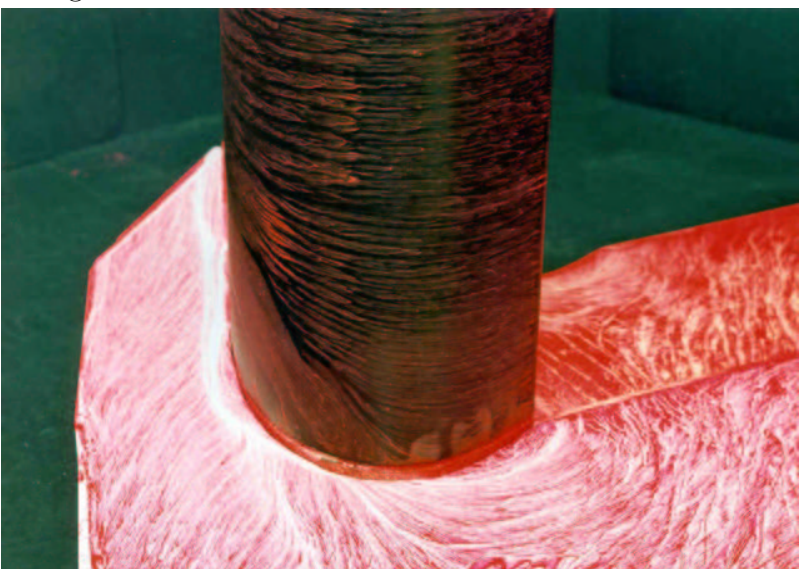


Figure 8.73: P0 Perspective View of Blade and Endwall.

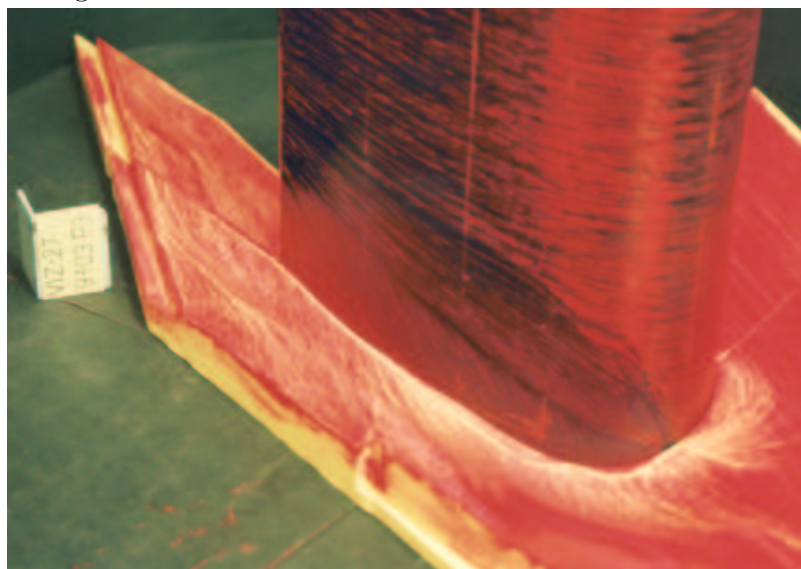


Figure 8.74: P3 Perspective View of Blade and Endwall

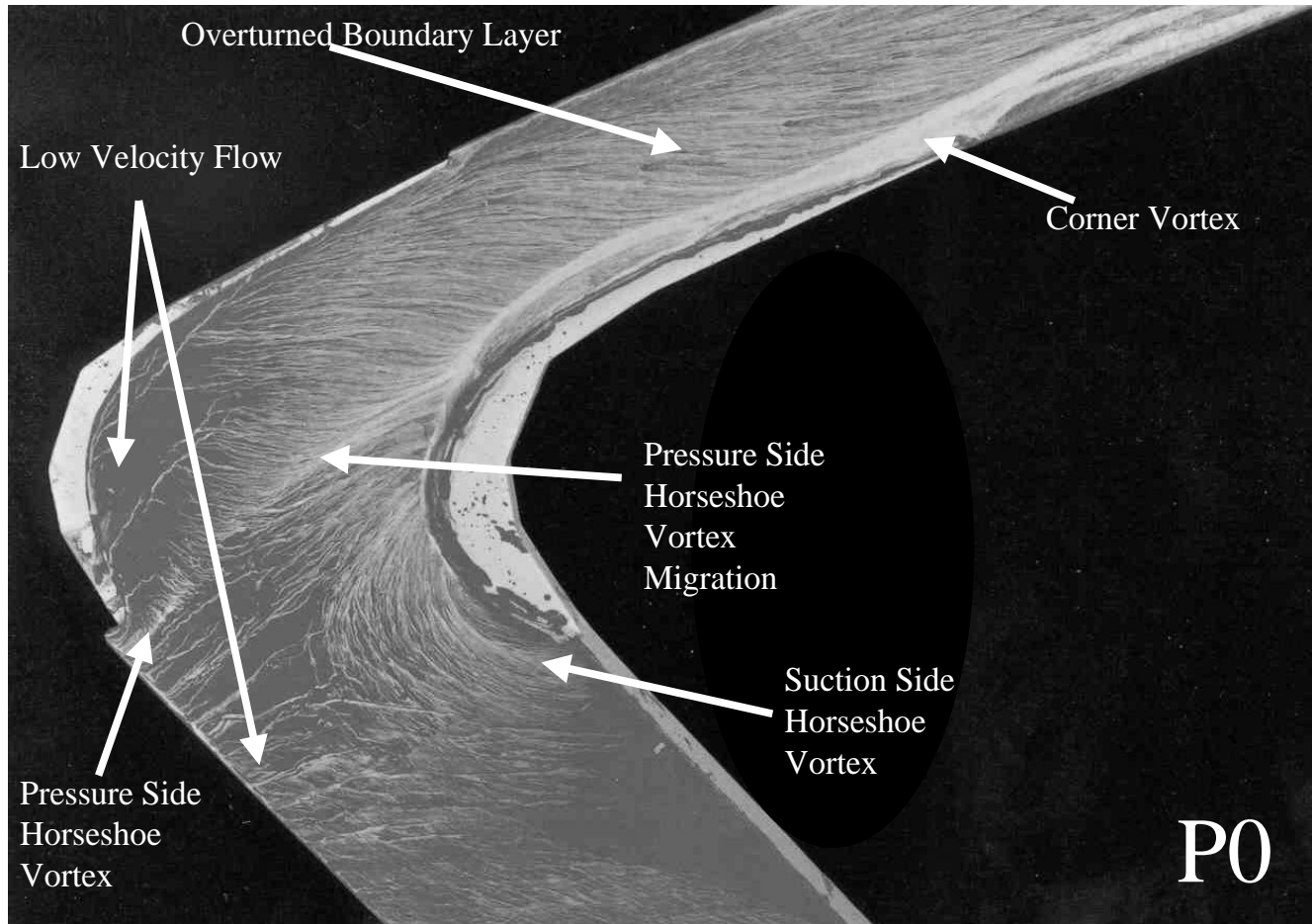


Figure 8.75: Annotated View of P_0 .

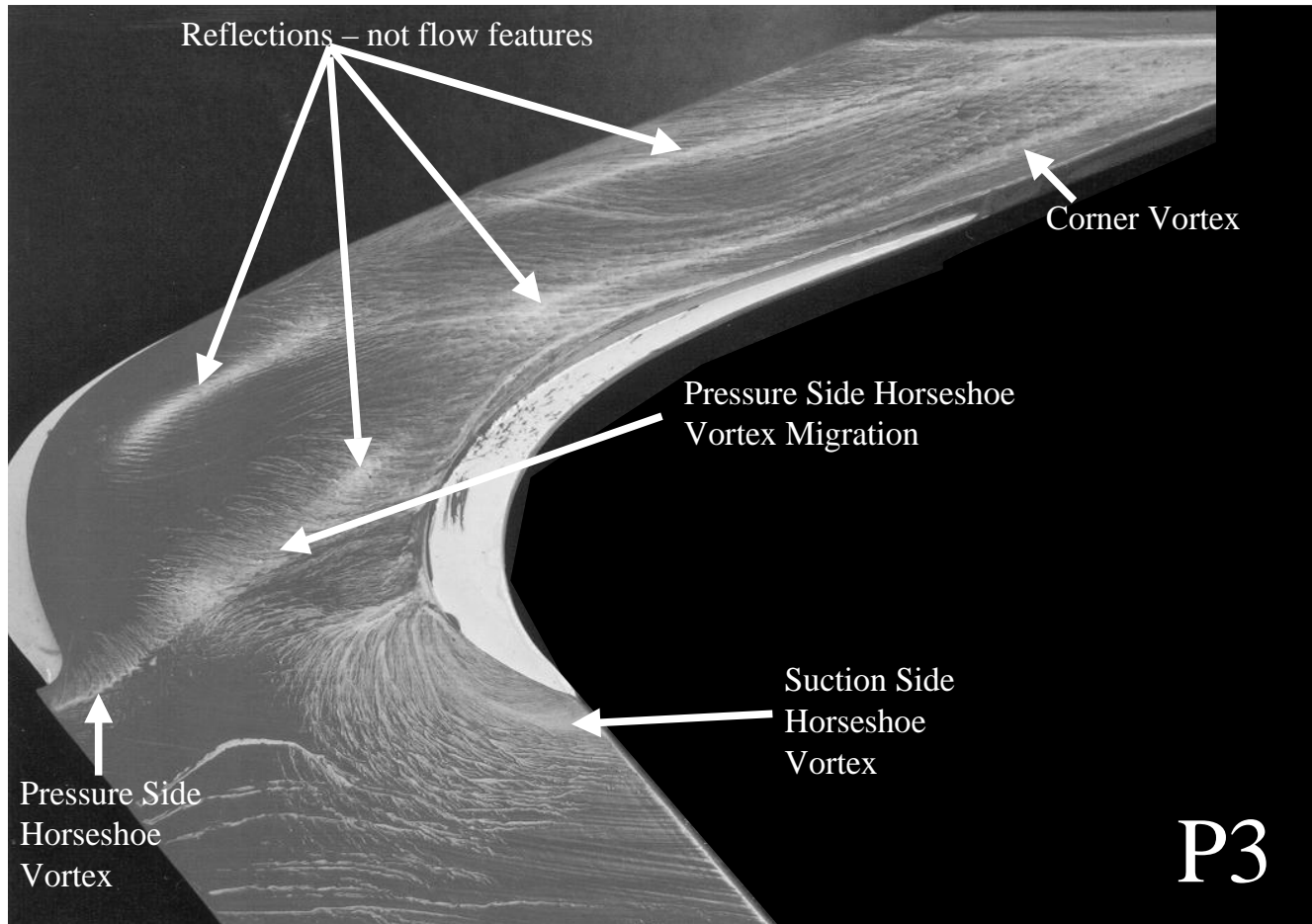


Figure 8.76: Annotated View of P3.

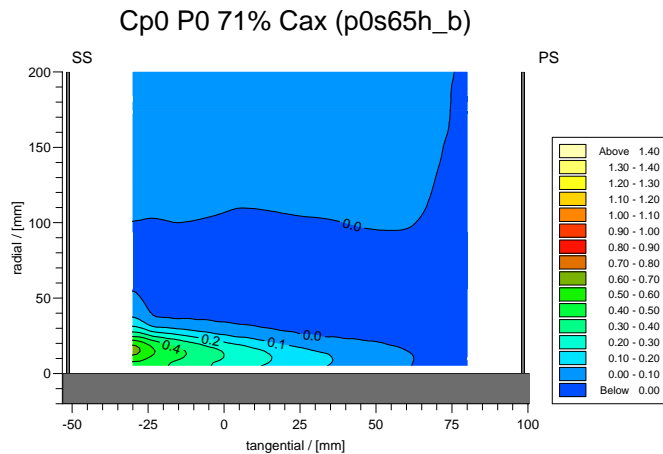


Figure 8.77: Planar Area Loss at Slot 6 - CFD.

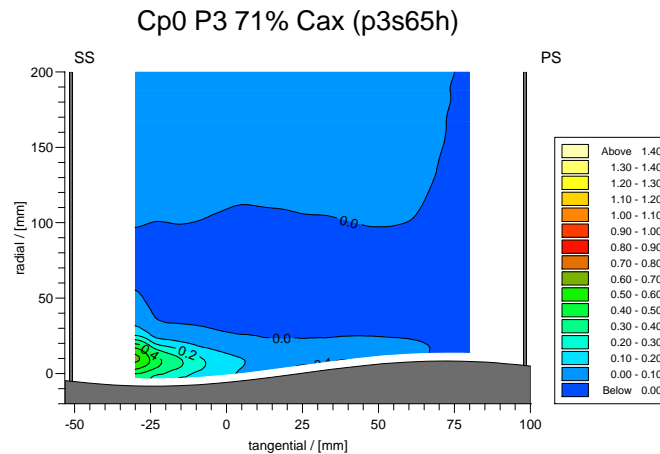


Figure 8.78: P3 Area Loss at Slot 6 - CFD.

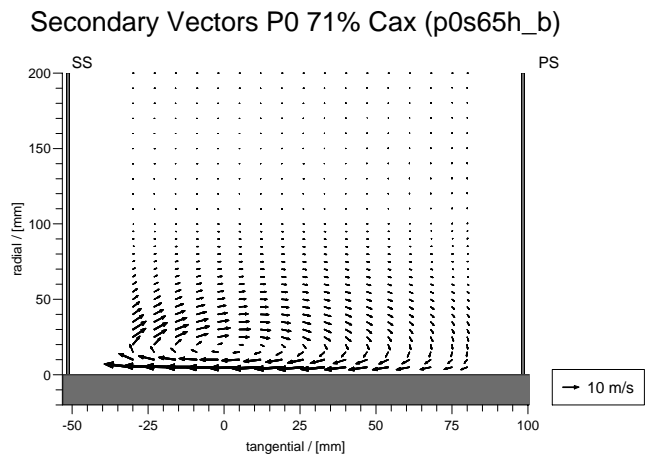


Figure 8.79: Planar Secondary Vectors at Slot 6 - CFD.

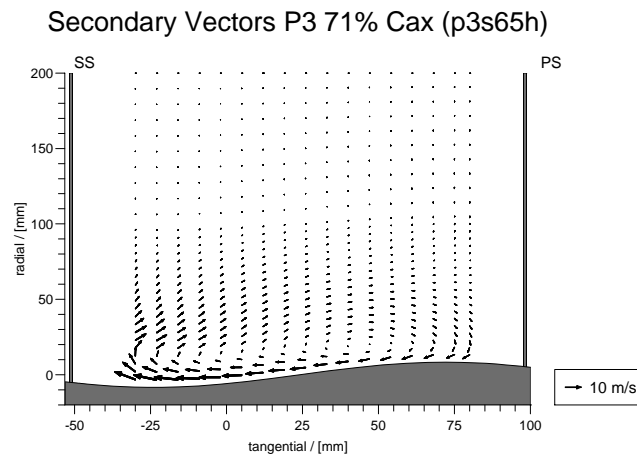


Figure 8.80: P3 Secondary Vectors at Slot 6 - CFD.

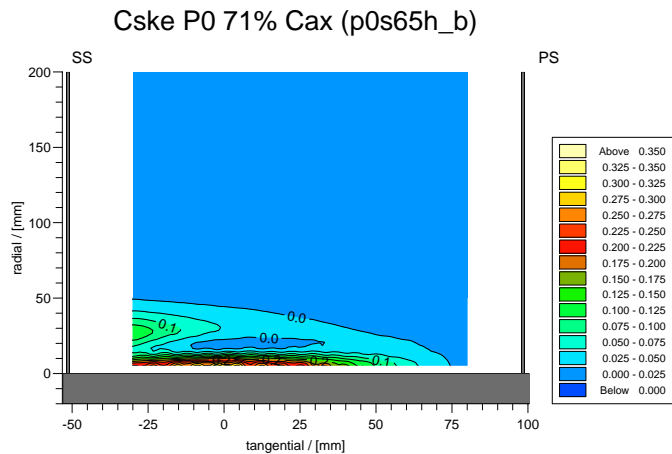


Figure 8.81: Planar C_{ske} at Slot 6 - CFD.

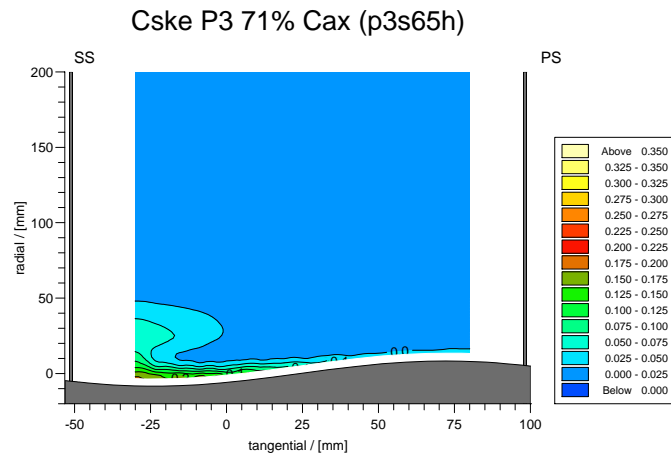


Figure 8.82: P3 C_{ske} at Slot 6 - CFD.

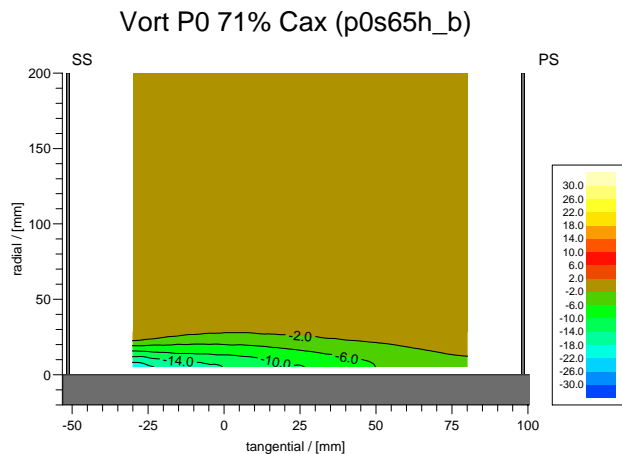


Figure 8.83: Streamwise Vorticity Coefficient at Slot 6 P0 - CFD.

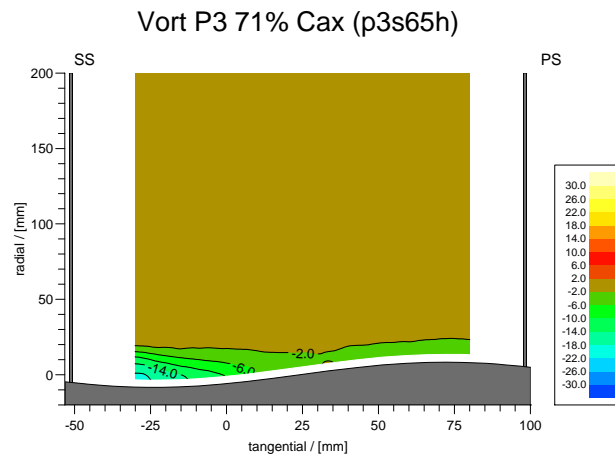


Figure 8.84: Streamwise Vorticity Coefficient at Slot 6 P3 - CFD.

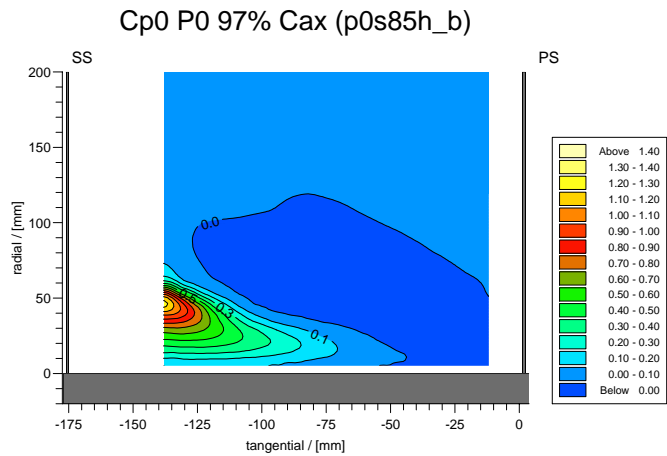


Figure 8.85: Planar Area Loss at Slot 8 - CFD.

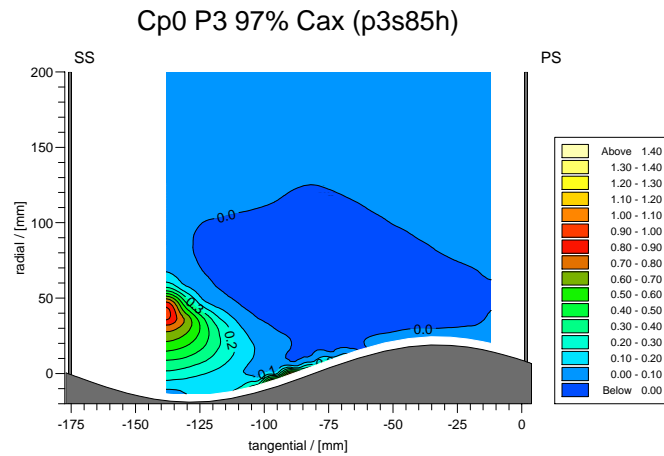


Figure 8.86: P3 Area Loss at Slot 8 - CFD.

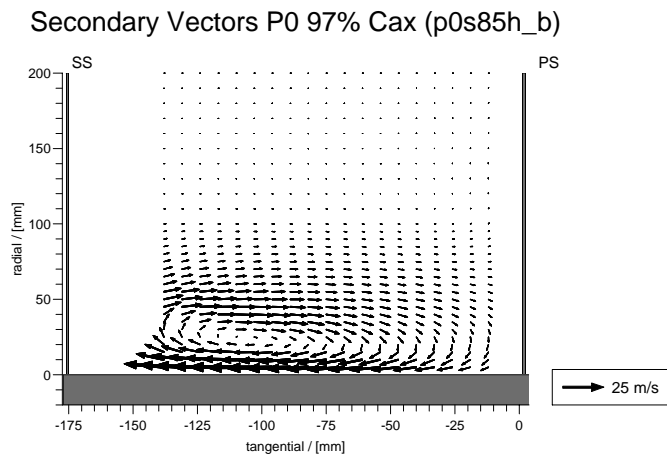


Figure 8.87: Planar Secondary Vectors at Slot 8 - CFD.

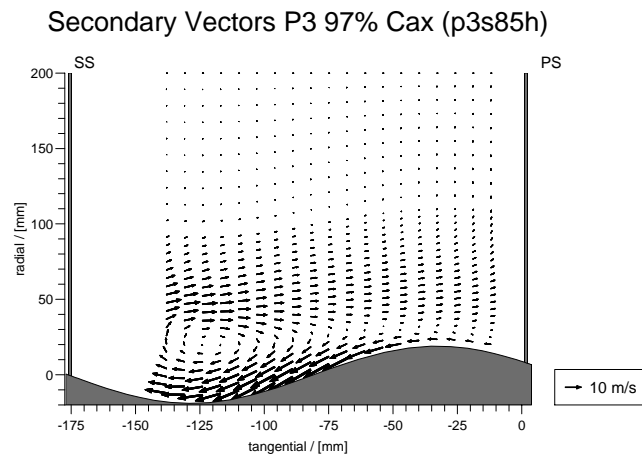


Figure 8.88: P3 Secondary Vectors at Slot 8 - CFD.

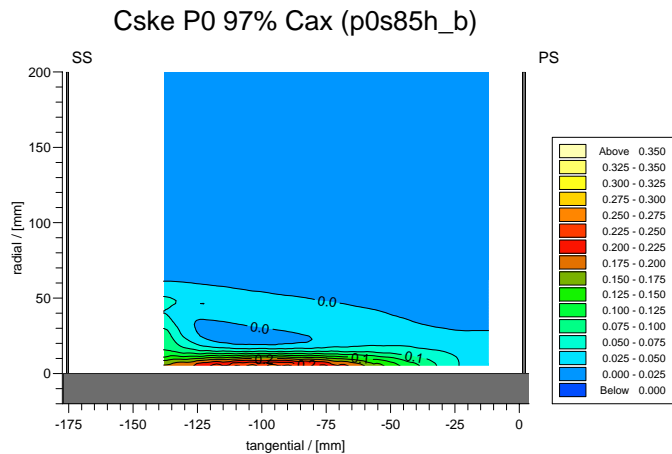


Figure 8.89: Planar C_{ske} at Slot 8 - CFD.

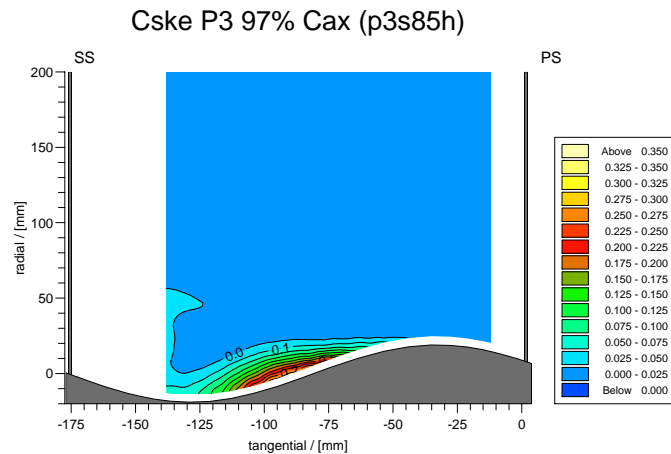


Figure 8.90: P3 C_{ske} at Slot 8 - CFD.

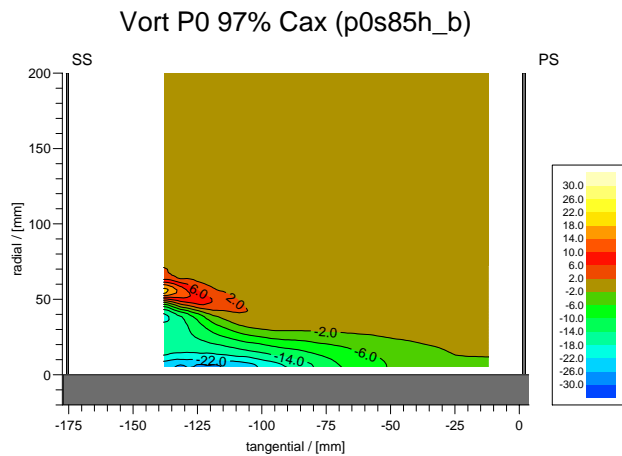


Figure 8.91: Streamwise Vorticity Coefficient at Slot 8 P0 - CFD.

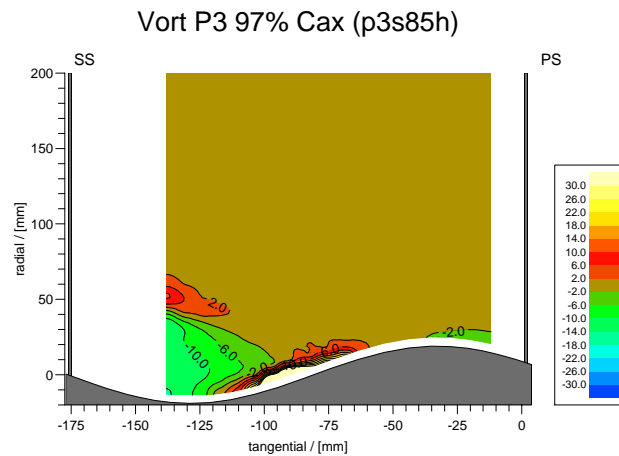


Figure 8.92: Streamwise Vorticity Coefficient at Slot 8 P3 - CFD.

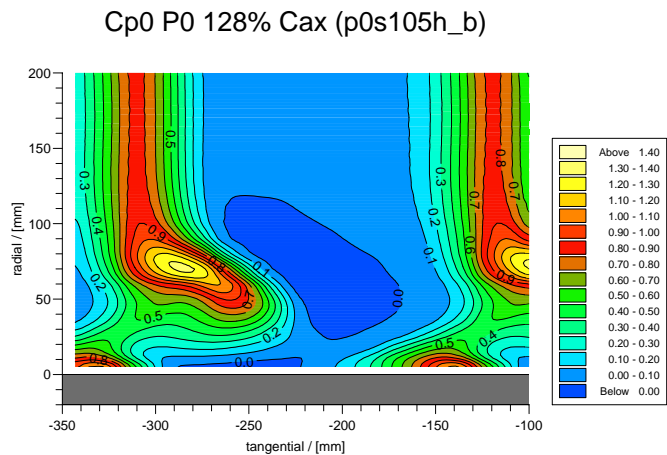


Figure 8.93: Planar Area Loss at Slot 10 - CFD.

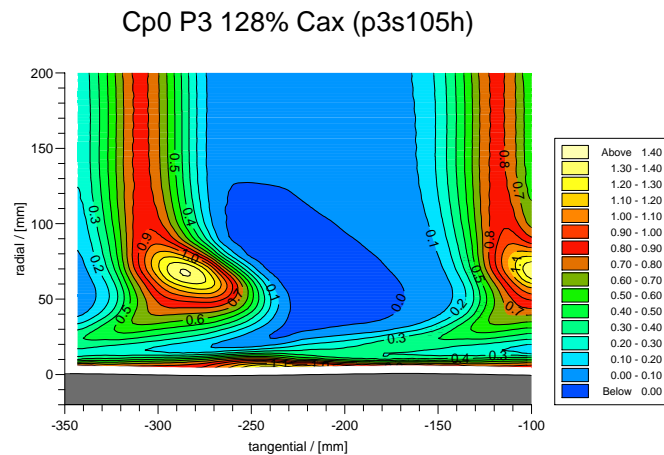


Figure 8.94: P3 Area Loss at Slot 10 - CFD.

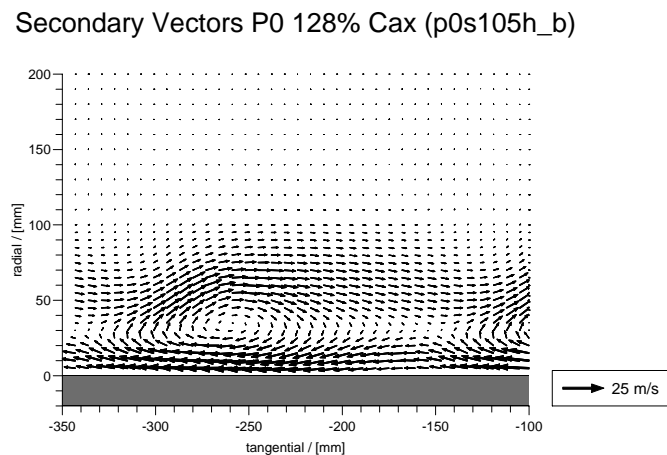


Figure 8.95: Planar Secondary Vectors at Slot 10 - CFD.

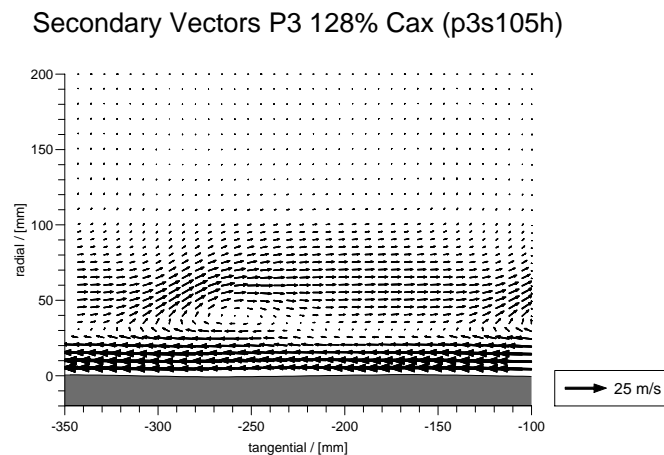


Figure 8.96: P3 Secondary Vectors at Slot 10 - CFD.

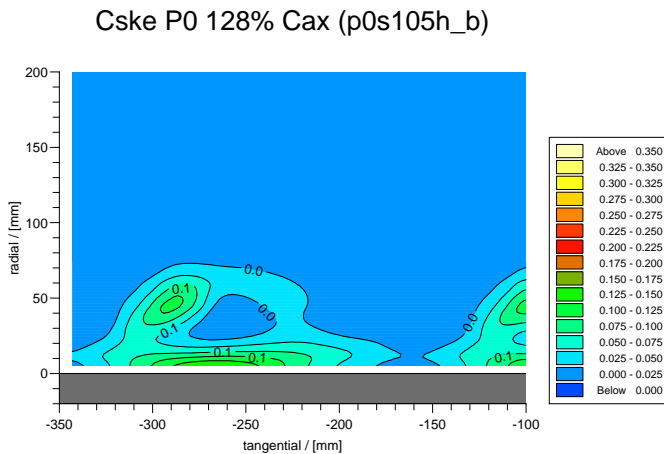


Figure 8.97: Planar C_{ske} at Slot 10 - CFD.

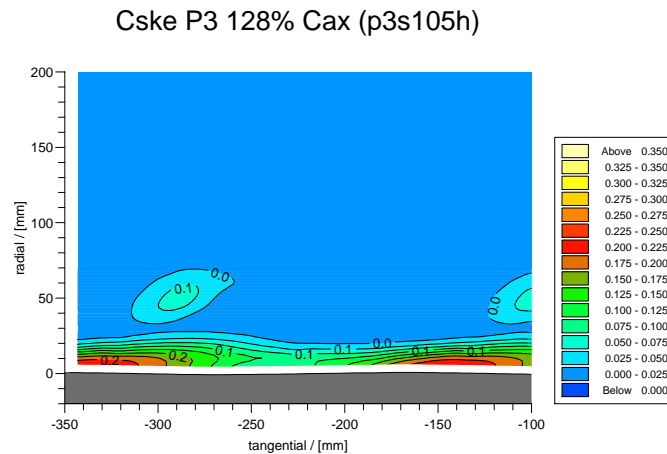


Figure 8.98: $P3 C_{ske}$ at Slot 10 - CFD.

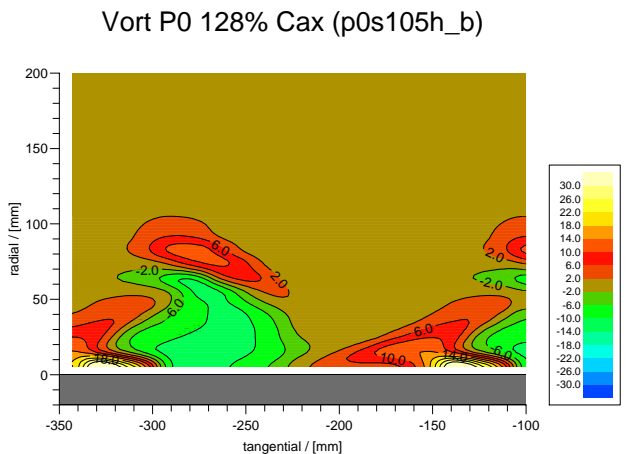


Figure 8.99: Streamwise Vorticity Coefficient at Slot 10 P0 - CFD.

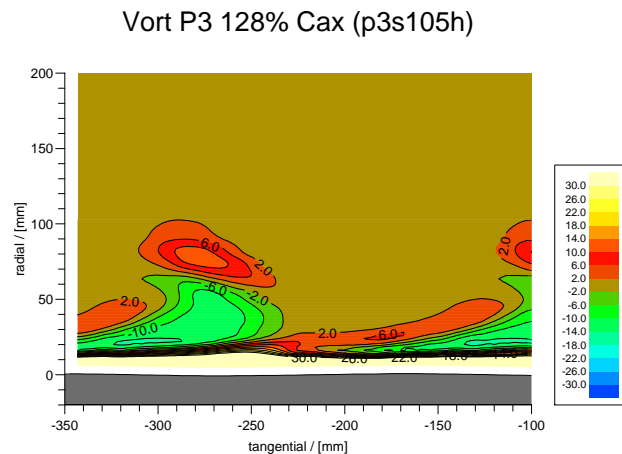


Figure 8.100: Streamwise Vorticity Coefficient at Slot 10 P3 - CFD.

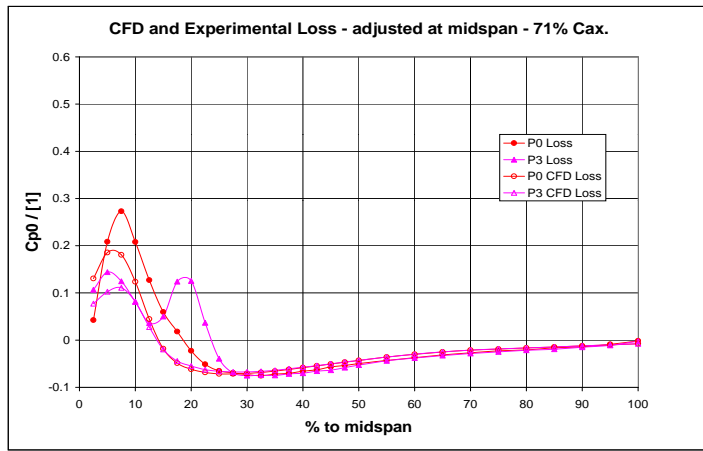


Figure 8.101: Pitch Averaged Loss at Slot 6 - CFD.

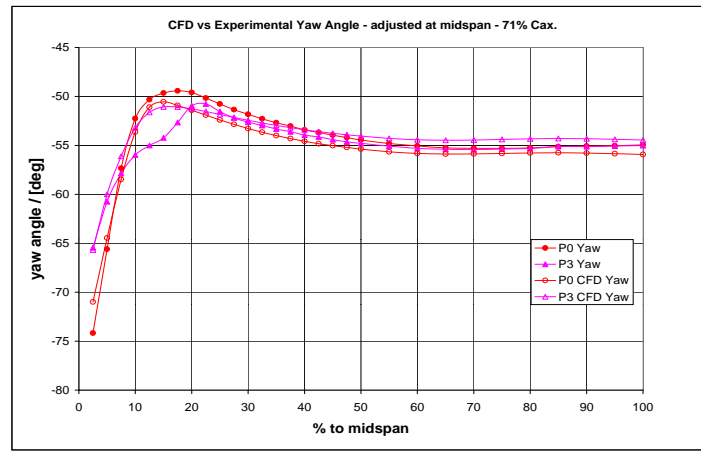


Figure 8.102: Pitch Averaged Yaw at Slot 6 - CFD.

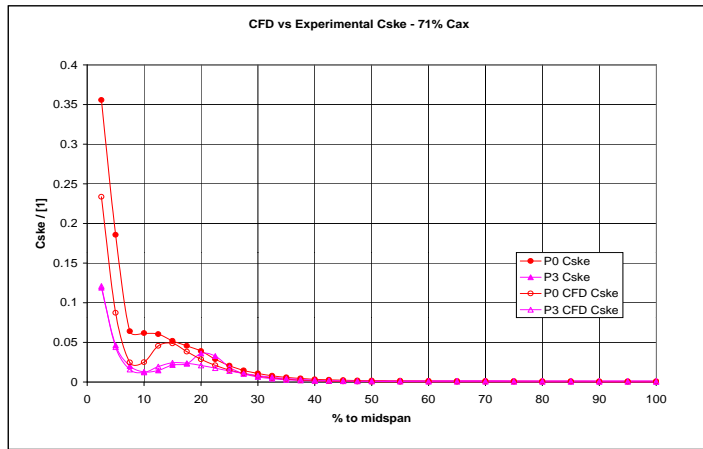


Figure 8.103: Pitch Averaged C_{ske} at Slot 6 - CFD.

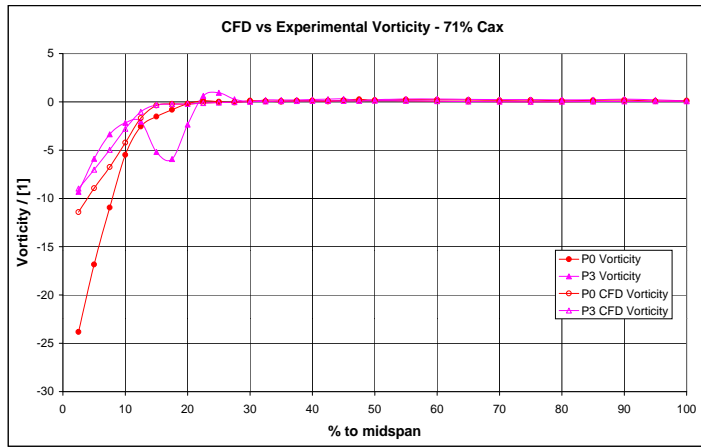


Figure 8.104: Pitch Averaged Streamwise Vorticity Coefficient at Slot 6 - CFD.

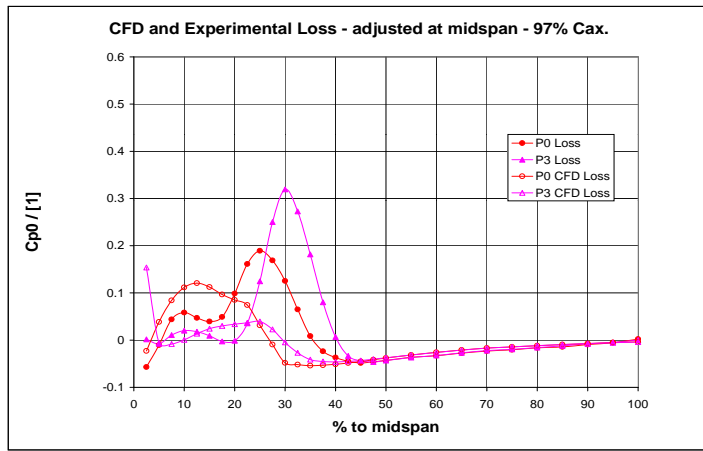


Figure 8.105: Pitch Averaged Loss at Slot 8 - CFD.

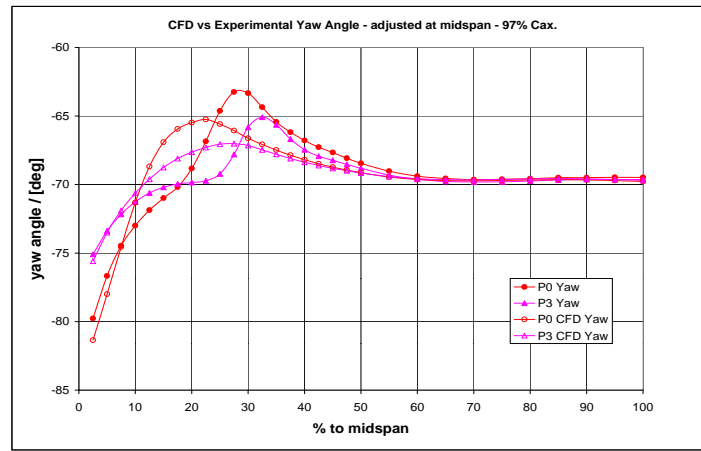


Figure 8.106: Pitch Averaged Yaw at Slot 8 - CFD.

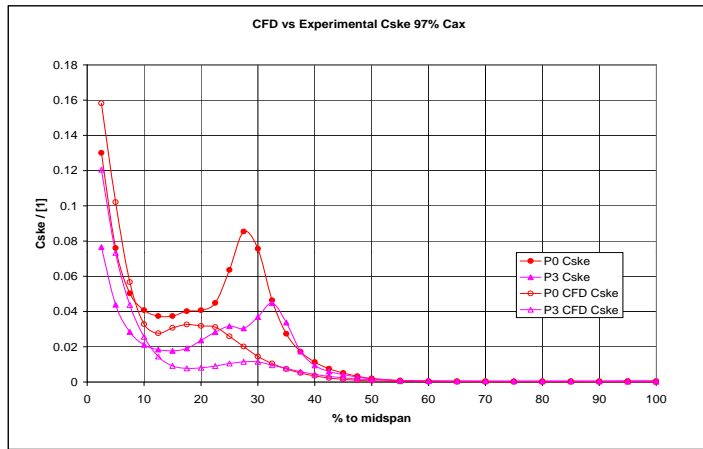


Figure 8.107: Pitch Averaged C_{ske} at Slot 8 - CFD.

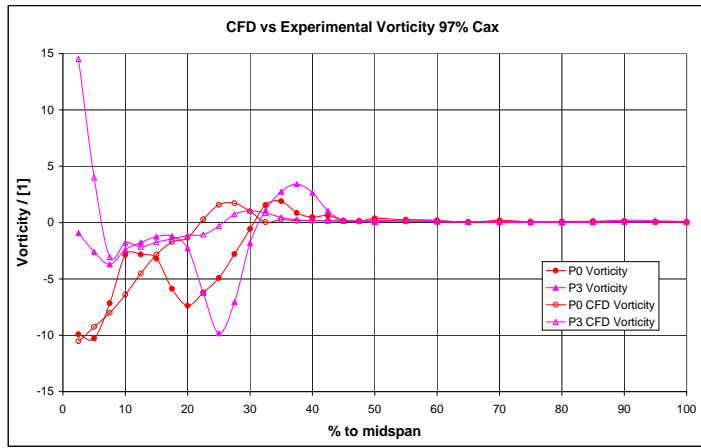


Figure 8.108: Pitch Averaged Streamwise Vorticity Coefficient at Slot 8 - CFD.

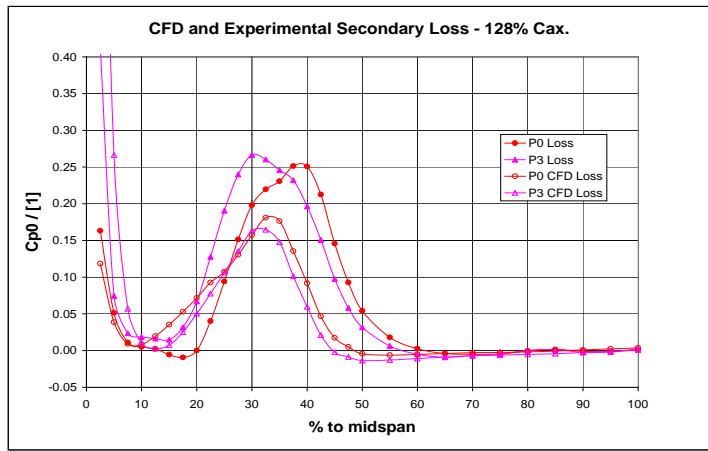


Figure 8.109: Pitch Averaged Loss at Slot 10 - CFD.

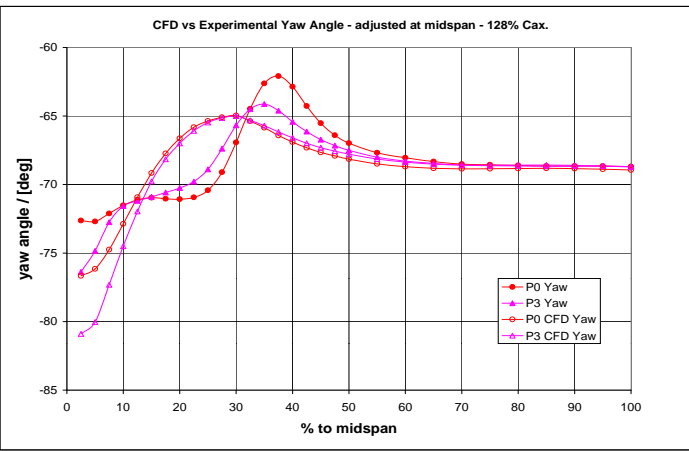


Figure 8.110: Pitch Averaged Yaw at Slot 10 - CFD.

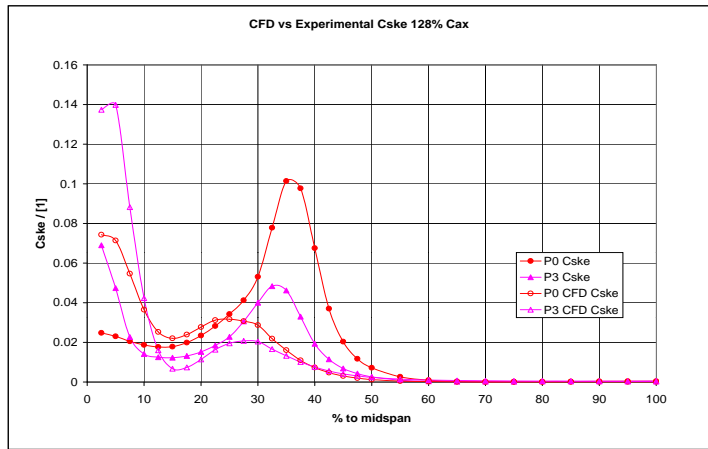


Figure 8.111: Pitch Averaged C_{ske} at Slot 10 - CFD.

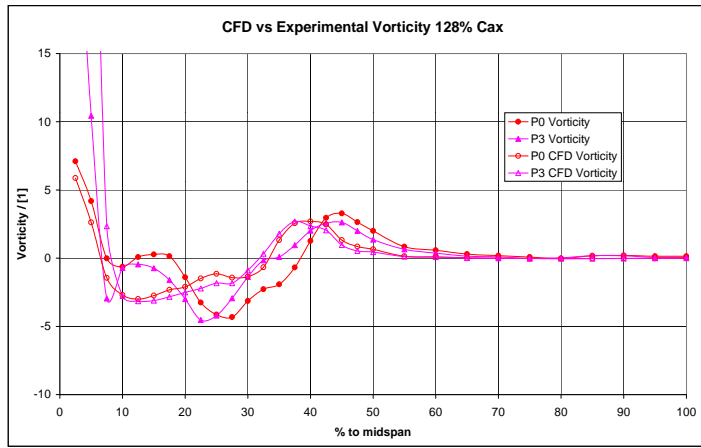


Figure 8.112: Pitch Averaged Streamwise Vorticity Coefficient at Slot 10 - CFD.

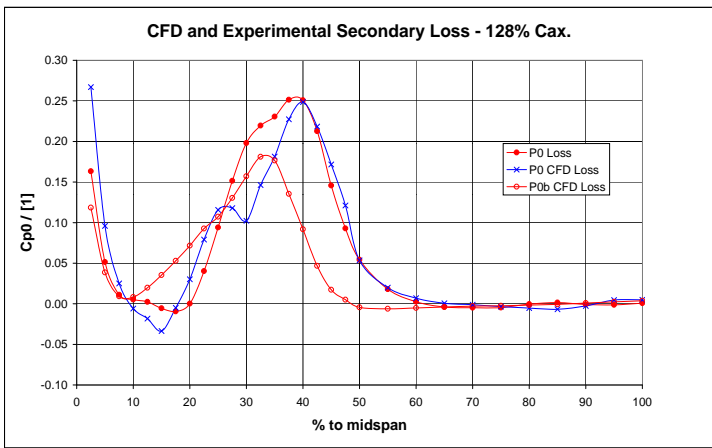


Figure 8.113: Loss predictions from the Two Planar CFD Solutions.

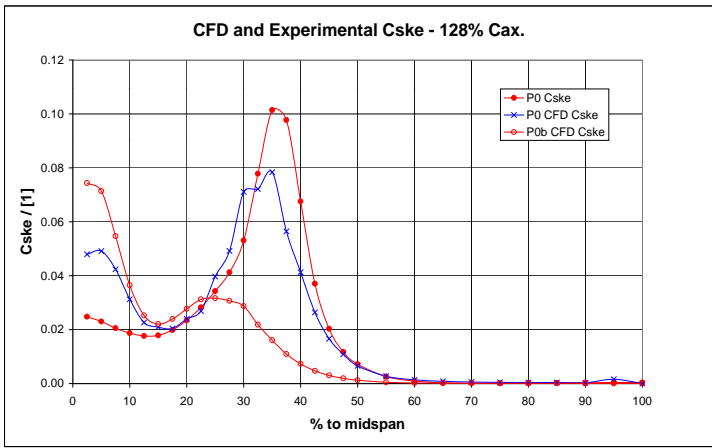


Figure 8.115: C_{ske} predictions from the Two Planar CFD Solutions

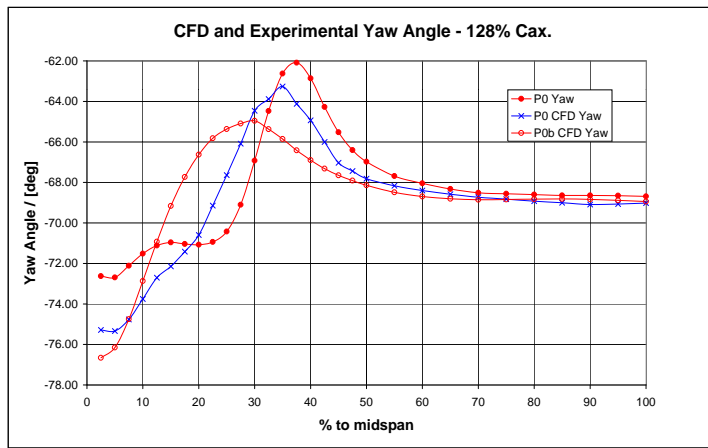


Figure 8.114: Yaw angle predictions from the Two Planar CFD Solutions.

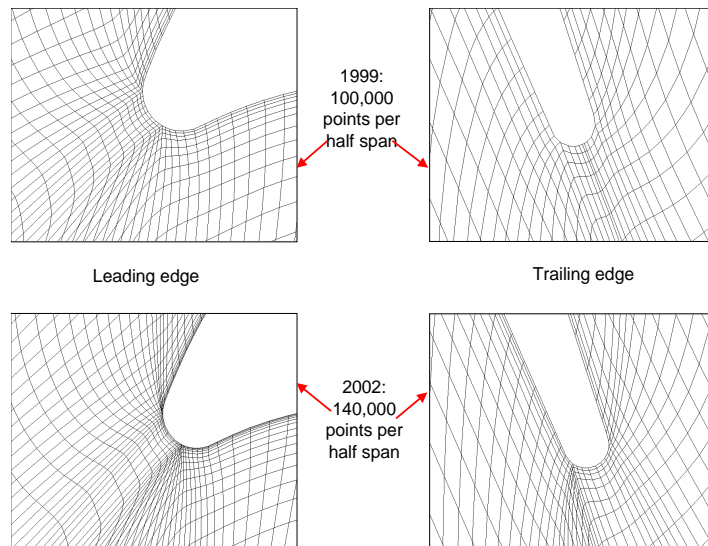


Figure 8.116: Comparison of Grids for the Two Planar CFD Solutions

Chapter 9

Overall Discussion

THE AIMS of this thesis were to understand the effects of three dimensional endwall profiling on loss reduction and provide information on a major engine manufacturers' design system for producing profiled endwalls. It is perhaps worth pointing out that understanding the effect of endwall profiling is an exceedingly ambitious aim to complete fully, the flow in the planar cascade features at least four major vortex structures, the production of loss from each is not well understood and the boundary layer flows on both the aerofoil and the endwalls are transitional. This chapter aims to highlight the understanding gained from the experiments conducted earlier, to make comparisons with other work and discusses ways the experiments and profiled endwalls could be improved.

9.1 Publication of Experimental Technique

The experimental techniques for flow visualisation results and pressure probe traversing were explained in detail in Chapter 3. Considerable space has also been devoted to the detailed data processing algorithms. The motivation behind this is to ensure that the experiments can be repeated and the results reproduced. Although there are descriptions of the experimental technique used in the Durham Cascade they often omit details which although trivial are vital to the understanding of the technique as a whole.

It is current practice for all calculations and algorithms to be embedded in computer programs as this allows calculations to proceed much faster than if they were done by hand. This also extends to experimental technique; the author has conducted something approaching one hundred and ten different traverses and nearly eight probe calibrations during the course of this work which would not be possible if they all had to be completed by hand. Having a reliable automated system means that multiple readings can be taken easily.

It is the author's view that where there is not a requirement for confidentiality both the data and the program sources used in a scientific publication should be made available. This leads to the possibility of detailed peer review and allows others to build on the work conducted.

9.2 Flow Visualisation

A comprehensive set of surface oil/dye flow visualisation measurements have been presented in this thesis. These images show a reduced passage vortex for P1 and P2 cases with no discernible trace of the passage/pressure side of the horseshoe vortex seen at all on the endwall. Significant changes are observed in the horseshoe vortex for P1 and P2 with a large stagnant area being observed for the P1 geometry. Blade surface visualisations confirm the reduced strength of the passage vortex for P1 and P2 but indicate that the fundamental flow dynamics are the same. For the third generation endwall the flow visualisation has highlighted a region of separated flow which explains the cause of the poor performance of the P3 endwall.

This shows that despite being a “tried and tested” technique surface oil/dye visualisation remains valuable. It is also apparent from the flow visualisation work that the orientation of the cascade (airflow exiting upwards) is a major impediment to getting high quality flow visualisation results in regions of low speed. For example we can contrast the flow visualisation of the horseshoe vortex see in Figure 8.75 on page 247 with those found in Langston et al. (1977) who used a horizontal endwall. Mounting the cascade with a horizontal endwall improves the flow visualisation quality substantially. However there are good practical reasons for the cascade discharge to be vertical, as the cascade is situated in a laboratory with a number of other cascades anything other than a vertical discharge would interfere with other experiments.

9.3 Transitional Flow in the Durham Cascade

Previous studies on the planar endwall Moore (1995) have shown significant areas of transitional flow. The Durham Cascade operates at a Reynolds number several times lower than that found in real machines. If the benefits of endwall profiling were derived significantly from altering the transition of the endwall or blade surface, the applicability of the technique to real machines would be in doubt.

Chapter 6 of this thesis described hot film work to determine the state of the boundary layer on the endwall and suction surface. This work shows that little change in the boundary layer state occurs on the aerofoil suction surface when endwall profiling is applied. There is clear evidence of transitional flow for the planar and P1 and P2 profiles. The endwall boundary layer is much less clear. However it would appear that endwall profiling does not dramatically change the state of the boundary layer.

The results from Chapter 6 suggest that the transitional nature of the boundary layers are not changed by the application of endwall profiling. This means the benefits of endwall profiling are due to bulk flow effects and not changing the state of the boundary layers. The results of engine representative rig tests (Brennan et al. (2001) and Harvey et al. (2002)) also suggest that the benefits of endwall profiling are applicable to real machines.

9.4 Comparison with previous work in the Durham Cascade

This thesis contradicts previous results from the Durham Cascade. Jayaraman (2000) reported on the manufacture and test of the second generation endwall and concluded that the P2 profile performed considerably worse than the P1 profile, although it still reduced loss. This conclusion is not supported by the current results and some comment is required. There are a number of reasons for the differing results:-

- Different experimenters use slightly different experimental techniques. This has a major effect on evaluating endwall designs as the differences between endwalls are very small. A major effort in the current work has been to standardise the experimental method so that comparable results can be achieved.
- No repeat of the datum case was made when Hartland and Jayaraman measured their profiled endwalls. As has been shown earlier even when repeating the results in a “back to back” manner relatively large changes occur - the author regards this as the main reason for the differences between the current work and that of his predecessors.
- Minor changes have been made to the test rig. Specifically the probe positioning methodology has been improved, the endwall mounting has been made more robust and minor repairs have been made to other areas of the cascade. These changes are unlikely to change the conclusions of this thesis but they introduce an extra level of variability into a comparison of the present work with that of Jayaraman (2000) and Hartland (2001).
- It is very rare for cascade or turbine rig experiments to be repeated. In fact the author knows of very little published work which repeats experiments on the same rig carried out several years later.

Although different processing of the experimental results has taken place this is not the cause of the change in ranking of the two profiled endwalls. The data from Hartland and Jayaraman has been processed using the current data processing methods and gives the same ranking in terms of loss production. The results from earlier papers are not directly comparable, for example earlier papers used the Slot 1 (-9% c_{ax}) results for the inlet boundary layer.

Figure 9.1 shows the pitch averaged loss values from a number of experimenters on the Durham cascade. This graph is for the planar case and includes the “state of the art” reading from the current data. There are two data sets compared, the one produced by Hartland (2001) (labelled JCH on the graph) and one distributed as the ERCOFTAC test case for the Durham Cascade¹ (labelled TEST on the graph). As can be seen from this graph the variations between Hartland (2001) and the current work are not atypical. The results are adjusted to give the same midspan value to allow easy comparison.

¹This data is publicly available on the world wide web.

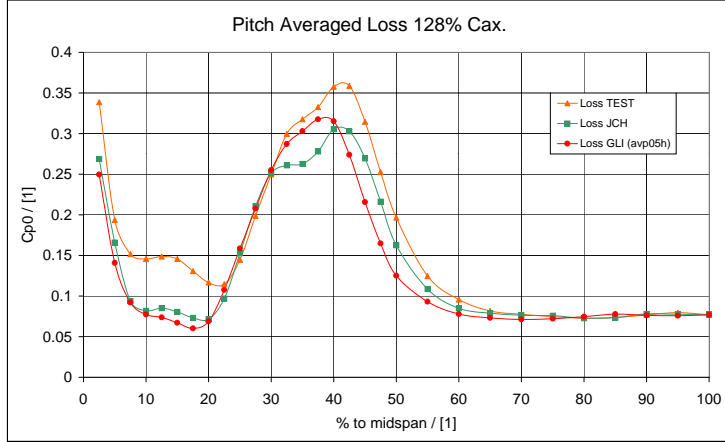


Figure 9.1: Pitch Averaged C_{P0} for a number of experimenters.

Figure 9.2 shows a similar figure for yaw angle, this figure includes data from Moore (1995) (labelled HM on the graph) taken from single rotate-able hot wire measurements which do not allow loss readings. The results are again adjusted to give the same midspan value. It would appear that it is easier to measure yaw angle than loss coefficient. The figure shows that at most there is a 1.5° variation between experimental results taken by different experimenters over a period of nearly ten years using different techniques.

It is important to avoid ignoring the significance of the change in loss ranking and also to avoid making too much of the changing conclusions. The current results support many of the conclusions drawn in the previous papers, the endwalls still reduce loss although the exact level of reduction has been clarified. It is also very easy to be “wise after the event”, the original work on profiled endwalls carried out by Hartland et al. (1999a) was extremely innovative, developing systems for manufacture and testing of profiled endwalls.

The discrepancy between the P2 flow dynamics and the loss reduction was quite clearly stated in Gregory-Smith et al. (2001) and the conclusions of Hartland et al. (1999a) are unchanged by the current results.

9.5 Pitch Averaged Yaw Angle Calculation

For all the results contained in this thesis the pitch averaged yaw angle was calculated as:-

$$\bar{\alpha} = \tan^{-1} \frac{\bar{V}_t}{\bar{V}_x} \quad (9.1)$$

However in earlier published work Ingram et al. (2003) and Ingram et al. (2002) a different method of calculating pitch averaged yaw angle was used namely:-

$$\bar{\alpha} = \frac{\int_0^s \alpha V_x \Delta r dt}{\int_0^s V_x \Delta r dt} \quad (9.2)$$

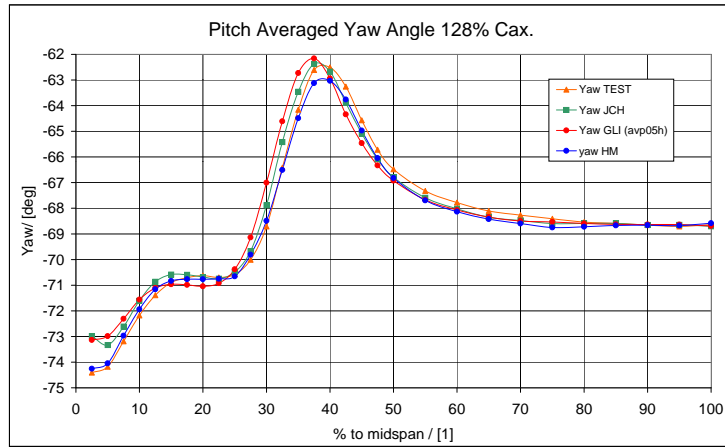


Figure 9.2: Pitch Averaged yaw angle for a number of experimenters.

This is analogous to the mass weighting used for the calculation of various coefficients; $\overline{C_{ske}}$, $\overline{\Omega_s}$, However the method used in this thesis is to be preferred as it associates the angle with the correct mass flow and tangential momentum. The changes between equation 9.1 and 9.2 are generally very small except near the endwall when differences of a few degrees may emerge.

The only substantive change that this results in is that using the mass weighted (Equation 9.2) method of calculating pitch averaged yaw results in much reduced overturning at the endwall for P1 compared to the planar case. Figure 5.110 on page 124 shows that for the correct calculation (Equation 9.1) the overturning is about the same for P0 and P1. The reasons for this are primarily due to the axial velocity distribution of P1 close to the endwall - low axial velocity is found in the regions of overturned flow. The current result is more consistent with the secondary vectors found in Figure 5.124 on page 128.

9.6 Absolute Yaw Angle Measurement.

As described in Chapter 3, adjustments to the experimental data are made for midspan yaw angle, midspan pitch angle and midspan midpitch loss coefficient. Due to the methods used in setting the yaw angle of the probe in the early stages of the work conducted for this thesis a low level of accuracy in yaw angle setting was obtained. This has necessitated large corrections to the experimental data in order to make some blade passage measurements comparable to each other and subsequently necessitated even larger corrections to the CFD data in order to make it comparable to the experimental data.

Clearly this situation is undesirable and in future more care must be taken when setting up traverses. It would also have been desirable to have examined the CFD midspan yaw angles in order to get an idea of what the experimental midspan yaw angles might have been. One would expect CFD to predict the two dimensional

Experimenter	Error exit P_{dyn}	Error inlet P_{dyn}
Current work (2003)	-	± 0.005
Biesinger (1993)	-	± 0.005
Harrison (1989)	± 0.003	-
Hodson and Dominy (1987)	± 0.005	-
Langston et al. (1977).	-	± 0.0044

Table 9.1: $\overline{\overline{C}_{P0}}$ error estimates from literature.

turning at midspan accurately. However for the first part of the project a detailed examination of Rolls-Royce CFD was not available. Nevertheless the result of these defects has been that this thesis discusses yaw angles relative to the planar case in most cases rather than absolute values. More accurate methods of setting up the probe have largely solved the problem but future projects should ensure that absolute yaw angle measurements are taken from the start.

9.7 Experimental Loss Evaluation

A major part of this thesis has been devoted to obtaining accurate measurements of loss production in a turbine cascade when endwall profiling is applied. This is much more difficult than was at first appreciated, the planar case is already quite efficient and the absolute level of loss reductions that are being measured is quite small. This thesis has attempted to provide accurate and repeatable loss measurements for several profiled geometries as well as a realistic estimate of the accuracy of the measurement.

This is a feature that is not found in other work in the field where repeating measurements appears to be somewhat unusual. For example the work of Sauer et al. (2000), Hartland (2001), Harrison (1989) and Hodson and Dominy (1987) do not contain repeats of the same experiment. This is not to suggest that the cited works are not high quality work but that providing an estimate of accuracy by repeating experiments is not common. One of the reasons for this may be that conducting experiments is time consuming and difficult and for many purposes is not required. For example the work described in this thesis on the third generation endwall has but one traverse conducted on it for the results. However since the loss is going up and not down it was not felt necessary to repeat the results.

The estimate of accuracy for secondary loss measurements conducted for this thesis was estimated at around $\pm 5\%$ of secondary loss or ± 0.005 in terms of loss coefficient. Table 9.1 shows error estimates for cascade tests conducted by Biesinger (1993), Harrison (1989), Hodson and Dominy (1987) and Langston et al. (1977). Note that some experimenters have defined C_{P0} using the exit dynamic head to normalise the coefficient, this is common turbine for turbine blade design. This thesis uses the *inlet* dynamic head to normalise pressure coefficients as the inlet conditions are well defined.

Table 9.1 suggests that the error margins that have been found in this thesis are typical of those found by other workers.

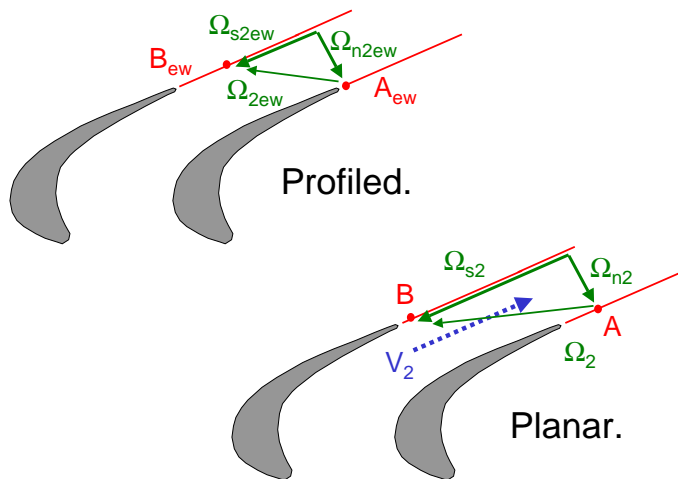


Figure 9.3: Effect of endwall Profiling on Streamwise Vorticity

9.8 Classical Secondary Flow Theory

Classical secondary flow theory can play an important part in understanding secondary flow. For example an appreciation of the Squire & Winter formula (Equation 9.3) leads to some useful insights into the flow. For example that turbulent boundary layers have the normal vorticity concentrated near the endwall, so the secondary flow will also be concentrated there.

$$\Omega_s = -2\Omega_n(\alpha_2 - \alpha_1) \quad (9.3)$$

Another important result from understanding classical secondary flow theory is that one cannot eliminate the secondary flow. Streamwise vorticity arises from the turning of the vorticity vector in a turbine. It is impossible to avoid turning the flow and hence the vorticity vector, so some secondary flow will always be present.

Endwall profiling introduces a three dimensional effect near the endwall. Thinking about this in terms of a pressure field, endwall profiling is designed to reduce the cross passage pressure gradient which drives the secondary flow.

Endwall profiling can also be thought of in terms of vorticity dynamics. Thinking in terms of vorticity dynamics endwall profiling reduces the velocity on the suction surface and increases it on the pressure surface by means of streamline curvature. This reduces the magnitude of the streamwise vorticity. This is illustrated in Figure 9.3.

Simple vorticity dynamics equations such as the Squire and Winter formula or the more comprehensive equations of Came and Marsh (1974) operate only on the flow angle and the inlet vorticity. Endwall profiling is a way of altering the endwall state without altering the bulk of the flow so it is impossible with simple vorticity theory to calculate quantitative effects of endwall profiling, or even to attempt to rank competing geometries. Furthermore Came and Marsh (1974) assume that the Bernoulli surfaces remain plane - this is clearly impossible with profiled endwalls.

Nevertheless classical secondary flow theory provides an insight into the fundamental mechanisms at work.

9.9 CFD predictions of endwall profiling

The design of these profiled endwalls would not be possible without the use of CFD technologies which allow the designer to select one out of a number of candidate geometries.

CFD does not however predict loss accurately, although the results from Chapter 7 show that CFD can predict roughly the right shape of the loss core (Figure 7.95 on page 203). A detailed examination of the origins of that loss suggest that the origins of the loss are incorrect. For CFD most of the loss peak (30-50% midspan) comes from boundary layer loss that is convected into the passage vortex loss core downstream of the blade row. In the experiments half the loss peak comes from the passage vortex itself. The point is that although a rough qualitative agreement of loss can be obtained this is not due to accurate modelling of the loss production in the flow field.

CFD does a better job of predicting yaw angle deviations as can be seen in Figure 7.96 on page 204. As is well known this is down to the fact that flows are dominated by mass and momentum conservation and not the detailed viscous interactions. In fact once a sheared boundary layer is present many of the detailed flow patterns can be predicted using an inviscid calculation. If the designer is aware of the limitations of the current “state of the art” CFD he or she can work around them as been demonstrated with the first two generations of endwall design. In fact the first generation endwall was designed with this very limitation in mind, using exit angle deviations as the guide to the performance of the endwall designs. More sophisticated methods have since been developed based (see Brennan et al. (2001)) which try to do the same thing for three dimensional geometries.

The third generation endwall demonstrates that CFD predictions are not perfect and can in fact lead to serious errors.

9.10 Third generation endwall

The third generation endwall was designed to achieve the best possible loss reduction and used the largest height perturbations that could be manufactured ($\pm 20\text{mm}$). This third generation endwall does not however reduce loss. In fact there is an increase in loss, this increase is due to the existence of a three dimensional separation associated with a region of sharp curvature. The fact that the third generation endwall increases loss does not however invalidate the approach of using three dimensional endwalls to reduce loss, the third generation endwall was an attempt to obtain the best possible loss reduction using the largest perturbations in height - it is not surprising therefore that a limit has been reached. It is also difficult to see how one would recognise that a limit had been reached and the design is going to fail without recourse to experiments.

It may however be possible to obtain the predicted benefits of the third generation endwall by reducing the sharpness of the curvature at the problem location. Examining the CFD results for P3 may also enable the designer to see if there were any indications of the separation from other parameters such as static pressure coefficient changes. Regrettably not enough time was available during the production of this thesis for the author to undertake such a task.

A lower freestream length scale could also be used as input to the CFD, this would reduce the turbulent viscosity and might lead to the separated region being successfully predicted. However it is not clear how this would be applicable to a routine design environment - the length scale that gives the best results is divorced from the measured length scale and was only discovered by a process of trial and error. Such a combination of measurement and computational results would not be routinely be available to the turbomachinery designer.

9.11 C_{ske} as a design parameter

Although the emphasis of this thesis is not on design practice for profiled endwalls a comment on the applicability of using C_{ske} or derived quantities for the design of endwalls is necessary.

It has been established in Chapters 7 and 8 that the computational fluid dynamics used in the design of profiled endwalls does not accurately predict loss either in terms of the absolute values of loss or the changes introduced by endwall profiling. Clearly therefore using loss is not a practical way of optimising a design, however since designs have to be produced some way of optimising designs needs to be found - even if it is less than ideal.

The approach used in the designs found in this thesis was firstly to design on the basis of reducing exit angle deviations - this was the basis of the first generation (P1) design. However this introduced an enhanced corner vortex which reduced the overturning at the endwall at the expense of additional loss. The approach used in the design of the second generation of profiled endwalls was to use C_{ske} as a parameter which represents the amount of secondary flow at the plane of interest, the theory being that if you minimise the amount of C_{ske} in the flow then the loss will reduce as well. More sophisticated methods to deal with more complex three dimensional geometries are available see Brennan et al. (2001).

The use of C_{ske} as a parameter for finding an acceptable design is clearly less than ideal as can be seen from Chapter 7. Even C_{ske} is not predicted correctly by CFD though the CFD does make a better job of it than loss. This thesis and the results from Rose et al. (2001) and Harvey et al. (2002) demonstrate that this approach can be highly successful. The third generation endwall shows that the system is not perfect and that the design of components still requires a great deal of skill on the part of the designer.

	P0	P1	P2	P3
η	89.34	90.21	90.89	88.32
change in %	-	0.87	1.55	-1.01

Table 9.2: Estimated Efficiencies with Profiled Endwalls

9.12 Application to Real Machines

The work of Brennan et al. (2001), Rose et al. (2001) and Harvey et al. (2002) has shown that profiled endwalls are applicable to real machines and produce real benefits. Rose et al. (2001) reported a stage efficiency increase of $0.59\% \pm 0.25\%$ and Harvey et al. (2002) reported a stage efficiency increase of $0.9\% \pm 0.4\%$. These efficiency changes are small but the power output of an aircraft engine turbine is very high so the actual energy savings are substantial.

It is possible to relate the results of cascade tests to stage efficiencies, a method is outlined in Cohen et al. (1996) and detailed in Appendix D. This method is approximate as it relies on a number of assumptions but it does allow the results of cascade tests to be put into context. Furthermore in the calculation described in Appendix D a comparison is made between different endwall geometries so the assumptions should apply equally to all endwalls. The results of this calculation are listed in Table 9.2.

The flow parameters (flow coefficient and temperature drop coefficient) are based on the Trent 500 HP turbine in Harvey et al. (2002) though educated guesses have been made where data is not publically available.

As can be seen from Table 9.2 the predicted benefits of endwall profiling are similar to those found in practice, this gives some confidence in the ability of simple cascade tests to represent the much more complicated flows in real machines.

9.13 Key Results

Table 9.3 provides an at-a-glance comparison for the key results in this thesis. Figure 9.4 provides a bar chart of this data. This table displays the net total, secondary and midspan losses for experimental and computational results. Table 9.3 also includes mixed out losses. The numbers in Table 9.3 are for five hole probe readings only as otherwise experimental results are not comparable to computational ones.

Care has to be taken therefore when quoting the results from Table 9.3 it can be argued that the synthesised data set which combines five and three hole probe readings is a much better measure of loss than the five hole probe readings alone. However since at the time of writing synthesised data sets were not available for CFD one must make do with a five hole probe comparison.

Further caution is suggested when compared when comparing P3 readings to the other readings in the table. In Chapter 8 all results are referenced to the planar reference case taken using the “back-to-back” methodology this is slightly different from the planar results in Table 9.3. Further details about the difference between the P3 reference case and the one used in Table 9.3 detail is found in Table 8.2 on page 211.

		Experimental				CFD			
		P0	P1	P2	P3	P0	P1	P2	P3
C_{ax} Plane	Total	0.1503	0.1336	0.1289	0.1599	0.2226	0.2212	0.2159	0.2574
	Secondary	0.0723	0.0554	0.0517	0.0821	0.0716	0.0723	0.0668	0.0519
	% Planar	100.0	76.5	71.4	109.2	100.0	101.0	93.3	100.6
Mixed Out Plane	Total	0.2346	0.1930	0.1828	0.1812	0.2525	0.2435	0.2390	0.2782
	Secondary	0.1046	0.0902	0.0694	0.1101	0.0914	0.0940	0.0798	0.0603
	% Planar	100	80.2	66.3	94.8	100.0	102.8	87.4	92.7

Table 9.3: Key Loss Results from this Thesis.

As discussed in Chapter 8 the CFD prediction for P3 was based on a different grid and inlet boundary layer than those for original P0, P1 and P2 computations which are shown in Table 9.3. This should be borne in mind when comparing P3 CFD results to the P0, P1 and P2 cases as the calculations were completed on a slightly different basis. A P0 calculation with the revised grid and inlet boundary layer is available and is discussed in Chapter 8.

Nevertheless Figure 9.4 and Table 9.3 provide an overview of the loss results found in this thesis.

9.14 Secondary flows and endwall profiling

As Denton and Xu (1999) have pointed out although the inviscid effects of three dimensional flow features are well understood, the viscous flow features are not well understood. The operation of non-axisymmetric endwall profiling is described here mainly using an inviscid description. For secondary flow to be present there needs to be an inlet boundary layer, but once this boundary layer is present inviscid flow theory will predict many of the features seen in real secondary flows.

The basic mechanics of endwall profiling appear to be as follows:-

- The horseshoe vortex dynamics are substantially altered by endwall profiling. In particular the flow is encouraged around the suction side of the blade, weakening the pressure side of the horseshoe vortex. See Figure 9.5.
- The cross passage pressure gradient in the blade row is reduced by the action of streamline curvature. i.e. convex curvature increases velocity and reduces static pressure and vice versa. In order to return to a flat endwall at exit curvature of an opposite direction needs to be added. This is generally done with a smooth a curvature as possible to reduce the adverse affects. See figure 9.5. This contributes to the over turning near the endwall as it enhances the cross passage pressure gradient at the blade exit.
- The reduced cross passage pressure gradient means that the passage vortex is smaller for profiled endwalls and generates less loss.
- The reduced cross passage pressure gradient means that the passage vortex does not migrate as near to the suction surface as the planar case. Therefore

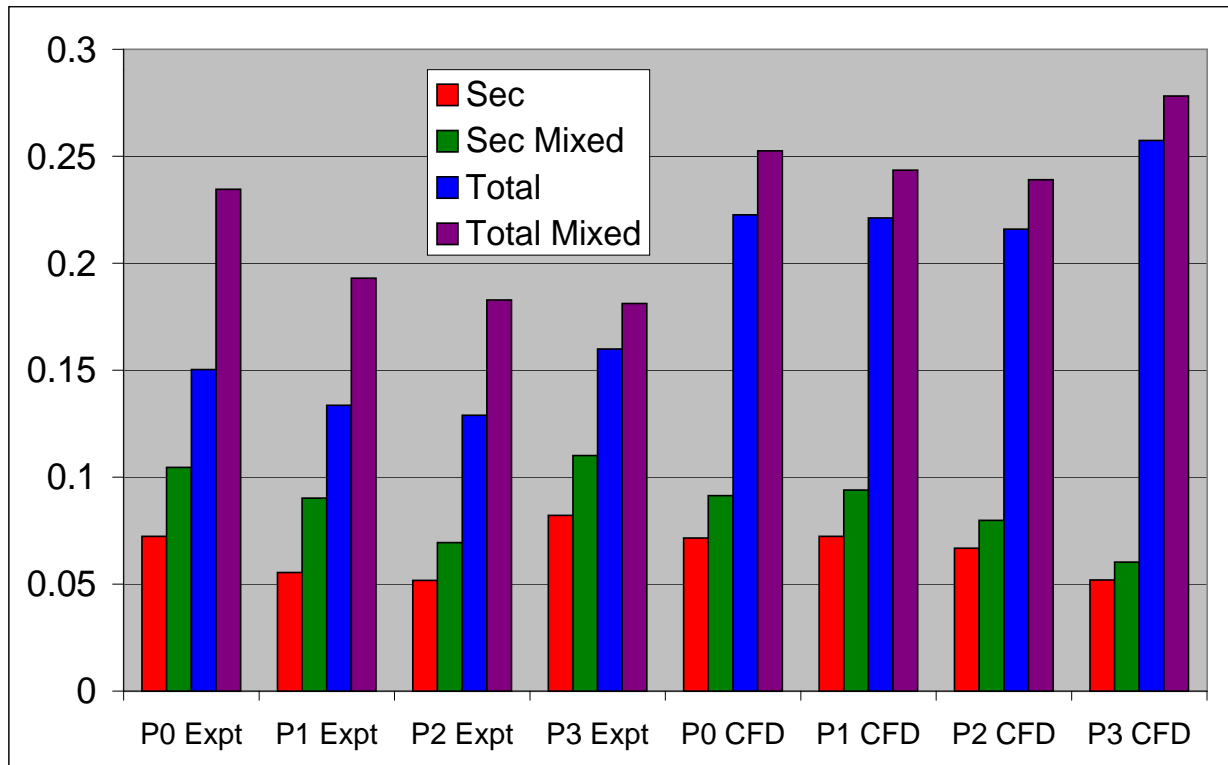
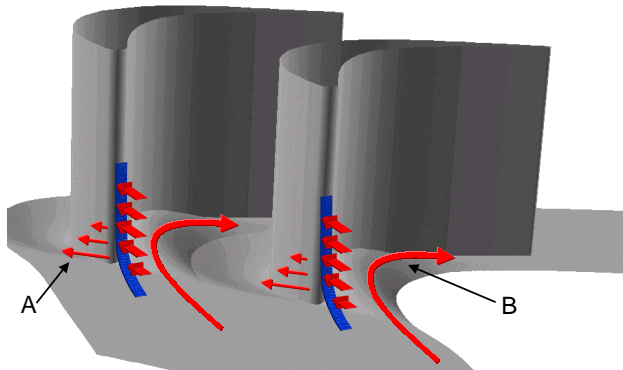


Figure 9.4: Bar Chart of Key Results from this Thesis.



- A. Profiling encourages the flow around the suction side of the blade at inlet.
- B. Reduced cross passage pressure gradient delays migration of passage vortex

Figure 9.5: Effect of endwall profiling on the horseshoe vortex

it interacts less with the corner vortex where very high relative velocities are introduced by the opposing vortices. The passage vortex also stays closer to the endwall reducing the radial spread of secondary flow.

- A consequence of the reduced secondary flows inside the blade passage is that less of the boundary layer inside the blade row is rolled up into the passage vortex. This means that overturning at the endwall is actually increased with endwall profiling unless measures such as the enhanced corner vortex for P1 are introduced.
- The reduced secondary flows mean that less mixing loss occurs downstream of the blade row.
- Transition on the blade surface is unaffected by endwall profiling.
- Transition on the endwall surface is much more difficult to determine but appears not to contribute to the reduction of loss from endwall profiling.

The horseshoe vortex reduction/encouragement around the suction side can be explained for P1 as the upstream ridge acting as a sort of upstream blade guiding the flow cleanly around to the suction surface. For P2 the effect is of a large blockage around the leading edge on the pressure side which encourages flow to locally flow around the suction surface by means of the upstream potential flow effect. P3 has a similar “hump” as P2 but the feature though is not as pronounced.

The horseshoe vortex dynamics are interesting as the leading edge effects may be similar to those found in Zess and Thole (2002) or Sauer et al. (2000) both of whom used leading edge bulbs to reduce secondary loss but did not contour their endwalls. This is to a large extent speculation as directly comparable figures for the Durham endwalls and the leading edge bulb work are not available. However it is not too far fetched to suppose some sort of similarity. In previous work, Sieverding (1985),

it was suspected that the horseshoe vortex was not important in the formation of secondary flows and losses, the work described in this thesis may suggest otherwise.

Chapter 10

Conclusions and Recommendations

ONE OF THE main aims of this thesis was to understand the effects of three dimensional endwall profiling on loss reduction. In order to do this a range of detailed measurements have been conducted on profiled endwalls. These measurements have encompassed pressure probe measurements, flow visualisation and hot film measurements of the boundary layer state. A comprehensive and detailed comparison with the computational fluid dynamics used to design the profiled endwalls and the above mentioned experimental results has also been conducted. This chapter brings together the key points from the previous nine chapters, recommendations for future work and experimental practices are also included.

10.1 Conclusions

- The experience from this work suggests that previous methods of error analysis such as those conducted by Biesinger (1993) produce good estimates of experimental accuracy when compared to the approach used in this thesis of repeating the experiments and determining the error estimate from the variability of the results.
- Non-axisymmetric endwall profiling reduces secondary flows and loss. The best profile (P2) so far tested in the Durham Cascade reduces secondary loss by around 31% ($\pm 5\%$) of the planar value, and reduces the under turning of the flow by 2.7° but increases the over turning by 2.4° . This profile also reduces the radial extent of secondary flow with passage vortex loss core being moved from around 40% of span to 30% of span. An important point is that as well as reducing loss within the blade row the flow at exit from the blade row is more uniform (the increased overturning is found only close to the endwall) and therefore may improve the efficiency of a downstream blade row.
- Non-axisymmetric endwall profiling has significant effects on the flow dynamics inside the blade row. The horseshoe vortex structure is altered significantly with flow being encouraged around to the suction side of the blade. The

passage vortex strength is much reduced and the under turning is reduced. However unless a special feature is added to compensate (The P1 enhanced corner vortex for example) the over turning at the endwall is actually increased.

- The ranking according to loss reduction for the geometries available for testing in the Durham cascade is P2, P1, P0 and then P3 in order of increasing loss. This ranking for P1 and P2 is different from that reported in previous work Gregory-Smith et al. (2001) and the new ranking is the result of repeating a number of experiments. The new ranking also provides a much more consistent relation of the flow dynamics (Secondary vectors, C_{ske} , ...) to loss production in the cascade.
- The third generation endwall increases loss rather than reduces it. This is due to a flow feature analogous to a conventional two dimensional flow separation which occurs at a sharp convex curvature on the endwall at entry to the blade row. It may be possible to redesign the profile to reduce the amplitude of this curvature and keep the benefits of endwall profiling.
- The benefits of endwall profiling are not due to altering the transitional nature of the boundary layers in the Durham cascade. The intermittency distribution appears to be unaffected by endwall profiling on the blade surfaces and on the endwalls.
- Flow visualisation shows that endwall profiling has dramatic effects on the flow pattern on the endwall. Care needs to be taken when interpreting surface oil/dye flow visualisations. Features which appear dramatic (The P1 “stagnant” region Figure 4.3 on page 63) may not actually be large loss producing features and features which appear much smaller (The P3 “separated region” Figure 8.76 on page 248) produce much more significant loss changes.
- The CFD method used here does not predict loss accurately.
- CFD does however predict the yaw angle deviations correctly and has more success predicting the location and extent of secondary flow features - provided no separated regions are present that are missed by the CFD. Considerable success has been achieved in non-axisymmetric endwall profiling design both in the Durham Cascade and in rig tests (Brennan et al. (2001) and Harvey et al. (2002)) by using predictors from the CFD other than loss such as yaw angle or secondary kinetic energy.

10.2 Recommendations

- Traversable hot wires are preferable to surface mounted hot films for carrying out intermittency measurements and should be used where possible in future. Not only is a higher frequency response possible but the amount of manual labour that goes into conducting an experiment is much less, meaning that much more data can be collected in a given amount of time.

- A quantification of the effects of using the correct inlet boundary layer for the CFD calculations should be carried out. This would involve carrying out two nearly identical computations one with the measured inlet boundary layer as a boundary condition (with negative loss) and one without.
- The P3 CFD calculation could be repeated with a smaller free stream length scale. This might predict the separated region associated with the region of sharp curvature on entry to the blade passage as a lower free stream length scale would produce a lower turbulent viscosity.
- Future work with a three hole probe should be plotted and process the radial position accurately. In the current work it was assumed that the closest point to the wall measured by a three hole probe was on the wall itself. In reality the non-zero probe thickness means that the measurements occur half a probe thickness from the wall and this should be taken into account in future work.
- The CFD close to the endwalls should be examined and contrasted to the experimental data taken close to the endwall. This would shed some light on the success the computation in capturing the changes on the endwall introduced by endwall profiling.
- Experimental technique should be carefully documented and published. Where the secrecy of novel techniques or designs is not required the data and program code should be made available. This allows the experiments to be repeated and allows a process of peer review to take place on the experiments conducted.
- Quantitative evaluation of the benefits of non-axisymmetric endwall profiling requires careful experimental technique. In particular to rank competing geometries that successfully reduce loss is a difficult task, there are several elements to providing a realistic estimate:- Firstly the measurements must be conducted using *exactly* the same technique - this is best conducted by measuring all the competing geometries in sequence. Secondly a robust system of error checking and validation should be introduced into the measuring process. Thirdly the process should be as clearly documented as possible. Fourthly a realistic estimate of the accuracy of the results needs to be obtained.
- The predicted benefits for the third generation endwall may be available if the design is altered locally in the region of sharp curvature that causes the separated region.
- The benefits of endwall profiling can be examined in a number of ways that have not been included in this thesis due to limitations on the authors time. One particularly promising approach is the so called “Denton $\int U^3 dA$ ” approach which examines entropy creation as being proportional to cube of the flow velocity (see Denton (1993) for more details). Haller and Anderton (2002) have claimed impressive performance increases using this approach to design three dimensional blading and it may provide insights into the operation of endwall profiling.

- The use of yaw angle and C_{ske} as quantities to optimise during the endwall profiling design has been successful as shown in this thesis and the work of Rose et al. (2001) and Harvey et al. (2002). Chapter 7 has shown a correlation between C_{ske} and loss reduction, this should be further investigated to see if it is applicable to other flow situations. Other parameters such as vorticity coefficient might also provide better insights into the flow and this should be investigated further.
- Real turbomachinery components include a number of features that are not modelled by the simple cascade. These include leading and trailing edge platforms, the small but non-negligible gap between each blade, corner fillets and cooling injection to name several. The effect of these features on endwall profiling is not clear although the results of rig tests Rose et al. (2001) suggest that they do not remove all the benefits of endwall profiling. Further research is needed in this area.
- The current method of designing endwalls is to design the endwalls after the blade shape has already been determined. This can be a useful design aim, i.e. to improve the performance of a machine without substantially altering the flow dynamics within it. However there is no reason not to be ambitious and aim in the future to design a three dimensional passage rather than designing an endwall after the event. There are many three dimensional features being researched at the moment such as blade lean and leading edge bulbs that might be combined with endwall profiling to produce an even better design.

Bibliography

- Ainley, D. and Mathieson, G. (1951). A method of performance estimation for axial-flow turbines. Technical Report Reports and Memoranda: No: 2874, Aeronautical Research Council, HMSO.
- Anderson, S. and Pendery, B. (2001). Steady and unsteady traverse measurements on a transonic industrial hp turbine stage. *Proceedings of the 4th European Conference on Turbomachinery*.
- Atkins, M. (1984). *Endwall profiling in axial flow turbines*. PhD thesis, Cambridge University.
- Aunapu, N., Volino, R., Flack, K., and Stoddard, R. (2000). Secondary flow measurements in a turbine passage with endwall flow modification. *ASME Paper 2000-GT-0212*.
- Barlow, Rae, and Pope (1999). *Low Speed Wind Tunnel Testing*. Number ISBN: 0-471-55774-9. Wiley & Sons, 3rd edition edition.
- Beazley, D. (2001). *Python Essential Reference*. New Riders.
- Bellhouse, B. and Schultz, D. L. (1966). Determination of mean and dynamic skin friction, separation and transition in low-speed flow with a thin-film heated element. *Journal of Fluid Mechanics*, Vol 24(2):pp379 to 400.
- Biesinger, T. (1993). *Secondary Flow Reduction Techniques in Linear Turbine Cascades*. PhD thesis, School of Engineering, University of Durham.
- Breisig, V., Giboni, A., Lerner, C., Peters, P., and Pfost, H. (2001). Experimental examination of the stator flow in a 1.5 stage axial turbine test stand. *Proceedings of the 4th European Conference on Turbomachinery*.
- Brennan, G., Harvey, N., Rose, M., Formison, N., and Taylor, M. (2001). Improving the efficiency of the trent 500 hp turbine using non-axisymmetric end walls: Part 1 turbine design. *ASME Paper 2001-GT-0444*.
- Burd, S. and Simon, T. (2002). Effects of slot bleed injection over a contoured end-wall on nozzle guide vane cooling performance: Part i : Flow field measurements. *ASME Paper 2000-GT-199*.
- Came, P. and Marsh, H. (1974). Secondary flow in cascades: Two simple derivations for the components of vorticity. *Journal of Mechanical Engineering Science*.

- Christiansen, T. and Bradshaw, P. (1981). Effect of turbulence on pressure probes. *J PHYS E SCI INSTRUMEN.*
- Cleak, J. (1989). *Validation of Viscous, Three-Dimensional Flow Calculations in an Axial Turbine Cascade*. PhD thesis, School of Engineering, University of Durham.
- Cohen, H., Rogers, G., and Saravanamuttoo, H. (1996). *Gas Turbine Theory*. Number ISBN: 0-582-23632-0. Addison Wesley Longman Limited, fourth edition edition.
- Day, C., Oldfield, M., and Lock, G. (1999). The influence of film cooling on the efficiency of an annular nozzle guide vane cascade. *Journal of Turbomachinery, Transactions of the ASME*.
- Day, C., Oldfield, M., and Lock, G. (2000). Aerodynamic performance of an annular cascade of film cooled nozzle guide vanes under engine representative conditions. *Experiments in Fluids*.
- Deich, M., Filipov, G., and Lazarev, L. (1965). Atlas of axial turbine blade characteristics. part i: Method of profiling and the aerodynamics of cascades. *Moscow: Masinostoenie Publishing House*.
- Denton, J. (1993). Loss mechanisms in turbomachines. *ASME Paper 93-GT-435*.
- Denton, J. and Cumpsty, N. (1987). Loss mechanisms in tubomachines. *Institution of Mechnaical Engineers: C260/87*.
- Denton, J. and Xu, L. (1999). The explotation of three-dimensional flow in turbomachinery design. *Proceedings of the Institution of Mechanical Engineers*, 213(Part C):125–137.
- Dominy, R. and Hodson, H. (1992). An investigation of factors influencing the calibration of 5-hole probes for 3-d flow measurements. *ASME 92-GT-216*.
- Dorney, D. and Gundy-Burlet, K. (2002). Effects of hot streak shape on rotor heating in a high-subsonic single-stage turbine. *ASME Paper 2000-GT-0449*.
- Dossena, V., Perdichizzi, A., and Savini, M. (1999). The influence of endwall contouring on the performance of a turbine nozzle guide vane. *Transactions of the ASME, Journal of Turbomachinery*, 121:200–208.
- Duden, A., Raab, I., and Fottner, L. (1999). Controlling the secondary flow in a turbine cascade by three dimensional airfoil design and endwall contouring. *Transactions of the ASME, Journal of Turbomachinery*, 121:191–199.
- Eckerle, W. and Langston, L. (1987). Horseshoe vortex formation around a cylinder. *Transaction of the ASME, Journal of Turbomachinery*, 109:278–285.
- Eymann, S., Reinmoller, U., Niehuis, R., Forster, W., Beversdorff, M., and Gier, J. (2002). Improving 3d flow characteristics in a multistage lp turbine by means of endwall contouring and airfoil design modifacaton- part 1: Design and experimental investigation. *ASME Paper GT-2002-30352*.

- Friedrichs, S., Hodson, H., and Dawes, W. (1996). Distribution of film-cooling effectiveness on a turbine endwall measured using the ammonia and diazo technique. *Transactions of the ASME, Journal of Turbomachinery*, 118:613–621.
- Galassi, M., Davies, J., Theiler, J., Gough, B., Jungman, G., Booth, M., and Rossi, F. (2001). *GNU Scientific Library Reference Manual*. Network Theory Ltd.
- Goldstein, R. and Spores, R. (1988). Turbulent transport on the endwall in the region between adjacent turbine blades. *Transactions of the ASME, Journal of Heat Transfer*, 110:862–869.
- Graves, C. (1985). *Secondary flows and losses in gas turbines*. PhD thesis, School of Engineering, University of Durham.
- Gregory-Smith, D. (1983). Secondary flows and losses in axial flow turbines. *ASME Paper 82-GT-19*.
- Gregory-Smith, D. (1995). Calculations of the secondary flow in a turbine cascade. *AD-Vol 49, Computational Fluid Dynamics in Aeropropulsion*, (ISBN: 0-7918-1730-X):77–87. Presented at the 1995 ASME International Mechanical Engineering Congress and Exposition.
- Gregory-Smith, D. (1997). Lecture 1: Physics of secondary flows lecture 2: Secondary flows and vorticity lecture 3: Secondary loss: Loss generation, effect of blade design, loss correlations and modelling. *von Karman Institute for Fluid Mechanics*. Secondary and Tip Clearance Flows in Axial Turbines.
- Gregory-Smith, D. and Graves, C. (1983). Secondary flows and losses in a turbine cascade. *AGARD-CP-351, AGARD Conference Proceedings No. 351: Viscous Effects in Turbomachines*.
- Gregory-Smith, D., Graves, C., and Walsh, J. (1987). Growth of secondary losses and vorticity in an axial turbine cascade. *ASME Paper 87-GT-114*.
- Gregory-Smith, D., Ingram, G., Jayaraman, P., Harvey, N., and Rose, M. (2001). Non-axisymmetric turbine end wall profiling. *Proceedings of the Institution of Mechanical Engineers*.
- Haller, B. (1997). Full 3d turbine blade design. *von Karman Institute for Fluid Mechanics*. Secondary and Tip Clearance Flows in Axial Turbines.
- Haller, B. and Anderton, J. (2002). Development of new high load/high lift transonic shrouded hp gas turbine stage design - a new approach for turbomachinery. *ASME Paper GT-2002-30363*.
- Harrison, S. (1989). *The Influence of Blade Stacking on Turbine Losses*. PhD thesis, Department of Engineering, University of Cambridge.
- Harrison, S. (1990). The influence of blade lean on turbine losses. *ASME 90-GT-55*.
- Hartland, J. (2001). *Secondary Loss Reduction in Rotor Blades by Non-axisymmetric end-wall profiling*. PhD thesis, University of Durham.

- Hartland, J., Gregory-Smith, D., , Harvey, N., and Rose, M. (1999a). Non-axisymmetric turbine end wall design: Part 2 experimental validation. *ASME Paper 99-GT-338*.
- Hartland, J., Gregory-Smith, D., , Harvey, N., and Rose, M. (1999b). Non-axisymmetric turbine end wall design: Part ii experimental validation. *ASME Paper 99-GT-338*, 1:1.
- Hartland, J., Gregory-Smith, D., and Rose, M. (1998). Non-axisymmetric endwall profiling in a turbine rotor blade. *ASME Paper 98-GT-525*.
- Harvey, N., Brennan, G., Newman, D., and Rose, M. (2002). Improving turbine efficiency using non-axisymmetric end walls: Validation in the multi-row environment and with low aspect ratio blading. *ASME Paper GT-2002-30337*.
- Harvey, N. and Ramsden, K. (2000). A computational study of a novel turbine rotor partial shroud. *ASME Paper 2000-GT-668*.
- Harvey, N., Rose, M., Taylor, M., Shahpar, S., Hartland, J., and Gregory-Smith, D. (1999). Non-axisymmetric turbine end wall design: Part i: Three dimensional linear design system. *ASME Paper 99-GT-337*, 1:1.
- Hodson, H. and Dominy, R. (1987). The off-design performance of a low-pressure turbine cascade. *Transactions of the ASME, Journal of Turbomachinery*, 109:201–209.
- Hodson, H. P. (1985). Boundary layer transition and seperation near the leading edge of a high speed turbine blade. *Transactions of the ASME, Journal of Engineering for Gas Turbines and Power*, Vol 107:pp127 to 134.
- Howell, R., Ramesh, O., Hodson, H., Harvey, N., and Schulte, V. (2000). High lift and aft loaded profiles for low pressure turbines. *ASME Paper 2000-GT-261*.
- Ingram, G. (2003). Manufacture of the third generation endwall. Technical report, School of Engineering, University of Durham.
- Ingram, G. and Gregory-Smith, D. (2002). Progress report no 7, endwall profiling for the reduction of secondary loss. Technical report, School of Engineering, University of Durham.
- Ingram, G., Gregory-Smith, D., and Harvey, N. (2003). Experimental quantification of the benefits of end-wall profiling in a turbine cascade. *ISABE 2003, Cleveland Ohio*.
- Ingram, G., Gregory-Smith, D., Rose, M., Harvey, N., and Brennan, G. (2002). The effect of end-wall profiling on secondary flow and loss development in a turbine cascade. *ASME Paper GT-2002-30339*.
- IntelligentLight (2001). *Reference Manual: Fieldview 8*. 1290 Wall Street West, Third Floor, Lyndhurst, NJ 07071, version 8.0 edition.

- Jayaraman, P. (2000). An investigation of secondary flow in a turbine blade with end wall profiling. Master's thesis, School of Engineering, University of Durham.
- Kernighan, B. and Ritchie, D. (1988). *The C Programming Language*. Prentice Hall.
- Kreyszig, E. (1983). *Advanced Engineering Mathematics*. John Wiley and Sons.
- Langston, L. (2001). Secondary flows in axial turbines-a review. *Annals of the New York Academy of Sciences: Heat Transfer in Gas Turbine Systems*.
- Langston, L., Nice, M., and Hooper, R. (1977). Three-dimensional flow within a turbine cascade passage. *Transactions of the ASME, Journal of Engineering for Power*.
- Main, A., Day, C., Lock, G., and Oldfield, M. (1996). Calibration of a four-hole pyramid probe and area traverse measurements in a short-duration transonic turbine cascade tunnel. *Experiments in Fluids*.
- Main, A., Oldfield, M., Lock, G., and Jones, T. (1997). Free vortex theory for efficiency calculations from annular cascade data. *Transactions of the ASME, Journal of Turbomachinery*.
- Maltby, R. (1962). Flow visualization in wind tunnels using indicators. *AGARDograph 70*.
- Marchal, P. and Sieverding, C. (1977). Secondary flows within turbomachinery bladings. *AGARD Conference Proceedings No. 214, Secondary Flows in Turbomachines.*, (AGARD-CP-214).
- Merzkirch (1974). *Flow Visualisation*. Number ISBN: 0-12-491350-4. Academic Press Inc, 1st edition edition.
- Miller, R., Moss, R., Ainsworth, R., and Harvey, N. (2001). Time-resolved vane-rotor-vane interaction in a transonic one and a half stage turbine. *Proceedings of the 4th European Conference on Turbomachinery*.
- Moore, H. (1995). *Experiments in a Turbine Cascade for the Validation of Turbulence and Transition Models*. PhD thesis, University of Durham.
- Moore, H. and Gregory-Smith, D. (1996). Transition effects on secondary flows in a turbine cascade. *ASME Paper 96-GT-100*.
- Moore, J. and Adhye, R. (1985). Secondary flows and losses downstream of a turbine cascade. *Transactions of the ASME, Journal of Engineering for Gas Turbines and Power*, 107:961.
- Moore, J. G. (1985). Calculation of 3d flow with numerical mixing. *AGARD-LS-140 on 3D Computation Techniques applied ot Internal Flows in Propulsion Systems*.
- Morris, A. and Hoare, R. (1975). Secondary loss measurements in a cascade of turbine blades with meridional wall profiling. *ASME 75-WA/GT-13*.

- Moustapha, S., Paron, G., and Wade, J. (1985). Secondary flows in cascades of highly loaded turbine blades. *Transactions of the ASME, Journal of Engineering for Gas Turbines and Power*, 107:1031–1038.
- Perdichizzi, A. (1990). Mach number effects on secondary flow development downstream of a turbine cascade. *Transactions of the ASME, Journal of Turbomachinery*, 112:643–651.
- Prasad, D. and Hendricks, G. (2000). A numerical study of secondary flow in axial turbines with application to radial transport of hot streaks. *ASME Paper 2000-GT-0448*.
- Rose, M. (1994). Non-axisymmetric endwall profiling in the hub regions of axial flow gas turbine. *ASME Paper 94-GT-249*.
- Rose, M., Harvey, N., Seaman, P., Newman, D., and McManus, D. (2001). Hub turbine using non-axisymmetric end walls. part ii: Experimental validation. *ASME Paper 2001-GT-0505*.
- Roy, R., Squire, K., Gerendas, M., Song, S., Howe, W., and Ansari, A. (2000). Flow and heat transfer at the hub endwall of inlet vane passages experiments and simulations. *ASME Paper 2000-GT-198*.
- Sargison, J., Guo, S., Oldfield, M., Lock, G., and Rawlinson, A. (2002a). A converging slot-hole film-cooling geometry - part 1: Low-speed flat-plate heat transfer and loss. *Transactions of the ASME, Journal of Turbomachinery*.
- Sargison, J., Guo, S., Oldfield, M., Lock, G., and Rawlinson, A. (2002b). A converging slot-hole film-cooling geometry - part 2: Transonic nozzle guide vane heat transfer and loss. *Transactions of the ASME, Journal of Turbomachinery*.
- Sauer, H., Muller, R., and Vogeler, K. (2000). Reduction of secondary flow losses in turbine cascades by leading edge modification at the endwall. *ASME Paper 2000-GT-0473*.
- Shahpar, S. (2000). A comparative study of optimisation methods for aerodynamic design of turbomachinery blades. *ASME Paper 2000-GT-523*.
- Sharma, O. and Butler, T. (1987). Predictions of endwall losses and secondary flows in axial flow turbine cases. *Transactions of the ASME, Journal of Turbomachinery*.
- Sieverding, C. (1985). Recent progress in the understanding of basic aspects of secondary flows in turbine blades passages. *Transactions of the ASME, Journal of Engineering for Gas Turbines and Power*, 107:248.
- Sieverding, C. and Bosche, V. D. (1983). The use of coloured smoke to visualize secondary flows in a turbine-blade cascade. *Journal of Fluid Mechanics, Cambridge University Press*, 134:85–89.
- Smith, D., Bubb, J., Popp, O., III, H. G., Diller, T., Schetz, J., and Ng, W. (2000). An investigation of heat transfer in a film cooled transonic turbine cascade, part i: Steady heat transfer. *ASME Paper 2000-GT-0202*.

- Squire, H. and Winter, K. (1951). The secondary flow in a cascade of airfoils in a nonuniform stream. *Journal of Aerodynamic Science*.
- Takeshi, K., Matsuura, M., Aoki, S., and Sato, T. (1989). An experimental study of heat transfer and film cooling on low aspect ratio turbine nozzles. *ASME 89-GT-187*.
- Treaster, A. and Yocum, A. (1979). The calibration and application of five hole probes. *ISA Transactions*, 18(2):23.
- Wallis, A., Denton, J., and Demargne, A. (2000). The control of shroud leakage flows to reduce aerodynamic losses in a low aspect ratio, shrouded axial flow turbine. *ASME Paper 2000-GT-475*.
- Walsh, J. (1987). *Secondary Flows and Inlet Skew in Axial Flow Turbine Cascades*. PhD thesis, School of Engineering, University of Durham.
- Wang, H., Olson, S., Goldstein, R., and Eckert, E. (1997). Flow visualization in a linear turbine cascade of high performance turbine blades. *Transactions of the ASME, Journal of Turbomachinery*, 119:1–8.
- Warner, R. and Tran, M. (1987). Recent developments to improve high-pressure and intermediate-pressure turbine efficiency. *Proceedings of the Institution of Mechanical Engineers, International Conference, Turbomachinery: Efficiency Prediction and Improvement*, t, (C278/87):287–292.
- Yamamoto (1987). Production and development of secondary flows and losses in two types of straight turbine cascades. part 1:a stator case. part 2: A rotor case. *Transactions of the ASME, Journal of Turbomachinery*, 109:186–200.
- Yan, J. (1999). *The Effect of End Wall Profiling on Secondary Flow in Nozzle Guide Vanes*. PhD thesis, School of Engineering, University of Durham.
- Zess, G. and Thole, K. (2002). Computational design and experimental evaluation of using a leading edge fillet on a gas turbine vane. *Transactions of the ASME, Journal of Turbomachinery*.

Appendix A

Profiled Endwall Geometries

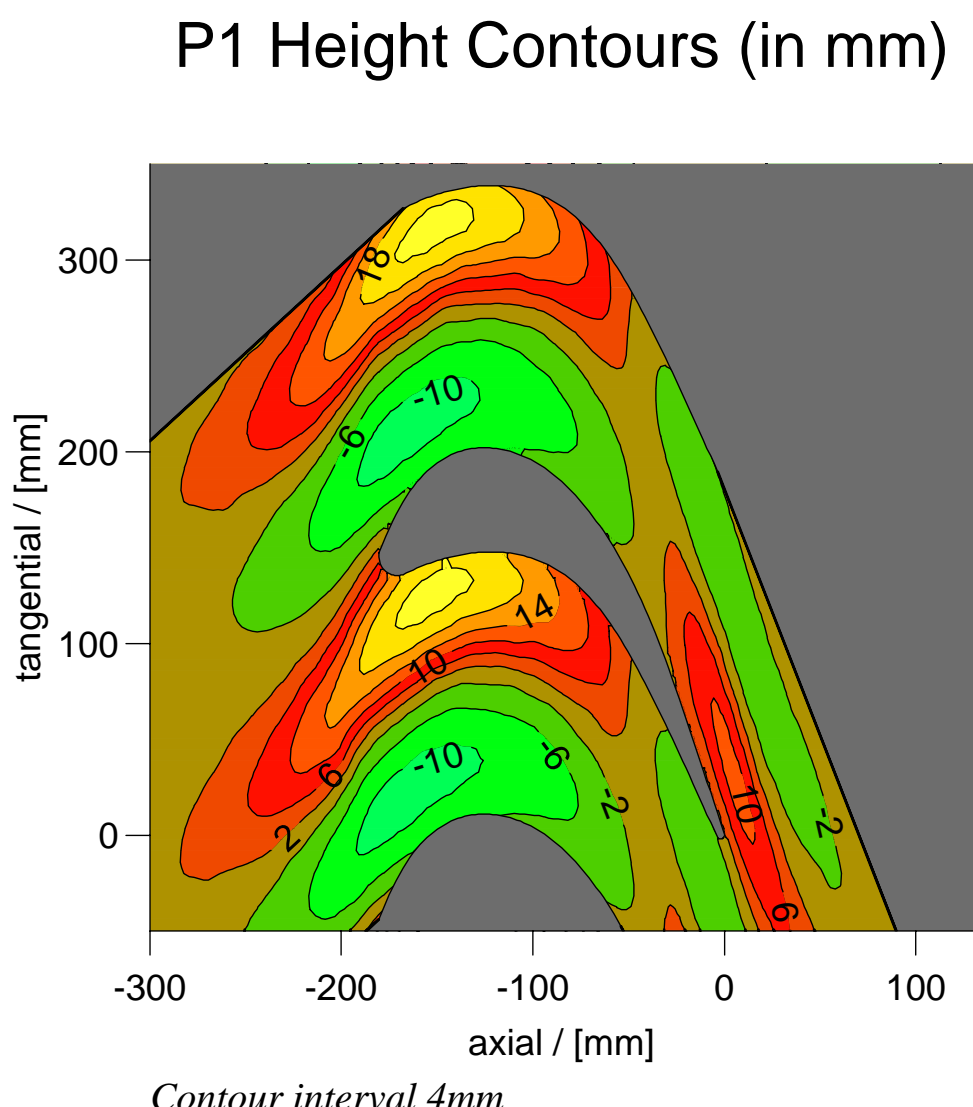


Figure A.1: P1 Geometry.

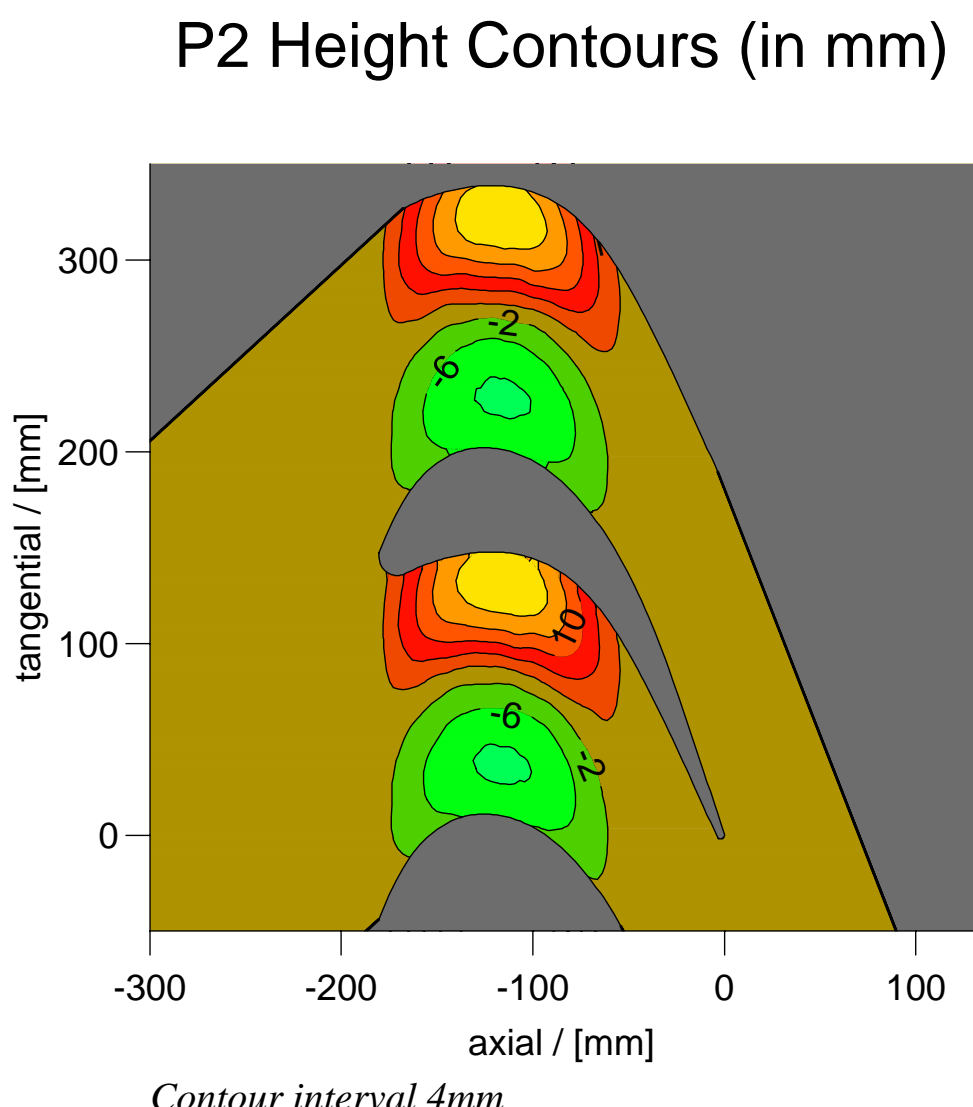


Figure A.2: P2 Geometry.

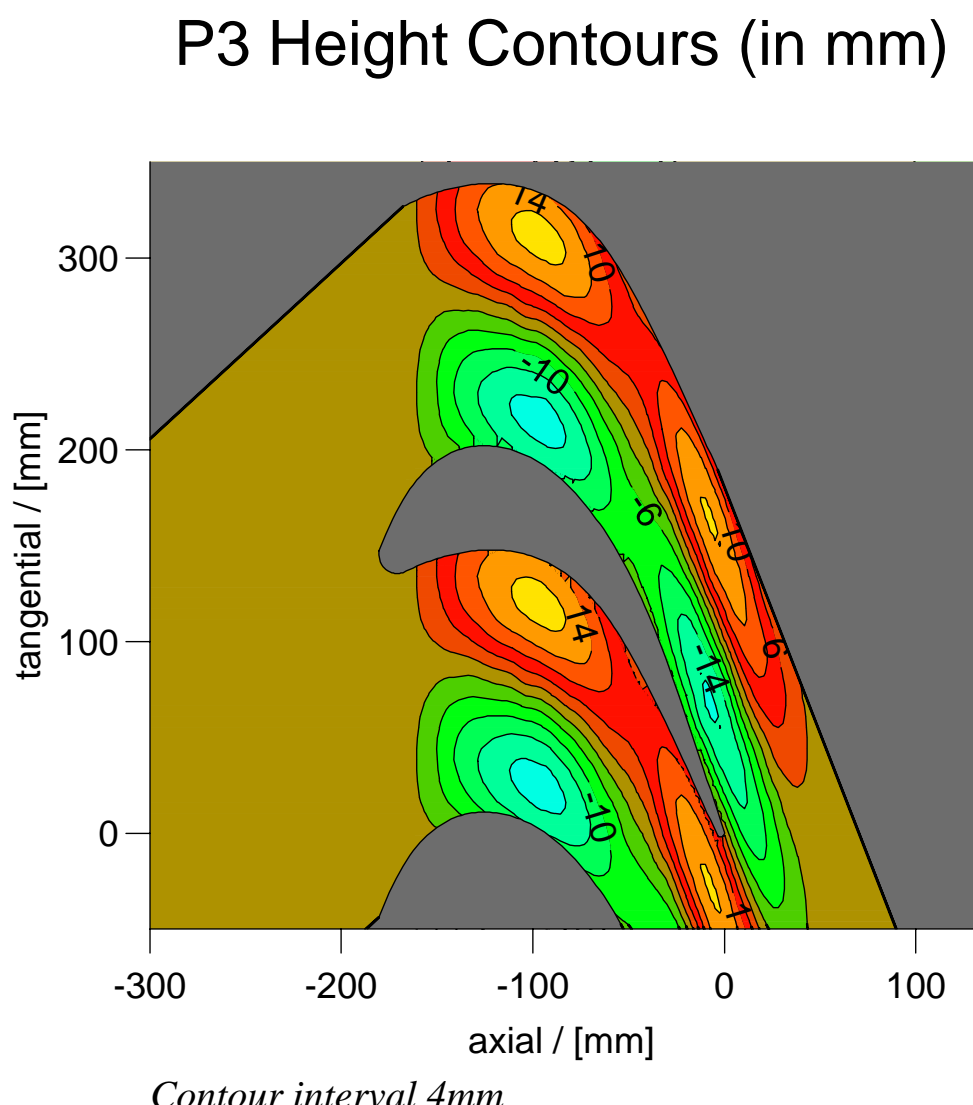


Figure A.3: P3 Geometry.

Appendix B

Cascade Coordinates

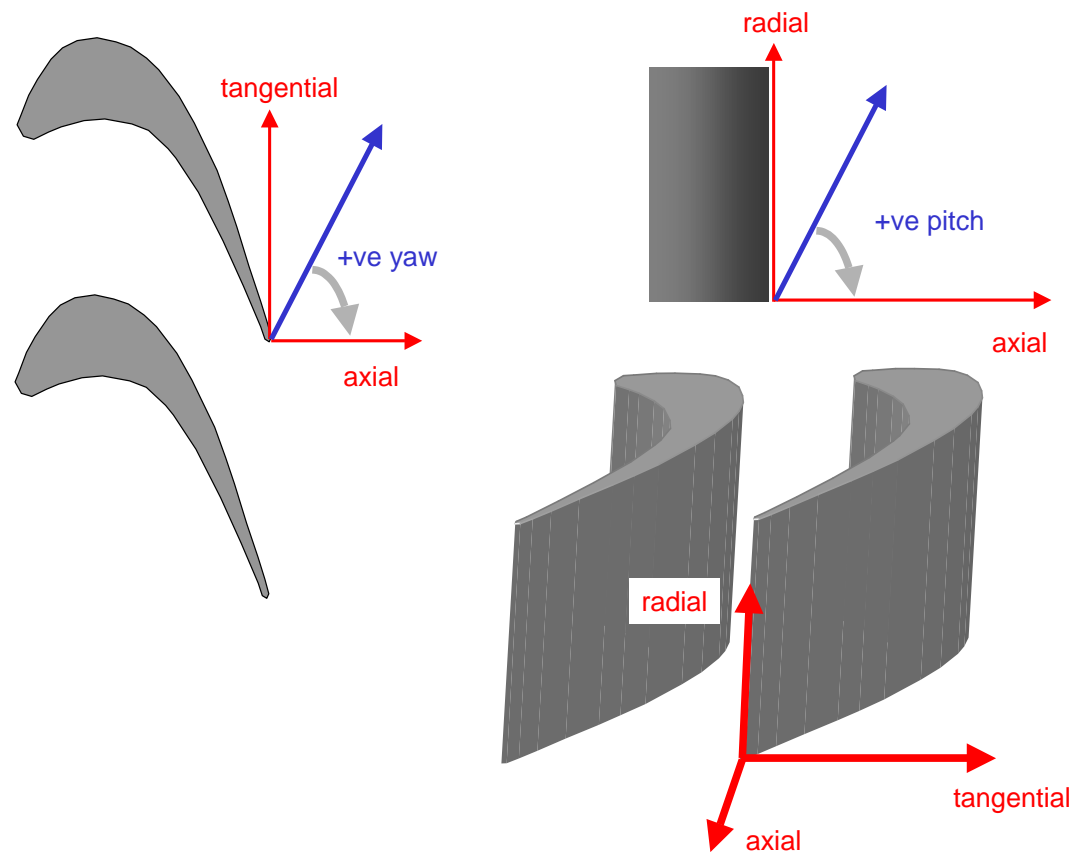


Figure B.1: Cascade Coordinates including sign of pitch and yaw angles.

Appendix C

Supplemental Information on Experiment Labels and Technique

C.1 Labels for Pressure Probe Traverses

There is a large amount of data presented in this thesis, so in order to improve the traceability of the data each experiment was given a label such as *trv29* or *hand5* to identify the data. The label is repeated on the illustration with the data in it so one can be sure which set of data one is looking at as some readings were repeated on different days (e.g. Slot 10). The label is important as it is generally the name of the data files associated with the experiment. For example *trv70* refers to a P0 Slot 10 traverse but the only way to find that out is to look in one of the datafiles, which would be called *trv70.vlt* and *trv70.pa*. Processed data is identified by the filename extension *trv70.t5c*, *trv70.fld*, *trv70.avg*. All files follow the MSDOS 8.3 filename convention.

Five hole probe traverse labels are located in Table C.1, three hole probe traverse labels are found in Table C.2 and the traverses conducted for the third generation endwall are listed in Table C.3.

Slot No.	P0	P1	P2	Calib
1	trv48	trv49	trv47	cal39
2	trv67	trv68	trv65	cal60
3	trv24	trv38	trv32	cal35
4	trv62	trv61	trv64	cal55
5	trv58	trv60	trv57	cal54
6	trv23	trv37	trv31	cal35
8	trv22	trv36	trv30	cal35
10(a)	trv70	trv69	trv72	cal61
10(b)	trv87	trv88	trv86	cal62
10(c)	trv91	trv90	trv92	cal62

Table C.1: Five Hole Traverse Labels and corresponding calibration.

Slot No.	P0	P1	P2	Calib
1	trv84	trv83	trv85	cal66
2	trv81	trv82	trv80	cal65
10(a3)	trv77	trv76	trv78	cal65
10(b3)	trv94	trv99	trv93	cal65
10(c3)	trv97	trv96	trv98	cal65

Table C.2: Three Hole Traverse Labels and corresponding calibration.

Slot No.	P0	P3	Calib
6	trv100	trv101	cal70
8	trv104	trv105	cal70
10	trv111	trv110	cal74
10 (3h)	trv108	trv109	cal73
4 (3H)	trv106	trv107	cal71

Table C.3: P3 Measurement Traverse Labels

C.2 Labels for Hot Film Readings

Chapter 6 describes the hot film readings, for each experiment described in that chapter a label was produced such as “P0EC7” or “P1S501”. As is evident the labels take the form of $P_n i l_{xx}$ this can be decoded as follows:-

- n - The first two letters e.g. “P0” refer to the profile under testing.
- i - The third letter indicates whether the trace is on the endwall (“E”) or on the suction surface (“S”)
- l - For the suction surface all measurements were taken at slot locations, the number refers to the slot number. For the endwall the measurements were all taken at pressure tapping locations, each axial line of pressure tappings was given a letter A to P and the letter refers to the line of pressure tappings.
- xx - For the suction surface this gives the radial height when multiplied by ten, e.g. 10 is 100mm from the radial zero and 05 is 50mm from the zero. For the endwall this gives the tapping number 1 being nearest the suction surface and 10 being closest to the pressure surface.

This means that a given experiment label uniquely determines the position and endwall of the hot film trace. For example “P0EC7” refers to endwall P0, line C of the pressure tapings and position seven which is near the pressure surface.

C.3 Different ways of calculating Table 7.1

Table 7.1 on 173 shows the CFD results compared to the “best” five hole probe experimental results. These $\overline{\overline{C}_{P0}}$ values are obtained by taking three $\overline{\overline{C}_{P0}}$ values and calculating the mean. A slightly different result will be obtained if one averages the three traverses used for the repeatability work at an earlier stage, i.e. when they

are still area data and not area *averaged* data and then process them through the programs to obtain a single $\overline{\overline{C_{P0}}}$ value. The pitch averaged values shown in the CFD comparison figures represent the latter case and the area averaged values represent the former case.

Strictly speaking therefore one cannot obtain the $\overline{\overline{C_{P0}}}$ values in the tables in Chapter 7 from the pitch averaged values shown for comparison in the graphs. However the change is minor and this note is mainly for the benefit of future researchers should they discover an apparently anomaly in the data.

C.4 Pressure Probe Data Processing Programs

calib program that returns flow variables from a calibration map (output from *coeff*) and traverse data (output from *log5h* or *log3h*)

coeff converts the output from *logpy* into a calibration map

field program used to process area output from *calib*

FAITH Forward And Inverse THree dimensional linear design system a Rolls-Royce program used for designing profiled end walls.

FIELDVIEW Post processing software program used to examine CFD

GSHARP Plotting package used to produce two dimensional contour plots and vector plots in this thesis

logpy logs calibration maps on the pitch-yaw traverse

log3h logs data for three hole traverses

log5h logs data for five hole traverses

pitch processed the output from *field* to produce pitch and are averaged data

The connection between the different data processing programs is shown in Figure C.1.

C.5 Repeatability Results

The % of planar value refers to the secondary loss rather than the total loss. The % of planar values is the % of the relevant P0 traverse, so for trv88 the loss is expressed as a % of the trv87 P0 run etc. The results for each of the repeatability test for a five hole probe are found in Table C.4.

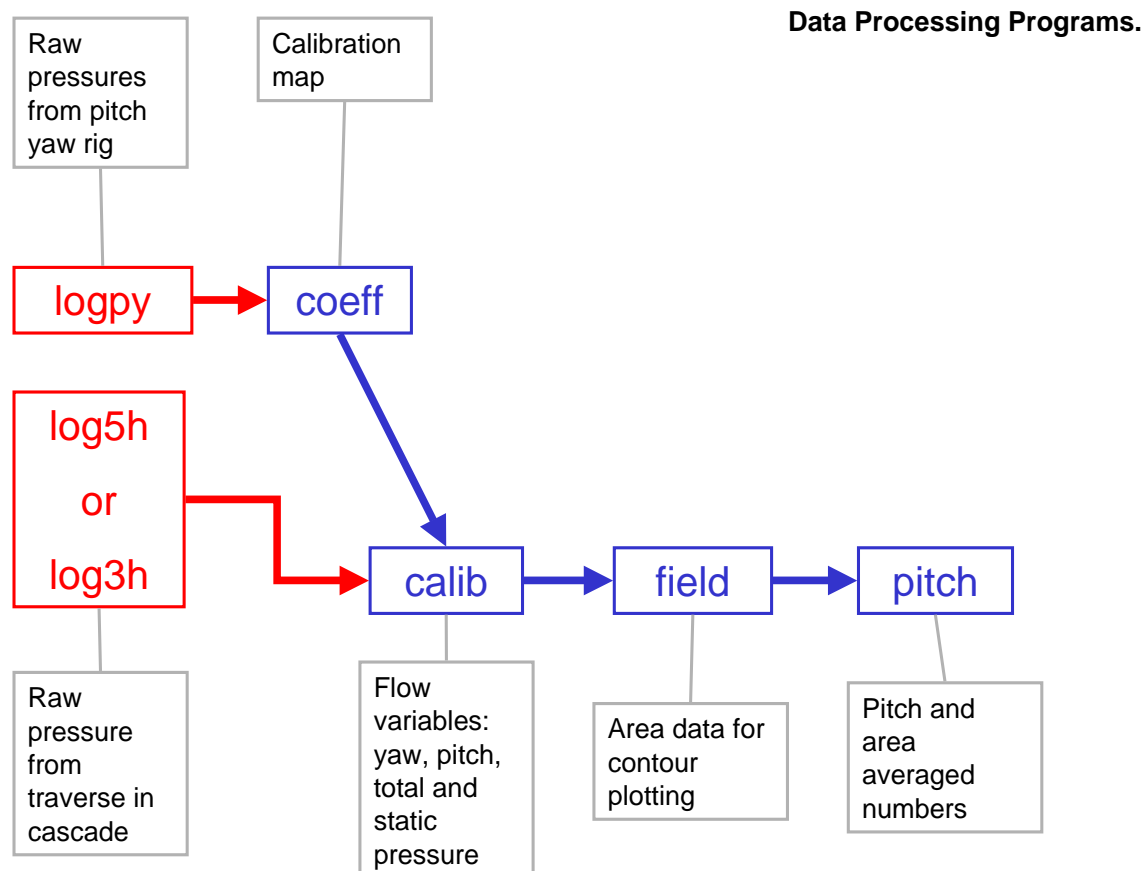


Figure C.1: Data Processing Programs written by the author.

	P0 trv87	P0 trv70	P0 trv91
Loss Coeff:	0.1351	0.1325	0.1379
Inlet b/l Loss:-	-0.0151	-0.0151	-0.0151
Net Total Loss Coeff:	0.1503	0.1476	0.1531
Midpsan Loss:	0.0782	0.0767	0.0790
Net Secondary Loss:	0.0721	0.0710	0.0740
% of planar value	100.0	100.0	100.0
	P1 trv88	P1 trv69	P1 trv90
Loss Coeff:	0.1169	0.1186	0.1198
Inlet b/l Loss:-	-0.0151	-0.0151	-0.0151
Net Total Loss Coeff:	0.1320	0.1338	0.1349
Midpsan Loss:	0.0778	0.0781	0.0787
Net Secondary Loss:	0.0542	0.0557	0.0562
% of planar value	75.2	78.5	76.0
	P2 trv86	P2 trv72	P2 trv92
Loss Coeff:	0.1163	0.1109	0.1139
Inlet b/l Loss:-	-0.0151	-0.0151	-0.0151
Net Total Loss Coeff:	0.1315	0.1260	0.1291
Midpsan Loss:	0.0786	0.0765	0.0764
Net Secondary Loss:	0.0529	0.0495	0.0527
% of planar value	73.4	69.8	71.1

Table C.4: Area Averaged Loss Results at Slot 10.

Appendix D

Estimating the effects of Profiled Endwalls on Stage Efficiency

Chapter 7 of Cohen et al. (1996) shows the isentropic efficiency of a stage can be related to the loss coefficients. In this appendix a different notation for α and β is used than that found in the rest of the thesis. Elsewhere α and β refer to yaw and pitch angle in the cascade, in this chapter they are used to refer to absolute and relative yaw angles respectively.

This performance estimate is based on two dimensional cascade flow theory, the numbering and the two angles used in the equation are shown in Figure D.1.

$$\eta = \left(1 + \frac{1}{2} \frac{V_x}{U} \left[\frac{Y_R \sec^2 \beta_3 (T_3/T_2) Y_N \sec^2 \alpha_2}{\tan \beta_3 + \tan \alpha_2 - (U/V_x)} \right] \right)^{-1} \quad (\text{D.0.1})$$

Y_R and Y_N are the rotor and nozzle loss coefficients based on *exit* dynamic head. U is the blade speed and V_x is axial velocity. α_2 is the nozzle exit angle relative to the nozzle. β_3 is the rotor exit angle relative to the nozzle. T_3 and T_2 are the static temperatures at stations 2 and 3 respectively.

The derivation may be found in Chapter 7, pages 279-280 of Cohen et al. (1996). Loss coefficients have to be related to the exit dynamic head to be used with the method, an exit dynamic head of 764 Pa is assumed in order to do this.

Values are obtained for equation D.0.1 as follows:-

- A blade speed of 340 m/s is assumed
- A flow coefficient (ϕ) of 0.39 is taken from Harvey et al. (2002). This gives V_X
- The temperature drop coefficient $\psi = \frac{2\Delta H}{U^2}$ of 3.08 is taken from Harvey et al. (2002). This gives the stage temperature drop.
- A turbine entry temperature of 1800 K is assumed.
- Y_N and Y_R are taken to be the same and are taken to be equal to the loss coefficients based on exit dynamic head taken from cascade tests. These are for the 128% c_{ax} case and NOT for the mixed out loss case.
- A 50% (Λ) reaction design is assumed.

	P0	P1	P2	P3
$V_x / [\text{m/s}]$	133	133	133	133
$U / [\text{m/s}]$	340	340	340	340
$Y_N / [1]$	0.04429	0.04027	0.0372	0.04905
$Y_R / [1]$	0.04429	0.04027	0.0372	0.04905
$\beta_3 / [^\circ]$	73	73	73	73
$\alpha_2 / [^\circ]$	73	73	73	73
$T_3 / [\text{K}]$	1555.6	1555.6	1555.6	1555.6
$T_2 / [\text{K}]$	1710.6	1710.6	1710.6	1710.6
$\eta / [\%]$	89.34	90.21	90.89	88.32
change / [%]	-	0.87	1.55	-1.01

Table D.1: Calculation of efficiency estimate.

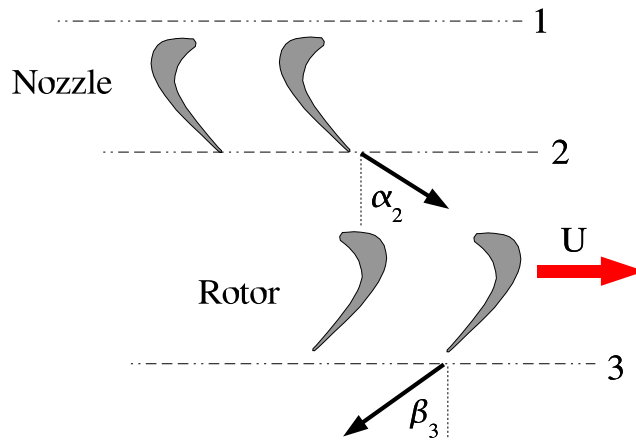


Figure D.1: Labelling for Simple Efficiency Estimate

- β_3 is obtained from $\tan \beta_3 = \frac{1/2\psi - 2\Lambda}{2\phi}$
- β_2 is obtained from $\tan \beta_2 = \frac{1/2\psi + 2\Lambda}{2\phi}$
- α_2 is obtained from $\tan \alpha_2 = \tan \beta_2 + \frac{1}{\phi}$
- Static temperatures are related to stagnation values by using $T_0 = T + \frac{V^2}{2C_p}$
- η is calculated from equation D.0.1

Table D.1 shows the values arrived at from the above calculation.

Appendix E

Photographs of Pressure Probes.

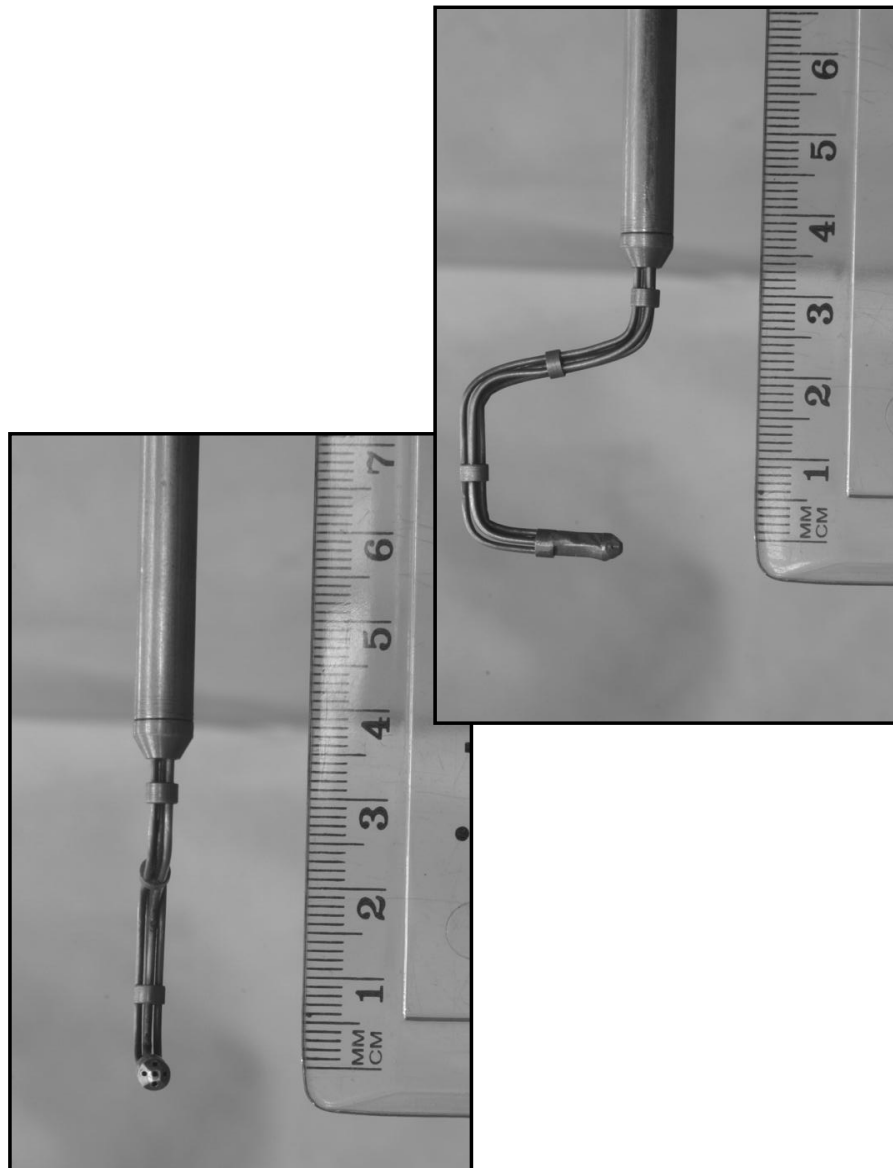


Figure E.1: Photograph of probe 5HB.

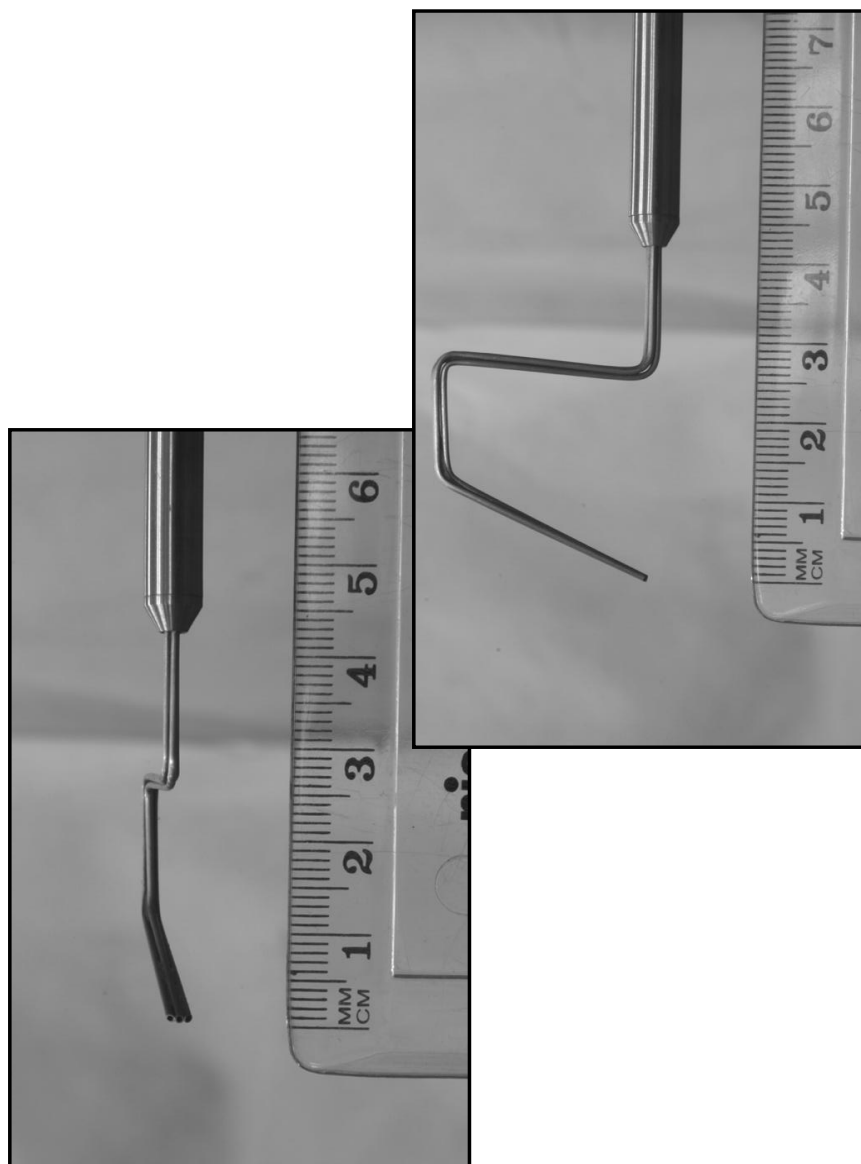


Figure E.2: Photograph of probe 3HE.